The fundamentals of crust generation: major tonalite intrusions associated with an oceanic plateau, Aruba, Dutch Caribbean

by

Rosalind Vanessa White M.A. (Cantab.)

A thesis submitted for the degree of
Doctor of Philosophy
at the University of Leicester

Department of Geology
University of Leicester
March 1999

UMI Number: U117714

All rights reserved

INFORMATION TO ALL USERS
The quality of this reproduction is dependent upon the quality of the copy submitted.

In the unlikely event that the author did not send a complete manuscript
and there are missing pages, these will be noted. Also, if material had to be removed,
a note will indicate the deletion.

UMI U117714
Published by ProQuest LLC 2013. Copyright in the Dissertation held by the Author.
Microform Edition © ProQuest LLC.
All rights reserved. This work is protected against
unauthorized copying under Title 17, United States Code.

ProQuest LLC
789 East Eisenhower Parkway
P.O. Box 1346
Ann Arbor, MI 48106-1346

This thesis is dedicated to my parents:
Alan and Glenys

Abstract

The fundamentals of crust generation: major tonalite intrusions associated with an oceanic plateau, Aruba, Dutch Caribbean

Rosalind V. White

The origin of the continents is of fundamental importance to Earth Scientists. There have been recent suggestions that crustal growth is linked to mantle plume activity, and this study focuses on a Cretaceous Caribbean example of juvenile additions to the continental crust. The basaltic-tonalitic rock association studied is reminiscent of greenstone belts, which are believed to represent some of the earliest continental crust.

The basaltic Aruba Lava Formation is part of the Cretaceous (predominantly 91 - 88 Ma) Caribbean oceanic plateau, which moved into the Caribbean region from the Pacific. The thick succession of submarine-to-emergent volcanic and sedimentary rocks on Aruba implies an intra-oceanic origin, and new petrographic, geochemical and isotopic data are all consistent with derivation of the Aruba Lava Formation from a mantle plume.

Intrusion of a predominantly tonalitic batholith (dated as 85 - 82 Ma) occurred concurrently with deformation of the Aruba Lava Formation. The batholith is interpreted as having formed in response to the earliest stages of subduction beneath the plateau. This occurred subsequent to a subduction polarity reversal caused by the reluctance of the Caribbean oceanic plateau to be subducted. Subduction-derived mafic magmas, originating from the remnant mantle plume source region, were added to the plateau crust, where they triggered intracrustal partial melting and tonalite generation.

This work demonstrates that rapid crustal growth can occur via accretion of oceanic plateaux: this mechanism does not require the presence of pre-existing crust, and may be analogous to the mechanism that generated the earliest continental nuclei. Addition of subduction-derived melts to the accreted material "ripens" the embryonic continent; this can happen within a few million years after the initial accretion event. Mantle plumes play an important part in transfer of mass and thermal energy from the mantle to the crust, and in reorganising tectonic plates. This allows reprocessing, remelting, and ripening of mantle-derived basalts to generate continental crust.

"I didn't get hold of the wrong end of the stick:
I got hold of the right end of a different stick...."

Ian Rushforth

Acknowledgements

Firstly, I would like to thank Mum, Dad, Fiona and the rest of my family for their love and support throughout my time at Leicester. Mum and Dad deserve particular thanks for taking me on childhood holidays to rocky places, and instilling in me an interest in the natural world, without which I would not have undertaken this Ph.D. Fiona and Calum merit a special mention for sending me a well-timed Victoria Wine gift voucher (Cheers!), and I am indebted to Grandma and Grandad for buying me a colour printer for Christmas. I think I've just about worn it in now...

My acknowledgements go to John Tarney for devising this project, which I have thoroughly enjoyed tackling; and to John, Andy Saunders and Andrew Kerr for their enthusiasm and admirable supervising skills. Fieldwork was made so much more fun by having the company of Sam Barr, Fred Custance and Pamela Kempton – I think they enjoyed it too. Funding for the project was provided by the Natural Environment Research Council, and I would also like to express my gratitude to the Government of Aruba for subsidising the fieldwork, and to the Harkness Scholarship fund (Cambridge) for providing the money for me to travel and present this work at conferences.

Big thanks go to Vivi Ruiz, Dirk Beets, Gerard Klaver, Bertil van Os, Jorica Baars, Leon Pors, Kally de Meyer and Armando Curet, (my colleagues in Holland and the Dutch Antilles), for their logistical and laboratory support and friendly encouragement. I would particularly like to thank Vivi for her hospitality on Aruba, and Jorica and Bertil (and his family) for putting me up when I was in Haarlem doing lab work.

I'd also like to thank those who have taught me various laboratory techniques: particularly Pamela Kempton at NIGL. The Ar-Ar dating was carried out under the instruction of Malcolm Pringle at SURRC. Thanks also to the analytical services staff at Leicester: Tim Brewer, Rob Wilson, Nick Marsh, Rob and Dougi for keeping me chirpy whilst doing all the XRF preparation, Emma Mansley and Kevin Sharkey for helping prepare the samples for ICP-MS, and Colin and Lin. Paul Denton and Dave York also deserve a mention for their friendship, and lunches in the park/pear drops, respectively. Thanks also to Norry and Dickson for their discussions on geochemical and tectonic matters relating to this project.

I will be eternally grateful for the friendship and excellent companionship of so many people at Leicester. A special mention should go to those who have put up with living with me: in particular, Tiffany, Mike and Loz (house) and Loz and Craig (office). I've actually quite enjoyed these last few days of writing up, and have been in the good company of Tiff (apple pie provider), Kate (choc-chip cookie donor) and Graeme (jammy doughnut man). Never again will the members of FRUStRATE (Fiendishly Riting Up Students Require Alcohol To Excel) have such a good excuse for this kind of indulgence. Although I'm sure we'll think of one...

Other people at Leicester who I would like to thank for their amity and company include Ph.D. students past and present, and academic staff: Lindsey, Sarah G., Duncan, Marion, Vassilis, Gawen, Trevor, Alan, Robin, Sam, Rich, Kim, Tanya, big Matt, Jane, Steve T., Pat, Karine, Neil, Hannah, Craig II and anyone else I might have forgotten. I'd also like to thank those who encouraged me to do things other than geology, for example, vegetable gardening and going to concerts (John Hudson); horn playing and subsequent drinking (Roger and Jo, Julian, etc.); swimming (Sam, Gawen, Kate), tennis (Trevor) and going to hilly places (lots of people). Thanks also to those who have provided entertainment and encouragement via e-mail: Emma Harrison, Helen Clark, Paul Matthews and Martin Goldberg, to name but a few.

Finally, I'd like to express my thanks to those who have provided me with tender loving care over the past few years: Fred and Andy.

Contents

Chapter 1

Origins of the continental crust: a history of controversy

1.1 Introduction 1.1
1.1.1 Characteristics of the continental crust and lithosphere 1.1
1.1.2 Early theories for the origins of the continents 1.2
1.1.3 Obstacles to crustal growth research 1.3

1.2 Models for crustal growth: volume additions 1.4
1.2.1 Oceanic plateau accretion 1.5
1.2.2 The andesite model: arc accretion 1.5
1.2.3 Continental arc magmatism 1.6
1.2.4 Continental flood basalts 1.6
1.2.5 Subduction-accretion terranes 1.6

1.3 Creation of the continental crust's geochemical signature 1.7
1.3.1 Tonalite-trondhjemite-granodiorite suites 1.9
1.3.2 Subduction zone magmatism 1.10
1.3.3 Small volume basaltic melt fractions 1.10

1.4 The age of the continental crust 1.10
1.4.1 Methodology used to determine crustal growth ages 1.11
1.4.2 Summary of growth models 1.13
1.4.3 Has a consensus been reached? 1.15

1.5 The earliest continents: Archaean crustal rocks 1.16
1.5.1 Lithological characteristics 1.17
1.5.2 Structure 1.18
1.5.3 Origins 1.18

1.6 Broad objectives of this study 1.19
1.6.1 Methodology 1.19

Chapter 2

Oceanic plateaux and their role in the tectonic and magmatic evolution of the Caribbean region

2.1 Introduction 2.1

2.2 Oceanic Plateaux 2.1
2.2.1 Fate of oceanic plateaux 2.3

2.3 The Caribbean-Colombian Cretaceous Igneous Province 2.4

2.3.1 Structure of the Caribbean oceanic plateau 2.4
2.3.2 Composition of the Caribbean oceanic plateau 2.5
2.3.3 Rates of volcanism and potential origin of the Caribbean oceanic plateau 2.6
2.3.4 Arc magmatism associated with the Caribbean oceanic plateau 2.6

2.4 Tectonic reconstructions of the Caribbean region 2.7

2.5 The South Caribbean plate boundary zone 2.10
2.5.1 The Aruba-La Blanquilla chain 2.11

2.6 Summary 2.12

Chapter 3

The Field Geology of Aruba

3.1 Introduction 3.1
3.1.1 Previous work on the geology of Aruba 3.2
3.1.2 Why Aruba? 3.2
3.1.3 Fieldwork logistics and aims 3.3
3.1.4 Sampling strategy 3.4

3.2 The Aruba Lava Formation 3.4
3.2.1 Lithologies of the Aruba Lava Formation 3.4
3.2.1.1 Basalts 3.4
3.2.1.2 Dolerites 3.5
3.2.1.3 Volcaniclastic material 3.5
3.2.2 Stratigraphy of the Aruba Lava Formation and its significance 3.7
3.2.3 Age of the Aruba Lava Formation 3.8
3.2.4 Metamorphism and Deformation of the Aruba Lava Formation 3.9
3.2.4.1 Amphibolites: purely contact metamorphism? 3.9
3.2.4.2 Deformation of the Aruba Lava Formation 3.10

3.3 The Aruba batholith 3.12
3.3.1 Lithological descriptions 3.12
3.3.1.1 Tonalite 3.12
3.3.1.2 Diorite 3.13
3.3.1.3 Hooibergite 3.13
3.3.1.4 Gabbro 3.14
3.3.1.5 Porphyritic rocks 3.14
3.3.1.6 Leucocratic material 3.15
3.3.1.7 Late mafic dykes 3.15
3.3.2 Relationships between members of the batholith 3.15
3.3.3 Origin of the hooibergites - case study of contradictory relationships. 3.17
3.3.4 Simplified intrusion sequence for the batholith 3.20

3.4 Relationships between the Aruba Lava Formation and the batholith 3.21

3.5 Summary 3.22

Chapter 4

Geochronology of Aruban rocks

4.1 Introduction 4.1

4.2 Previous work dating Aruban rocks 4.1

4.2.1 The Aruba Lava Formation 4.1

4.2.2 The Aruba batholith 4.2

4.2.3 Dating uplift and erosion: fission track studies 4.2

4.2.4 Regional constraints 4.3

4.3 An ^{40}Ar-^{39}Ar study of Aruban rocks 4.3

4.3.2 Interpretation of ^{40}Ar-^{39}Ar data 4.4

4.3.3 ^{40}Ar-^{39}Ar results for the Aruba Lava Formation 4.6

4.4 Conclusions 4.9

Chapter 5

Petrography and Mineral Chemistry of the Aruba Lava Formation

5.1 Introduction 5.1

5.2 Basalts and dolerites 5.2

5.2.1 Petrography 5.2

5.2.1.1 Petrography of the basalts 5.2

5.2.1.2 Petrography of the dolerites 5.3

5.2.2 Mineral chemistry of plagioclase 5.3

5.2.3 Mineral chemistry of clinopyroxene 5.4

5.2.4 Mineral chemistry of opaque phases 5.7

5.2.5 Mineralogy of secondary phases 5.7

5.3 Volcaniclastic rocks 5.7

5.3.1 Petrography of the basaltic conglomerate 5.7

5.3.2 Petrography of the fine-grained volcaniclastic rocks 5.8

5.3.3 Petrography of the ignimbrite 5.9

5.3.4 Petrography of the accretionary lapilli tuff 5.10

5.4 Deformed and metamorphosed members of the Aruba Lava Formation 5.10

5.4.1 Petrography and mineral chemistry of the amphibolites 5.10

5.4.1.1 Hornblende-plagioclase geothermometry 5.11

5.4.2 Petrography of deformed chlorite-schists 5.13

5.5 Summary 5.13

Chapter 6

Petrogenesis of the Aruba Lava Formation

6.1 Introduction 6.1

6.2 Alteration and metamorphism of the Aruba Lava Formation 6.2

6.2.1 Major element mobility - previous studies 6.3

6.2.2 Trace element mobility - previous studies 6.4

6.2.3 Element mobility in the Aruba Lava Formation 6.5
6.2.3.1 Element mobility in basalts and dolerites 6.5
6.2.3.2 Element mobility in amphibolites 6.6
6.2.3.3 Element mobility in deformed chlorite schists 6.9
6.2.3.4. Element mobility in volcaniclastic rocks 6.10

6.3 Classification of the Aruba Lava Formation rocks 6.11

6.4 Determining the composition of the most primitive magma 6.12
6.4.1 Characteristics of a primary magma 6.12
6.4.2 Identification of cumulus olivine in altered rocks 6.13
6.4.3 Identification of cumulus phases in dolerites 6.16
6.4.4 The most primitive liquids 6.17
6.4.5 Comparison of the most primitive basalt with Curaçao and Ontong Java basalts 6.19

6.5 Fractional crystallisation 6.19
6.5.1 Is the variability caused by fractional crystallisation alone? 6.22
6.5.2 Comparison of fractionation trends for Aruba, Curaçao and Ontong Java 6.25
6.5.3 Are Curaçao-type magmas parental to the Aruba Lava Formation? 6.25

6.6 Constraints on the mantle source of the Aruba Lava Formation 6.26
6.6.1 Isotopic composition of the mantle source 6.26
6.6.2 Trace element composition of the mantle source 6.30

6.7 Melting processes 6.33

6.8 Conclusions 6.37

Chapter 7

Petrography and Mineral Chemistry of the Aruba Batholith

7.1 Introduction 7.1

7.2 Petrography and mineral chemistry discussed by lithology 7.1
7.2.1 Hooibergites 7.2
7.2.2 The layered gabbro series 7.3
7.2.2.1 Plagioclase-rich gabbroic rocks 7.4
7.2.2.2 Olivine- and pyroxene-rich gabbroic rocks 7.4
7.2.3 Gabbros 7.5
7.2.4 Diorites 7.6
7.2.5 Tonalites 7.8
7.2.6 Leucotonalites 7.9
7.2.7 Granites 7.9
7.2.8 Leucocratic veins 7.9
7.2.9 Porphyritic rocks 7.9

7.3 Alteration of the batholith rocks: summary 7.11

7.4 Synthesis 7.11
7.4.1 Crystallisation sequence for the batholith 7.11
7.4.2 Minor elements in pyroxenes: pressure/temperature constraints? 7.12
7.4.3 Pressure/temperature constraints from amphiboles 7.14
7.4.4 Significance of zoning of plagioclase 7.16

7.5 Summary 7.18

Chapter 8

Geochemistry of the Aruba Batholith

8.1 Introduction 8.1
8.1.1 Chemical and mineralogical criteria used for lithological classification 8.1
8.1.2 Broad geochemical characteristics of the suite 8.2

8.2 Presentation of geochemical data for the batholith 8.3
8.2.1 Major and minor element data 8.3
8.2.2 Trace element data 8.4
8.2.3 Isotope data 8.8
8.2.4 Uncertainty in batholith geochemical analyses: sampling and alteration 8.10

8.3 Mineralogical controls on whole-rock compositions 8.12
8.3.1 The cumulate problem 8.13
8.3.2 Comparison of whole-rock compositions with phase compositions 8.14
8.3.3 Verification of cumulate characteristics using whole rock data 8.15
8.3.4 Implications of cumulates for the evolution of the batholith 8.19

8.4 Dykes cross-cutting the batholith 8.19

8.5 Summary 8.21

Chapter 9

Petrogenesis of the Aruba batholith and implications for the generation of continental crust

9.1 Crustal growth via plateau accretion 9.1
9.1.1 Summary of key constraints from earlier chapters 9.2

9.2 Overview of model for silicic magmas associated with oceanic plateaux 9.3

9.3 Isotopic constraints on the generation of the Aruba batholith suite 9.4
9.3.1 Sr and Nd isotope constraints 9.4
9.3.2 Pb isotope constraints 9.4
9.3.2.1 Characteristics and composition of the unradiogenic-Pb endmember 9.4
9.3.2.2 Incorporation of the unradiogenic-Pb endmember into the batholith magmas 9.8

9.4 Generation of the gabbros of the batholith 9.11
9.4.1 The most primitive liquid of the batholith 9.11
9.4.2 Subduction zone origin for the batholith gabbros? 9.13
9.4.3 Mantle plume origin for the batholith gabbros? 9.16
9.4.4 Generation of the gabbros: summary 9.17

9.5 Generation of the tonalites of the batholith 9.18
9.5.1 Fractionation from the gabbros 9.18
9.5.2 Direct melts of a metasomatised mantle wedge 9.19
9.5.3 Melting of metabasalt 9.19
9.5.3.1 Melting of metabasaltic streaks in a heterogeneous mantle plume 9.21
9.5.3.2 Melting of the downgoing slab in a subduction zone 9.24
9.5.3.3 Melting of metabasalt of the plateau 9.25

9.6 Clues from the diorites: a combination of processes? 9.29

9.7 Sweaty basalts and hot flushes 9.32

9.7.1 Generation of the most silicic material in the batholith 9.34

9.8 Detailed model for silicic magmatism associated with oceanic plateaux 9.35

9.8.1 Key constraints on the model 9.35

9.8.2 Description of the model, and its relation to Caribbean tectonics 9.36

9.8.3 Implications for Caribbean tectonics and magmatism 9.39

9.8.3.1 Reversal in subduction polarity 9.39

9.8.3.2 The Caribbean 76 Ma thermal event 9.41

9.9 Implications for crustal growth models 9.42

9.10 Scope for further research 9.43

Appendix A

Sample information

A.1 Location Map (in pocket inside back cover) A.1

A.2 Sample location and lithological information A.1

A.3 Information sources by sample A.10

Appendix B

^{40}Ar-^{39}Ar geochronology

B.1 Principles of the ^{40}Ar-^{39}Ar method of dating B.1

B.2 Limitations of the ^{40}Ar-^{39}Ar method and sources of error B.6

B.3 Sample preparation techniques B.8

B.4 Analytical techniques B.10

Appendix C

XRF analyses

C.1 Selection of samples for analysis C.1

C.2 Sample preparation C.1

C.3 XRF machine conditions C.2

C.4 Results of XRF analyses C.2

Appendix D

Rare Earth Element Analyses

D.1 Introduction D.1

D.2 Inductively Coupled Plasma Mass Spectrometry (ICP-MS) analyses D.1

D.2.1 Sample selection and preparation D.1

D.2.2 ICP-MS analysis D.2

D.2.3 ICP-MS results D.3

D.3 Inductively Coupled Plasma Optical Emissions Spectrometry (ICP-OES) analyses D.3

D.3.1 Sample selection and preparation D.3

D.3.2 ICP-OES analysis D.4

D.3.2 ICP-OES results D.5

D.4 Instrumental Neutron Activation analyses (INAA) D.5

D.4.1 Sample preparation D.5

D.4.2 Detection, counting and processing D.5

D.4.3 Results D.6

Appendix E

Data Quality for XRF and REE Analyses

E.1 XRF E.1

E.1.1 Major elements E.1

E.1.2 Trace elements E.1

E.2 REE analyses E.14

E.2.1 Comparison with international reference materials E.14

E.2.2 Comparison between different analytical methods for REE determination E.14

E.2.3 The Eu correction E.15

Appendix F

Radiogenic isotope analyses

F.1 Sample selection and preparation F.1

F.1.1 Weighing and spiking of samples F.1

F.1.2 Digestion and conversion to bromides F.2

F.2 Ion exchange chromatography column chemistry F.3

F.2.1 Pb separation F.3

F.2.2 U separation F.4

F.2.3 Separation of Sr and REEs from the bulk solution F.4

F.2.4 Separation of Sm and Nd from the REE fraction F.5

F.3 Measurement of isotope ratios F.5

F.3.1 Loading F.5

F.3.2 Analysis F.5

F.3.3 Blanks and reference materials F.5

F.4 Age correction F.6

Appendix G

Electron microprobe analyses

G.1 Analytical techniques _____ **G.1**

G.2 Results _____ **G.1**

Appendix H

Presentation and Publication of this study

H.1 Publications _____ **H.1**

H.2 Oral and poster presentations _____ **H.1**

References

References _____ **R.1**

Addenda

Sample location map belonging to Appendix A.1 _____ **pocket inside back cover**

Reprint of White *et al.* (1999) _____ **pocket inside back cover**

List of figures

Note that (for example) Page 2.4a follows Page 2.4.

		Page
Fig. 1.1	Methods by which volume is added to the continental crust: oceanic plateau accretion, island arc accretion, continental flood basalt magmatism, continental arc magmatism and subduction-accretion.	1.4
Fig. 1.2	Models for tonalite-trondhjemite-granodiorite genesis; a) slab melting; b) melting of mafic underplated material in a continental arc; and c) melting of metasomatised mantle.	1.9
Fig. 1.3	Estimates of the rate of growth of the continental crust by various authors (updated from Reymer and Schubert (1984) and Windley (1995) and references therein).	1.11
Fig. 1.4	Stratigraphic age versus crustal residence age for sedimentary rocks (after Miller *et al.*, 1986).	1.13
Fig. 1.5	The main categories of crustal growth models (discussed in text); 1) increasing growth rate; 2) progressive growth (a - approximately linear; b - episodic); 3) rapid early growth; and 4) no growth.	1.14
Fig. 1.6	World map showing distribution of Archaean cratons that contain greenstone belts (adapted from de Wit and Ashwal, 1997).	1.17
Fig. 2.1	Modern day distribution of oceanic and continental large igneous provinces, after Saunders *et al.* (1992).	2.2
Fig. 2.2	Neotectonic map of the Caribbean region (after Mann *et al.*, 1990) showing the location of Aruba with respect to other exposed fragments of the Caribbean-Colombian Cretaceous Igneous Province.	2.4a
Fig. 2.3	Reconstructions of the tectonics of the Caribbean area, compiled from Pindell and Barrett (1990); Kerr *et al.* (in press).	2.8a
Fig. 2.4	Map of the South Caribbean Plate Boundary Zone (adapted from Avé Lallement, 1997; Silver *et al.*, 1975; Maresch, 1974).	2.10a
Fig. 3.1	Simplified geological map of Aruba, after Beets *et al.*, 1996.	3.1a
Fig. 3.2	Localities mentioned in the text of Chapter 3, in order of appearance.	3.1a
Fig. 3.3	(Photo): General view of Aruba, taken from the hills of the Aruba Lava Formation, looking towards the outcrop area of the batholith. The cone-shaped hills are mafic parts of the batholith. The largest of these, in the distance, is the Hooiberg[2].	3.4a
Fig. 3.4	(Photo): View shows a range of rock types within the batholith. Mafic rocks tend to form hills.	3.4a
Fig. 3.5	(Photo):"Corestones" of tonalite derived from the underlying bedrock by spheroidal weathering.	3.4a
Fig. 3.6	(Photo): General view of the Aruba Lava Formation showing the abundant surface debris.	3.4a
Fig. 3.7	(Photo): Pillow basalts within the Aruba Lava Formation.	3.4a
Fig. 3.8	(Photo): Fine sand- to silt-grade volcaniclastic sediment in the Aruba Lava Formation shows ripple cross-bedding.	3.4a

Fig. 3.9	(Photo): Convolute bedding (by hammer head) in a volcaniclastic sandstone of the Aruba Lava Formation.	3.6a
Fig. 3.10	(Photo): Graded bed in volcaniclastic sandstone of the Aruba Lava Formation.	3.6a
Fig. 3.11	(Photo): Tuff consisting of accretionary lapilli in the Aruba Lava Formation. The lapilli have been deformed (flattened and elongated) since their deposition.	3.6a
Fig. 3.12	(Photo): Coarse volcaniclastic rock with eutaxitic texture.	3.6a
Fig. 3.13	(Photo): Breccio-conglomerate in the Aruba Lava Formation. Clasts consist almost entirely of basalt and dolerite.	3.6a
Fig. 3.14	(Photo): Fine scale graded beds interbedded within the basaltic conglomerate.	3.6a
Fig. 3.15	(Photo): Amphibolite showing signs of partial anatexis: the white areas are silicic segregations and the very dark regions are interpreted as amphibole-rich residues.	3.10a
Fig. 3.16	(Photo): Shear bands in an amphibolite facies member of the Aruba Lava Formation suggest top-to-the-north displacement.	3.10a
Fig. 3.17	(Photo): A xenolith of foliated amphibolite in a trondhjemitic melt.	3.10a
Fig. 3.18	(Photo): Bedding-cleavage relationships in the Aruba Lava Formation: cleavage is sub-vertical.	3.10a
Fig. 3.19	Stereographic analysis of structural data (bedding and cleavage) from volcaniclastic rocks of the Aruba Lava Formation.	3.11a
Fig. 3.20	(Photo): Tonalite boudins within a shear zone of the Aruba Lava Formation.	3.10a
Fig. 3.21	(Photo): Chevron folds in a shear zone of the Aruba Lava Formation. These fold the earlier shear cleavage.	3.10a
Fig. 3.22	(Photo): Six phases of intrusion within a small outcrop of the batholith.	3.13a
Fig. 3.23	(Photo): The texture of a typical tonalite.	3.13a
Fig. 3.24	(Photo): Magmatic layering, defined by bands of different mineralogical composition, in a hooibergite.	3.13a
Fig. 3.25	(Photo): Cuspate contacts between three sub-lithologies of hooibergite. These suggest that different magmas co-existed in a liquid state.	3.13a
Fig. 3.26	(Photo): Magmatic layering in a gabbro-norite is displaced by syn-magmatic faults.	3.13a
Fig. 3.27	(Photo): A thin mafic dyke cross-cuts the batholith.	3.13a
Fig. 3.28	(Photo): Cross-cutting relationships within the batholith are frequently well-exposed.	3.16a
Fig. 3.29	(Photo): Veins of silicic material cut diorite and a tonalite vein.	3.16a
Fig. 3.30	(Photo): Mafic dykes are younger than the silicic veins.	3.16a
Fig. 3.31	(Photo): Lack of chilled margin between an enclave-bearing and an enclave-free tonalite.	3.16a
Fig. 3.32	(Photo): Tonalite-hosted inclusions of a variety of compositions. Most are elongated and deformed.	3.16a
Fig. 3.33	(Photo): Tonalite containing inclusions of microdiorite, porphyry and meladiorite.	3.16a
Fig. 3.34	(Photo): Highly flattened and aligned inclusions.	3.17a
Fig. 3.35	(Photo): Porphyritic inclusion showing clear evidence of duc(k)tile deformation; dioritic inclusions are angular.	3.17a
Fig. 3.36	(Photo): Gabbro xenoliths within tonalite tend to be angular.	3.17a
Fig. 3.37	(Photo): Jigsaw breccia consisting of diorite "clasts" separated by tonalitic veins.	3.17a
Fig. 3.38	(Photo): Tonalitic dyke cuts hooibergite at Warawara[8].	3.17a
Fig. 3.39	(Photo): Inclusions of tonalite in hooibergite, also at Warawara[8]. The age relationship shown here is contradictory to that of Fig. 3.38.	3.17a
Fig. 3.40	(Photo): Contact between tonalite and hooibergite at Canashito[9]. A finger of tonalite intrudes the hooibergite on the right-hand side; the hill is cut by a fault in the centre.	3.19a
Fig. 3.41	(Photo): Magmatic breccia where acidic veins cut hooibergite.	3.19a

Fig. 3.42 (Photo): Acidic veins have partially assimilated hooibergite. Note the reaction rim between the hooibergite xenoliths and the acidic melt. 3.19a
Fig. 3.43 (Photo): Acidic melt has almost completely disaggregated this hooibergite. Here, no reaction rims are present. 3.19a
Fig. 3.44 (Photo): Brittle acidic veins cut a layered hooibergite. A dark reaction rim is present. 3.19a
Fig. 3.45 (Photo): Contact between tonalite and a dolerite of the Aruba Lava Formation. No chilling is apparent. 3.19a

Fig. 4.1 Age spectra, K/Ca plots and isochron correlation diagrams for members of the Aruba Lava Formation: amphibolite, dolerite and basalts. 4.7a
Fig. 4.2 Age spectra, K/Ca plots and isochron correlation diagrams for tonalites and diorites from the Aruba batholith. 4.8a
Fig. 4.3 Age spectra, K/Ca plots and isochron correlation diagrams for a mela-diorite and a late mafic dykes from the Aruba batholith. 4.8b

Fig. 5.1 (Photomicrograph): Basalt sample in a representative state of preservation for the Aruba Lava Formation. (ARU94-29) 5.2a
Fig. 5.2 (Photomicrograph): One of the freshest basalt samples. The original equigranular texture is well-preserved. (ARU96-31). 5.2a
Fig. 5.3 (Photomicrograph): An amphibolite collected from the ALF adjacent to the contact with the batholith. (ARU97-8) 5.2a
Fig. 5.4 (Photomicrograph): Dolerite with a subophitic texture. (ARU94-22) 5.2a
Fig. 5.5 (Photomicrograph): Dolerite with a more equigranular texture than that shown in Fig. 5.4. (ARU96-38). 5.2a
Fig. 5.6 An-Ab-Or plot showing compositions of plagioclase from the Aruba Lava Formation. 5.4
Fig. 5.7 Pyroxene analyses from the Aruba Lava Formation: using the classification of Morimoto *et al.* (1988), all analysed pyroxenes are Mg-rich augites. 5.5
Fig. 5.8 Al and Ti (molecular proportions, calculated to 6 oxygen atoms per formula unit) values for pyroxenes from the Aruba Lava Formation. 5.6
Fig. 5.9 (Photomicrograph): Basaltic conglomerate. (ARU97-138) 5.8a
Fig. 5.10 (Photomicrograph): The matrix of a basaltic conglomerate consists of smaller basaltic clasts, individual crystal fragments (mainly plagioclase) and brown cryptocrystalline material. (ARU97-139) 5.8a
Fig. 5.11 (Photomicrograph): Fine-grained volcaniclastic rock, with a small basaltic clast and fragments of plagioclase, clinopyroxene and quartz. (ARU96-76) 5.8a
Fig. 5.12 (Photomicrograph): Volcaniclastic rock composed of cryptocrystalline (once glassy?) clasts of basaltic material. (ARU94-24) 5.8a
Fig. 5.13 (Photomicrographs): a: Syn-sedimentary fault in a reworked volcaniclastic rock. The bedding is defined by different proportions of clasts to matrix and the clast size;
b: Magnified view of a coarse-grained, plagioclase-rich bed in the same thin section to demonstrate that the clasts are predominantly plagioclase feldspar. (ARU96-77) 5.8a
Fig. 5.14 (Photomicrograph): Pyroclastic rock with eutaxitic texture. The magnified mineral is clinopyroxene. It is not known whether this is an equilibrium phase in a now-silicified rock, or a xenocryst in a silicic magma. (ARU96-13) 5.10a
Fig. 5.15 (Photomicrograph): Accretionary lapilli tuff: the lapilli have been deformed and are now oval shaped in cross-section. (ARU97-69) 5.10a
Fig. 5.16 (Photomicrograph): Typical amphibolite, consisting of green amphibole and plagioclase, with some quartz and clinopyroxene. (ARU97-40) 5.10a

Fig. 5.17 (Photomicrograph): Amphibolite with a different bulk composition from that shown in Fig. 5.16, dominated by colourless (rather than green) amphibole. (ARU96-142) 5.10a
Fig. 5.18 (Photomicrograph): This amphibolite shows segregation into mafic (amphibole-dominated) and felsic (plagioclase and quartz-dominated) layers. This is interpreted as the onset of melting (see text). (ARU97-147) 5.10a
Fig. 5.19 Estimates of hornblende-plagioclase equilibration temperatures, using the method of Blundy and Holland (1990). 5.12
Fig. 5.20 (Photomicrograph): Deformed chlorite schist, demonstrating that an original cleavage (probably formed by shearing: see quartz pods) has been crenulated by a second deformation event. (ARU96-88) 5.10a

Fig. 6.1 Plots of major elements vs. Zr, to assess major element mobility in various lithologies of the Aruba Lava Formation. 6.5a
Fig. 6.2 Plots of HFSE and selected REE vs. Zr, to assess trace element mobility in various lithologies of the Aruba Lava Formation. 6.5b
Fig. 6.3 Plots of LIL, Th and U vs. Zr, to assess mobility in various lithologies of the Aruba Lava Formation. 6.6a
Fig. 6.4 Plots of transition metal elements and Ga vs. Zr, to assess their mobility in various lithologies of the Aruba Lava Formation. 6.6b
Fig. 6.5 a: Classification of the Aruba Lava Formation rocks on a total alkalis vs. silica diagram (Le Maitre *et al.*, 1989). 6.11a
b: The K_2O vs. silica diagram further subdivides the sub-alkalic rock series.
c: The diagram of alkali index vs. alumina further confirms the tholeiitic affinites of the less-altered basalts and dolerites.
Fig. 6.6 Diopside-hypersthene-olivine-nepheline-quartz diagram showing CIPW normative data for the Aruba Lava Formation. 6.11b
Fig. 6.7 a: Plot of Ni vs. MgO showing olivine addition vectors to initial magmas of varying MgO contents (shown for "Scenario 2" - see text and Fig. 6.7b). Also shown for comparison are lines showing liquid evolution during olivine fractionation. 6.14a
b: Plot of Ni vs. MgO showing the three scenarios used in modelling Ni addition via olivine accumulation.
Fig. 6.8 a: MgO vs. Zr plot showing vector due to olivine addition; MgO content may also be enhanced by growth of chlorite during alteration/metamorphism. 6.15a
b: Ni vs. Zr plot showing vector due to olivine addition.
c: Cr vs. Zr plot showing vector due to accumulation of a Cr-bearing phase (probably Cr-spinel) concomitant with olivine addition.
Fig. 6.9 a-d: Liquid lines of descent calculated by TRACE3 (Nielsen, 1988) for the primitive end members (compositions reported in Table 6.2) of the Aruba Lava Formation, the Curaçao Lava Formation and the Ontong Java Plateau, compared with data from samples of the Aruba Lava Formation. 6.24a
e-h: as above. 6.24b
i-l: as above. 6.24c
Fig. 6.10 Initial $^{87}Sr/^{86}Sr$ vs. ε_{Nd} (all corrected to time of emplacement: 88 Ma for Aruba Lava Formation), comparing the Aruba Lava Formation rocks with a range of data from the Caribbean region and Pacific plateaux (Fig. 6.10a) and data from the Caribbean region only (for clarity) in 6.10b. 6.28a
Fig. 6.11 Lead isotope data for the Aruba Lava Formation, compared with data from a wide range of Caribbean mafic rocks and Pacific plateaux. 6.29a
Fig. 6.12 Multi-element diagram, normalised to bulk silicate earth (McDonough and Sun, 1995), showing basalts and dolerites of the Aruba Lava Formation. 6.31a

Fig. 6.13 Compositional range of Aruba Lava Formation rocks in terms of La/Sm vs. Zr/Nb compared with the Ontong Java Plateau and Curaçao. 6.31a
Fig. 6.14 Nb/Y vs. Zr/Y for the Aruba Lava Formation, compared with other Pacific plateau and Caribbean basalts, after Fitton *et al.*, 1997. 6.31b
Fig. 6.15 Bulk silicate earth-normalised (McDonough and Sun, 1995) Th/Nd and Nd/Yb for samples from the Aruba Lava Formation, the Ontong Java Plateau and Curaçao. 6.31b
Fig. 6.16 Multi-element diagrams for the Aruba Lava Formation, normalised to bulk silicate earth (McDonough and Sun, 1995). 6.33a
Fig. 6.17 Rare earth element plots for the Aruba Lava Formation, normalised to C1 chondrite (McDonough and Sun, 1995). Fields for Curaçao lavas (Kerr *et al.*, 1996b) and the Ontong Java Plateau (Babbs, 1997) are included for comparison. 6.33b
Fig. 6.18 Bulk silicate earth-normalised (McDonough and Sun, 1995) La/Sm and Sm/Yb for samples from the Aruba Lava Formation, the Ontong Java Plateau and Curaçao. 6.33c
Fig. 6.19 a: Average $Na_{8.0}$ vs. average $Fe_{8.0}$ for the Aruba Lava Formation basalts and dolerites, compared with data from a worldwide compilation by Klein and Langmuir (1987) and average values for the Ontong Java Plateau (OJP) by Mahoney *et al.* (1993) and Babbs (1997). 6.34a
b: Average CaO/Al_2O_3 vs. average $Fe_{8.0}$ for the Aruba Lava Formation basalts and dolerites, showing data from oceanic plateaux and MORB for comparison.

Fig. 7.1 Pyroxene analyses from the Aruba batholith, classified according to Morimoto *et al.* (1988). 7.1a
Fig. 7.2 Classification of amphiboles (Leake *et al.*, 1997). The majority of amphiboles analysed for the whole lithological range are magnesiohornblende. 7.1a
Fig. 7.3 An-Ab-Or plot showing compositions of feldspar analyses from various lithologies of the batholith. 7.1b
Fig. 7.4 Plagioclase compositions displayed in terms of An mol. percent. Each row of symbols represents a single rock. 7.1b
Fig. 7.5 Analyses of opaque minerals: most of the analyses are almost pure magnetite, although some show solid solution towards ulvöspinel. 7.1c
Fig. 7.6 Olivine compositions from two rocks that both belong to the ol/cpx-rich gabbro group. 7.1c
Fig. 7.7 Biotite compositions from diorites and tonalites show a restricted range. 7.1c
Fig. 7.8 (Photomicrograph): Typical hooibergite, showing the large equant magnesio-hornblendes, and small diopside crystals poikilitically enclosed by plagioclase. (ARU96-57) 7.2a
Fig. 7.9 (Photomicrograph): Hooibergite that is extremely rich in diopside, which locally makes up 100% of the rock volume. (ARU97-133) 7.2a
Fig. 7.10 (Photomicrograph): The large magnesiohornblende crystals in this hooibergite contain numerous diopside inclusions, which are smaller and more irregularly shaped than those included by plagioclase (andesine to oligoclase). (ARU97-164) 7.2a
Fig. 7.11 (Photomicrograph): Region of a hooibergite sample that has small euhedral hornblendes enclosed by plagioclase (cloudy white in top half) and quartz (clear white in bottom half). (ARU94-4b) 7.2a
Fig. 7.12 (Photomicrograph): Plagioclase-rich hooibergite where the plagioclase crystals show remarkable heterogeneity, with irregularly-shaped cores (An_{89} to An_{87}) mantled by more sodic rims (An_{53} to An_{33}). (ARU97-75) 7.2a
Fig. 7.13 (Photomicrograph): Large corroded(?) hornblende crystal from an acidic vein cutting the hooibergite. This hornblende contains clinopyroxene inclusions, so is unlikely to have nucleated and grown within the silicic magma. (ARU97-134) 7.2a

Fig. 7.14 (Photomicrograph): Bytownite-rich gabbro from the layered series. Clinopyroxene (diopside to augite) is the other major phase present. (ARU97-173) 7.4a
Fig. 7.15 (Photomicrograph): Hornblende oikocryst enclosing plagioclase, clinopyroxene and opaque chadacrysts. (ARU97-174) 7.4a
Fig. 7.16 (Photomicrograph): Vermicular intergrowth of an opaque mineral and orthopyroxene, probably arising from replacement of olivine. (ARU97-173) 7.4a
Fig. 7.17 (Photomicrograph): Vermicular intergrowth of an opaque mineral and orthopyroxene, which appears to have nucleated on the opaque mineral crystal, and grown outwards into the olivine crystal. (ARU97-111) 7.4a
Fig. 7.18 (Photomicrograph): Enstatite oikocryst enclosing chadacrysts of olivine (Fo_{79} to Fo_{75}), plagioclase (bytownite), augite and magnetite/ilmenite. (ARU97-111) 7.4a
Fig. 7.19 (Photomicrograph): Bytownite oikocryst enclosing chadacrysts of olivine ($Fo_{\sim 76}$) and augite. (ARU96-154) 7.4a
Fig. 7.20 (Photomicrograph): Typical gabbro from the layered series. a: plane polarised light; b: crossed polars. (ARU97-172) 7.7a
Fig. 7.21 (Photomicrograph): A diorite having textural similarities with the hooibergites, in particular, the large equant euhedral magnesiohornblende crystals, which may contain clinopyroxene inclusions. (ARU97-163) 7.7a
Fig. 7.22 (Photomicrograph): Diorite that is texturally similar to the tonalites. Magnesiohornblende crystals are smaller and more elongate than those in the hooibergites, but still euhedral. (ARU97-161) 7.7a
Fig. 7.23 (Photomicrograph): Porphyritic microdiorite from an enclave within the tonalite. The large hornblende crystals may be twinned. (ARU97-74) 7.7a
Fig. 7.24 (Photomicrograph): Microdiorite (from enclave within tonalite) containing biotite oikocrysts surrounding plagioclase chadacrysts. (ARU97-54a) 7.7a
Fig. 7.25 (Photomicrograph): Representative tonalite from the batholith. (ARU96-59) 7.9a
Fig. 7.26 (Photomicrograph): Part of a large plagioclase crystal (the whole crystal is approximately 7 mm in length) from a tonalite, showing intricate zoning (An_{58} to An_{31}). (ARU97-78) 7.9a
Fig. 7.27 (Photomicrograph): A complexly zoned plagioclase from a tonalite. This crystal has been partially resorbed during its growth. (ARU94-18) 7.9a
Fig. 7.28 (Photomicrograph): A representative leucotonalite, with a granular texture. (ARU94-15) 7.9a
Fig. 7.29 (Photomicrograph): Aplite, consisting of quartz, plagioclase and potassium feldspar. The granophyric intergrowth at the bottom right has quartz blebs in potassium feldspar. (ARU96-41) 7.9a
Fig. 7.30 (Photomicrograph): This aplite has a radial granophyric growth of quartz and plagioclase. (ARU97-51) 7.9a
Fig. 7.31 (Photomicrograph): a: Porphyritic andesite from dyke, containing twinned clinopyroxene and plagioclase phenocrysts set in a groundmass of the same minerals. b: The same rock, at higher magnification. (ARU96-8) 7.10a
Fig. 7.32 (Photomicrograph): Plagioclase-hornblende porphyry of dacitic composition, representative of the majority of porphyritic rocks within the batholith. The plagioclase phenocrysts are complexly zoned, similar to those found in the tonalite (Figs. 7.26 and 7.27) and the hornblendes are euhedral. (ARU97-178) 7.10a
Fig. 7.33 (Photomicrograph): Complex plagioclase glomerocryst within a plagioclase-hornblende porphyry of andesitic composition. Each plagioclase crystal forming the glomerocryst shows evidence of resorption at some point in its history. (BK77-043) 7.10a

Fig. 7.34 (Photomicrograph): Altered porphyritic rock of dacitic composition, with large anhedral quartz, euhedral partly-sericitised plagioclase and very altered amphibole (bright colours). (ARU94-27) 7.10a
Fig. 7.35 (Photomicrograph): Magnified view of plagioclase phenocryst from a porphyritic enclave in tonalite. (ARU97-6) 7.10a
Fig. 7.36 Synthesis of the order of crystallisation in various lithologies of the batholith. 7.11a
Fig. 7.37 Ti-Al compositions in clinopyroxenes of the batholith, calculated to 6 oxygen atoms. 7.13a
Fig. 7.38 Equilibration temperatures calculated by the hbl-plag computer program of Blundy and Holland (1990). 7.13a
Fig. 7.39 Zoning profile across the plagioclase crystal pictured in Fig. 7.26. 7.17

Fig. 8.1 Plot showing normative data for all samples from the Aruba batholith having more than 10% normative quartz after Barker (1979). 8.2a
Fig. 8.2 QAP plot (after Streckeisen, 1976) showing normative data for all samples from the Aruba batholith. 8.2a
Fig. 8.3 Total alkali vs. silica plot for the batholith reveals its subalkaline character. 8.3a
Fig. 8.4 The K_2O vs. SiO_2 diagram further divides the subalkaline rock series. 8.3a
Fig. 8.5 Diagram of alkali index vs. alumina suggests that the mafic rocks of the batholith have tholeiitic affinities. 8.3a
Fig. 8.6 AFM plot for the rocks of the batholith. 8.3b
Fig. 8.7 According to a plot of $Fe_2O_{3(t)}$/MgO and the dividing line of Miyashiro (1974), the rocks of the batholith are calc-alkaline. 8.3b
Fig. 8.8 K-Ca-Na plot for the Aruba batholith (after Defant and Drummond, 1993) showing that samples of the Aruba batholith trend into the trondhjemite-tonalite-dacite (TTD) field rather than following a typical calc-alkaline trend. 8.3b
Fig. 8.9 a-e: Plots of major elements vs. SiO_2 and MgO for the batholith. 8.4a
f-j: as above. 8.4b
Fig. 8.10 a-h: Plots of trace elements vs. SiO_2 for the batholith. 8.5a
i-p: as above. 8.5b
Fig. 8.11 Multi-element plots for selected samples from the Aruba batholith. 8.6a
Fig. 8.12 Comparison of trace element data for the batholith, with abundances normalised to bulk silicate earth (McDonough and Sun, 1995). 8.6b
Fig. 8.13 Chondrite-normalised REE plots for selected samples from the Aruba batholith. 8.7a
Fig. 8.14 a: Measured Sr and Nd isotope ratios for the Aruba batholith compared to data age-corrected to 85Ma. 8.8a
b: Age-corrected (85 Ma) Sr isotope ratios and $\varepsilon_{Nd\ (t=85\ Ma)}$ for the batholith, compared with equivalent data for the Aruba Lava Formation (t=88Ma).
Fig. 8.15 a: Measured $^{207}Pb/^{204}Pb$ vs. $^{206}Pb/^{204}Pb$ for the Aruba batholith compared to data age-corrected to 85 Ma. The age-corrected (88 Ma) field of the ALF samples is included for comparison. 8.8a
b: Measured $^{208}Pb/^{204}Pb$ vs. $^{206}Pb/^{204}Pb$ for the Aruba batholith compared to data age-corrected to 85 Ma. The age-corrected (88 Ma) field of the ALF samples is included for comparison.
Fig. 8.16 Plots of loss on ignition vs. SiO_2 and MgO for rocks of the batholith. 8.12a
Fig. 8.17 a: Ba vs. K_2O demonstrates that there is a consistent relationship between these elements for most lithologies of the batholith. 8.12a
b: Rb vs. K_2O is similar.
Fig. 8.18 Sr vs. Al_2O_3 for rocks of the batholith. 8.12a

Fig. 8.19	Plots of major elements vs. SiO_2 for the batholith compared with electron microprobe analyses.	8.16a
Fig. 8.20	Plots of major elements vs. CaO for the batholith compared with electron microprobe analyses.	8.16b
Fig. 8.21	Results of modelling hooibergite REE abundances via crystal accumulation.	8.18a
Fig. 8.22	a: Trace element plot for the late mafic dykes. b: REE plot for the late mafic dykes.	8.21
Fig. 9.1	Initial ε_{Nd} and $^{87}Sr/^{86}Sr$ for the batholith compared with the Aruba Lava Formation and other suites from the Caribbean/Pacific region. The samples from the batholith plot within a restricted field that overlaps with the compositions of the ALF basalts and dolerites.	9.4a
Fig. 9.2	Pb isotope data for the batholith, age corrected to 85 Ma compared with fields for the Aruba Lava Formation (this study: age corrected to 88 Ma) and other suites from the Caribbean and Pacific regions.	9.4a
Fig. 9.3	Plot of Sr isotopes vs. $^{206}Pb/^{204}Pb$, showing results of calculations for admixtures of various sources (in the mantle, prior to melting).	9.5a
Fig. 9.4	Plots to demonstrate the compositional characteristics of the unradiogenic-Pb end-member. There is a correlation between La/Nb and $^{206}Pb/^{204}Pb$, suggesting that the unradiogenic-Pb endmember is characterised by high La/Nb.	9.5a
Fig. 9.5	Possible locations for the involvement of a sedimentary unradiogenic-Pb endmember in the petrogenesis of the batholith, notably the more mafic rocks.	9.9
Fig. 9.6	Multi-element plot showing range of compositions of the non-layered gabbros from the batholith, i.e., those that are more likely to represent liquid compositions.	9.15a
Fig. 9.7	Nb/Y vs. Zr/Y plot for samples from the Aruba batholith, after Fitton *et al.*, 1997.	9.15a
Fig. 9.8	Results of calculations designed to show whether the trace element abundances in the gabbros can be explained via mixing of a tonalitic melt and an Aruba Lava Formation-type mafic melt.	9.16a
Fig. 9.9	a: Chondrite-normalised (McDonough and Sun, 1995) REE plots for the Aruba tonalites and a 17% modal batch melt of ALF. b: Results of REE modelling: Ce/Yb represents the steepness of the pattern (due to residual garnet); Gd/Yb represents the curvature (due to residual amph/cpx). c: Trace element plot, normalised to bulk silicate earth (McDonough and Sun, 1995), for the Aruba tonalites, the same model melt as Fig. 9a, and model melt (arbitrarily) corrected for major phases and fluids.	9.20a
Fig. 9.10	Possible tectonic and thermal regimes where melting of meta-basalt could occur.	9.23a
Fig. 9.11	Sr/Y vs. Y diagram for the Aruba batholith (after Defant and Drummond, 1993).	9.23a
Fig. 9.12	La/Nb vs. $^{206}Pb/^{204}Pb$ plot, showing mixing lines between Aruba Lava Formation (ALF) basalt, partial melt of ALF basalt and hypothesised gabbro endmembers with a subduction zone signature (high La/Nb, low $^{206}Pb/^{204}Pb$).	9.31a
Fig. 9.13	Trace element and REE data for the most leucocratic members of the batholith.	9.31a
Fig. 9.14	a-c: Model for tectonic evolution of the Caribbean region in relation to the petrogenesis of the Aruba batholith. d-f: the same, continued.	9.37a 9.37b
Fig. 9.15	Possible mechanism for rapid subduction polarity reversal.	9.40a

List of tables

Table		Page
1.1	Estimates of composition of the upper, middle lower and bulk continental crust.	1.8
4.1	Summary of reliability criteria for ^{40}Ar-^{39}Ar data, discussed in text.	4.6
4.2	Summary of $^{40}Ar/^{39}Ar$ incremental heating experiments of leached whole rocks and hornblende separates from the Aruba Lava Formation.	4.6
4.3	Summary of $^{40}Ar/^{39}Ar$ incremental heating experiments of biotite and hornblende separates from the Aruba batholith and a cross-cutting dyke.	4.8
6.1	Results of olivine accumulation modelling for the Aruba Lava Formation (see also Figs. 6.7a and 6.7b).	6.14
6.2	Comparison of estimated parental liquid compositions for Aruba, Curaçao and the Ontong Java Plateau.	6.18
6.3	Range of age-corrected (t = 88 Ma) isotope ratios for all five analysed basalts and dolerites from the Aruba Lava Formation.	6.28
8.1	Chemical characteristics of late mafic dykes.	8.20
9.1	Comparison of Aruba tonalite with adakites (Drummond and Defant, 1990).	9.25

Chapter 1

Origins of the continental crust: a history of controversy

1.1 Introduction

This study is concerned primarily with the processes that can generate silicic material in an environment dominated by extrusive mafic igneous rocks, and the implications of these processes for the generation of continental crust throughout Earth history. The island of Aruba, located in the southern Caribbean region, is used as a case study of a relatively modern environment where mafic and silicic rocks are intimately associated with one another, both in space and time. The mafic rocks are thought to be part of the plume-related Cretaceous Caribbean oceanic plateau sequence, and the silicic rocks are predominantly tonalitic in composition: similar to the average composition of the upper continental crust.

This chapter aims to place the present study into context by outlining current thinking on the origin and growth of the continental crust, in order to give the reader a broader scale appreciation of the applications of this research. Additionally, the main features of Archaean greenstone belts will be described, in order to allow comparison with Aruba. Some of the oldest preserved continental rocks occur in greenstone belts, and comparison with Aruba is of particular interest because greenstone belts have a similar association of mafic and silicic rock types to Aruba; moreover, the lithologies occur in a comparable age sequence.

1.1.1 Characteristics of the continental crust and lithosphere

The continental crust covers approximately 40% of the Earth's surface and represents less than 0.5% of the total mass of the Earth, but is disproportionately important because it preserves information about the majority of Earth history. The oldest preserved remnants of continental crust on the Earth's surface include the tonalitic Amîtsoq gneisses in western Greenland (dated as 3822 Ma by ion microprobe methods: Kinny, 1986) and the Acasta gneisses in the western Slave Province, Canada (up to 4031 Ma: Bowring and Williams, 1999), although older $^{207}Pb/^{206}Pb$ ages (up to 4270 Ma) have been obtained from zircons occurring as detrital particles within ~3500 Ma metasedimentary rocks in western Australia (Maas *et al.*, 1992). This implies that the very earliest continental crust to form on the Earth

was subsequently destroyed either by erosion, and/or recycling into the mantle. The mean age of the continents, determined from neodymium model ages of many modern and ancient clastic sediment samples (Miller *et al.*, 1986), has been estimated as 2.0 ± 0.2 Ga.

Continental crust is on average 35 km thick, but varies from 7 km in tectonically thinned regions (Horsefield *et al.*, 1994) to ~70 km in orogenic belts (e.g., Tibet; Zhao *et al.*, 1991). The lithosphere which includes this crust is normally about 100 km thick, but can be significantly thicker beneath Archaean crust: up to 250 km as attested to by fast seismic velocities beneath Archaean cratons (Polet and Anderson, 1995) and presence of lithosphere-derived diamonds (created at depths of more than ~150 km) in kimberlites (Mitchell, 1986).

The continental crust is enriched in incompatible trace elements with respect to the Earth's mantle, which shows a crudely complementary depletion. Trace element modelling shows that *if* the continental crust were generated by a single melting event of the mantle, a melt fraction of the order 1% would be required to explain the observed trace element enrichment (O'Nions and McKenzie, 1988). Although this scenario is clearly simplistic, it illustrates the necessity for either small degree melts, or repeated melting episodes, to concentrate the trace elements into the crust to such an extent. The bulk composition of the *upper* continental crust is approximately granodioritic (66% SiO_2; Taylor and McLennan, 1985), although it is generally accepted that the composition of the entire continental crust is somewhat more mafic than this (57.3% SiO_2; Taylor and McLennan, 1985), firstly because seismic velocities tend to increase with depth, indicating a progressively more mafic composition with increasing depth (Christensen and Mooney, 1995), and secondly because many lower crustal xenoliths recovered from volcanic rocks are of metabasic composition (Rudnick and Taylor, 1987).

1.1.2 Early theories for the origins of the continents

The origin and evolution of the continental areas, on which human life evolved, has been a topic of considerable debate since the inception of geological science. During the late 18th Century, the opposing schools of thought were the Neptunists, who believed that granites (*sensu lato*) were precipitated from a universal ocean and formed the foundation for sedimentary rocks, and the Plutonists, who considered granites to be formed by the consolidation of molten matter. The Plutonists, and their main protagonist, James Hutton, eventually triumphed in this altercation, but the granite controversy continued nevertheless. Hutton maintained that granites were igneous in origin, but Lyell noted that many were closely

associated with metamorphic rocks, and the concept of granitization was proposed. By the 1940s, the deliberations had swung in favour of an igneous origin - granites were extreme differentiates of basaltic magmas. As tends to occur in scientific debate, it was assumed that there was only one "correct" answer; however, a solution to the "granite problem" was proposed by Read (1948): there are "granites and granites". It is now accepted that granitic rocks fall into several categories, and research continues to this day into how they became separated from the Earth's mantle to form the continental crust.

1.1.3 Obstacles to crustal growth research

One of the principal difficulties in determining the origin of granitic rocks and the continental crust is that the principles of uniformitarianism cannot necessarily be applied. The Earth has changed over geological time, particularly in terms of its heat production and dissipation. This may have led to different types of rock suites dominating different periods of Earth history; for example, greenstone belts (discussed in Section 1.5) and komatiites are important in the Archaean, but have become comparatively rarer since. Additionally, because granitic (crustal) rocks solidify beneath the Earth's surface, all our observations must come from exhumed crustal rocks. Interpretations of these observations are rarely straightforward, because many parts of the continental crust have suffered long histories of deformation and metamorphism. Meanwhile, large volumes of the present-day lower crust remain essentially inaccessible (apart from seismic and xenolith studies).

Another problem is that significant volumes of the crust may have been destroyed. There is no record of any crust before 4270 Ma (i.e., there are no reported radiometric dates or Nd model ages of either whole-rocks or single mineral grains before this time), but that does not necessarily mean that no crust existed: one possibility is that the Earth's primordial crust was destroyed by meteorite bombardment (McLennan and Taylor, 1982). The destruction of continental crust also occurs at the present day, with recycling of eroded material into the mantle at subduction zones, and it is likely that this process has been operative to some extent throughout Earth history. Indeed, constraining the volumes of continental material returning to the mantle has become a key point for discussion (e.g., Reymer and Schubert, 1984; Veizer and Jansen, 1985).

The complexity of the topic of the origin and growth of the continents has resulted in several emphases: exploring when the crust was generated; investigating the processes which add volume to the crust; and scrutinising its growth in terms of addition of chemical elements.

These approaches need to be recombined before the origin of the continental crust will be fully understood.

1.2 Models for crustal growth: volume additions

Several models have been proposed for the processes which increase the volume of the continental crust (Fig. 1.1): oceanic plateau accretion (Abbot and Mooney, 1995), island arc accretion (Taylor, 1967; 1977), continental arc magmatism (Tarney *et al.*, 1976), continental plume magmatism (White *et al.*, 1987), and subduction-accretion (Barr *et al.*, 1999). The latter three models require the pre-existence of earlier continents, and cannot represent mechanisms for the earliest growth of the continents. The first two models do not require pre-existing continents, but have one problematic feature in common: the material that they add to the crust does not seem to match the overall composition of the continents. The present study attempts to solve this apparent paradox by concentrating more on the processes which add the required chemical elements to the continental crust. This is discussed further in Section 1.3. An interesting feature of some of the models for addition of mass to the continents (discussed below) is that they inherently imply some sort of episodicity in crustal growth, whether that be episodicity in periods of accretion or periods of plume magmatism. Additionally, some are candidates for primary crustal growth, in that they do not require pre-existing continent, and so are essential for the formation of the very earliest continental crust.

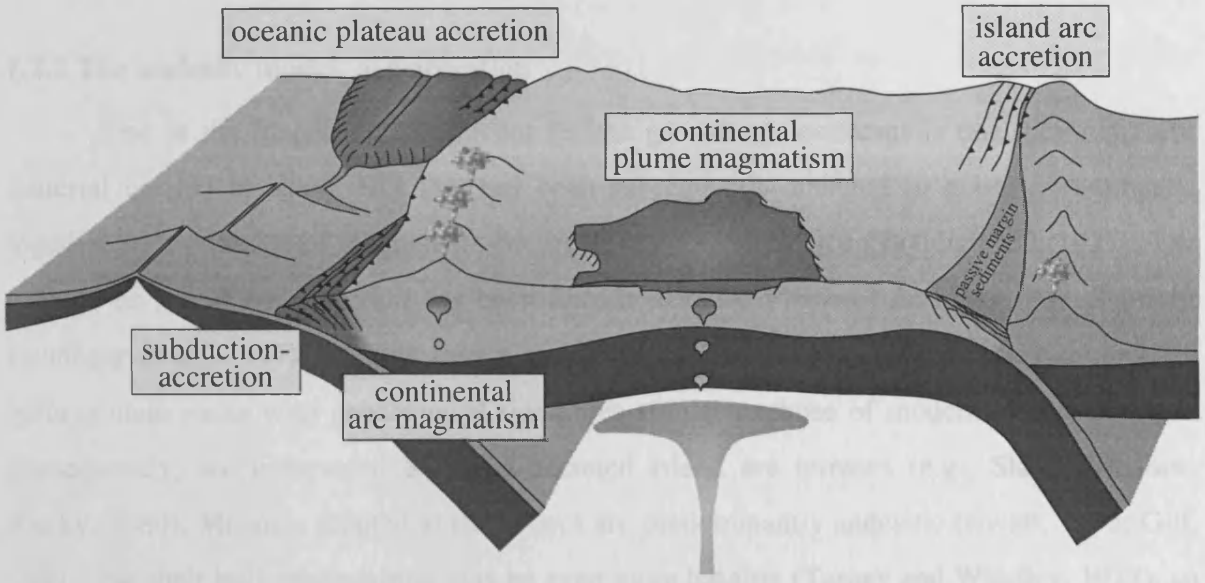

Figure 1.1: Methods by which volume is added to the continental crust: oceanic plateau accretion, island arc accretion, continental flood basalt magmatism, continental arc magmatism and subduction-accretion.

1.2.1 Oceanic plateau accretion

Oceanic plateaux represent vast outpourings of basaltic magma, thought to be linked to the presence of anomalously hot mantle plumes (Campbell and Griffiths, 1990). (The general features of oceanic plateaux, in particular the Caribbean-Colombian Cretaceous Oceanic Plateau will be discussed further in Chapter 2.) Several authors have proposed that the growth of the continental crust may be connected to the presence of these oceanic plateaux (e.g., Stein and Hofmann, 1994; Abbot and Mooney, 1995; Stein and Goldstein, 1996), although the nature of this link is not well-constrained and many questions remain unanswered. One interesting feature of oceanic plateaux is that the periods of their formation may be episodic, related to major mantle overturn events, and it has been suggested that this may be a cause of the episodicity (see Section 1.4) in growth of the continents (Stein and Hofmann, 1994). Plateaux are potentially extremely important in adding mass to the continents because they are thick, possibly still hot, and consequently more buoyant than normal oceanic crust. Because of this, they may be inclined to resist subduction (Cloos, 1993), becoming accreted to, or obducted onto the edges of continents (as well as being accreted to island arcs: Petterson *et al.*, 1999). Their large volume (Schubert and Sandwell, 1989) means that plateau accretion may be able to explain periods of rapid continental growth better than the volcanic arc accretion model (see below); however there is a problem regarding the bulk composition of the accreted material not matching that of the bulk continental crust, and some subsequent ripening is required (White *et al.*, 1999).

1.2.2 The andesite model: arc accretion

One of the longest-standing ideas for the growth of continents is that they represent material created at island arcs that has been subsequently accreted to existing continents, together with products of magmatism occurring at continental arcs (Taylor, 1967; 1977). The process of island arc accretion has been documented for Phanerozoic rocks (e.g., Taiwan; Lundberg *et al.*, 1997) and may have also been operative in the Archaean: some greenstone belts contain rocks with geochemical signatures similar to those of modern island arcs, and consequently, are interpreted as being accreted island arc terranes (e.g., Slave Province; Kusky, 1989). Magmas erupted at island arcs are predominantly andesitic (Ewart, 1976; Gill, 1981), but their bulk composition may be even more basaltic (Tarney and Windley, 1977), so if accreted arc material is the precursor to a tract of continental crust, some secondary process is required to modify its composition, making it richer in incompatible elements and silica.

Additionally, there have been suggestions (Reymer and Schubert, 1986) that an unrealistic number of accreting island arcs would be required to account for the rapid growth rates of some crustal segments. This implies that arc accretion cannot be the only process that contributes to crustal growth.

1.2.3 Continental arc magmatism

Present day addition of volume to the continents occurs predominantly at continental active margins (e.g., the Andes: Tarney *et al.*, 1976). This model differs from the two described above in that material of the correct composition (i.e., granodioritic to tonalitic) is added to the continental crust: magmas erupted at (and intruded into) continental arcs tend to be more silicic than those at island arcs. It should be cautioned, however, that the silicic magmas which approach the Earth's surface may be matched by voluminous mafic rocks (and cumulates) at depth. This model requires pre-existing crust, and cannot be responsible for the earliest growth of the continents; additionally, the rates of continental arc magmatism at the present day are insufficient to account for the periods of rapid continental growth proposed throughout Earth history.

1.2.4 Continental flood basalts

Growth of the continental crust can arise directly from a plume ascending beneath continental lithosphere, particularly if accompanied by rifting and concomitant decompression melting (e.g., White *et al.*, 1987). However, unlike accreted oceanic plateaux, it is difficult to find a mechanism whereby this new basaltic crust can be ripened into something more silicic: this is because continental flood basalts are located within tectonic plates, far from areas of potential tectonism and magmatism, i.e., plate boundaries.

1.2.5 Subduction-accretion terranes

In addition to volcanic arcs and oceanic plateaux being accreted to pre-existing continents, large sedimentary accretionary complexes can form at sites of subduction. These are dominated by sedimentary rocks derived from adjacent continental regions, but may also include sediments of an oceanic affinity as well as slivers of oceanic crust and associated seamounts. Considerable areas of continental crust can grow in this way, and are stabilised by transfer of accretionary material from the footwall of the system into the hanging-wall (Barr *et al.*, 1999).

1.3 Creation of the continental crust's geochemical signature

The chemical composition of the continental crust is difficult to constrain accurately because of the difficulties in sampling such a large heterogeneous volume in a truly representative fashion. Constraints on the lithological composition of the entire continental crust are provided by seismic velocity structure data (Christensen and Mooney, 1995), but most of the other methods which give more detailed information about crustal composition are somewhat restricted to the upper continental crust. One notable exception is the study of lower crustal xenoliths (e.g., Rudnick and Taylor, 1987), which are predominantly metabasic in composition; these data corroborate the evidence from seismic studies and some exposed lower crustal sections (e.g., the Ivrea Zone: Fountain and Salisbury, 1981) that show that the lower crust contains substantial amounts of mafic rocks. In contrast, sampling of rocks exhumed from various depths in Precambrian shields (Shaw *et al.*, 1986) suggests that the upper crust is dominated by rocks of granodioritic and tonalitic compositions, which matches conclusions from studies of terrigenous shales (e.g., Taylor and McLennan, 1985).

Table 1.1 shows various estimates of the composition of the continental crust. In summary, the upper continental crust is granodioritic or tonalitic in composition; the lower crust is significantly more mafic. In terms of trace elements, the continents are very enriched in the incompatible elements, particularly Rb, Ba, Th, U and K, and form a crudely complementary reservoir to the depleted mantle (i.e., the source of mid-ocean-ridge basalts (MORB)) and other mantle components, e.g., the ocean island basalt source. Some elements, such as Ta, Nb, P and Ti are less enriched in the continental crust than would be expected from their distribution coefficients in normal pyrolite mantle. It is these characteristics which are discussed below, with an emphasis on the processes that can produce the observed concentrations of elements.

It is generally accepted that a silicic continental crust cannot be simply extracted from the mantle in a single melting event for two reasons: firstly, a melt fraction of only 1-2% would be required to explain the trace element enrichments (O'Nions, 1992), and a viscous silicic melt of this degree would not be able to separate from the mantle on geologically reasonable timescales (McKenzie, 1989); secondly, generation of such a silicic magma directly from a melting of a mantle peridotite is not consistent with experimental phase equilibria (O'Hara, 1968). This implies that processes of secondary modification must occur in order to convert the predominantly basaltic additions from the mantle into something richer in silica and incompatible trace elements, i.e., upper continental crust. Condie (1997)

speculates that the Earth may be unique in providing an environment in which this reprocessing can occur: Earth's stable hydrosphere facilitates hydration of basaltic rocks, making them more prone to episodes of remelting, and plate tectonics (or a primitive equivalent) provides the driving force for transporting rocks towards potential melting regions.

	Upper			Middle		Lower			Bulk			
Source	Condie 1993	Shaw 1967	T & M 1985	R & F 1995	W & T 1981	R & F 1995	W & T 1981	T & M 1985	Condie 1997	Taylor 1977	W & T 1984	T & M 1985
SiO_2	66.3	64.9	66.0	60.6	68.1	52.3	63.0	54.4	59.7	58.0	64.8	57.3
TiO_2	0.70	0.52	0.50	0.80	0.35	0.54	0.55	1.00	0.68	0.80	0.51	0.90
Al_2O_3	14.9	14.6	15.2	15.5	16.3	16.6	16.1	16.1	15.7	18.0	16.1	15.9
$FeO_{(t)}$	4.7	4.0	4.5	6.4	3.3	8.4	5.5	10.6	6.5	7.5	4.8	9.1
MgO	2.5	2.2	2.2	3.4	1.4	7.1	3.5	6.3	4.3	3.5	2.7	5.3
MnO	0.07	0.07	0.08	0.10	-	0.10	-	-	0.09	0.14	-	0.18
CaO	3.6	4.1	4.2	5.1	3.3	9.4	5.8	8.5	6.0	7.5	4.6	7.4
Na_2O	3.4	3.5	3.9	3.2	5.0	2.6	4.5	2.8	3.1	3.5	4.4	3.1
K_2O	2.9	3.1	3.4	2.0	2.2	0.6	1.0	0.3	1.8	1.5	2.0	1.1
P_2O_5	0.12	0.15	-	0.10	-	0.10	-	-	0.11	-	-	-
Ni	60	19	20	70	20	88	58	135	73	30	39	105
Cr	112	35	35	150	32	215	88	235	159	55	61	185
Ba	626	1070	550	402	710	259	760	150	429	350	-	250
Rb	87	110	112	62	74	11	11	5	53	42	-	32
Sr	269	316	350	281	580	348	570	230	299	400	-	260
Nb	10	26	25	8	6	5	5	6	8	11	-	11
Zr	162	240	190	125	190	68	200	70	118	100	-	100
Y	25	21	22	22	7	16	9	19	21	22	-	20
Th	9.1	10.0	10.7	6.1	8.4	1.2	0.4	1.1	5.5	4.8	5.1	3.5
U	2.4	2.5	2.8	1.6	-	0.2	-	0.3	1.4	1.3	1.3	0.9
La	29	32	60	17	36	8	22	11	18	19	-	16
Ce	59	65	64	45	69	20	44	23	42	38	-	33
Pr	-	-	7.1	-	-	-	-	2.8	-	4.3	-	3.9
Nd	-	26	26	-	30	-	19	13	-	16	-	16
Sm	4.8	4.5	4.5	4.4	4.4	2.8	3.3	3.2	4.0	3.7	-	3.5
Eu	1.1	0.9	0.9	1.5	1.1	1.1	1.2	1.2	1.2	1.1	-	1.1
Gd	-	2.8	3.8	-	-	-	-	3.1	-	3.6	-	3.3
Tb	-	0.48	0.64	-	0.41	-	0.43	0.59	-	0.64	-	0.60
Dy	-	-	3.5	-	-	-	-	3.6	-	3.7	-	3.7
Ho	-	0.62	0.80	-	-	-	-	0.77	-	0.82	-	0.78
Er	-	-	2.3	-	-	-	-	2.2	-	2.3	-	2.2
Tm	-	-	0.33	-	0.14	-	0.19	0.32	-	0.32	-	0.32
Yb	2.0	1.5	2.2	2.3	0.8	1.5	1.2	2.2	1.9	2.2	-	2.2
Lu	-	0.23	0.32	-	-	-	-	0.29	-	0.30	-	0.30

Table 1.1: Estimates of composition of the upper, middle lower and bulk continental crust. Shaw - Shaw *et al.*; T & M - Taylor and McLennan; W & T - Weaver and Tarney; R + F - Rudnick and Fountain. Major elements in weight percent; trace elements in ppm.

1.3.1 Tonalite-trondhjemite-granodiorite suites

The generation of tonalite-trondhjemite-granodiorite (TTG) suites is of particular interest to the continental growth mechanisms controversy because TTGs are chemically similar to various estimates of the composition of the upper crust (Table 1.1). Moreover, rocks of tonalitic composition make up a significant volume of the Earth's Archaean shield areas (e.g., Barker and Arth, 1976). Current models for TTG generation fall into three categories (Fig. 1.2): a) remelting of hydrated basaltic oceanic crust during subduction, where the subducting plate is young and hot (Drummond and Defant, 1990); b) remelting of hydrated basaltic material that has been underplated beneath thickened continental arcs (Atherton and Petford, 1993); and c) melting of peridotitic mantle that has been metasomatised by fluids derived from a subducting slab, followed by fractional crystallisation (Evans and Hanson, 1997). The genesis of TTG suites is considered in the context of the present study in Chapter 9.

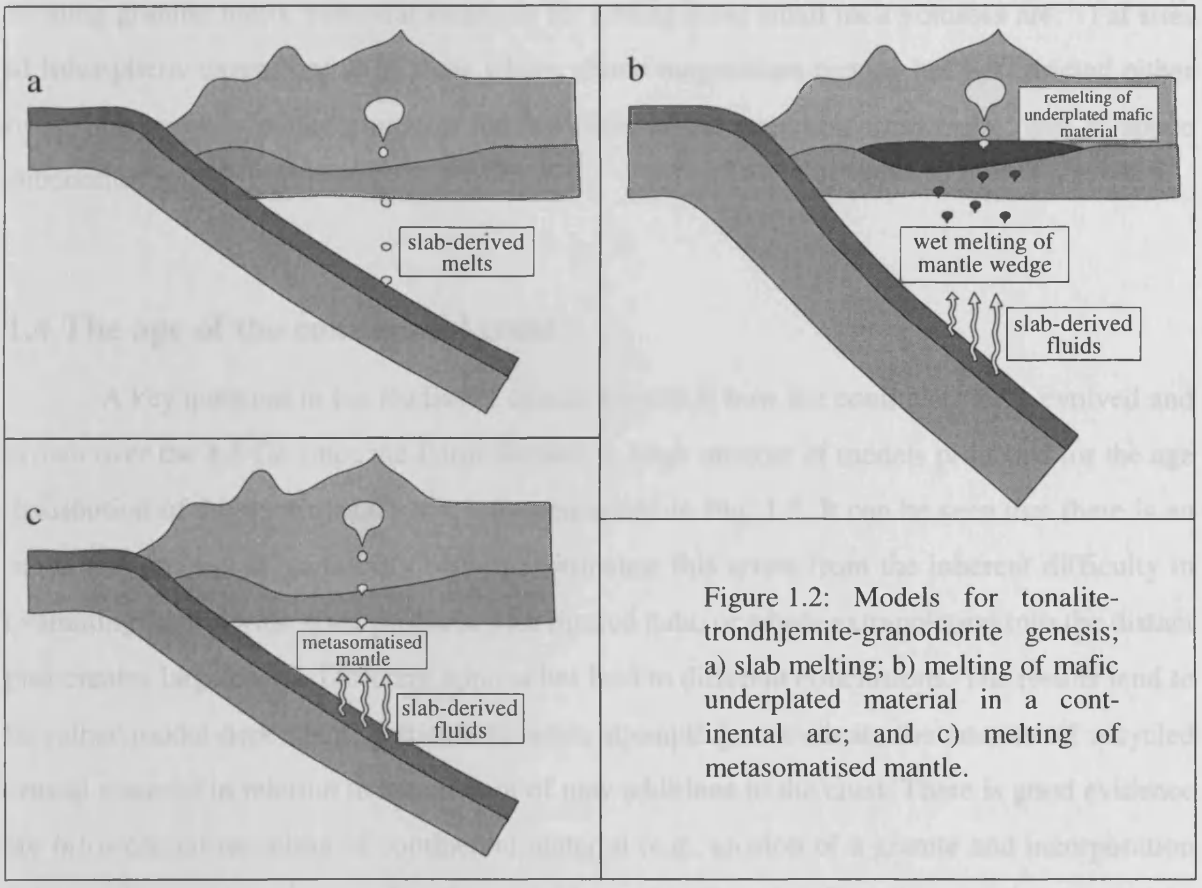

Figure 1.2: Models for tonalite-trondhjemite-granodiorite genesis; a) slab melting; b) melting of mafic underplated material in a continental arc; and c) melting of metasomatised mantle.

1.3.2 Subduction zone magmatism

Aside from the proposed generation of TTG suites in various subduction-related settings (discussed in the previous section), it is generally accepted that subduction zone magmatism adds not only mass to the continents, but also material which is broadly similar in composition to the continental crust (Tarney *et al.*, 1976; Taylor, 1977). This is true particularly of magmatism at continental active margins, where large volumes of silicic magmas (showing enrichments in light rare earth (LREE) and large ion lithophile elements (LILE) and depletions in Nb and Ta) are added (Pearce, 1982).

1.3.3 Small volume basaltic melt fractions

O'Nions (1992) points out that granitic rocks are relatively ineffective at fractionating trace elements to produce the required enrichments because they result from high degree melts of their protolith. He argues instead that trace element enrichments originate by the addition of small volume basaltic melt fractions from the mantle, and are subsequently inherited by crust-forming granitic melts. Potential locations for adding these small melt volumes are: 1) at sites of lithospheric extension; 2) in areas where plume magmatism occurs, but is restricted either by the temperature of the plume or the thickness of the overlying lithosphere; and 3) above subduction zones.

1.4 The age of the continental crust

A key question in the studies of crustal growth is how the continents have evolved and grown over the 4.5 Ga since the Earth formed. A large number of models proposed for the age distribution of the continental crust are summarised in Fig. 1.3. It can be seen that there is an incredible amount of variability between estimates: this arises from the inherent difficulty in evaluating such a wide scale problem with limited data, or where extrapolation into the distant past creates large errors. Different approaches lead to different conclusions. The results tend to be rather model-dependent, particularly when attempting to evaluate the amount of recycled crustal material in relation to the amount of new additions to the crust. There is good evidence for *intra*-crustal recycling of continental material (e.g., erosion of a granite and incorporation into a sedimentary sequence) but this should not significantly affect the growth rate models. What is considerably more difficult to constrain is the rate of recycling of crustal material to the mantle throughout Earth history, either at subduction zones, or during continental delamination (Fyfe, 1978; Armstrong, 1981; Armstrong, 1991).

1.4.1 Methodology used to determine crustal growth ages

A variety of methods have been used to constrain both the ages of exposed continental material, and the timing of the mantle's depletion in crust-forming trace elements. It is important here to be able to distinguish between the radiometric age of a rock, which can be reset by periods of tectonism and metamorphism, and the age of its extraction from the mantle. The approaches fall into two main categories: determining the timing of mantle derivation of continental material (igneous and sedimentary) from neodymium "model" (or "crustal residence") ages, and establishing the complementary evolution of the upper mantle by studying mantle-derived rocks (i.e., basalts) of various ages now preserved within the continental crust. However, because both approaches utilise only trace element data, the results may only be applicable to the addition of trace elements to the continental crust: trace element behaviour may be decoupled from major element behaviour (O'Nions, 1992) and the associated growth in mass of the continents.

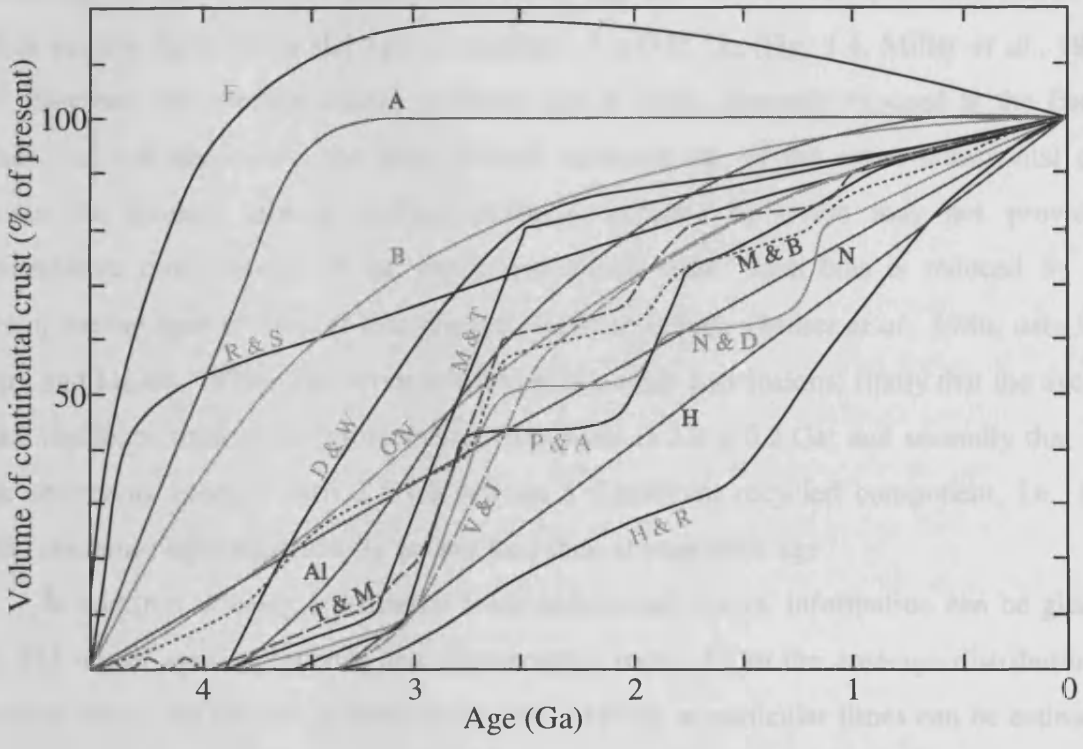

Figure 1.3: Estimates of the rate of growth of the continental crust by various authors (updated from Reymer and Schubert (1984) and Windley (1995) and references therein). A - Armstrong (1981); Al - Allegré (1982); B - Brown (1979); D & W - Dewey and Windley (1981); F - Fyfe (1978); H - Hurley (1968); H & R - Hurley and Rand (1969); M & B - McCulloch and Bennett (1994); M & T - McLennan and Taylor (1982); N - Nelson (1991); N & D - Nelson and DePaolo (1985); O'N - O'Nions *et al.* (1979); P & A - Patchett and Arndt (1986); R & S - Reymer & Schubert (1984); T & M - Taylor and McLennan (1995); V & J - Veizer and Jansen (1979).

Calculation of Nd model ages assumes that the Nd isotopic ratio of the source mantle region is known (or can be estimated). The age of crustal extraction from this known source region is a function of the $^{147}Sm/^{144}Nd$ ratio of the sample and its $^{143}Nd/^{144}Nd$ ratio (Faure, 1986). Results of these calculations are somewhat model-dependent, i.e., it becomes important whether the rock of interest was derived from a depleted-mantle or primitive-mantle source, although in practice, a depleted mantle source is usually assumed, consistent with interpretations of trace element and isotopic data showing progressive depletion of the upper mantle with time (e.g., O'Nions *et al.*, 1978). Another complication is that the Nd model age does not necessarily represent a geologically meaningful event, because it is a weighted average of contributions from potentially many sources. However, the Sm/Nd isotopic system is relatively robust in that the elements tend not to be fractionated from one another during sedimentary or metamorphic reprocessing; therefore the technique is not just restricted to igneous rocks.

Substantial progress has been made in constraining the ages of the continental masses by studying Nd model ages of sediments. Present day well-mixed sediments from fluvial and aeolian sources have Nd model ages averaging 1.7 ± 0.35 Ga (Fig. 1.4, Miller *et al.*, 1986). This represents the average crustal residence age of rocks presently exposed at the Earth's surface, but not necessarily the mean crustal residence age of the entire continental crust because the modern erosion surface presently sampled by rivers may not provide a representative cross-section of the entire continental crust. Such bias is reduced by also studying model ages of ancient fine-grained clastic sediments (Miller *et al.*, 1986; data from Veizer and Jansen, 1979). This work resulted in two main conclusions: firstly that the average crustal residence time of the entire sedimentary mass is 2.0 ± 0.2 Ga; and secondly that only those sediments younger than 2.5 Ga contain a significant recycled component, i.e., have crustal residence ages significantly greater than their stratigraphic age.

In addition to using information from sedimentary rocks, information can be gleaned from Nd model ages of igneous and metamorphic rocks. From the area-age distribution of basement rocks, the amount of continental crust existing at particular times can be estimated, and it is on these estimates that some of the crustal growth curves (e.g., O'Nions *et al.*, 1979) shown in Fig. 1.3 are based. However, these are minimum estimates, because there are no constraints on what volume of the continental crust may have been subsequently destroyed by being returned to the mantle. Nd model ages of igneous rocks can represent either a single extraction event from the mantle, or a weighted average of new material plus recycled crust,

but are particularly useful in that they can identify new magmatic additions to the continents, i.e., bodies where the intrusive age and the crustal residence age are identical.

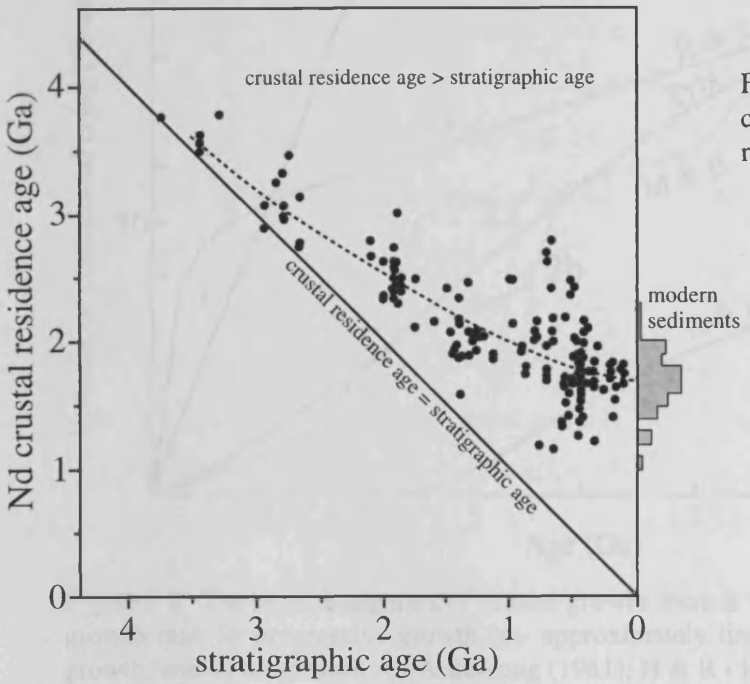

Figure 1.4: Stratigraphic age versus crustal residence age for sedimentary rocks (after Miller *et al.*, 1986).

Geochemical tracers of mantle depletion can also provide important constraints on the timing of extraction of incompatible trace elements to leave a complementary reservoir, and Nd isotopes are also useful for this. The presence of very old rocks (4.0 - 3.8 Ga) with positive ε_{Nd} values indicates that a significant mantle depletion event had occurred by this time (Bowring and Housh, 1995); yet if a sizeable amount of crust had been extracted from the mantle at this time, we see little evidence for its survival now. This lends credibility to the arguments that extensive crustal recycling into the mantle may have occurred. Similar studies using a wider range of isotopic systems (O'Nions *et al.*, 1978; 1980) and other trace elements (e.g., Nb/U; Sylvester *et al.*, 1997) also support early depletion of the upper mantle (or at least, some of it) in incompatible trace elements.

1.4.2 Summary of growth models

Although there are a large number of estimates for the timing of the growth of continents, most fall into the following categories (Fig. 1.5):

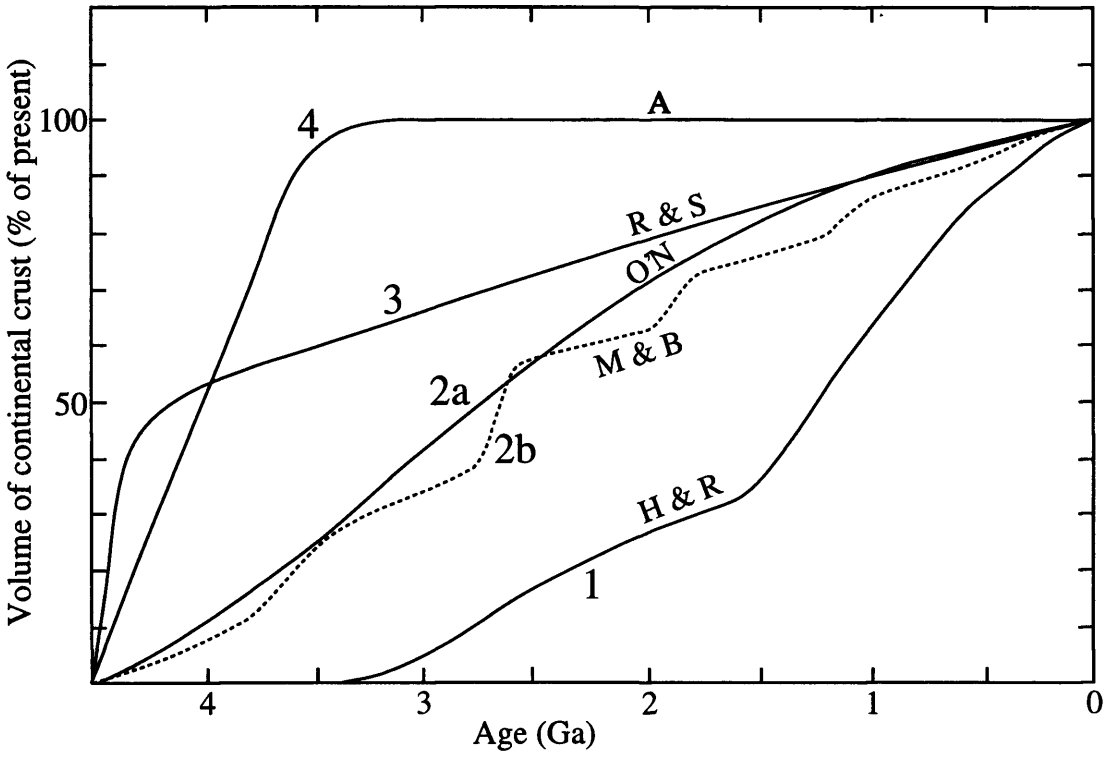

Figure 1.5: The main categories of crustal growth models (discussed in text); 1) increasing growth rate; 2) progressive growth (a - approximately linear; b - episodic); 3) rapid early growth; and 4) no growth. A - Armstrong (1981); H & R - Hurley and Rand (1969); M & B - McCulloch and Bennett (1994); O'N - O'Nions *et al.* (1979); R & S - Reymer & Schubert (1984).

1) Increasing growth rate with time

One of the earliest models (Hurley and Rand, 1969) for the growth of the continents suggested that the growth rate has increased with time. This was based on isotopic ages of exposed rocks - we now know that isotopic ages can be reset by metamorphism, and so their evaluation was biased towards younger rocks.

2) Progressive, approximately linear growth

Many authors advocate a growth rate which has remained *approximately* constant with time (e.g., O'Nions *et al.*, 1979). These models arise primarily from observations of Nd model age versus crustal area, and do not preclude recycling of some material into the mantle, providing that this amount does not exceed juvenile additions. Some variations on this model include episodic periods of rapid growth inferred from major peaks in ages of granitoids and greenstones (e.g., 3.1-2.7 Ga and 2.0-1.7 Ga, Patchett and Arndt, 1986; 1.9-1.7 Ga, Nelson and DePaolo, 1985), but with an overall trend of increasing crustal volume with time.

3) Rapid early growth and slower subsequent growth

Reymer and Schubert (1984) estimated the present net growth rate of the continents at 1.06 km^3yr^{-1} by evaluating the volumes of new additions and removals of crustal material. At this rate of addition, the continents would take almost 7 Ga to grow to their present size. This implies that the net rate of addition of material to the continental crust must have slowed with time. Brown (1979) suggests that the rate of crustal growth is directly determined by the Earth's thermal energy, which has also decreased with time.

4) No growth or negative growth

Armstrong (1981) based a no-growth model on the observation that most silicic crustal material had mantle-like isotopic characteristics at the time of formation, indicating recent extraction from the mantle rather than reworking of older crust. If continental volume were to be preserved (Wise, 1974), these juvenile additions had to be balanced by extensive recycling into the mantle. This recycling may have been achieved because the hotter mantle would have been more vigorously convecting; however, an increased mantle temperature would make the crustal material prone to being remelted in subduction zones, and consequently, being returned to the crust. Although the *no growth* model explains the observation that the small existing volume of ancient continental material is extremely evenly distributed between the continents, no mechanism has been proposed for how such a large amount of continental crust could grow so quickly. Fyfe (1978) postulated a more extreme model still, where the continental crust grew extremely quickly during the early history of the Earth, but thereafter, destruction rate has exceeded addition rate, and the continents are shrinking.

1.4.3 Has a consensus been reached?

Models which involve no or negative modern crustal growth are now largely abandoned, much to the dismay of Armstrong (1991): *"crustal growth [is a] geochemical dogma [that has] survived by inertia and repetition and endless self-citation..."*! This is because large juvenile additions to the continental crust have been observed throughout the Phanerozoic that do not appear to have been counterbalanced by recycling into the mantle. However, a number of models which lie between the minimum growth rate curve of O'Nions *et al.* (1979) and the constant mass model of Armstrong (1981) show a reasonable degree of propinquity. Nevertheless, Rudnick (1995) seems resigned to the fact that the growth rate of the continents is poorly constrained: "anywhere between 40 to 100% of the present mass of the continents may have existed since the end of the Archaean". The best supported general

model is one of progressive crustal growth with episodic surges at around 2.7-2.6 Ga and 2.0-1.8 Ga (Condie, 1997). The question remains as to exactly what caused these surges.

1.5 The earliest continents: Archaean crustal rocks

Exposed portions of the Archaean continental crust fall into two main categories: greenstone-granite belts and granulite-gneiss belts. The latter, which can contain significant proportions of gneisses belonging to the tonalite-trondhjemite-granodiorite association, represent exhumed Archaean mid-lower crust: they have suffered high-grade metamorphism, and the majority have been reworked during younger orogenic events (Nutman *et al.*, 1993). Although they are useful sources of information concerning the mode of evolution of the deep continental crust in the early part of Earth history, their multi-stage evolution makes them considerably more complex than the Caribbean region that is the focus of the present study; a thorough discussion of granulite-gneiss belts is, therefore, beyond the scope of this thesis.

Greenstone-granite belts, however, have more similarities with the Caribbean rocks of interest, and a review of their main features is of relevance to the present study. Greenstone belts are important features in the continental growth debate because they, together with high-grade gneissic terranes, represent a significant proportion of the earliest continental crust preserved. A map showing the location of the world's greenstone belts is shown in Fig. 1.6. The term "greenstone" refers to a basic igneous rock metamorphosed to greenschist facies, and greenstone belts are so termed because they contain a high proportion of these rocks. There is some confusion, however, about the actual definition of a "greenstone belt". Historically, the term has been reserved for ancient (Archaean) rocks (Hunter and Stowe, 1997), whereas Condie (1997) suggests that a greenstone should be defined as "a supracrustal succession in which the combined submarine mafic volcanic and volcaniclastic sediment component exceeds 50%", and therefore includes examples of all ages.

Studies of ancient greenstone belts (and their modern analogues) may be more instructive in constraining the history of the Earth's continental crust than studies of ancient granulite-gneiss terranes, because the former have not undergone as severe deformation and metamorphism, and their history is more easily determined. However, all Archaean/ Proterozoic greenstone belts have suffered some degree of tectonic overprinting, and their interpretation is far from trivial.

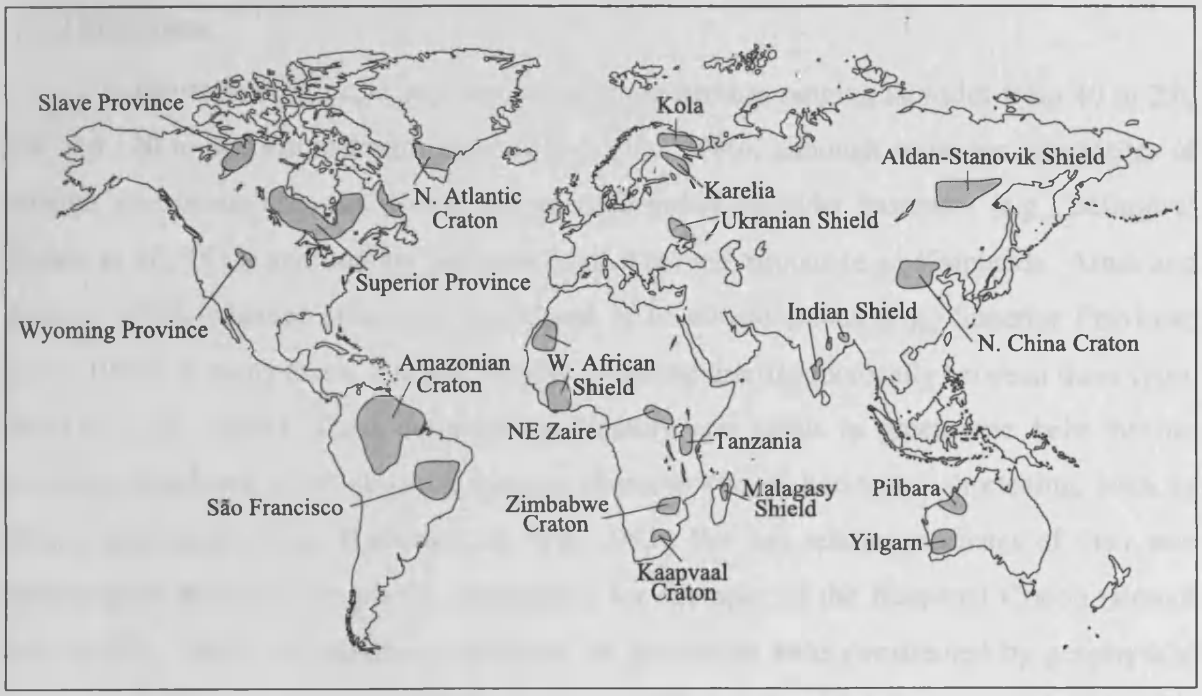

Figure 1.6: World map showing distribution of Archaean cratons that contain greenstone belts (adapted from de Wit and Ashwal, 1997).

1.5.1 Lithological characteristics

Greenstone belts can be lithologically very diverse, and the following description (summarised from Condie (1997) and Windley (1995)) is somewhat generalised:

The lower tectonostratigraphic unit is predominantly volcanic, and contains ultramafic komatiitic extrusive rocks and submarine basalts commonly overlain by volcanic rocks of a more felsic, often calc-alkaline composition. With increasing height in the succession, the amount of komatiite and basalt decreases, and there is a concomitant increase in the proportion of volcaniclastic rocks (as opposed to lava flows) and evolved compositions. Sedimentary rocks associated with the lower volcanic unit are jaspers, cherts and banded iron formations. The upper stratigraphic unit consists mainly of terrigenous siliciclastic rocks.

The overall stratigraphy is interpreted in terms of a shallowing upward sequence, beginning with submarine mafic volcanism. As the system matured, volcanism became localised and progressively more emergent; finally, intervening sedimentary basins developed.

Many greenstone belts are associated with syntectonic granitoid bodies belonging to tonalite-trondhjemite-granodiorite (TTG) suites. These are chemically similar to felsic volcanics within the greenstone belt succession. Later post-tectonic discordant plutons are granitic *(sensu stricto)* in composition.

1.5.2 Structure

Greenstone belts occur as irregular or linear terranes ranging in width from 40 to 250 km and 120 to 800 km in length (Kearey and Vine, 1996), although some are composites of smaller greenstone domains. Some rest unconformably on older basement (e.g., Belingwe; Bickle *et al.*, 1975) and contain populations of inherited zircons (e.g., Kambalda; Arndt and Jenner, 1986), whereas others are considered to be allochthonous (e.g., Superior Province; Card, 1990); in many cases, it is not possible to distinguish unequivocally between these types (Bickle *et al.*, 1994). Their deformational history can result in greenstone belts having complex structures, often showing features characteristic of horizontal shortening, such as thrusts and nappes (e.g., Barberton; de Wit, 1982). For this reason, estimates of their true stratigraphic thickness are poorly constrained, for example, in the Kaapvaal Craton (Brandl and de Wit, 1997), the maximum thickness of greenstone belts constrained by geophysical methods is 10 km compared with the estimate of 25 km determined stratigraphically - this implies significant tectonic duplication of stratigraphic units. Late emplacement of silicic plutons into greenstone belts adds a further element of structural complication.

1.5.3 Origins

A variety of models have been proposed for the origin of greenstone belts, and it has only relatively recently become accepted that the many differences between specific examples are a function of their different origins, i.e., not all can be explained by a single model. The preponderance of structures indicative of horizontal shortening suggests that accretion or obduction tectonics may have played an important role in their development. This has resulted in some greenstone belts being interpreted as accreted fragments, either of oceanic plateaux (e.g., Desrochers *et al.*, 1993), Archaean oceanic crust (Helmstaedt *et al.*, 1986) or island arcs (e.g., Kusky, 1989), depending on the geochemistry of the basaltic rocks present. For cases showing geochemical evidence for crustal contamination and populations of inherited zircons, which require that the basalts and komatiites were erupted through pre-existing continental crust, models involving continental plume-related magmatism (Lesher and Arndt, 1995) and back-arc extension (Tarney *et al.*, 1976) were proposed. As the quantity of observational evidence has increased, models for the formation of greenstone belts have become increasingly elaborate, for example, subduction of mid-ocean ridges near continental hotspots (Abbott, 1996).

1.6 Broad objectives of this study

Despite all the work targeting the problem of crustal generation, several questions remain unanswered. The timing of the major periods of crust generation remains a topic of considerable debate; the temporally-focused and local nature of this study cannot assist in solving this problem. Nonetheless, the association of continent-like silicic material with juvenile basaltic rocks derived from the mantle may provide important clues on how continental crust generation processes operated in the very earliest history of the Earth, i.e., before there was any pre-existing continental crust.

In particular, it is hoped that the results of this study will enable an evaluation of the oceanic plateau model of crustal growth, answering some of the following questions:

- how important is plateau accretion to crustal growth?
- by what mechanism does chemical modification of plateau material occur, and could this mechanism also be responsible for the modification of accreted island arc material?
- how quickly can this modification occur, and how quickly can continental lithosphere/crust be stabilised?

In addition, the project provides a valuable data set for studies of Caribbean tectonics and magmatism, which will be discussed further in the following chapter.

1.6.1 Methodology

A variety of techniques were used in this study to elucidate the nature of the mafic and silicic rock types on Aruba and their inter-relationships. Detailed fieldwork was carried out to describe the range of rock types and study their mutual contacts and samples were taken for geochemical and isotopic analysis. Geological mapping was not considered a priority, since a new geological map of Aruba was already in preparation (Beets *et al.*, 1996). Field identifications were substantiated with petrographic and electron microprobe work. The samples were analysed by XRF, INAA and ICP-OES (Leicester University) and ICP-MS (Rijks Geologische Dienst, Netherlands) for a wide range of major, minor and trace elements, and selected samples were analysed by TIMS (NERC Isotope Geosciences Laboratory) for Sr, Nd and Pb isotopes. Nine samples were dated by ^{40}Ar-^{39}Ar techniques (Scottish Universities Research and Reactor Centre).

Chapter 2

Oceanic plateaux and their role in the tectonic and magmatic evolution of the Caribbean region

2.1 Introduction

This chapter aims to put the present study into a regional context by summarising previous relevant work carried out in the Caribbean area, and discussing the tectonic and magmatic evolution of the region. The Caribbean seaway originated in the early Jurassic, when North and South America began to rift from one another following the break-up of western Pangaea (Pindell and Barrett, 1990). However, the arrival of a Cretaceous oceanic plateau into the area appears to have had a profound effect on its subsequent history, controlling both the development and location of plate boundaries and associated magmatism.

2.2 Oceanic Plateaux

Oceanic plateaux represent vast outpourings of basaltic magmas, and together with continental flood basalts, are known as *large igneous provinces* (Fig. 2.1). These vast magmatic provinces, which can cover areas of the order 1 million km^2, are of particular interest because: 1) they can provide constraints on mantle processes and dynamics (Saunders *et al.*, 1992); 2) the ash and volatile output arising from their voluminous eruptions may have had pronounced effects on global climate and biodiversity (Courtillot *et al.*, 1986); and 3) they may have played an important rôle in the development of the continental crust (Stein and Hofmann, 1994).

The formation of an oceanic plateau can be extremely rapid, with large volumes of magma being extruded (and intruded) in timescales of the order of a few m.y. (Tarduno *et al.*, 1991). The crust produced is considerably thicker than normal oceanic crust, with values of ~32 km being recorded for the Ontong Java Plateau (Gladczenko *et al.*, 1997), although the majority of plateaux are 10-20 km thick (Coffin and Eldholm, 1993; 1994). The volumes of magma involved can be in excess of 50×10^6 km^3 (Ontong Java Plateau: Mahoney, 1987), which indicates that an enormous volume of mantle must have been partially melted. The

anomalously high rates of magma production associated with oceanic plateaux can best be explained by the presence of large volumes of mantle material with an unusually high potential temperature (T_p: defined by McKenzie and Bickle (1988) as the temperature of a portion of mantle if it were allowed to ascend to the surface without melting, expanding and cooling adiabatically; T_p may vary from 1280°C for normal mantle to as much as 1480°C (McKenzie and Bickle, 1988)). The large volumes of hot mantle required to create oceanic plateaux could be supplied via a starting mantle plume (Campbell and Griffiths, 1990), a solitary diapir (Olson, 1994) or a steady state mantle plume (White and McKenzie, 1989). Some plateaux show evidence for a multi-phase genesis, e.g., the Ontong Java Plateau, with radiometric ages clustering at 121 Ma and 90 Ma (Mahoney *et al.*, 1993), although the bulk of activity appears to have occurred at 121 Ma.

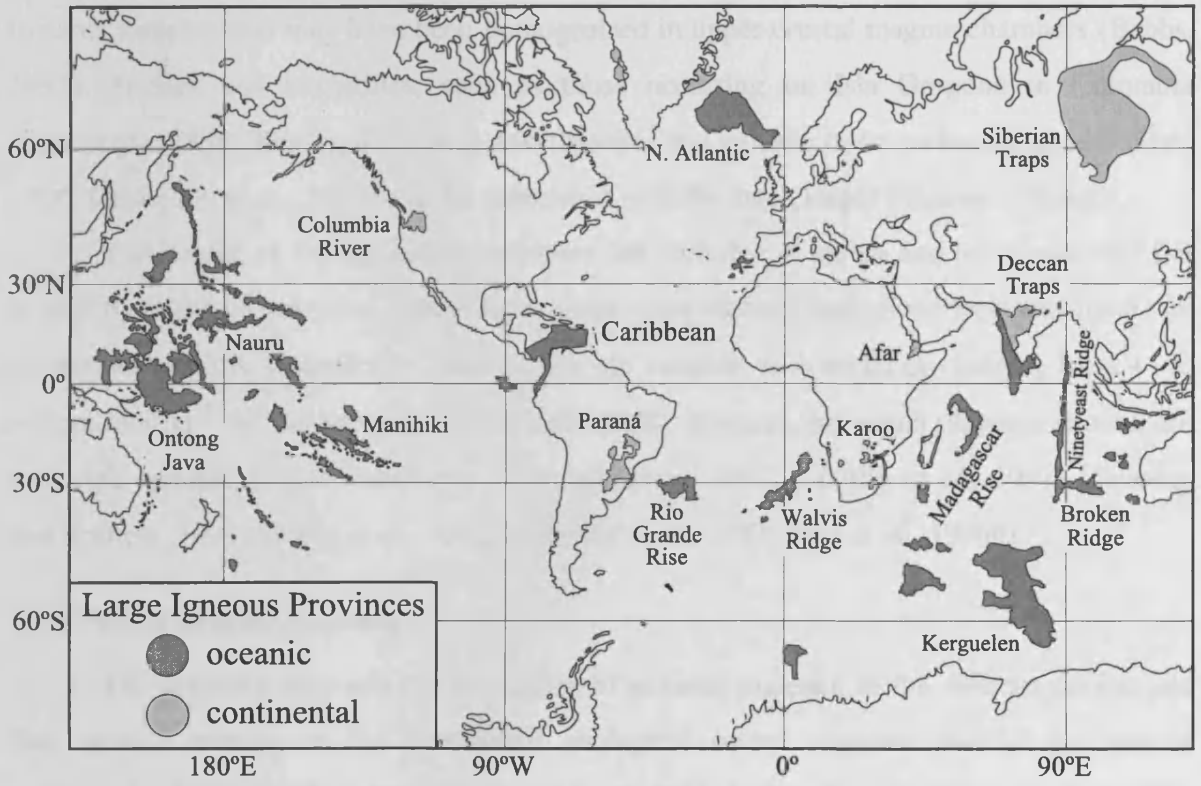

Figure 2.1: Modern day distribution of oceanic and continental large igneous provinces, after Saunders *et al.* (1992).

The link between oceanic plateaux and mantle plumes is further strengthened by the association of modern day examples of large scale basaltic magmatism (e.g., Iceland, Hawai'i) with large scale geophysical anomalies. Low seismic velocities indicate the presence of hot underlying mantle (Wolfe, 1997), and gravity anomalies, which are positive, but smaller than would be expected for the observed ocean floor elevation, imply some dynamic uplift

(Courtney and White, 1986). For these modern examples, the volume of magma observed is larger when the volcanism is associated with a mid-ocean ridge (e.g., Iceland), because for mantle of the same potential temperature, more decompression melting can occur if the lithosphere is thin (McKenzie and Bickle, 1988). This fact, and the geographical location of certain plateaux, has led to the hypothesis that some existing oceanic plateaux may have also formed at, or close to, spreading centres (e.g., Ontong Java, Kerguelen: Saunders *et al.*, 1996), although this need not necessarily be the case, as the temperature and size of the now-inactive mantle plumes that may have been responsible for these provinces are poorly constrained.

Oceanic plateaux are predominantly basaltic and can be remarkably uniform in their compositions of major elements, trace elements and radiogenic isotopes (e.g., the Ontong Java Plateau: Tejada *et al.*, 1996). This apparent uniformity may arise from the fact that it is logistically difficult to sample the deeper portions of oceanic plateaux, resulting in a bias towards samples that may have been homogenised in upper crustal magma chambers (Babbs, 1997). Picrites and komatiites, such as those occurring on Isla Gorgona in Colombia (Echeverría, 1980; Kerr *et al.*, 1996a), and rhyolites and volcaniclastic rocks (Iceland: Walker, 1966; Calderone *et al.*, 1990) may be associated with the much larger volumes of basalts.

The basalts of Pacific oceanic plateaux are tholeiitic in nature and have relatively flat to slightly enriched primitive mantle-normalised multi-element and chondrite-normalised rare earth element plots. Isotopically, these basalts are variable, with initial ε_{Nd} ranging from +1 to +10 and initial $^{87}Sr/^{86}Sr$ between 0.7028 and 0.7050, although individual plateaux show more restricted isotopic ranges (Saunders, 1985; Mahoney, 1987; Castillo *et al.*, 1991; Mahoney and Spencer, 1991; Storey *et al.*, 1992; Mahoney *et al.*, 1993; Kerr *et al.*, 1996b).

2.2.1 Fate of oceanic plateaux

The disparity between the abundance of oceanic plateaux in the modern oceans and their relative paucity in the continental geological record suggests that, *if* the rate of production of plateaux has not been anomalously high during the last 150 m.y., then either plateaux are eventually subducted, or they are processed and converted into material which is no longer easily recognisable as oceanic plateau crust (Stein and Goldstein, 1996; Saunders *et al.*, 1996).

Because oceanic plateaux are considerably thicker than normal oceanic crust, they are more buoyant, and less prone to being recycled into the mantle at subduction zones. This disinclination to subduct is more extreme if a plateau (and its underlying mantle) is still hot when it encounters a subduction zone, and further buoyancy is achieved from the existence of

lower density mantle depleted by partial melting (Hill, 1993). Instead of being returned to the mantle at a subduction zone, plateau material may be accreted against or obducted onto continental margins (Ben-Avraham *et al.*, 1981). Cloos (1993) argues, however, that basaltic plateaux with crustal thicknesses of less than 30 km should eventually become negatively buoyant and susceptible to subduction, particularly if the lower portions are converted into eclogite (Saunders *et al.*, 1996).

The presence of oceanic plateaux and their interaction with subduction zones may be instrumental in determining the configuration of plate boundaries (Nur and Ben-Avraham, 1982), with subduction "flip" (e.g., Solomon Arc: Cooper and Taylor, 1985) or backstep (e.g., Colombia: Millward *et al.*, 1984) being potential consequences of a plateau-subduction zone collision. Additionally, numerical simulations by Ratcliff *et al.* (1998) indicate that reorganisation of plate motions can be accomplished merely due to the "lubricating effects of mantle plume heads". It follows, therefore, that the existence of mantle plumes and the oceanic plateaux created therefrom can have a far-reaching influence in the tectonic (and consequently, magmatic) evolution of a particular area.

2.3 The Caribbean-Colombian Cretaceous Igneous Province

The region covered by the Caribbean Sea is the site of an oceanic large igneous province of Cretaceous age (Donnelly *et al.*, 1990), termed the Caribbean-Colombian Cretaceous Igneous Province by Kerr *et al.* (1997b). This province, which covers an area of approximately 6×10^5 km^2, includes both oceanic plateau and arc-related rocks (Fig. 2.2). Detailed studies of this large igneous province have relied on the fact that portions of it have been uplifted at the margins of the Caribbean plate, and now crop out subaerially.

2.3.1 Structure of the Caribbean oceanic plateau

Several lines of evidence suggest that the Caribbean crust is oceanic plateau crust. Drilling during DSDP Leg 15 (Donnelly *et al.*, 1973) and ODP Leg 165 (Site 1001) penetrated oceanic basement of basaltic composition, interbedded with late Cretaceous pelagic sediments. The Caribbean sea floor lies at a depth of approximately 4 km (Burke, 1988), which is significantly shallower than expected for Cretaceous sea floor of a normal thickness (5.6 km for 88 Ma oceanic crust: Parsons and McKenzie, 1978). This implies that the

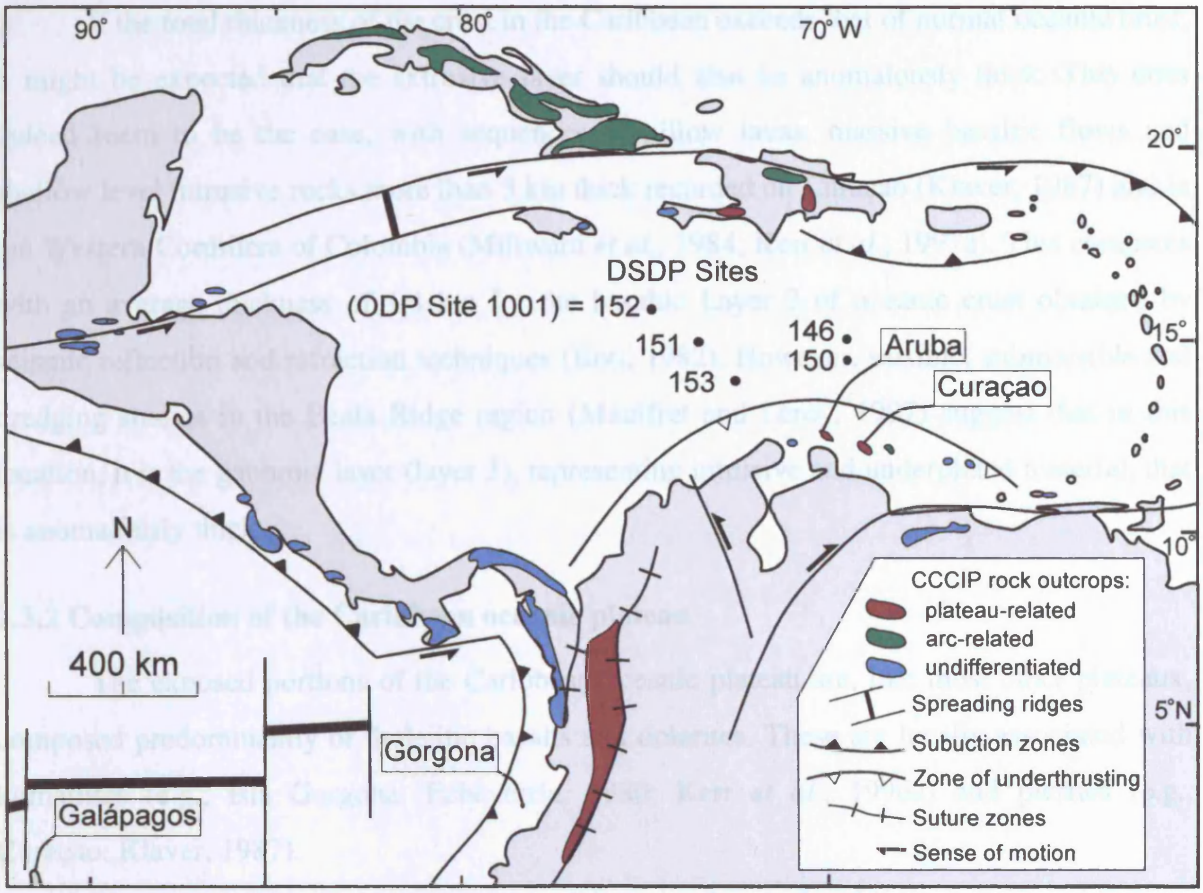

Figure 2.2: Neotectonic map of the Caribbean region (after Mann *et al.*, 1990) showing the location of Aruba with respect to other exposed fragments of the Caribbean-Colombian Cretaceous Igneous Province (CCCIP: after Kerr *et al.*, 1997b). Rock outcrops described as "undifferentiated" have either an unknown affiliation, or one that is disputed. Deep Sea Drilling Project (DSDP) sites are also marked. ODP Leg 165 redrilled the area: Site 1001 is 40 km to the SW of Site 152.

Caribbean crust is anomalously thick, and is in accordance with seismic studies of the region (Edgar *et al.*, 1971), which obtained values of 8 to 20 km.

If the total thickness of the crust in the Caribbean exceeds that of normal oceanic crust, it might be expected that the extrusive layer should also be anomalously thick. This does indeed seem to be the case, with sequences of pillow lavas, massive basaltic flows and shallow level intrusive rocks more than 5 km thick recorded on Curaçao (Klaver, 1987) and in the Western Cordillera of Colombia (Millward *et al.*, 1984; Kerr *et al.*, 1997a). This compares with an average thickness of 1.4 km for the basaltic Layer 2 of oceanic crust obtained by seismic reflection and refraction techniques (Bott, 1982). However, seismic, submersible and dredging studies in the Beata Ridge region (Mauffret and Leroy, 1997) suggest that in this location, it is the gabbroic layer (layer 3), representing intrusive and underplated material, that is anomalously thick.

2.3.2 Composition of the Caribbean oceanic plateau

The exposed portions of the Caribbean oceanic plateau are, like most other plateaux, composed predominantly of tholeiitic basalts and dolerites. These are locally associated with komatiites (e.g., Isla Gorgona: Echeverría, 1980; Kerr *et al.*, 1996a) and picrites (e.g., Curaçao: Klaver, 1987).

The range of lithologies observed, and their geochemical and isotopic composition, are all consistent with a mantle plume origin, with the picrites and komatiites representing higher degrees of melting of the source (30% proposed for Curaçao picrites: Beets *et al.*, 1982). The highly magnesian lavas are variable in chemistry (moderately enriched in the Duarte Complex in Hispaniola (Lapierre *et al.*, 1997), exhibiting flat chondrite-normalised rare earth element patterns in Curaçao (Kerr *et al.*, 1996b) and ranging from extremely depleted to enriched in Gorgona (Kerr *et al.*, 1996a)); such variations would be unlikely to be found in rocks from a MORB source. The light rare earth element enrichments and isotopic compositions in particular are inconsistent with derivation from a depleted MORB source. The variability in isotopic and elemental chemistry from rocks throughout the Caribbean oceanic plateau implies that the source was heterogeneous, and systematically high ε_{Nd} (ranging from +5 to +9) across the province reveal a long term history of depletion in the source region (Kerr *et al.*, 1997a).

2.3.3 Rates of volcanism and potential origin of the Caribbean oceanic plateau

A compilation of ^{40}Ar-^{39}Ar dates from the Caribbean oceanic plateau by Sinton *et al.* (1998) reveals that most of the dates are clustered around 91-88 Ma. These dates come from widely spaced on-land sections. The large volume of magma (approximately 6×10^6 km^3, assuming an area covering 6×10^5 km^2 has 10 km thick plateau crust) extruded in this short timescale, and over such a large area, adds weight to arguments invoking a mantle plume origin for the province, because the averaged eruption rate of 3 km^3/yr is much greater than can be explained by normal ocean floor (mid ocean ridge) magmatism (a 1000 km length of ridge producing normal 7 km thick oceanic crust at a half-spreading rate of 5 cm/yr produces ~0.7 km^3 of new crust per year). A second, less voluminous, phase of magmatism appears to have occurred throughout the province at about 78-72 Ma (Kerr *et al.*, 1997a; Sinton *et al.*, 1998), and there is mounting evidence for some older plateau material in the province (e.g., Lapierre *et al.*, 1997, Kerr *et al.*, in press). No convincing magnetic anomaly patterns indicating normal spreading oceanic crust are present in the Caribbean region (Fox and Heezen, 1975). However, long wavelength NE-SW and E-W linear magnetic anomalies over the Venezuelan and Colombian basins are interpreted by Hall (1995) as resulting from an Early Cretaceous phase of seafloor spreading at the Farallon-Pacific-Phoenix triple junction. If this were the case, the 88-91 Ma oceanic plateau material would have to have been erupted as a mantle plume impinged upon this pre-existing crust and lithosphere.

2.3.4 Arc magmatism associated with the Caribbean oceanic plateau

In addition to voluminous mafic magmatism belonging to the Caribbean oceanic plateau, significant magmatism with subduction-related characteristics has been identified (e.g., Donnelly *et al.*, 1990). It is important to note that it is the subduction-related sequences associated with the plateau that can potentially provide information about the positions and ages of plate boundaries, allowing tectonic reconstructions of the region to be made.

The subduction-related rocks have been broadly classified into two suites – the tholeiitic primitive island arc suite of Donnelly and Rogers (1967) (which is roughly equivalent to the island arc tholeiite suite of Jakes and Gill (1970)) and the calc-alkaline suite. The significance of the two different suites is not yet clear, although there is a general tendency for the tholeiitic rocks to be older than the calc-alkaline volcanics (Donnelly *et al.*, 1971).

Rocks of the tholeiitic suite occur in the Virgin Islands, Puerto Rico, Bonaire and Tobago, and the majority were erupted during the Aptian-Albian (Donnelly *et al.*, 1990), although locally, tholeiitic arc volcanism continued until the Coniacian (e.g., Bonaire: Priem *et al.*, 1979). There have been no proven examples of tholeiitic arc rocks being intercalated with basalts of the Caribbean oceanic plateau: it is likely that these rocks have been tectonically accreted to the oceanic plateau.

Calc-alkaline magmatism in the Caribbean region appears to have begun in the late Cretaceous, and continues to the present day in the Greater Antilles and Central American arcs. The abrupt appearance of calc-alkaline magmas at ~90 Ma is interpreted by Donnelly *et al.* (1990) as signalling a major change in plate movements, including the beginning of persistent compression and subduction. The close (i.e., intrusive) association of some of the calc-alkaline plutons with plateau basalts contrasts strongly with the discrete, probably allochthonous, occurrences of tholeiitic arc rocks.

2.4 Tectonic reconstructions of the Caribbean region

Fig. 2.2 shows obducted fragments of rocks belonging to the Caribbean-Colombian Cretaceous Igneous Province, together with present plate boundaries. To the north and south the Caribbean plate is bounded by complex broad zones of strike-slip movement, along which the Caribbean is moving eastwards relative to North and South America at a rate of 2 to 4 cm/yr (Sykes *et al.*, 1982). Subduction zones dipping beneath the plateau form the eastern and western boundaries. This present geometry arises from the complex tectonic history of the Caribbean plate.

The Caribbean plate, floored by the Caribbean oceanic plateau, is allochthonous with respect to the Americas. This was first recognised by Wilson (1966), who noticed similarities between the morphology of the Caribbean region and ice-rafting structures, and several lines of evidence have subsequently confirmed the exotic origin of the Caribbean plate (e.g., Case *et al.*, 1984). A Pacific origin for the Caribbean plate seems most likely. This is based upon: 1) present-day eastward motions from earthquake seismology; 2) 1000 km of pull-apart offset in the Cayman Trough; 3) magnetic anomalies in the Caribbean not reflecting spreading history between the Americas; 4) continuous Lesser Antilles volcanism since at least the Eocene, indicating progressive consumption of the Atlantic plate; and 5) diachronous deformation and basin development along the northern and southern margins of the Caribbean, younging towards the east (summarised from Pindell and Barrett, 1990).

Several plate reconstructions agree about the major features of the history of the region (summarised in Figs. 2.3a-f) even if they differ in detail (e.g., Duncan and Hargraves, 1984; Burke, 1988; Pindell and Barrett, 1990). Sea floor spreading between North and South America began in the early-middle Jurassic (Figs. 2.3a-b), and the Proto-Caribbean seaway had attained its present ~3000 km extent by the time of magnetic anomaly 34 at about 84 Ma (Pindell *et al.*, 1988), with minimal displacement between the Americas thereafter.

At 91 - 88 Ma (Sinton *et al.*, 1998), a major plateau-constructing event occurred in the eastern Pacific region (Fig. 2.3d). It is generally accepted that the plateau formed as part of the Farallon plate (Burke, 1988), although it remains unclear whether it was extruded onto pre-existing oceanic crust (as favoured by Hall, 1995), or formed at a spreading ridge (e.g., Iceland). A mantle plume related origin for the province is now also broadly agreed upon, since this seems to be the only reasonable explanation for the anomalously thick crust, the large magma volumes emplaced within a short timescale, and the trace element compositions and high MgO contents of (some of) the lavas. Duncan and Hargraves (1984) suggested that the plateau was formed above the starting Galápagos mantle plume, although recent palaeomagnetic work on Gorgona (MacDonald *et al.*, 1997) suggests that (at least) this part of the province may have originated further south (~26°S), and may instead be related to the Easter or Sala y Gomez hotspot.

At this time, east- or north-eastward-directed subduction was occurring beneath the Proto-Caribbean region and continental North and South America, consuming the Farallon plate (Fig. 2.3c) and carrying the newly-formed Caribbean plateau towards the Americas. As the thick, possibly still hot, oceanic plateau approached these subduction zones, it may have resisted subduction due to its buoyancy (Burke *et al.*, 1978). In the Caribbean region, where the plateau interacted with an intra-oceanic subduction zone, a reversal in subduction polarity ensued (Fig. 2.3d), possibly analogous to that in the Solomon Islands where attempts to subduct the Ontong Java Plateau failed (Hughes and Turner, 1977). The timing of the subduction polarity reversal in the Caribbean is not yet well-constrained, with estimates ranging from 100 Ma to 60 Ma (Burke, 1988; Draper *et al.*, 1996). This uncertainty has led to considerable debate over the cause of the reversal. The general consensus (Burke *et al.*, 1984; Duncan and Hargraves, 1984; Pindell and Barrett, 1990) is that it was the arrival of the 88-91 Ma phase of the Caribbean plateau and its collision with the Proto-Greater Antilles Arc that clogged the subduction zone and caused the polarity reversal. Alternative explanations include: 1) there being an earlier phase of plateau magmatism (Lebron and Perfit, 1993;

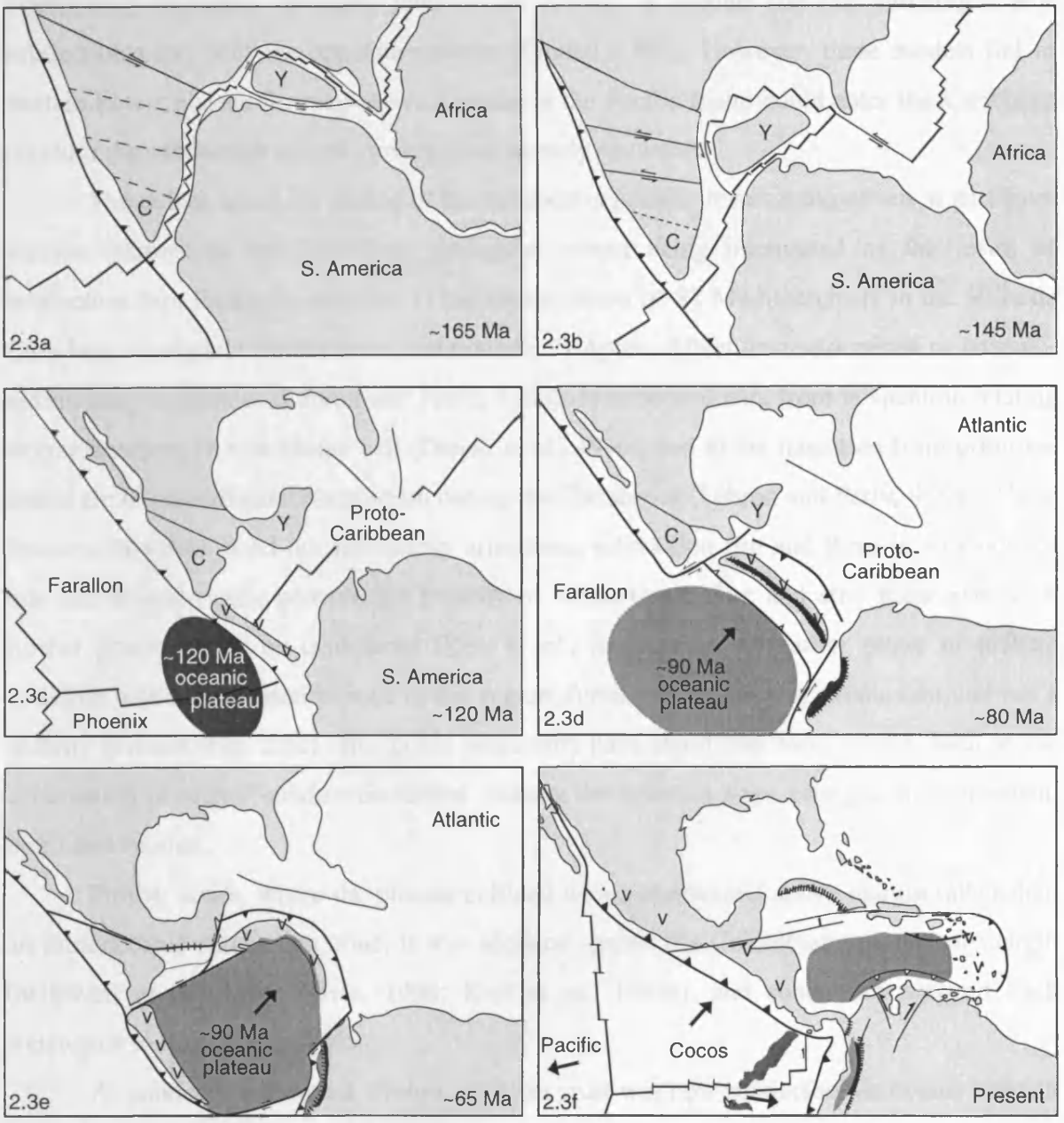

Figures 2.3a to f: Reconstructions of the tectonics of the Caribbean area, compiled from Pindell and Barrett (1990); Kerr *et al.* (in press).

C: Chortis Block
Y: Yucatan
v: active volcanism

↗ sense of plate motion

↗ sense of motion on strike-slip fault

subduction zone

zone of underthrusting

suture zone

spreading ridge and transform faults

Lapierre *et al.*, 1997) which blocked the subduction zone, triggering subduction "flip"; and 2) significantly increased spreading rates in the Atlantic at around 100 Ma initiating a new subduction zone with the opposite polarity (Pindell, 1993). However, these models fail to explain how a plateau forming above a plume in the Pacific realm could enter the Caribbean region if the subduction polarity reversal had already occurred.

The debate about the timing of the subduction polarity reversal has arisen in part from various features in the Caribbean geological record being interpreted as the result of subduction flip. Examples include: 1) the identification of 97 Ma blueschists in the Villa de Cura belt, Venezuela (Smith *et al.*, submitted); 2) Aptian-Albian unconformities in volcano-sedimentary sequences (Lebron and Perfit, 1993); 3) structural data from Hispaniola relating to emplacement of a peridotite belt (Draper *et al.*, 1996); and 4) the transition from primitive island arc to calc-alkaline magmatism during the Cretaceous (Lebron and Perfit, 1994). These features, however, need not necessarily arise from subduction flip and there is no evidence that can unequivocally point to the polarity of subduction before and after these events. A further possibility to be considered (Kerr *et al.*, in press) is an earlier phase of plateau colliding with the subduction zone in this region, forcing a step-back in subduction, but not a polarity reversal (Fig. 2.3c). This could potentially have significant local results, such as the exhumation of high-P subduction-related rocks at the collision zone, changes in magmatism, uplift and erosion.

Further south, where the plateau collided with a continental active margin rather than an intra-oceanic subduction zone, it was accreted against the Colombian continental margin (Millward *et al.*, 1984; Nivia, 1996; Kerr *et al.*, 1997a), and subduction stepped back westwards to its present position.

As subduction resumed, Proto-Caribbean crust was now subducted westwards beneath the plateau (Fig. 2.3e), which moved northwards and eastwards into the Caribbean region as strike-slip plate margins developed on the northern and southern margins. The Antilles arc was built up on the leading edge of the advancing plateau, and a north-east directed subduction zone formed beneath the trailing edge of the plateau (the present day Central American subduction zone). As the Caribbean plateau advanced past the Americas on its way to its present location, fragments of it were obducted and accreted along the margins.

A later phase (38 Ma to present) of N-S directed convergence between North and South America has complicated the situation further, resulting in further deformation at the margins of the Caribbean plate (e.g., underthrusting of the Caribbean plate beneath South

America resulting in a deformed sedimentary wedge: Ladd and Watkins, 1979) as well as internal deformation of the plate (Burke *et al.*, 1978). This deformation is most prominent where collision of Panama with South America has resulted in the northwards expulsion of the Santa Marta block (Burke *et al.*, 1984). Immediately to the north of this location, Kellogg and Bonini (1982) identified a seismic zone dipping south-eastwards beneath the South American plate that they interpreted as representing 390 km of non-magmatic subduction of the Caribbean plate, leading to deformation of the Southern Caribbean belt and 7 to 12 km of uplift in the last 10 m.y.

Because of this complex history, the initial size of the Caribbean oceanic plateau is difficult to determine. Exactly how much of the plate is floored by oceanic plateau (rather than normal oceanic crust) is poorly constrained; additionally unknown amounts of plateau material may have been subducted or subcreted, and what remains is frequently, although heterogeneously deformed.

2.5 The South Caribbean plate boundary zone

Although the relative motion between the Caribbean plate and South America (Sykes *et al.*, 1982) is east-west oriented (i.e. approximately parallel to the plate boundary), the border between the two plates is actually a ~ 400 km wide zone of deformation (Fig. 2.4) involving strike-slip faulting in addition to extensional and compressional folding and faulting (Ladd *et al.*, 1990). This transpressive orogenic belt is characterised by diffuse modern seismicity (McCann and Pennington, 1990), but with significant historic earthquakes occurring along the dextral El Pilar fault (Aggarwal, 1983).

The plate boundary zone has been divided, from north to south, into the following belts (summarised from Ladd *et al.*, 1990; Avé Lallement, 1997): 1) the *South Caribbean deformed belt*, consisting of deformed sediments resulting from the recent convergence of the Caribbean and South American plates; 2) the *Aruba-La Blanquilla chain*, discussed in detail in section 2.5.1; 3) the *Falcón and Bonaire basins*, thought to be a consequence of Oligocene and Miocene extensional pull-apart tectonics associated with a dextral strike-slip regime (Muessig, 1984); and 4) the *Venezuelan Andes and Caribbean coastal range*, which are superposed sequences of several nappes thrust southwards over the South American foreland during a period of deformation which lasted from the Cretaceous to the Eocene (Maresch, 1974).

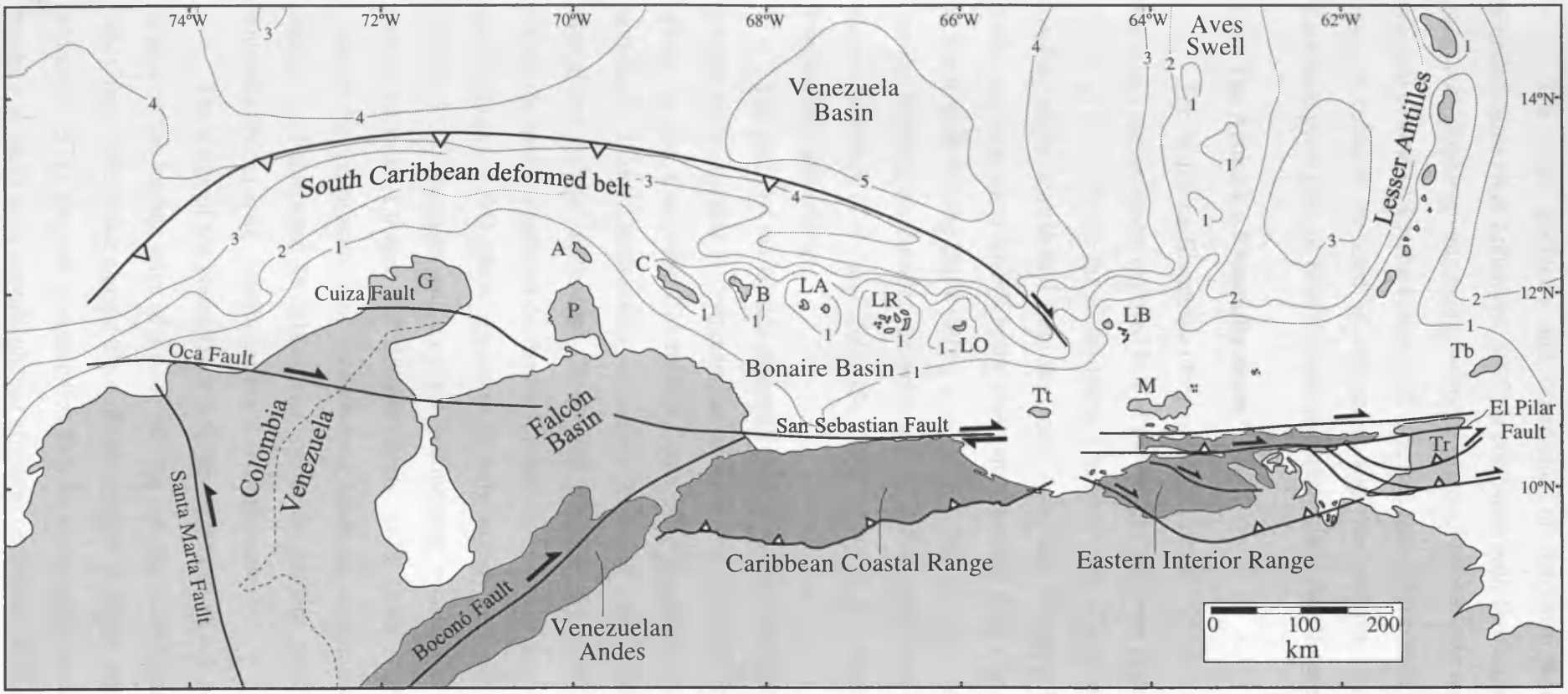

Figure 2.4: Map of the South Caribbean Plate Boundary Zone (adapted from Avé Lallement, 1997; Silver *et al.*, 1975; Maresch, 1974).

Bathymetric contours shown in metres (× 1000)

G: Guajira Peninsula
P: Paraguaná Peninsula
A: Aruba
C: Curaçao
B: Bonaire

LA: Las Aves
LR: Los Roques
LO: La Orchila
LB: La Blanquilla

Tt: Tortuga
M: Margarita
Tr: Trinidad
Tb: Tobago

Thrust fault
Strike-slip fault
Mountainous areas

The style, geometry and orientation of deformation occurring within the plate boundary zone (Avé Lallement, 1997) is consistent with formation in a right-oblique collision zone, with displacements being partitioned into a N-S directed thrust component and an E-W oriented dextral strike-slip component. The fact that deformation appears to be systematically younger towards the east is consistent with the relative eastward advancement of the Caribbean plate past the South American margin since the Cretaceous.

2.5.1 The Aruba-La Blanquilla chain

The Aruba-La Blanquilla chain of islands lies to the north of the Venezuelan coastline, and is the northernmost exposed belt of the South Caribbean plate boundary zone. The largest islands in the chain are the Netherlands Antilles: Aruba, Curaçao and Bonaire. The east-west trending chain is separated from the South American continent by the 2000m deep Bonaire Basin, and individual islands in the chain are separated from one another by grabens bounded by north-west-striking faults (Silver *et al.*, 1975). Seismic, gravity and geological data suggest that the Netherlands Antilles are underlain by a thick (~32 km) high density crust, probably oceanic in nature (Case and Holcomb, 1980), although this large thickness may arise in part from tectonic thickening.

The rocks of the islands generally belong to two groups: Cretaceous igneous or meta-igneous rocks, fringed by Neogene-Recent limestone terraces. The Cretaceous igneous rocks belong to the Caribbean-Colombian Cretaceous Igneous Province and comprise thick, moderately folded, successions of mainly tholeiitic lavas and volcaniclastic rocks, with intercalated pelagic sediments (Beets and MacGillavry, 1977). Tonalitic/dioritic plutons intrude the mafic sequences on Aruba, Curaçao and some of the Venezuelan Antilles (Jackson and Robinson, 1994): these appear to be only slightly younger than the basaltic rocks (see Chapter 4). Campanian and younger sedimentary successions unconformably overlie the igneous rocks on Curaçao and Bonaire (Beets, 1977; Beets *et al.*, 1977), and there is strong evidence for the proximity of a continental landmass at this time (e.g., Precambrian exotic cobbles in a Palaeocene fluviatile conglomerate on Bonaire, possibly derived from the Guajira Peninsula (Priem *et al.*, 1986b; see Fig. 2.4 for location).

The rocks of the Netherlands Antilles were once all considered to be arc-related rocks formed on the leading edge of a plate moving into the Caribbean from the west (Beets *et al.*, 1984), that were thrust against the northern margin of South America in the late Cretaceous (Maresch, 1974), but this interpretation may be oversimplified, as it does not account for the presence of rocks with oceanic plateau affinities on islands such as Curaçao (Klaver, 1987). It

seems to be commonly assumed (e.g., Avé Lallement, 1997) that because the islands form a contiguous chain, they must have a common origin, whereas in reality, it is not known exactly how the exposures in the different islands are related to one another, because of the complexity of the tectonic environment in which they now lie. What is certain is that the chain contains rocks which seem to belong to both arc-related (e.g., Bonaire: Beets *et al.*, 1984) and plateau-related (e.g., Curaçao: Klaver, 1987) parts of the Caribbean-Colombian Cretaceous Igneous Province.

The islands have undergone recent uplift, resulting in the sub-aerial exposure of limestone terraces that reflect late Pleistocene sea level maxima (Herweijer & Focke, 1978). Additionally, there is palaeomagnetic evidence for large clockwise rotations (up to 90°) having occurred on (at least) Aruba and Bonaire at some point after the late Cretaceous (Stearns *et al.*, 1986). It is not known whether these rotations relate to the initial juxtaposition of the plateau and arc sequences next to the South American continent, or to their subsequent history in a dextral transpressive plate boundary zone.

2.6 Summary

- Oceanic plateaux, which are massive basaltic large igneous provinces formed via mantle plume activity, can have profound effects on the tectonic and magmatic evolution of a region, because their inherent buoyancy (especially when young and still hot) can result in a reorganisation of the tectonic plates and subduction zones around them.
- The dominant control on the complex tectonic and magmatic evolution of the Caribbean region was the arrival of the Caribbean oceanic plateau, which formed in the Pacific region, and moved eastwards relative to the Americas until it reached its present location in the Caribbean region.
- The Caribbean oceanic plateau was constructed at ~ 91 - 88 Ma (Sinton *et al.*, 1998).
- Arc-related sequences associated with the Caribbean plateau fall into two categories: tholeiitic arc rocks that may be tectonically accreted to the plateau, and calc-alkaline rocks that have erupted through (or intruded into) the plateau.
- The area studied as part of this thesis – Aruba – is located within the South Caribbean plate boundary zone, adjacent to the Venezuelan continental margin: this area is the focus of the following chapter.

Chapter 3

The Field Geology of Aruba

3.1 Introduction

The island of Aruba is located in the southern Caribbean region, approximately 40 km from the Paraguanà peninsula of the Venezuelan mainland (Figs. 2.2; 2.4). Aruba is one of a chain of islands, the "Aruba - La Blanquilla" chain, which extends for 600 km in an E-W orientation, parallel to the northern margin of South America. This island chain is separated from the mainland by the Bonaire Basin, which reaches a maximum depth of over 2000 metres; to the north, beyond the Curaçao ridge, lies the Venezuela Basin. Aruba and the neighbouring islands of Curaçao and Bonaire are the three largest islands in the chain.

Aruba is an elongate island about 30 km long and 10 km wide (Fig. 3.1). The long axis of the island lies NW-SE. Trade winds blow across Aruba from east to west, and calcareous beach deposits have accumulated along west- and south-west facing shorelines. Precipitation is low, and falls mainly in November and December. Most evaporates or runs off rapidly, and the scrubby vegetation, such as cactus and mimosa, is indicative of the arid environment. Geologically, Aruba consists of a Cretaceous sequence of mafic lavas and sediments, the Aruba Lava Formation, intruded by a predominantly tonalitic batholith. The igneous core of the island is fringed by unconformably overlying Neogene and Quaternary limestones, which have now been uplifted.

The island has low topography, reaching a maximum of 190 metres (Jamanota[1]) in the outcrop area of the Aruba Lava Formation (Fig. 3.1). The outcrop area of the Aruba Lava Formation is the most undulating, due to the large contrast in resistance to erosion of its lavas, tuffs and deformed equivalents: valleys trend E-W, parallel to the structural grain of the rocks. The area where the batholith is exposed has lower relief and altitude, although there are a number of small, often conical, hills which have developed where the more resistant mafic parts of the batholith are exposed (Fig. 3.3). The largest of these is the Hooiberg[2] (168 metres), the type locality of a coarse amphibole-rich gabbroid rock, named "hooibergite" by Westermann (1932). The topography of the batholith is closely linked to lithology - hilly, mafic portions of the batholith are more abundant along the NE coast (Fig. 3.4). The

[1, 2]: Throughout this chapter, numerals in superscript refer to localities indicated on the map of Aruba (Fig. 3.2).

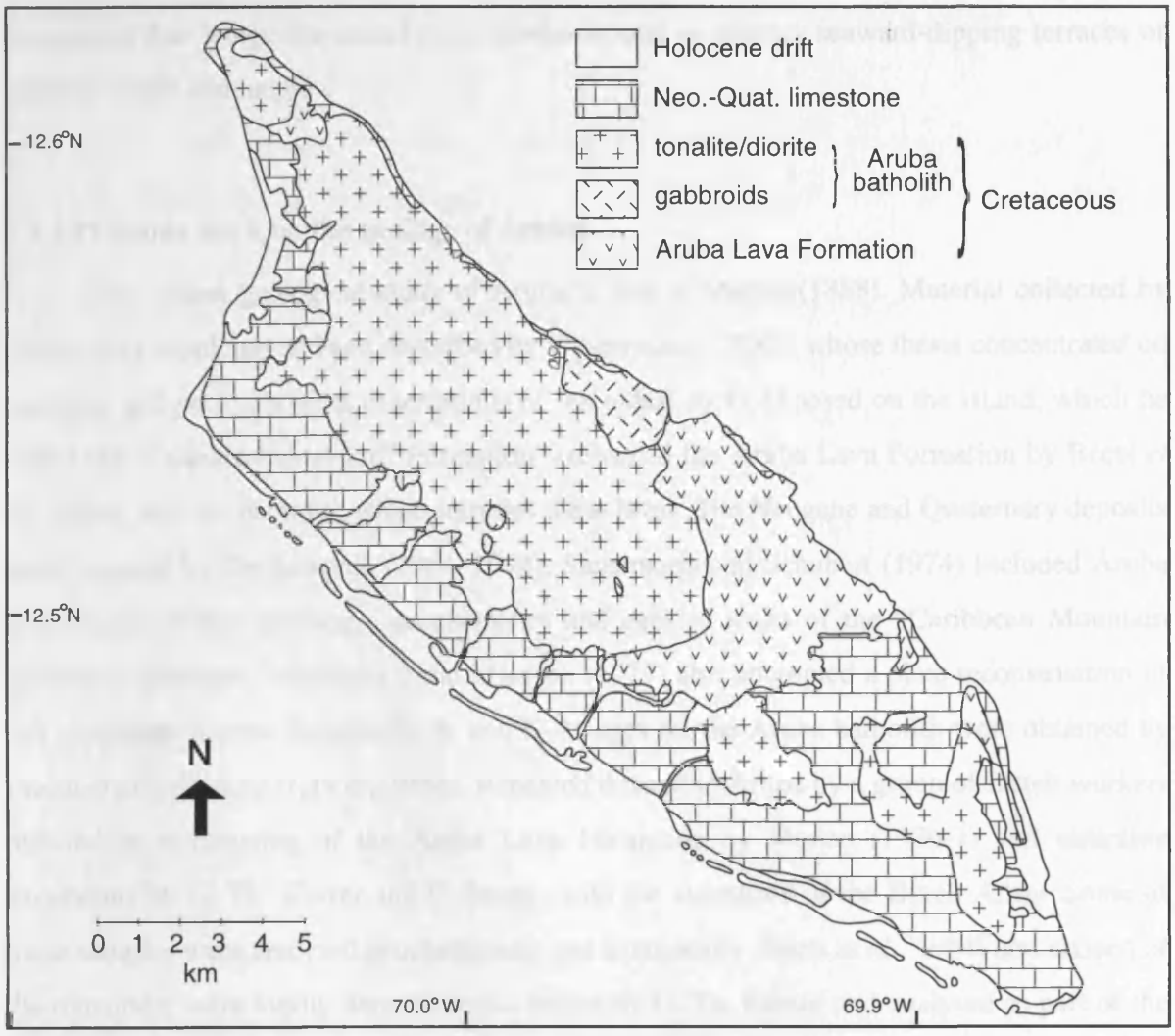

Fig. 3.1: Simplified geological map of Aruba, after Beets *et al.*, 1996.

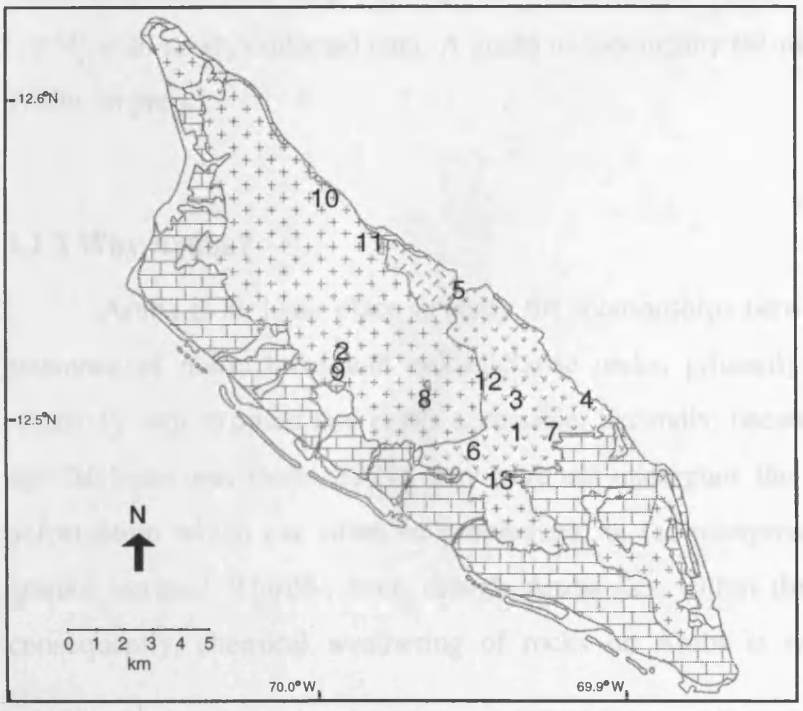

Fig. 3.2: Localities mentioned in the text of Chapter 3, in order of appearance.

1. Jamanota
2. Hooiberg
3. Mira La Mar
4. Dos Playa
5. Andicuri
6. Wela
7. Juditi
8. Warawara
9. Canashito
10. Sero Pos di Nord
11. Wariruri
12. Arikok
13. Shidiharaca

limestones that fringe the island form sub-horizontal or slightly seaward-dipping terraces of variable width and height.

3.1.1 Previous work on the geology of Aruba

The oldest geological study of Aruba is that of Martin (1888). Material collected by Martin was supplemented and described by Westermann (1932), whose thesis concentrated on mapping and petrographical descriptions of the oldest rocks exposed on the island, which he called the "Diabase-Schist-Tuff Formation" (renamed the Aruba Lava Formation by Beets *et al.*, 1984), and the batholith which intrudes these lavas. The Neogene and Quaternary deposits were mapped by De Buisonjé (1964, 1974). Santamaría and Schubert (1974) included Aruba in a review of the petrology, geochemistry and ages of rocks of the "Caribbean Mountain System of Northern Venezuela", and Maresch (1974) also attempted a plate reconstruction of this mountain system. Several Rb-Sr and K-Ar ages for the Aruba batholith were obtained by Priem *et al.* (1966;1977;1978;1986a). Renewed interest in Aruba by a group of Dutch workers resulted in re-mapping of the Aruba Lava Formation by Monen (1976-7) and sampling excursions by G. Th. Klaver and F. Beunk, with the assistance of the Dutch Army. Some of these samples were analysed geochemically and isotopically (Beets *et al.*, 1984) and sixteen of the remainder were kindly donated to the author by G. Th. Klaver and analysed as part of the present study. A new geological map of Aruba has recently been published (Beets *et al.*, 1996) which combines data from the maps of Westermann (1932), Monen (1977) and De Buisonjé (1974) with newly collected data. A guide to accompany the map is in preparation (Beets and White, in prep.).

3.1.2 Why Aruba?

Aruba is an ideal place to study the relationships between a tonalitic batholith and a sequence of mafic lavas and volcaniclastic rocks, primarily because both rock types are relatively well exposed and easily accessible. Secondly, because the rocks are Cretaceous in age (Helmers and Beets, 1977), they have not undergone the significant metamorphism and deformation which can often be problematic in the interpretation of Archaean greenstone-granite terranes. Thirdly, even though Aruba lies within the tropics, it is relatively arid; consequently, chemical weathering of rocks on Aruba is much less severe than that on

northern Caribbean islands, making it ideal for the collection of fresh samples for geochemical analysis.

Aruba does, however, also have several problems. In many places, "exposure" of the batholith actually consists mainly of giant rounded boulders derived from the underlying bedrock by spheroidal weathering (Fig. 3.5). This means that orientations of structures observed cannot be determined unequivocally, although the "corestones" have probably not been moved very far from their original location, and some may be *in situ*. Likewise, true exposure of the Aruba Lava Formation is in many places covered by loose debris (Fig. 3.6). Intrusion of the batholith has led to variable degrees of contact metamorphism of the Aruba Lava Formation (Helmers and Beets, 1977) and so Aruba is not the best place for a detailed petrographic, geochemical or geochronological study of the basalts. In contrast, the neighbouring island of Curaçao has a sequence of basalts and picrites of a similar age (Beets and MacGillavry, 1977), which have not been significantly affected by metamorphism. Published data from Curaçao (Kerr *et al.*, 1996b) have therefore been used for comparison with the Aruba Lava Formation.

Additionally, palaeomagnetic studies of Aruba and Bonaire (Stearns *et al.*, 1986) have demonstrated that the island may have rotated by up to 90° clockwise since intrusion of the batholith. This rotation may be related to Aruba's present location in a complex dextral strike-slip plate boundary zone (Mann *et al.*, 1990), or possibly to earlier events. This leads to uncertainly in the interpretation of structural information.

3.1.3 Fieldwork logistics and aims

Approximately three months were spent in the field in Aruba. This time was divided between two field seasons, in the winters of 1996 and 1997.

The specific aims of the fieldwork were:

- to document and describe the range of lithologies present in the Aruba Lava Formation and the Aruba batholith.
- to provide appropriate samples for geochemical and isotopic analysis of the whole range of lithologies observed.
- to determine the field relationships between the Aruba Lava Formation and the batholith, i.e., to determine whether they are in intrusive or tectonic contact.

- to elucidate the relationships between the various lithologies of the batholith, particularly the age relationships.
- to collect information on the structure of the Aruba Lava Formation.

Geological mapping of Aruba was not considered a priority for this study, since many of the relationships of interest occur on too small a scale for mapping to be useful, and because a recent geological map already exists (Beets *et al.*, 1996).

3.1.4 Sampling strategy

In total, 212 samples were collected for geochemical analysis, in addition to those donated by G. Th. Klaver, and a number of samples taken purely for petrographic and microprobe study. Care was taken to ensure that the samples selected accurately represented the range of lithologies present, and the freshest rocks possible were targeted. Weathered surfaces were removed in the field. Not all of the samples came from *in situ* exposures, especially for the batholith, where very little of the rock was truly *in situ* and any that was seemed determined to stay there; however, great care was taken to choose samples which were clearly not far removed from their original location. Samples ranged in size from 0.5 kg for basalts to 4 kg for tonalites, reflecting the increasing mass of rock required for a representative sample as the grain (crystal) size of the rock increases. For some of the very coarse-grained (~2 cm) members of the batholith (e.g., the "hooibergites"), it was logistically unrealistic to collect and transport truly representative samples, and this has been considered when interpreting the geochemical results.

3.2 The Aruba Lava Formation

3.2.1 Lithologies of the Aruba Lava Formation

The rocks of the Aruba Lava Formation can be subdivided into three lithological varieties: basalts, dolerites and interbedded volcaniclastic rocks. Their occurrence and appearance is discussed below.

3.2.1.1 Basalts

The basalts occur mainly as sheets and flows with some pillow lavas (Fig. 3.7), and are usually fine-grained (occasionally aphanitic) and aphyric. No glassy chilled margins to the

Fig. 3.3: General view of Aruba, taken from the hills of the Aruba Lava Formation, looking towards the outcrop area of the batholith. The cone-shaped hills are mafic parts of the batholith. The largest of these, in the distance, is the Hooiberg[2].

Fig. 3.4: View shows a range of rock types within the batholith. Mafic rocks tend to form hills.

Fig. 3.5: "Corestones" of tonalite derived from the underlying bedrock by spheroidal weathering.

Fig. 3.6: General view of the Aruba Lava Formation showing the abundant surface debris.

Fig. 3.7: Pillow basalts within the Aruba Lava Formation.

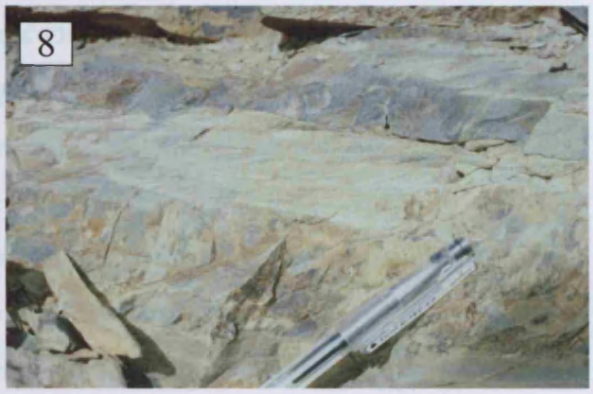

Fig. 3.8: Fine sand- to silt-grade volcaniclastic sediment in the Aruba Lava Formation shows ripple cross-bedding.

pillows have been preserved. Often, vesicles are present in a zone parallel to the pillow margin, and, in some cases, these are the only visible evidence for the basalt being pillowed (e.g., Mira La Mar[3]). In other cases, there is no evidence for pillow structures, and the basalts are interpreted as being massive flow units. Quality of exposure of these units is not sufficient to determine thicknesses of individual flows.

3.2.1.2 Dolerites

Dolerites occur as sill-like thick sheets, successions of which can reach thicknesses of up to 400 metres. They are found throughout the formation. From the field relationships, it is impossible to tell if their origin is intrusive, or if they represent the bases of thick flows. However, the presence of some very coarse grained variants suggests the former interpretation. Because of their hardness and resistance to erosion, the dolerites form topographic highs.

In general, they are texturally equigranular and medium grained. The colour index is high, and the rocks are homogeneous. In the freshest samples, plagioclase and pyroxene can be distinguished in hand specimen.

3.2.1.3 Volcaniclastic material

Reworked volcaniclastic siltstones and sandstones

Most of the volcaniclastic material in the Aruba Lava Formation occurs as reworked sedimentary deposits interbedded with the basalts. Its volcanogenic origin is testified by its chemical and textural immaturity - the angular grains consist predominantly of feldspars and mafic minerals with some quartz, and crystal or cleavage faces can sometimes be observed. Sorting is generally good, but this is more likely to result from reworking of the sediment rather than the original size distribution of the volcanic-derived grains. Grain size varies from coarse sand to fine silt, and bed thickness ranges from millimetre-scale to decimetre-scale. Colour on a fresh surface is usually greyish green, while weathered samples are always brown.

Sedimentary structures preserved include:

1. Ripple-scale cross laminations (Fig. 3.8), suggesting reworking of material in shallow water (i.e., above the storm wave-base) or by turbidity currents.
2. Contorted bedding (Fig. 3.9), which could have arisen either from deposition of material on a slope too steep for the sediment to be stable, or movement of unconsolidated sediment during an earthquake. Either or both mechanisms are reasonable for sediment deposited on the flank of an erupting volcano.

3. Graded bedding (Fig. 3.10), suggesting re-deposition of sediment from turbidity or storm currents. It is also possible that the graded bedding could be a primary (i.e., not reworked sedimentary structure arising from air-fall of material from an ash cloud into shallow water, but it is difficult to distinguish between these modes of origin with the limited data available.

These sedimentary structures suggest that the volcaniclastic deposits were laid down in a dynamic sedimentary environment, close to an eruptive centre. Re-working of material by turbidity currents is consistent with 1) the observation of graded bedding and ripple cross bedding; and 2) the inference that slope instability resulted in the convoluted bedding.

Non-reworked pyroclastic material

Pyroclastic sediments occur in which accretionary lapilli are preserved (Fig. 3.11). This suggests that extensive reworking of this sediment has probably not occurred, since none of the lapilli seem to be broken or damaged.

A very coarse-grained rock of probable pyroclastic origin (Fig. 3.12) is found in the section at Dos Playa[4]. It consists of clasts ranging from 2 mm to 4 cm, which are light grey in colour and very irregular in outline. The clasts appear to be flattened parallel to bedding, giving the rock a coarse eutaxitic texture. A small proportion (less than 1%) of the clasts are made of black, very fine-grained cherty material. The abundant pale grey clasts are also extremely hard and fine-grained, and may also be siliceous. The extreme hardness and toughness of this lithology, and the sharp surfaces produced on fracturing suggest that the rock has been extensively silicified - this leads to difficulties in determining the original composition of the pale grey clasts. However, the texture of the rock suggests an ignimbritic origin.

Basaltic conglomerates and breccias

At the summit of Jamanota[1] and several other localities in the southern part of the outcrop region of the Aruba Lava Formation, breccio-conglomerates occur (Fig. 3.13). According to Monen (1977), these are restricted to one stratigraphic horizon, and have correspondingly been used to elucidate the large-scale structure. The sequence of conglomerates is up to 50 metres thick.

Clasts within these rudaceous rocks range in size from a few mm to 15 cm and are usually sub-rounded, although at a few localities angular to sub-angular clasts occur. The

Fig. 3.9: Convolute bedding (by hammer head) in a volcaniclastic sandstone of the Aruba Lava Formation.

Fig. 3.10: Graded bed in volcaniclastic sandstone of the Aruba Lava Formation.

Fig. 3.11: Tuff consisting of accretionary lapilli in the Aruba Lava Formation. The lapilli have been deformed (flattened and elongated) since their deposition.

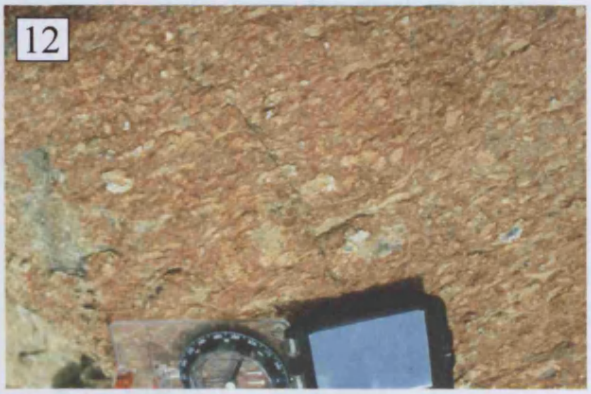

Fig. 3.12: Coarse volcaniclastic rock with eutaxitic texture.

Fig. 3.13: Breccio-conglomerate in the Aruba Lava Formation. Clasts consist almost entirely of basalt and dolerite.

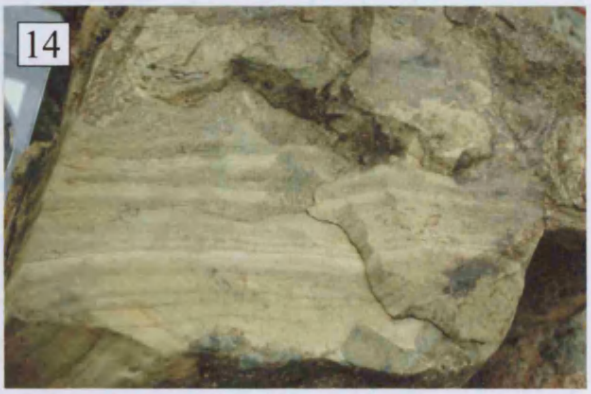

Fig. 3.14: Fine scale graded beds interbedded within the basaltic conglomerate.

composition of the clasts is almost entirely basaltic and doleritic, although a few small clasts of volcaniclastic sandstone are present. The conglomerate is usually clast-supported, but, at a few horizons, interbedded graded medium-fine sandstones are seen (Fig. 3.14). It has been argued that the deposition of the conglomerates represents a period of sub-aerial sedimentation in a fluviatile environment (Beets *et al.*, 1984), but certain features of the deposit are more consistent with a debris avalanche origin, particularly the massive bedding, the presence of occasional graded beds within the deposit, the lack of any cross-bedding or imbrication and the relatively poor sorting of the clasts. Consequently, in this study, the lithology is interpreted as resulting from a debris avalanche into a sedimentary environment usually dominated by small-scale turbiditic flows, which are represented by the fine-grained volcaniclastic material. Whether an origin in a fluviatile or turbiditic environment is preferred, subaerial erosion of basalts and dolerites seems to be necessary to derive the clasts initially.

3.2.2 Stratigraphy of the Aruba Lava Formation and its significance

According to the map of Monen (1977), the approximate proportions of the different lithologies exposed are:

dolerites	24%	~5 km^2
basalts	41%	~8 km^2
pyroclastic/volcaniclastic sediments	35%	~7 km^2

There seems to be no overall gradation (e.g., from basalt-dominated to volcaniclastic-dominated) in the mapped sequence.

Three points must be emphasised about this stratigraphy - firstly, the dominance of material of a mafic composition; secondly, the absence of any sedimentary material of an obviously continental provenance (confirmed in thin section: see Chapter 5); and finally, the high abundance of volcaniclastic deposits compared with the neighbouring island of Curaçao. These observations provide constraints on the environment of formation.

The deficiency of continental-derived sediments implies that the Aruba Lava Formation was deposited a significant distance from any continental source. This implication, compared with Aruba's present location, only 40 km from the South American mainland, supports models (e.g., Pindell and Barrett, 1990) suggesting that the whole Caribbean plate, including Aruba, is allochthonous. The abundance of pillowed basaltic material also supports

an entirely oceanic association; however, the sequence cannot represent normal ocean floor material, because of the presence of so much volcaniclastic material.

The presence of abundant vesicles in pillowed basalts points to a relatively shallow sub-aqueous environment, with hydrostatic pressure being insufficient to inhibit degassing of the magma. (Note that it is difficult to assign a value to the maximum water depth at which vesicles can form, because it is also dependent on the volatile content of the magma). Sedimentological features of the volcaniclastic rocks also suggest reworking in relatively shallow water above the storm wave-base, or by turbidity currents. Convolute bedding indicates sediment instability, which could arise from deposition on a slope, nearby earthquake activity, or both. Clasts in the basaltic conglomerate have probably been derived via sub-aerial erosion. Together, these features imply deposition of the Aruba Lava Formation on the flanks of an emergent volcano.

One noticeable paradox in the stratigraphy is the association of uniformly mafic extrusive and intrusive magmas with such a large volume of volcaniclastic material, because under normal circumstances, basaltic magma tends not to be involved in explosive volcanic activity. Does the volcaniclastic material represent explosive eruption of more evolved compositions? The lack of any observed corresponding lava compositions suggests that this is unlikely. Instead, if the sub-aqueous/sub-aerial environment is considered, it seems likely that basaltic magmas could have become involved in explosive hydromagmatic activity, resulting in copious fragmental matter. The accretionary lapilli, too, suggest the existence of moist eruption clouds.

Both an oceanic arc environment and an oceanic plateau environment are broadly consistent with the lithological and stratigraphic observations, although the dominance of mafic material fits better with the oceanic plateau scenario. Geochemical and isotopic studies are required to distinguish unequivocally between these environments, and are discussed in Chapter 6.

3.2.3 Age of the Aruba Lava Formation

No palaeontological evidence for the age of the Aruba Lava Formation was found during the present study; however, imprints of ammonites have previously been recovered from a pebbly mudstone intercalated between basaltic flows near Dos Playa[4]. None have been formally described or identified, but MacDonald (1968) and Wiedmann (reported in Beets *et al.*, 1984) independently concluded that the fauna have a Turonian age (93.3 - 88.7 Ma).

Radiometric dating has so far been inconclusive, and is discussed further in Chapter 4.

3.2.4 Metamorphism and Deformation of the Aruba Lava Formation

The rocks of the Aruba Lava Formation are metamorphosed to prehnite-pumpellyite, greenschist or amphibolite facies. The metamorphism appears to be at least partly due to the intrusion of the batholith, because the metamorphic grade increases from east to west, towards the margins of the batholith. The maximum metamorphic grade achieved at the margin of the batholith is amphibole-hornfels facies.

3.2.4.1 Amphibolites: purely contact metamorphism?

Amphibolite-facies rocks which occur at the margins of the batholith have previously been interpreted purely as contact amphibolites (Beets *et al.*, 1984), which is true in some localities. These amphibolites are homogeneous and isotropic. However, a second class of amphibolites has also been identified close to the margins of the batholith. These have a well-developed foliation defined by alignment of tabular plagioclase crystals, and therefore cannot have formed simply by contact metamorphic processes. This class was also observed by Westermann (1932), and occurs primarily at Andicuri[5]. Sometimes a lineation, defined by elongated amphibole crystals, is preserved.

These amphibolites are highly heterogeneous, consisting of bands of different compositions, ranging from almost pure amphibole through amphibole + plagioclase (the dominant mineral assemblage) to purely felsic segregations (Fig. 3.15). This range of mineral assemblages, and the observed textures, are consistent with partial anatexis of a meta-basic amphibolite facies rock, where the amphibole-rich parts represent a residue of melting and the quartz-plagioclase segregations represent liquid compositions (Winther, 1996). Such migmatisation would require high temperatures. It is possible that the high-T contribution is provided by the batholith; however, some movement is also required to produce the foliation and lineation. At Andicuri[5], the foliation is orientated approximately 050°/50° SE and the lineations plunge roughly 40° to the south. Shear bands (Fig. 3.16) suggest top-to-the-north displacement, i.e., a sinistral oblique thrust sense of shear.

The significance of these sheared (as opposed to isotropic) amphibolites remains unclear. At Andicuri[5], the amphibolites are separated from less-metamorphosed, non-deformed members by a ~50m wide zone that has been heavily intruded by tonalitic composition melts. This region appears to have been a zone of substantial fluid movement

thereafter; the rocks observed here are heavily altered and occasionally silicified. This boundary is interpreted as a fault zone.

If the Andicuri[5] amphibolites are indeed regional amphibolites created at some depth, then their exhumation poses a problem, given the absence of any large scale structural features usually required to uplift and expose these sorts of rocks. The working hypothesis in this study is that they did not come from a particularly deep level, but are at amphibolite facies because of the extra heat provided by the batholith. Because the outcrops of the sheared amphibolites are extremely localised (they occur on a scale of ~100 m close to the margins of the batholith), it is possible that they could have been exhumed as the neighbouring batholith ascended through the crust, pulling some of the adjacent country rocks with it. This mechanism would also explain the apparent fault zone between the amphibolites and the less metamorphosed, non-deformed members.

If the process were occurring, could it have been responsible for forming the foliation? Three observations suggest not. Firstly, the foliation is better-developed farther away from the contact with the batholith, suggesting that thermal input from the batholith has overprinted and destroyed the foliation. Secondly, mineral lineations in the amphibolite together with poorly developed shear sense indicators suggest oblique sinistral thrusting in the amphibolite. The foliation in the amphibolite dips away from the tonalite contact, therefore, if the foliation had been formed by a magma body trying to push up through the amphibolite, the lineation should be steeply plunging and the shear sense indicators should show a normal displacement. Thirdly, foliated xenoliths of amphibolite were found in the tonalite (Fig. 3.17). These observations all indicate that the foliation-forming event at amphibolite facies occurred earlier than the intrusion of the batholith. This is consistent with a regional-metamorphic origin for the amphibolites.

3.2.4.2 Deformation of the Aruba Lava Formation

Folding

According to Monen (1977), the structure of the Aruba Lava Formation consists of, from south to north, a faulted syncline and anticline. The majority of the outcrop area represents the northward dipping north limb of the anticline.

At certain localities, a cleavage is observed that has many of the features of an axial planar cleavage (Fig. 3.18). It cross-cuts bedding in fine-grained volcaniclastic sediments, but the bedding is not disrupted, so it is not a shear cleavage. In places, the cleavage is refracted where the grain size of the sedimentary rock changes.

Fig. 3.15: Amphibolite showing signs of partial anatexis: the white areas are silicic segregations and the very dark regions are interpreted as amphibole-rich residues.

Fig. 3.16: Shear bands in an amphibolite facies member of the Aruba Lava Formation suggest top-to-the-north displacement.

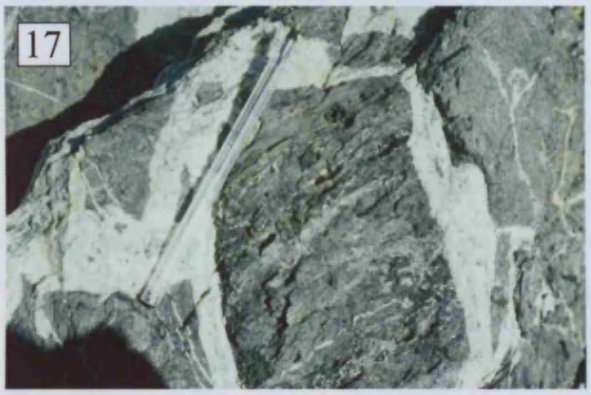

Fig. 3.17: A xenolith of foliated amphibolite in a trondhjemitic melt.

Fig. 3.18: Bedding-cleavage relationships in the Aruba Lava Formation: cleavage is sub-vertical.

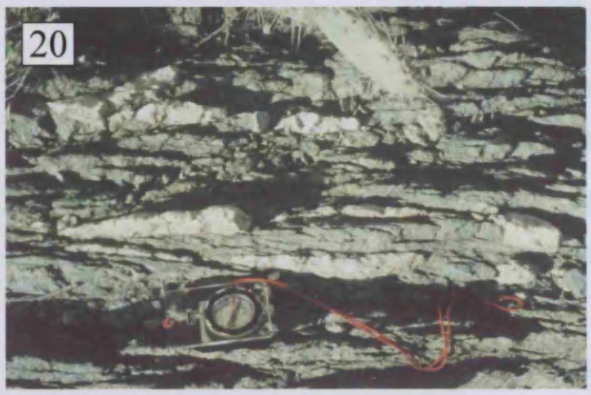

Fig. 3.20: Tonalite boudins within a shear zone of the Aruba Lava Formation.

Fig. 3.21: Chevron folds in a shear zone of the Aruba Lava Formation. These fold the earlier shear cleavage.

Stereographic analysis (Fig. 3.19) of the structural data obtained for the northward-dipping northern limb and the axial-planar cleavage predicts that the other limb of the fold should have an attitude of 128°/28° SW. Beds with this attitude are not observed, suggesting that the structures in the south of the region are not related to those at Dos Playa[4]. Unfortunately, a thorough search of this area failed to uncover a coherent structural story. Five bedding measurements were found that were not dipping to the NE, but these seemed to be randomly dispersed over the stereonet. At one locality, the bedding and cleavage were at roughly 90 degrees to one another (i.e., the definition of a fold hinge zone) but again, when plotted on the stereonet, they did not produce a coherent story. The following conclusions can be drawn:

1. The area has been compressed and folded sufficiently strongly for an axial planar cleavage to develop. The other limb, which theoretically should be shallowly dipping approximately SW, appears to be missing.
2. The area is dissected by numerous small faults, thus beds are effectively no longer *in situ*, and may have been rotated. This may explain the nonsensical hinge bedding measurements. It should be possible to determine if rotation has occurred by looking at the orientation of the cleavage, but in these localities the rock was so heavily faulted and jointed that it was not possible to tell exactly which set of planes was cleavage.
3. The area has also been affected by intrusion of porphyritic tonalite bodies, probably related to the Aruba batholith, which may have also resulted in re-orientation of bedding in the Aruba Lava Formation.

Ductile deformation

Another cleavage with a different orientation from the axial planar cleavage described above occurs in a 1 km wide zone near Jamanota[1] (Fig. 3.20) and Wela[6]. This foliation is a shear foliation: it is anastamosing and small shear sense indicators are seen (albeit rarely). No bedding is preserved and quartz veins cutting the main foliation are deformed. At Juditi[7], a rock consisting of deformed accretionary lapilli is found (Fig. 3.11) - the once spherical lapilli are now flattened elongate ellipsoids. This cannot be accounted for by compaction and flattening alone, as this would result in non-elongate disc-shaped lapilli. Therefore, an element of simple shear is required to explain the observed shape distribution. The shear foliation strikes approximately E-W and is subvertical.

Fig. 3.19: Stereographic analysis of structural data (bedding and cleavage) from volcaniclastic rocks of the Aruba Lava Formation. Only one limb of this large-scale fold is exposed on Aruba.

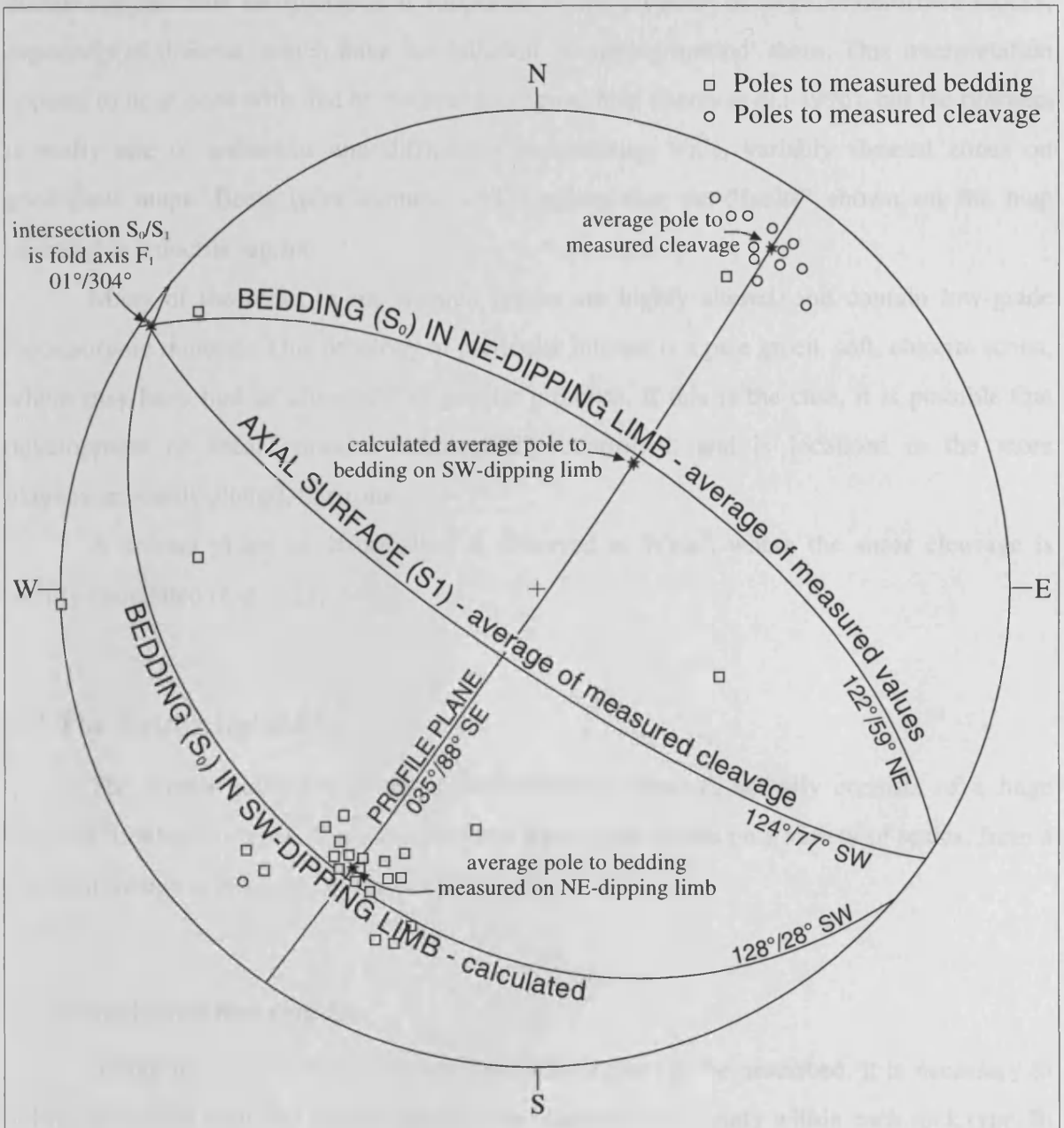

Result: given the attitude of one limb and the axial planar cleavage, the attitude of the other limb is estimated to be 128°/28° SW.

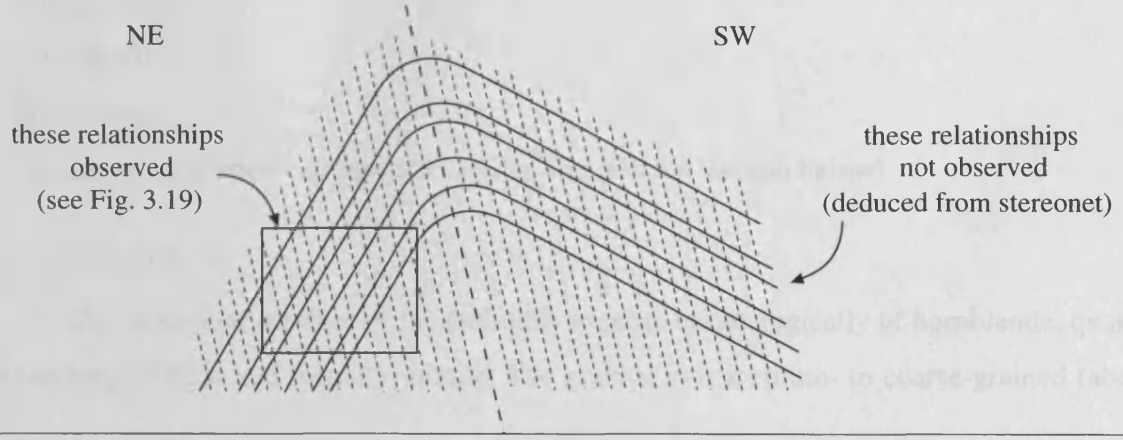

This shear cleavage is interpreted as having formed in a wide shear zone operating in a ductile regime. This interpretation is supported by the presence of large, undeformed blocks, especially of dolerite, which have the foliation 'wrapping around' them. This interpretation appears to be at odds with that of the new geological map (Beets *et al.*, 1996), but the problem is really one of semantics and difficulties representing wide, variably sheared zones on geological maps. Beets (pers. comm., 1997) agrees that the "faults" shown on the map operated in a ductile regime.

Many of the rocks in the sheared region are highly altered, and contain low-grade metamorphic minerals. One lithology of particular interest is a pale green, soft, chlorite schist, which may have had an ultramafic or picritic protolith. If this is the case, it is possible that development of shear zones is lithologically controlled, and is localised in the more magnesian, easily altered, horizons.

A second phase of deformation is observed at Wela[6], where the shear cleavage is locally crenulated (Fig. 3.21).

3.3 The Aruba batholith

The Aruba batholith, although predominantly tonalite, actually consists of a huge range of lithological types. Variation between these types occurs on a variety of scales, from a few centimetres to hundreds of metres (Fig. 3.22).

3.3.1 Lithological descriptions

Before the relationships between these lithologies can be described, it is necessary to define the names used and discuss the features observed and variety within each rock type. In general, four field criteria enabled classification of the lithologies. Those were:

1. Colour index
2. Crystal size
3. Mineralogy
4. Certain textural observations (discussed in the relevant section below).

3.3.1.1 Tonalite

This abundant member of the batholith consists mineralogically of hornblende, quartz, plagioclase feldspar and (usually) biotite. The grain size is medium- to coarse-grained (about

3 mm), although hornblendes are often larger (up to 10 mm: Fig. 3.23). The colour index varies from 10% to about 30% mafic minerals, with varieties at the high end of the range being termed mela-tonalites. Trondhjemite was used for varieties with less than 10% ferromagnesian minerals. The hornblendes in an average tonalite are quite elongate, with an aspect ratio greater than 3. Some show crucifix twinning. The prefixes fine- and micro- were used for types with, respectively, finer than average grain size and grain size less than 1 mm. Often, a slight foliation is developed, but this is not ubiquitous.

3.3.1.2 Diorite

The diorites are texturally similar to the tonalites, with a grain size of 2 - 3 mm. They tend to be more equigranular, because the hornblendes are the same size as the other minerals. Diorites differ from tonalite mainly in terms of their colour index, which ranges from 30% to 55%, with the darker varieties being called mela-diorites. Similarly, finer-grained varieties have been given the prefix micro-. The mineralogy is the same as that of the tonalite, except that the increase in abundance of hornblende is mirrored by a decrease in the felsic minerals, and biotite is significantly less common.

In addition to the "normal" diorites, two textural sub-groups are defined: "stubby" diorite, where the hornblende crystals have a distinctly different equant shape with aspect ratio <2, compared to the "normal" diorites with their more elongate hornblendes; and "hooibergitic diorite", where large 1-2 cm hornblende crystals poikilitically enclose the other minerals.

3.3.1.3 Hooibergite

This term applies to a melanocratic, coarse-grained, plutonic rock containing essential hornblende, with varying amounts of plagioclase, clinopyroxene and occasionally quartz. The name is reserved exclusively for a rock with a particularly distinctive texture where the rock is visually dominated by large (5 mm - 50 mm) euhedral, sub-equant hornblende crystals. The epithet was originally introduced by Westermann (1932), after "a beautiful, darkcoloured, igneous rock, in which many big hornblende crystals are particularly striking" was found to make up a hill known locally as the Hooiberg[2] (Dutch for haystack).

In this thesis, the above terminology is preserved, because the more correct terms of meladiorite or hornblende-gabbro, in my opinion, neither adequately describe this lithology, nor distinguish between it and other texturally "normal" meladiorites or hornblende-gabbros.

Fig. 3.22: Six phases of intrusion within a small outcrop of the batholith.

Fig. 3.23: The texture of a typical tonalite.

Fig. 3.24: Magmatic layering, defined by bands of different mineralogical composition, in a hooibergite.

Fig. 3.25: Cuspate contacts between three sub-lithologies of hooibergite. These suggest that different magmas co-existed in a liquid state.

Fig. 3.26: Magmatic layering in a gabbro-norite is displaced by syn-magmatic faults.

Fig. 3.27: A thin mafic dyke cross-cuts the batholith.

Hooibergites are highly variable, with colour index ranging from 55% to 100% (hornblendite). The large euhedral hornblende crystals sit in a finer grained, often greenish coloured, matrix of plagioclase ± clinopyroxene (± quartz). In some places, banding of probable cumulus origin occurs in the hooibergite (Fig. 3.24). Gradational contacts between sub-groups of this lithology are present, as are rare cuspate contacts (Fig. 3.25).

The term "dioritic hooibergite" has been adopted for a hooibergite where the plagioclase in the matrix is coarse-grained and prominent, and "hooibergitic" has also been used as a textural adjective to describe, for example, a diorite or gabbro with a poikilitic overgrowth of large equant hornblendes.

3.3.1.4 Gabbro

Gabbros in the Aruba batholith are transitional from the diorites, and in the field the distinction between the two is somewhat arbitrary. They are relatively coarse-grained (2 - 4 mm), equigranular and have a colour index of 55% to about 80%. Mineralogically, they contain plagioclase, hornblende and pyroxene. Olivine, biotite and quartz occur, but rarely. Some of the hornblende may be secondary after pyroxene.

In some places, the gabbro possesses prominent magmatic layering (e.g., the Wariruri[11] layered gabbro series), sometimes showing spectacular structures such as syn-magmatic faulting (Fig. 3.26). This layering is interpreted as being of cumulus origin; however, when observed *in situ*, it dips steeply to the south. If the cumulus interpretation is correct, and the layers originally formed with a horizontal attitude, this implies that (at least these portions of) the batholith have undergone significant rotations. Other gabbro bodies show either no distinctive magmatic layering, or very subtle layering.

3.3.1.5 Porphyritic rocks

At least two distinctive porphyry types occur within the Aruba batholith, and are also intrusive into the Aruba Lava Formation.

The first type, hornblende-plagioclase porphyry, consists of 2 - 3 mm phenocrysts of hornblende and plagioclase in a fine grained mid-to-light grey coloured matrix. The morphology of the phenocrysts is very similar to that of the same mineral where it occurs in the tonalite, and consequently, they are interpreted as more quickly-cooled relatives of the tonalite. This link is strengthened by the presence of occasional porphyries bearing biotite phenocrysts, and the petrographic and geochemical studies (see Chapters 7 and 8) are also consistent with a close relationship between the two rock groups.

The second type of porphyry appears to be considerably more mafic. The phenocrysts are mainly amphiboles, and the matrix is darker-coloured and often finer-grained. These rocks could be more quickly-cooled relatives of the diorites, or may be related to the aphyric mafic dykes (see below).

3.3.1.6 Leucocratic material

Much of the material cross-cutting the batholith is extremely leucocratic, containing no ferromagnesian minerals. The quartz- and feldspar-bearing acid material can be either pegmatitic or aplitic in texture. Quartz veins with coarse grain sizes cross both the batholith and the Aruba Lava Formation. These veins have been of historical and economic importance for Aruba, because they are gold-bearing. The first gold discovery was of a nugget in 1824 (reported in Beets and White, in prep.), and exploitation ceased in 1914 (Westermann, 1932).

3.3.1.7 Late mafic dykes

Mafic dykes also cross-cut the batholith. These range from 1 cm (Fig. 3.27) to approximately 2 m in thickness. The thinnest sheets are very fine grained and dark coloured, but thicker ones may begin to develop a porphyritic texture with amphibole phenocrysts. Occasional large feldspar crystals appear to have been assimilated from the surrounding tonalite and are xenocrysts rather than true phenocrysts. A different group of mafic dykes has a greenish colour and a granular, medium grained texture.

3.3.2 Relationships between members of the batholith

One of the primary aims of the fieldwork was to determine a sequence of intrusion for the different members of the batholith. This turned out not to be a straightforward task, since many of the relationships were ambiguous, or gave opposing conclusions in different localities. Observations utilised included:

Cross-cutting relationships

A relative age sequence can be determined if one lithology cross cuts another, truncating some of the features of the earlier lithology (Fig. 3.28). The morphology of the contact can give clues about the relative temperatures and rheologies of the lithologies involved.

This turned out to be particularly diagnostic for the late history of the batholith. All of the major members of the batholith are cut by relatively thin (cm to dm scale) veins of

leucocratic material (Fig. 3.29). These in turn are cut by the mafic dykes (Fig. 3.30) and thin planes of epidote mineralisation.

Cross-cutting trends between the major members of the batholith are somewhat less well-defined, although an overall sequence of more mafic to more felsic was determined. It was not possible to determine directly any age relationships between the hooibergites and the gabbros, because these lithologies had no observed mutual contacts.

The presence or absence of *chilled margins* gives qualitative information about the duration of the age difference between lithologies. The only pronounced chilling observed was at the margins of the late mafic dykes, and occasionally at the margins of hornblende-plagioclase porphyry bodies that showed a clear sheet-like morphology.

In the absence of chilled margins in the majority of the outcrops studied, some age relationships could not be resolved. This occurred where, for example, two rock types had a mutual contact with a planar morphology and no chilling (Fig. 3.31). Additionally, contacts of this type were frequently exploited by subsequent magma pulses, resulting in a banded structure with no way of elucidating the intrusion order.

Inclusions

The tonalitic members of the batholith frequently contain numerous inclusions, ranging from a few percent to about 80 percent of the rock volume (Fig. 3.32). Inclusions in hosts other than tonalite are present, but rare. Tonalite-hosted inclusions cover a vast range of lithologies and morphologies (Fig. 3.33). They range in size from 1cm to 3 metres, with the majority falling in the 5 - 30cm range. Abundances of the different lithologies were counted for a variety of size ranges at six localities, to provide constraints on the order of intrusion.

By far the most abundant lithologies are microdiorite and hornblende-plagioclase porphyry. These have diffuse contacts with the host rock, and irregular globule shapes. Sometimes they are highly flattened and aligned parallel to one another (Fig. 3.34). This alignment is also parallel to the margins of the host intrusion, where this is observed. This type of inclusion is interpreted as being at least partially liquid when included into the tonalite. Observations which point to this conclusion include:

1. the flattening of inclusions (Fig. 3.34).
2. clear evidence of ductile deformation in some examples (Fig. 3.35).
3. extremely high abundances (up to 80%: Fig. 3.32) in some ~ 2 m thick tonalitic sheets – if the inclusions had been completely solid, this would have significantly increased the bulk

Fig. 3.28: Cross-cutting relationships within the batholith are frequently well-exposed.

Fig. 3.29: Veins of silicic material cut diorite and a tonalite vein.

Fig. 3.30: Mafic dykes are younger than the silicic veins.

Fig. 3.31: Lack of chilled margin between an enclave-bearing and an enclave-free tonalite.

Fig. 3.32: Tonalite-hosted inclusions of a variety of compositions. Most are elongated and deformed.

Fig. 3.33: Tonalite containing inclusions of microdiorite, porphyry and meladiorite.

viscosity of the magma, making it rheologically impossible for a sheet of this thickness to flow.

Other common inclusions are diorites and gabbro, which mainly occur close to localities where tonalite intrudes these rocks. The inclusions are commonly much more angular, and appear to have been derived from fracturing of the wall rock by tonalite (Fig. 3.36). Occasionally, jigsaw breccias (Fig. 3.37) of diorite occur as inclusions. Even though the inclusions are angular, as if the diorite had been completely solid when stoping occurred, chilled margins are still absent, indicating that it was at least still hot. In fact, a viscous magma need not necessarily be solid in order to fracture in a brittle manner, depending on the strain rate imposed upon it, i.e., the fluid pressure of the intruding magma.

Transitional rock types

These occasionally occur on up to 100 m distance scales between two end-member lithologies. These could be interpreted as zones of complete mixing between two co-existing liquids, or, alternatively, could represent re-oriented layered sequences where the rock types are related to one another by fractional crystallisation. These transitional zones are discussed further in the following section.

3.3.3 Origin of the hooibergites - case study of contradictory relationships.

Much discussion has focused on the relationship of the hooibergites to the other members of the batholith, in terms of both age and composition.

Martin (1888) concluded that the hooibergites represented concentrations of amphibole and augite in the common tonalite, whereas Westermann (1932) considered them to be first-solidification differentiates. Later, Helmers and Beets (1977) suggested that the presence of mylonite zones at the margins pointed to a "late ultimate emplacement". It has become apparent during the present study that these contrasting opinions arise in part from apparently contradictory field relationships.

The suggestion that the rocks of the Hooiberg[2] were younger intrusions arose partly from the cone-like morphology of the hill (Fig. 3.3) and the circular outcrop pattern of the hooibergite, which evoked a vision of a plug-like intrusion morphology. This was supported by observation of foliated material at the margins, implying that the hooibergite had pushed its way through the surrounding tonalite. (In reality, foliated, weathered zones can be found distributed throughout the entire outcrop area of the tonalite, and are probably related to later faulting.) Another line of evidence was that the hooibergite, in particular the margins thereof,

Fig. 3.34: Highly flattened and aligned inclusions.

Fig. 3.35: Porphyritic inclusion showing clear evidence of duc(k)tile deformation; dioritic inclusions are angular.

Fig. 3.36: Gabbro xenoliths within tonalite tend to be angular.

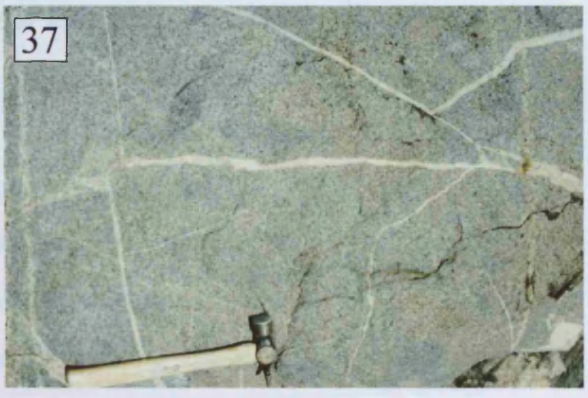

Fig. 3.37: Jigsaw breccia consisting of diorite "clasts" separated by tonalitic veins.

Fig. 3.38: Tonalitic dyke cuts hooibergite at Warawara[8].

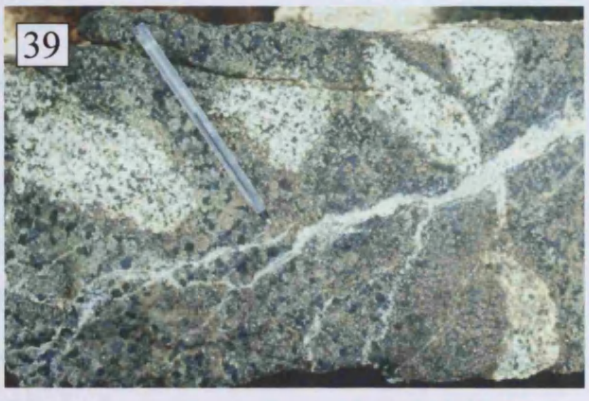

Fig. 3.39: Inclusions of tonalite in hooibergite, also at Warawara[8]. The age relationship shown here is contradictory to that of Fig. 3.38.

is veined by acidic material. Because of the concentration of this at the edges of the body, it was interpreted as acid back-veining after intrusion of hooibergite partially melted the surrounding tonalite. However, if the vein material was a late-stage differentiate derived from the tonalite, it would also be more abundant close to the tonalitic source, i.e., at the margins of the hooibergite massif.

A significant proportion of time in the field, therefore, was devoted to finding the appropriate outcrops to solve this problem. The conclusion finally reached is that the hooibergite bodies fall into two categories: earlier than the main tonalite, and synchronous with the main tonalite, i.e., they are emplaced throughout the entire sequence.

An example of the early category is the main Hooiberg[2], in that places are found where the hooibergite is definitely cut by tonalite. Tonalite outcrops occur halfway up the hill on the north side - this is not conclusive in itself, as they could be large xenoliths included into a later hooibergite, but on the south side it is clear that tonalitic dykes cut the hooibergite. This occurs also at Warawara[8] (Figs. 38 and 39) and Canashito[9]. At Canashito[9] Quarry, a tiny (10 metre high) dissected hooiberg reveals that the hooibergite overlies the tonalite (Fig. 3.40), and the contact is sub-horizontal, with small-scale 'fingers' of tonalite extending into the hooibergite. If the hooibergite was a later plug-like intrusion, the contact would be expected to be sub-vertical, and hooibergite 'fingers' would intrude the tonalite. At some (but not all) places within this exposure, shearing has occurred along the contact, complicating the relationships.

At Warawara[8], banding of possible cumulus origin is found *in situ* (Fig. 3.24) and has a dip to the north of approximately 60 degrees. Assuming that this banding was originally horizontal, there are two options: either the rotation occurred as a solid hooibergite mass descended into a liquid tonalite body, or the whole batholith has been tilted by 60 degrees since emplacement. However, the layering at Warawara[8] dips in the opposite direction to that observed in the gabbroic rocks at the north coast of Aruba, suggesting the former explanation.

The acid veining at the main Hooiberg[2] remains a problem. If the hooibergite was older, then the leucocratic material cannot be acid back-veining. The acid veining in the rest of the batholith is quite a late brittle feature, but at the Hooiberg[2] both brittle and ductile behaviour can be seen - sometimes the veins cut straight through (Fig. 3.41), sometimes they are deflected around hornblende crystals (Fig. 3.42), and sometimes the acid material appears to completely disaggregate the hooibergite (Fig. 3.43). This could be a function of magma flux - a large flux of acid melt would heat up and disaggregate the hooibergite more, but this does

not fit well with the observations: small volume non-brittle intrusion can be observed as well as relatively high volume brittle intrusion. The preferred interpretation is that the hooibergite existed at a range of temperatures and rheological states as it was veined, but real proof is lacking.

Transitional rock types between hooibergite and diorite occur at the Hooiberg. These either coexist with normal hooibergite, or are slightly later than it.

The hooibergite at Sero Pos di Nord[10] appears to be synchronous with the surrounding tonalite. Sero Pos di Nord[10] is a hill which has tonalite at its base and hooibergite at the top. As the hill is ascended (travelling southwards), there is a transition from paler to darker rocks – the concentration of hornblende increases until the rock resembles a diorite. Then the hornblende becomes more equant and prominent. Finally, pyroxene appears in the matrix. Unfortunately, close to the summit of the hill, a later tonalitic dyke cuts everything, obscuring the transitional sequence. Beyond this dyke is the hooibergite. At this well-exposed locality, there is no evidence of either tonalite intruding hooibergite or the converse, and even though "absence of evidence is not evidence of absence," it is concluded that the broad transitional zone is reasonably convincing evidence that the rock types are approximately synchronous. One explanation is that the sequence represents a layered series, where crystal fractionation processes have differentiated a parental magma into pyroxene-bearing hooibergites (cumulate) and evolved liquids (diorites and tonalites). However, the geometry observed is difficult to reconcile with such a hypothesis: the more mafic rocks currently reside at the top of the hill. Even if the batholith has been reoriented by tectonic movements, as suggested to explain the layering in the gabbro that dips steeply to the south, these movements would have had to have been severe enough to overturn originally horizontal magmatic units to explain the present distribution of rock types.

One of the other problems with the interpretation of the hooibergites is whether the hornblendes are primary or secondary. The observational evidence suggests that two processes occur – primary crystallisation from a melt and secondary overgrowth, probably prompted by additional fluid or melt input.

Evidence for primary crystallisation from a melt:

1. In the areas where rock types transitional between tonalite and hooibergite occur, the changes from outcrop to outcrop are very subtle. Going from tonalite to hooibergite (e.g., at Sero Pos di Nord[10]), firstly the concentration of elongate hornblende (as seen in the

Fig. 3.40: Contact between tonalite and hooibergite at Canashito[9]. A finger of tonalite intrudes the hooibergite on the right-hand side; the hill is cut by a fault in the centre.

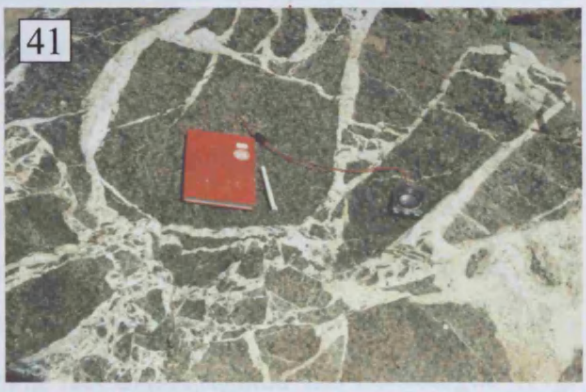

Fig. 3.41: Magmatic breccia where acidic veins cut hooibergite.

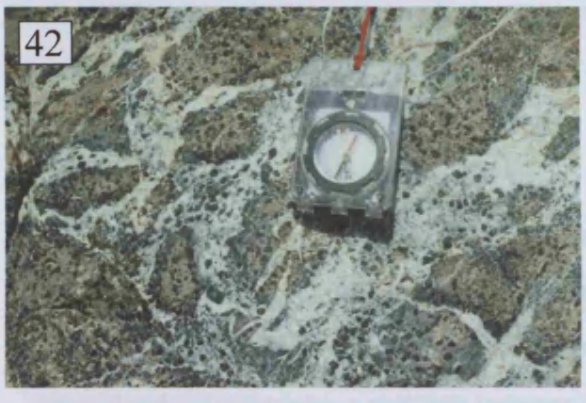

Fig. 3.42: Acidic veins have partially assimilated hooibergite. Note the reaction rim between the hooibergite xenoliths and the acidic melt.

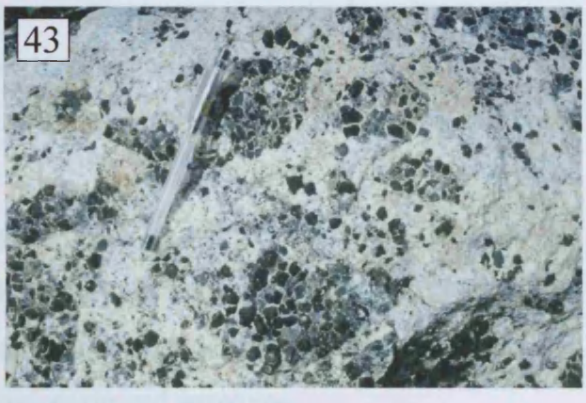

Fig. 3.43: Acidic melt has almost completely disaggregated this hooibergite. Here, no reaction rims are present.

Fig. 3.44: Brittle acidic veins cut a layered hooibergite. A dark reaction rim is present.

Fig. 3.45: Contact between tonalite and a dolerite of the Aruba Lava Formation. No chilling is apparent.

tonalite) increases until there is a normal looking diorite, then the concentration continues to increase and the shape changes to a less elongate one until the rock type "stubby diorite" (see page 3.13 for definition) occurs. Finally, pyroxene is found in the matrix and the rock resembles a hooibergite. (These hooibergites in general have a smaller hornblende crystal size than those found at the main Hooiberg.) Because of the continuum of rock types observed, an argument for secondary hornblende in the hooibergite would also have to be applied to the diorite and tonalite, which would be unrealistic.

2. At the main Hooiberg[2], extensive acid veining has disaggregated the hooibergite (Fig. 3.43). In this lithology, the hornblende crystals are morphologically identical to those in the un-veined hooibergite, suggesting that they existed prior to the acid veining event and have been removed from the host hooibergite as the veining (± assimilation) occurred. This field observation is consistent with petrographic studies (see Section 7.2.1 and Fig. 7.13).

Evidence for secondary overgrowth or coarsening:

1. Adjacent to some acidic veins cutting the hooibergite, there is a rim enriched in hornblende. It seems that this is a reaction rim between the hooibergite and the acid vein (Figs. 3.42 and 3.44).
2. At some localities, extremely dark hooibergites were found, which appear to have no matrix. The hornblendes can be seen poikilitically enclosing another ferromagnesian mineral, confirmed in thin section as diopside. Plagioclase is absent, suggesting that the hornblende results from a reaction between plagioclase and pyroxene.
3. At the gabbro locality (Wariruri[11]), some rocks have ~1 cm hornblende crystals poikilitically overgrowing the anhydrous gabbro mineralogy. These appear to be secondary.

3.3.4 Simplified intrusion sequence for the batholith

The first rocks to crystallise were gabbroic and hooibergitic cumulates. These may have crystallised at the same time as one another, but with the textural and mineralogical differences reflecting different bulk compositions (and volatile contents) of the melt phase. Rocks of a dioritic composition are the next in the sequence, and are in places transitional from the gabbros and hooibergites. A voluminous phase of tonalitic magmatism followed. This magma locally stoped xenoliths from its wall rocks, and entrained magmas of a slightly different, more dioritic composition. Some of these magmas may have been completely mixed into the tonalite, whereas others are preserved as deformed enclaves. Phases of veining by

magmas of more and more acidic composition occurred next. These magmas may represent late stage differentiates of the tonalite.

Finally, suites of mafic dykes intruded the whole complex, which was by then cool enough for the dykes to chill, but hot enough for hydrothermal circulation and epidote mineralisation to continue.

3.4 Relationships between the Aruba Lava Formation and the batholith

One of the priorities of the fieldwork was to determine the nature of the map-scale contact between the Aruba Lava Formation and the batholith, to find whether the batholith was genuinely intrusive, or whether the two were merely faulted next to one another. At least three localities[5,12,13] were found where the tonalite was seen to be intruding the lava sequence – once into a basalt, once into a dolerite (Fig. 3.45) and once into an amphibolite. Interestingly, the tonalite was not chilled against the dolerite or the amphibolite, implying that the country rocks were either still warm, or had been substantially heated by earlier intrusive phases of the batholith before the final contact formed. Locally, the contact between the batholith and the Aruba Lava Formation is faulted, but this is a later complication - the intrusive nature of the batholith into the lavas has been established beyond doubt.

Near Jamanota[1], it can be seen that intrusion of the batholith is penecontemporaneous with movement along the shear zone - tonalite preferentially intrudes the weak sheared rock, but is then itself deformed into boudins by further movement (Fig. 3.20).

The situation at Andicuri[5], where tonalite intrudes foliated amphibolite, is different. There, the foliation developed before intrusion of the tonalite, as foliated amphibolite blocks are included as xenoliths within the tonalite (Fig. 3.17). Indeed, the extra heat provided by the batholith, in addition to possibly causing the amphibolite to partially melt, appears to be causing the foliation to be thermally overprinted - the foliation is much better developed further from the margin of the batholith.

Intrusion of the batholith into the pre-existing lava sequence has had a profound effect on the geology of Aruba. Not only did it contribute to the metamorphism of the lavas, but it also enabled development of a hydrothermal circulation system, which resulted in epidote mineralisation as well as formation of (historically) economically viable gold deposits.

3.5 Summary

- The Aruba Lava Formation consists of a sequence of basalts, dolerites and volcaniclastic sedimentary rocks deposited on the flanks of an emergent volcano located in an oceanic environment. It is a viable candidate for an oceanic plateau sequence.
- The Aruba batholith represents a highly complex magmatic system, with magmas of extremely variable compositions being intruded contemporaneously. The overall sequence of emplacement is from mafic to acidic, with a further late mafic pulse.
- The Aruba batholith is intrusive into the Aruba Lava Formation.
- The Aruba Lava Formation is folded, and in places, cut by shear zones. Intrusion of the batholith occurred at approximately the same time as movement along those shear zones.

Chapter 4

Geochronology of Aruban rocks

4.1 Introduction

The field observations described in Chapter 3 raise some interesting questions about the timing of the emplacement of the various rock series on Aruba. In particular, the field observations suggest that the Aruba Lava Formation and the Aruba batholith may be close in age to one another. In order to develop a model that can explain the transition in magmatic environment, and hence the origin of these two different magmatic suites, time constraints are extremely important. Additionally, in order to enable an evaluation to be made of the Aruba Lava Formation as a potential member of the Caribbean oceanic plateau, the timing of its eruption must be considered together with its geochemical composition (discussed in Chapter 6).

This chapter discusses previous work that constrains the ages of Aruban rocks and reports new ^{40}Ar-^{39}Ar incremental heating results obtained from nine Aruban samples: four from the Aruba Lava Formation, four from the batholith and one dyke cross-cutting the batholith. The analyses of the basalt and dolerite samples from the Aruba Lava Formation were performed on leached whole rocks; other analyses were carried out on hornblende or biotite mineral separates (see Table B.1 for details of the preparation procedure for individual samples).

4.2 Previous work dating Aruban rocks

4.2.1 The Aruba Lava Formation

No radiometric dating of the Aruba Lava Formation has been attempted prior to this study, and all the existing information on its age is derived from stratigraphic and palaeontological studies. Westermann (1932) could not determine its age because of the "absence of index fossils", but suggested that it correlates with similar, but fossil-bearing, Cretaceous formations on other Antillean islands. This assumption was strengthened by the discovery of imprints of ammonites in a sedimentary intercalation within the Aruba Lava

Formation. No formal description or identification of these ammonites has taken place, but MacDonald (1968) and Wiedmann (reported in Beets *et al.*, 1984) independently concluded that the fauna are Turonian in age (90.4-88.5 Ma: Harland *et al.*, 1990).

4.2.2 The Aruba batholith

The Aruba batholith is constrained from field evidence to be younger than the Aruba Lava Formation. Intrusive contacts between the batholith and the lavas are observed, meaning that the batholith is not tectonically emplaced. Westermann (1932) suggests that the "diorite" intruded during orogenesis of the Aruba Lava Formation, in late Mesozoic or early Tertiary (Lower Eocene) time, based on the presence of an unconformably overlying limestone dated palaeontologically as Upper Eocene to Lower Miocene.

Subsequent radiometric studies have refined this estimate: Priem *et al.* (1966) dated biotite concentrates from the Aruba batholith by Rb-Sr and K-Ar methods, and obtained 3 ages ranging from 75 ± 4 to 71 ± 4 Ma. Santamaría and Schubert (1974) obtained a K-Ar age of 67 ± 4 Ma, also on a biotite concentrate. An older age for the batholith became apparent when Priem *et al.* (1978) obtained two Rb-Sr isochrons for the Aruba batholith, and concluded that it resulted from at least two phases of episodic intrusion, dated at 85.1 ± 0.5 Ma and 70.5 ± 2.2 Ma respectively. However, a subsequent Rb-Sr and K-Ar study (Priem *et al.*, 1986a) found that, for some samples, biotite separates gave younger ages than the corresponding hornblende separates, and concluded that intrusion of the composite batholith occurred at 88.5 ± 0.8 Ma, with thermal events at ~72 Ma and ~62 Ma leading to a degree of isotopic resetting. It should be noted that the 88.5 ± 0.8 Ma date could be somewhat misleading, because it actually represents an average value of the five oldest ages obtained, and was calculated in order to eliminate the effects of any minor isotopic resetting: however, eleven of the original data points lie in the range 89.5 - 83.5 Ma, and there is no firm evidence against intrusion of the batholith over this slightly longer time period.

4.2.3 Dating uplift and erosion: fission track studies

Unpublished fission track work on apatite ($T_{closure} \approx 80°C$) and zircon ($T_{closure} \approx 260°C$) from the Aruba batholith has been carried out by Paul Andriessen at the Vrije Universiteit (pers. comm.). Apatite dates fall in the range 40-30 Ma (Upper Eocene - Lower Oligocene), indicating that uplift of the batholith to a depth of ~3 km occurred at this time (assuming a geothermal gradient of ~30°C/km). Interestingly, this is also the approximate age of the

earliest preserved limestone on Aruba (Westermann, 1932). The zircon data are less easily interpreted because the dates obtained are not consistent, i.e., closure dates as diverse as 70 Ma and 40 Ma are reported.

4.2.4 Regional constraints

Voluminous mafic rocks from the Caribbean region have been dated by Sinton *et al.* (1998) using ^{40}Ar-^{39}Ar methods. These samples, thought to belong to the Caribbean oceanic plateau, yield ages ranging from 91 to 88 Ma, although a volumetrically secondary, but region-wide, event occurred at ~76 Ma (Kerr *et al.*, 1997a; Sinton *et al.*, 1998). Some reported ages are as young as 63 Ma (Sinton *et al.*, 1997), but these probably represent material accreted to the plateau. Two basalt samples from the nearby Curaçao Lava Formation gave ages of 89.5 ± 1.0 and 88.0 ± 1.2 Ma, and a sill intrusive into this unit has a 75.8 ± 2.0 Ma age. Re-Os isochron results for Curaçao basalts indicate a crystallisation age of 85.6 ± 8.1 Ma (Walker *et al.*, in press).

Santamaría and Schubert (1974) obtained K-Ar ages of between 84 ± 6 Ma and 62 ± 3 Ma for a wide range of intrusive and extrusive "calc-alkaline" lithologies from many locations within the Caribbean-Venezuela plate boundary zone. A compilation of data from calc-alkaline (*sensu lato*) plutonic rocks by Donnelly *et al.* (1990) gives a similar range, with the majority falling between 90 and 65 Ma. However, there is strong evidence for thermal events resetting isotopic clocks in this region, and it cannot be ruled out that some of these younger dates may arise from this. For example, Rb-Sr and K-Ar dating of samples from the Washikemba Formation on Bonaire was inconclusive, because the dates obtained were significantly younger than the stratigraphic age of the Formation, with thermal resetting events occurring at 78 ± 2 Ma and 61 ± 4 Ma (Priem *et al.*, 1979). Similarly, thermal resetting events have been reported rocks on for Aruba (see previous section). It is interesting to speculate whether these periods of isotopic resetting correspond to younger phases of mafic magmatism associated with the Caribbean oceanic plateau.

4.3 An ^{40}Ar-^{39}Ar study of Aruban rocks

4.3.1 Rationale for sample selection

For the Aruba Lava Formation, sample selection involved choosing the coarsest grained basalts or dolerites, with the smallest amount of groundmass glass or fine-grained alteration products, and the highest possible proportion of original preserved mineralogy. Note

that none of the Aruba Lava Formation samples is pristine: all have been altered or metamorphosed to some degree and contain secondary minerals (see Chapter 5 for details of petrography of these rocks). It was hoped that the contribution from these secondary minerals could be minimised by leaching the samples prior to irradiation (see Appendix B for details). A hornblende separate was obtained from one amphibolite sample belonging to the Aruba Lava Formation.

Samples from the batholith were chosen to cover a range of lithologies and geographical locations. Biotite separates were preferred, due to their higher potassium content, but hornblende separates were prepared from biotite-free lithologies. Thin section study ensured that the minerals to be separated were as free as possible from alteration products.

To assess precision, one experiment was performed on duplicate sub-samples (ARU96-131a and b).

4.3.2 Interpretation of ^{40}Ar-^{39}Ar data

Incremental heating ^{40}Ar-^{39}Ar analysis yields three estimates of the sample age: the plateau age, isochron age and total fusion age. The *plateau age* is derived from selected plateau-forming increments of the age spectrum (e.g., Fig. 4.1), weighted according to the amount of ^{39}Ar released and the inverse of the variance for each step. (Note that *plateau age* used in this sense should not be confused with the age of the [Caribbean] plateau). The *isochron age* is obtained from the gradient of a plot of $^{40}Ar/^{36}Ar$ versus $^{39}Ar/^{36}Ar$ for the selected steps. The *total fusion age* reflects the apparent age of the total Ar degassed from the sample during the entire step-heating experiment, and is therefore considerably less reliable than the plateau and isochron ages, especially for altered samples.

The isochron ages are strongly preferred over the weighted mean plateau ages because they combine quantitative estimates of analytical precision and internal disturbance of the sample (scatter about the isochron), without making any assumption about the composition of the non-radiogenic, or trapped, argon component. It has been noted (Singer and Pringle, 1996) that, at least for sub-aerial lavas, non-atmospheric $^{40}Ar/^{36}Ar$ intercepts on isotope correlation diagrams are often not an indication of a non-atmospheric trapped component but, rather, reflect irradiation-induced experimental artefacts in fine-grained phases. The observation that the $^{40}Ar/^{36}Ar$ intercept is not statistically different from 295.5 (the atmospheric value) is an important indication that these experimental artefacts are not significant.

Rigorous criteria (Pringle, 1993) have been adopted to determine whether an incremental heating experiment has given meaningful results. Briefly, these criteria include:

1) a well-defined, high-temperature age spectrum plateau formed by at least three contiguous steps that are *all* concordant in age at the 95% confidence level and represent ≥ 50% of the ^{39}Ar released;
2) a well-defined isochron exists for the plateau points as defined by the F-variate statistic SUMS/(N-2) for the York2 regression used in this study (York, 1969);
3) the plateau and isochron ages are concordant at the 95% confidence level;
4) the $^{40}Ar/^{36}Ar$ intercept on the isochron diagram does not differ from the atmospheric value of 295.5 at the 95% confidence level.

Table 4.1 indicates, for each experiment performed, whether the data obtained are acceptable according to each of the above criteria. The final "total" column gives a score out of 5 for each experiment, so that the reliability of each experiment can be assessed at a glance. Ideally, for a result to be considered reliable, all of the criteria should be met. However, all but one of the experiments carried out in this study violate at least one of the criteria.

The most commonly contravened criterion is the value of the F-variate statistic, SUMS/(N-2). This statistic gives an indication of the scatter about the isochron compared to the scatter expected from analytical uncertainty alone. Unacceptably high values, as observed in most of these experiments, can arise due to either geological or experimental disturbance, or underestimation of the analytical precision. In these circumstances, it seems judicious to lower the rigorous standards somewhat, and consequently, for the purposes of this study, a score of 4 or more is deemed acceptable for a reasonably reliable age determination, although a greater degree of caution must be exercised in the geological interpretation of the results.

According to Table 4.1, none of the age determinations from the Aruba Lava Formation basalt and dolerite samples meet sufficient criteria to be considered reliable. Possible reasons for this are discussed in section 4.3.3.

It should also be noted that the errors quoted in the following sections are analytical uncertainty alone. They do not include any uncertainty in the age of the neutron flux monitor used. This results in a systematic error that cannot easily be quantified. As a guide, the values quoted are relative to a value of 27.92 Ma for TCR sanidine (Singer and Pringle, 1996), which corresponds to an age of 513.9 Ma for the hornblende standard MMhb-1 (Pringle, 1992). This compares to a recommended value of 523.1 Ma for MMhb-1 reported in Renne *et al.* (1998), and leads to the possibility that the absolute ages quoted for the Aruba samples could be anything up to 1.8%, or approximately 1.5 Ma, too young.

Table 4.1: Summary of reliability criteria for ^{40}Ar-^{39}Ar data, discussed in text.

Experiment	Material	Lithology	Tests (see below for description): 1a	1b	c	d	e	total
Aruba Lava Formation								
ARU96-2	whole rock	basalt	?	YES	NO	NO	NO	1.5
ARU96-30	whole rock	dolerite	NO	YES	N/A	N/A	N/A	1
ARU96-31	whole rock	basalt	?	YES	NO	YES	YES	3.5
ARU96-147	hornblende	amphibolite	YES	YES	NO	YES	YES	4
Aruba batholith								
ARU96-131a	biotite	tonalite	YES	YES	NO	YES	YES	4
ARU96-131b	biotite	tonalite	YES	YES	NO	YES	YES	4
ARU96-158	biotite	diorite	YES	YES	NO	YES	YES	4
BK77-165	hornblende	diorite	YES	YES	YES	YES	YES	5
ARU96-152	hornblende	meladiorite	?	YES	NO	NO	NO	1.5
ARU96-123	hornblende	mafic dyke	YES	YES	NO	YES	YES	4

Criterion 1a well defined plateau: ≥3 steps concordant at 95% confidence level
Criterion 1b plateau represents ≥50% ^{39}Ar released
Criterion 2 SUMS/N-2 value acceptable
Criterion 3 plateau and isochron ages concordant at 95% confidence level
Criterion 4 intercept within error of atmospheric value (295.5)

4.3.3 ^{40}Ar-^{39}Ar results for the Aruba Lava Formation

A summary of the numerical results of incremental heating of samples from the Aruba Lava Formation is presented in Table 4.2, and age spectra, isochron correlation diagrams and K/Ca plots can be found in Fig. 4.1.

Table 4.2: Summary of $^{40}Ar/^{39}Ar$ incremental heating experiments of leached whole rocks and hornblende separates from the Aruba Lava Formation. Full data for each experiment are located in Appendix B.

					Age spectrum				Isochron Analysis		
Sample	Material	Lithology	K/Ca total	Total gas age (Ma)	Increments used	^{39}Ar (%)	Age ± 1 s.d. (Ma)	MSWD	SUMS (N-2)	$^{40}Ar/^{39}Ar$ ± 1 s.d. intercept	Age ± 1 s.d. (Ma)
ARU96-2	whole rock	basalt	0.024	74.00 ± 0.23	4 of 18	63.9	76.43 ± 1.13	14.55	3.42	224.5 ± 17.2	81.73 ± 1.36
ARU96-30	whole rock	dolerite	0.009	53.70 ± 0.43	16 of 16	100.0	50.64 ± 2.68	193.6	no isochron analysis attempted		
ARU96-31	whole rock	basalt	0.009	87.76 ± 0.31	9 of 14	52.1	77.68 ± 0.79	9.25	12.90	290.5 ± 11.6	78.90 ± 3.07
ARU96-147	hornblende	amphibolite	0.017	77.68 ± 0.33	10 of 16	93.4	80.48 ± 0.48	3.95	5.86	308.8 ± 45.9	79.34 ± 3.44

Analytical methods and data reduction after Singer and Pringle (1996).

All ages calculated relative to 27.92 Ma for TCR sanidine; all errors reported as 1 σ of analytical precision.

Although the ages quoted in Table 4.2 for the basalts and dolerite seem to be relatively consistent (i.e. about 80 Ma), Table 4.1 shows that the experiments are clearly unreliable. This is illustrated graphically in Fig. 4.1, where none of the experiments yields a convincing plateau. Consequently, any rigorous geological interpretation of these data is likely to be suspect. The most logical explanation for the poor data is that all the samples were severely thermally disturbed due to intrusion of the batholith, and this perturbed their Ar systematics.

In spite of this, however, the data for samples ARU96-2 and ARU96-31 show certain features, which may be mere coincidences, but are interesting nonetheless. Both reveal poorly-defined age spectrum plateaux at ages that are indistinguishable at the 95% confidence level. These ages (76.4 ± 1.1 and 77.7 ± 0.8 Ma, respectively) are remarkably similar to the 76 Ma date given for a secondary magmatic event in the Caribbean region (Kerr *et al.*, 1997a; Sinton *et al.*, 1998). It is clearly impossible that these lavas were extruded during that event, because this is inconsistent with both the palaeontological and field evidence (i.e. intrusion by a batholith previously dated as 88.5 ± 0.8 Ma: Priem *et al.*, 1986a). However, this event could have been responsible for resetting of the Ar isotopic system of these samples. Alternatively, these pseudo-plateaux could represent a cooling age for these samples after metamorphism by the batholith.

A second feature of ARU96-31 is that the recombined total fusion age of the sample is ~88 Ma, consistent with the Turonian palaeontological age of the Aruba Lava Formation, and radiometric data from the adjacent island of Curaçao. This can only represent the true age of this rock if all subsequent thermal disturbance of this sample only resulted in internal redistribution of the argon isotopes within the sample.

The experiment on the hornblende separate from amphibolite ARU96-147 gave acceptable results, with a plateau age of 80.5 ± 0.5 Ma and a statistically indistinguishable isochron age of 79.3 ± 3.4 Ma. This amphibolite is thought to represent a member of the Aruba Lava Formation that was highly metamorphosed by intrusion of the batholith: it was collected from within 100 metres of the Aruba Lava Formation-batholith contact. The date determined in this study is a cooling age subsequent to this metamorphism, rather than the age of the protolith. Consequently, ~80 Ma may be used as a minimum age for the protolith of the Aruba Lava Formation; this further rules out the possibility that the ~77 Ma pseudo-plateaux observed in ARU96-2 and ARU96-31 represent ages of extrusion of the Aruba lavas, and lends weight to the argument that these represent reset ages.

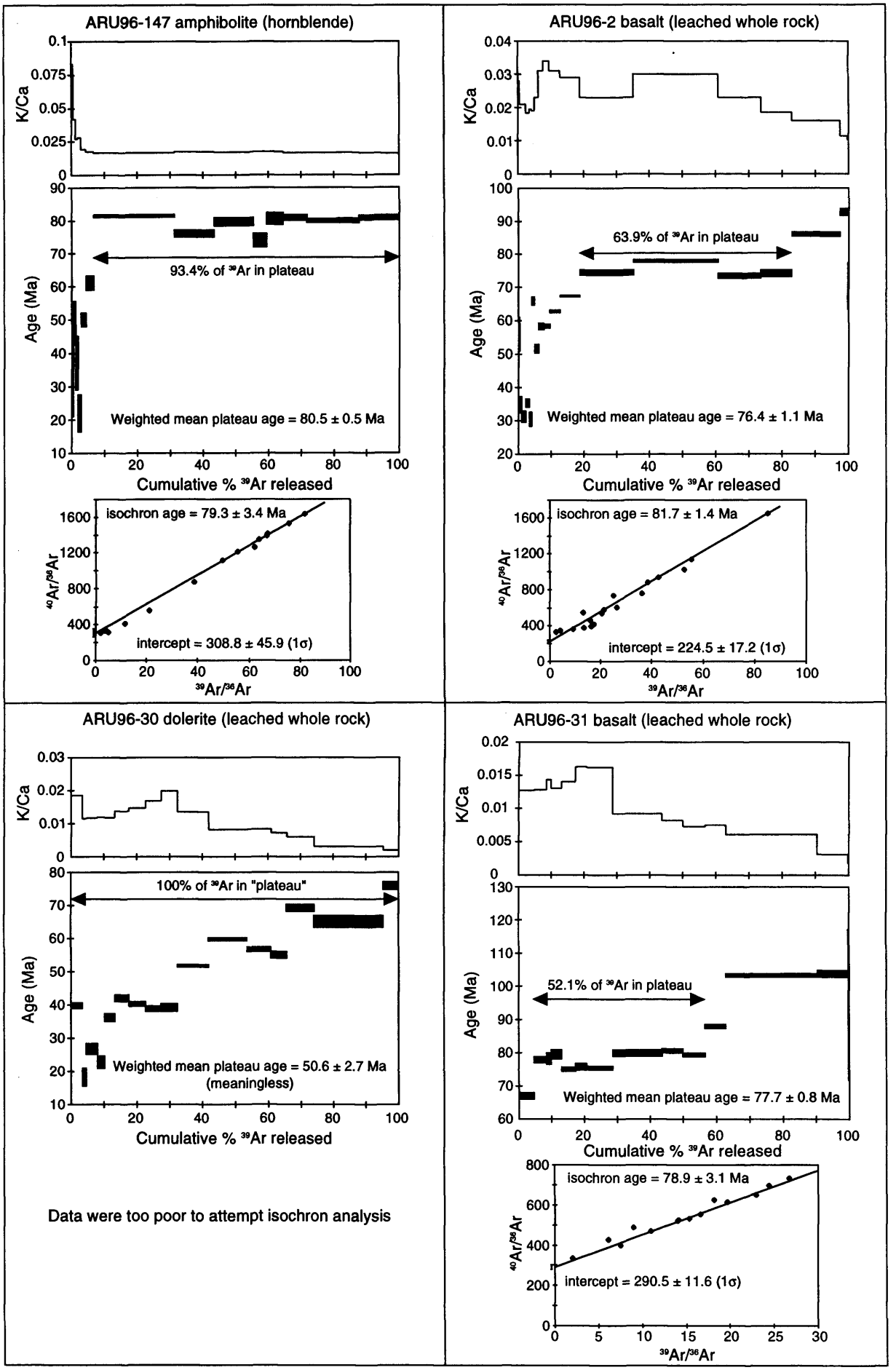

Figure 4.1: Age spectra, K/Ca plots and isochron correlation diagrams for members of the Aruba Lava Formation: amphibolite, dolerite and basalts.

4.3.4 ^{40}Ar-^{39}Ar results for the Aruba batholith

Table 4.3 summarises numerical data for the incremental heating experiments on samples from the Aruba batholith. Age spectra, K/Ca plots and isochron correlation diagrams are shown in Figs. 4.2 and 4.3.

Table 4.3: Summary of $^{40}Ar/^{39}Ar$ incremental heating experiments of biotite and hornblende separates from the Aruba batholith and a cross-cutting mafic dyke. Full data for each experiment are located in Appendix B.

					Age spectrum				Isochron Analysis		
Sample	Material	Lithology	K/Ca total	Total gas age (Ma)	Increments used	^{39}Ar (%)	Age ± 1 s.d. (Ma)	MSWD	SUMS (N-2)	$^{40}Ar/^{39}Ar$ ± 1 s.d. intercept	Age ± 1 s.d. (Ma)
ARU96-131a	biotite	tonalite	3.1	82.69 ± 0.20	5 of 5	100.0	82.95 ± 0.42	15.58	25.17	296.2 ± 6.5	82.71 ± 0.53
ARU96-131b	biotite	tonalite	6.0	82.29 ± 0.18	14 of 17	98.9	83.03 ± 0.32	14.17	14.85	279.2 ± 14.5	83.06 ± 0.43
ARU96-158	biotite	diorite	3.9	84.29 ± 0.20	12 of 16	94.1	84.99 ± 0.27	4.53	4.25	245.7 ± 29.2	85.40 ± 0.46
BK77-165	hornblende	diorite	0.037	81.09 ± 0.39	10 of 18	71.3	81.80 ± 0.26	1.43	1.49	287.4 ± 7.7	82.20 ± 0.51
ARU96-152	hornblende	meladiorite	0.059	84.58 ± 0.27	8 of 17	91.5	87.21 ± 1.67	113	54.5	365.7 ± 25.2	79.92 ± 2.76
ARU96-123	hornblende	late mafic dyke	0.063	75.57 ± 0.24	10 of 17	75.5	79.59 ± 0.62	10.5	11.4	320.8 ± 25.7	77.46 ± 2.09

Analytical methods and data reduction after Singer and Pringle (1996).

All ages calculated relative to 27.92 Ma for TCR sanidine; all errors reported as 1 σ of analytical precision.

Table 4.1 shows that all of the experiments apart from ARU96-152 yielded acceptable results according to the criteria adopted during this study.

Two biotite separates prepared from tonalite sample ARU96-131 gave plateau ages and isochron ages, all four of which are indistinguishable at the 95% confidence level, indicating that analytical precision and sample reproducibility are both excellent. The weighted mean isochron age for the two experiments is 83.0 ± 0.3 Ma and the weighted mean plateau age is 82.9 ± 0.3 Ma.

The diorite samples analysed gave isochron ages of 85.4 ± 0.5 Ma and 82.2 ± 0.5 Ma. These ages are statistically distinguishable from each other at the 95% confidence level, but the dates still fit extremely well with the field observations, which can be summarised as some diorites being earlier than the tonalites and some being contemporaneous. These ^{40}Ar-^{39}Ar data show that sample ARU96-158 definitely belongs to an early diorite phase, whereas sample BK77-165 has an age statistically indistinguishable from the tonalite.

Although the experiment on meladiorite ARU96-152 did not meet the criteria laid down in this study, field evidence suggests the Matividiri gabbro body, from which this sample was derived, is older than the tonalites (and most of the diorites); therefore the 87.2 ± 1.67 Ma plateau age is probably a reasonable reflection of the true age of the gabbro body. The lower

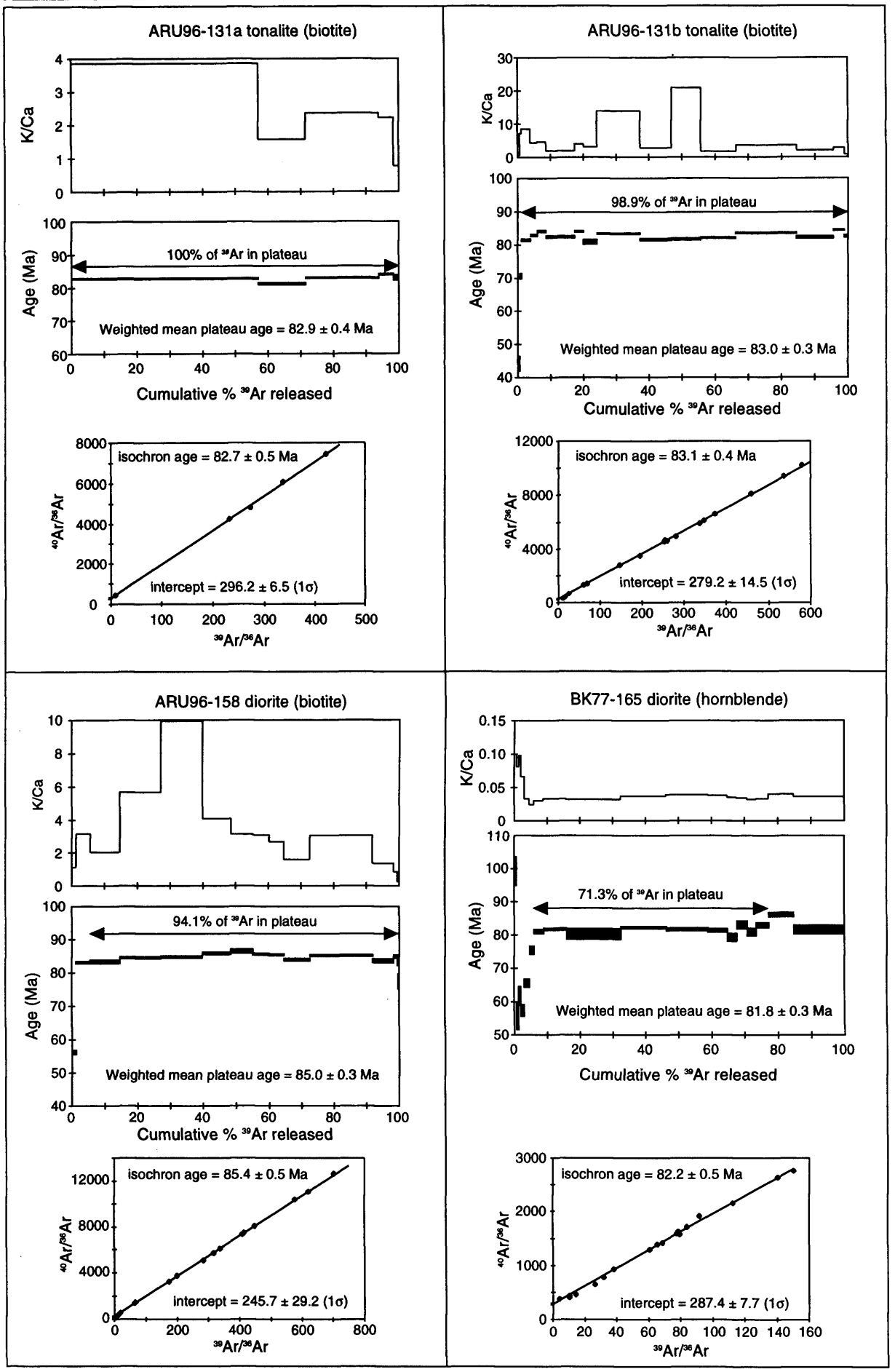

Figure 4.2: Age spectra, K/Ca plots and isochron correlation diagrams for tonalites and diorites from the Aruba batholith.

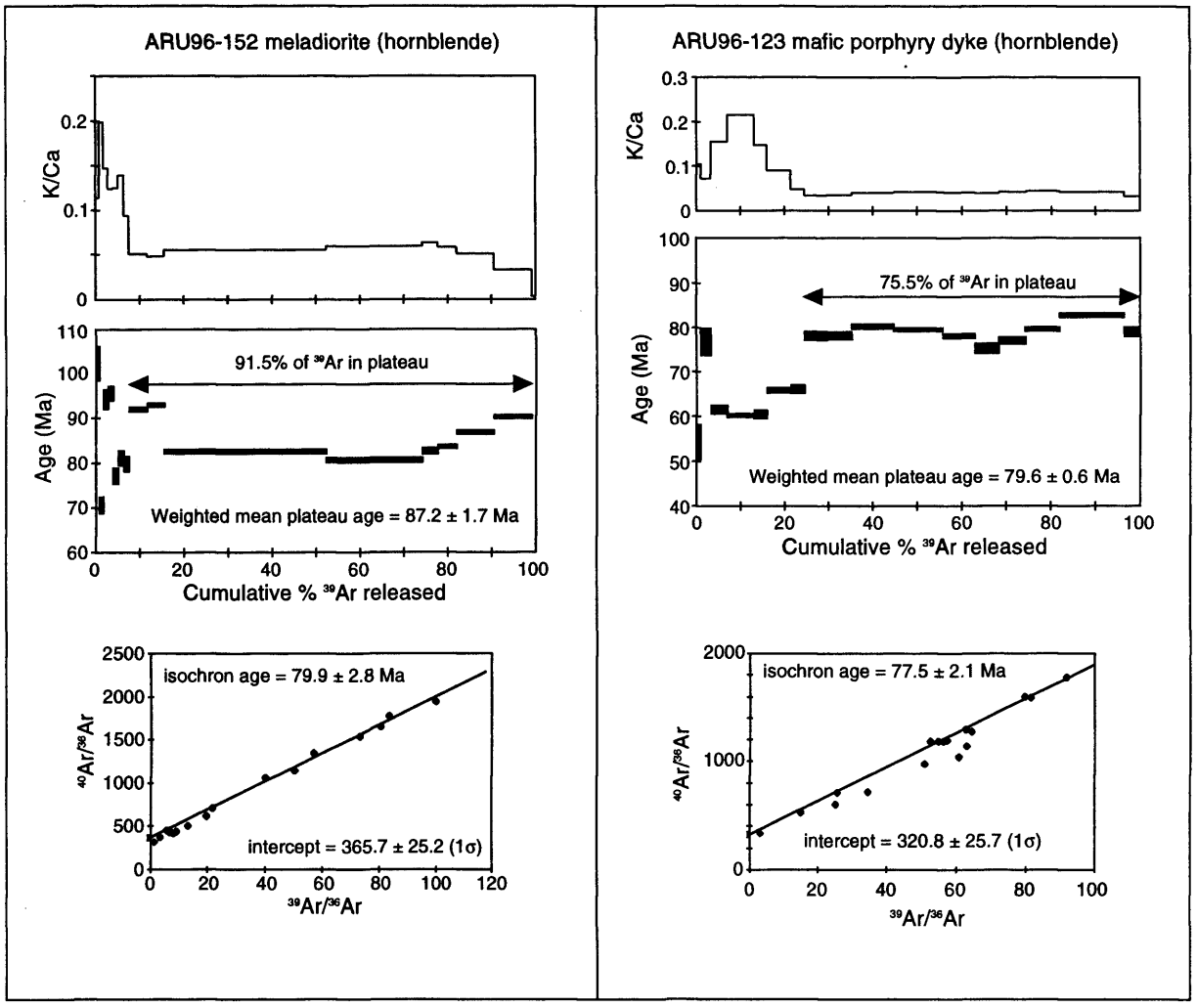

Figure 4.3: Age spectra, K/Ca plots and isochron correlation diagrams for a mela-diorite and a late mafic dyke from the Aruba batholith.

isochron age may reflect the higher than atmospheric $^{40}Ar/^{36}Ar$ intercept for this sample, which could be due to not fitting the lower temperature steps (for which there was a lot of scatter: see Fig. 4.3). The initial ratios *were* probably atmospheric, and therefore the plateau age better reflects the true crystallisation age.

The cross-cutting porphyritic mafic dyke ARU96-123 yielded an isochron age of 77.5 ± 2.1 Ma. This is in accordance with all the other data. Field relationships show that this dyke cuts the tonalite, is intruded along a brittle fracture, and has chilled margins, i.e. it intruded after cooling of the main mass of the batholith.

4.4 Conclusions

- The ^{40}Ar-^{39}Ar incremental heating data obtained in this study were unable to contribute significant knowledge about the age of the Aruba Lava Formation, because the Ar systematics of the obtained samples had been disturbed, and none reached an acceptable age plateau. The most likely explanations for this perturbation are either the intrusion of the adjacent Aruba batholith, or the later "thermal events" that appear to have affected many radiometric age determinations of igneous rocks throughout the Caribbean region. Even though reliable radiometric dates could not be obtained for the Aruba Lava Formation, its geographical proximity with a similar unit from Curaçao (dated as 88.9 ± 0.8 Ma: Sinton *et al.*, 1998) and the discovery of ?Turonian (90.4-88.5 Ma: Harland *et al.*, 1990) ammonites means that the most likely age of the Aruba Lava Formation is also approximately 88-91 Ma.
- The amphibolite sample from next to the contact with the batholith revealed an age of ~ 80 Ma. In addition to representing a minimum age for the protolith of the Aruba Lava Formation, it also represents the time of cooling of the country rock (i.e., the Aruba Lava Formation) through the closure temperature for the Ar isotopic system (approx. 500°C for hornblende).
- The Aruba Lava Formation is folded, and in places, cut by shear zones. Intrusion of the batholith occurred at approximately the same time as movement along those shear zones (Chapter 3), and thus the deformation of the Aruba Lava Formation can be dated as ~85 to ~82 Ma.

- The samples from the batholith yielded more convincing plateaux, and reliable isochron ages range from 82.2 ± 0.5 to 85.4 ± 0.5 Ma. The ^{40}Ar-^{39}Ar data are in agreement with the field evidence in that mafic members of the batholith are either earlier than, or contemporaneous with, the dominant tonalitic phase. Porphyritic mafic dykes cut the batholith approximately 5 m.y. later, after the batholith had cooled.
- The data obtained in this study, together with previously reported data, indicate that "thermal events" have been significant throughout the province. One thermal event seems to have occurred in Aruba at about 77 Ma: this is the age of both the mafic dyke cutting the batholith, and the poorly-defined plateau ages given by rocks of the Aruba Lava Formation, and is only marginally older than some of the old (reset) Rb-Sr and K-Ar dates for the batholith. This thermal event may be related to the younger phase of Caribbean plateau magmatism (~76Ma) reported by Kerr *et al.* (1997a) and Sinton *et al.* (1998). Other purported thermal events (~72 Ma and ~62 Ma: Priem *et al.*, 1986) appear to have only local significance, although it is interesting to note that the 62 Ma age corresponds with the youngest reported dates for Caribbean plateau magmatism (Sinton *et al.*, 1998) and calc-alkaline magmatism of the Southern Caribbean Plate Boundary Zone (Santamaría and Schubert, 1974).
- The most striking conclusion arising from this ^{40}Ar-^{39}Ar dating study of Aruba is that the Aruba batholith intruded the Aruba Lava Formation shortly after eruption of the basaltic sequence, within a period of ~3 to ~9 m.y. This is in accordance with the results from the fieldwork (Chapter 3), and places important constraints on the tectonic environment(s) in which these magmas were produced.

Chapter 5

Petrography and Mineral Chemistry of the Aruba Lava Formation

5.1 Introduction

This chapter describes the petrographic features (from thin section studies) and mineral chemistry (from electron microprobe studies carried out at the University of Leicester: see Appendix G for analytical techniques and data) of the rocks of the Aruba Lava Formation. The majority of the rocks contain high proportions of secondary minerals: these are briefly studied, mainly to provide constraints on the ways in which their development could have altered the whole rock chemistry. The bulk of the work in this chapter, however, concentrates on the least altered and least metamorphosed rocks, because it is the primary mineralogical and textural features that hold the most information of relevance to the overall story presented in this thesis. All of the main textural and compositional groups are represented.

The specific aims of the petrographic and microprobe work are as follows:

- to identify the crystallising phases in the basalts and dolerites; to determine their relative proportions and order of crystallisation.
- to build up a database of the compositions of the crystallising phases, thus providing constraints on the fractionation modelling carried out in Chapter 6.
- to constrain the metamorphic/alteration histories of these rocks.
- to determine compositions of secondary (alteration and metamorphic) phases, so that their effects on the whole-rock geochemistry can be assessed.
- to ascertain the compositional features of clasts within the volcaniclastic rocks, in order to place controls on their likely provenance.
- to study textural features of volcaniclastic rocks that are not reworked, so that information on the original style of volcanic eruptions can be gleaned.

5.2 Basalts and dolerites

5.2.1 Petrography

5.2.1.1 Petrography of the basalts

The majority of the basalts are highly altered, and primary minerals other than plagioclase are rarely preserved. The degree of alteration is greatest in the western part of the outcrop area (Westermann, 1932), suggesting that the growth of secondary minerals is a contact metamorphic process controlled by the intrusion of the batholith. The photomicrographs (Figs. 5.1, 5.2 and 5.3) show the range of degrees of alteration and metamorphism suffered by these rocks: Fig. 5.1 shows the most common state of alteration; Fig. 5.2 is a relatively fresh sample, and Fig. 5.3 is a contact amphibolite collected from within a few metres of the contact with the batholith.

The basalts are aphanitic, and do not contain phenocrysts or phenocrystic pseudomorphs. The basalts consist of plagioclase laths, which vary in size from approximately 0.2 to 1 mm, set in a groundmass dominated by green amphibole, which is probably of secondary origin (Fig. 5.1). The amphibole crystals are subequant to elongate, and generally very small – about 0.2 mm; occasionally the amphibole has a fibrous habit and is associated with chlorite and other cryptocrystalline clay minerals. No olivine was discovered in these rocks, and very few samples contain any fresh pyroxene. Opaque minerals (including ilmenite and Cr-spinel) are ubiquitous, forming up to ~ 5% of the rock volume, and occur either disseminated throughout the rock, or in densely-packed clusters. The ilmenite and Cr-spinel may represent primary igneous phases, but the proportion of opaque phases in the rock could be modified by formation of secondary opaque minerals (e.g., haematite or sulphides). Rutile occurs as an accessory phase.

The highly altered nature of the basalts means that little information about the primary igneous textures can be deduced, except that the protoliths were aphyric, and contained euhedral to subhedral plagioclase crystals. Where pyroxene is preserved, it occurs as small (0.2 mm), anhedral, slightly elongate crystals that are intergranular to the plagioclase (Fig. 5.2). Some samples contain amygdales, filled with a variety of secondary minerals, including quartz, ?prehnite, epidote, calcite and chlorite.

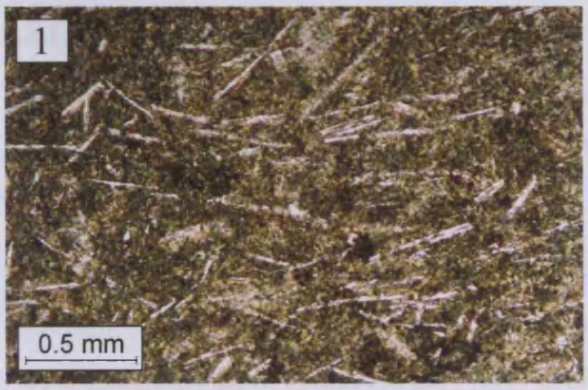

Fig. 5.1: Basalt sample in a representative state of preservation for the Aruba Lava Formation. Plagioclase laths (showing a degree of alignment) are preserved, but no other primary minerals remain. The groundmass consists of green amphibole and opaque minerals. Plane polarised light. (ARU94-29)

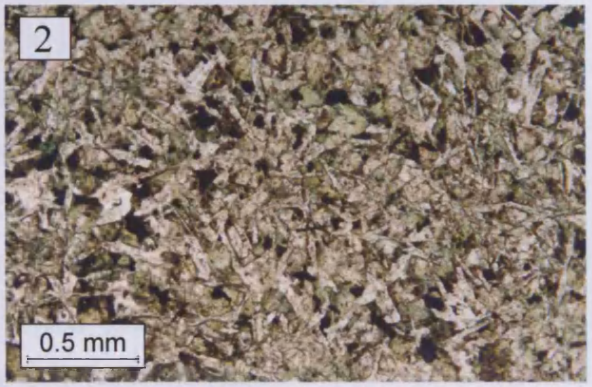

Fig. 5.2: One of the freshest basalt samples. The original equigranular texture is well-preserved, as is the plagioclase, but clinopyroxene crystals are partially altered to amphibole. Plane polarised light. (ARU96-31)

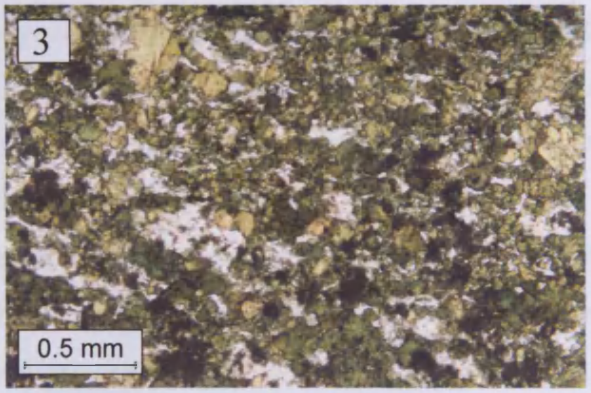

Fig. 5.3: An amphibolite collected from the ALF adjacent to the contact with the batholith. Although the rock macroscopically and chemically resembles a basalt, no original textures are preserved, and the rock is dominated by relatively large green amphibole crystals. Plane polarised light. (ARU97-8)

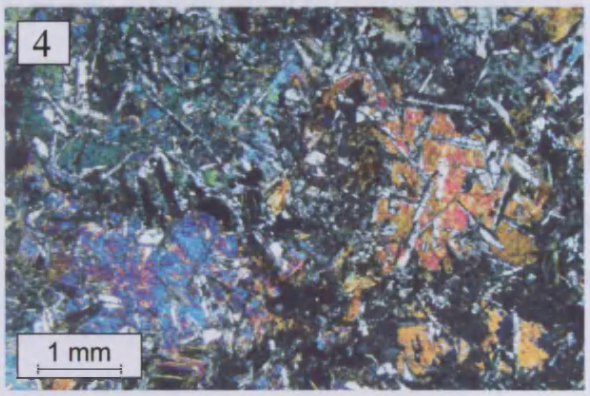

Fig. 5.4: Dolerite with a subophitic texture, having large (~3 mm) augite crystals enclosing (or partially enclosing) small plagioclase laths. Crossed polars. Note the difference in scale between Figs. 5.4 and 5.5. (ARU94-22)

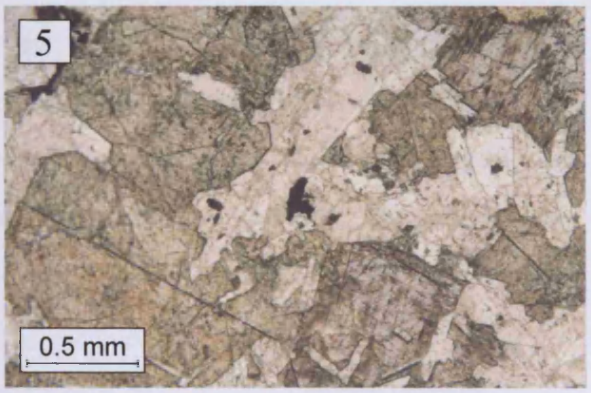

Fig. 5.5: Dolerite with a more equigranular texture than that shown in Fig. 5.4. Clinopyroxene and plagioclase crystals are comparable in size. At the bottom of the picture is a subophitic domain, with pyroxene enclosing plagioclase. Plane polarised light. (ARU96-38)

5.2.1.2 Petrography of the dolerites

The dolerites appear to have suffered less alteration than the basalts, and primary minerals are identifiable in most samples. They are phanerocrystalline, with crystal size varying from fine (~ 1 mm) in some samples to coarse (~ 5 mm) in others. In general terms, the degree of alteration, as well as being geographically controlled by proximity to the batholith, appears to correlate negatively with crystal size, i.e., the finer grained dolerites suffer more pervasive alteration than their coarser grained counterparts.

Although no olivine is identifiable in the dolerites, clinopyroxene (augite) is frequently preserved, and plagioclase is present in all samples. The plagioclase crystals are euhedral to subhedral and show multiple twinning; the augite is usually subhedral to anhedral and occasionally has simple twins. The majority of samples have approximately equal proportions of plagioclase and clinopyroxene. Opaque minerals (ilmenite, magnetite, titanomagnetite and Cr-spinel) are also present, as is quartz (both as a primary mineral and a secondary infill in vughs). The augite crystals in the dolerites frequently are altered to green amphibole; in the most extreme cases, they are almost completely overgrown by the secondary amphibole. Chlorite, apatite, epidote and sphene are also present as alteration products.

The dolerites exhibit a high degree of textural variability. Some samples have a well-developed subophitic texture, with large (~ 3 mm) augite crystals enclosing (or partially enclosing) small plagioclase laths (Fig. 5.4). For the more altered samples, where pyroxene is not preserved, the amphibole replacing it occurs as small crystals that are intergranular between the plagioclase, and it is difficult to determine whether the original texture was equigranular or subophitic. Either is possible, because equigranular (usually subhedral granular) textures are also observed (Fig. 5.5).

The textural relationships observed in the dolerites allow the construction of a crystallisation sequence. For the subophitic dolerites, small plagioclase laths crystallised early, followed by crystallisation of pyroxene. The subhedral granular dolerites suggest that pyroxene and plagioclase crystallisation occurred concurrently; however, these rocks also contain some subophitic domains, where plagioclase crystallised earlier and became (partially) enclosed by pyroxene.

5.2.2 Mineral chemistry of plagioclase

Electron microprobe analyses of plagioclase crystals from the basalts and dolerites rocks range from An_{87} to An_{31}, and are presented in Fig. 5.6. All of the analyses from the

cores of plagioclase crystals fall within the bytownite and labradorite fields; the andesine analyses are exclusively from the rims of crystals in dolerite ARU96-37. Chemical zonation can be distinguished in some thin sections: the zoning is discontinuous, with homogeneous calcic cores mantled by sodic rims. The maximum compositional change observed in any single crystal is from An_{64} to An_{31} (in dolerite sample ARU96-37). The plagioclase compositions fall within the ranges observed for oceanic plateau basalts (e.g., the Ontong Java Plateau; Babbs, 1997), with the more albite-rich analyses (from rims) representing late stage growth of the plagioclase crystals as the liquid became more evolved.

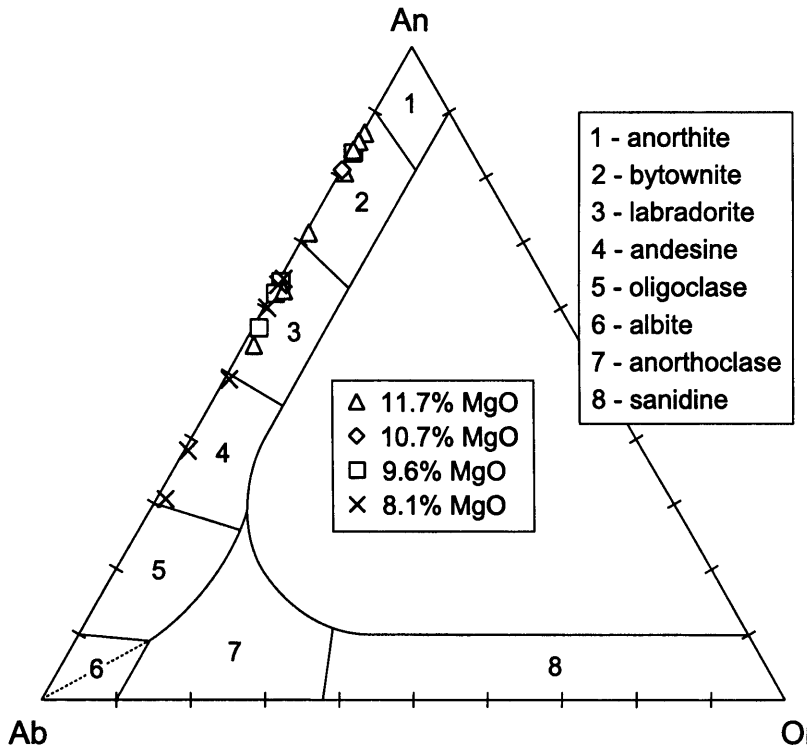

Fig. 5.6: An-Ab-Or plot showing compositions of plagioclase from the Aruba Lava Formation. The symbols represent different samples, and the MgO content of the whole rock for each sample is given. Full whole-rock analyses can be found in Appendix C (XRF) and Appendix D (ICP-MS).

5.2.3 Mineral chemistry of clinopyroxene

Clinopyroxene analyses from members of the Aruba Lava Formation are displayed in the pyroxene quadrilateral (Fig. 5.7). These analyses are all from dolerites, because the clinopyroxenes in the basalts were too small and altered to be successfully analysed. All of the analysed clinopyroxenes are Mg-rich augites (IUGS pyroxene classification: Morimoto *et al.*, 1988) and the range of compositions observed is limited. The Mg numbers of these pyroxenes range from 86 to 71: using a Fe-Mg exchange distribution coefficient of 0.23 (at 1200°C:

derived from Pearce and Parkinson (1993)) these pyroxenes were in equilibrium with melts having Mg# between 59 and 36. This implies that clinopyroxene crystallisation was occurring during a significant fractionation interval of the host melts.

In addition to the major pyroxene constituents (i.e., MgO, FeO, CaO and SiO_2), the clinopyroxenes contain TiO_2 (0.2 to 0.8 wt.%), Cr_2O_3 (0 to 0.9 wt.%), Al_2O_3 (1.5 to 3 wt.%), MnO (0.15 to 0.35 wt.%) and Na_2O (0.15 to 0.25 wt.%). There is a general tendency for TiO_2, MnO and Na_2O contents of the pyroxenes to increase with decreasing Mg#. This is consistent with these components being concentrated in the melt phase during crystallisation such that the later-crystallising pyroxenes, i.e., those with lower Mg#, have higher concentrations of these incompatible elements. The opposite is true for Cr_2O_3, where concentrations decrease with decreasing Mg#. Al_2O_3 contents also decrease very slightly with decreasing Mg#, mirroring the gentle decrease in Al_2O_3 content of the melts during fractional crystallisation (see Section 6.5.1).

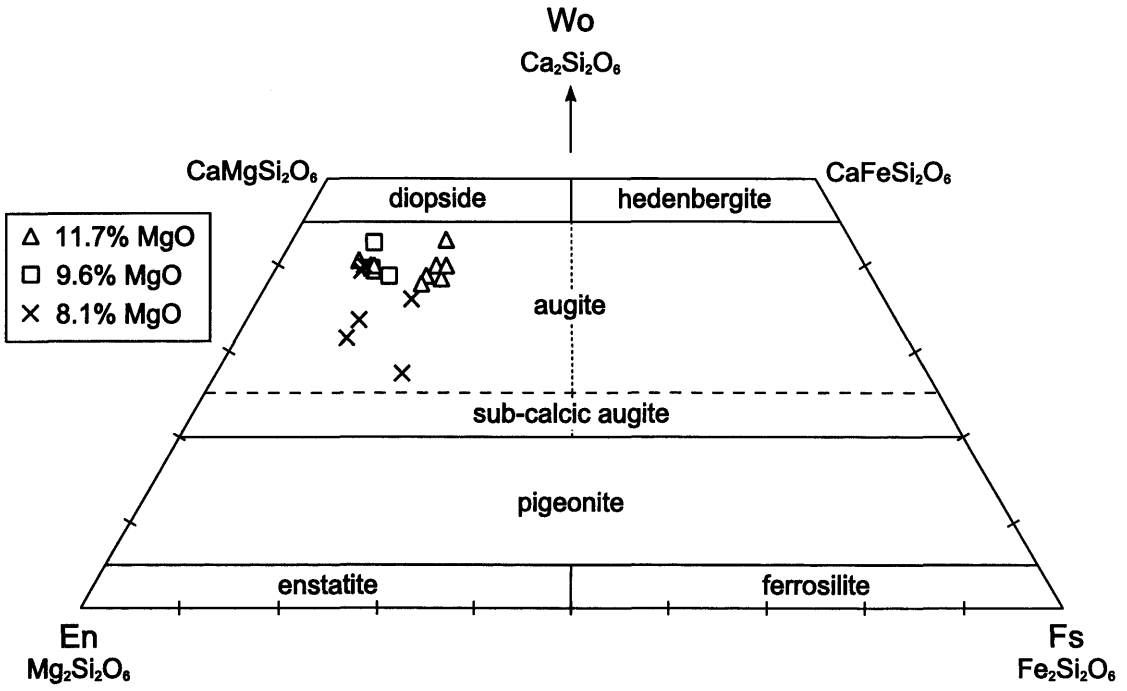

Fig. 5.7: Pyroxene analyses from the Aruba Lava Formation: using the classification of Morimoto *et al.* (1988), all analysed pyroxenes are Mg-rich augites. Symbols refer to different samples: the key gives the MgO content (wt.%) of the corresponding whole rock (full data can be found in Appendix C).

The minor element concentrations in clinopyroxenes are controlled by a range of substitutions, some of which are coupled. In some rock suites (e.g., the Shiant Isles sill: Gibb, 1973), there is a positive correlation between Al_2O_3 and TiO_2 contents of pyroxenes, thought to be due to the substitution $(Fe^{2+}, Mg^{2+}) + 2Si^{4+} \Rightarrow Ti^{4+} + 2Al^{3+}$. In this case the ideal Al:Ti ratio (molecular proportion) in the pyroxene should be 2. For the Aruba Lava Formation

dolerites, no positive correlation between Al_2O_3 and TiO_2 exists, and Al:Ti > 2 (Fig. 5.8), indicating that introduction of Al^{3+} cations must occur also by other substitutions. These include the Tschermak substitution: $(Fe^{2+}, Mg^{2+}) + Si^{4+} \Rightarrow 2Al^{3+}$, and derivatives thereof (e.g., Cr^{3+} or Fe^{3+} instead of Al^{3+}). The amount of Tschermak substitution may be related to temperature, with more Al^{3+} being accommodated into the pyroxene structure at high temperature (e.g., Herzberg and Chapman, 1976); however, experimental studies (Thy, 1991a) have related the Al:Ti ratio to pressure, with increased Tschermak substitution at greater pressures. In real magmatic systems, these conclusions are not necessarily contradictory: for example, crystallisation in a deep magma chamber occurs at both elevated temperature *and* elevated pressure. It seems, therefore, that some of the crystallisation of pyroxene in the Aruba Lava Formation magmas occurred at high temperatures and/or pressures, although given the apparently contradictory data in the literature (Herzberg and Chapman, 1976; Thy, 1991a), it is difficult to determine which of these factors is the more significant, and no real conclusions can be drawn about where this crystallisation actually took place. Another possibility is that the basaltic liquids inherited pyroxene crystals from either their source region, or gabbroic rocks crystallised at depth; however, the lack of pyroxene xenocrysts in any of the basalts studied does not support this hypothesis.

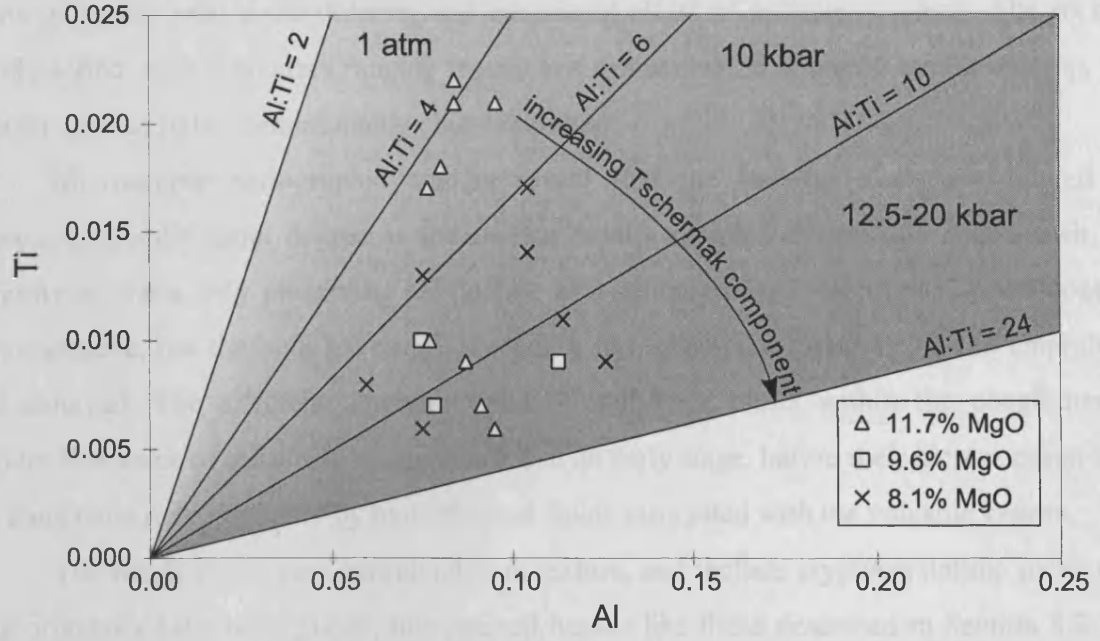

Fig. 5.8: Al and Ti (molecular proportions, calculated to 6 oxygen atoms per formula unit) values for pyroxenes from the Aruba Lava Formation. Symbols refer to different samples: the key gives the MgO content (wt.%) of the corresponding whole rock. All Aruba samples have Al:Ti > 2, suggesting they have a significant Tschermak component. The arrow gives the direction of increasing Tschermak substitution, which correlates with increasing temperature (Herzberg and Chapman, 1976) and/or increasing pressure (Thy, 1991) of crystallisation. The pressure values that relate to different Al:Ti values are from Thy (1991).

5.2.4 Mineral chemistry of opaque phases

The opaque phases in the Aruba Lava Formation basalts and dolerites are ilmenite, magnetite, titanomagnetite and Cr-spinel. Very few microprobe analyses of these phases were successful, because of their small size and irregular surface morphology, arising from the fact that many "crystals" were actually fine-grained aggregates of opaque phases intermingled with other minerals. Acceptable analyses are presented in Appendix G.

5.2.5 Mineralogy of secondary phases

A few microprobe analyses of secondary amphiboles were obtained: these are all magnesiohornblendes, according to the classification scheme of Leake *et al.* (1997), and have a restricted range of compositions within this category.

A secondary chlorite from a dolerite has Mg# ≈ 54 and MgO ≈ 16 wt.%.

5.3 Volcaniclastic rocks

5.3.1 Petrography of the basaltic conglomerate

The basaltic conglomerate consists macroscopically of sub-rounded to sub-angular clasts of basalt, with some dolerite, and occasional clasts of sedimentary rock. The rock is poorly sorted, with clast sizes ranging from a few millimetres to about 15 cm. In outcrop, the deposit appears to be predominantly clast-supported.

Microscopic petrographic studies reveal that the basaltic clasts are altered to approximately the same degree as the *in situ* basalts sampled during this study, with the majority of clasts only preserving plagioclase as a primary phase. Occasional clasts contain clinopyroxene, but the bulk have only secondary ferromagnesian minerals (green amphibole and chlorite). The different alteration state of individual clasts within the conglomerate implies that some of the clasts became altered at an early stage, before their incorporation into the composite rock, probably by hydrothermal fluids associated with the volcanic system.

The basalt clasts vary considerably in texture, and include cryptocrystalline rocks that may originally have been glassy, fine grained basalts like those described in Section 5.2.1.1, and basalts containing phenocrysts or glomerocrysts of plagioclase or plagioclase and clinopyroxene (Fig. 5.9). The textural variability observed in the clasts of the basaltic conglomerate is greater than that seen in the basalt flows, indicating either that the basalts sampled during this study did not cover the whole textural range, or that the clasts in the

basaltic conglomerate were derived from a wider catchment area than is presently exposed on Aruba. The paucity of dolerite clasts in the basaltic conglomerate compared to the present outcrop area is hardly surprising: given that the basaltic conglomerate occurs interbedded within the Aruba Lava Formation, it must have been deposited at the same time as the volcanic activity, and so preferentially samples lithologies that were exposed at the surface, i.e., basalts rather than dolerites. The clasts of sedimentary rock in the conglomerate are petrographically akin to some of the fine-grained volcaniclastic rocks discussed in the next section (Section 5.3.2).

The matrix of the basaltic conglomerate consists of smaller basaltic clasts, individual crystals of plagioclase (and occasional pyroxenes), and brownish-coloured cryptocrystalline material (Fig. 5.10) that is similar in appearance to the matrix of the fine-grained volcaniclastic rocks (see Section 5.3.2).

5.3.2 Petrography of the fine-grained volcaniclastic rocks

The fine-grained volcaniclastic rocks are generally well sorted, and vary in grain size from silt to coarse sand grade. Bedding is usually present, and is manifest on a millimetre to decimetre scale. It commonly shows sedimentary structures such as grading, ripple cross-bedding and convolute bedding, indicating that the sediments have been reworked. In general, the volcaniclastic rocks with the most basaltic compositions show the least evidence for reworking, and these may represent original, unmodified, volcanogenic deposits. This implies that the reworking processes may be changing the bulk composition of the rocks to something more silicic, consistent with the higher resistance of minerals like plagioclase and quartz to weathering and sedimentary processes.

A typical non-reworked basaltic volcaniclastic rock is pictured in Fig. 5.11. This crystal-rich sample contains plagioclase, augite and quartz, together with small lithic clasts, which are also basaltic in composition. The existence of a volcaniclastic rock of this composition suggests that some of the basaltic volcanism on Aruba was explosive. The clasts are bound by a brown-coloured cryptocrystalline matrix which contains some patches of calcite. The deposit is relatively poorly sorted and does not contain any fine-scale sedimentary lamination. A few of the plagioclase crystals are euhedral, but the majority have irregular, angular shapes, conceivably arising from fracture during an explosive eruption.

Fig. 5.12 shows another type of volcaniclastic rock that also appears to have been formed via explosive eruption of basaltic material. It consists of extremely fine-grained clasts

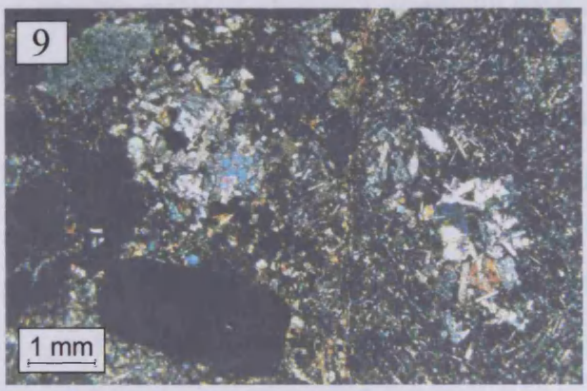

Fig. 5.9: Basaltic conglomerate (shown with crossed polars). The clast making up the right-hand third of the picture is a basalt with a large glomerocryst of plagioclase and clinopyroxene. The oblong-shaped black clast in the lower left is an extremely fine-grained (glassy) basalt. (ARU97-138)

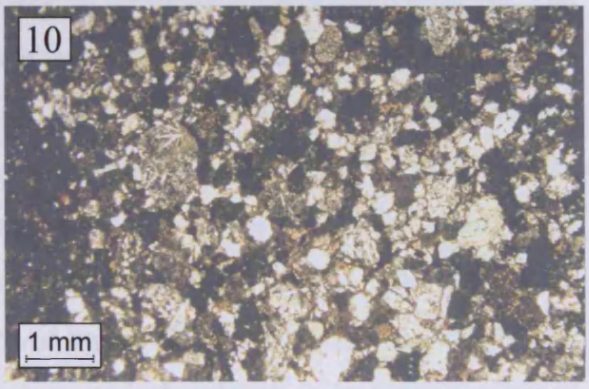

Fig. 5.10: The matrix of a basaltic conglomerate consists of smaller basaltic clasts, individual crystal fragments (mainly plagioclase) and brown cryptocrystalline material. Plane polarised light. (ARU97-139)

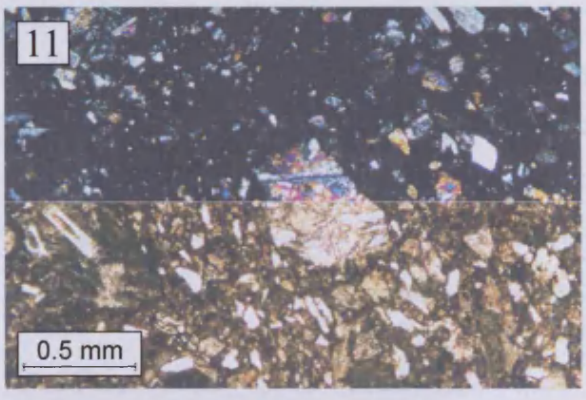

Fig. 5.11: Fine-grained volcaniclastic rock, with a small basaltic clast and fragments of plagioclase, clinopyroxene and quartz. Top half: crossed polars; bottom half: plane polarised light. (ARU96-76)

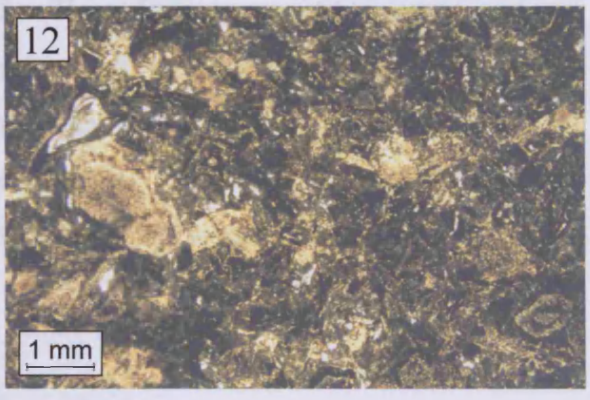

Fig. 5.12: Volcaniclastic rock composed of crypt-ocrystalline (once glassy?) clasts of basaltic material. Plane polarised light. (ARU94-24)

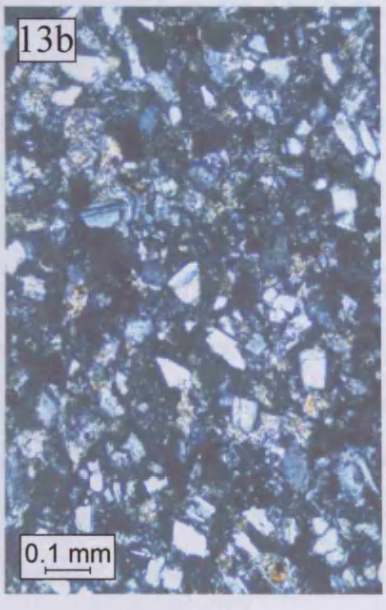

Fig. 5.13a: Syn-sedimentary fault in a reworked volcaniclastic rock. The bedding is defined by different proportions of clasts to matrix and the clast size. Plane polarised light. (ARU96-77)

Fig. 5.13b: Magnified view of a coarse-grained, plagioclase-rich bed in the same thin section (crossed polars) to demonstrate that the clasts are predominantly plagioclase feldspar. (ARU96-77)

of basaltic material, that may originally have been glassy and are now cryptocrystalline. The only identifiable minerals in this lithology are a few small plagioclase laths.

The reworked volcaniclastic rocks contain crystals of plagioclase, and a small amount of quartz and pyroxene (mostly altered to amphibole), in a brown-coloured cryptocrystalline matrix, probably composed of clay minerals. Other minerals present are calcite, epidote and chlorite, but these appear to be secondary. The bedding is defined by the grain size of the plagioclase crystals and variation in the proportion of crystal clasts to matrix (Fig. 5.13). In the finer-grained, clay-mineral-rich layers, a spaced cleavage is developed at an oblique angle to bedding.

No clasts of a continental provenance were observed in these rocks. The observed mineral grains have all been found in the basalts and dolerites (mainly plagioclase, with some pyroxene and quartz), and all of the lithic clasts are different textural varieties of basaltic rocks, or occasionally different volcaniclastic rocks. The sediments are poor in quartz, and any quartz that is present does not have any petrographic features characteristic of a long history (e.g., undulose extinction). The only metamorphic minerals present are those that are also present in the basalts and dolerites. It is concluded, therefore, that the fine-grained volcaniclastic sedimentary rocks are locally derived, from weathering and reworking of basalts, dolerites and volcaniclastic sediments.

5.3.3 Petrography of the ignimbrite

Close to Dos Playa (see Fig. 3.2 and Section 3.2.1.3) is a horizon in the Aruba Lava Formation which has the field appearance of an ignimbrite, having clasts ranging from 2 mm to 4 cm that are flattened parallel to bedding, giving the rock a eutaxitic texture. The rock appears to be more silica-rich than any other volcanic rock on Aruba, and this is confirmed by the chemical analysis (see Appendix C) and the preponderance of felsic minerals in thin section. It is not known whether the high silica content is an original feature of the rock, or whether the rock has been subsequently silicified.

In thin section, the clasts are composed almost entirely of very fine (< 0.1 mm) granular quartz and feldspar, set in a matrix of even finer, almost cryptocrystalline material of a similar composition. Very occasionally, clinopyroxene crystals (~ 0.3 mm) are found within the clasts (Fig. 5.14). The matrix between the clasts also consists of very fine granular quartz (?and feldspar) together with clay minerals, which make the matrix appear brownish in plane polarised light, compared with the essentially colourless clasts. Some clasts consist entirely of an extremely fine aggregate of ?quartz crystals: these could represent chert (lithic) clasts, or

devitrified silicic volcanic glass. The extremely fine granular textures observed in this rock do not appear to be original, and may have resulted from silicification or recrystallisation. The presence of occasional clinopyroxene crystals hints that the magma from which this rock was derived was not necessarily as silicic as its present (dacitic; $SiO_2 \approx 66\%$) bulk composition, consistent with the silicification hypothesis.

The eutaxitic texture of this rock gives rise to the question of the emplacement temperature of this lithology: was the rock emplaced at high enough temperatures to become welded? Although this lithology is presently highly indurated, this could be a function of secondary processes, for example, recrystallisation or silicification. Petrographic studies of young ignimbritic rocks can sometimes answer this question: if the rock has a glassy matrix, or perlitic cracks arising from glass devitrification, it can be concluded that the rock was emplaced at high enough temperatures to become welded. For the Aruba ignimbrite, no glass or perlitic cracks are present, but in this case, because the rock appears to be recrystallised, the temperature of emplacement cannot be deduced.

5.3.4 Petrography of the accretionary lapilli tuff

The lapilli tuff consists of flattened accretionary lapilli in a matrix of a similar composition. The lapilli have an oval shape (in two dimensions) due primarily to flattening, and their concentric internal structure (Fig. 5.15) is defined by bands that are darker in plane polarised light. With the exception of scarce small plagioclase crystals, no primary minerals can be identified, and the rock is almost completely cryptocrystalline apart from some overgrowths of secondary minerals (epidote and amphibole). Accretionary lapilli are the result of aggregation of miniscule ash particles from a moist eruption cloud (Cas and Wright, 1987), indicating once more that some of the volcanic activity contributing to the Aruba Lava Formation was explosive, and probably phreatomagmatic, in nature.

5.4 Deformed and metamorphosed members of the Aruba Lava Formation

5.4.1 Petrography and mineral chemistry of the amphibolites

In thin section, the amphibolites consist predominantly of green amphibole and plagioclase, with minor quartz and occasional clinopyroxene crystals (Fig. 5.16). Magnetite, sphene, epidote, apatite and calcite occur as accessory phases. The amphibolites are markedly heterogeneous, and some samples have a different bulk composition, characterised by having

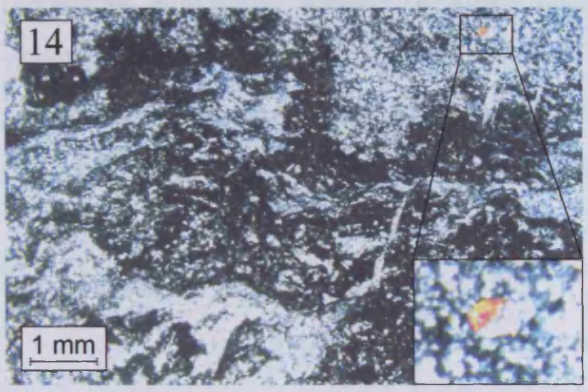

Fig. 5.14: Pyroclastic rock with eutaxitic texture (crossed polars). The magnified mineral is clinopyroxene. It is not known whether this is an equilibrium phase in a now-silicified rock, or a xenocryst in a silicic magma. (ARU96-13)

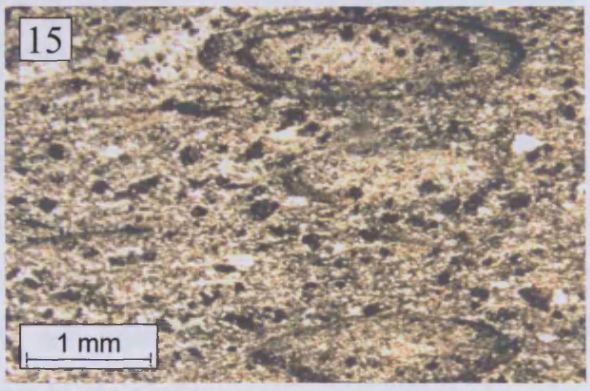

Fig. 5.15: Accretionary lapilli tuff: the lapilli have been deformed and are now oval shaped in cross-section. The dark patches are secondary minerals overgrowing the original texture. Plane polarised light. (ARU97-69)

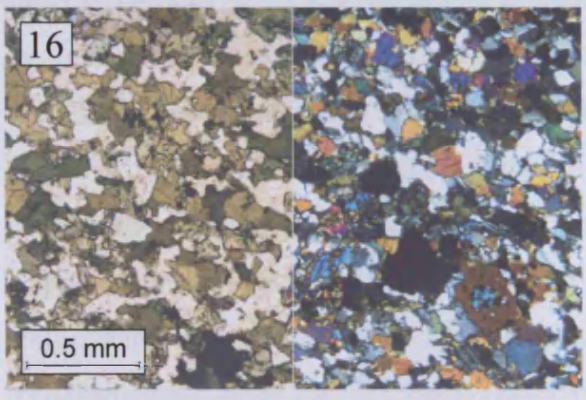

Fig. 5.16: Typical amphibolite, consisting of green amphibole and plagioclase, with some quartz and clinopyroxene. Left side: plane polarised light; right side: crossed polars. (ARU97-40)

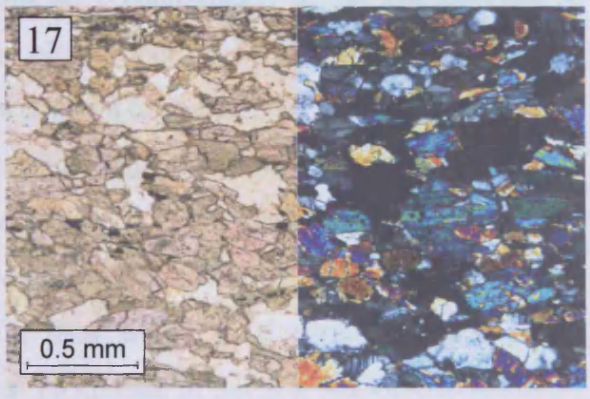

Fig. 5.17: Amphibolite with a different bulk composition from that shown in Fig. 5.16, dominated by colourless (rather than green) amphibole. Left side: plane polarised light; right side: crossed polars. (ARU96-142)

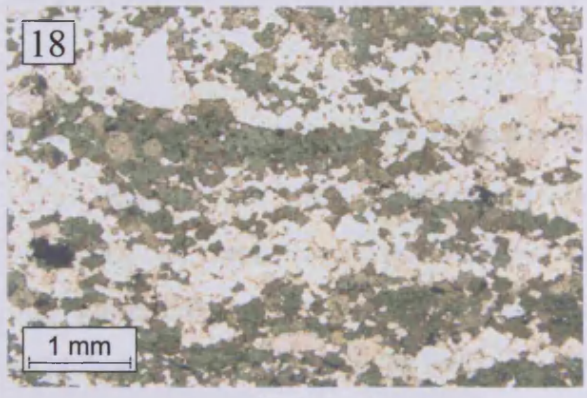

Fig. 5.18: This amphibolite shows segregation into mafic (amphibole-dominated) and felsic (plagioclase and quartz-dominated) layers. This is interpreted as the onset of melting (see text). Plane polarised light. (ARU97-147)

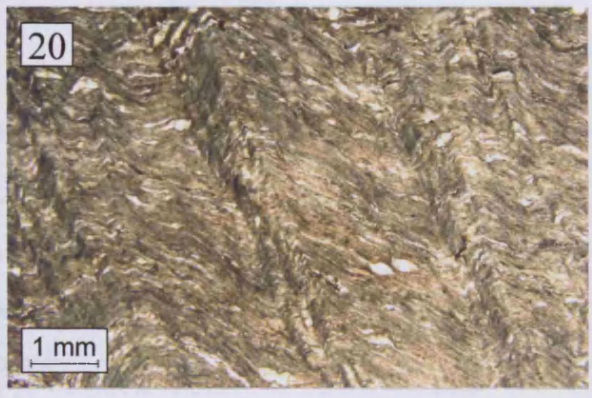

Fig. 5.20: Deformed chlorite schist (plane polarised light), demonstrating that an original cleavage (probably formed by shearing: see quartz pods) has been crenulated by a second deformation event. (ARU96-88)

colourless amphibole instead of green amphibole (Fig. 5.17). This probably represents compositional variation in the protoliths of the amphibolites, with some more-MgO-rich samples being dominated by colourless MgO-rich amphiboles. Amphibole analyses reveal that the green amphiboles fall into the magnesiohornblende category (Leake *et al.*, 1997) and have Mg# ranging from 50 to 80 and MgO ≈ 10 to 14 wt.%, whereas the colourless amphiboles are cummingtonites having Mg# ≈ 70 and MgO ≈ 22 wt.%.

Some samples are segregated into mafic and felsic layers, the mafic layers being dominated by green amphibole and the felsic layers by plagioclase and quartz (Fig. 5.18). This is interpreted as the onset of melting, with silicic liquids being extracted from the bulk rock, leaving an amphibole-rich residue.

The amphibolites are texturally well-equilibrated, and have granular textures, with equal-sized plagioclase and amphibole crystals that are predominantly equant and anhedral in the poorly-foliated amphibolites (Fig. 5.16) and elongate in the well-foliated amphibolites (Fig. 5.17). This equilibrated texture is in marked contrast to some of the contact amphibolites (e.g., Fig. 5.3) found adjacent to the batholith margins in other regions. This could be simply because the equilibrated amphibolites are found mainly at Andicuri, adjacent to a gabbroic massif of the Aruba batholith. This gabbro would have intruded at a significantly higher temperature than the tonalites of the batholith, and would have promoted more rapid recrystallisation in the country rocks. However, as mentioned in Section 3.2.4.1, the Andicuri amphibolites cannot be explained simply by contact metamorphism: many samples have a well-defined foliation (Fig. 5.17). This is seen in thin section by alignment of tabular plagioclase crystals and alignment of amphibole crystals. Lineations are also present in some samples, and are defined by alignment of amphiboles.

5.4.1.1 Hornblende-plagioclase geothermometry

Approximate temperatures of equilibration for hornblende-plagioclase mineral pairs have been calculated according to the methods of Blundy and Holland (1990). The amphibole-plagioclase thermometer is based on the exchange equilibrium of Al in tetrahedral sites in amphiboles and albite due to the following reactions:

edenite	+ quartz =	tremolite	+ albite
$NaCa_2(Mg,Fe)_5[Si_7AlO_{22}](OH)_2$	$+ 4\ SiO_2$ =	$Ca_2(Mg,Fe)_5Si_8O_{22}(OH)_2$	+ $NaAlSi_3O_8$

pargasite	+ quartz =	hornblende	+ albite
$NaCa_2(Mg,Fe)_4Al[Si_6Al_2O_{22}](OH)_2$	$+ 4\ SiO_2$ =	$Ca_2(Mg,Fe)_4Al[Si_7AlO_{22}](OH)_2$ +	$NaAlSi_3O_8$

The method is appropriate for both metamorphic and igneous rocks, as long as they contain calcic amphibole (having less than 7.8 Si atoms per formula unit) in equilibrium with plagioclase (less calcic than An_{92}) in a silica-saturated rock. Calibration has been carried out within the temperature range 500° - 1100°C, and the inherent errors due to the method and its calibration are estimated as ± 75°C (2σ). This error estimate also includes uncertainty in electron microprobe analyses for typical mineral compositions, but does not include geological error, for example, incomplete equilibration of mineral phases. The pressure dependence of the above reactions is poorly constrained, but is thought to be much less significant than the effect of temperature.

The equilibration temperatures were determined for mineral pairs from three samples. The results from two of the samples are very consistent, and the third sample gives temperatures that are slightly lower. These temperatures are presented in Fig. 5.19.

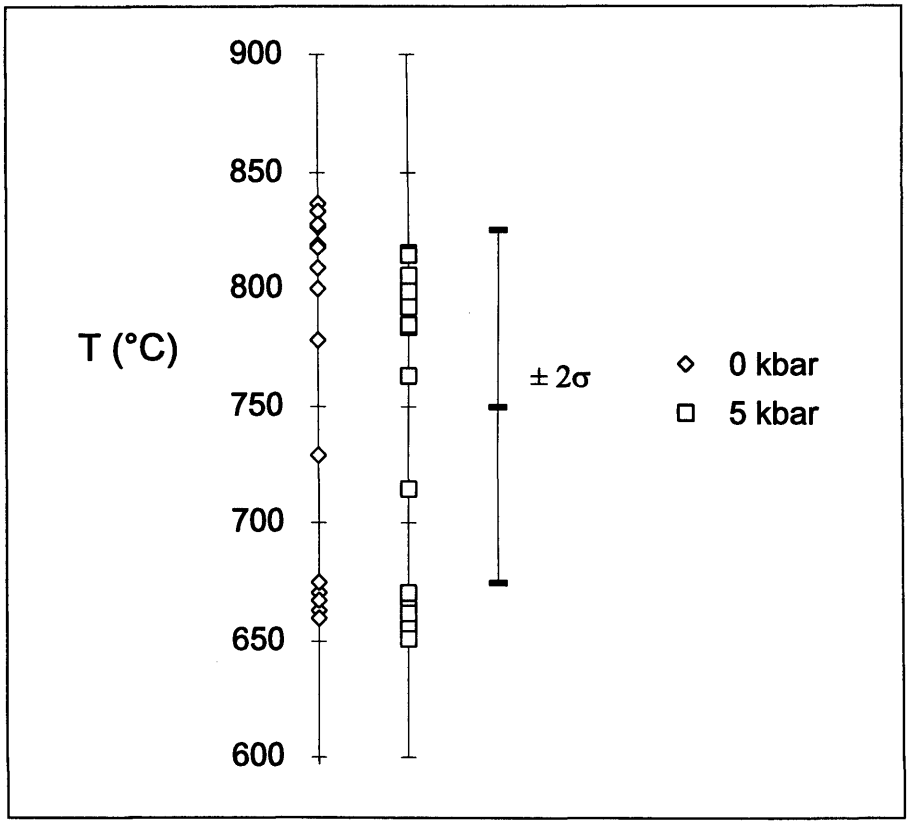

Figure 5.19: Estimates of hornblende-plagioclase equilibration temperatures, using the method of Blundy and Holland (1990). The temperatures obtained for the 5 kbar calculations are only slightly lower than those for the 0 kbar estimate, because the Al-exchange reactions involved are not particularly pressure-sensitive.

Because no independent estimate of pressure could be made for the amphibolites, the equilibration temperatures were calculated for 0 kbar and 5 kbar, corresponding to depths of 0 km and ≈ 15 km, respectively. None of the amphibolites studied contained any garnet, and 15 km is a reasonable estimate (in fact, probably an overestimate) of their maximum depth. The temperatures for both pressure estimates all fall between 650°C and 850°C, with a greater number of samples at the high temperature end of this range. These temperatures are somewhat high for low pressure (i.e., non-garnet bearing) amphibolites, consistent with their location adjacent to a large gabbro body. Additionally, the temperatures obtained using the hornblende-plagioclase geothermometer corroborate the petrographic evidence for melting (Fig. 5.18), as the highest temperatures recorded in the amphibolites approach estimates for the wet basalt solidus temperature at <5 kbar (e.g., Green, 1982; Wolf and Wyllie, 1994; Rapp and Watson, 1995).

5.4.2 Petrography of deformed chlorite-schists

The deformed chlorite schists are very well foliated rocks dominated by cryptocrystalline chlorite. Sometimes the primary foliation is crenulated (Fig. 5.20), and in some locations, secondary amphibole crystal overprint the foliation. X-ray diffraction analysis (R. Wilson, pers. comm.) of these rocks demonstrates that they consist of clinochore (the Mg-rich chlorite endmember), although the clinochore peak is coincident with the magnesiohornblende peak, indicating that the overprinting amphibole phase is probably magnesiohornblende. The Mg-rich chlorite found in these rocks is different from the chlorite alteration product of the dolerites, suggesting either that the protolith of the deformed chlorite schists was richer in MgO, or that the fluids responsible for alteration of this lithology were richer in MgO than those fluids altering the dolerite.

5.5 Summary

- The Aruba Lava Formation basalts and dolerites are (or, for the altered rocks, were) composed predominantly of plagioclase and pyroxene, in approximately equal proportions. Opaque accessory phases include ilmenite, Cr-spinel, magnetite and titanomagnetite, and no olivine was found in any of the samples.
- The basalts are highly altered, with the secondary assemblages dominated by green amphibole (magnesiohornblende) and chlorite. These secondary phases also occur in the

dolerites, although the primary mineralogical and textural features of the dolerites are much better preserved than those of the basalts.

- Textural relationships in the dolerites suggest that plagioclase crystallisation commenced prior to clinopyroxene crystallisation, but for the majority of the crystallisation interval, both phases grew concurrently.
- The clasts in the basaltic conglomerate and the fine grained volcaniclastic rocks are all consistent with a local derivation, i.e., from within the Aruba Lava Formation. None of these rocks contain material with an obviously continental provenance.
- The non-reworked fine-grained basaltic tuffs suggest that explosive eruption of basaltic magma accompanied the effusive magmatism. The presence of tuffs bearing accretionary lapilli indicates that at least some of this explosive activity was due to interaction of magma with water.
- Amphibolite-facies rocks found near Andicuri consist of magnesiohornblende and/or cummingtonite with plagioclase and minor quartz and clinopyroxene. Equilibration temperatures for these assemblages range from 650°C to almost 850°C, close to the onset of melting for water-saturated basaltic rocks. This substantiates the field and petrographic evidence for melting, i.e., small-scale silicic segregations.

Chapter 6

Petrogenesis of the Aruba Lava Formation

6.1 Introduction

This chapter examines whole-rock geochemical and isotopic analyses, together with the petrographic and mineralogical characteristics discussed in the previous chapter, in order to evaluate the processes that have influenced the composition of the Aruba Lava Formation rocks. The composition of a suite of (predominantly) basaltic rocks such as this is controlled by a myriad of processes and variables: firstly, the composition of the mantle from which the parental magmas were derived, and the melting processes involved. The second group of processes to be appraised involve those that modified these parental magmas between the time of their extraction from the mantle and their emplacement at (or near) the surface. This second group potentially includes processes such as fractional crystallisation and assimilation of pre-existing crustal rocks during magma ascent, as well as mixing with other magma batches. Finally, it is necessary to assess how post-emplacement processes have changed the observed compositions: these processes could include hydrothermal alteration occurring shortly after emplacement, metamorphism occurring at the time of intrusion of the Aruba batholith, and subsequent secondary alteration.

The approach used here is "youngest first". It is vital, in a study of this nature, to consider the effects of the younger processes before deciding which data can reasonably be used to model the petrogenetic history, which is the ultimate aim of this chapter. Throughout this section, the Aruba Lava Formation rocks will be compared with other, apparently similar, rock suites from the adjacent island of Curaçao and the Ontong Java Plateau in the W. Pacific. The reason for this is simple: a detailed and totally meaningful geochemical study of the Aruba Lava Formation is difficult because the rocks are not pristine (see Chapter 5). If it can be shown, however, that these rocks are very similar to other better-preserved and better-studied suites, the conclusions of those earlier studies can perhaps be applied to Aruba. Data from the Curaçao Lava Formation have been chosen for comparison because of: 1) Curaçao's geographical proximity to Aruba; 2) the similarity in age of the two Formations; and 3) the lower degree of alteration/metamorphism of the Curaçao rocks. The Ontong Java Plateau has

also been chosen for comparison because 1) it is well documented as an oceanic plateau, both geochemically and geophysically (e.g., Mahoney, 1987; Gladczenko *et al.*, 1997; Babbs, 1997); and 2) there is a large database of both geochemical and isotopic data available.

6.2 Alteration and metamorphism of the Aruba Lava Formation

It has been shown in Chapters 3 and 5 that the rocks of the Aruba Lava Formation are metamorphosed and altered, and only rarely preserve their original mineralogy. For the purposes of a geochemical study, it is essential to consider how interaction with metamorphic fluids and growth of secondary minerals have influenced the resulting chemical composition. Certain elements (e.g., Sr, Ba) are considered to be highly mobile during alteration (e.g., Ludden *et al.*, 1982), so use of these elements for understanding igneous processes is prone to error. Conversely, some elements remain essentially immobile, even during metamorphism, and abundances of these elements *can* be used to constrain the magmatic processes of interest.

Although many previous studies (e.g., Hart *et al.*, 1974; Humphris and Thompson, 1978; Gelinas *et al.*, 1982; Ludden and Gelinas, 1982; Dostal and Strong, 1983; Schiano *et al.*, 1993) have considered element mobility during alteration and/or metamorphism, their conclusions are not necessarily applicable to the Aruba Lava Formation, because the relative mobility of elements depends on an array of complex factors that vary according to lithology and locality as well as degree and style of alteration (Kerr, 1993). In spite of this complexity, certain elements may have general tendencies towards being either relatively immobile or mobile, and a knowledge of these general tendencies is required before the specific questions of elemental mobility in the different lithologies can be addressed.

Elemental mobility can be assessed by determining the degree of correlation between pairs of elements: if a high degree of correlation is achieved, it can mean either that both elements can be considered immobile, or that both elements behave in exactly the same way during metamorphism or secondary alteration. A low degree of correlation, on the other hand, means that one or both of the elements being considered have had a history of mobility. Although the two previous statements suggest non-unique solutions for any one pair of elements, when a wide range of elements is considered, their relative mobilities can be deduced. This type of analysis assumes that in a genetically related suite of *pristine* rocks, all elements show a high degree of correlation, an assumption that is not necessarily true, but usually seems to be the case, especially in basaltic systems.

6.2.1 Major element mobility - previous studies

Major element mobility is controlled predominantly by the composition of the newly-forming secondary phases. This varies according to degree of alteration/metamorphism, the composition of the circulating fluids, and the bulk composition of the protolith. When considering mobility of the major elements, it is also important to include the effects of apparent mobility due to mass balance effects: for example, if a rock is heavily silicified, the concentrations of other oxides (and trace elements) will be reduced by dilution, although they may not have been physically removed from the system (Dostal and Strong, 1983).

In many studies of altered basaltic rocks, major element mobility is somewhat neglected with respect to trace element mobility (e.g., Borsi *et al.*, 1995). However, there is good evidence that major elements are significantly mobile. Reduced concentrations of SiO_2, Al_2O_3, CaO, Na_2O and K_2O have been reported from vesicular flow margins of the Mull lava succession (Morrison, 1979) due to leaching by hydrothermal fluids. In different alteration environments, other major constituents may become mobile: Kempton and Casey (1997) reported enrichments in MgO and depletions in CaO, FeO and TiO_2 in hydrothermally altered diabase dykes from ODP Leg 153, due primarily to growth of secondary chlorite. CaO depletion (with accompanying Na_2O enrichment) will also occur if calcic plagioclase is altered to albite. Cann (1979) found that lower greenschist facies metamorphism of ocean-floor basalts resulted in significant losses of CaO and Al_2O_3, and variable gains in SiO_2, $FeO_{(t)}$ and Na_2O, whereas MnO, K_2O, TiO_2 and P_2O_5 remained essentially unaffected.

It should be stressed that the studies summarised above are relevant to rocks altered in conditions only as extreme as lower greenschist facies. It seems logical that alteration and metamorphism at higher grades will lead to enhanced mobility. However, it becomes extremely difficult to determine the effects of element mobility at these higher grades, chiefly because assumptions are required about the original composition of the rock. Attempts to circumvent these problems include the use of molecular proportion ratio diagrams (e.g., FeO/Al_2O_3 vs. SiO_2/Al_2O_3: Pearce, 1968). Using this method, Beswick (1982) argued that SiO_2, Al_2O_3, TiO_2, $FeO_{(t)}$, MgO and CaO were not discernibly mobile in low grade metamorphism of most greenstone belt volcanics, in contrast to Na_2O and K_2O. However, it has been demonstrated both statistically and empirically (Rollinson and Roberts, 1986) that molecular proportion ratio diagrams may produce spurious correlations, i.e., the apparent immobility of certain elements may, in fact, be a statistical artefact. Gelinas *et al.* (1982) carefully considered the mobility of major elements in mafic metavolcanics (up to upper

greenschist facies) and concluded that, even though Na_2O, K_2O, CaO, FeO, and MgO had been mobile, the chemical changes in the rocks were not sufficient to obliterate their original (tholeiitic or calc-alkaline) affinities, which were determined independently using immobile trace elements.

6.2.2 Trace element mobility - previous studies

The mobility of trace elements in altered and metamorphosed basaltic rocks appears to be better known than that of major elements, and only a brief review will be attempted here.

In general, the high-field-strength elements (HFSE: Nb, Zr, Y, P, Ti, Hf) are considered immobile for a wide range of lithologies and degrees of alteration/metamorphism as high as amphibolite facies (Sheraton *et al.*, 1989). The rare earth elements (REE: La, Ce, Pr, Nd, Sm, Eu, Gd, Tb, Dy, Ho, Er, Tm, Yb, Lu) are also usually regarded as immobile, at least up to greenschist facies (Humphris *et al.*, 1978; Ludden and Thompson, 1979) and sometimes at even higher metamorphic grades (Bernard-Griffiths *et al.*, 1991). However, several authors consider the REE, particularly the LREE to be more susceptible to mobility during alteration than the HFSE (e.g., Wood *et al.*, 1976; Ludden *et al.*, 1982; Lahaye *et al.*, 1995). This may be because the REE, being highly incompatible elements, become concentrated in the residual liquid during crystallisation, and eventually may be incorporated into late-crystallising glasses that are preferentially altered (Humphris *et al.*, 1978). In certain circumstances, however, both HFSE and REE may become extremely mobile, for example, in zones of carbonation associated with shear zones in the Abitibi belt (Kerrich, 1994). This is because CO_2-rich fluids are capable of stabilising the REE and HFSE as carbonate complexes (e.g., Cantrell and Byrne, 1987; Hynes, 1980).

The behaviour of the large-ion-lithophile elements (LILE: Rb, Sr, Pb, K, Ba, Na) contrasts markedly with that of the REE and HFSE discussed above. This is principally because of the large size and low ionic potential of the LILE, which makes them liable to dissolution in aqueous fluids. These elements are deemed mobile, even at low degrees of alteration (e.g., Staudigel *et al.*, 1981; Ludden *et al.*, 1982; Dostal and Strong, 1983).

The mobility of transition metals (e.g., Sc, V, Cr, Co, Ni, Zn, Cu) depends to an extent on temperature (more mobile at higher temperatures: Seewald and Seyfried, 1990). Mn, Zn and Cu tend to be more mobile than Co, Ni, V, Sc and Cr (Humphris and Thompson, 1978; Annesley, 1990; Rollinson, 1993).

6.2.3 Element mobility in the Aruba Lava Formation

An evaluation of element mobility in the Aruba Lava Formation has been made by studying bivariate element plots. The element Zr was chosen as the abscissa, because not only is it considered to be one of the most immobile elements (see Section 6.2.2), but it occurs in the rocks at abundances that can be easily analysed by XRF with reasonable analytical precision (see Appendix E). The plots shown in Figs. 6.1 to 6.4 display all the available data, divided by lithology. However, because element mobility does appear to vary with lithology, different groups of lithologies are discussed separately in the following section.

6.2.3.1 Element mobility in basalts and dolerites

Major elements: In Fig. 6.1, fields that encompass the majority of basalts and dolerites are shown. Dotted fields extend the former to include *all* basalts and dolerites. For MgO and Al_2O_3, all of the basalts and dolerites show a well defined, tightly-clustered trend, suggesting that these elements have not been mobile during alteration and metamorphism. The majority of samples show well defined trends for SiO_2, $Fe_2O_{3(t)}$, and K_2O: these elements have been mobilised only for the few samples that lie away from the main trend. MnO, CaO and Na_2O show linear clusters of points with a few outlying samples. The clusters are not as well-defined as the trends for SiO_2, $Fe_2O_{3(t)}$ and K_2O, suggesting that MnO, CaO and Na_2O are generally slightly mobile, becoming more so for certain samples. Interestingly, the highest SiO_2, $Fe_2O_{3(t)}$, MnO, CaO and Na_2O mobility has predominantly affected basalts, whereas K_2O mobility has affected both basalts and dolerites. The greater elemental mobility for the basalts suggests the alteration is chiefly a consequence of sea water percolation following extrusion of the lava, rather than secondary alteration during (for example) intrusion of the batholith.

Loss on ignition (LOI): All except one of the basalts and dolerites have LOI < 2%. There is no coherent relationship between LOI and Zr content. Sample ARU96-119, with an LOI of 2.34% also has the highest Sr, K_2O and Na_2O contents, and appears to be the most altered sample. There is also no systematic relationship between LOI and lithology, i.e., basalts and dolerites have comparable LOI values.

HFSE and REE: The fields shown in Fig. 6.2 include all analysed basalt and dolerite samples, even those which appeared to have suffered some major element mobility. TiO_2, P_2O_5, Nb and the REEs show well-defined linear trends, suggesting that they are immobile in these rocks. Importantly, these figures demonstrate that Zr is also immobile, and that other

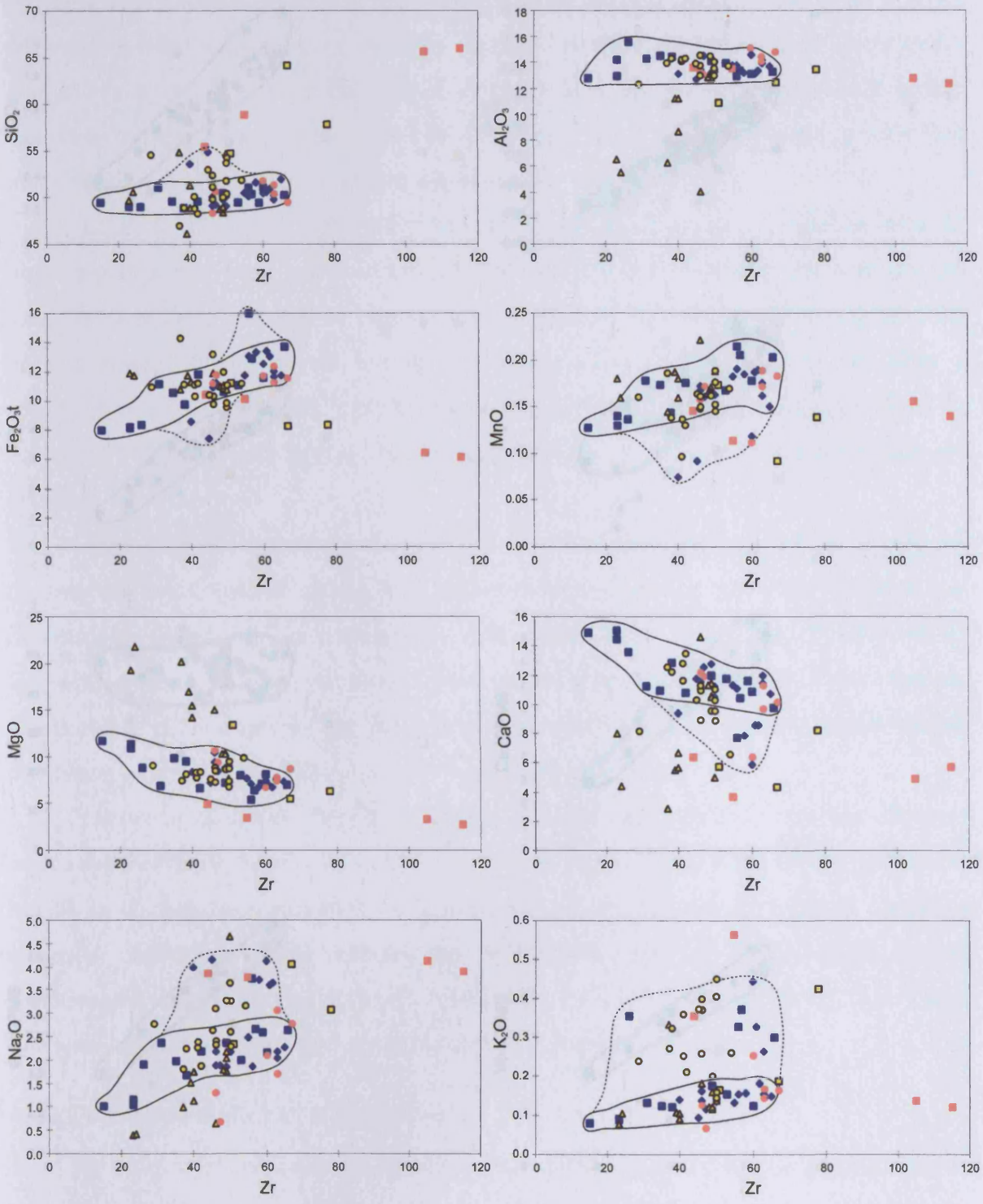

Fig. 6.1 Plots of major elements vs. Zr, to assess major element mobility in various lithologies of the Aruba Lava Formation. Solid fields surround all or most of the reasonably fresh basalts and dolerites. Dotted fields are extensions of the solid fields to include those that have been significantly altered. All analyses by XRF: Zr in ppm, major elements in wt.%.

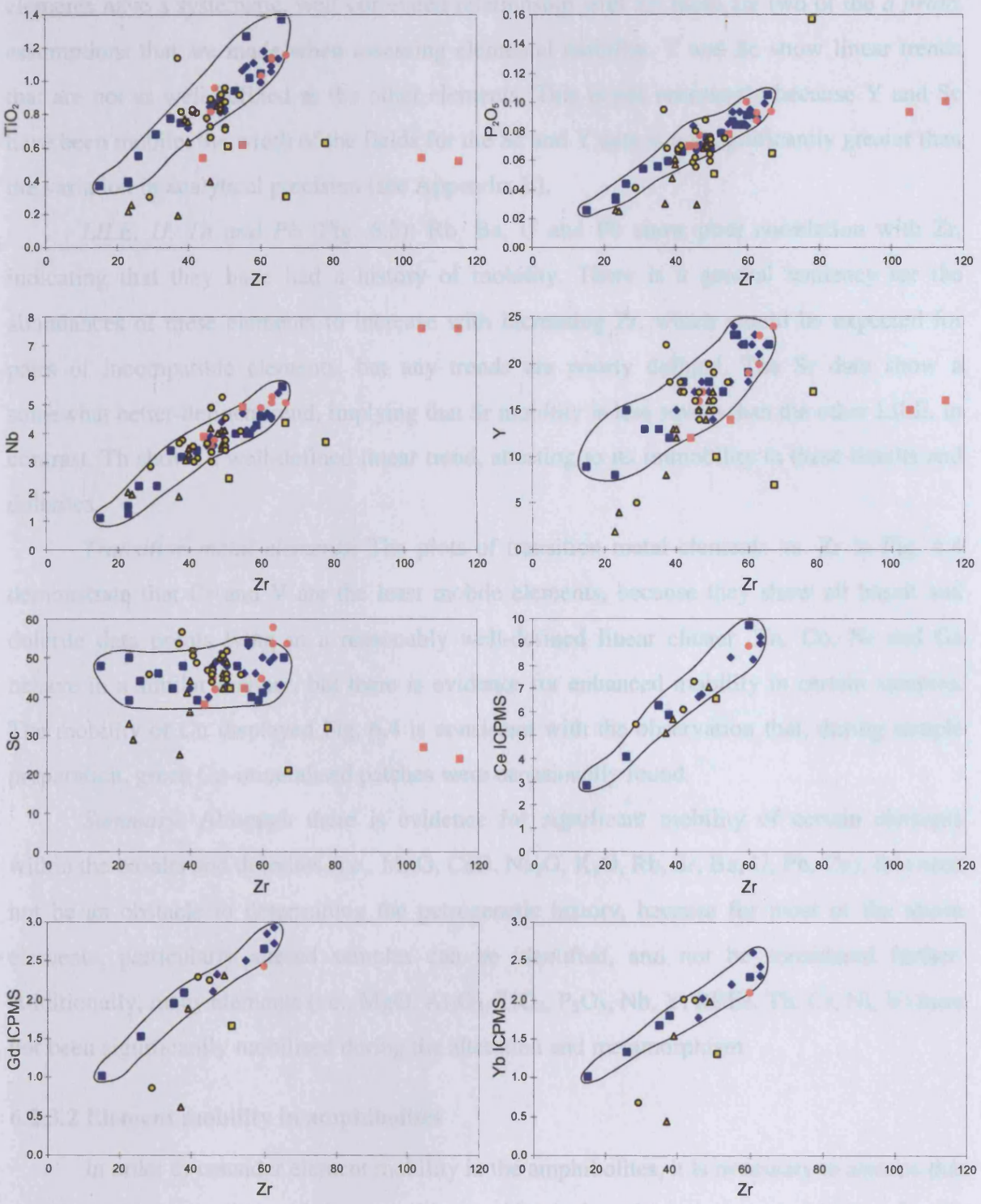

Fig. 6.2 Plots of HFSE and selected REE vs. Zr, to assess trace element mobility in various lithologies of the Aruba Lava Formation. Selected REE are representative of light, middle and heavy REEs. The Aruba basalts and dolerites show tight linear arrays against Zr (shown by solid lines), attesting to their immobility. All analyses by XRF except REE, which were done by ICP-MS. All values quoted in ppm except TiO_2 and P_2O_5 (wt. %).

elements have a systematic, well-correlated relationship with Zr: these are two of the *a priori* assumptions that are made when assessing elemental mobility. Y and Sc show linear trends that are not as well-defined as the other elements. This is not necessarily because Y and Sc have been mobile: the width of the fields for the Sc and Y data is not significantly greater than the variation in analytical precision (see Appendix E).

LILE, U, Th and Pb (Fig. 6.3): Rb, Ba, U and Pb show poor correlation with Zr, indicating that they have had a history of mobility. There is a general tendency for the abundances of these elements to increase with increasing Zr, which would be expected for pairs of incompatible elements, but any trends are poorly defined. The Sr data show a somewhat better-defined trend, implying that Sr mobility is less severe than the other LILE. In contrast, Th shows a well-defined linear trend, attesting to its immobility in these basalts and dolerites.

Transition metal elements: The plots of transition metal elements vs. Zr in Fig. 6.4 demonstrate that Cr and V are the least mobile elements, because they show all basalt and dolerite data points lying in a reasonably well-defined linear cluster. Zn, Co, Ni and Ga behave in a similar manner, but there is evidence for enhanced mobility in certain samples. The mobility of Cu displayed Fig. 6.4 is consistent with the observation that, during sample preparation, green Cu-mineralised patches were occasionally found.

Summary: Although there is evidence for significant mobility of certain elements within the basalts and dolerites (i.e., MnO, CaO, Na_2O, K_2O, Rb, Sr, Ba, U, Pb, Cu), this need not be an obstacle to determining the petrogenetic history, because for most of the above elements, particularly altered samples can be identified, and not be considered further. Additionally, many elements (i.e., MgO, Al_2O_3, TiO_2, P_2O_5, Nb, Y, REEs, Th, Cr, Ni, V) have not been significantly mobilised during the alteration and metamorphism.

6.2.3.2 Element mobility in amphibolites

In order to consider element mobility in the amphibolites, it is necessary to assume that the chemical composition of the protolith was identical to the basalts and dolerites. In this way, the chemical changes that have occurred during amphibolite-facies metamorphism can be deduced. The above assumption is reasonable for the Aruba Lava Formation, because of its limited geographical extent, and the fact that a transition in lithology from greenschist facies to amphibolite facies occurs as the contact with the batholith is approached. This situation of being able to compare directly the compositions of amphibolites with their protoliths is

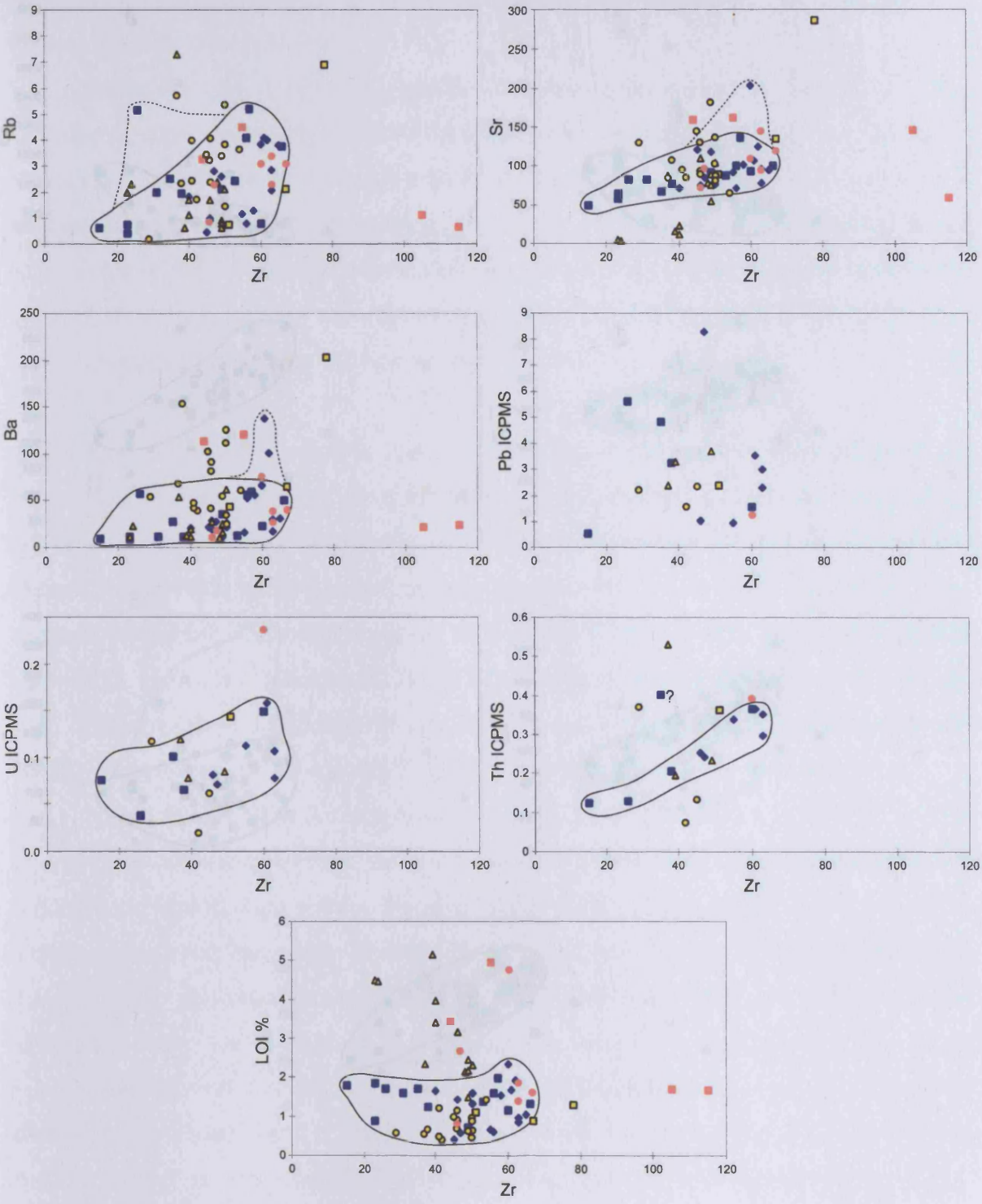

Key: Aruba Lava Formation
- basalts
- dolerites
- deformed chlorite rocks
- amphibolites (basaltic)
- amphibolites (not basaltic)
- volcaniclastics (basaltic)
- volcaniclastics (not basaltic)

Fig. 6.3 Plots of LIL, Th and U vs. Zr, to assess mobility in various lithologies of the Aruba Lava Formation. Also shown for comparison is a plot of loss on ignition (LOI %) vs. Zr. All analyses by XRF except Th, U and Pb, which were done by ICP-MS. Values quoted are ppm except LOI. Fields as in Fig. 6.1.

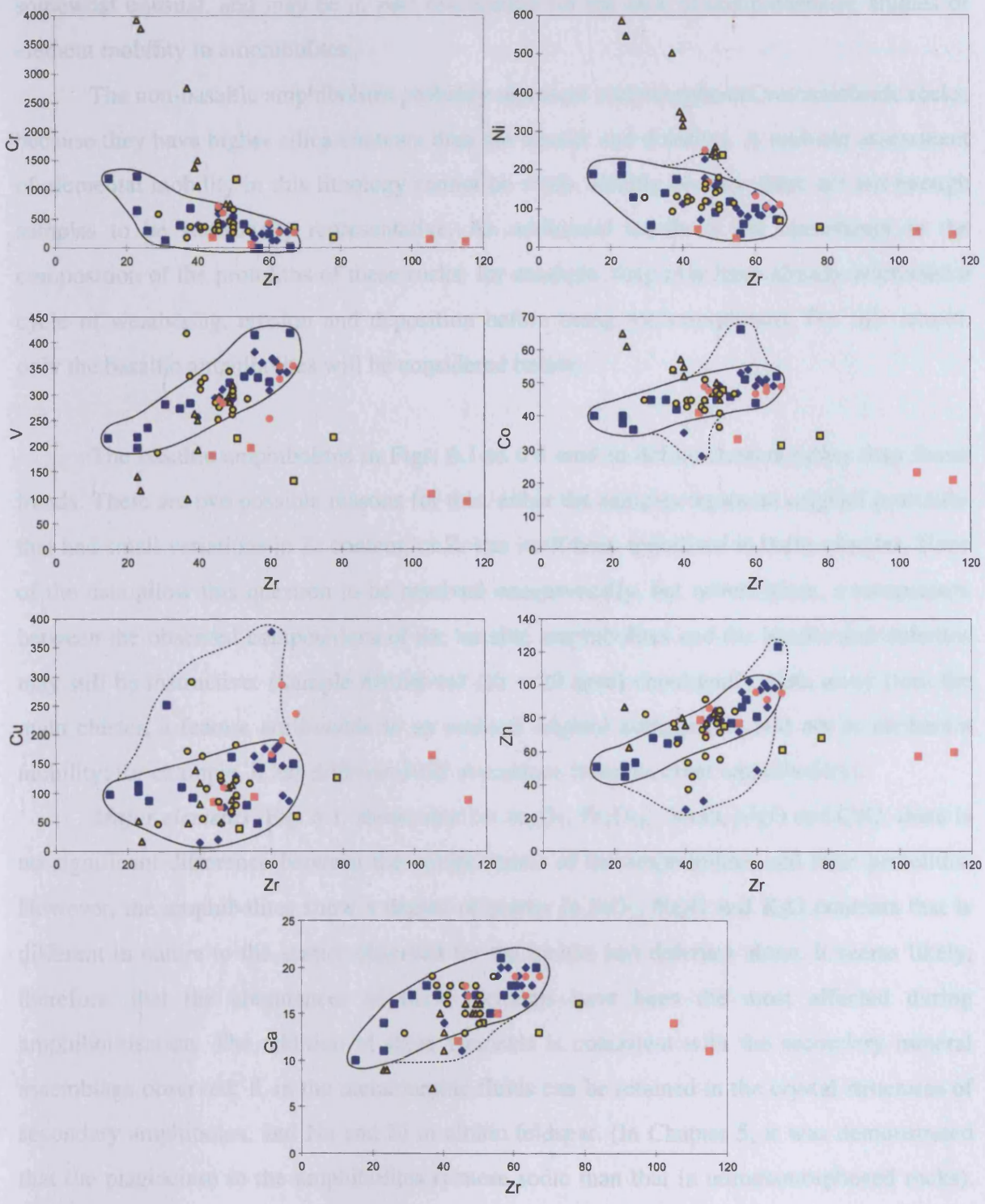

Fig. 6.4 Plots of transition metal elements and Ga vs. Zr, to assess their mobility in various lithologies of the Aruba Lava Formation. All analyses shown here are by XRF, and all values are in ppm. Fields as for Fig. 6.1.

somewhat unusual, and may be in part responsible for the lack of comprehensive studies of element mobility in amphibolites.

The non-basaltic amphibolites probably represent metamorphosed volcaniclastic rocks, because they have higher silica contents than the basalts and dolerites. A realistic assessment of elemental mobility in this lithology cannot be made, mainly because there are not enough samples to be statistically representative. An additional hurdle is the uncertainty in the composition of the protoliths of these rocks: for example, they may have already witnessed a cycle of weathering, erosion and deposition before being metamorphosed. For this reason, only the basaltic amphibolites will be considered below.

The basaltic amphibolites in Figs. 6.1 to 6.4 tend to define clusters rather than linear trends. There are two possible reasons for this: either the samples represent original protoliths that had small variations in Zr content, or Zr has itself been mobilised in these samples. None of the data allow this question to be resolved unequivocally, but nevertheless, a comparison between the observed compositions of the basaltic amphibolites and the basalts and dolerites may still be instructive. (Sample ARU96-147 (Zr = 29 ppm) consistently plots away from the main cluster, a feature attributable to an unusual original composition and not to elemental mobility; for example, it has different REE abundance from the other amphibolites).

Major elements: Fig. 6.1. shows that for Al_2O_3, $Fe_2O_{3(t)}$, MnO, MgO and CaO, there is no significant difference between the compositions of the amphibolites and their protoliths. However, the amphibolites show a degree of scatter in SiO_2, Na_2O and K_2O contents that is different in nature to the scatter observed for the basalts and dolerites alone. It seems likely, therefore, that the abundances of these elements have been the most affected during amphibolitisation. The addition of these elements is consistent with the secondary mineral assemblage observed: K in the metamorphic fluids can be retained in the crystal structures of secondary amphiboles, and Na and Si in albitic feldspar. (In Chapter 5, it was demonstrated that the plagioclase in the amphibolites is more sodic than that in unmetamorphosed rocks). The coupled substitution (Ca, Al $\Rightarrow$ Na, Si) involved in albitisation of feldspars could result in the depletion in the rock of both Ca and Al; however, in the assemblage under consideration, Al can reside in the newly-growing amphiboles. The Ca content is somewhat more problematic: Fig 6.1. shows that Ca contents of amphibolites are similar to those of the basalts and dolerites even though the principal phases making up the amphibolites are less calcic than those in the unmetamorphosed rocks (i.e., amphibole (~11% CaO) instead of clinopyroxene

(~15 to 20% CaO), and more sodic plagioclase (~8 to 11% CaO) instead of calcic plagioclase (~11 to 17% CaO)). The additional Ca must, therefore, be retained in accessory phases, such as epidote, calcite, sphene and apatite. Petrographic work (Chapter 5) has revealed that these phases are present in the amphibolites, but are volumetrically minor.

Loss on ignition: The amphibolites, in general, have lower losses on ignition than the basalts and dolerites (Fig. 6.3). This is because the basalts and dolerites are altered at a lower metamorphic grade, and contain secondary clay minerals that have a greater structural water content than amphiboles.

HFSE and REE: The basaltic amphibolites generally overlap in composition with the basalts and dolerites for TiO_2, P_2O_5, Nb, Y and Sc, indicating that mobility during metamorphism has not altered the concentrations of these elements by large amounts. Nevertheless, the clusters (rather than trends) observed do suggest slight mobility of either these elements, or Zr, or both. One possible reason for the limited mobility of these elements, even at amphibolite facies, is that amphibole can accommodate HFSE in its structure, and consequently, HFSE are unlikely to be removed from the system completely, although they may be mobilised within it (i.e., a closed system). The limited REE data for basaltic amphibolites suggest that the REE have been immobile during metamorphism (this is confirmed later in Fig. 6.17).

LILE, U, Th and Pb: The abundances of these elements show no consistent interrelationships. Even Th (Fig. 6.3), which was considered immobile for the basalts and dolerites, shows very poor correlation with Zr. It is concluded that this variability is due in part to mobility during initial alteration of the protolith and in part (in whole for Th) to mobility during metamorphism. The higher concentrations of Rb, Sr and Ba in the amphibolites may be linked to the composition of the fluids responsible for metamorphism (i.e., a closed system does not exist for these elements): these fluids are likely to have been derived from the intruding Aruba batholith, which has significantly higher concentrations of these elements than the basalts and dolerites.

Transition metal elements: Examination of Fig. 6.4 reveals that the basaltic amphibolites plot in the basalts and dolerites field for Cr, Ni, V, Co and Ga, and therefore mobility during metamorphism has not been an important process. For Cu and Zn, there is some scatter outside the basalt and dolerite field, which could be due to elemental mobilisation during metamorphism.

Summary: Comparison between compositions of the basaltic amphibolites and their purported protoliths suggests that SiO_2, Na_2O, K_2O, Rb, Sr, Ba, U, Th, Pb, Cu and Zn were mobilised during the amphibolite facies metamorphism. The loss of well-defined linear trends for the HFSE (including Zr) suggests that these too may be slightly mobile.

6.2.3.3 Element mobility in deformed chlorite schists

A brief inspection of Figs. 6.1 to 6.4 reveals that the deformed chlorite-bearing rocks bear very little resemblance to the basalts and dolerites for MgO, Al_2O_3, CaO, Na_2O, Cr and Ni. Possible reasons for this include 1) different original compositions; and 2) different mobility of elements during metamorphism. A combination of approaches can be used to decipher which of the reasons above is more important: the coherency of trends defined by the chlorite schists give information about elemental mobility; where coherent trends *are* observed, the differences between these and trends observed for the basalts and dolerites should reflect differences in the original compositions.

Major elements: No coherent trends are displayed for SiO_2, Al_2O_3, MnO and CaO (Fig. 6.1), indicating that these elements have been mobile. For MnO and SiO_2, the abundances observed in the chlorite schists are similar to those in the basalts and dolerites. For Al_2O_3 and CaO, the abundances in the chlorite schists are markedly lower than those in the basalts and dolerites. The appearance of reasonably well-defined trends for MgO, K_2O and $Fe_2O_{3(t)}$, and a less well-defined trend for Na_2O, suggests that these components may have been less mobile, and the abundances of these elements may reflect the approximate original composition of the rocks. It will be argued in Section 6.4.2 that the observed trends are consistent with the addition of cumulus olivine: the low Al_2O_3 and CaO contents of these rocks are, therefore, likely to be original features, if somewhat distorted by subsequent mobility. Another explanation for the high MgO content of these rocks is growth of secondary chlorite. This cannot be ruled out as a contributory factor for these chlorite-rich rocks, although it is not likely to be the *primary* reason for their high MgO contents (see Section 6.4.2).

Loss on ignition: The deformed chlorite-bearing rocks have losses on ignition that range from ~1.5 to ~5.2%, reflecting their high content of minerals containing structurally-bound water (i.e., chlorite).

HFSE and REE: The poor correlation between TiO_2, P_2O_5 and Zr for the chloritic rocks demonstrates that one or more of these elements has been mobile. For Nb, Y and Sc, there is an overall positive correlation, but the trends are not well-defined, and some elemental

mobility is likely. Two out of the three samples analysed by ICP-MS for REE plot within the basalt and dolerite field; the third again appears to have an unusual composition, similar to the amphibolite ARU96-147. These data alone plotted against Zr are not sufficient to assess REE mobility, although the smoothness of the REE profiles (Fig. 6.17; discussed in Section 6.6.2) suggest that the REE have not been particularly mobile.

LILE, U, Th and Pb: The samples show no coherent relationship with Zr for Sr, Rb, Ba, Pb and U: these elements have been mobile, either before or during metamorphism of these rocks. Some samples have extremely low Sr contents (<25 ppm), suggesting either that Sr has been leached during metamorphism/alteration, or that the rocks initially had very low Sr contents. Either scenario is feasible. The two samples analysed by ICP-MS again plot within the basalt/dolerite field for Th, suggesting that Th mobility is not significant for this lithology.

Transition metal elements: On plots of Cr, Ni and Co vs. Zr (Fig 6.4), the chlorite schists show a systematic negative correlation. The most probable explanation for this is their original composition (rather than element mobility). The reasonable correlations observed on these diagrams also suggest that Zr has been relatively immobile in this lithology. V, Zn and Ga show positive correlations with Zr, although these are poorly-defined, implying a degree of mobility. The low Ga values compared to the basalts and dolerites mirror the low Al contents, because Ga and Al behave similarly in igneous processes.

Summary: Relatively few elements have escaped mobility in this lithology: the least-affected elements are $Fe_2O_{3(t)}$, MgO, K_2O, Nb, Y, Zr, REEs, Th, Cr, Ni and Co. The distribution of some of these elements is markedly different from that observed for the basalts and dolerites, hinting at a different protolith for these rocks. This aspect is discussed and developed further in Section 6.4.2.

6.2.3.4. Element mobility in volcaniclastic rocks

A thorough assessment of element mobility in these rocks is beyond the scope of this study, because it requires a knowledge of their initial compositions that cannot be gleaned from the available (limited) data. However, it is interesting to note that the basaltic volcaniclastics plot within the basalt and dolerite field for all elements except Sc, U, V, and Cu, strongly suggesting that the basaltic volcaniclastic rocks have the same ultimate origin as the basalts and dolerites. Elemental mobility for the *non*-basaltic volcaniclastic rocks is even more difficult to determine, as these have been reworked and/or silicified (Chapter 5).

6.3 Classification of the Aruba Lava Formation rocks

This section is concerned with identifying salient compositional features of the Aruba Lava Formation basalts and dolerites in order to determine their geochemical affinities. The diagrams presented in this section include only the least altered basalt and dolerite samples, i.e., those that fall within the solid-line fields on *all* the plots in Figs. 6.1 to 6.4. The other lithologies have been included in these diagrams for comparison, although it should be noted that, because of element mobility, their locations on Figs. 6.5 to 6.6 may not be petrogenetically meaningful.

On the total alkalis vs. silica diagram (Fig. 6.5a), all samples plot in the sub-alkaline field of Irvine and Baragar (1971). All the basalts, basaltic volcaniclastics and dolerites have SiO_2 < 52 wt.%: they fall within the basalt field of Le Maitre *et al.* (1989). The other lithologies are more variable. The "basaltic amphibolite" and "deformed chlorite rock" groups actually span the basalt and basaltic andesite fields, but this is probably due to the addition of SiO_2 during metamorphism rather than any primary variation in composition of the protolith. The higher SiO_2 contents of the non-basaltic amphibolites and volcaniclastic rocks could be due to a combination of processes: 1) differentiation from basaltic magmas; 2) selective preservation of quartz during weathering cycles; 3) addition of silica during metamorphism (amphibolites) or silicification (volcaniclastics: see Section 5.3.3).

The subalkaline rock series of Irvine and Baragar (1971) can be subdivided on the basis of the K_2O vs. SiO_2 diagram (Fig. 6.5b). The basalts and dolerites plot in a very restricted area, well within the low-K tholeiite field (Rickwood, 1989). Even the amphibolites, for which there is clear evidence of K_2O addition (Section 6.2.3.2), still plot within the low-K field. Examination of the alkali index vs. Al_2O_3 plot (Fig. 6.5c) confirms the tholeiitic character of the Aruba Lava Formation.

CIPW normative compositions of the Aruba Lava Formation are displayed in Fig. 6.6. CIPW norms were calculated using the CIPW Norms computer program of D. R. Mason (1990), using Fe_2O_3/FeO = 0.2 (Middlemost, 1989). Using the classification of Thompson (1984), the Aruba Lava Formation contains both silica-saturated and silica-oversaturated rocks: olivine-tholeiites and quartz-tholeiites, respectively. However, these classifications may not be entirely robust for this rock suite, because the proportions of CIPW norm phases are sensitive to relatively minor variations in composition, such as those introduced during alteration (e.g., Ca addition increases normative diopside; Na addition increases normative feldspar, and consequently decreases the amount of silica available for formation of quartz).

Fig. 6.5a

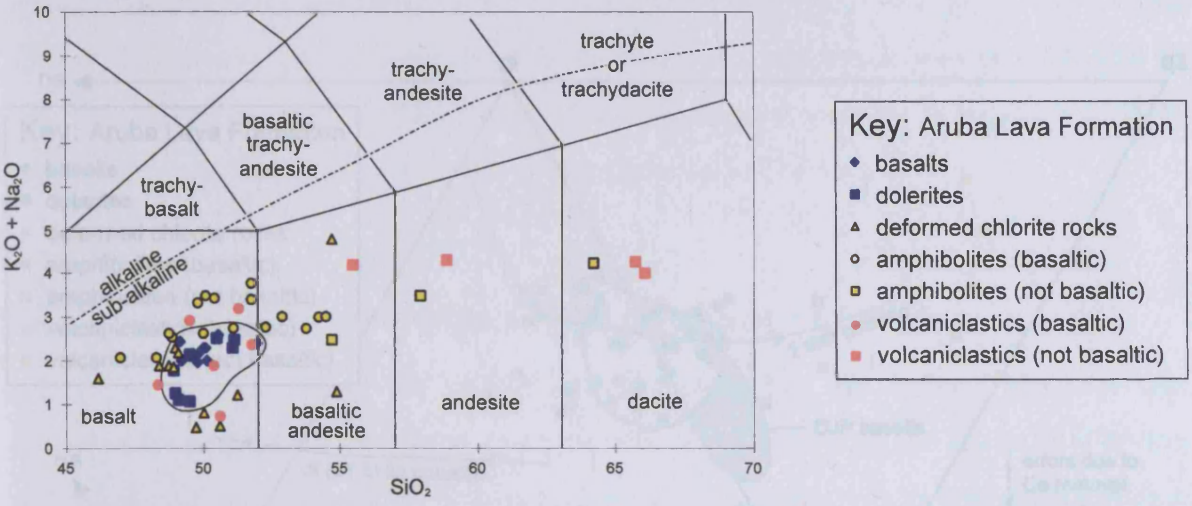

Figure 6.5a: Classification of the Aruba Lava Formation rocks on a total alkalis vs. silica diagram (Le Maitre *et al.*, 1989). The field surrounds the basalts and dolerites, after screening to remove heavily altered samples (see text). The dashed line dividing alkaline from sub-alkaline rocks is after Irvine and Baragar (1971).

Fig. 6.5b

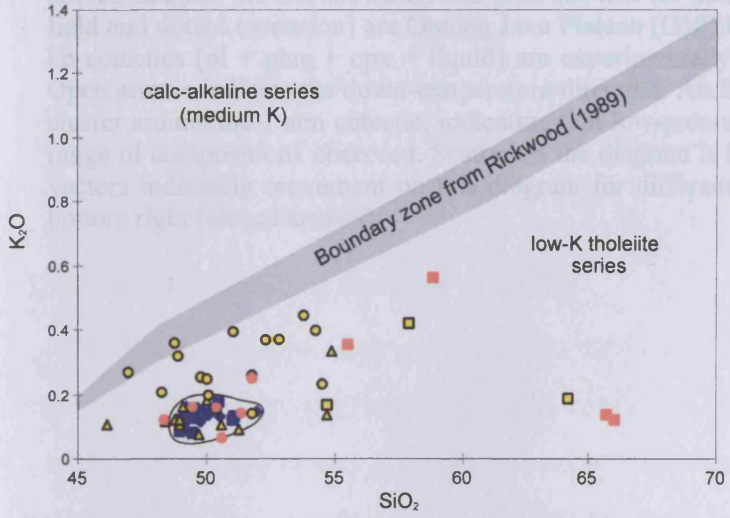

Figure 6.5b: The K_2O vs. silica diagram further subdivides the sub-alkalic rock series. The basalts and dolerites (screened for alteration) plot in a restricted area of the low-K tholeiite field. The boundary zone is from a compilation of boundary lines by Rickwood (1989). The location of the amphibolite samples closer to the tholeiite/calc-alkaline boundary is a result of K addition during metamorphism (see Section 6.2.3.2).

Fig. 6.5c

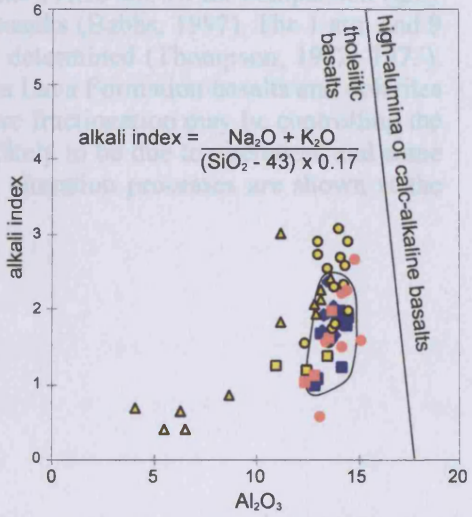

Figure 6.5c: The diagram of alkali index vs. alumina further confirms the tholeiitic affinites of the less-altered basalts and dolerites. Dividing line from Middlemost (1975).

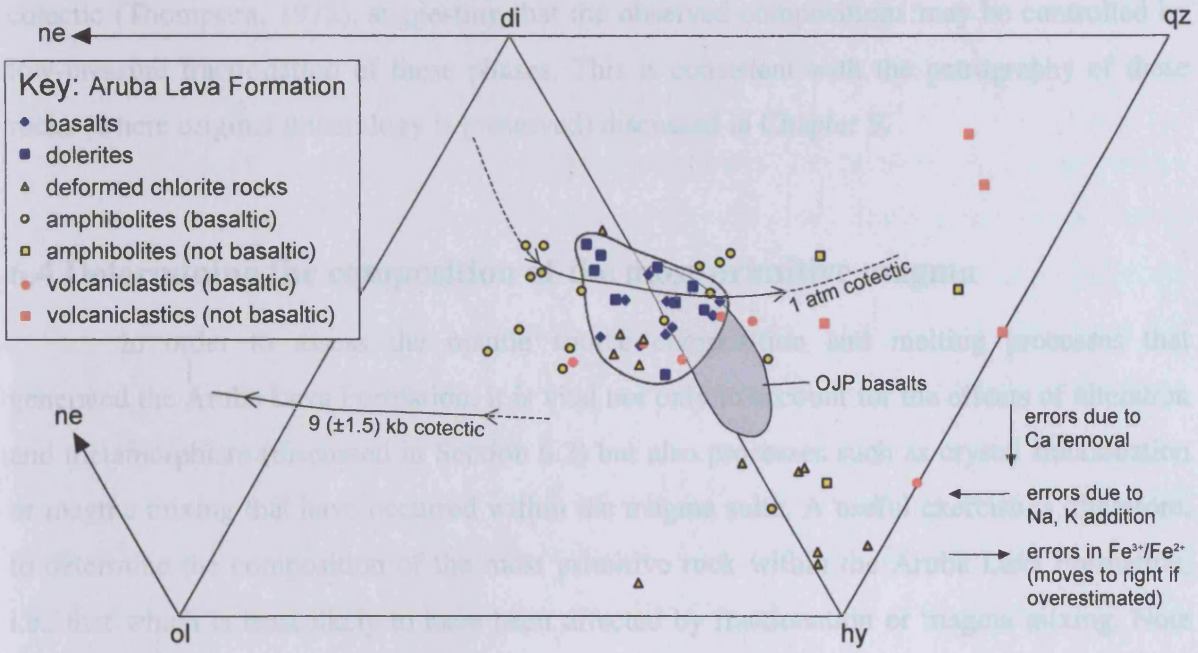

Fig. 6.6: Diopside-hypersthene-olivine-nepheline-quartz diagram showing CIPW normative data for the Aruba Lava Formation. The white field surrounds the basalts and dolerites (the most altered samples are not shown on this plot: see text for details). Also shown for comparison (grey field and dotted extension) are Ontong Java Plateau (OJP) basalts (Babbs, 1997). The 1 atm and 9 kb cotectics (ol + plag + cpx + liquid) are experimentally determined (Thompson, 1972; 1973). Open arrows indicate the down-temperature direction. Aruba Lava Formation basalts and dolerites cluster around the 1 atm cotectic, indicating that low-pressure fractionation may be controlling the range of compositions observed. Scatter on the diagram is likely to be due to alteration, and some vectors indicating movement on this diagram for different alteration processes are shown at the bottom right (closed arrows).

The data field for the basalts and dolerites partially overlaps with that of the Ontong Java Plateau (Babbs, 1997), and the data cluster around the 1 atmosphere ol + plag + cpx + liquid cotectic (Thompson, 1972), suggesting that the observed compositions may be controlled by low-pressure fractionation of these phases. This is consistent with the petrography of these rocks (where original mineralogy is preserved) discussed in Chapter 5.

6.4 Determining the composition of the most primitive magma

In order to assess the mantle source composition and melting processes that generated the Aruba Lava Formation, it is vital not only to account for the effects of alteration and metamorphism (discussed in Section 6.2) but also processes such as crystal fractionation or magma mixing that have occurred within the magma suite. A useful exercise is, therefore, to determine the composition of the most primitive rock within the Aruba Lava Formation, i.e., that which is least likely to have been affected by fractionation or magma mixing. Note that this composition is unlikely to correspond to the primary magma extracted from the mantle source region: the differences between the most primitive observed magma and a postulated primary magma (in equilibrium with a mantle residue) will give insights into the processes that modified the magmas between their extraction from the underlying mantle and emplacement at (or near) the surface. A further complication arises because the most primitive (i.e., highest MgO) rocks may not reflect original liquid compositions: the addition of cumulus olivine enhances MgO contents, and must also be considered.

6.4.1 Characteristics of a primary magma

Primary magmas must be in equilibrium with mantle olivine and orthopyroxene at the depth of melt segregation from the mantle. Liquids in equilibrium with mantle olivine (~Fo_{89-92}) should have Mg numbers (Mg#: defined as molecular $(100 \times Mg)/(Mg + Fe^{2+})$) of 71 (in equilibrium with Fo_{89}) to 78 (in equilibrium with Fo_{92}), using the Fe^{2+}-Mg distribution coefficient between olivine and melt of 0.3 ± 0.03 determined by Roeder and Emslie (1970). The Mg# of the liquid does not vary significantly with extent of melting, because mantle olivine always remains a residual phase. Similarly, Ni and Cr contents for primary melts can be calculated. These are also buffered by the residual mantle phases, and insensitive to degree of melting in the source. Ni contents of a primary mantle melt are approximately 250-350 ppm

and Cr contents are 500 - 600 ppm (Green *et al.*, 1974; Green, 1976; Hanson and Langmuir, 1978; Sun and Nesbitt, 1979).

6.4.2 Identification of cumulus olivine in altered rocks

In suites of pristine basaltic rocks, the identification of enhanced MgO contents due to the presence of cumulus olivine is relatively simple: possible olivine accumulation should be considered if the sample is highly olivine phyric. In the rocks of the Aruba Lava Formation, however, this technique is impossible, because the rocks are altered to such an extent that olivine (if it ever existed in these rocks) is no longer present. Cumulus olivine must, therefore, be identified using geochemical techniques.

One of the most sensitive probes for determining involvement of olivine is the Mg# of the rock: addition of cumulus olivine increases Mg#, whereas removal of olivine from a liquid preferentially depletes it in Mg, and the Mg# decreases. This characteristic cannot be used alone, because it requires a preliminary knowledge of the Mg# of the original liquid, i.e., it cannot be assumed that the parental (or most primitive) magma of a suite is in equilibrium with mantle olivine and has Mg#≈0.7.

Seven (out of twelve) of the deformed samples have Mg# ≥73, indicating either that: 1) the samples were primary liquids in equilibrium with mantle olivine; 2) the samples contain(ed) cumulus Mg-rich phase(s); or 3) MgO has been added to the rocks during alteration to chlorite. Using Mg# data alone, it is not possible to distinguish which of the three above hypotheses are correct, and other geochemical parameters need to be consulted.

Olivine involvement may also be fingerprinted using Ni abundances. Ni and MgO are highly correlated for all lithologies, including altered and deformed members. The trend observed is linear, and cannot be modelled by removal of olivine from the most MgO-rich composition, since this would result in a curved trend due to the dependence of the Ni-Mg olivine-liquid partition coefficient (D_{Ni}) on MgO content (Hart and Davis, 1978). Instead, the data are better explained by olivine accumulation: the linear trends observed are essentially mixing lines between the original liquid and an olivine end-member. The slope of this line depends on D_{Ni}, and therefore on the MgO content of the liquid.

Using the method described in Hart and Davis (1978), vectors representing accumulation of 5% olivine (of equilibrium composition) to a range of melts have been added to the Ni vs. MgO plot in Fig. 6.7a. The best estimate of the original liquid composition (to which the olivine was added) is given by the MgO content where the olivine addition vector is

parallel to the observed trend. For the Aruba Lava Formation, it is not completely clear what this observed trend is, because the high-MgO samples are mineralogically dominated by chlorite, and the chloritisation process may have increased the MgO contents. For this reason, the analysis has been carried out using three different scenarios (shown in Fig. 6.7b):

1) the best fit line through all Aruba Lava Formation samples except non-basaltic volcaniclastics represents the real trend, and intersects the high MgO deformed samples (i.e., no allowance for MgO addition during formation of chlorite).

2) the best fit line through the basalts represents the real trend: this passes to the low-MgO side of the deformed samples and therefore allows for some chloritisation.

3) high-MgO and Ni Curaçao samples (Kerr *et al.*, 1996b) are used to constrain a realistic maximum estimate for the gradient of the olivine accumulation vector: this scenario allows for significant MgO addition due to chloritisation, but assumes that the high-MgO Aruba samples are derived from similar liquids to Curaçao olivine cumulate rocks.

Results for the three scenarios are presented in Table 6.1.

Table 6.1: Results of olivine accumulation modelling for the Aruba Lava Formation (see also Figs. 6.7a and 6.7b.)

	1	2	3
Initial liquid composition: MgO	5.2 wt.%	6.2 wt.%	8.5 wt.%
Initial liquid composition: Ni	32 ppm	51 ppm	116 ppm
Initial liquid comp.: $FeO_{(t)}$ (assumed*)	10 wt.%	10 wt.%	10 wt.%
Fo content of olivine crystallising	Fo ≈ 76	Fo ≈ 79	Fo ≈ 83
MgO content of olivine crystallising	28.2 wt.%	29.6 wt.%	31.9 wt.%
Ni content of olivine crystallising	746 ppm	984 ppm	1584 ppm
Amount of cumulus olivine required to explain high MgO rocks.	~ 65 to 75 %	~ 48 to 55 %	~ 26 to 33 %
Maximum MgO added during chloritisation	2.8 wt.%	3.7 wt.%	5.3 wt.%

* This modelling is not sensitive to FeO content: varying FeO from 5 wt.% to 15 wt.% had a negligible effect on all results except the Fo content of the crystallising olivine.

These calculations give estimates for the composition of a melt, from which the high-MgO Aruba Lava Formation samples could have been derived via olivine accumulation. The best estimate appears to be that of Scenario 2. The initial liquid composition for Scenario 1 has lower MgO than that observed for any of the rocks apart from the non-basaltic volcaniclastic rocks, and extremely large amounts of olivine accumulation are required to match the observed high MgO contents; moreover, the position of the data points for some of

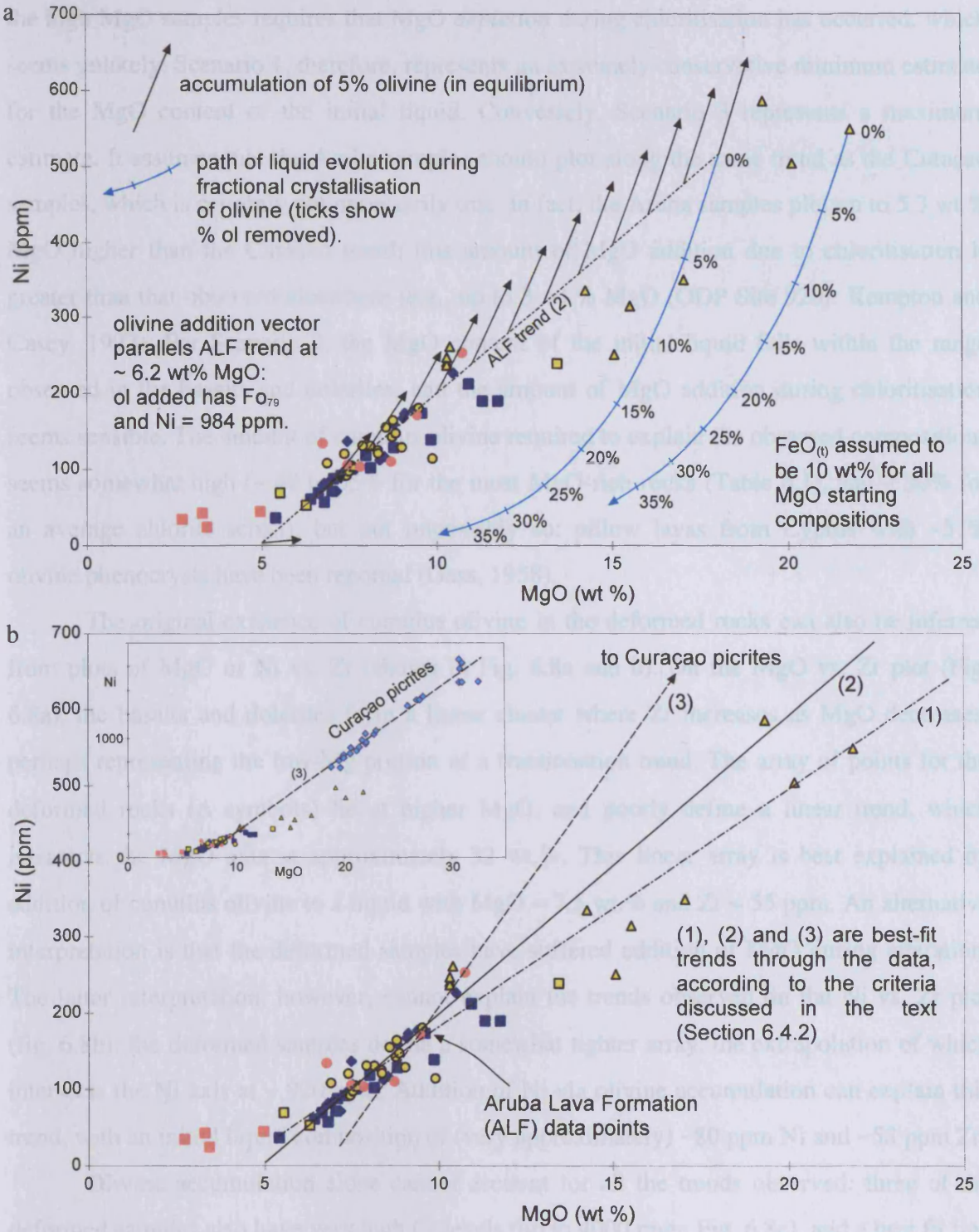

Key: Aruba Lava Formation
- basalts
- dolerites
- deformed chlorite rocks
- amphibolites (basaltic)
- amphibolites (not basaltic)
- volcaniclastics (basaltic)
- volcaniclastics (not basaltic)

Fig. 6.7a: Plot of Ni vs. MgO showing olivine addition vectors to initial magmas of varying MgO contents (shown for "Scenario 2" - see text and Fig. 6.7b). Also shown for comparison are lines showing liquid evolution during olivine fractionation.

Fig. 6.7b: Plot of Ni vs. MgO showing the three scenarios used in modelling Ni addition via olivine accumulation. These are discussed in the text. The inset figure gives the location of the Curaçao picrites (Kerr *et al.*, 1996b; Klaver, unpubl. data) used to constrain the slope of line (3).

the high MgO samples requires that MgO *depletion* during chloritisation has occurred, which seems unlikely. Scenario 1, therefore, represents an extremely conservative minimum estimate for the MgO content of the initial liquid. Conversely, Scenario 3 represents a maximum estimate. It assumes that the Aruba samples should plot along the same trend as the Curaçao samples, which is certainly not necessarily true. In fact, the Aruba samples plot up to 5.3 wt.% MgO higher than the Curaçao trend: this amount of MgO addition due to chloritisation is greater than that observed elsewhere (e.g., up to 3 wt.% MgO (ODP Site 920): Kempton and Casey, 1997). For Scenario 2, the MgO content of the initial liquid falls within the range observed in the basalts and dolerites, and the amount of MgO addition during chloritisation seems sensible. The amount of cumulus olivine required to explain the observed compositions seems somewhat high (~ 48 to 55% for the most MgO-rich rocks (Table 6.1), and ~ 30% for an average chlorite schist), but not impossibly so: pillow lavas from Cyprus with ~57% olivine phenocrysts have been reported (Gass, 1958).

The original existence of cumulus olivine in the deformed rocks can also be inferred from plots of MgO or Ni vs. Zr (shown in Fig. 6.8a and b). On the MgO vs. Zr plot (Fig. 6.8a), the basalts and dolerites form a linear cluster where Zr increases as MgO decreases, perhaps representing the low-Mg portion of a fractionation trend. The array of points for the deformed rocks (Δ symbols) lie at higher MgO, and poorly define a linear trend, which intersects the MgO axis at approximately 32 wt.%. This linear array is best explained by addition of cumulus olivine to a liquid with MgO ≈ 7.5 wt.% and Zr ≈ 55 ppm. An alternative interpretation is that the deformed samples have suffered addition of MgO during alteration. The latter interpretation, however, cannot explain the trends observed on the Ni vs. Zr plot (fig. 6.8b): the deformed samples define a somewhat tighter array, the extrapolation of which intersects the Ni axis at ~ 920 ppm. Addition of Ni via olivine accumulation can explain this trend, with an initial liquid composition of (very approximately) ~80 ppm Ni and ~58 ppm Zr.

Olivine accumulation alone cannot account for all the trends observed: three of the deformed samples also have very high Cr levels (up to 4000 ppm; Fig. 6.8c), and a best fit line through the deformed samples intersects the Cr axis at ~6800 ppm, equivalent to ~ 1 wt.% Cr_2O_3. Because olivine does not readily accommodate Cr^{3+} in its structure, Cr-spinel is likely to have also been a cumulus phase in the protoliths of these rocks. Although the Cr-spinel crystals alone would be too small to be effectively separated from any melt phase, if they occurred as inclusions in co-crystallising olivine, their incorporation as cumulus phases becomes more likely.

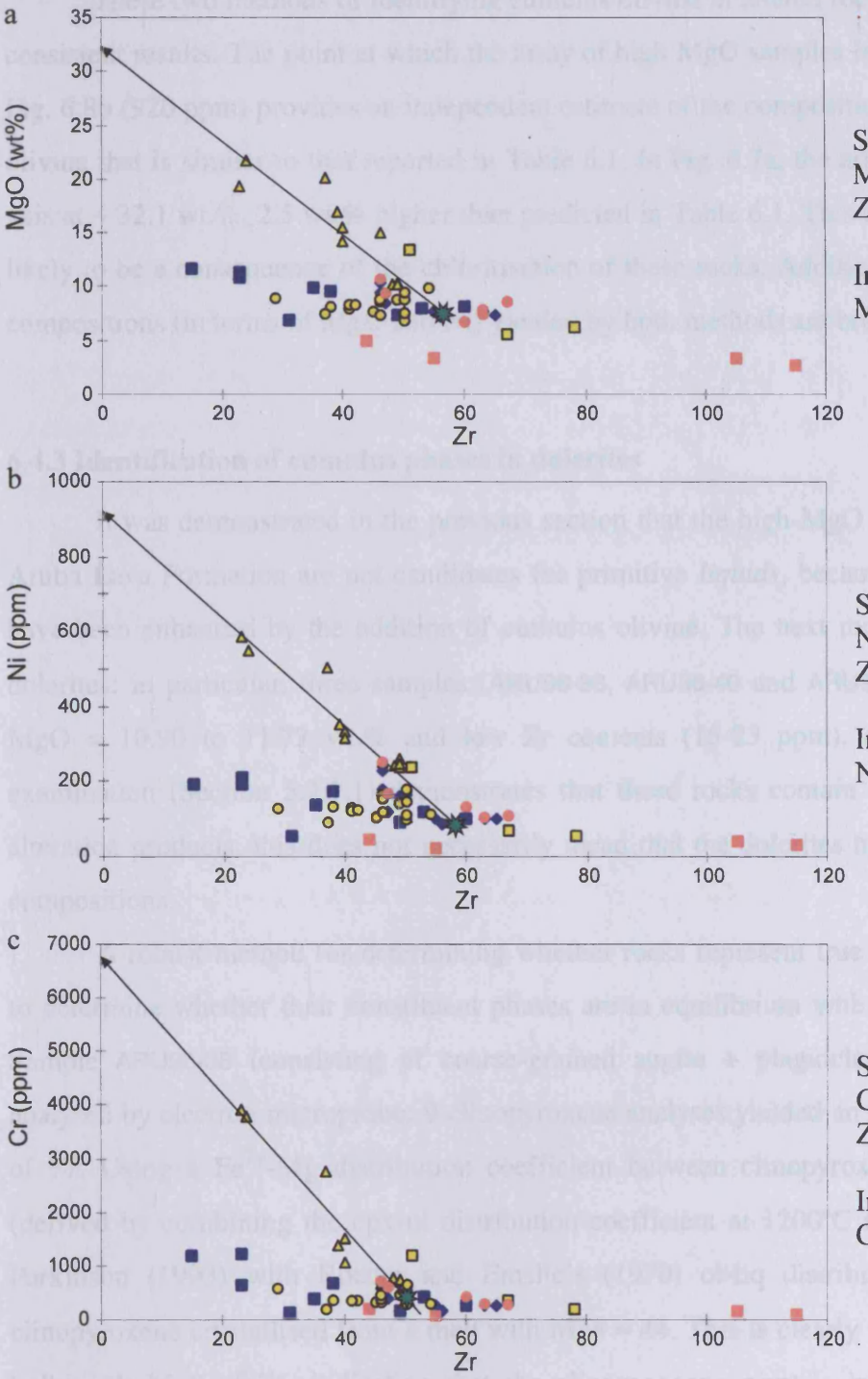

Fig. 6.8a: MgO vs. Zr plot showing vector due to olivine addition; MgO content may also be enhanced by growth of chlorite during alteration/metamorphism.

Fig. 6.8b: Ni vs. Zr plot showing vector due to olivine addition.

Fig. 6.8c: Cr vs. Zr plot showing vector due to accumulation of a Cr-bearing phase (probably Cr-spinel) concomitant with olivine addition.

These two methods of identifying cumulus olivine in altered rocks provide remarkably consistent results. The point at which the array of high MgO samples intersects the Ni axis in Fig. 6.8b (920 ppm) provides an independent estimate of the composition of the accumulating olivine that is similar to that reported in Table 6.1. In Fig. 6.7a, the array intersects the MgO axis at ~ 32.1 wt.%, 2.5 wt.% higher than predicted in Table 6.1. This extra 2.5 wt.% MgO is likely to be a consequence of the chloritisation of these rocks. Additionally, the initial liquid compositions (in terms of MgO and Ni) yielded by both methods are broadly similar.

6.4.3 Identification of cumulus phases in dolerites

It was demonstrated in the previous section that the high-MgO deformed rocks of the Aruba Lava Formation are not candidates for primitive *liquids*, because their MgO contents have been enhanced by the addition of cumulus olivine. The next most primitive rocks are dolerites: in particular, three samples (ARU96-38, ARU96-40 and ARU96-72) with Mg# ≈ 75, MgO = 10.90 to 11.73 wt.% and low Zr contents (15-23 ppm). Although petrographic examination (Section 5.2.1.1) demonstrates that these rocks contain neither olivine nor its alteration products, this does not necessarily mean that the dolerites have to represent liquid compositions.

A robust method for determining whether rocks represent true liquid compositions is to determine whether their constituent phases are in equilibrium with the bulk composition. Sample ARU96-38 (consisting of coarse-grained augite + plagioclase (up to An_{85})) was analysed by electron microprobe: 9 clinopyroxene analyses yielded an average value for Mg# of 77. Using a Fe^{2+}-Mg distribution coefficient between clinopyroxene and melt of 0.23 (derived by combining the cpx-ol distribution coefficient at 1200°C reported in Pearce and Parkinson (1993) with Roeder and Emslie's (1970) ol-liq distribution coefficient), this clinopyroxene crystallised from a melt with Mg# ≈ 44. This is clearly very different from the bulk rock Mg# of 76, indicating that the clinopyroxene crystals in ARU96-38 are not in equilibrium with the bulk composition, and are therefore of cumulus origin. This conclusion is confirmed by using the TRACE3 computer program (Nielsen, 1988) to determine the initial crystallising phases for the ARU96-38 bulk composition: the first minerals to crystallise "should be" Cr-spinel and olivine (Fo_{90}), followed by clinopyroxene (Mg# = 90) and later by plagioclase (An_{83}): quite different from the observed assemblage.

Similarly, clinopyroxene analyses of ARU96-30 (Mg# = 68; MgO = 9.56) have an average Mg# = 80, which should be in equilibrium with a melt having Mg# ≈ 47. This sample, although considerably less primitive than the other dolerite samples, still contains cumulus phases, and cannot be considered a parental liquid to the other rocks of the Aruba Lava Formation.

Samples ARU96-40, ARU94-22 and ARU96-72 are petrographically and chemically similar to ARU96-38 and ARU96-30, and it is therefore likely that these also do not represent liquid compositions. In contrast, sample ARU96-37 (Mg# = 60, MgO = 8.12 wt.%) contains clinopyroxene that is (approximately) in equilibrium with the bulk composition: the clinopyroxenes have Mg# up to 80, and should be in equilibrium with a liquid having Mg# = 57. However, this dolerite is less primitive than some of the basalts (see next section).

6.4.4 The most primitive liquids

It can be seen from Sections 6.4.2 and 6.4.3 that neither the high-MgO deformed rocks nor the dolerites with MgO > 9 wt.% can be considered to be representative of liquid compositions because they contain (or contained) cumulus MgO-rich phases (either olivine or clinopyroxene). The basalts, on the other hand, do not appear to contain any olivine phenocrysts (or pseudomorphs thereafter), and are more likely to be representative of liquid compositions. The most magnesian basalts are ARU96-21 (10.47 wt.% MgO; Mg# = 67.7) and ARU96-101 (9.36 wt.% MgO; Mg# = 65.8). Both of these samples have 46 ppm Zr. An average composition is shown in Table 6.2. In contrast to the dolerites, no clinopyroxenes from basalts were analysed by electron microprobe, and it is therefore not possible to state whether or not the crystal phases present are in equilibrium with the bulk rock composition. However, the lack of phenocrysts within the basalts suggests that they are unlikely to contain significant volumes of cumulus phases. According to the criteria listed in Section 6.4.1, these magmas are near-primary, and have only undergone minor compositional modification since their extraction from the mantle.

Table 6.2: Comparison of estimated parental liquid compositions. "Aruba" is the average of the two highest MgO Aruba basalts; "OJP" is the average of the two most primitive Ontong Java Plateau basalts sampled by Babbs (1997). The sample chosen to represent Curaçao (CUR-3; Kerr *et al.*, 1996b) is not one of the highest-MgO samples of that suite, because it is likely that samples with significantly higher than MgO ≈ 15wt.% may contain cumulus olivine. All data have been recalculated to give totals of 100% (not including loss on ignition) to enable comparison.

	Aruba	OJP	Curaçao
SiO_2	50.32	49.63	47.94
TiO_2	0.87	1.12	0.82
Al_2O_3	13.59	13.64	13.00
$Fe_2O_{3(t)}$	11.24	12.38	10.69
MnO	0.17	0.18	0.19
MgO	10.05	10.13	15.29
CaO	11.48	11.20	10.06
Na_2O	2.06	1.49	1.86
K_2O	0.15	0.13	0.06
P_2O_5	0.07	0.09	0.08
total	100	100	100
Mg#	66.8	64.8	76.3
Rb	1.0	3.4	0.6
Sr	75	147	59
Ba	24	24	18
Zr	46	56	45
Nb	3.9	3.4	3.9
Y	15	21	17
Sc	47	45[§]	47
V	292	249	276
Cr	636	171	1081
Ni	204	161	335
Cu	84	111	23
Zn	77	66	64
Ga	16	17	10
La	2.7	5.4	2.8
Ce	6.7	9.1	6.1
Nd	5.4	7.9	5.4

[§]: INAA data

6.4.5 Comparison of the most primitive basalt with Curaçao and Ontong Java basalts

It can be seen from Figs. 6.1 and 6.2 that the basalts are relatively restricted in composition: SiO_2 = 49.14 to 51.99 wt.%; TiO_2 = 0.81 to 1.14 wt.%; Al_2O_3 = 13.2 to 14.5 wt.%; $Fe_2O_{3(t)}$ = 10.74 to 13.09 wt.%; MgO = 7.14 to 10.47 wt.%; and CaO = 10.5 to 12.76 wt.%. (The dolerites are more variable, probably because some of them contain cumulus material (Section 6.4.3).) A restricted range of compositions is also observed in basalts from Malaita (Ontong Java Plateau; Babbs, 1997), and may be due to efficient homogenisation of batches of magma in sub-volcanic magma chambers. The most primitive magmas from Aruba and the Ontong Java Plateau (Table 6.2) are very similar to one another, but are both very different from the most primitive rocks found on Curaçao (liquid compositions having 15-17 wt.% MgO: Kerr *et al.*, 1996b). This may reflect the nature of the magmatic plumbing systems in these locations: picritic liquids are denser than basaltic liquids and may be trapped by density filters, such as crustal rocks or magma chambers containing fractionated basaltic melts (e.g., Sparks *et al.*, 1980). The presence of picritic rocks on Curaçao implies that the mantle-derived melts did not encounter such a density filter. In contrast, picritic liquids do not appear to have been erupted on Aruba and Malaita (Ontong Java Plateau), although this does not necessarily mean that picritic liquids were not generated in the mantle beneath these locations. (Alternatively, any picrites present, which are likely to be volumetrically minor, could simply have been overlooked.) The evolved nature and homogeneity of most of the basalts erupted on Aruba hints that there may have been a well-established magma chamber at some level beneath the volcanic edifice(s), and this would have contributed to the non-eruption of any picritic magmas.

6.5 Fractional crystallisation

A number of features thus far discovered suggest that the process of fractional crystallisation has been important in the genesis of the basalts and dolerites (and, by inference, also the other members of the Aruba Lava Formation). The aim of this section is to determine how much of the compositional variation *could* be due to fractional crystallisation, since this is one of the simplest models for introducing compositional variability into a suite of rocks. Any variation that cannot be explained either by elemental mobility or fractional crystallisation *must* then be due to other processes, such as different batches of parental magma arising from varying degrees of melting of source regions that may themselves have

some compositional heterogeneity. It is noted, however, that from these data it is not possible to distinguish unequivocally the exact relative importance of these processes, because some of the compositional features could be explained either by fractional crystallisation or different parental magmas.

The first feature that suggests that the Aruba Lava Formation rocks have undergone crystal fractionation is the clustering of the data around the low-P cotectic (Thompson, 1982) in the normative ol-di-hy-qz diagram (Fig. 6.6), whereas primary melts extracted from depth within the mantle would be expected to plot closer to the olivine apex. Secondly, not even the most primitive basalts fully satisfy the criteria for being primary magmas described in Section 6.4.1: the maximum Mg# is 67.7 and Cr and Ni contents are less than 700 and 230 ppm, respectively. These two observations together suggest that crystal fractionation must have occurred between extraction of the primary magmas from the mantle and eruption of the basalts. The depth at which the bulk of this fractionation occurred is difficult to constrain; however, at least some of it appears to have occurred at relatively shallow levels, resulting in the clustering around the 1 atm cotectic in Fig. 6.6. The linear trends displayed in Figs. 6.1 to 6.4 also suggest that the basalts and dolerites are related to one another by fractional crystallisation. Additionally, some of the dolerites show evidence for *in situ* fractionation (Section 6.4.3), where the mineral phases present are not in equilibrium with the bulk rock composition, suggesting that a liquid fraction has been removed from them during crystallisation. This is in accordance with the inference from Fig. 6.6 that fractionation has occurred at low pressures. *In situ* fractionation in shallow-seated dolerites sills has also been reported on Curaçao (Klaver, 1987).

Computer modelling of fractional crystallisation has been carried out using the TRACE3 program of Nielsen (1988). The aims of this modelling are threefold:

1) to determine whether it is feasible that the members of the Aruba Lava Formation are related to one another by fractional crystallisation alone, or whether different parental magmas are required to explain the variation within the suite;
2) to compare the Aruba Lava Formation data with Curaçao and the Ontong Java Plateau; and
3) to investigate the possibility that the Aruba Lava Formation magmas are related to the Curaçao lavas by fractional crystallisation.

The TRACE3 program models, for a range of major and trace elements, the liquid lines of descent that arise from fractional crystallisation of olivine, orthopyroxene, clinopyroxene, plagioclase, spinel, ilmenite and pigeonite from an anhydrous (usually

basaltic) end member composition at 1 atm pressure. This is achieved by combining a major element phase equilibrium model with trace element partitioning. The proportions and compositions of the fractionating phases are also calculated. For the results reported in Fig. 6.9, the oxygen fugacity was set at the FMQ buffer, because this yielded Fe_2O_3/FeO ratios for the resulting liquids that were close to 0.15. The modelling carried out was the simplest allowed by the program, i.e., a closed system, with no recharge, assimilation or eruption of magmas. The end member compositions chosen were the estimated most primitive liquid compositions from the regions of interest (see Section 6.4.4. and Table 6.2). Zr and Mg# have been used as indices of fractionation, firstly because they are not affected by mobility during alteration, and secondly because the basalts and dolerites span a reasonably wide range of values for these parameters.

For the Aruba Lava Formation, TRACE3 predicts that the initial crystallising phase is olivine (with minor Cr-spinel); olivine is joined by plagioclase at ~7% crystallisation (MgO ≈ 8 wt.% and Mg# ≈ 61.7) and shortly after by clinopyroxene at ~10% crystallisation (MgO ≈ 7.9 wt.% and Mg# ≈ 60.9). Thereafter, plagioclase and clinopyroxene (in approximately equal proportions) dominate the crystallising assemblage until the liquid is considerably more evolved than any of the basalts and dolerites. However, the program does predict that olivine (up to 10%) continues to crystallise together with the plagioclase and clinopyroxene. These predictions broadly agree with petrographic studies, which show that the basalts and dolerites are dominated by plagioclase and clinopyroxene in approximately equal proportions (Section 5.2.1.2). One significant discrepancy between the modelling and petrographic studies is that no olivine has been observed in any of the rocks. This is not necessarily surprising, since the high degree of alteration/metamorphism makes it unlikely that olivine would have been preserved. Note that there is *indirect* evidence (in the form of high Ni and MgO contents) for olivine accumulation in some of the rocks (Section 6.4.2).

The fractionating phases for the Ontong Java Plateau endmember are very similar to those calculated for the Aruba Lava Formation. Olivine is the first phase to crystallise: this time it is not accompanied by Cr-spinel fractionation, possibly reflecting the significantly lower Cr content of the Ontong Java Plateau starting composition (Table 6.2). Plagioclase joins the fractionating assemblage at ~6% crystallisation (MgO ≈ 8.3 wt.%; Mg# ≈ 60.2), and clinopyroxene also begins to crystallise somewhat later in the sequence, at ~16% crystallisation (MgO ≈ 7.7 wt.%; Mg# ≈ 57.1).

The crystallisation sequence computed by TRACE3 for the Curaçao endmember is markedly different from those reported for Aruba and the Ontong Java Plateau. Olivine and Cr-spinel crystallise together until ~19% crystallisation, where they are joined by plagioclase (the liquid at this point has MgO ≈ 8.8 wt.% and Mg# ≈ 65.2). Cr-spinel ceases crystallising shortly thereafter, and clinopyroxene joins the fractionating assemblage at ~34% crystallisation, where MgO ≈ 8.0 wt.% and Mg# ≈ 60.0.

6.5.1 Is the variability caused by fractional crystallisation alone?

In theory, if all the chemical variation observed in the basalts and dolerites is due to crystal fractionation processes, all of the samples should lie either along the liquid line of descent calculated by TRACE3 (if they represent evolved liquids), or along a backwards projection of some portion of the trend (if they represent crystal cumulates). If this is not the case, the possibility that the Aruba Lava Formation rocks are derived from a range of different parental magmas must be considered.

Figure 6.9 shows liquid lines of descent calculated by TRACE3 superimposed on plots of the Aruba Lava Formation data, using Zr and Mg# as fractionation indices. Only a selection of elements is shown, chosen to represent the range of behaviour observed. For some elements, the data points and the calculated trend are coincident: exactly what would be expected if all the basalts and dolerites were related simply by fractionation (e.g., K_2O (Fig. 6.9f), P_2O_5 (Fig. 6.9g), La (Fig. 6.9h), $Fe_2O_{3(t)}$ (Fig. 6.9b) and also TiO_2, MgO, MnO, Nb, Y, Sr and the other REEs (not shown)). The dolerites lie close to a back-projection of the liquid line of descent, suggesting that they have an accumulative crystal component - but note that, in order to fit the observed data, this must be a back-projection of the plag + cpx dominated part of the trend (Zr > 51 ppm; Mg# < 61) rather than the olivine-controlled segment.

The modelled trends for SiO_2, Al_2O_3 and CaO (Figs. 6.9a, 6.9c and 6.9d, respectively) show initial enrichments in the liquid that do not appear to correspond with the data. These enrichments result from the initial olivine and Cr-spinel fractionation modelled by TRACE3. There are two likely reasons for the discrepancy: either the phase equilibria used by TRACE3 to calculate the fractionating phases are slightly displaced from the real system (due to differences in pressure or $P_{(H_2O)}$, for example), resulting in initial olivine crystallisation that is an artefact of the calculations; or the Aruba Lava Formation is derived not from one parental magma, but a spectrum of compositions - in Fig. 6.9, this would result in a range of parallel liquid lines of descent that could adequately explain the data. The minor scatter in Figs. 6.9b,

6.9f, 6.9g, and 6.9h could also be due to varying parental magma compositions, although another possibility is that the scatter arises from slight elemental mobility.

TRACE3 predicts rapid depletion of Ni in the liquid that is not observed in the data points (Fig. 6.9l). The observed data could again be explained by different batches of parental magma or mixing between primitive and more evolved magmas. Alternatively, because the slope of the plag + cpx dominated portion of the trend parallels the trend for the Aruba Lava Formation samples, the data can be explained satisfactorily by plag + cpx (+ minor ol) fractionation; the rapid depletion in Ni results from the initial olivine crystallisation modelled by TRACE3 that is not necessarily truly representative of the evolution of this suite of rocks.

For Al_2O_3 (Fig. 6.9c) and Na_2O (Fig. 6.9e), the low-Zr high-Mg# dolerites do not all lie close to a back-projection of the plag + cpx dominated portion of the liquid line of descent. They have lower Al_2O_3 and Na_2O contents than would be predicted by accumulation of plag + cpx (+ minor ol) in the proportions predicted by TRACE3. However, these data can be explained if proportionately more cpx than plag has accumulated. An interesting point for speculation at this juncture is what might cause an enhanced proportion of cpx to be preserved in a cumulate rock. One possibility is that, if crystallisation were occurring at greater pressures, a greater proportion of cpx could crystallise (Thompson, 1974); alternatively, even if cpx and plag crystallised in approximately equal proportions (as predicted by TRACE3 at 1 atm), plagioclase crystals might be preferentially retained in the liquid phase because of their lower density compared to clinopyroxene.

This model of proportionately greater cpx accumulation in the dolerites can be tested by looking at those elements which are abundant in cpx, but not in plag. The higher-than-predicted V contents (Fig. 6.9i) of the dolerites are consistent with an increased proportion of cpx ($V \approx 130$ ppm) rather than plag ($V \approx 10$ ppm); however, even small amounts of Cr-spinel ($V > 7000$ ppm) in the rocks can drastically increase V contents, and it may be Cr-spinel, rather than cpx, that is controlling the V concentrations. This is confirmed by the Cr data (Fig. 6.9k), where the dolerites show a lot of scatter because their Cr contents are very sensitive to even small variations in the amount of Cr-spinel present.

The horizontal trend displayed by the data for Sc (Fig. 6.9j) fits very poorly with the trend predicted by TRACE3, and the dolerites lie significantly lower than the back-projection of the cpx + plag control line. This appears to negate the arguments discussed above that cpx accumulation has been more significant than plag accumulation - in fact, the Sc data would appear to suggest that plag accumulation is dominant. However, the distribution coefficient

for Sc in cpx is rather poorly constrained (with estimates ranging from ~0.5 (Ulmer, 1989) to ~4 (Gallahan and Nielsen, 1992)), and varies with cpx composition; for example, a clinopyroxene with a high acmite component ($NaFe^{3+}Si_2O_6$) could accommodate more Sc in its structure due to the substitution $Fe^{3+} \Rightarrow Sc^{3+}$. Because the data for all elements except Sc appear to be consistent with the accumulation of cpx and plag (predominantly cpx), it is suggested that the D_{Sc} used by TRACE3 (which ranges from ~2.5 to ~3 depending on the bulk composition) is inappropriate for this particular suite of rocks.

The data displayed in Figs. 6.9a to 6.9l suggest that the basalts and dolerites are broadly related to one another by fractional crystallisation: for most elements the modelled liquid line of descent from the most primitive basalt passes close to the more evolved basalts of the sequence. Approximately 30% fractional crystallisation of the primitive endmember (Mg# $\approx$ 67) is required to generate the more evolved basalts (Mg# $\approx$ 55). The low-Zr, high Mg# dolerites lie close to a back-projection of the plag + cpx portion of the liquid line of descent, implying that they are cumulate plag-cpx-bearing rocks, consistent with the petrographic observations and the conclusions of Section 6.4.3.

The discrepancies between the observed compositions and the modelled trends for some elements can be explained by a number of factors. These include:

1) different batches of parental magmas with slightly different compositions;

2) mixing between primitive and evolved magmas derived from similar parents;

3) sensitivity of compositions to proportions of phases accumulating (e.g., Cr);

4) inaccuracies in the proportions of fractionating phases predicted by TRACE3 due to shifts in the phase equilibria used for modelling compared to the real magma system (for example, TRACE3 models 1 atm. fractionation);

5) uncertainty in some of the partition coefficients used by TRACE3, notably D_{Sc}; and,

6) elemental mobility;

The data do not allow a precise identification to be made of which of the above factors are the most influential in controlling the compositions. Nevertheless, the main conclusion from this section is robust: that the majority of the variation observed in the compositions of the basalts and dolerites can be explained by fractional crystallisation. The involvement of different parental magmas is required to explain some of the data, but these parental magmas can differ only subtly in composition from the one used for the modelling.

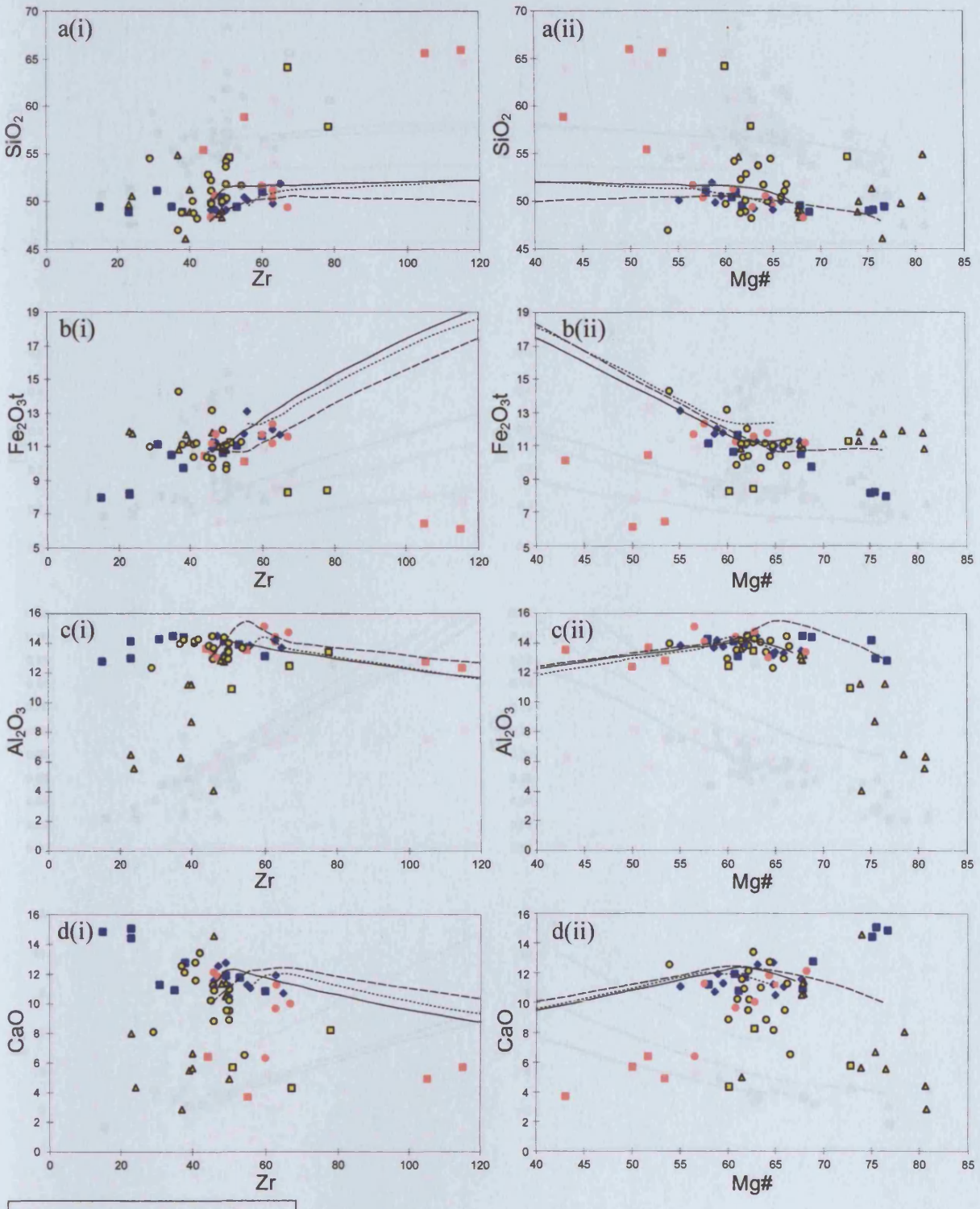

Fig. 6.9a-d: Liquid lines of descent calculated by TRACE3 (Nielsen, 1988) for the primitive end members (compositions reported in Table 6.2) of the Aruba Lava Formation, the Curaçao Lava Formation and the Ontong Java Plateau, compared with data from samples of the Aruba Lava Formation. Major elements reported in wt. %; Zr in ppm; Mg# defined in text (Section 6.4.1). All data by XRF.

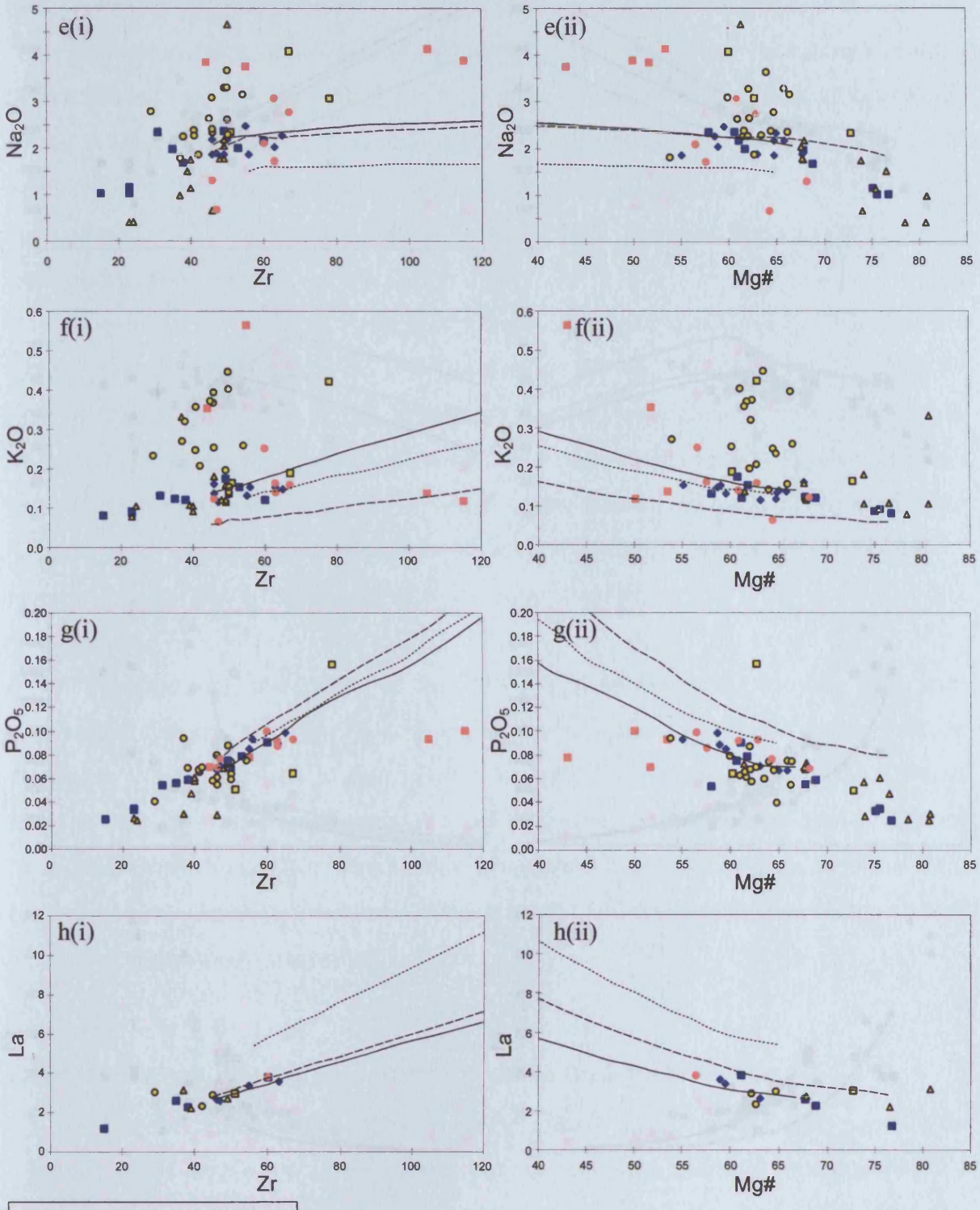

Fig. 6.9e-h: Liquid lines of descent calculated by TRACE3 (Nielsen, 1988) for the primitive end members (compositions reported in Table 6.2) of the Aruba Lava Formation, the Curaçao Lava Formation and the Ontong Java Plateau, compared with data from samples of the Aruba Lava Formation. Major elements reported in wt. %; Zr and La in ppm; Mg# defined in text (Section 6.4.1). All data by XRF, except La, which is by ICP-MS.

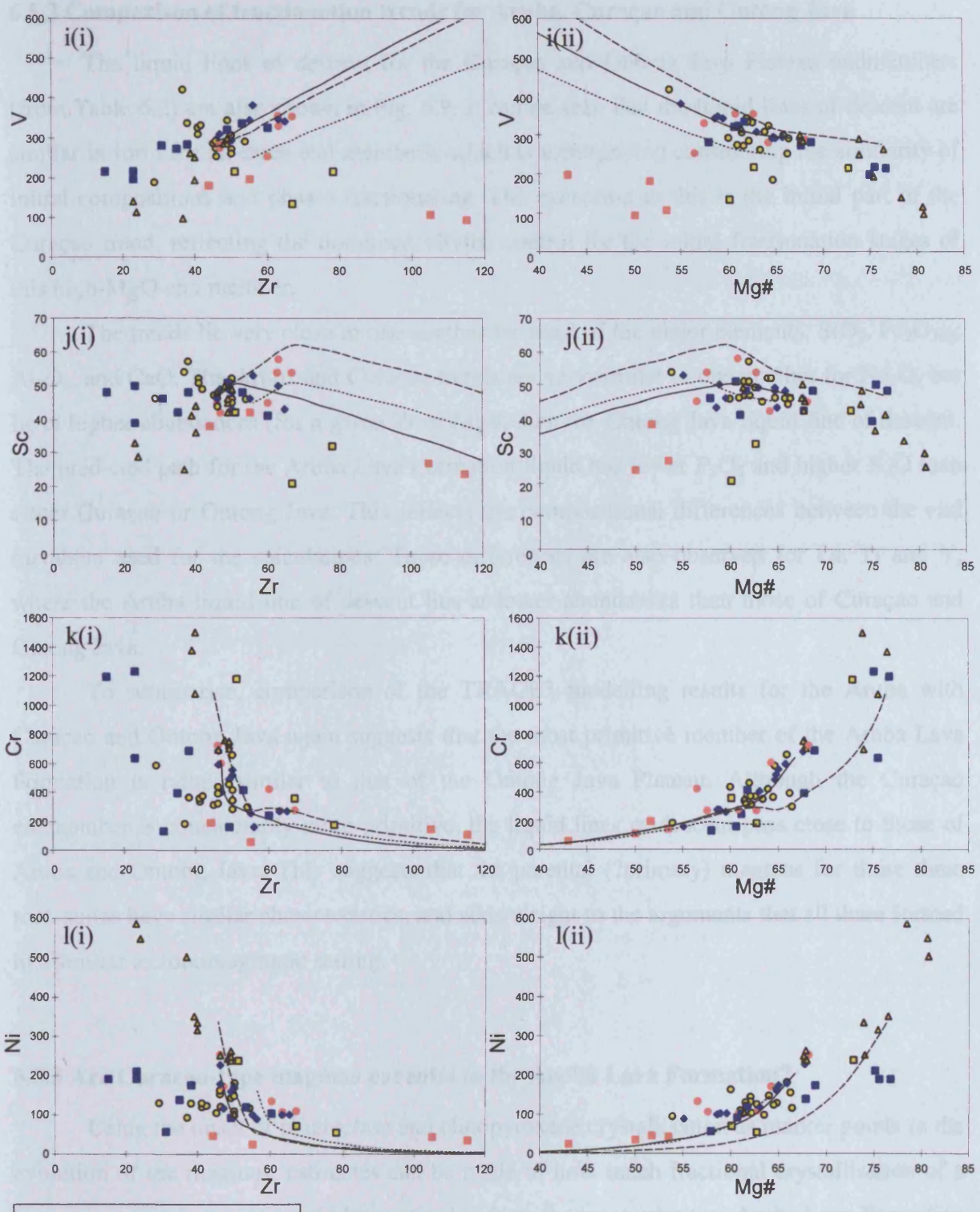

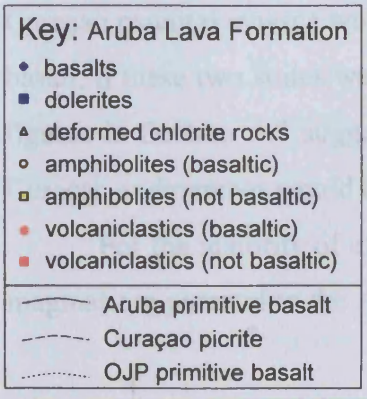

Fig. 6.9i-l: Liquid lines of descent calculated by TRACE3 (Nielsen, 1988) for the primitive end members (compositions reported in Table 6.2) of the Aruba Lava Formation, the Curaçao Lava Formation and the Ontong Java Plateau, compared with data from samples of the Aruba Lava Formation. All analyses by XRF; reported in ppm, except Mg#, which is defined in text (Section 6.4.1).

6.5.2 Comparison of fractionation trends for Aruba, Curaçao and Ontong Java

The liquid lines of descent for the Curaçao and Ontong Java Plateau endmembers (from Table 6.2) are also shown in Fig. 6.9. It can be seen that the liquid lines of descent are similar in form for all three end members, which is unsurprising considering the similarity of initial compositions and phases fractionating. The exception to this is the initial part of the Curaçao trend, reflecting the dominant olivine control for the initial fractionation stages of this high-MgO end member.

The trends lie very close to one another for most of the major elements: SiO_2, $Fe_2O_{3(t)}$, Al_2O_3, and CaO. The Aruba and Curaçao trends are very similar to one another for Na_2O, but lie at higher abundances (for a given Zr or Mg#) than the Ontong Java liquid line of descent. The predicted path for the Aruba Lava Formation liquid has lower P_2O_5 and higher K_2O than either Curaçao or Ontong Java. This reflects the compositional differences between the end members used for the calculations. These differences are also observed for La, Ti and Y, where the Aruba liquid line of descent lies at lower abundances than those of Curaçao and Ontong Java.

To summarise, comparison of the TRACE3 modelling results for the Aruba with Curaçao and Ontong Java again suggests that the most primitive member of the Aruba Lava Formation is rather similar to that of the Ontong Java Plateau. Although the Curaçao endmember is considerably more primitive, the liquid lines of descent pass close to those of Aruba and Ontong Java. This suggests that the parental (?primary) magmas for these three rock suites have similar characteristics, and adds weight to the arguments that all three formed in a similar tectonomagmatic setting.

6.5.3 Are Curaçao-type magmas parental to the Aruba Lava Formation?

Using the onset of plagioclase and clinopyroxene crystallisation as marker points in the evolution of the magmas, estimates can be made of how much fractional crystallisation of a Curaçao parental magma would be required to form the most primitive Aruba Lava Formation basalt, if these two suites were indeed related by fractional crystallisation. Examination of the figures in Section 6.5 suggests that between 12% and 24% fractional crystallisation of the Curaçao endmember would be required to form the Aruba endmember.

For the majority of elements displayed in Fig. 6.9, it is plausible that the Curaçao-type magmas are parental to the Aruba Lava Formation magmas; there are, however, a few notable

exceptions. The modelled K_2O trend for Curaçao passes to the low-K_2O side of all of the Aruba basalts and dolerites: it appears that the Curaçao endmember has a significantly lower K_2O content than any of the Aruba basalts. This is not necessarily an original feature: brief inspection of the Curaçao dataset reported in Kerr *et al.* (1996b) demonstrates that K_2O contents cover a large range, probably due to elemental mobility during secondary processes. Nonetheless, some of the differences observed between Aruba and Curaçao do appear to reflect original differences in the parental magmas. The Aruba Lava Formation has lower P_2O_5, La, V and Sc for a given Mg#; these are relatively immobile elements (see Section 6.2.3.1), so this difference is likely to represent a difference in parental magma compositions. Additionally, the Ni contents of the Aruba magmas cannot be explained by olivine-dominated fractional crystallisation of a Curaçao-type parent, because the resulting liquid becomes depleted too quickly in Ni. It is therefore concluded that, although the compositions of the parental magmas for the Aruba and Curaçao lavas were similar in many respects, it is not possible that the Curaçao lavas and the Aruba Lava Formation were both derived from simple fractional crystallisation of a single parental magma.

6.6 Constraints on the mantle source of the Aruba Lava Formation

6.6.1 Isotopic composition of the mantle source

Sr, Nd and Pb isotope ratios are not modified during mantle melting processes or subsequent fractional crystallisation, and so can be used as tracers of mantle sources or to identify contamination of mantle-derived magmas with material having different isotope ratios. However, caution needs to be exercised when interpreting isotope ratios. Before comparing the isotope ratios of rocks of different ages, an age-correction should be made. All data reported in this section are, therefore, *initial* ratios (denoted, for example, $(^{87}Sr/^{86}Sr)_i$), age-corrected to 88 Ma for the Aruba Lava Formation. The age correction introduces a error into the reported values, especially for $(^{87}Sr/^{86}Sr)_i$ and the Pb ratios, because the parent isotopes (Rb, U and, to a lesser extent, Th) have been shown to be mobile during metamorphism and alteration. Fortunately, the Rb, U and Th contents are ubiquitously low, and any error arising due to the age correction will be small.

The mobility of the daughter elements should also be considered before interpreting the isotope data. It was shown in Section 6.2.3 that Sr is a mobile element: the measured Sr isotope ratios may not, therefore, be truly meaningful. This is especially important for the

more deformed or metamorphosed rocks. It is well known that equilibration with seawater during hydrothermal alteration can result in modified (usually elevated) $^{87}Sr/^{86}Sr$ (e.g., Staudigel *et al.*, 1981; Mahoney, 1987). Altered Sr isotope ratios could also result from modification of Rb contents during alteration, but only if Rb/Sr changes, and the system has time to mature; the half-life of $^{87}Rb \Rightarrow {}^{87}Sr$ is approximately 50 Ga (Steiger and Jäger, 1977), so this is unlikely to be a problem for the ~88 Ma Aruban rocks.

In some cases, the effects of isotopic mobility during alteration can be accounted for by leaching the powdered sample in hydrochloric acid. This tends to dissolve and remove the secondary phases that contribute to the modified isotope ratios (e.g., clay minerals, zeolites). The isotopic analysis is then carried out on the dissolved residue, which should contain (ideally) only primary igneous phases that preserve the magmatic isotope ratios.

Isotopic mobility is less problematic for Nd. Both Nd and the parent element, Sm, have been shown to be immobile in the Aruba Lava Formation rocks, and so the measured ratios should reflect the original isotopic composition. Seawater has very low concentrations of Nd, and is incapable of significantly changing the Nd isotopic composition of altered rocks. Moreover, even if alteration were to modify the parent/daughter (i.e., Sm/Nd) ratio, the half life for $^{147}Sm \Rightarrow {}^{143}Nd$ is even greater than that for the Rb-Sr system, and any secondary modification of Sm/Nd requires an immensely long time period for a significant difference to the isotopic signature to be recorded. However, Mahoney (1987) did report that for very altered basalts, $(\varepsilon_{Nd})_i$ could be elevated by up to 1.5 units in the leached compared to the unleached sample.

Pb isotope ratios also do not appear to be substantially modified during alteration. Mahoney and Spencer (1991) and Mahoney *et al.* (1993) found that there was minimal difference between the Pb isotope ratios of leached and unleached samples. In contrast, Babbs (1997) concludes that Pb isotopes as well as Pb abundances have been modified by seawater alteration, although the differences may arise from the inclusion of altered veins within samples. Babbs' work (1997) showed that the leached samples were considerably more radiogenic than the unleached: the maximum displacements recorded were 0.37, 0.045 and 0.284 for $^{206}Pb/^{204}Pb$, $^{207}Pb/^{204}Pb$ and $^{208}Pb/^{204}Pb$, respectively.

Although it was acknowledged that the isotope ratios (in particular, $^{87}Sr/^{86}Sr$) of the Aruba Lava Formation rocks could have been modified by alteration, a decision was made *not* to leach the samples prior to isotopic analysis. The rocks are so altered that, in some cases, it was suspected that *no* primary mineralogy remained. In this situation, leaching actually

contributes an extra layer of uncertainty to the results, because it is difficult to determine which phases are removed during leaching, and which remain to be analysed.

The five analysed basalts and dolerite samples show a restricted range of isotope ratios (Table 6.3; Figs. 6.10 and 6.11). In addition to these five samples, four deformed and metamorphosed rocks (chlorite-schists and amphibolites) were analysed. The Sr isotope ratios for three of these samples (with values as high as 0.705294) extend beyond the restricted ranges reported for the basalts and dolerites. The deformed and metamorphosed samples also extend the range of Pb isotopes to less radiogenic values (down to 18.655 for $(^{206}Pb/^{204}Pb)_i$ and 38.292 for $(^{208}Pb/^{204}Pb)_i$), although the values for $(^{207}Pb/^{204}Pb)_i$ fall within the range of the basalts and dolerites. $(^{143}Nd/^{144}Nd)_i$ ratios for the deformed samples, however, are indistinguishable from those of the basalts and dolerites.

Table 6.3: Range of age-corrected (t = 88 Ma) isotope ratios for all five analysed basalts and dolerites from the Aruba Lava Formation. The 1σ reported is analytical error only; a more realistic estimate of the error is given by the external reproducibility on the standard (see Appendix F). Errors arising from age-correction are also not included.

Ratio	Minimum	error (1 σ)	Maximum	error (1σ)
$(^{87}Sr/^{86}Sr)_i$	0.703256	± 5	0.703842	± 7
$(^{143}Nd/^{144}Nd)_i$	0.512870	± 5	0.512930	± 4
$(\varepsilon_{Nd})_i$	+ 6.75		+ 7.91	
$(^{206}Pb/^{204}Pb)_i$	18.771	± 0.002	19.111	± 0.002
$(^{207}Pb/^{204}Pb)_i$	15.538	± 0.002	15.594	± 0.003
$(^{208}Pb/^{204}Pb)_i$	38.322	± 0.005	38.768	± 0.007

In Figs. 6.10 and 6.11, the Aruba Lava Formation isotope data are compared with data from elsewhere in the Caribbean region, and Pacific oceanic plateaux, for example the Ontong Java Plateau. On the $(\varepsilon_{Nd})_i$ vs. $(^{87}Sr/^{86}Sr)_i$ plot (Fig. 6.10), the Aruba basalts and dolerites plot in the upper left quadrant, indicating a long term history of depletion in the source region. The mantle source of the Aruba Lava Formation is not as depleted as the mantle from which MORB is derived: for example, East Pacific Rise MORB has $(^{87}Sr/^{86}Sr)_i$ values down to ~ 0.7025 and $(\varepsilon_{Nd})_i$ up to + 11 (Mahoney *et al.* (1993) and references therein). The Sr and Nd isotope ratios analysed for the Aruba basalts, in addition to closely resembling those of Curaçao picrites and basalts (Kerr *et al.*, 1996b), are very similar to those reported for a

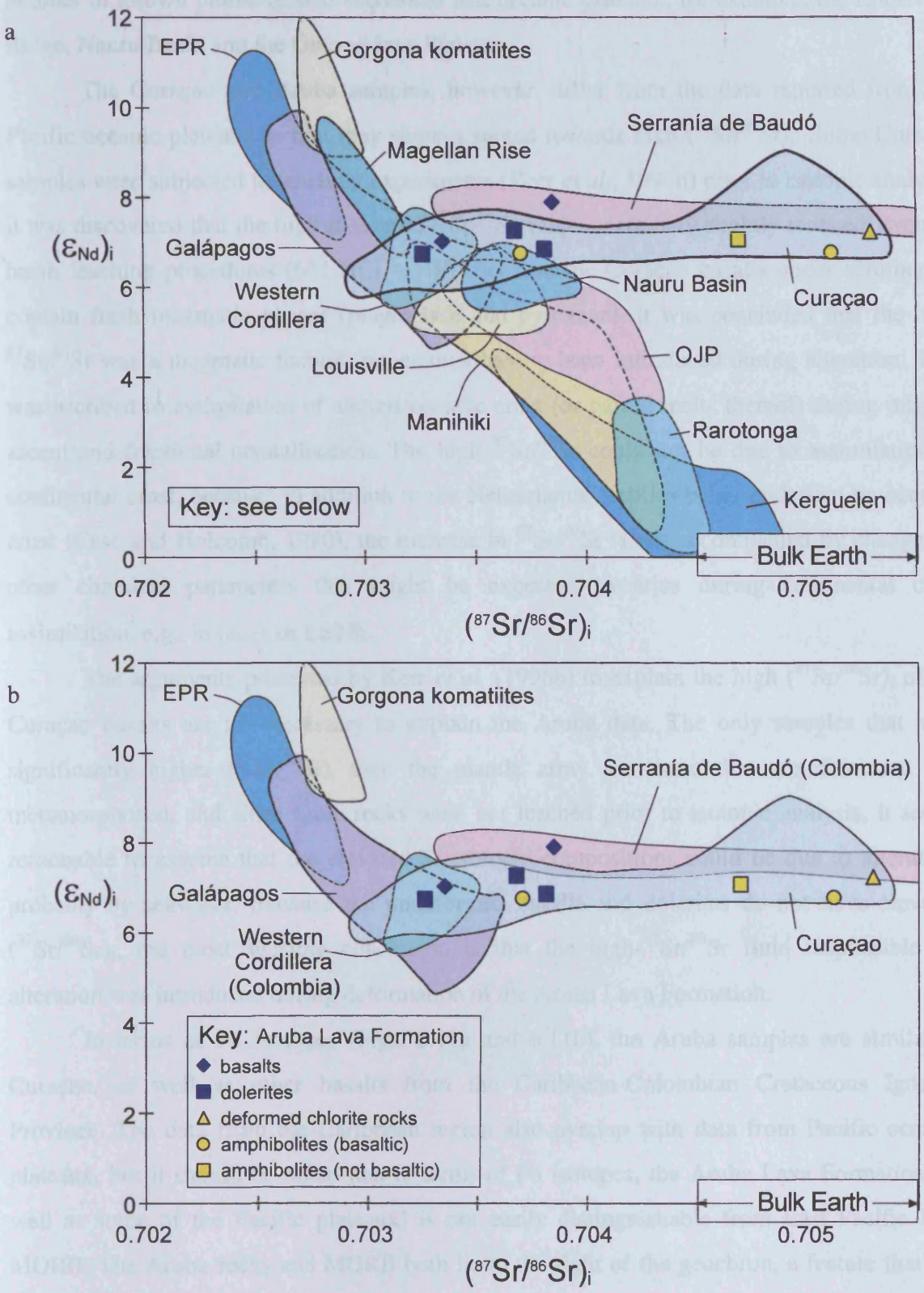

Fig. 6.10: Initial $^{87}Sr/^{86}Sr$ vs. ε_{Nd} (all corrected to time of emplacement: 88 Ma for Aruba Lava Formation), comparing the Aruba Lava Formation rocks with a range of data from the Caribbean region and Pacific plateaux (Fig. 6.10a) and data from the Caribbean region only (for clarity) in 6.10b. Data for Curaçao and Colombia from Hauff *et al.* (submitted): Serranía de Baudó field extends to $^{87}Sr/^{86}Sr \approx 0.706$. Other data from Mahoney *et al.* (1993) and Kerr *et al.* (1996b) and references therein. Range of Bulk Earth estimates for Sr isotopes from Faure (1986).

number of known plume-related sequences and oceanic plateaux, for example, the Louisville Ridge, Nauru Basin and the Ontong Java Plateau.

The Curaçao and Aruba samples, however, differ from the data reported from the Pacific oceanic plateaux in that they show a spread towards high $(^{87}Sr/^{86}Sr)_i$. Some Curaçao samples were subjected to leaching experiments (Kerr *et al.*, 1996b) prior to isotopic analysis: it was discovered that the high measured $^{87}Sr/^{86}Sr$ values were only slightly reduced, even by harsh leaching procedures (6M HCl + HF). Because the Curaçao basalts under scrutiny *do* contain fresh magmatic phases (plagioclase and pyroxene), it was concluded that the high $^{87}Sr/^{86}Sr$ was a magmatic feature, rather than having been introduced during alteration. This was ascribed to assimilation of altered oceanic crust (or partial melts thereof) during magma ascent and fractional crystallisation. The high $^{87}Sr/^{86}Sr$ could not be due to assimilation of continental crust, because, in addition to the Netherlands Antilles being underlain by oceanic crust (Case and Holcomb, 1980), the increase in $^{87}Sr/^{86}Sr$ is not accompanied by changes in other chemical parameters that might be expected to arise during continental crust assimilation, e.g., in $(\varepsilon_{Nd})_i$ or La/Nb.

The arguments presented by Kerr *et al.* (1996b) to explain the high $(^{87}Sr/^{86}Sr)_i$ of the Curaçao basalts are not necessary to explain the Aruba data. The only samples that have significantly higher $(^{87}Sr/^{86}Sr)_i$ than the mantle array are those that are deformed and metamorphosed, and since these rocks were not leached prior to isotopic analysis, it seems reasonable to assume that the elevated Sr isotopic compositions could be due to alteration, probably by seawater. Because the undeformed basalts and dolerites do not have elevated $(^{87}Sr/^{86}Sr)_i$, the most sensible conclusion is that the high-$^{87}Sr/^{86}Sr$ fluid responsible for alteration was introduced during deformation of the Aruba Lava Formation.

In terms of Pb isotopes (Figs. 6.11a and 6.11b), the Aruba samples are similar to Curaçao, as well as other basalts from the Caribbean-Colombian Cretaceous Igneous Province. The data from the Caribbean region also overlap with data from Pacific oceanic plateaux, but it should be noted that in terms of Pb isotopes, the Aruba Lava Formation (as well as some of the Pacific plateaux) is not easily distinguishable from East Pacific Rise MORB. The Aruba rocks and MORB both lie to the right of the geochron, a feature that has long puzzled geochemists (e.g., Allègre, 1969): a source region that has undergone prior melt extraction events should be depleted in U and Th relative to Pb, and should therefore evolve to give relatively unradiogenic Pb isotope ratios, lying to the left of the geochron. It has been proposed (e.g., White and Hofmann, 1982; Saunders *et al.*, 1988; Chauvel *et al.*, 1995) that

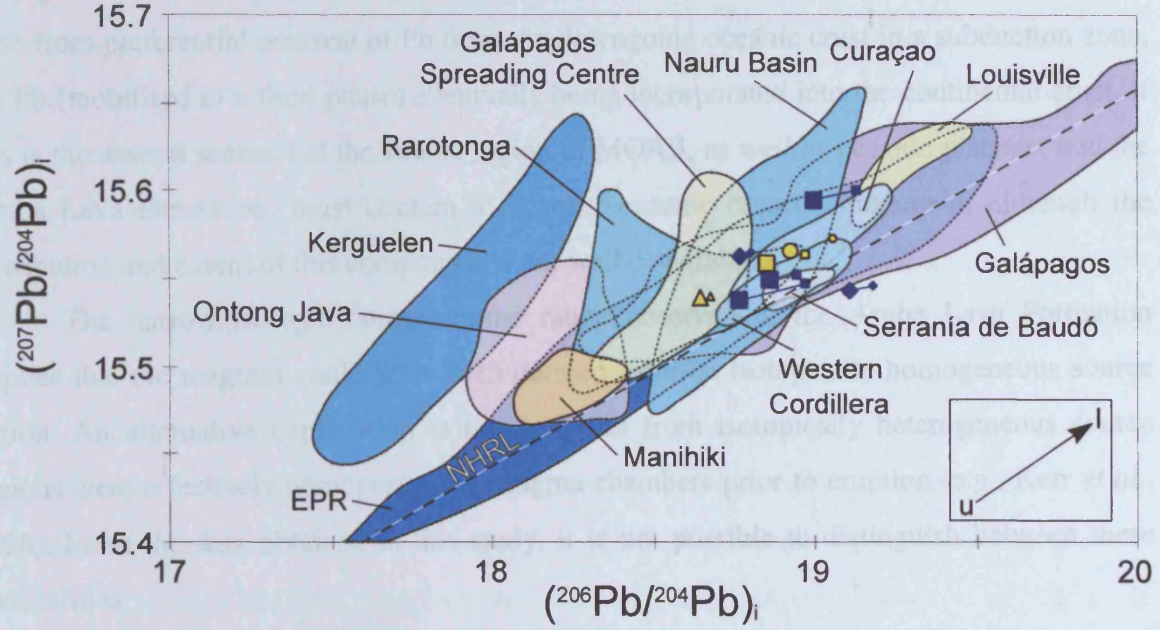

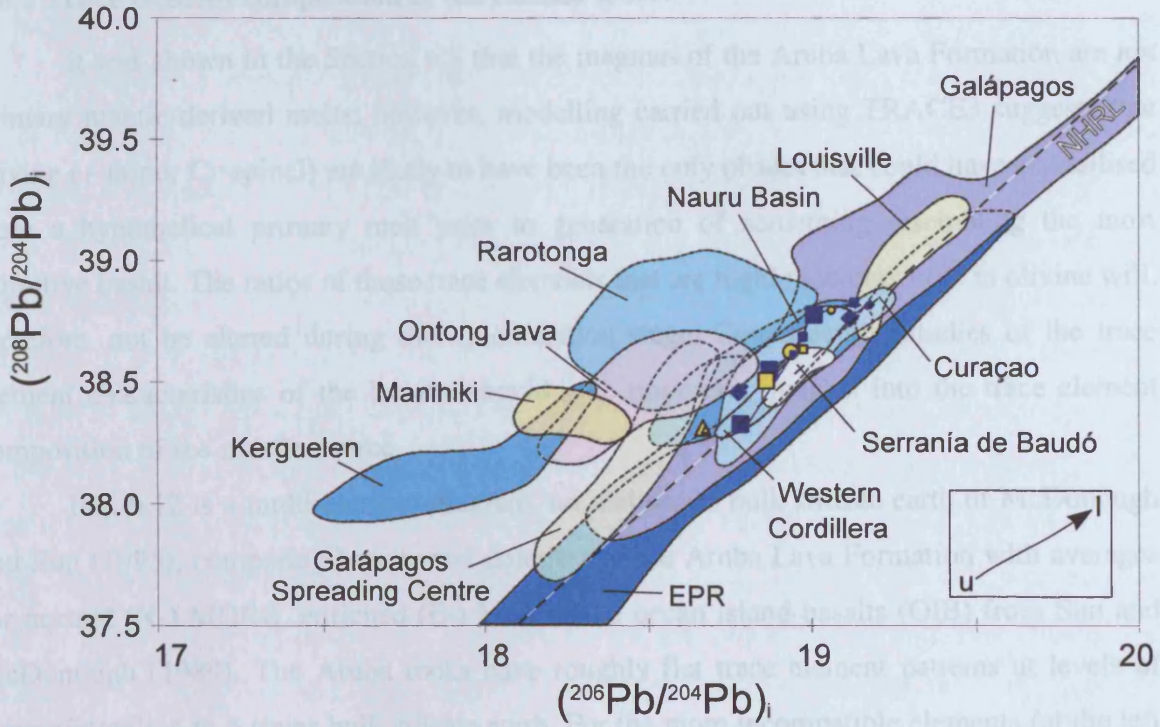

Key: Aruba Lava Formation
- basalts
- dolerites
- deformed chlorite rocks
- amphibolites (basaltic)
- amphibolites (not basaltic)

Fig. 6.11: Lead isotope data for the Aruba Lava Formation, compared with data from a wide range of Caribbean mafic rocks and Pacific plateaux. Data is age-corrected to the time of emplacement. For the Aruba Lava Formation, large symbols represent age-corrected data, and small symbols represent the measured isotope ratio for the same sample (these are linked with a line if there is any danger of ambiguity). Data sources as in Fig. 6.10. Arrow from "u" to "l" represents the *maximum* shift (from leached to unleached) reported for the Ontong Java basalts by Babbs (1997).

the high U-Pb ratio required to evolve an isotopic signature to the right of the geochron could arise from preferential removal of Pb from the downgoing oceanic crust in a subduction zone, the Pb (mobilised in a fluid phase) eventually being incorporated into the continental crust. If this is the case, it seems that the source region of MORB, as well as oceanic plateaux and the Aruba Lava Formation, must contain a recycled oceanic crustal component, although the distribution and extent of this component is not well constrained.

The narrow isotopic compositional range observed in the Aruba Lava Formation implies that the magmas could have been derived from an isotopically homogeneous source region. An alternative explanation is that magmas from isotopically heterogeneous source regions were effectively homogenised in magma chambers prior to eruption (e.g., Kerr *et al.*, 1998). From the data obtained in this study, it is not possible to distinguish between these possibilities.

6.6.2 Trace element composition of the mantle source

It was shown in the Section 6.5 that the magmas of the Aruba Lava Formation are *not* primary mantle-derived melts; however, modelling carried out using TRACE3 suggests that olivine (+ minor Cr-spinel) are likely to have been the only phases that could have crystallised from a hypothetical primary melt prior to generation of something resembling the most primitive basalt. The ratios of those trace elements that are highly incompatible in olivine will, therefore, not be altered during this fractionation stage. Consequently, studies of the trace element characteristics of the basalts should give important insights into the trace element composition of the mantle source.

Fig. 6.12 is a multi-element diagram, normalised to bulk silicate earth of McDonough and Sun (1995), comparing basalts and dolerites of the Aruba Lava Formation with averages for normal (N-) MORB, enriched (E-) MORB and ocean island basalts (OIB) from Sun and McDonough (1989). The Aruba rocks have roughly flat trace element patterns at levels of approximately 4 to 6 times bulk silicate earth. For the more incompatible elements (at the left hand side of the diagram), the abundances of trace elements lie between N-MORB and E-MORB; this implies a source that is somewhat less depleted than the N-MORB source, but not as enriched as the E-MORB source. The scatter at the left-hand side of the diagram is likely to be due to alteration, as it is most pronounced for Ba, Rb and K, which have been shown to be mobile. However, Th is not mobile in the basalts and dolerites, and the low abundances of Th compared to the other immobile trace elements hint at a slightly depleted source region. Nevertheless, the abundances of highly incompatible trace elements in the

basalts and dolerites suggest that they were derived from a mantle source that was less depleted than the normal MORB source: this relatively enriched source region may have been located within a mantle plume.

The composition of the Aruba Lava Formation magmas also lies on a mixing line between N-MORB and E-MORB in $(La/Sm)_{BSEN}$ vs. Zr/Nb space (Fig. 6.13). ($_{BSEN}$ denotes a ratio normalised to bulk silicate earth (McDonough and Sun, 1995), also equivalent to a chondrite-normalised (McDonough and Sun, 1995) ratio). Note that the extent of depletion is dependent on the element studied; i.e., some elements have near-chondritic ratios (e.g., La/Sm, Zr/Nb) whereas others show depletions relative to chondritic ratios (e.g., Th). Fig. 6.13 also shows data from Curaçao and Ontong Java for comparison: these data also fall between N-MORB and E-MORB, close to the bulk silicate earth value, implying that the mantle source trace element compositions of the three suites are similar. If anything, the Ontong Java basalts have slightly higher Zr/Nb than the Aruba Lava Formation, whereas the Curaçao lavas have lower Zr/Nb.

If there is a depleted mantle source component contributing to the genesis of the Aruba Lava Formation magmas, this need not necessarily be the N-MORB source. It has been proposed that mantle plumes can be markedly heterogeneous (e.g., Hart, 1988; Hart *et al.*, 1992; Kerr *et al.*, 1995), containing both depleted and enriched components. The depleted plume component is compositionally distinct from the N-MORB source, as demonstrated by Fitton *et al.* (1997) for Icelandic basalts on a plot of Nb/Y vs. Zr/Y (Fig. 6.14). This arises because N-MORB has a more marked depletion in Nb than other incompatible elements, due to previous melt extraction events, whereas Nb is relatively enriched in plume material. The Aruba and Curaçao data fall close to bulk silicate earth, within the field of Iceland basalts. This field also encompasses other oceanic plateau data (e.g., Ontong Java and Manihiki) as well as most ocean island basalts. The location of the Aruba Lava Formation, within the Iceland array, suggests that the slightly depleted component (inferred from the isotopic composition and some trace element data, e.g., Th) may be intrinsic to the plume source region, rather than resulting from entrained N-MORB source material.

The abundances in the Aruba Lava Formation rocks of the less incompatible elements (i.e., Nd to Lu; Fig. 6.12) are *less* than those in N-MORB. This is unlikely to be due to the source region being more depleted than the N-MORB source, because that would result in lower abundances for the whole range of elements, but particularly the most incompatible elements. This leaves two possible explanations: firstly, that the trace element abundances in

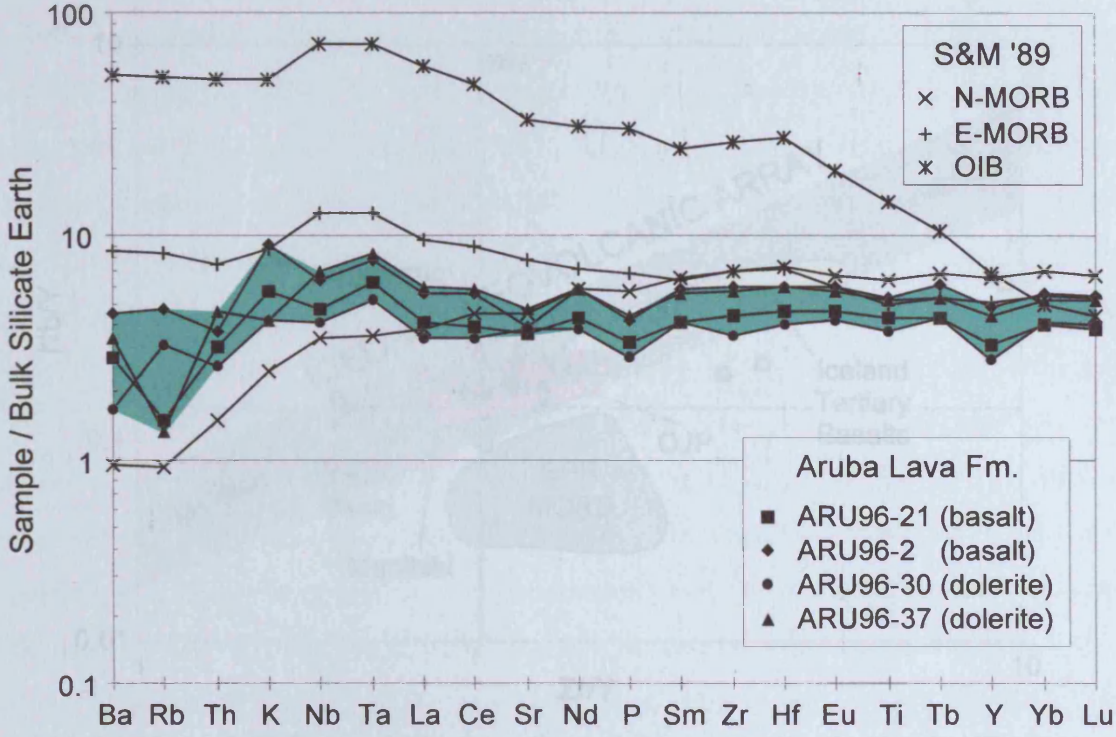

Fig. 6.12: Multi-element diagram, normalised to bulk silicate earth (McDonough and Sun, 1995), showing basalts and dolerites of the Aruba Lava Formation. These show essentially flat patterns, with a slight depletion of the very incompatible elements (e.g., Th), although this effect is obscured by elemental mobility for Ba, Rb and K. Average normal MORB (N-MORB), enriched MORB (E-MORB) and ocean island basalt (OIB) are shown for comparison (from Sun and McDonough, 1989). Green field accentuates position of Aruba Lava Formation samples. Analyses by XRF (Ba, Rb, K, Sr, P, Zr, Ti, Y), ICP-MS (Th, Nb and REEs) and INAA (Ta, Hf).

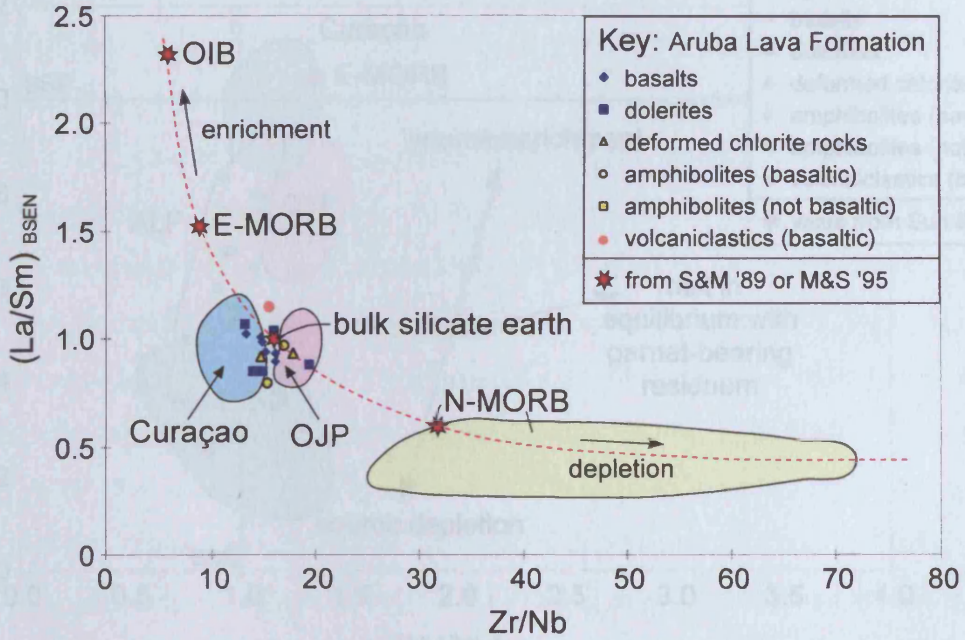

Fig. 6.13: Compositional range of Aruba Lava Formation rocks (Zr and Nb by XRF; La and Sm by ICP-MS) compared with the Ontong Java Plateau (OJP: Babbs, 1997) and Curaçao (Kerr *et al.*, 1996b; G. Klaver, unpubl. data: *most* data fall into the field drawn). All three suites fall close to bulk silicate earth (McDonough and Sun, 1995; equivalent also on this plot to C1 chondrite), having compositions intermediate between those of N-MORB (field from A.D. Saunders, unpubl. data) and E-MORB. BSEN: normalised to bulk silicate earth (McDonough and Sun, 1995).

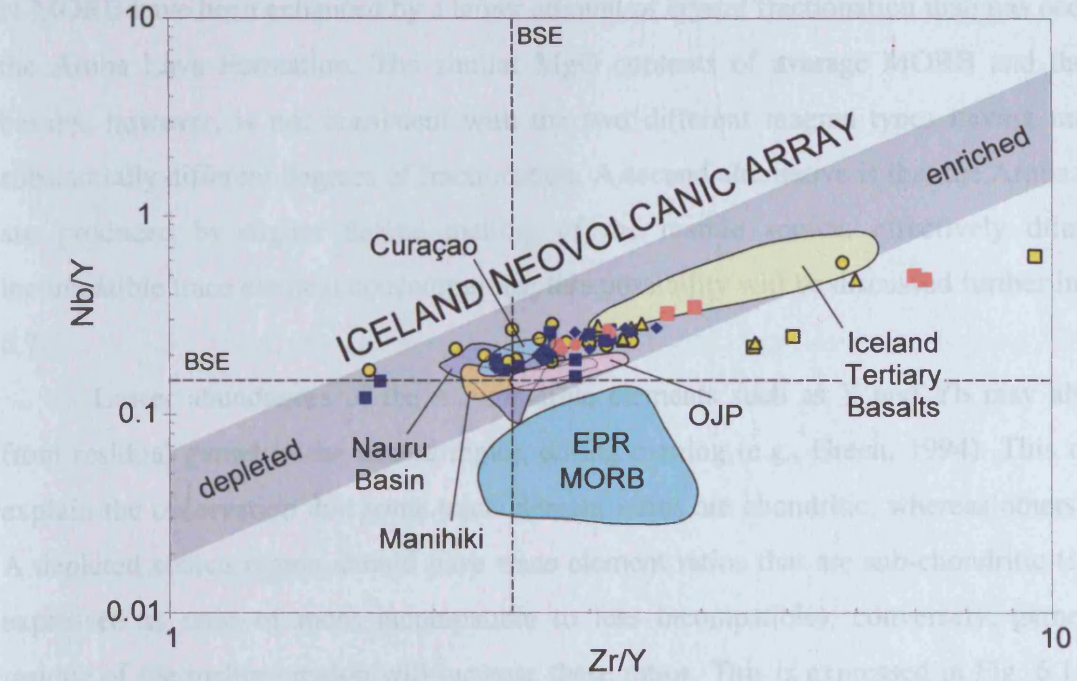

Fig. 6.14: Nb/Y vs. Zr/Y for the Aruba Lava Formation, compared with other Pacific plateau and Caribbean basalts. All mafic neovolcanic rocks from Iceland plot in the "Iceland Neovolcanic Array" (Fitton *et al.*, 1997): some of these have a depleted component that is distinct in composition from N-MORB (here represented by the East Pacific Rise (EPR); A. D. Saunders, unpubl. data). Other data sources: Ontong Java (OJP) - Babbs (1997); Curaçao - Kerr *et al.* (1996b); Nauru Basin - Saunders (1985); Manihiki - A. D. Saunders and G. F. Marriner (unpubl. data); Iceland Tertiary Basalts - Fitton *et al.* (1997). BSE: bulk silicate earth of McDonough and Sun (1995). Aruba symbols: see key below.

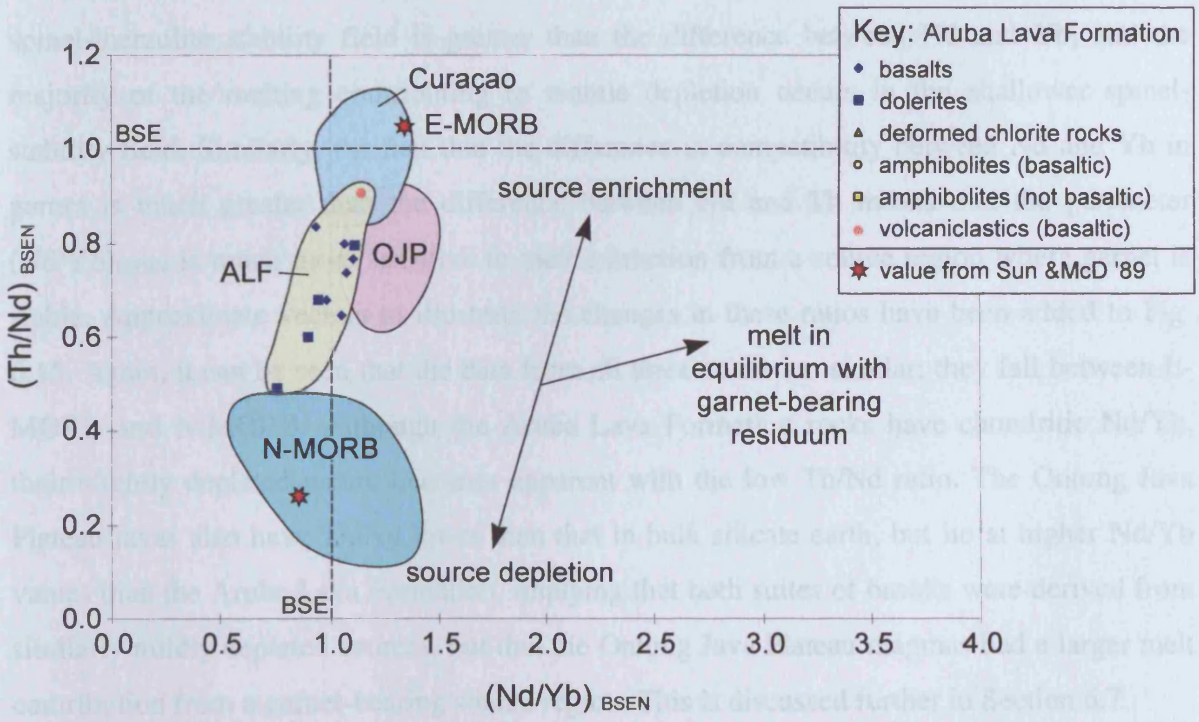

Fig. 6.15: Bulk silicate earth-normalised (McDonough and Sun, 1995) Th/Nd and Nd/Yb for samples from the Aruba Lava Formation (ALF), the Ontong Java Plateau (OJP: Babbs, 1997) and Curaçao (Kerr *et al.*, 1996b). The ALF samples are intermediate between E-MORB and N-MORB (field from A. D. Saunders, unpubl. data), and show no evidence for significant equilibration with a garnet-bearing residue. BSE: as Fig. 6.14. Amphibolites not included on this plot because of Th mobility.

N-MORB have been enhanced by a larger amount of crystal fractionation than has occurred in the Aruba Lava Formation. The similar MgO contents of average MORB and the Aruba basalts, however, is not consistent with the two different magma types having undergone substantially different degrees of fractionation. A second alternative is that the Aruba magmas are produced by higher degree melting of the mantle source, effectively diluting the incompatible trace element concentrations; this possibility will be discussed further in Section 6.7.

Lower abundances of the incompatible elements such as Y and Yb may also result from residual garnet in the source region during melting (e.g., Green, 1994). This may also explain the observation that some trace element ratios are chondritic, whereas others are not. A depleted source region should have trace element ratios that are sub-chondritic (if always expressed as ratio of more incompatible to less incompatible); conversely, garnet in the residue of the melting region will increase these ratios. This is expressed in Fig. 6.15, which uses the parameters $(Th/Nd)_{BSEN}$ and $(Nd/Yb)_{BSEN}$ as tracers of depletion and enrichment of mantle sources arising from melting in the spinel and garnet stability fields. Although both of these ratios in the melt are increased by melting in either source region, $(Th/Nd)_{BSEN}$ is much more sensitive to the degree of incompatible element depletion of the mantle source. This is because the incompatibility difference between Th and Nd during mantle melting in the spinel-lherzolite stability field is greater than the difference between Nd and Yb, and the majority of the melting contributing to mantle depletion occurs in the shallower spinel-stability field. Similarly, the fact that the difference in compatibility between Nd and Yb in garnet is much greater than the difference between Nd and Th means that the parameter $(Nd/Yb)_{BSEN}$ is much more sensitive to melt extraction from a source region where garnet is stable. Approximate vectors to illustrate the changes in these ratios have been added to Fig. 6.15. Again, it can be seen that the data from all three suites are similar; they fall between E-MORB and N-MORB. Although the Aruba Lava Formation rocks have chondritic Nd/Yb, their slightly depleted nature becomes apparent with the low Th/Nd ratio. The Ontong Java Plateau lavas also have Th/Nd lower than that in bulk silicate earth, but lie at higher Nd/Yb values than the Aruba Lava Formation, implying that both suites of basalts were derived from similarly mildly depleted sources, but that the Ontong Java Plateau magmas had a larger melt contribution from a garnet-bearing source region. This is discussed further in Section 6.7.

Another important feature of the bulk silicate earth-normalised multi-element diagram (Fig. 6.12) is that there is no evidence for any subduction-related component, for example,

there are no depletions in Nb or Ta (e.g., Saunders *et al.*, 1991). Figure 6.16 displays bulk silicate earth-normalised values for other members of the Aruba Lava Formation for comparison with the basalts and dolerites. (Note that these are abridged versions of the multi-element diagram, because good quality analytical data for the range of trace elements shown in Fig. 6.12 were not available). For all lithologies, the patterns observed are essentially flat, with the exception of those elements that have previously been shown to be relatively mobile. Again, there is no evidence of a subduction-related signature. The trace element similarities between the basalts, dolerites and other members of the Aruba Lava Formation strengthens their genetic link, which was inferred from the fieldwork and major element data.

The similarities between the basalts and dolerites and the amphibolites and volcaniclastic rocks extend also to the rare earth elements. Chondrite-normalised ($_{CN}$) REE plots display remarkably flat patterns (Fig. 6.17) at abundances of approximately 10 times chondrite. They are extremely similar to the plots for other localities documented as belonging to the Caribbean plateau, e.g., Curaçao (Kerr *et al.*, 1996b). The data are, however, not identical to the Ontong Java Plateau data – the REE patterns for Ontong Java tend to have greater curvature, with higher $(Sm/Yb)_{CN}$. This is shown in Fig. 6.18, which is analogous to Fig. 6.15 (Note that for *ratios* of REE, bulk silicate earth-normalised values are the same as chondrite-normalised values). A depleted source region has sub-chondritic La/Sm, and slightly sub-chondritic Sm/Yb. Residual garnet in the melting region results in a steepening of the REE patterns (e.g., Fig. 6.17), such that both ratios increase; however, the increase in Sm/Yb is much more extreme. The Aruba data plot between N-MORB and E-MORB, but lie to lower Sm/Yb than the Ontong Java data. This implies either that residual garnet in the source region of the Ontong Java magmas was more important than for the Aruba magmas, or that the Aruba Lava Formation source had lower Sm/Yb; however, the very flat REE patterns observed in Fig. 6.17 suggest that garnet involvement in the petrogenesis of the Aruba Lava Formation was minimal, and this is likely to be the primary control on the differences between this suite and the Ontong Java magmas.

6.7 Melting processes

The trace element and isotopic compositions of the Aruba Lava Formation magmas strongly suggest that they were derived from a mantle plume source. It is, therefore, of interest to consider the melting processes via which these magmas were derived, to see if these too are

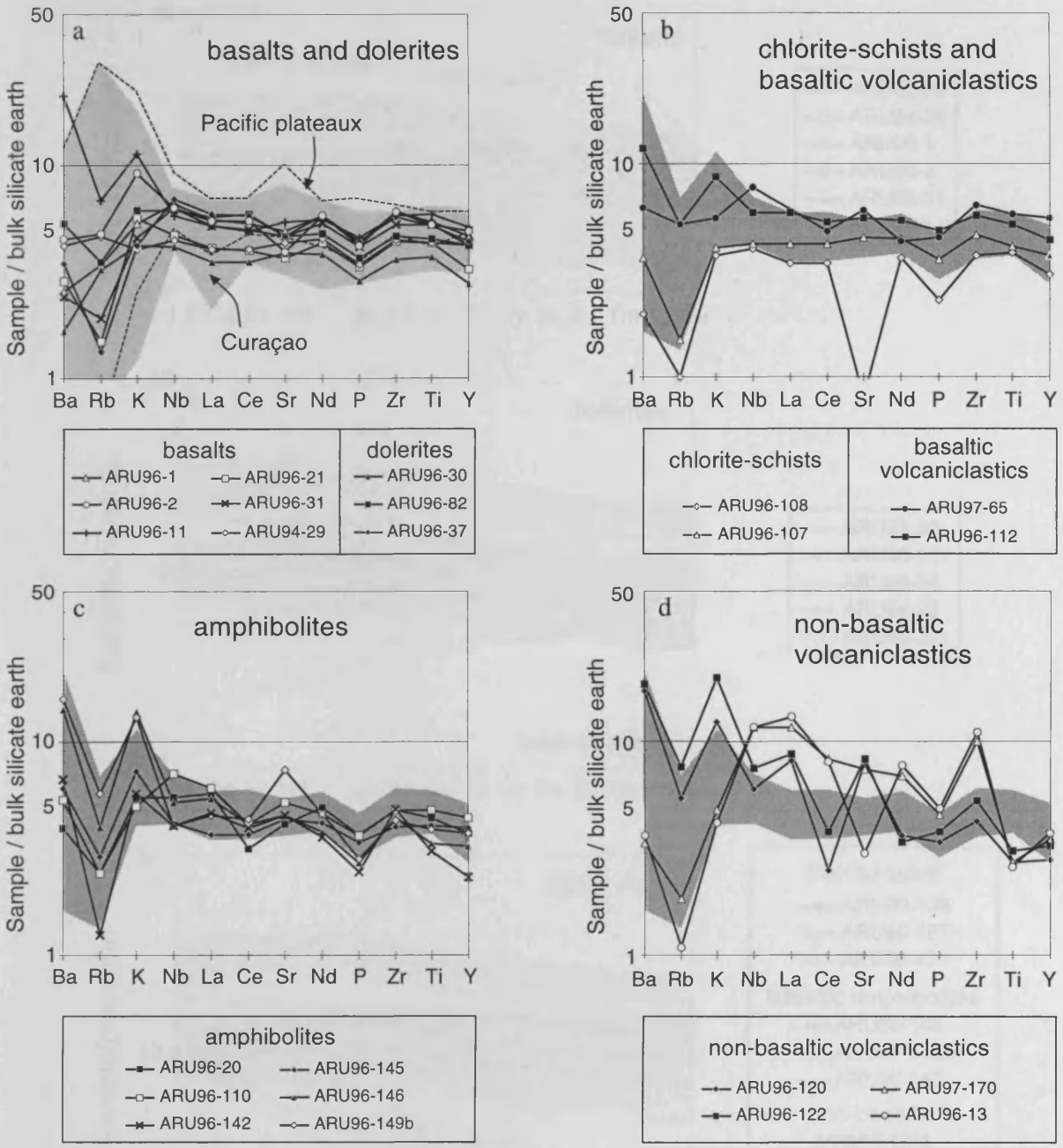

Fig. 6.16: Multi-element diagrams for the Aruba Lava Formation, normalised to bulk silicate earth (McDonough and Sun, 1995). In Fig. 6.16a, Aruba Lava Formation basalts and dolerites are compared to mafic volcanic rocks from Curaçao (grey field) and Pacific oceanic plateau (dashed field); data from Kerr *et al.* (1996b) and references therein. In Figs. 6.16a, b and c, other lithologies of the Aruba Lava Formation are compared with the basalts and dolerites (darker grey fields). For the chlorite schists, basaltic volcaniclastic rocks and amphibolites, almost all analyses fall within the basalt and dolerite field.

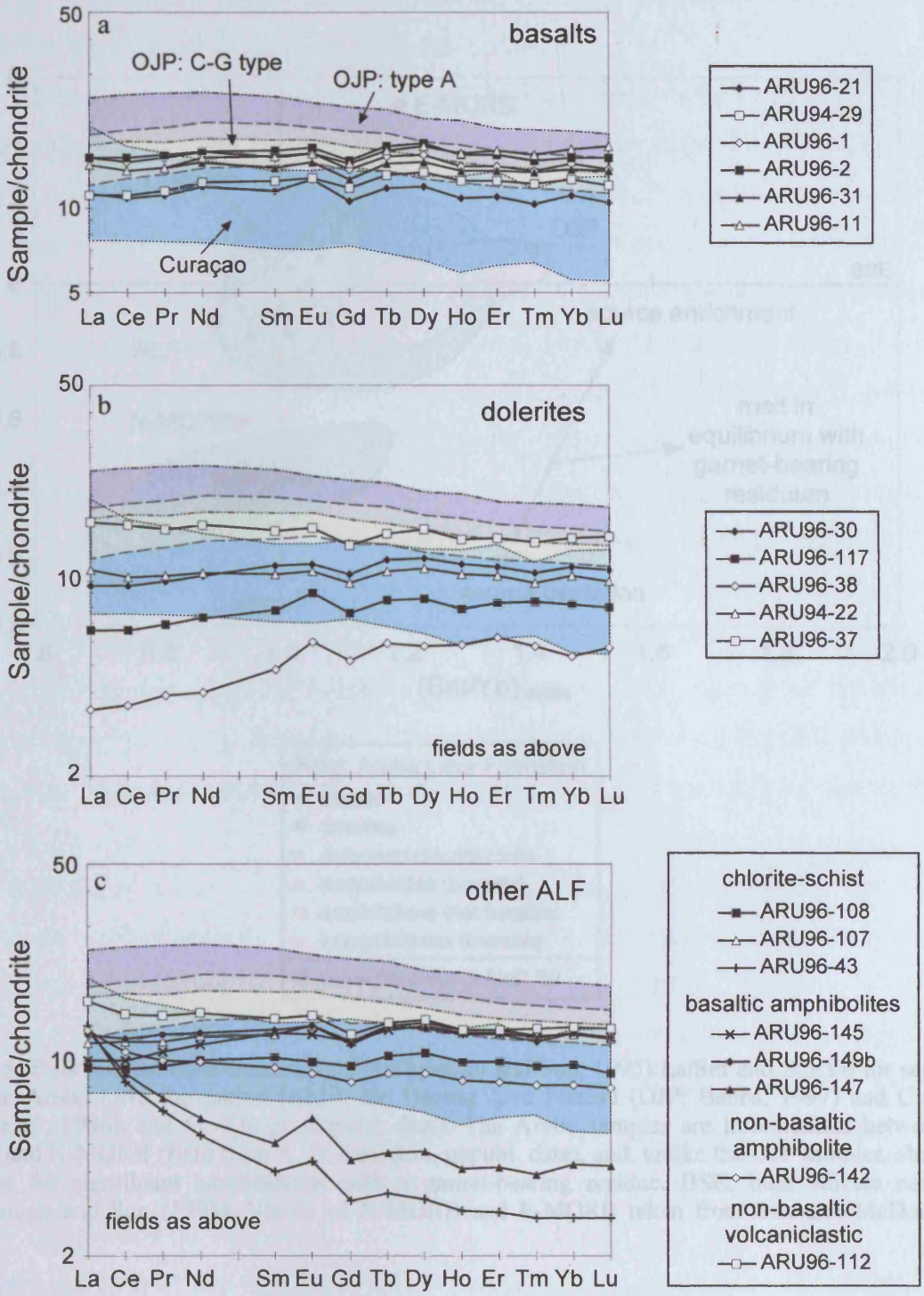

Fig. 6.17: Rare earth element plots for the Aruba Lava Formation, normalised to C1 chondrite (McDonough and Sun, 1995). Fields for Curaçao lavas (Kerr *et al.*, 1996b) and the Ontong Java Plateau (Babbs, 1997) are included for comparison. The Aruba basalts are remarkably homogeneous, and have near-chondritic REE ratios.The dolerites have generally lower REE abundances, consistent with the interpretation of many dolerites representing cumulates. Most "other" Aruba Lava Formation (ALF) samples are similar in composition to the basalts.

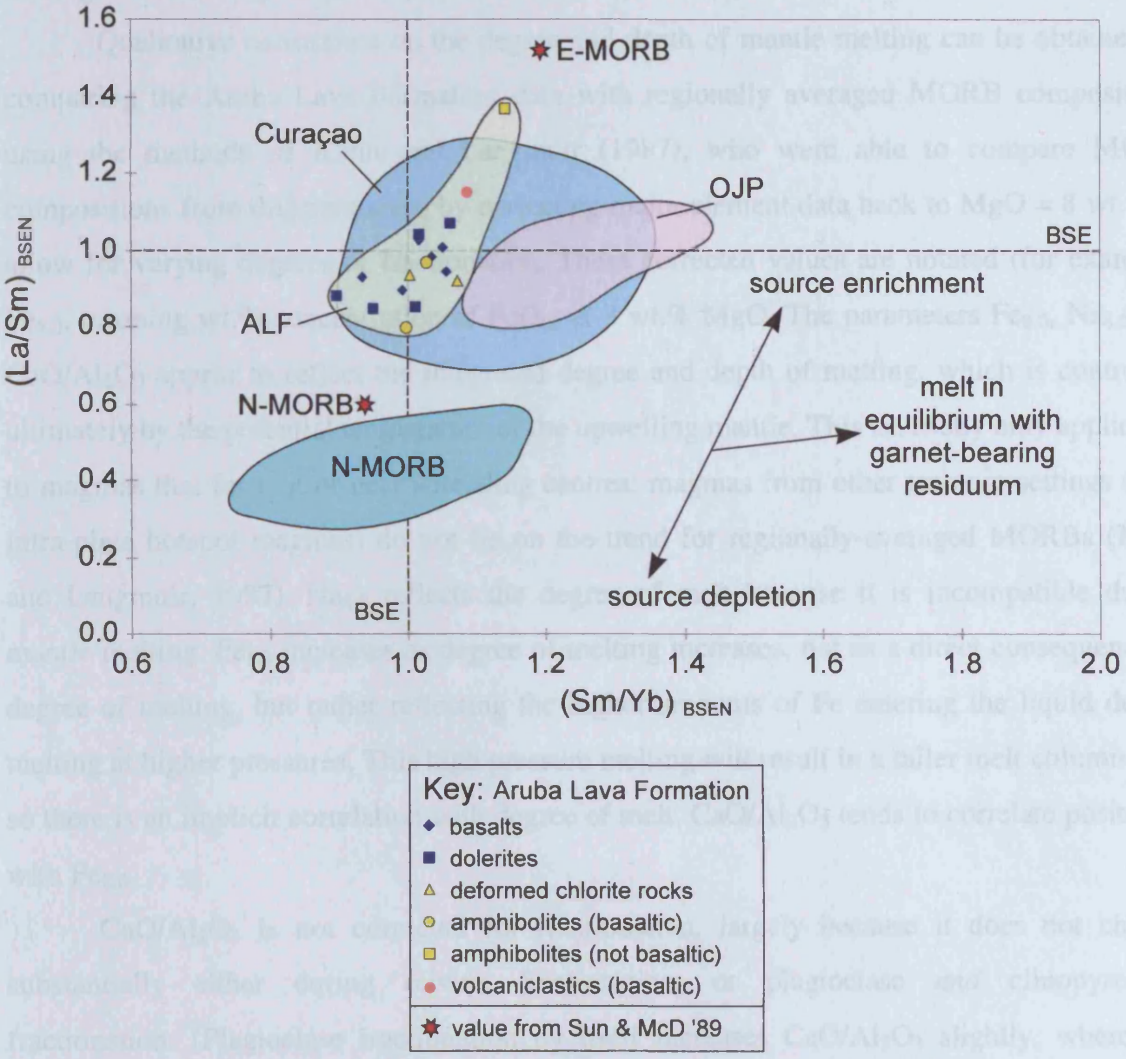

Fig. 6.18: Bulk silicate earth-normalised (McDonough and Sun, 1995) La/Sm and Sm/Yb for samples from the Aruba Lava Formation (ALF), the Ontong Java Plateau (OJP: Babbs, 1997) and Curaçao (Kerr *et al.*, 1996b and G. Klaver, unpubl. data). The Aruba samples are intermediate between E-MORB and N-MORB (field from A. D. Saunders, unpubl. data), and, unlike the OJP samples, show no evidence for significant equilibration with a garnet-bearing residue. BSE: bulk silicate earth of McDonough and Sun (1995). Values of N-MORB and E-MORB taken from Sun and McDonough (1989).

compatible with a mantle plume source. The parameters under consideration are, specifically, the degree of melting and the depth at which this occurred.

Qualitative constraints on the degree and depth of mantle melting can be obtained by comparing the Aruba Lava Formation data with regionally averaged MORB compositions using the methods of Klein and Langmuir (1987), who were able to compare MORB compositions from different areas by correcting major element data back to MgO = 8 wt.% to allow for varying degrees of fractionation. These corrected values are notated (for example) $Fe_{8.0}$, meaning wt.% concentration of $FeO_{(t)}$ at 8 wt.% MgO. The parameters $Fe_{8.0}$, $Na_{8.0}$ and CaO/Al_2O_3 appear to reflect the integrated degree and depth of melting, which is controlled ultimately by the potential temperature of the upwelling mantle. This is strictly only applicable to magmas that form at or near spreading centres: magmas from other tectonic settings (e.g., intra-plate hotspot magmas) do not lie on the trend for regionally-averaged MORBs (Klein and Langmuir, 1987). $Na_{8.0}$ reflects the degree of melt because it is incompatible during mantle melting. $Fe_{8.0}$ increases as degree of melting increases, not as a direct consequence of degree of melting, but rather reflecting the higher amounts of Fe entering the liquid during melting at higher pressures. This high pressure melting will result in a taller melt column, and so there is an implicit correlation with degree of melt. CaO/Al_2O_3 tends to correlate positively with $Fe_{8.0}$.

CaO/Al_2O_3 is not corrected for fractionation, largely because it does not change substantially either during olivine fractionation, or plagioclase *and* clinopyroxene fractionation. (Plagioclase fractionation by itself increases CaO/Al_2O_3 slightly, whereas a decreasing CaO/Al_2O_3 ratio may reflect fractionation at higher pressures where clinopyroxene (without plagioclase) may be a liquidus phase (e.g., Bender *et al.*, 1978).) The TRACE3 modelling for the Aruba lavas (Section 6.5) predicted that plagioclase and clinopyroxene joined the fractionation assemblage at approximately the same time, so having no correction of CaO/Al_2O_3 is valid in this case.

For the Aruba Lava Formation, $Fe_{8.0} \approx 10.6$ wt.%, $Na_{8.0} \approx 2.12$ wt.% and $CaO/Al_2O_3 \approx 0.84$. These data plot within the MORB array of Klein and Langmuir (1987). Fig. 6.19 demonstrates that the Aruba data lie close to the high-degree melting end of the MORB spectrum, close to samples from hotspot-affected ridges such as Iceland, and samples from the Ontong Java Plateau (Mahoney *et al.*, 1993; Babbs, 1997). It must be cautioned, however, that parameters such as $Fe_{8.0}$ and $Na_{8.0}$ cannot always be interpreted directly in terms of pressure and degree of melting, especially when plume-related mantle sources are involved (e.g.,

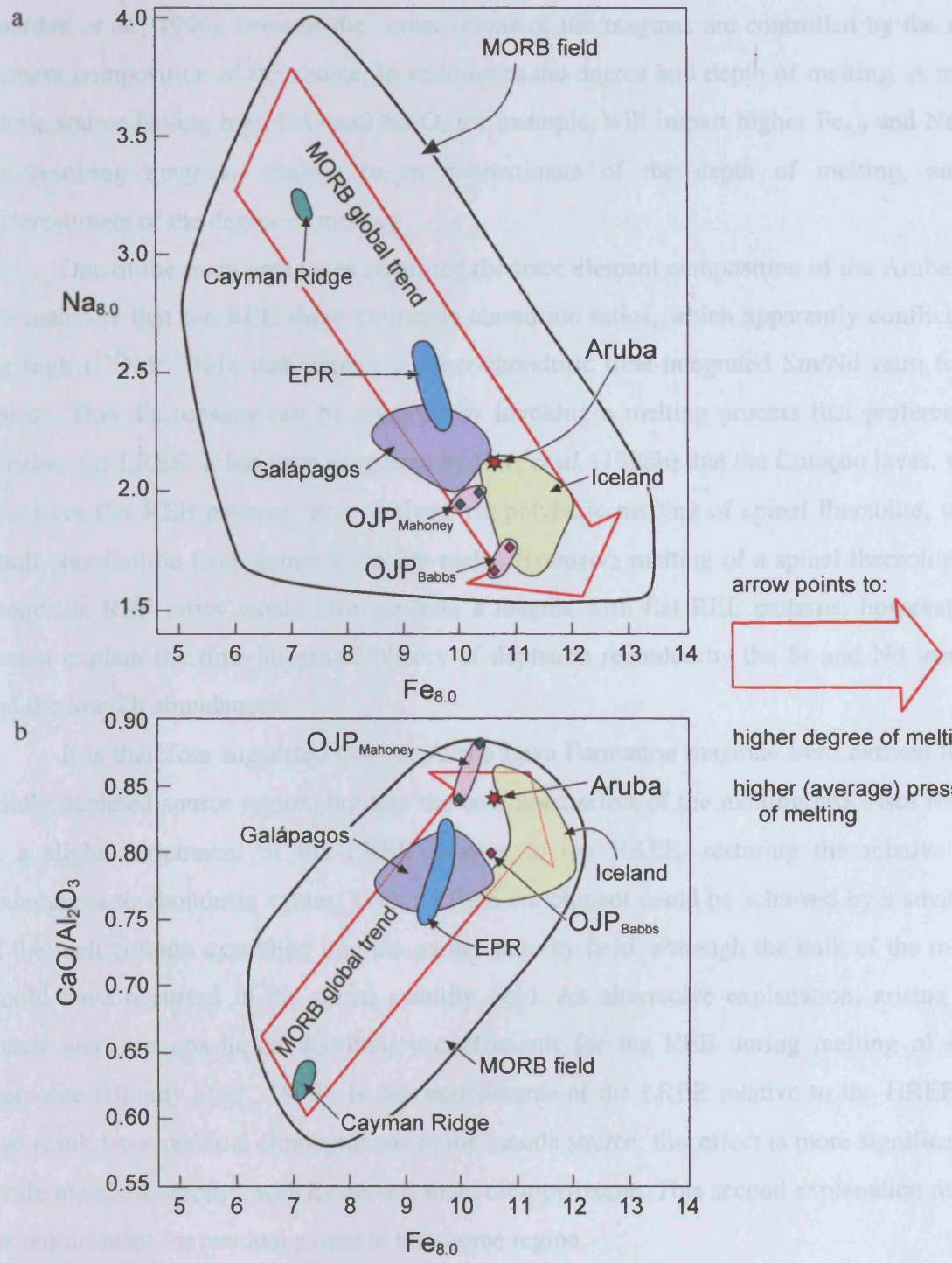

Fig. 6.19a: Average $Na_{8.0}$ vs. average $Fe_{8.0}$ for the Aruba Lava Formation basalts and dolerites, compared with data from a worldwide compilation by Klein and Langmuir (1987) and average values for the Ontong Java Plateau (OJP) by Mahoney *et al.* (1993) and Babbs (1997). The Aruba datum plots towards the high $Fe_{8.0}$ - low $Na_{8.0}$ end of the MORB global trend, reflecting a relatively high degree of melting of the mantle source, similar to the values observed for MORB regions affected by mantle plumes, where the mantle potential temperature is high (e.g., Iceland). Figure adapted from Mahoney *et al.*, 1993; "MORB global trend" arrow points towards higher degree, higher (average) pressure melting.

Fig. 6.19b: Average CaO/Al_2O_3 vs. average $Fe_{8.0}$ for the Aruba Lava Formation basalts and dolerites, showing data from oceanic plateaux and MORB for comparison (references same as above). The average Aruba Lava Formation value again plots close to Iceland and the Ontong Java Plateau.

Bourdon *et al.*, 1996), because the compositions of the magmas are controlled by the major element composition of the source, in addition to the degree and depth of melting. A mantle plume source having high FeO and Na_2O, for example, will impart higher $Fe_{8.0}$ and $Na_{8.0}$ to the resulting magmas, leading to an overestimate of the depth of melting, and an underestimate of the degree of melting.

One of the main paradoxes regarding the trace element composition of the Aruba Lava Formation is that the REE show uniformly chondritic ratios, which apparently conflict with the high $(^{143}Nd/^{144}Nd)_i$ that implies a super-chondritic time-integrated Sm/Nd ratio for the source. This discrepancy can be resolved by invoking a melting process that preferentially enriches the LREE. It has been suggested by Kerr *et al.* (1996b) that the Curaçao lavas, which also have flat REE patterns, were derived via polybaric melting of spinel lherzolite, with a small contribution from garnet lherzolite melts. Extensive melting of a spinel lherzolite with chondritic REE ratios would also generate a magma with flat REE patterns; however, this cannot explain the time-integrated history of depletion recorded by the Sr and Nd isotopes, and the low Th abundances.

It is therefore suggested that the Aruba Lava Formation magmas were derived from a mildly depleted source region, but that the combined effect of the melting processes resulted in a slight enrichment of the LREE relative to the HREE, restoring the relative REE abundances to chondritic values. Such a LREE enrichment could be achieved by a small part of the melt column extending into the garnet stability field, although the bulk of the melting would have occurred in the spinel stability field. An alternative explanation, arising from recent work on cpx-liquid distribution coefficients for the REE during melting of spinel lherzolite (Blundy *et al.*, 1998), is that enrichments of the LREE relative to the HREE may also result from residual clinopyroxene in the mantle source: this effect is more significant for fertile mantle lherzolite, which contains more clinopyroxene. This second explanation reduces the requirement for residual garnet in the source region.

This maximum amount of melting occurring in the garnet stability field can be quantified somewhat by comparison with the results of REE inversion modelling (McKenzie and O'Nions, 1991) carried out for the Ontong Java Plateau (Mahoney *et al.*, 1993). It has already been shown (Fig. 6.19) that the extent of melting to create the Ontong Java magmas is comparable to that which generated the Aruba lavas, according to Klein and Langmuir's (1987) data compilation, and assuming a similar mantle source composition for both provinces. The REE inversion modelling of Mahoney *et al.* (1993) suggests that the degree of

melting of the Ontong Java mantle source is ≈ 28 to 30% (after correction for ≈ 40% olivine fractionation). Of this melting, between ≈ 4% (assuming N-MORB type source) and ≈ 11% (assuming primitive mantle source) occurred within the garnet stability field. The HREE depletion of the Aruba Lava Formation is much less than that of the Ontong Java basalts (Fig. 6.18). Consequently, the amounts of melting in the garnet stability field reported for the Ontong Java Plateau represent the *maximum* estimate of degree of melting in the garnet stability field that generated the Aruba magmas; i.e., the Aruba magmas were produced by 0 - 11% melting of garnet lherzolite, with the remaining ≈ 30 - 19% occurring in the spinel stability field. For a source having depletion intermediate between primitive mantle and N-MORB (as suggested by the isotopic composition of both the Aruba Lava Formation and the Ontong Java Plateau, as well as Figs. 6.12, 6.13, 6.15 and 6.18), a more realistic estimate for the Aruba Lava Formation is 0 - 8% melting of garnet lherzolite, with 22 - 30% melting of spinel lherzolite. The proportion of melting occurring in the garnet stability field for both provinces is further reduced if some of the HREE depletion is a function of clinopyroxene in the source (Blundy *et al.*, 1998).

These estimates have two further consequences. Firstly, if the total degree of melt for the Aruba Lava Formation is similar to that of the Ontong Java Plateau, but a higher proportion of the Aruba Lava Formation source melted in the spinel stability field, this suggests that the melting column beneath Aruba must have extended to shallower levels; i.e., the lithospheric cap above the Aruba melting column was thinner than above the Ontong Java melting column. This implies that the environment of formation of the Aruba Lava Formation was closer to a mid-ocean ridge than the Ontong Java Plateau. The second consequence is that, if the Aruba melting column did extend to shallower levels, but the total degree of melt for both sequences is comparable, then the plume source for the Aruba magmas must have been at a lower potential temperature (or less fertile) than the Ontong Java plume. This latter inference is consistent with the larger volume and crustal thickness reported for the Ontong Java Plateau (Schubert and Sandwell, 1989; Gladczenko *et al.*, 1997).

6.8 Conclusions

- Although the Aruba Lava Formation is variably altered and metamorphosed, a study of the mobility of major and trace elements allows the identification of primary compositional features. For the basalts and dolerites, MgO, Al_2O_3, TiO_2, P_2O_5, Nb, Y, REEs, Th, Cr, Ni and V have not been significantly mobilised during alteration or metamorphism, and these elements can therefore be used to model the petrogenetic history of the suite. The other lithologies have suffered greater elemental mobility. Isotopic mobility becomes important for the deformed or metamorphosed members of the Aruba Lava Formation - they have, in particular, elevated $^{87}Sr/^{86}Sr$.
- The Aruba Lava Formation consists of rocks that are predominantly basaltic in composition. They are sub-alkaline, low-K tholeiites; some are quartz-normative and some are olivine-normative. The basalts and dolerites display a limited range of major and trace element compositions.
- None of the basalts or dolerites satisfies the criteria for being *primary* mantle-derived melts. The most primitive *liquid* composition found during this study has MgO $\approx$ 10.5 wt.% and Mg# $\approx$ 68. More magnesian rocks are present, but these do not necessarily represent liquid compositions, and can be instead explained by olivine accumulation and subsequent chloritisation (chlorite schists) or clinopyroxene accumulation (dolerites).
- The major and trace element compositions of the basaltic amphibolites and volcaniclastic rocks are very similar to those of the basalts and dolerites, demonstrating their consanguineous origin.
- The compositions of the basalts and dolerites appear to be controlled by olivine (+ Cr-spinel) fractionation from a primary mantle melt, followed by low pressure fractionation of olivine + plagioclase, and thereafter olivine + plagioclase + pyroxene. This is consistent with the loci of data points near the low P eutectic in CIPW norm space, the predominance of plagioclase and clinopyroxene in thin section, the geochemical evidence that plagioclase and pyroxene accumulation controls the composition of some of the dolerites, and the results of the TRACE3 modelling. Approximately 30% fractional crystallisation of the most primitive basalt is required to explain the more evolved basalt compositions. These magmas were probably derived from a range of parental liquids, but these must have been compositionally similar to one another.

- Many of the geochemical features of the Aruba Lava Formation strongly suggest that it has oceanic plateau affinities: the basalts are tholeiitic in nature, there is no evidence of a subduction-related signature (e.g., anomalously low Nb abundances), and the ratios of the REE and many other incompatible elements are approximately chondritic, and distinct from N-MORB. For a range of geochemical parameters, the Aruba rocks are intermediate between N-MORB and E-MORB. These features indicate that the melting that generated the Aruba Lava Formation magmas probably occurred in an upwelling mantle plume.
- The mantle plume source region was depleted in nature: $(^{87}Sr/^{86}Sr)_i \approx 0.7032$ to 0.7038; $(\varepsilon_{Nd})_i \approx +6.7$ to +7.9. However, like most other oceanic basalts, the source had been enriched in U relative to Pb over its history: Pb isotope ratios plot to the right of the geochron.
- The depletion in the mantle plume source of the Aruba Lava Formation does not arise from entrainment of depleted upper mantle material (N-MORB source) into the plume. The Zr/Y and Nb/Y ratios fall within the range reported for the Iceland neovolcanic array (Fitton *et al.*, 1997): the Iceland plume is thought to have an *intrinsic* depleted component that is compositionally distinct from the surrounding MORB source.
- The Aruba Lava Formation has many similarities with basalts from the Ontong Java plateau, as well as other Pacific plateaux, although the mantle source region of the Ontong Java Plateau was slightly more depleted in incompatible trace elements than that of the Aruba magmas.
- Comparison of the $Na_{8.0}$, $Fe_{8.0}$ and CaO/Al_2O_3 for the Aruba Lava Formation and the Ontong Java plateau implies that the two suites were derived from similar degrees of partial melting of their mantle source region (about 30%). However, the HREE depletions for the Aruba samples are less prominent, indicating a lower proportion of melting in the garnet stability field than for the Ontong Java samples.
- Many features of the Aruba Lava Formation are consistent with it having erupted in a near-ridge environment. The data plot within Klein and Langmuir's (1987) global array for near-ridge oceanic basalts, and the high degree of melting inferred ($\approx$ 30%), without significant melting occurring in the garnet stability field, is compatible with a melt column that extended to shallow levels, i.e., a near-ridge environment. This location also complies with the field evidence for the Aruba Lava Formation having been erupted in an emergent (i.e., partially subaerial, partially submarine) environment.

- The similar extent of melting inferred for the Aruba and Ontong Java basalts, combined with the deduction that smaller degree of melting occurred in the garnet stability field for the Aruba magmas, can only be reconciled with one another if the Caribbean plume was not as hot as the Ontong Java plume.
- An apparent paradox is created by the conclusion that the Aruba and Ontong Java basalts were derived by similar extents of melting of a mantle source, because of the much larger volume and crustal thickness reported for the Ontong Java Plateau. This paradox can be resolved by the Ontong Java plume being more vigorous, i.e., having more rapid cycling of hot mantle material through the melting region.
- The Aruba Lava Formation shares many geochemical similarities with the Curaçao Lava Formation, for example, ratios of incompatible trace elements, flat chondrite-normalised REE plots and Sr, Nd and Pb isotope ratios. The principal difference between the two suites is the preponderance of high-MgO lavas in the Curaçao succession, which can be explained by the Aruba Lavas being more effectively homogenised and fractionated in sub-surface magma chambers. The cognate nature of the Aruba and Curaçao basalts justifies the assumptions used in Chapter 4 that the two suites may be similar in age, although the fractional crystallisation modelling precludes derivation of the Aruba magmas by simple fractional crystallisation of a single Curaçao parental magma.

Chapter 7

Petrography and Mineral Chemistry of the Aruba Batholith

7.1 Introduction

This chapter describes the petrography and mineral chemistry of the rocks of the Aruba batholith. Studies of thin sections from all the lithological groups have been carried out to provide information on compositional and textural features, and these data are supplemented by electron microprobe analyses (presented in Appendix G). The chapter is organised by lithology; both petrographic features and mineral compositions are discussed concurrently.

The specific aims of this chapter are:

- to identify the crystallising phases in the various batholith lithologies.
- to study textural features of the rocks to determine crystallisation order and any other magmatic or subsolidus processes.
- to determine compositions of the minerals present, and ascertain any relationship between the mineral compositions and bulk compositions for the different lithologies.
- to evaluate the style and degree of alteration of these rocks, in order to assess how alteration may have affected the whole rock geochemistry (Chapter 8).

7.2 Petrography and mineral chemistry discussed by lithology

The lithological groupings used in this chapter will also be used in Chapters 8 and 9. Subdivision of the Aruba batholith into discrete lithological classes is not straightforward, because of the extreme textural variability, even when the bulk rock composition is similar. Additionally, the rock types are transitional to one another. For these reasons, the preferred classification scheme is based on the bulk chemical composition of the rock, as discussed in Section 8.1.1. There are two exceptions to this – the hooibergites and porphyries – because these rocks are texturally distinct from others having the same bulk composition.

Figs. 7.1 to 7.7 display electron microprobe analyses for minerals from rocks of the batholith. Each of these diagrams includes data for the whole range of lithologies; these figures should be referred to throughout Section 7.2.

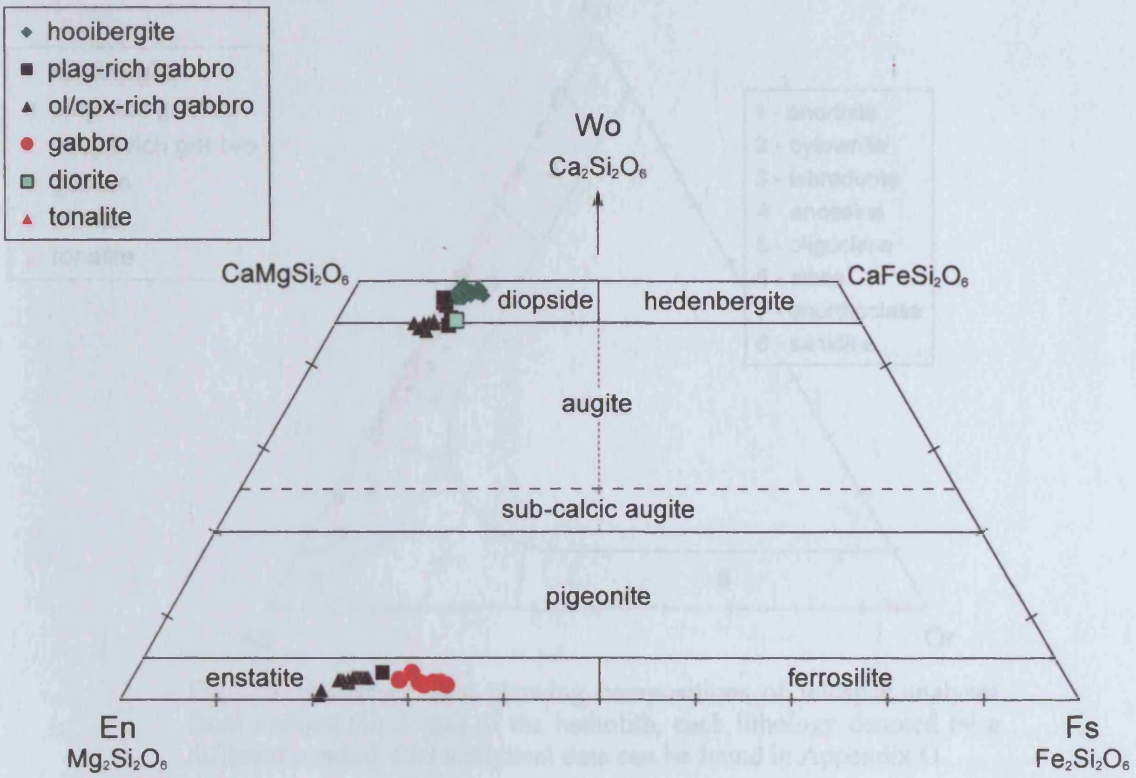

Fig. 7.1: Pyroxene analyses from the Aruba batholith, classified according to Morimoto *et al.* (1988): different symbols represent different lithologies (see key). Both orthopyroxene and clinopyroxene are present in the rocks of the batholith. The orthopyroxene analyses appear to show a trend towards lower Mg as the Mg content of the host rock decreases. No clear trends are apparent in the clinopyroxenes.

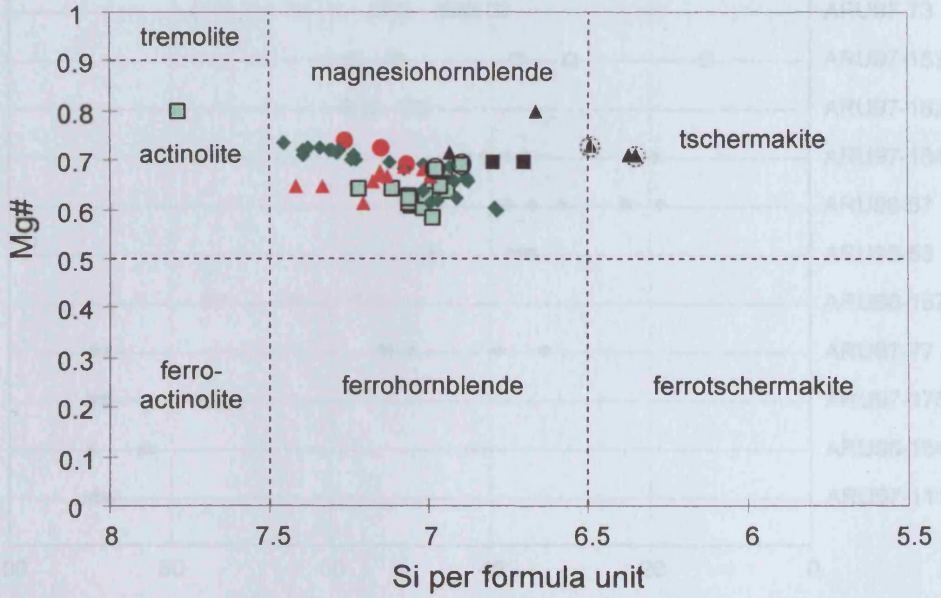

Fig. 7.2: Classification of amphiboles (Leake *et al.*, 1997). The majority of amphiboles analysed for the whole lithological range are magnesiohornblende. This diagram is only applicable for amphiboles with (Na + K) in A sites ≤ 0.5. Ringed samples do not satisfy this criterion: solid rings denote samples that are strictly edenites, and dashed rings are magnesiohastingsite.

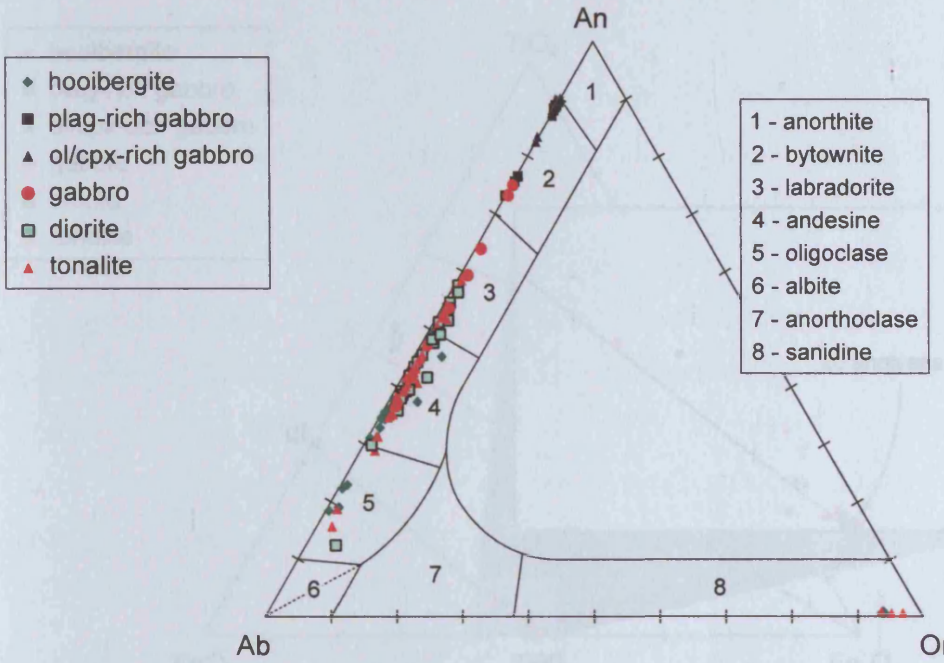

Fig. 7.3: An-Ab-Or plot showing compositions of feldspar analyses from various lithologies of the batholith, each lithology denoted by a different symbol. Full analytical data can be found in Appendix G.

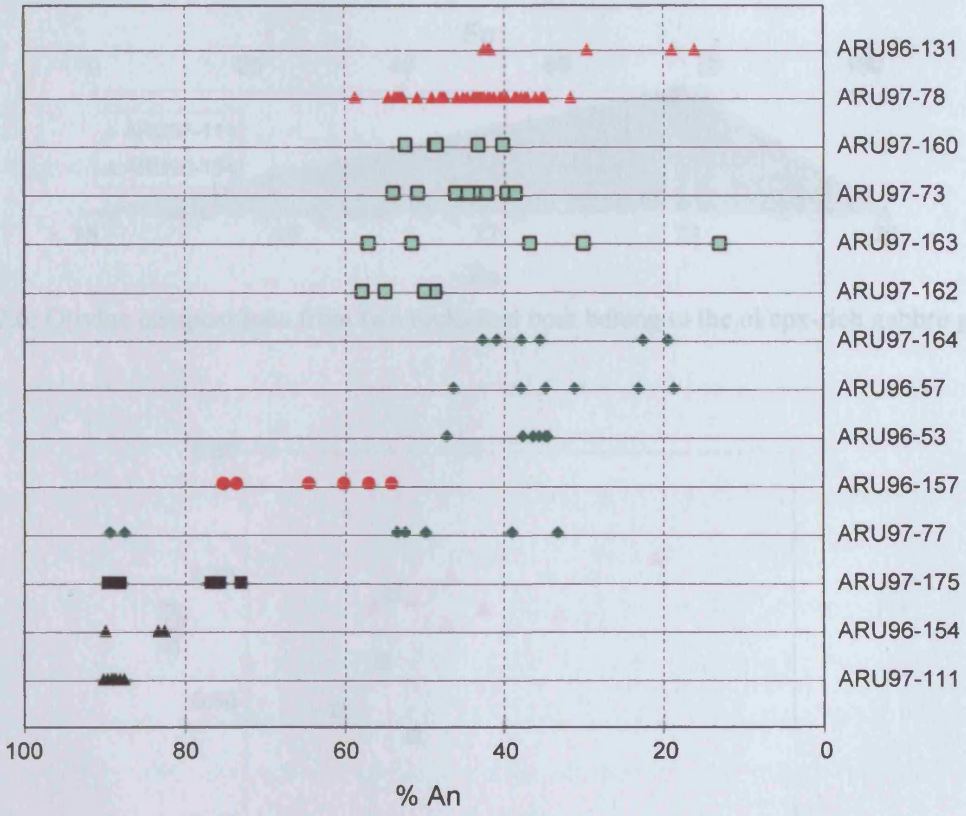

Fig. 7.4: Plagioclase compositions displayed in terms of An mol. percent. Each row of symbols represents a single rock, and the symbol used denotes the lithology. This diagram shows more clearly the variation in feldspar composition observed in a single thin section (or, in the case of ARU97-78, a single crystal). All analyses have less than 2 mol. percent Or.

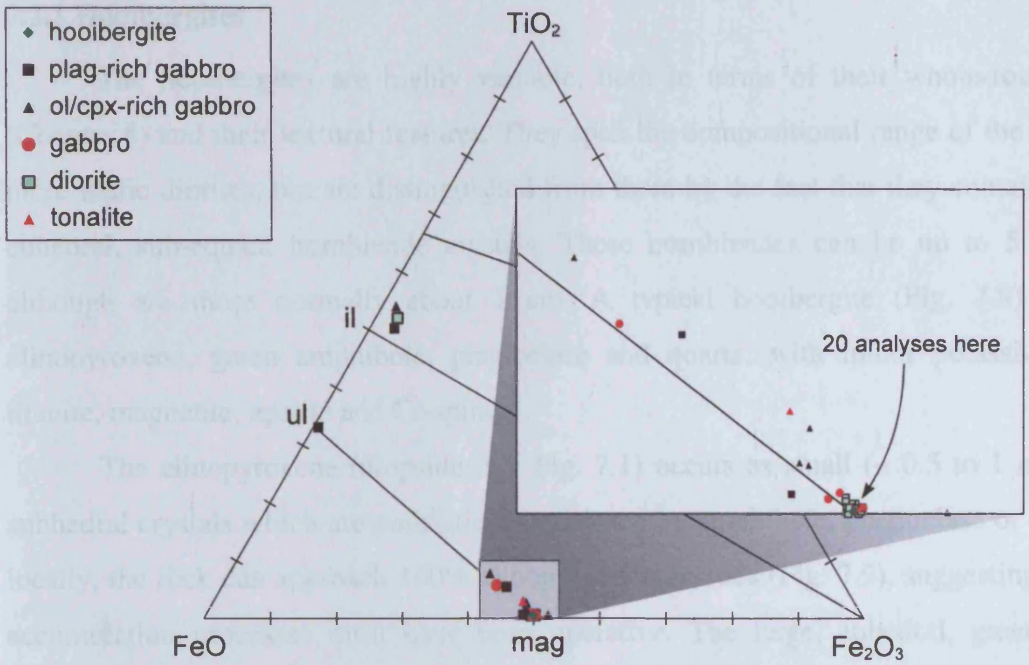

Fig. 7.5: Analyses of opaque minerals: most of the analyses are almost pure magnetite, although some show solid solution towards ulvöspinel. The single pure ulvöspinel analysis is from a bleb within magnetite, and may represent an exsolution feature.

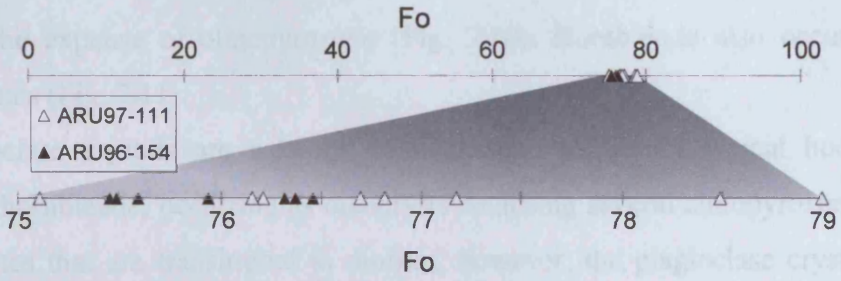

Fig. 7.6: Olivine compositions from two rocks that both belong to the ol/cpx-rich gabbro group.

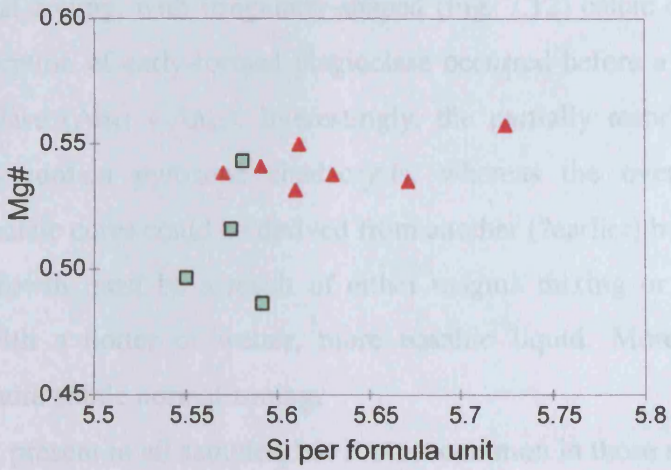

Fig. 7.7: Biotite compositions from diorites and tonalites show a restricted range.

7.2.1 Hooibergites

The hooibergites are highly variable, both in terms of their whole-rock chemistry (Chapter 8) and their textural features. They span the compositional range of the gabbros and more mafic diorites, but are distinguished from them by the fact that they contain ubiquitous euhedral, sub-equant hornblende crystals. These hornblendes can be up to 5 cm in size, although are more normally about 1 cm. A typical hooibergite (Fig. 7.8) consists of clinopyroxene, green amphibole, plagioclase and quartz, with minor potassium feldspar, titanite, magnetite, apatite and Cr-spinel.

The clinopyroxene (diopside: see Fig. 7.1) occurs as small (~ 0.5 to 1 mm), equant, subhedral crystals which are poikilitically enclosed by amphibole, plagioclase or quartz. Very locally, the rock can approach 100% clinopyroxene crystals (Fig. 7.9), suggesting that crystal accumulation processes must have been operative. The large, euhedral, green amphibole crystals that define the hooibergitic texture are magnesiohornblendes (according to the classification of Leake, 1997: Fig. 7.2). Where the hornblende crystals poikilitically enclose clinopyroxene, the latter tend to be smaller and more irregularly shaped than those found in adjacent plagioclase or quartz, suggesting that growth of at least some of the hornblende has occurred at the expense of clinopyroxene (Fig. 7.10). Hornblende also occurs as smaller euhedral crystals (Fig. 7.11).

Plagioclase crystals are anhedral to subhedral, and, in a typical hooibergite, are interstitial to hornblende, occurring as oikocrysts enclosing several clinopyroxene crystals. In the hooibergites that are transitional to diorites, however, the plagioclase crystals are more euhedral, and do not contain clinopyroxene chadacrysts. The plagioclase compositions found in hooibergites are highly variable (Figs. 7.3 and 7.4), ranging from An_{89} to An_{19}. Some have discontinuous normal zoning, with irregularly-shaped (Fig. 7.12) calcic cores (An_{89} - An_{87}), suggesting that resorption of early-formed plagioclase occurred before a phase of growth of more sodic plagioclase (An_{53} - An_{33}). Interestingly, the partially resorbed calcic cores of plagioclase do not contain pyroxene chadacrysts, whereas the overgrowth rims may, suggesting that the calcic cores could be derived from another (?earlier) batch of magma. This resorption and re-growth must be a result of either magma mixing or replenishment of a magma chamber with a hotter or wetter, more basaltic liquid. More usually, however, plagioclase shows more subtle normal zoning.

Quartz is not present in all samples, but is most common in those samples that are also rich in plagioclase. It occurs interstitially to plagioclase and hornblende, and may contain

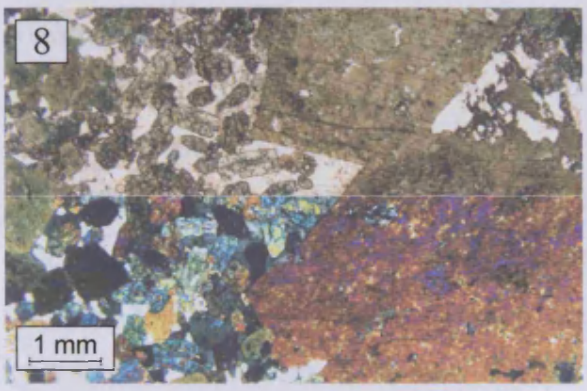

Fig. 7.8: Photomicrograph of a typical hooibergite, showing the large equant magnesiohornblendes, and small diopside crystals poikilitically enclosed by plagioclase (andesine to oligoclase) and quartz. Top half: plane polarised light; bottom half: crossed polars. (ARU96-57)

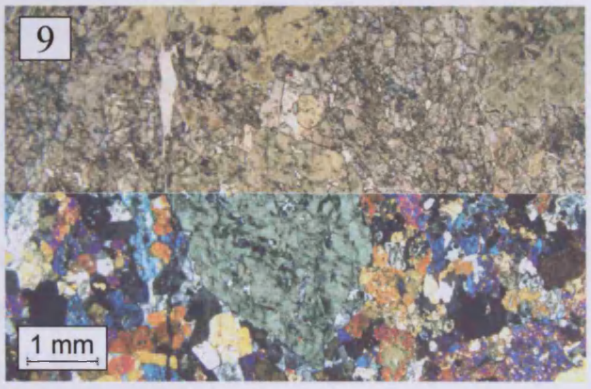

Fig. 7.9: Hooibergite that is extremely rich in diopside, which locally makes up 100% of the rock volume. Top half: plane polarised light; bottom half: crossed polars. (ARU97-133)

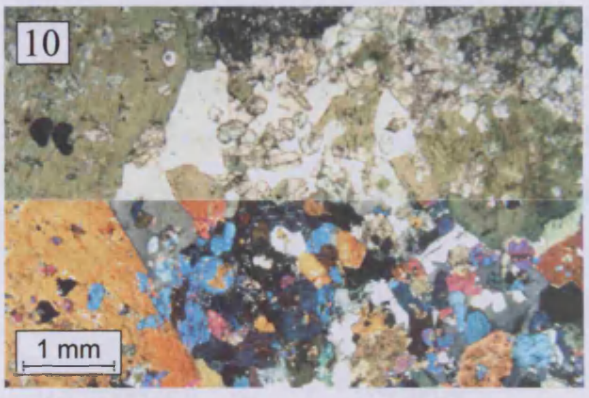

Fig. 7.10: The large magnesiohornblende crystals in this hooibergite contain numerous diopside inclusions, which are smaller and more irregularly shaped than those included by plagioclase (andesine to oligoclase). Top half: plane polarised light; bottom half: crossed polars. (ARU97-164)

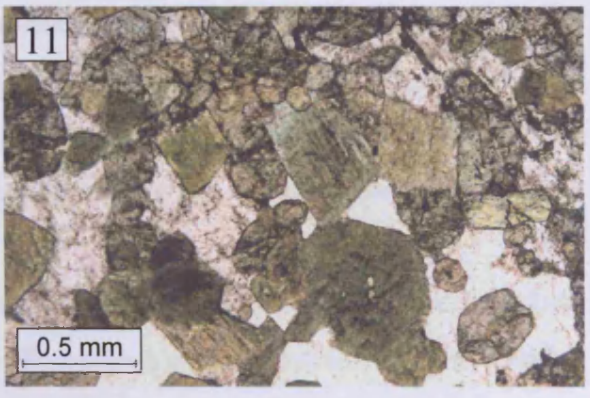

Fig. 7.11: Region of a hooibergite sample that has small euhedral hornblendes enclosed by plagioclase (cloudy white in top half) and quartz (clear white in bottom half). Plane polarised light. (ARU94-4b)

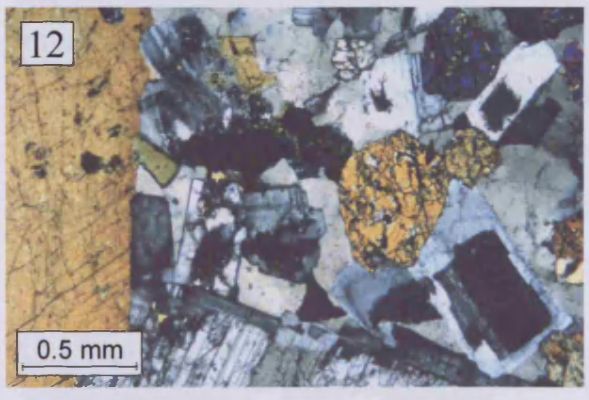

Fig. 7.12: Plagioclase-rich hooibergite where the plagioclase crystals show remarkable heterogeneity, with irregularly-shaped cores (An_{89} to An_{87}) mantled by more sodic rims (An_{53} to An_{33}). Crossed polars. (ARU97-75)

Fig. 7.13: Large corroded(?) hornblende crystal from an acidic vein cutting the hooibergite. This hornblende contains clinopyroxene inclusions, so is unlikely to have nucleated and grown within the silicic magma. See text for a fuller discussion. Plane polarised light. (ARU97-134)

clinopyroxene and/or hornblende chadacrysts. Potassium feldspar occurs as a minor phase, and is also interstitial to plagioclase and hornblende. Accessory phases present are apatite, titanite and opaque minerals.

The textural relationships between minerals demonstrate that clinopyroxene was the first mineral to crystallise, followed by hornblende, then plagioclase, quartz and potassium feldspar. The field relationships demonstrate that at least some of the hornblende growth continued at subsolidus temperatures (see Fig. 3.44, where hornblende concentrations are elevated adjacent to late acidic veins intruding the hooibergite via brittle fractures). However, the thin section studies reveal that formation of the large, euhedral hornblende crystals must have occurred before complete crystallisation of the hooibergite: Fig. 7.13 shows a photomicrograph of a hornblende crystal from a hooibergite that has been disaggregated by an acidic vein before the hooibergite was completely solidified (Fig. 3.43): because the hornblende crystal contains clinopyroxene inclusions, it clearly must have been derived from the adjacent hooibergite, rather than growing *in situ* in the acidic melt. Elsewhere, hornblende does appear to have nucleated and grown in the acidic veins, but this hornblende contains no inclusions, and is acicular in habit.

Rock types occur that are transitional (texturally) to other members of the batholith. Examples include gabbros and biotite-bearing diorites with a subhedral granular texture that is locally overgrown by large (up to 2 cm) equant hornblende crystals. These textures appear to be secondary, and are likely to be either late magmatic, or subsolidus. Another transitional (to diorite) rock type (e.g., ARU97-61) has little or no clinopyroxene, euhedral to subhedral plagioclase, and smaller euhedral hornblende that contains no clinopyroxene inclusions, and appears to be a primary magmatic phase, rather than having partially grown by replacement of or reaction with clinopyroxene.

The hooibergites have suffered small degrees of alteration. Plagioclase may be partially altered to sericite, and clinopyroxene by hornblende. Locally, patches are epidotised, and epidote and chlorite-bearing veins cut the rock.

7.2.2 The layered gabbro series

The layered gabbro series at Wariruri (see Fig. 3.26) is characterised by having modal layering, with some layers rich in plagioclase and others rich in olivine and other ferromagnesian minerals. Although members transitional between these groups also occur, only the two end members are discussed below.

7.2.2.1 Plagioclase-rich gabbroic rocks

This rock type has a subhedral granular texture (Fig. 7.14), dominated by subhedral plagioclase (Figs. 7.3 and 7.4: An_{88} - An_{73}) and anhedral clinopyroxene (Fig. 7.1: predominantly diopsidic). Plagioclase may represent up to ~70% of the rock (by volume) and is usually not zoned, although occasional crystals show normal, continuous zoning. Plagioclase crystals sometimes show alignment. Minor minerals present include anhedral opaque phases (ilmenite, titanomagnetite and magnetite: Fig. 7.5), orthopyroxene ($En_{\sim 71}$: Fig. 7.1), olivine and magnesiohornblende. Locally, hornblende dominates the assemblage, where it occurs as large (~1 cm) oikocrysts, enclosing chadacrysts of predominantly plagioclase, together with some clinopyroxene and opaque minerals (Fig. 7.15). Elsewhere, minor hornblende occurs intimately associated with clinopyroxene, indicating that it may be a secondary alteration product thereof. The large hornblende oikocrysts may also be secondary, late magmatic or subsolidus minerals.

Instead of being altered to hornblende, clinopyroxene may occasionally be altered to pumpellyite. Olivine, where present, is sometimes altered to chlorophaeite, or a vermicular intergrowth of an opaque phase and orthopyroxene (Figs. 7.16 and 7.17), or has a rim rich in opaque phases.

The inclusion of occasional clinopyroxene crystals within plagioclase enables the construction of a crystallisation sequence:

$$\text{cpx} + \text{opaques} \Rightarrow \text{cpx} + \text{plag} + \text{opaques} \Rightarrow \text{hbl}.$$

It is not known where olivine and orthopyroxene fall within this sequence, because they are volumetrically minor, and unequivocal crystallisation order indicators are not abundant enough for firm conclusions to be drawn.

7.2.2.2 Olivine- and pyroxene-rich gabbroic rocks

Some rocks of the Wariruri layered gabbro sequence are extremely rich in ferromagnesian minerals (up to ~80%): predominantly olivine, clinopyroxene and orthopyroxene. Different textural varieties occur: some are subhedral- to anhedral granular in texture, whereas others have a poikilitic texture. These two varieties may occur within a single thin section. Proportions of the different phases may differ markedly between samples, and even within the same sample.

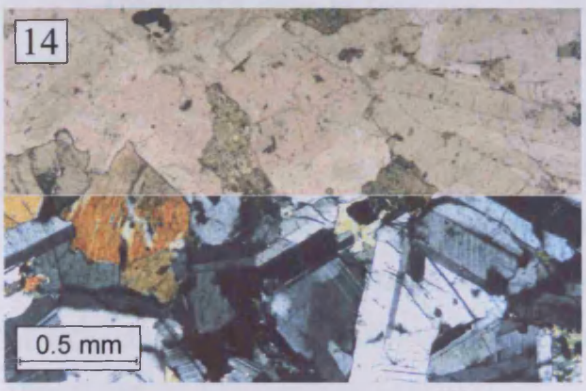

Fig. 7.14: Bytownite-rich gabbro from the layered series. Clinopyroxene (diopside to augite) is the other major phase present. Top half: plane polarised light; bottom half: crossed polars. (ARU97-173)

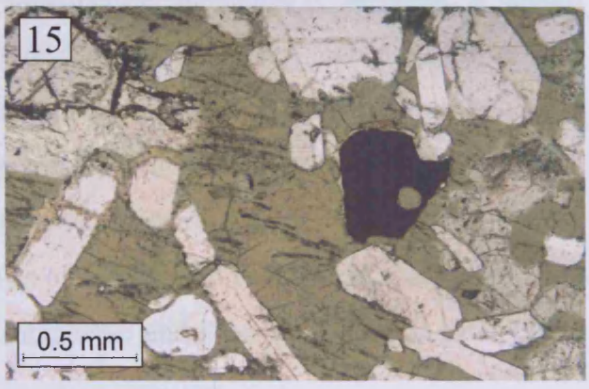

Fig. 7.15: Hornblende oikocryst enclosing plagioclase, clinopyroxene and opaque chadacrysts. This may be a late magmatic or subsolidus texture. Plane polarised light. (ARU97-174)

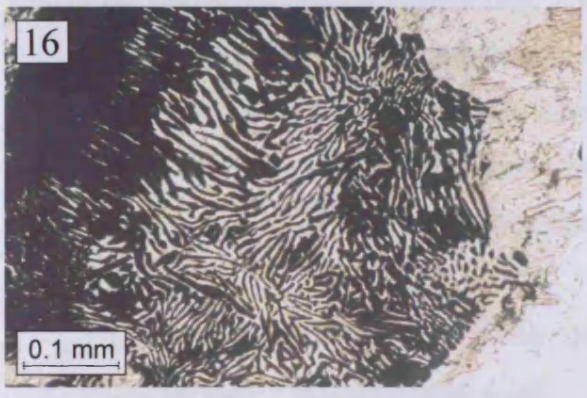

Fig. 7.16: Vermicular intergrowth of an opaque mineral and orthopyroxene, probably arising from replacement of olivine (see Fig. 7.17). Plane polarised light. (ARU97-173)

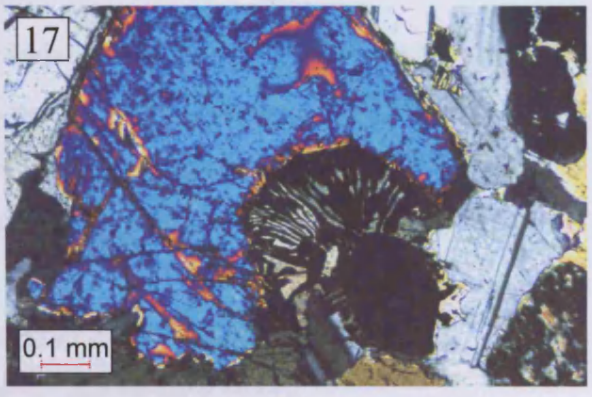

Fig. 7.17: Vermicular intergrowth of an opaque mineral and orthopyroxene, which appears to have nucleated on the opaque mineral crystal, and grown outwards into the olivine crystal. Crossed polars. (ARU97-111)

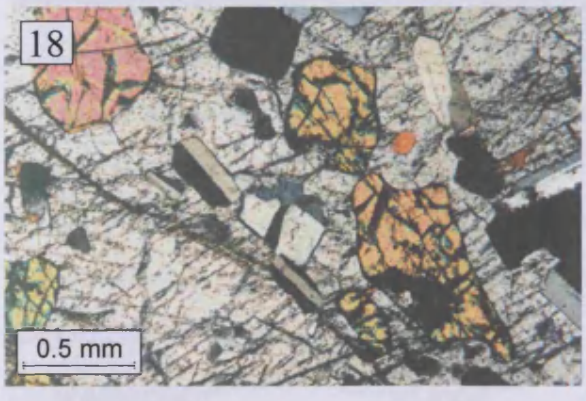

Fig. 7.18: Enstatite oikocryst enclosing chadacrysts of olivine (Fo_{79} to Fo_{75}), plagioclase (bytownite), augite and magnetite/ilmenite. Crossed polars. (ARU97-111)

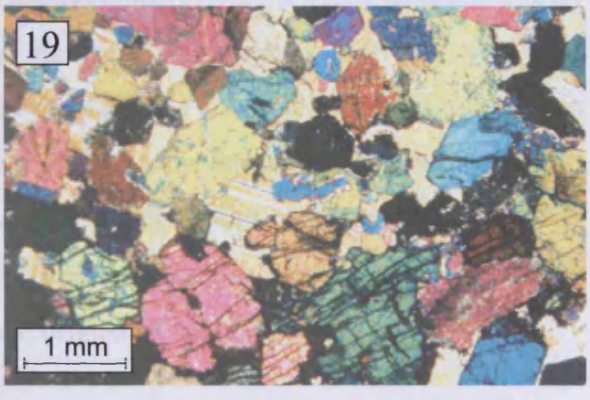

Fig. 7.19: Bytownite oikocryst enclosing chadacrysts of olivine ($Fo_{\sim 76}$) and augite. This section is slightly thick, giving the twinned plagioclase a yellow colour in crossed polars. (ARU96-154)

The olivine (Fo_{79} to Fo_{75}: Fig. 7.6) may be euhedral, subhedral or anhedral, is equant or slightly elongate, and can be up to 3 mm in size. Clinopyroxene crystals (diopside or Mg-rich augite: Fig. 7.1) are euhedral to subhedral, sometimes twinned, and up to 5 mm in length, although some are small and equant. The orthopyroxene (En_{79} to En_{73}: Fig. 7.1) shows pink pleochroism, and is subhedral to anhedral in the granular textured gabbros. In some of the poikilitic rocks, however, orthopyroxene occurs as oikocrysts (up to 6 mm in size) containing olivine, clinopyroxene, plagioclase and opaque (magnetite and ilmenite: Fig. 7.5) chadacrysts (Fig. 7.18).

Plagioclase (An_{90} to An_{83}: Figs. 7.3 and 7.4) is generally anhedral, and interstitial to olivine and pyroxene (with the exception mentioned above where it occurs as chadacrysts in orthopyroxene). It is not usually zoned. Occasionally, plagioclase occurs as oikocrysts containing olivine and clinopyroxene (Fig. 7.19).

Green-brown amphibole, which may be twinned, surrounds all the other phases, and occurs either as oikocrysts, or intimately associated with clinopyroxene as alteration rims. It is, therefore, either late magmatic, or subsolidus in origin. The amphibole in this lithology is variable in composition, with magnesiohornblende, magnesiohastingsite and tschermakite all being present.

The crystallisation sequence for this rock type can be summarised as follows:

$$ol + opq \Rightarrow ol + opq + cpx \Rightarrow opx \Rightarrow plag \Rightarrow hbl$$

although in some samples, plagioclase commences crystallisation before orthopyroxene, i.e.,

$$ol + opq \Rightarrow ol + opq + cpx \Rightarrow plag \Rightarrow opx \Rightarrow hbl$$

Most of the samples of this rock type are not heavily altered, and preserve original mineralogical and textural features. Pumpellyite and prehnite, or brown-green amphibole, may be associated with the pyroxenes. The olivine varies between relatively fresh, with only iddingsite alteration along cracks, to being partially replaced by a vermicular intergrowth of an opaque phase and orthopyroxene (Figs. 7.16 and 7.17). In the most altered samples of this category, the rock may consist almost entirely of hornblende and clinopyroxene: although these rocks have petrographic affinities with the hooibergites, the chemical composition is MgO-rich (see Chapter 8), and the rocks may have originally contained olivine.

7.2.3 Gabbros

In Section 8.1.1, the gabbro classification is defined according to chemical composition (> 6% MgO at < 55% SiO_2). Not all rocks that fall into the chemical classification are gabbro *sensu stricto*, i.e., containing clinopyroxene and plagioclase ($An_{>50}$);

some are gabbronorites, and some are meladiorites (petrography of this latter group is discussed together with the diorites). The gabbros discussed in this section (predominantly from the Matividiri massif) are distinguished from those in the previous section by their lack of any obvious magmatic layering; additionally, some samples are microgabbros.

The gabbros consist of clinopyroxene, orthopyroxene, plagioclase and opaque minerals, with minor green amphibole (probably secondary: see below), and occasionally, quartz and/or biotite (Fig. 7.20). The texture is subhedral granular, and there is a macroscopic modal layering, defined by changes in the relative abundances of plagioclase and the ferromagnesian minerals.

The clinopyroxene (augite) is up to 3 mm in size, sometimes twinned, and subhedral. In some samples, green amphibole occurs as coronas around the clinopyroxene. Subhedral orthopyroxene crystals (En_{65} - En_{70}: Fig. 7.1) are also up to 3 mm and subhedral. The plagioclase crystals (Figs. 7.3 and 7.4) are up to 4 mm in length, subhedral, and often zoned on a very fine scale. Opaque minerals (Fig. 7.5) occur as small (< 0.5 mm), anhedral inclusions in clinopyroxene or orthopyroxene, or are associated with pyroxene-rich patches. Quartz, where present, is interstitial to the plagioclase; biotite occurs only rarely.

The order of crystallisation is deduced as follows:

$$opq \Rightarrow opq + cpx + opx + plag \Rightarrow qtz \Rightarrow hbl$$

i.e., clinopyroxene, orthopyroxene and plagioclase are on the liquidus together for most of the crystallisation interval; quartz crystallises late in interstices, and hornblende is a secondary alteration product.

The orthopyroxene is the most altered mineral in this rock type, being often almost completely replaced by brown cryptocrystalline clay minerals. Clinopyroxene has suffered minor alteration to green amphibole (in addition to the coronas mentioned in the previous paragraph). The plagioclase is occasionally sericitised, and epidote may be present in the rock.

7.2.4 Diorites

The diorites of the Aruba batholith are extremely variable. There are (at least) three texturally distinct varieties:

1) diorites with textural affinities with hooibergites
2) diorites similar in texture to the tonalites
3) fine-grained diorites

The diorites that fall into category 1 above (Fig. 7.21) contain small, equant, subhedral clinopyroxene (diopside or Mg-rich augite) and large, equant, euhedral green amphibole,

which is occasionally twinned, and may poikilitically enclose the clinopyroxene. The amphibole present is predominantly magnesiohornblende (Fig. 7.2), but edenite and actinolite were also analysed. Plagioclase (An_{58} to An_{30}: Figs. 7.3 and 7.4) in these rocks can be very large (up to 8 mm), and is euhedral to subhedral. It may have calcic cores that are irregular in shape and appear to have been resorbed, then continued growing. Plagioclase may also poikilitically enclose clinopyroxene. Quartz is a minor constituent of this rock type, and poikilitically encloses clinopyroxene, hornblende and plagioclase. Other minor phases include opaque minerals and apatite. The crystallisation sequence for this lithology is:

$$cpx \Rightarrow hbl + plag \Rightarrow qtz.$$

The second group of diorites (Fig. 7.22) have a subhedral granular texture, with a crystal size of approximately 4 mm being common. The plagioclase (An_{42} to An_{16}: Figs. 7.3 and 7.4) is euhedral to subhedral, and up to 5 mm in size. The largest crystals, in particular, often have complex oscillatory zoning with resorbed horizons; these oscillatory zones are superimposed on a pattern of zoning that is normal. Anhedral magnetite (Fig. 7.5) can be abundant, and is spatially associated with ferromagnesian minerals, which include clinopyroxene and hornblende (and occasionally biotite). Some samples contain all three ferromagnesian phases, but most just contain two of the three. The amphibole (magnesiohornblende: Fig. 7.2) forms euhedral to subhedral elongate crystals, and is frequently twinned. Occasionally, it occurs in patches with a small crystal size: the patches appear to pseudomorph the diamond-shaped cross sections of pre-existing euhedral hornblende crystals. Clinopyroxene (Fig. 7.1), where present, either occurs within large hornblende crystals, or has a hornblende corona. This suggests either that the clinopyroxene became unstable within an evolving melt, or that the clinopyroxene is xenocrystic. Additionally, clinopyroxene is locally altered to an aggregate of green amphibole. Biotite (Fig. 7.7), where present, is a minor phase, and is locally altered to chlorite. Quartz and potassium feldspar are also minor phases, are anhedral, and interstitial to the plagioclase. Titanite and apatite are present as accessory minerals. The crystallisation sequence deduced for this lithology is:

$$opq\ (+ cpx) \Rightarrow hbl \Rightarrow plag \Rightarrow (bi) \Rightarrow (qtz)$$

The fine-grained diorites are found within the batholith either as enclaves, or as thin dykes cutting the tonalite of the batholith, or as minor constituents of hooibergitic massifs. Most have an equigranular texture (subhedral granular) with an average crystal size of ~0.5 to 1 mm, and the dominant minerals are amphibole, plagioclase and quartz. The amphibole

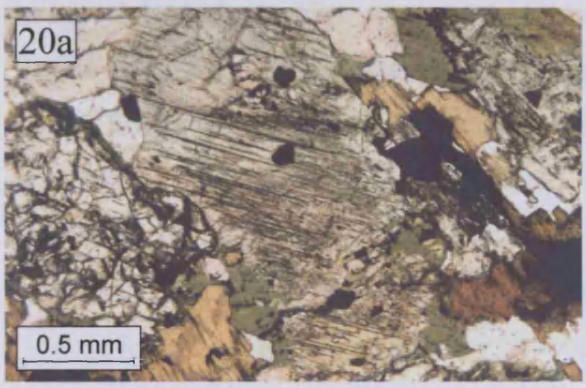

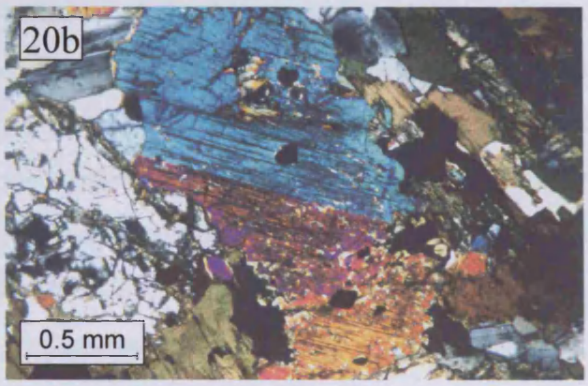

Fig. 7.20: Typical gabbro from the layered series. This photomicrograph shows twinned clinopyroxene, orthopyroxene, amphibole (at edges of clinopyroxene), biotite and plagioclase, with minor quartz and opaque minerals (a: plane polarised light; b: crossed polars). (ARU97-172)

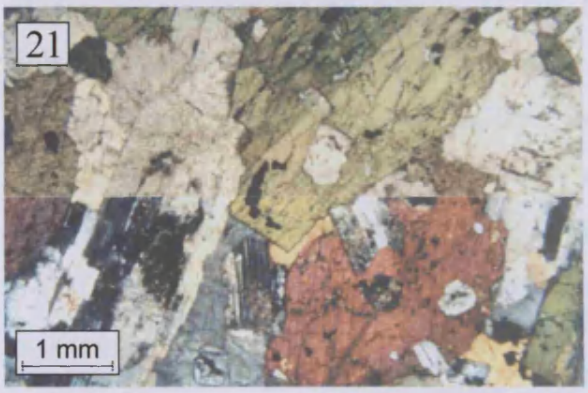

Fig. 7.21: A diorite having textural similarities with the hooibergites, in particular, the large equant euhedral magnesiohornblende crystals, which may contain clinopyroxene inclusions. Top half: plane polarised light; bottom half: crossed polars. (ARU97-163)

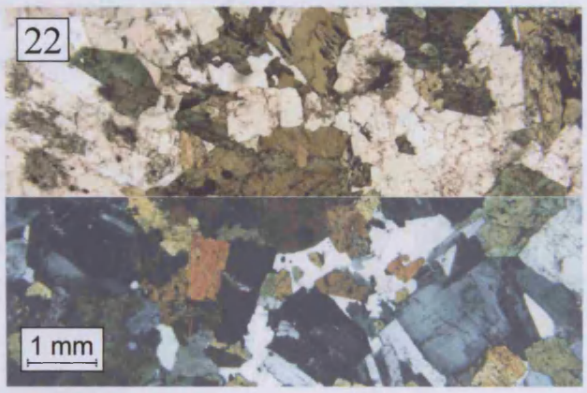

Fig. 7.22: Diorite that is texturally similar to the tonalites. Magnesiohornblende crystals are smaller and more elongate than those in the hooibergites, but still euhedral. Biotite is present, and plagioclase (labradorite to andesine) is frequently twinned. Top half: plane polarised light; bottom half: crossed polars. (ARU97-161)

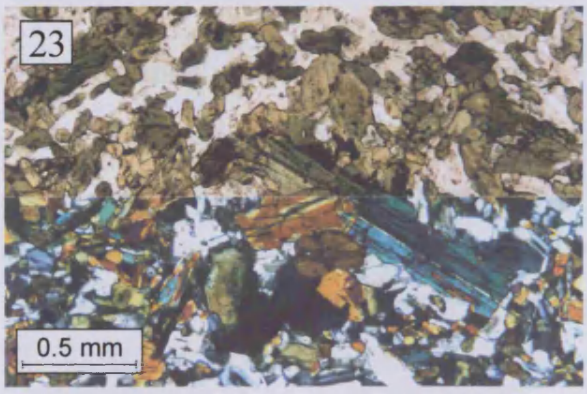

Fig. 7.23: Porphyritic microdiorite from an enclave within the tonalite. The large hornblende crystals may be twinned. Top half: plane polarised light; bottom half: crossed polars. (ARU97-74)

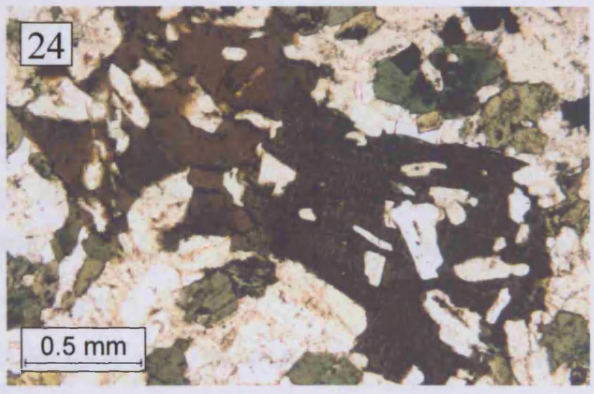

Fig. 7.24: Microdiorite (from enclave within tonalite) containing biotite oikocrysts surrounding plagioclase chadacrysts. Plane polarised light. (ARU97-54a)

(magnesiohornblende: Fig. 7.2) is euhedral to subhedral, and sub-equant. It sometimes shows simple twinning. The plagioclase (An_{54} - An_{38}: Figs. 7.3 and 7.4) is subhedral, and often zoned. Where anhedral plagioclase occurs, it is interstitial to the hornblende. Quartz occurs as anhedral, equant, grains that are interstitial to the hornblende and plagioclase; occasionally quartz oikocrysts contain hornblende. Anhedral opaque minerals (including ilmenite) and apatite occur as minor phases, as does subhedral biotite (often partially altered to chlorite).

Not all of the microdiorites have an equigranular texture: some are porphyritic, particularly those found as enclaves within the tonalite (Fig. 7.23). Hornblende phenocrysts (sometimes twinned) or glomerocrysts are found in a matrix of: elongate euhedral hornblende; subhedral plagioclase; and anhedral quartz and opaque minerals. Sometimes, zoned plagioclase phenocrysts may also be present. Occasionally, these microdiorites have a pseudo-doleritic texture, with plagioclase chadacrysts sub-ophitically enclosed by hornblende. Biotite, where present, sometimes occurs as oikocrysts around small plagioclase chadacrysts (Fig. 7.24). Although the groundmass is usually microcrystalline, the presence of spherulites in some samples suggest that the groundmass may have originally been glassy.

The crystallisation order for both the porphyritic and the equigranular fine-grained diorites is:

$$opq + hbl \Rightarrow hbl + plag \Rightarrow bi \Rightarrow qtz.$$

The diorites have generally suffered only minor alteration. Where clinopyroxene is present, it has been altered to hornblende along cracks. Plagioclase is sometimes altered to sericite, particularly in the calcic cores. Biotite is often partially altered to chlorite, and in extreme cases, may be completely replaced by chlorite and epidote.

7.2.5 Tonalites

The tonalites typically have a subhedral granular or granular texture (Fig. 7.25), and show considerably less textural variation than the diorites. They consist of plagioclase, hornblende, quartz and magnetite, with subhedral biotite (Fig. 7.7) present in most (but not all) samples, and apatite and titanite as accessory phases.

The subhedral plagioclase crystals are up to 4 mm in size, and frequently show complex zoning (An_{58} to An_{31}: Figs. 7.3, 7.4, 7.26 and 7.27). A few samples appear to have mixed populations of plagioclase: some crystals with intricate zoning, and some with none. Magnesiohornblende (Fig. 7.2) occurs as elongate euhedral to subhedral crystals, and is often twinned. Less frequently, the hornblende is anhedral. Magnetite (Fig. 7.5) tends to be spatially

associated with the hornblende, although not exclusively. The anhedral quartz is interstitial to the plagioclase, as is minor potassium feldspar.

The crystallisation sequence deduced is:

$$opq + hbl + plag \Rightarrow (bi) \Rightarrow qtz + kfsp$$

The tonalites show small degrees of alteration. Plagioclase may be slightly sericitised, and biotite often shows small degrees of chloritisation. Veins of epidote, chlorite and quartz may cut the tonalite.

7.2.6 Leucotonalites

The leucotonalites (Fig. 7.28) have a granular texture and are usually not as coarse-grained as the tonalites and diorites, having an average grain size of approximately 1 mm. They are dominated by plagioclase and quartz, with volumetrically minor biotite, potassium feldspar and opaque minerals.

7.2.7 Granites

The granites are texturally similar to the leucotonalites: they are generally relatively fine grained (0.5 to 1 mm) and have a granular texture. They consist of plagioclase, quartz and potassium feldspar, with small amounts of opaque minerals and biotite. Zircon and apatite are present as accessory minerals. Occasionally, the granites may contain some larger, zoned, plagioclase crystals.

7.2.8 Leucocratic veins

The leucocratic veins generally have a granular, fine-grained texture (0.5 to 1 mm), and consist of plagioclase, quartz and potassium feldspar, in varying proportions. Locally, they have a granophyric texture, with intergrowths of quartz and potassium feldspar (Fig. 7.29), or quartz and plagioclase (Fig. 7.30). These rocks contain no ferromagnesian minerals. One unusual sample (ARU97-118) appears to consist entirely of calcic plagioclase feldspar. Additionally, coarser grained pegmatitic veins occur: these tend to be very rich in quartz.

7.2.9 Porphyritic rocks

The porphyritic rocks belonging to the batholith occur as dykes within the Aruba Lava Formation or sheets within the batholith, as well as occurring as tonalite-hosted enclaves in the batholith. They are chemically equivalent to the diorites and tonalites (see Chapter 8),

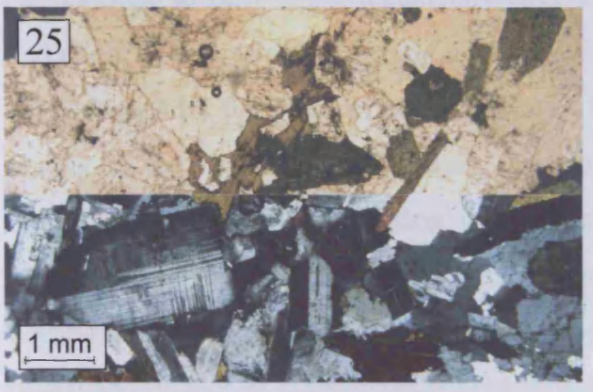

Fig. 7.25: Photomicrograph of a representative tonalite from the batholith. This example contains magnesiohornblende and biotite in addition to plagioclase, quartz and magnetite. Top half: plane polarised light; bottom half: crossed polars. (ARU96-59)

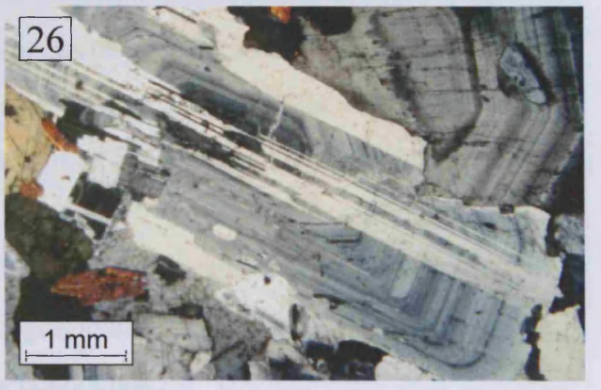

Fig. 7.26: Part of a large plagioclase crystal (the whole crystal is approximately 7 mm in length) from a tonalite, showing intricate zoning (An_{58} to An_{31}). Results of an electron microprobe traverse across this crystal are displayed in Fig. 7.39. Crossed polars. (ARU97-78)

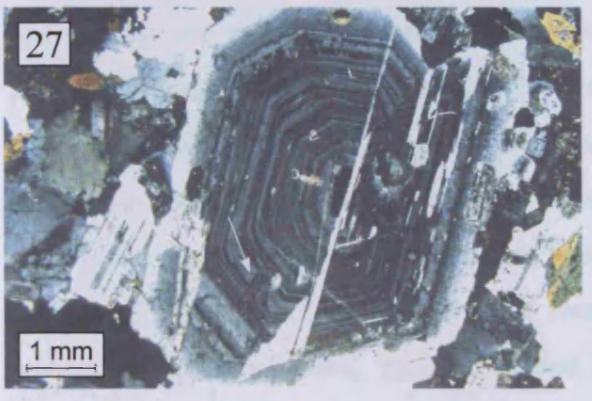

Fig. 7.27: A complexly zoned plagioclase from a tonalite. This crystal has been partially resorbed during its growth (for example, see arrow). Crossed polars. (ARU94-18)

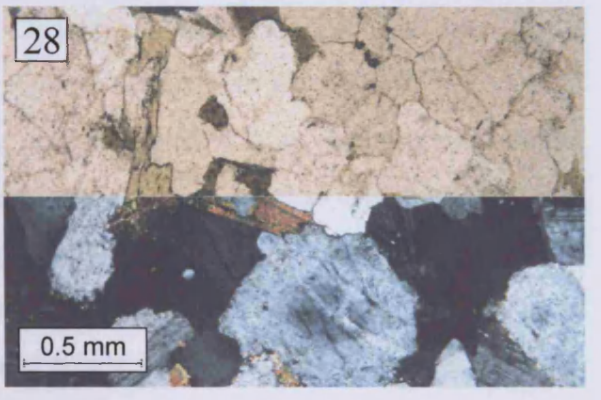

Fig. 7.28: A representative leucotonalite, with a granular texture. These differ from the tonalites in having more quartz and less ferromagnesian minerals, in some cases, none. Top half: plane polarised light; bottom half: crossed polars. (ARU94-15)

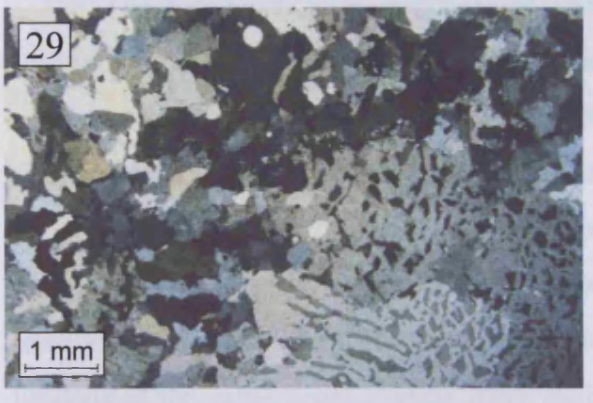

Fig. 7.29: Aplite, consisting of quartz, plagioclase and potassium feldspar. The granophyric intergrowth at the bottom right has quartz blebs in potassium feldspar. Crossed polars. (ARU96-41)

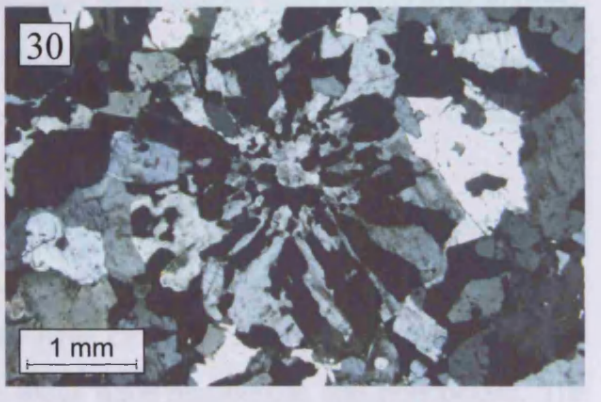

Fig. 7.30: This aplite has a radial granophyric growth of quartz and plagioclase. Crossed polars. (ARU97-51)

having 53% to 68% SiO_2, technically equivalent to porphyritic basaltic andesites, andesites and dacites. The proposed genetic link between the porphyritic rocks and the plutonic rocks is strengthened by the phenocryst assemblages in the former being similar to the crystallising phases in the tonalites and diorites. The populations of phenocrysts observed appears to depend on the bulk composition of the rock. Observed phenocryst assemblages include: clinopyroxene + plagioclase (Fig. 7.31); hornblende + plagioclase (Figs. 7.32 and 7.33); hornblende + plagioclase + quartz (Fig. 7.34); plagioclase + quartz. The most commonly observed phenocryst assemblage is hornblende + plagioclase.

Plagioclase phenocrysts tend to be large (up to 3 or 4 mm), and are complexly zoned. They contain oscillatory zoning, and may have been partially resorbed at various stages of their history (Fig. 7.35). The hornblende phenocrysts are euhedral and elongate, and are sometimes replaced by an aggregate of finer-grained hornblende. Occasionally, the hornblende phenocrysts are rimmed by opaque minerals. Opaque minerals also occur as phenocryst phases, although they are volumetrically minor. Quartz occurs both as embayed phenocrysts and multi-grained, partially resorbed xenocrysts, probably derived from the adjacent tonalite. Clinopyroxene phenocrysts occur only in a few samples: they are euhedral and show twinning.

The groundmass of the porphyries is composed of hornblende + plagioclase ± quartz, often with elongate hornblende. In some samples, the groundmass has a very fine granular texture, comprising quartz, plagioclase and only minor hornblende. A few samples have spherulites in the groundmass, indicating that the rock cooled sufficiently quickly for the matrix to be glassy, although the rocks containing spherulites are quartz-phyric (i.e., silicic in composition) and need not necessarily have cooled more quickly than their more mafic counterparts.

The porphyritic rocks appear to be considerably more altered than their coarse-grained, equigranular counterparts (i.e., the diorites and tonalites). The plagioclase crystals are almost always sericitised, and hornblende phenocrysts are in some cases completely replaced by calcite, which may also be present in the groundmass.

The phenocryst populations in the porphyritic rocks provide an independent line of evidence for comparison with the crystallisation sequences observed in the equigranular members of the batholith. The more mafic rocks have clinopyroxene and plagioclase on the liquidus at the same time; slightly more acidic rocks have hornblende and plagioclase. The presence of porphyries with hornblende, plagioclase and quartz phenocrysts show that these were co-crystallising phases. This demonstrates that, for the other batholith rocks, the

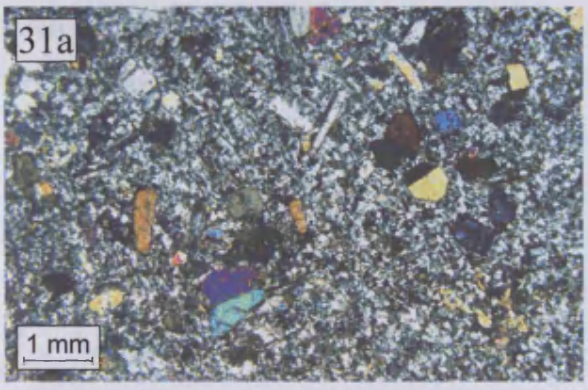

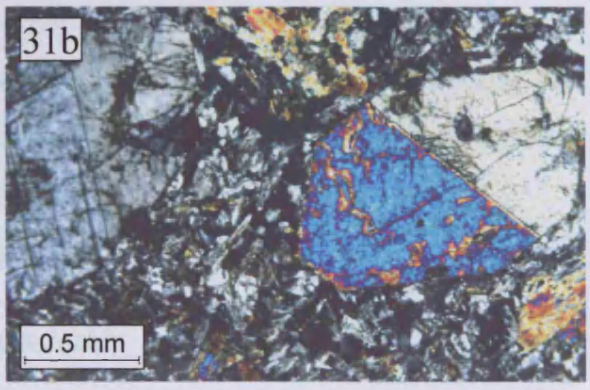

Fig. 7.31a: Porphyritic andesite from dyke, containing twinned clinopyroxene and plagioclase phenocrysts set in a groundmass of the same minerals. Crossed polars. b: The same rock, at higher magnification. Crossed polars. (ARU96-8)

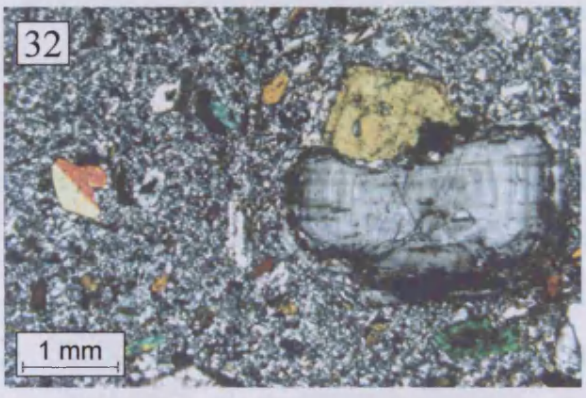

Fig. 7.32: Plagioclase-hornblende porphyry of dacitic composition, representative of the majority of porphyritic rocks within the batholith. The plagioclase phenocrysts are complexly zoned, similar to those found in the tonalite (Figs. 7.26 and 7.27) and the hornblendes are euhedral. Crossed polars. (ARU97-178)

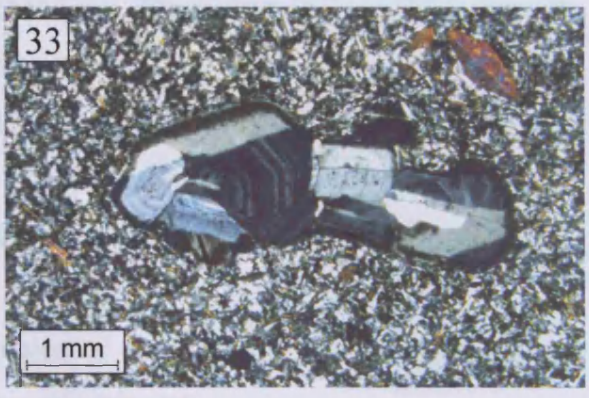

Fig. 7.33: Complex plagioclase glomerocryst within a plagioclase-hornblende porphyry of andesitic composition. Each plagioclase crystal forming the glomerocryst shows evidence of resorption at some point in its history. The whole glomerocryst does not appear to be in equilibrium with the surrounding medium. Crossed polars. (BK77-043)

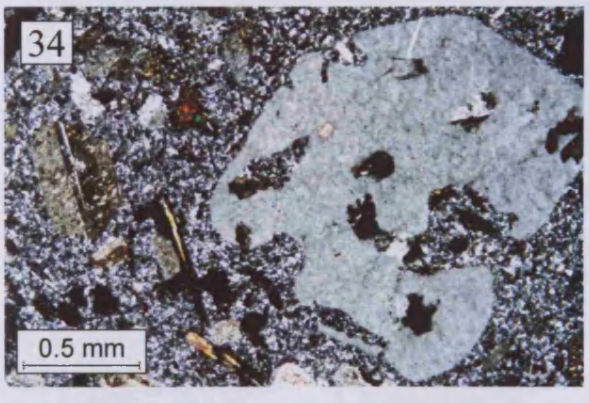

Fig. 7.34: Altered porphyritic rock of dacitic composition, with large anhedral quartz, euhedral partly-sericitised plagioclase and very altered amphibole (bright colours). Crossed polars. (ARU94-27)

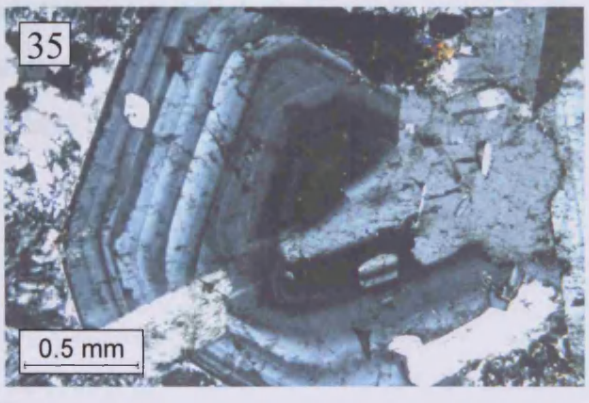

Fig. 7.35: Magnified view of plagioclase phenocryst from a porphyritic enclave in tonalite. The crystal shows an overall normal zoning, but consists of a number of discrete zones, most of which also show continuous normal zoning. The transition to a new calcic zone may be accompanied by resorption of the previous zone, and probably represents the crystal coming into contact with a hotter, or wetter magma. (ARU97-6)

presence of anhedral quartz in interstices need not necessarily mean that quartz was late crystallising: rather, the quartz merely tends to show a smaller degree of euhedralism. The most silicic porphyritic rocks have only plagioclase and quartz as phenocrysts, showing once again that these minerals crystallise concurrently.

7.3 Alteration of the batholith rocks: summary

Although the alteration of the Aruba batholith rocks is not severe, a summary of the secondary alteration phases observed is instructive when considering the effect that the alteration could have had on the whole-rock chemistry. These data are compiled from the descriptions of individual lithologies in the previous section.

- Olivine: may be altered along cracks to iddingsite or chlorophaeite; occasionally replaced by vermicular intergrowth of orthopyroxene and an opaque phase.
- Clinopyroxene: often altering to hornblende along cracks and at margins; occasionally altering to pumpellyite and/or prehnite.
- Orthopyroxene: sometimes altered to hornblende; occasionally replaced (partially or almost completely) by cryptocrystalline brown clay minerals.
- Biotite: often altered to chlorite, particularly at margins; occasionally completely replaced by chlorite and titanite, with minor epidote and quartz.
- Hornblende: occasionally altered to chlorite and epidote; very rarely replaced by calcite, especially in porphyritic rocks.
- Plagioclase: often shows some degree of sericitisation, particularly in calcic cores; in the most altered samples, plagioclase may be associated with epidote.
- The batholith is cross-cut by epidote-bearing veins that also contain quartz and chlorite.

7.4 Synthesis

7.4.1 Crystallisation sequence for the batholith

Construction of a single crystallisation sequence for the whole range of lithologies in the batholith is a difficult task because the order of crystallisation is not necessarily consistent from one lithology to another. However, a synthesis of the deductions made for all lithologies is displayed in Fig. 7.36.

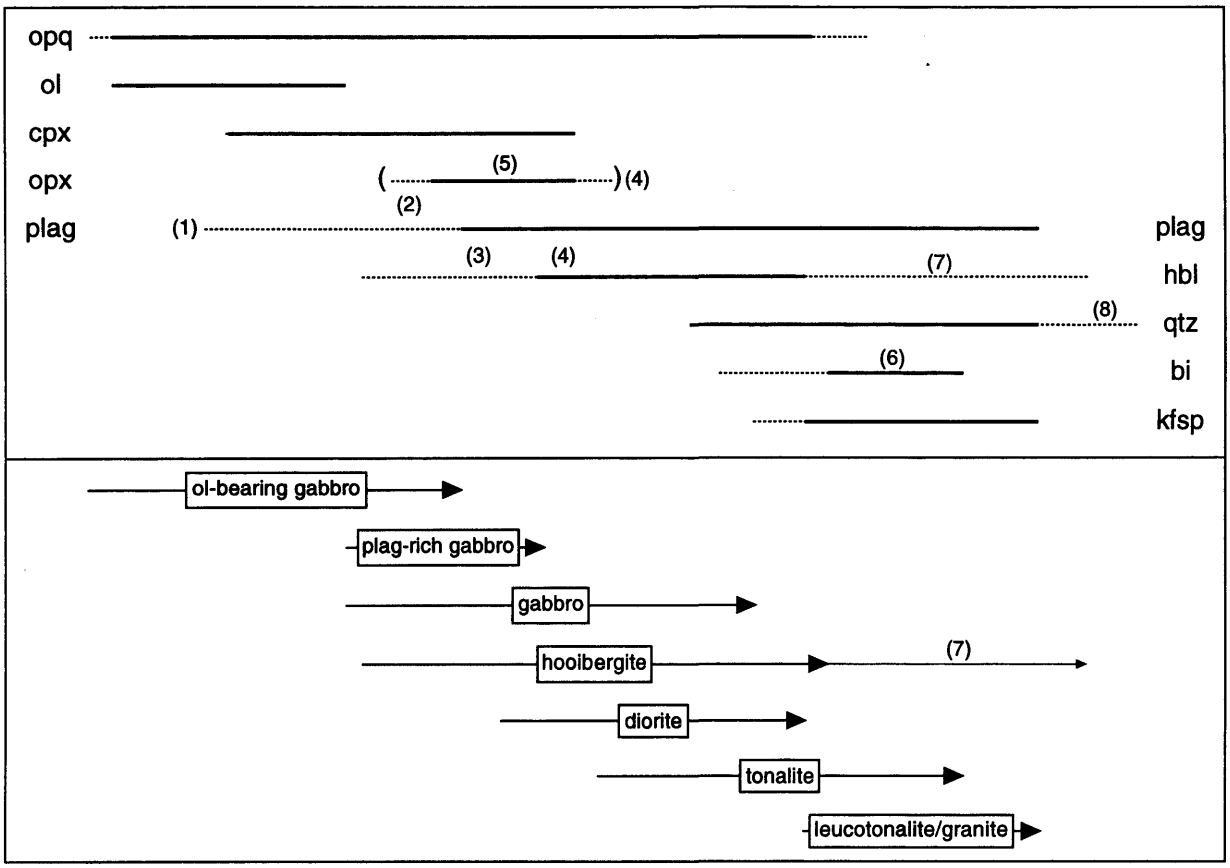

Fig. 7.36: Synthesis of the order of crystallisation of minerals in various lithologies of the batholith. The chart should be read from left to right as crystallisation occurs. Because the more mafic rocks in the batholith tend to be older (see Chapter 3), the chart can also act as a proxy for the evolution of the whole batholith, with the horizontal axis representing a larger-scale time dimension. Crystallisation ranges for selected lithologies are indicated, and the numbers refer to the comments below. This diagram is schematic only, and actual horizontal distances have no real meaning. Dotted lines represent crystallisation of a particular mineral in unusual circumstances, for example, usually cpx commences crystallisation before plagioclase, but the dotted extension of the plagioclase line indicates that occasionally, plagioclase crystallises before clinopyroxene.

Comments:

(1) Occasionally plagioclase crystallises before clinopyroxene.

(2) Sometimes plagioclase crystallises before orthopyroxene; sometimes the opposite.

(3) Sometimes plagioclase crystallises before hornblende; sometimes the opposite.

(4) Magmatic orthopyroxene and hornblende are never observed in the same rock. Hornblende may be present in gabbroic rocks, but appears to be an alteration phase after clinopyroxene. Orthopyroxene is never found in hooibergitic rocks.

(5) Orthopyroxene is not present in all the gabbroic rocks.

(6) Biotite is not present in all tonalites.

(7) The dotted extension to the hornblende line represents late growth (e.g., in the hooibergites adjacent to acidic veins) that occurs at various stages, including at subsolidus temperatures.

(8) The dotted extension to the quartz line represents crystallisation in late ?hydrothermal quartz veins.

The inferred crystallisation sequence for the gabbroic rocks is consistent with expectations from phase equilibrium constraints (e.g., Andersen, 1915). The slight differences in crystallisation order observed in the gabbro samples probably reflect subtle variations in bulk magma composition, and the extent to which equilibrium was maintained during crystallisation, for example, whether or not the crystallising assemblage was able to interact with the residual liquid.

The hooibergites, however, appear to behave differently: although they span the compositional range of the gabbros (see Chapter 8), their mineralogy is dominated by clinopyroxene, and olivine and orthopyroxene are never present. This difference is probably due to the gabbroic and hooibergitic cumulates being derived from melts with different bulk compositions: a more evolved mafic magma, for example, with higher CaO/MgO and higher SiO_2 will crystallise clinopyroxene more readily. Additionally, the hooibergites contain hornblende, which co-crystallised with the clinopyroxene for at least some of the crystallisation interval, again suggesting that the hooibergites were derived from a more evolved melt than the gabbros. The presence of magmatic hornblende also suggests that these magmas were wetter than those from which the gabbros crystallised; this will also have had an effect on the stability of the various crystallising phases. This discussion is complicated by the fact that the whole-rock compositions of the plagioclase-rich or olivine-bearing gabbros and the hooibergites are extremely unlikely to represent liquid compositions, and will be considered further, together with the whole rock geochemical data, in Chapter 8.

The more silicic members of the batholith also behave as expected, with the dominant ferromagnesian mineral changing from clinopyroxene to hornblende to biotite. This evolution can be seen in individual rocks, but also appears to be representative of the batholith as a whole.

7.4.2 Minor elements in pyroxenes: pressure/temperature constraints?

Fig. 7.37 shows that the pyroxenes in the rocks of the Aruba batholith contain a high Tschermak component (see Section 5.2.3 for discussion of Ti and Al substitution into pyroxenes). According to Thy (1991), this could indicate that these pyroxenes formed at pressures as high as 12.5 to 20 kbar, or ~38 to 60 km. An alternative viewpoint (Herzberg and Chapman, 1976) is that the amount of calcium Tschermak molecule ($CaAl_2SiO_6$) in clinopyroxene increases with temperature and is essentially independent of pressure. There is no independent evidence for the batholith having solidified at high pressures: for example, a much higher metamorphic grade than that observed would be expected in the country rocks

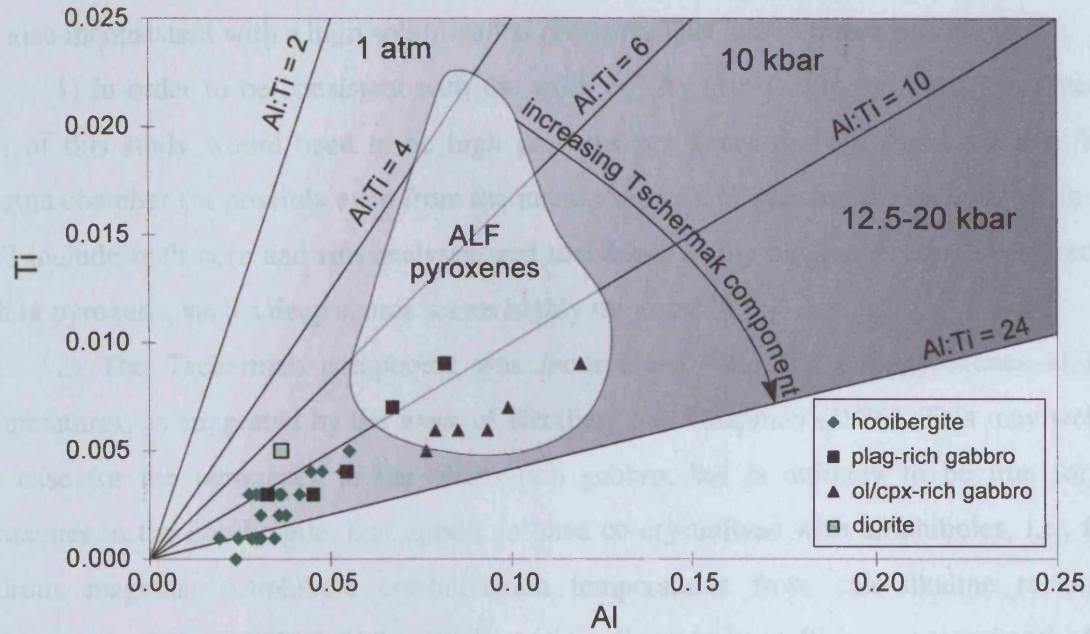

Fig. 7.37: Minor element compositions in clinopyroxenes of the batholith, plotted as atoms per formula unit (calculated to 6 oxygen atoms). The high Al:Ti ratios of these pyroxenes suggest that they have large Tschermak component. The field for the Aruba Lava Formation pyroxenes is shown for comparison. Conventional wisdom suggests that Tschermak substitution in pyroxenes may be a function of either increased pressure (Thy, 1991: pressure estimates indicated on diagram) or temperature (Herzberg and Chapman, 1976). See text for discussion.

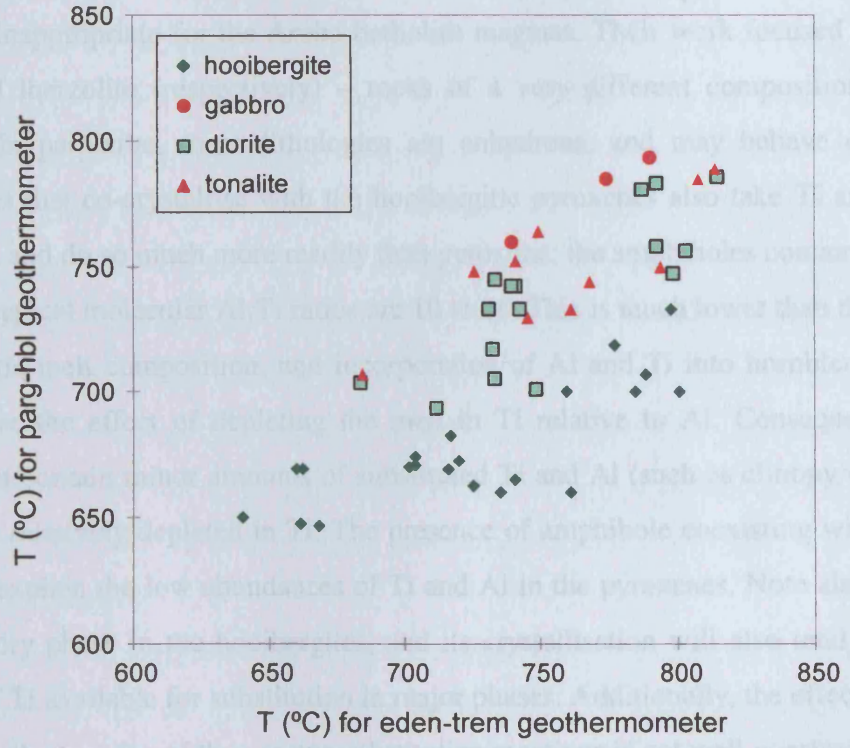

Fig. 7.38: Equilibration temperatures calculated by the hbl-plag computer program of Blundy and Holland (1990). All data reported are for 0 kbar pressure. The poor agreement between the geotherm-ometers for the hooibergites suggests that these may not be equilibrium hornblende-plagioclase assemblages; nevertheless, the data are included for comparison.

(i.e., the Aruba Lava Formation). Pressure constraints from the amphiboles (see next section) are also inconsistent with a high solidification pressure. This leaves three options:

1) In order to be consistent with the work of Thy (1991), the pyroxenes analysed as part of this study would need to be high pressure pyroxenes derived from a deeper level magma chamber (or possibly even from the mantle source). Given that the data shown in Fig. 6.37 include both core and rim analyses, and that some of the analysed rocks are extremely rich in pyroxene, such a deep source seems highly improbable.

2) The Tschermak component was incorporated into the clinopyroxenes at high temperatures, as suggested by the work of Herzberg and Chapman (1976). This may well be the case for the pyroxenes in the ol/cpx-rich gabbro, but is unlikely to be true for the pyroxenes in the hooibergite, that appear to have co-crystallised with amphiboles, i.e., from hydrous magmas. Amphibole crystallisation temperatures from calc-alkaline rocks are estimated at ~950 to 650°C (Helz, 1982), so any diopside crystallising concomitantly from such a magma is doing so at significantly lower temperature than diopside that crystallises from an anhydrous magma (e.g., 1270°C for the ternary eutectic in the system forsterite-anorthite-diopside: Osborn and Tait, 1952).

3) The third possibility is that the work of Thy (1991) and Herzberg and Chapman (1976) is inappropriate for the Aruba batholith magmas. Their work focused on alkali basalt and spinel lherzolite (respectively) – rocks of a very different composition to the Aruba magmas. In particular, these lithologies are anhydrous, and may behave differently. The amphiboles that co-crystallise with the hooibergitic pyroxenes also take Ti and Al into their structures, and do so much more readily than pyroxene; the amphiboles contain up to 1.5 wt.% TiO_2 and typical molecular Al:Ti ratios are 10 to 16. This is much lower than the Al:Ti ratio in any realistic melt composition, and incorporation of Al and Ti into hornblende in this ratio would have the effect of depleting the melt in Ti relative to Al. Consequently, any other phases that contain minor amounts of substituted Ti and Al (such as clinopyroxene) will also tend to be relatively depleted in Ti. The presence of amphibole coexisting with the pyroxene may also explain the low abundances of Ti and Al in the pyroxenes. Note also that titanite is an accessory phase in the hooibergites, and its crystallisation will also tend to decrease the amount of Ti available for substitution in major phases. Additionally, the effect of water in the magma on the kinetics of the various substitution reactions is not well-constrained.

7.4.3 Pressure/temperature constraints from amphiboles

Equilibration temperatures (calculated according to the methods of Blundy and Holland, 1990: see Section 5.4.1.1 for theoretical background) of co-crystallising hornblende-plagioclase assemblages are shown in Fig. 7.38. In addition to the ± 75°C (2σ) error inherent in the method, sensitivity analysis was carried out to determine how changes in plagioclase compositions during crystallisation (i.e., zoning) affect the results: for all samples displayed on Fig. 7.38, the maximum variation in temperature due to plagioclase compositional variability is ± 50°C, and values plotted are those obtained for the best estimate of the plagioclase composition.

Blundy and Holland's (1990) "hbl-plag" computer program calculates temperatures for two geothermometer reactions for a range of pressures. It was found that the temperatures obtained for 0 kbar had the best agreement between the two values for each data point; therefore, any data quoted in this section are 0 kbar data. For the higher pressure calculations, the pargasite-hornblende geothermometer yielded consistently higher temperatures than the edenite-tremolite values. Although this is not scientifically rigorous because "the pressure dependence is poorly constrained and the equilibria are not suitable for barometry" (Blundy and Holland, 1990), using low-pressure data is consistent with the field observations that the country rocks of the batholith do not appear to have been metamorphosed at high pressures.

The data for the diorites and tonalite range between ~680 and 800°C, consistent with the crystallisation temperatures reported for amphiboles in calc-alkaline magmas by Helz (1982). There does not appear to be any correlation between temperature and lithology; for example, it might be expected that the diorite assemblage would yield a higher temperature than a tonalite assemblage. This implies that equilibration between hornblende and plagioclase may have continued to lower temperatures than the crystallisation temperature of the minerals. The hooibergites tend to give lower temperatures still, and the values for the two geothermometers are not in as good agreement as for the tonalites and diorites. This may indicate that the hornblende-plagioclase assemblages in the hooibergite are not in complete chemical equilibrium.

Pressures of crystallisation of hornblende in plutonic rocks may be estimated using the aluminium-in-hornblende geobarometer (Hammarstrom and Zen, 1986; Hollister *et al.*, 1987). The barometer only works because, if a number of conditions are satisfied, compositional and temperature variables can be included in the geobarometer calibration, and the hornblende composition is expressed only as a function of pressure. The conditions are:

1. The rock has ten components (major oxides and water) and nine phases that were in equilibrium during crystallisation: plagioclase, quartz, hornblende, biotite, orthoclase, magnetite and titanite coexisting with a melt phase and a vapour phase (H_2O and CO_2). Using the phase rule (phases + degrees of freedom = components + 2), this leaves a system with a variance of 3, the degrees of freedom being P, T and composition of one phase. Because all of the above phases are only in equilibrium towards the end of crystallisation, only analyses of rim compositions should be used.
2. If the plagioclase composition is known, the degrees of freedom falls to 2. The geobarometer is calibrated for plagioclase rim compositions between An_{35} and An_{25}.
3. Because solidus curves for hornblende-bearing calc-alkaline liquids are relatively insensitive to pressure above 2 kbar, the temperature can be fixed at a reasonable value to allow calibration of the geobarometer.

Different calibrations of the geobarometer yield slightly different equations:

1. $P\ (\pm 3\ kbar) = -3.92 + 5.03Al_T$ (Hammarstrom and Zen, 1986)
2. $P\ (\pm 1\ kbar) = -4.76 + 5.03Al_T$ (Hollister *et al.*, 1987)

where Al_T is the total Al cations per formula unit of hornblende (23 oxygen atoms), cations having been normalised to total 15, excluding Na and K.

The tonalites (and some diorites) satisfy the first two conditions: the pressure of crystallisation is, of course, the aim of using the geobarometer in the first place. The values obtained for 19 amphibole analyses from 3 samples (two tonalites and a diorite) give the following results (numbers refer to the equation used):

1. 1.72 kbar ($\pm$ 0.57 1σ)
2. 1.56 kbar ($\pm$ 0.63 1σ)

The errors quoted above are the statistical uncertainty in the mean of the nineteen values used, and do not include the error inherent in the method, i.e., ± 3 kbar and ± 1 kbar, respectively.

These values are below the 2 kbar limit recommended for use of the barometer by Hollister *et al.* (1987). Below this pressure, temperature of solidification increases, and the total Al present in hornblende is more dependent on this temperature change. Nevertheless, it can be concluded from these data that the Aruba batholith must have crystallised at a relatively shallow level, i.e., less than 2 kbar (6 km). This is in accordance with the field observations and the better agreement of the 0 kbar data obtained from Blundy and Holland's (1990) hornblende-plagioclase geothermometers.

7.4.4 Significance of zoning of plagioclase

Many of the rocks of the batholith contain zoned plagioclase crystals. In general, the plagioclase crystals within the gabbros (both the layered and unlayered varieties) are relatively homogeneous in composition (see Fig. 7.4); the biggest variation in plagioclase composition is found in the hooibergites, diorites, tonalites and porphyries. In some of the rocks, the plagioclase compositions are bimodal (see, for example, Section 7.2.1); however, in most cases, the zoning is intricate and complex, with only a small compositional variation between zones. A compositional profile across the plagioclase crystal pictured in Fig. 7.26 is displayed in Fig. 7.39.

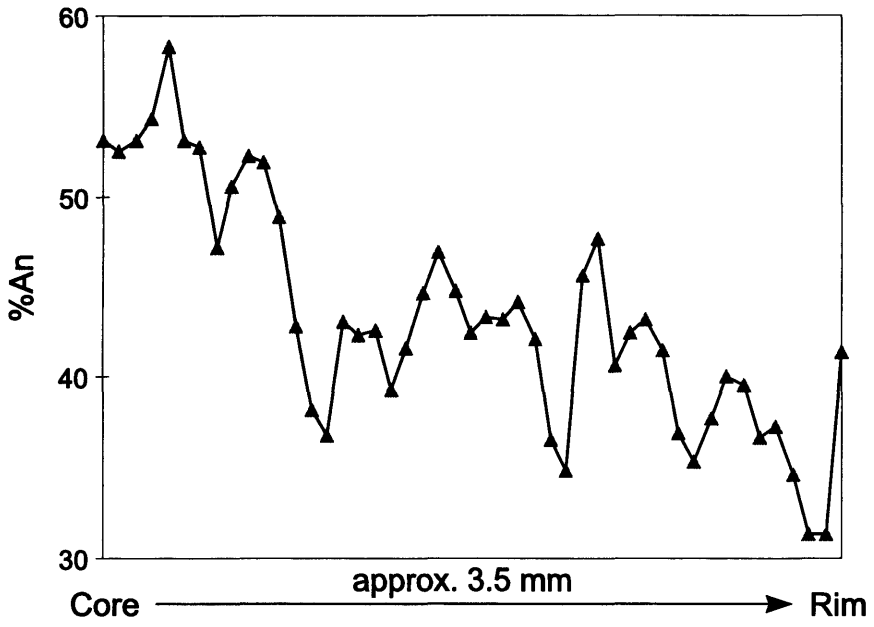

Fig. 7.39: Zoning profile across the plagioclase crystal pictured in Fig. 7.26. There is a gross-scale zoning from more calcic to more sodic, but superimposed upon this are several oscillations.

In this particular crystal, there are (at least) eight horizons where the zoning is reversed. Reversed zoning can occur in a number of instances:

1. If the temperature of the magma increases, the equilibrium plagioclase crystallising becomes more anorthite-rich.
2. If the magma becomes more hydrous, the liquidus and solidus of the plagioclase drop in temperature (Yoder *et al.*, 1957; Johannes, 1989), and the equilibrium plagioclase becomes more calcic.

The most simple mechanism for increasing the temperature of a magma, or increasing its volatile content, is to allow it to interact with another magma batch: in order to achieve the

temperature increase, this would normally be of a more mafic composition. Note that magma mixing such as this would also change the bulk composition, adding a further variable in determining the plagioclase composition. In reality, it is impossible to separate and quantify the importance of these different effects; however, it is reasonable to conclude that reverse zoning in plagioclase results from mixing between magma batches.

In contrast to the plagioclase pictured in Fig. 7.26, the plagioclase phenocryst in Fig. 7.35 contains conspicuous areas where a previous zone appears to have been resorbed prior to regrowth. It is interesting to speculate under what conditions resorption can occur: it must occur if the temperature and/or water content of the melt increase to such an extent that the crystal is above its liquidus temperature. If the temperature or H_2O change is smaller, such that the plagioclase crystal becomes located in the field between the solidus and the liquidus, whether resorption or growth of a more calcic (i.e., reversed) zone occurs will depend upon a complex interplay of growth rates of the calcic plagioclase versus dissolution rates of the more sodic plagioclase (kinetic factors), in addition to the rate at which the melt composition is changing, and thermodynamic factors such as the latent heat of crystallisation. This implies that to generate resorbed horizons, rather than reversed zoning, in plagioclase crystals, a more drastic, or rapid, change in the melt composition and/or temperature must occur. This is easily achieved if an existing magma or crystal population is mixed with a fresh batch of hotter, wetter, magma.

7.5 Summary

- The rocks of the batholith span a wide range of compositions, with gabbros dominated by olivine, augite, enstatite and plagioclase; hooibergites dominated by pyroxene and hornblende; diorites dominated by hornblende and plagioclase; and tonalites dominated by plagioclase, hornblende, biotite and quartz.
- Many of the petrographic features (in addition to the field characteristics: see Chapter 3) of the gabbros and hooibergites are consistent with an origin by accumulative processes. In particular, the very high diopside content of some of the hooibergites is impossible to achieve via equilibrium crystallisation of any realistic liquid.
- Many of the diorites, tonalites and porphyritic rocks contain plagioclase crystals that have complex zoning, indicating a history of interaction between different magma batches. This is consistent with the field evidence for magma mingling (see Chapter 3).
- The rocks of the batholith are slightly altered. Common secondary phases include, epidote, chlorite, amphibole and sericite.
- Amphibole compositions from suitable lithologies suggest solidification of the batholith at pressures of less than 2 kbars. Equilibration temperatures of hornblende and plagioclase assemblages are between 680°C and 800°C.

Chapter 8

Geochemistry of the Aruba Batholith

8.1 Introduction

The whole-rock geochemical features of the rocks of the Aruba batholith are described in this chapter, together with an introductory discussion and interpretation. The aim of this chapter is to provide the reader with the facts about the compositions of the different lithologies in the batholith. The analytical methods used to generate the data presented herein include XRF for major, minor and trace elements (see Appendix C), ICP-MS (see Appendix D), and thermal ionisation mass spectrometry (see Appendix F).

These data will be discussed more fully in Chapter 9, where relationships between different lithologies will be clarified, and a model is presented which interprets the data in terms of how and where the magmas were generated, and how they have been modified by various magmatic processes, for example, magma mixing and fractional crystallisation.

8.1.1 Chemical and mineralogical criteria used for lithological classification

The batholith rocks have been classified into lithological groups, and the symbols used on diagrams to reflect these groups are consistent throughout this chapter. The divisions are based primarily on chemical and/or mineralogical criteria, but occasionally also on textural features. Although divisions used are somewhat arbitrary, they are devised so that the majority of rocks are classified correctly according to a variety of classification schemes.

Hooibergites are defined by their textural and mineralogical features: they have visually prominent, equant, euhedral, large hornblende crystals in a matrix containing essential plagioclase, and often clinopyroxene and/or quartz. All hooibergites have less than 56 wt.% SiO_2 and most have greater than 8 wt.% MgO.

The *olivine- and pyroxene-rich gabbros* have >14 wt.% MgO (but are distinguished from MgO-rich hooibergites because they lack large euhedral hornblende crystals); they also have low TiO_2 contents compared to the other mafic rocks of the batholith. The *plagioclase-rich gabbros* have very low silica contents (less than 47%), whilst not having particularly high MgO (< 10%), and also do not contain large hornblende crystals. The *gabbros* have $SiO_2 < 55$ wt.% and MgO > 6 wt.%.

Diorites have between 55 wt.% and 62 wt.% SiO_2, but this category also includes three samples that have less than 55 wt.% SiO_2, because they also have significantly lower MgO than the gabbros, i.e., MgO < 6 wt.%. *Tonalites* encompass all rocks with between 62 and 72% SiO_2 that are not strongly porphyritic in texture. The *porphyries* range in chemical composition from 53 wt.% to 68 wt.% SiO_2 and 6.7 wt.% to 1.7 wt.% MgO, but are classified in a group of their own because of their porphyritic texture.

The rocks with more than 72 wt.% SiO_2 are classified according to alkali content. The *granites* have >2.5 wt.% K_2O, and the *leucotonalites* have <2.5 wt.% K_2O. This division results in the samples falling into the correct fields on a plot of normative An, Ab and Or (Fig. 8.1). The leucotonalite category includes some samples that are, strictly speaking, trondhjemites. The *leucocratic veins* category refers to samples which have high Na_2O (up to 8 wt.%) and high SiO_2 (> 77 wt.%), with the exception of sample ARU97-118, which appears to consist entirely of anorthitic plagioclase. The leucocratic veins also differ from the granites and leucotonalites by their lack of ferromagnesian minerals.

The divisions used here are broadly in agreement with the classification of samples on a quartz - alkali feldspar - plagioclase feldspar triangular plot (Streckeisen, 1976; Fig. 8.2). Although this diagram should, strictly, only be used for *modal* mineral proportions, normative proportions are plotted in Fig. 8.2, with A representing orthoclase and P representing albite plus anorthite. (A small number of samples were point-counted to ensure that the actual modal proportions of the salic minerals did not vary significantly from those predicted by the norm calculations.) With the exception of a few slightly more potassic samples, the gabbros and hooibergites all fall into the "gabbro" or "quartz gabbro" fields; the diorites span the "quartz diorite" and "tonalite" fields; the tonalites and leucotonalites fall in the "tonalite" or "granodiorite" fields; and the granites are classified as "granodiorite" or "monzogranite". This illustrates the difficulty in classification and nomenclature of samples, because using different classification schemes results in different answers.

8.1.2 Broad geochemical characteristics of the suite

Fig. 8.3 displays data for the batholith on a total alkalis ($Na_2O + K_2O$) versus silica plot, and compares them with data from the Aruba Lava Formation. All of the data fall into the sub-alkaline field; they cover a wide range of SiO_2 contents, with their volcanic equivalents ranging from basalt to rhyolite. There appears to be a marked compositional gap between the tonalites and leucotonalites, with only two samples (tonalites) having between 68

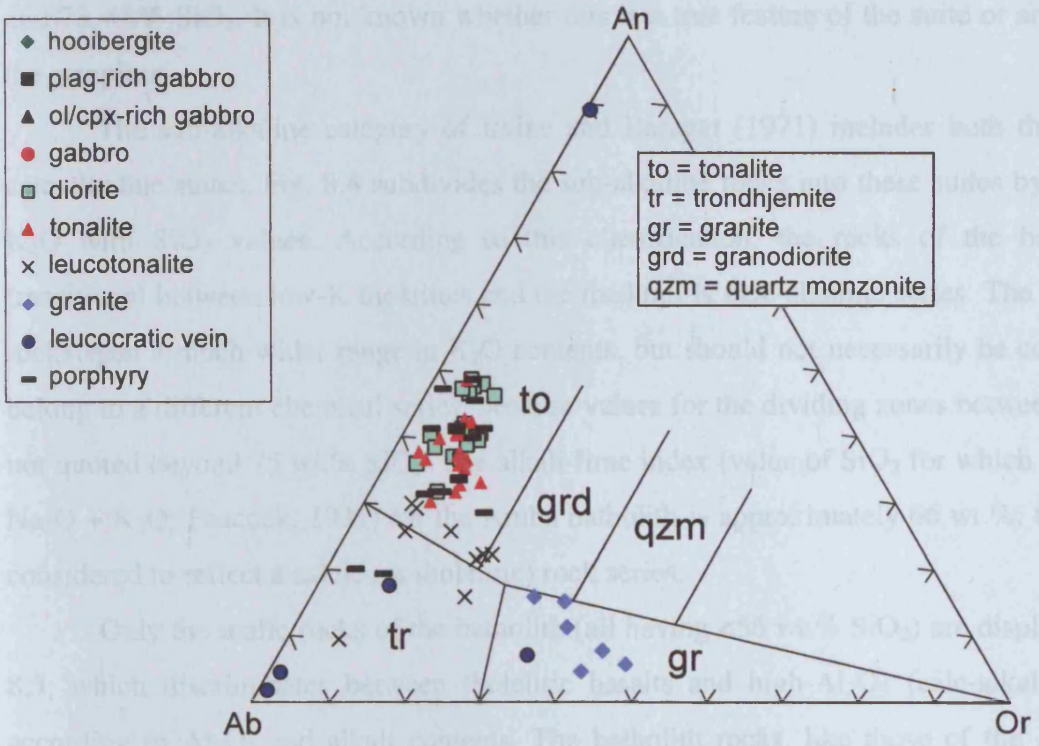

Fig. 8.1: Plot showing normative data for all samples from the Aruba batholith having more than 10% normative quartz after Barker (1979).

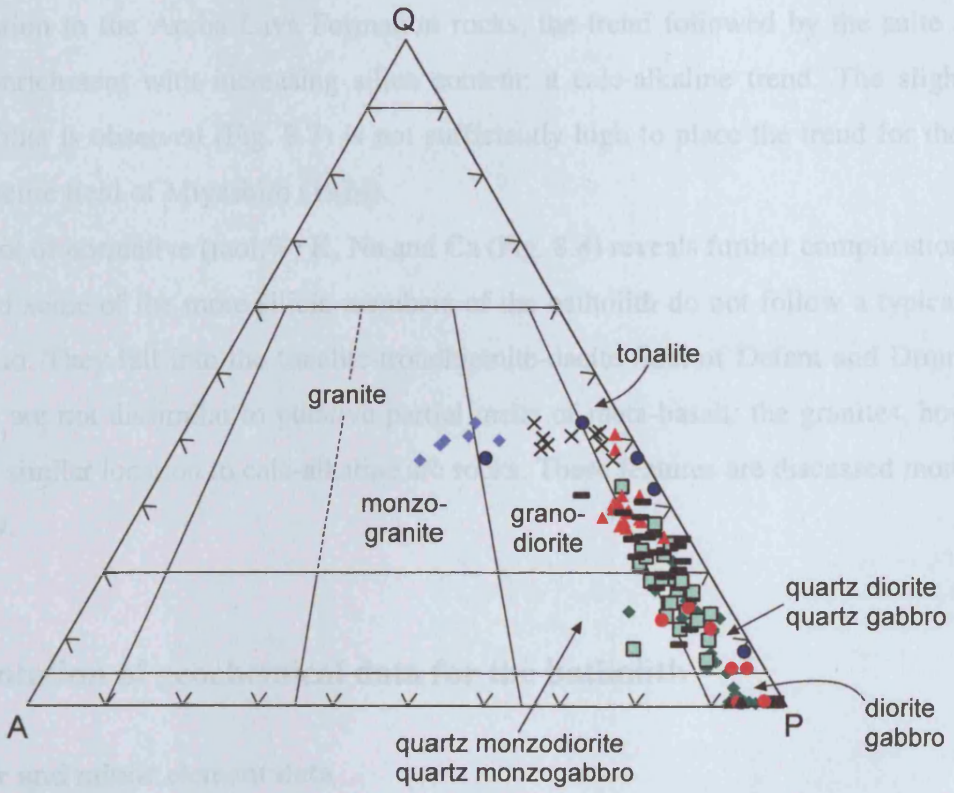

Fig. 8.2: QAP plot (after Streckeisen, 1976) showing normative data for all samples from the Aruba batholith. Some samples were point-counted to verify that the normative and modal mineralogies do not differ significantly. Q = quartz, A = orthoclase, P = anorthite + albite.

and 73 wt.% SiO_2. It is not known whether this is a true feature of the suite or an artefact of the sampling.

The sub-alkaline category of Irvine and Baragar (1971) includes both tholeiitic and calc-alkaline suites. Fig. 8.4 subdivides the sub-alkaline rocks into these suites by comparing K_2O with SiO_2 values. According to this classification, the rocks of the batholith are transitional between low-K tholeiites and the medium-K calc-alkaline series. The most silicic rocks span a much wider range in K_2O contents, but should not necessarily be considered to belong to a different chemical series, because values for the dividing zones between series are not quoted beyond 75 wt.% SiO_2. The alkali-lime index (value of SiO_2 for which CaO equals $Na_2O + K_2O$: Peacock, 1931) for the Aruba batholith is approximately 66 wt.%: this value is considered to reflect a calcic (or tholeiitic) rock series.

Only the mafic rocks of the batholith (all having <56 wt.% SiO_2) are displayed in Fig. 8.5, which discriminates between tholeiitic basalts and high-Al_2O_3 (calc-alkaline) basalts according to Al_2O_3 and alkali contents. The batholith rocks, like those of the Aruba Lava Formation, seem to have tholeiitic affinities. Inspection of the AFM plot (Fig. 8.6), however, demonstrates that the suite as a whole is not tholeiitic - although the mafic rocks plot in a similar location to the Aruba Lava Formation rocks, the trend followed by the suite shows little iron enrichment with increasing silica content: a calc-alkaline trend. The slight iron enrichment that is observed (Fig. 8.7) is not sufficiently high to place the trend for the suite into the tholeiite field of Miyashiro (1974).

A plot of normative (mol.%) K, Na and Ca (Fig. 8.8) reveals further complications: the tonalites and some of the more silicic members of the batholith do not follow a typical calc-alkaline trend. They fall into the tonalite-trondhjemite-dacite field of Defant and Drummond (1993), and are not dissimilar to putative partial melts of meta-basalt; the granites, however, do plot in a similar location to calc-alkaline arc rocks. These features are discussed more fully in Chapter 9.

8.2 Presentation of geochemical data for the batholith

8.2.1 Major and minor element data

Major and minor element data for the batholith (obtained by XRF: see Appendix C) are presented in Figs. 8.9a to 8.9j. The batholith lithologies cover a range in SiO_2 contents from 45 to 80 wt.%; MgO ranges from 18 wt.% to zero. There is a consistent relationship

Fig. 8.3

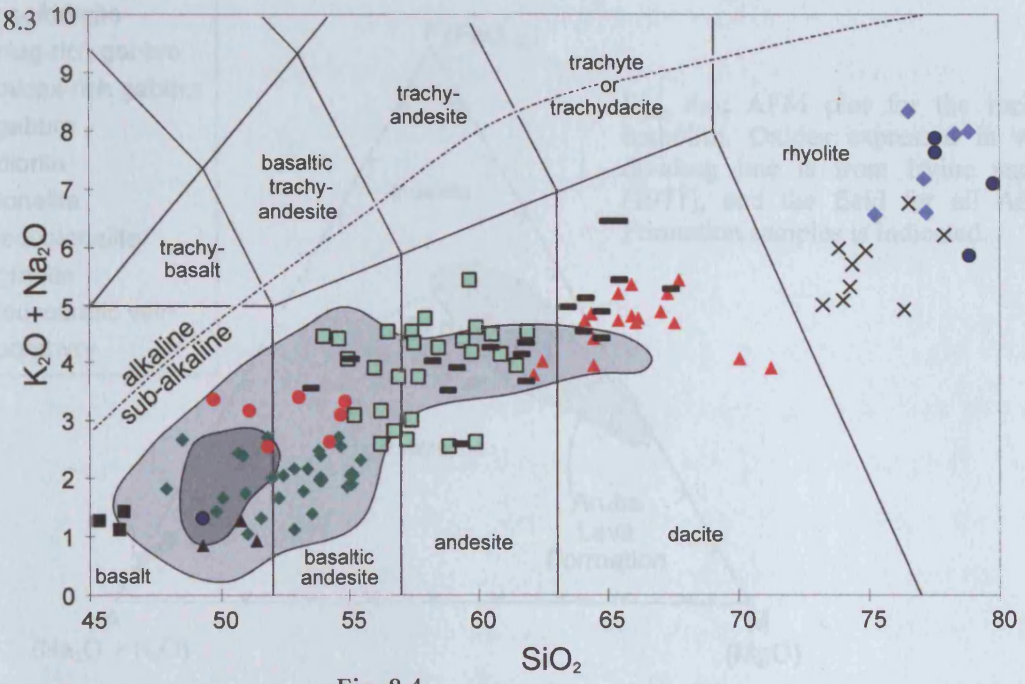

Fig. 8.4

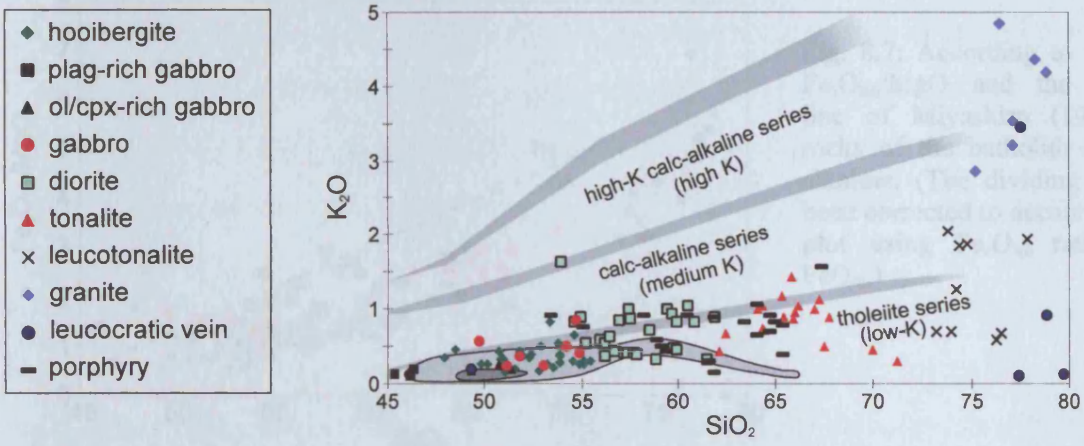

Fig. 8.5

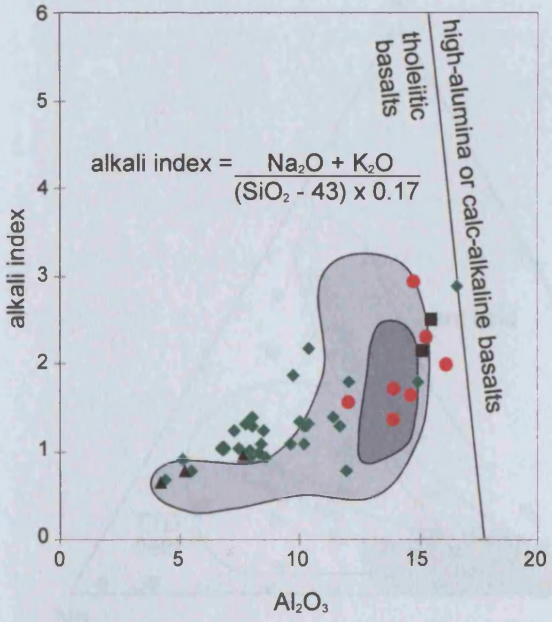

Fig. 8.3 (top): Total alkali vs. silica plot for the batholith reveals its subalkaline character. Darker field encompasses Aruba Lava Formation (ALF) basalts and dolerites; lighter field includes all ALF samples. Dividing line from Irvine and Baragar (1971).

Fig. 8.4 (middle): The K_2O vs. SiO_2 diagram further divides the subalkaline rock series. According to this plot (and the dividing fields from Rickwood, 1989), the batholith spans the tholeiite and calc-alkaline fields. ALF fields as described above.

Fig. 8.5 (bottom): Diagram of alkali index vs. alumina suggests that the mafic rocks of the batholith have tholeiitic affinities. One extremely plagioclase-rich gabbro plots to the right of the diagram area. Dividing line from Middlemost (1975). ALF fields as described in Fig. 8.3.

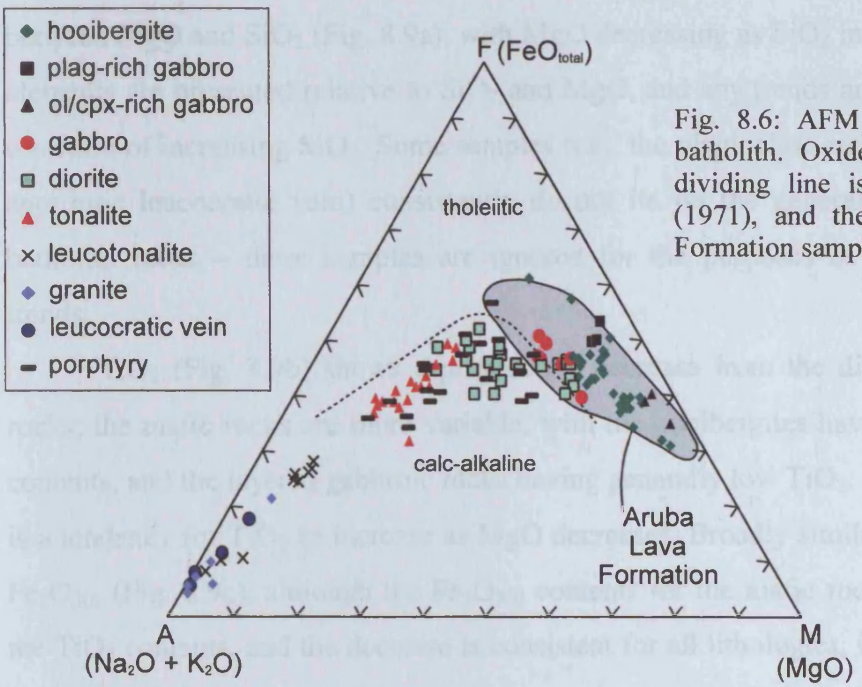

Fig. 8.6: AFM plot for the rocks of the batholith. Oxides expressed in wt.%. The dividing line is from Irvine and Baragar (1971), and the field for all Aruba Lava Formation samples is indicated.

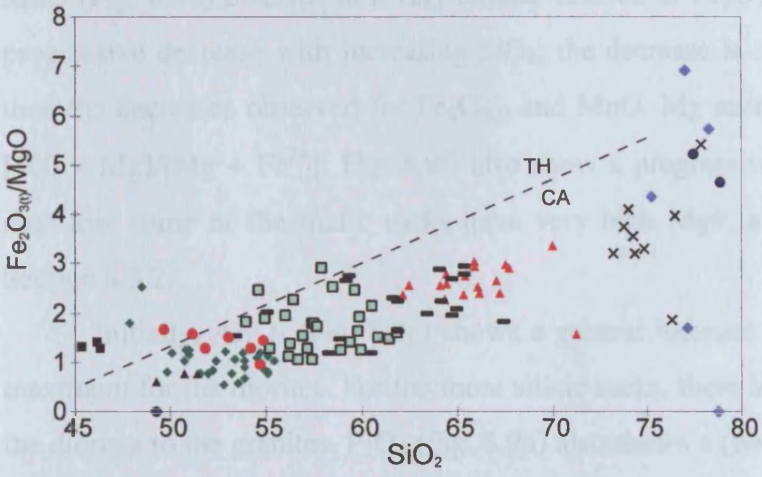

Fig. 8.7: According to a plot of $Fe_2O_{3(t)}$/MgO and the dividing line of Miyashiro (1974), the rocks of the batholith are calc-alkaline. (The dividing line has been corrected to account for this plot using $Fe_2O_{3(t)}$ rather than $FeO_{(t)}$.)

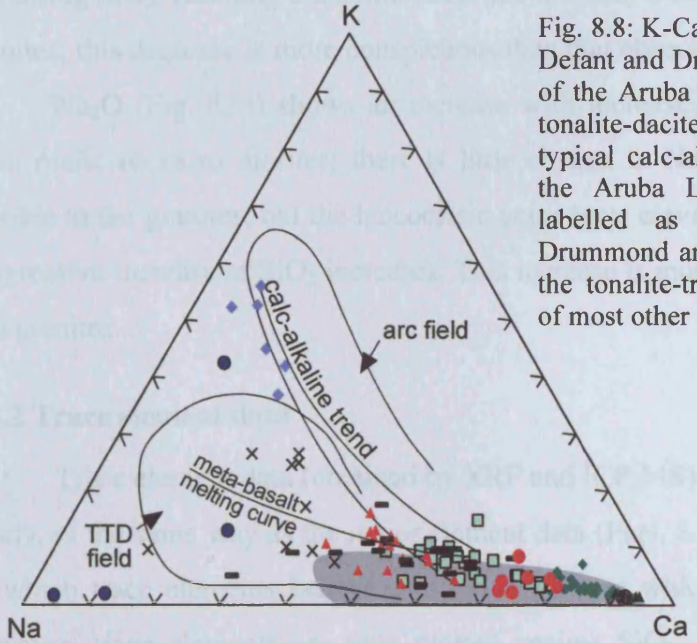

Fig. 8.8: K-Ca-Na plot for the Aruba batholith (after Defant and Drummond, 1993) showing that samples of the Aruba batholith trend into the trondhjemite-tonalite-dacite (TTD) field rather than following a typical calc-alkaline trend. The grey field includes the Aruba Lava Formation samples. The field labelled as "TTD" uses the terminology of Drummond and Defant (1993), and is equivalent to the tonalite-trondhjemite-grano-diorite (TTG) suite of most other authors.

between MgO and SiO_2 (Fig. 8.9a), with MgO decreasing as SiO_2 increases. Data for all other elements are presented relative to SiO_2 and MgO, and any trends are always discussed in the direction of increasing SiO_2. Some samples (i.e., the plagioclase-rich layered gabbros and the anorthitic leucocratic vein) consistently do not lie on the general trends observed for the batholith rocks – these samples are ignored for the purposes of describing these general trends.

TiO_2 (Fig. 8.9b) shows a progressive decrease from the diorites to the more acidic rocks; the mafic rocks are more variable, with the hooibergites having a large range in TiO_2 contents, and the layered gabbroic rocks having generally low TiO_2. For the mafic rocks, there is a tendency for TiO_2 to increase as MgO decreases. Broadly similar trends are observed for $Fe_2O_{3(t)}$ (Fig. 8.9c), although the $Fe_2O_{3(t)}$ contents for the mafic rocks are less scattered than the TiO_2 contents, and the decrease is consistent for all lithologies, including the mafic rocks. MnO (Fig. 8.9d) behaves in a very similar fashion to $Fe_2O_{3(t)}$. CaO (Fig. 8.9e) also shows a progressive decrease with increasing SiO_2; the decrease is more marked for the mafic rocks than the decreases observed for $Fe_2O_{3(t)}$ and MnO. Mg numbers (Mg# defined as molecular $[100 \times Mg]/[Mg + Fe^{2+}]$; Fig. 8.9f) also show a progressive decrease with increasing SiO_2; note that some of the mafic rocks have very high Mg#, a feature discussed more fully in Section 8.3.2.

Initially, Al_2O_3 (Fig. 8.9g) shows a general increase with increasing SiO_2, reaching a maximum for the diorites. For the more silicic rocks, there is a gentle decrease in Al_2O_3 from the diorites to the granites. P_2O_5 (Fig. 8.9h) also shows a (poorly-defined) initial increase with increasing SiO_2, reaching a maximum for the diorites, then decreasing from the diorites to the granites; this decrease is more conspicuous than that observed for Al_2O_3.

Na_2O (Fig. 8.9i) shows an increase with increasing SiO_2. The increase is consistent from mafic rocks to diorites; there is little change in Na_2O contents from the more silicic diorites to the granites, but the leucocratic veins have elevated Na_2O. K_2O (Fig. 8.9j) shows a progressive increase as SiO_2 increases. This increase is much more rapid for the leucotonalites and granites.

8.2.2 Trace element data

Trace element data (obtained by XRF and ICP-MS) are presented in a number of ways: firstly, in the same way as the major element data (Figs. 8.10a to 8.10p), to give an indication of which trace elements behave in similar ways to which major elements. To save space, however, trace elements are only plotted against SiO_2, except for elements where it was

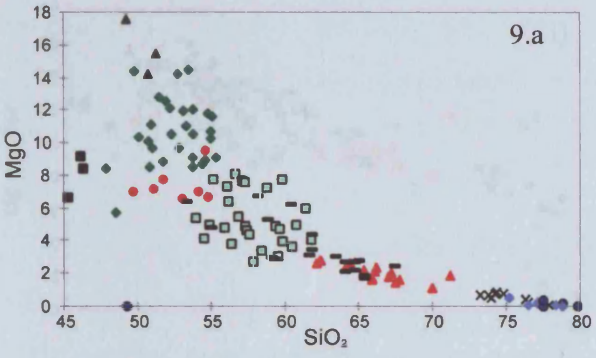

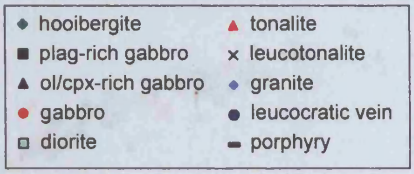

Figs. 8.9 a-e: Plots of major elements vs. SiO_2 and MgO for the batholith. Figs. 8.9 f-j can be found on the next page.

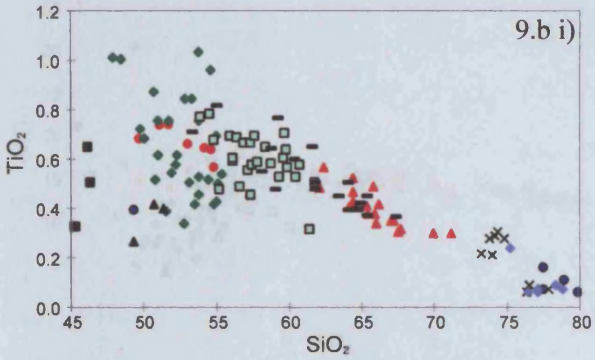

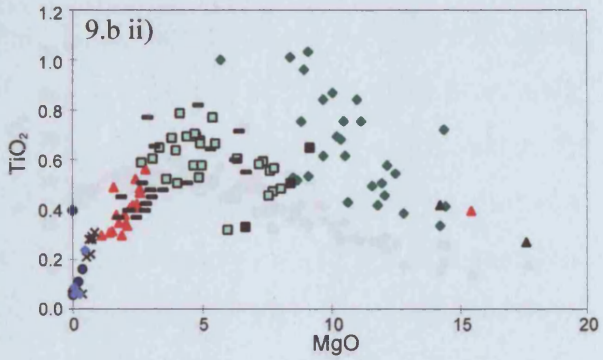

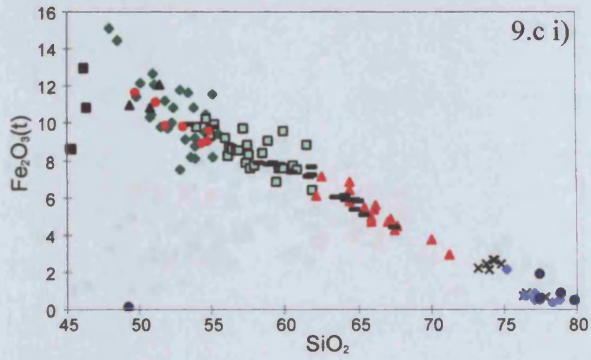

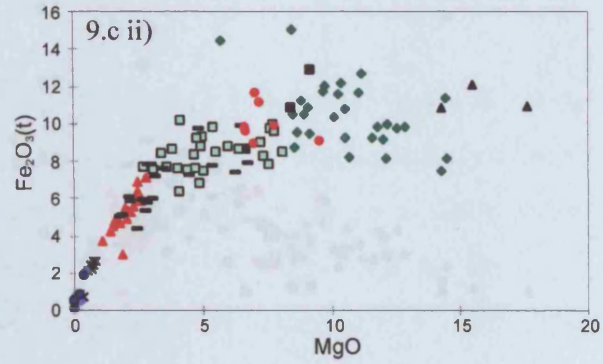

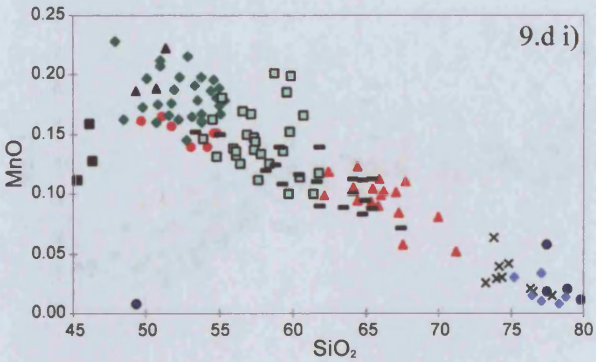

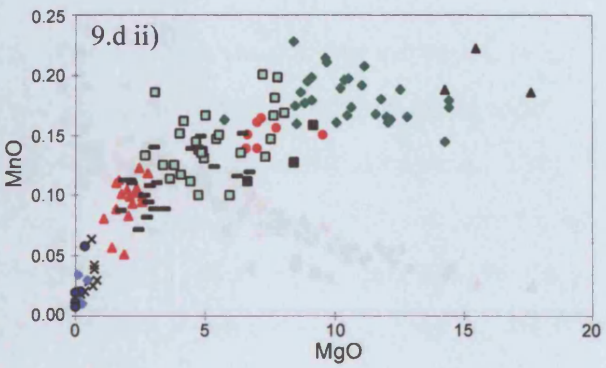

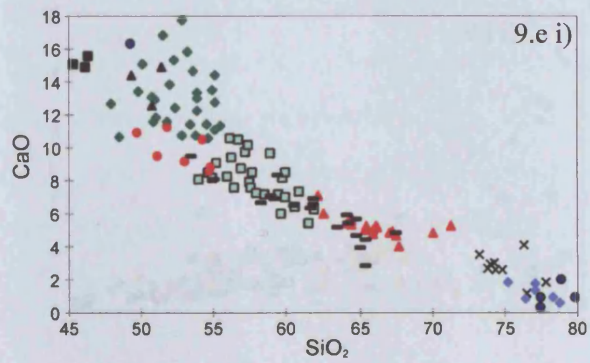

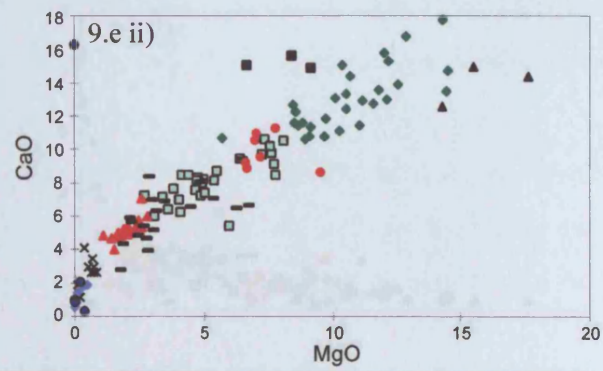

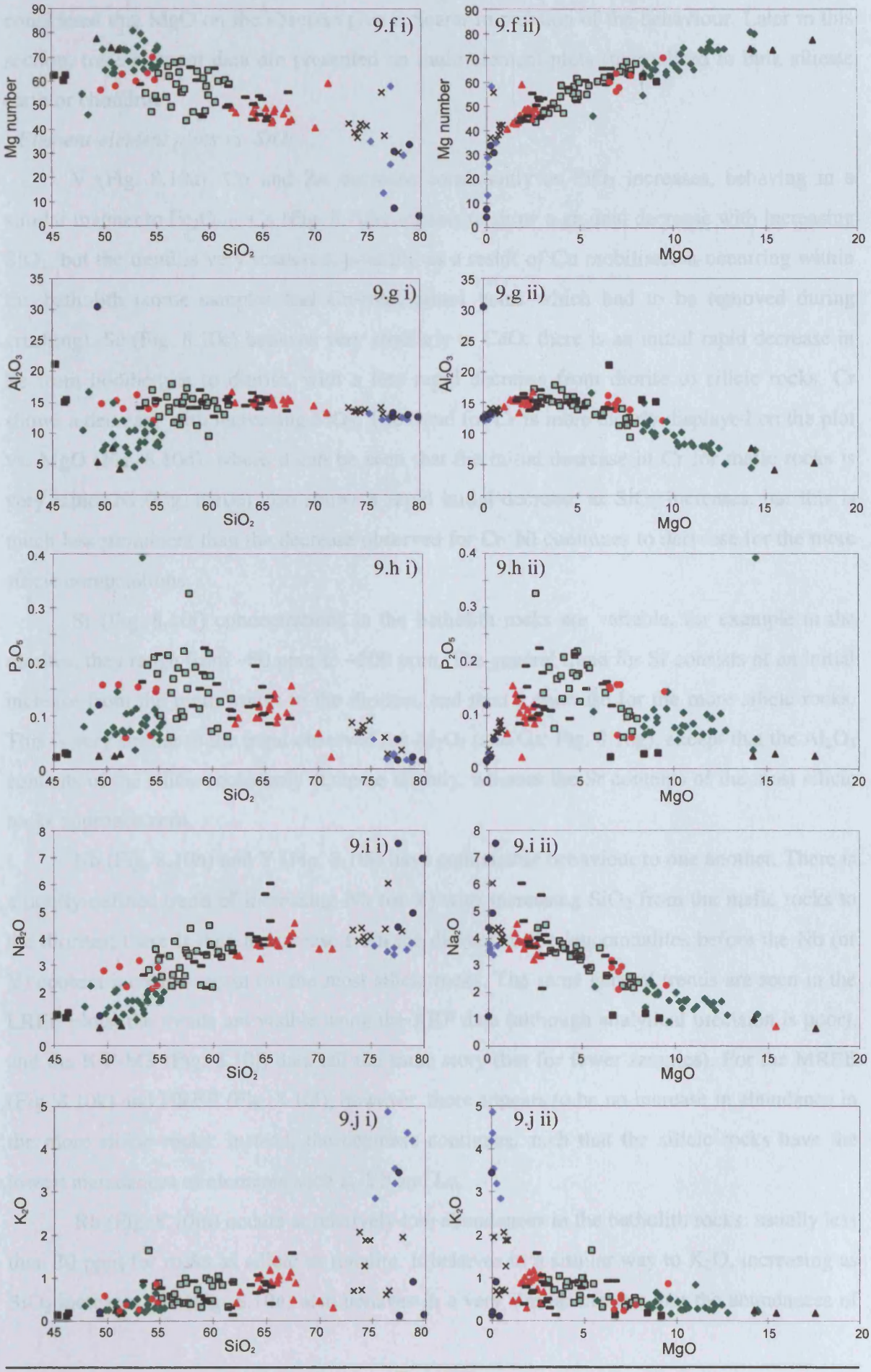
9.f i)
Mg number
SiO2
9.f ii)
Mg number
MgO
9.g i)
Al2O3
SiO2
9.g ii)
Al2O3
MgO
9.h i)
P2O5
SiO2
9.h ii)
P2O5
MgO
9.i i)
Na2O
SiO2
9.i ii)
Na2O
MgO
9.j i)
K2O
SiO2
9.j ii)
K2O
MgO

considered that MgO on the abscissa give a clearer impression of the behaviour. Later in this section, trace element data are presented on multi-element plots (normalised to bulk silicate earth or chondrite).

Element-element plots vs. SiO_2.

V (Fig. 8.10a), Co and Zn decrease consistently as SiO_2 increases, behaving in a similar manner to $Fe_2O_{3(t)}$. Cu (Fig. 8.10b) appears to show a gradual decrease with increasing SiO_2, but the trend is very scattered, possibly as a result of Cu mobilisation occurring within the batholith (some samples had Cu-mineralised veins which had to be removed during crushing). Sc (Fig. 8.10c) behaves very similarly to CaO: there is an initial rapid decrease in Sc from hooibergite to diorite, with a less rapid decrease from diorite to silicic rocks. Cr shows a decrease with increasing SiO_2. The trend for Cr is more clearly displayed on the plot vs. MgO (Fig. 8.10d), where it can be seen that the initial decrease in Cr for mafic rocks is very rapid. Ni (Fig. 8.10e) also shows a rapid initial decrease as SiO_2 increases, but this is much less prominent than the decrease observed for Cr. Ni continues to decrease for the more silicic compositions.

Sr (Fig. 8.10f) concentrations in the batholith rocks are variable, for example in the diorites, they range from ~80 ppm to ~500 ppm. The general trend for Sr consists of an initial increase from the mafic rocks to the diorites, and then a decrease for the more silicic rocks. This is very similar to the trend observed for Al_2O_3 (and Ga: Fig. 8.10g), except that the Al_2O_3 contents of the silicic rocks only decrease slightly, whereas the Sr contents of the most silicic rocks approach zero.

Nb (Fig. 8.10h) and Y (Fig. 8.10i) have comparable behaviour to one another. There is a poorly-defined trend of increasing Nb (or Y) with increasing SiO_2 from the mafic rocks to the diorites; there is then a decrease from the diorites to the leucotonalites before the Nb (or Y) content increases again for the most silicic rocks. The same general trends are seen in the LREE plots: the trends are visible using the XRF data (although analytical precision is poor), and the ICP-MS (Fig. 8.10j) data tell the same story (but for fewer samples). For the MREE (Fig. 8.10k) and HREE (Fig. 8.10l), however, there appears to be no increase in abundance in the more silicic rocks; instead, the decrease continues, such that the silicic rocks have the lowest abundances of elements such as Yb and Lu.

Rb (Fig. 8.10m) occurs at relatively low abundances in the batholith rocks: usually less than 30 ppm for rocks as silicic as tonalite. It behaves in a similar way to K_2O, increasing as SiO_2 increases. Ba (Fig. 8.10n) also behaves in a very similar manner, but the abundances of

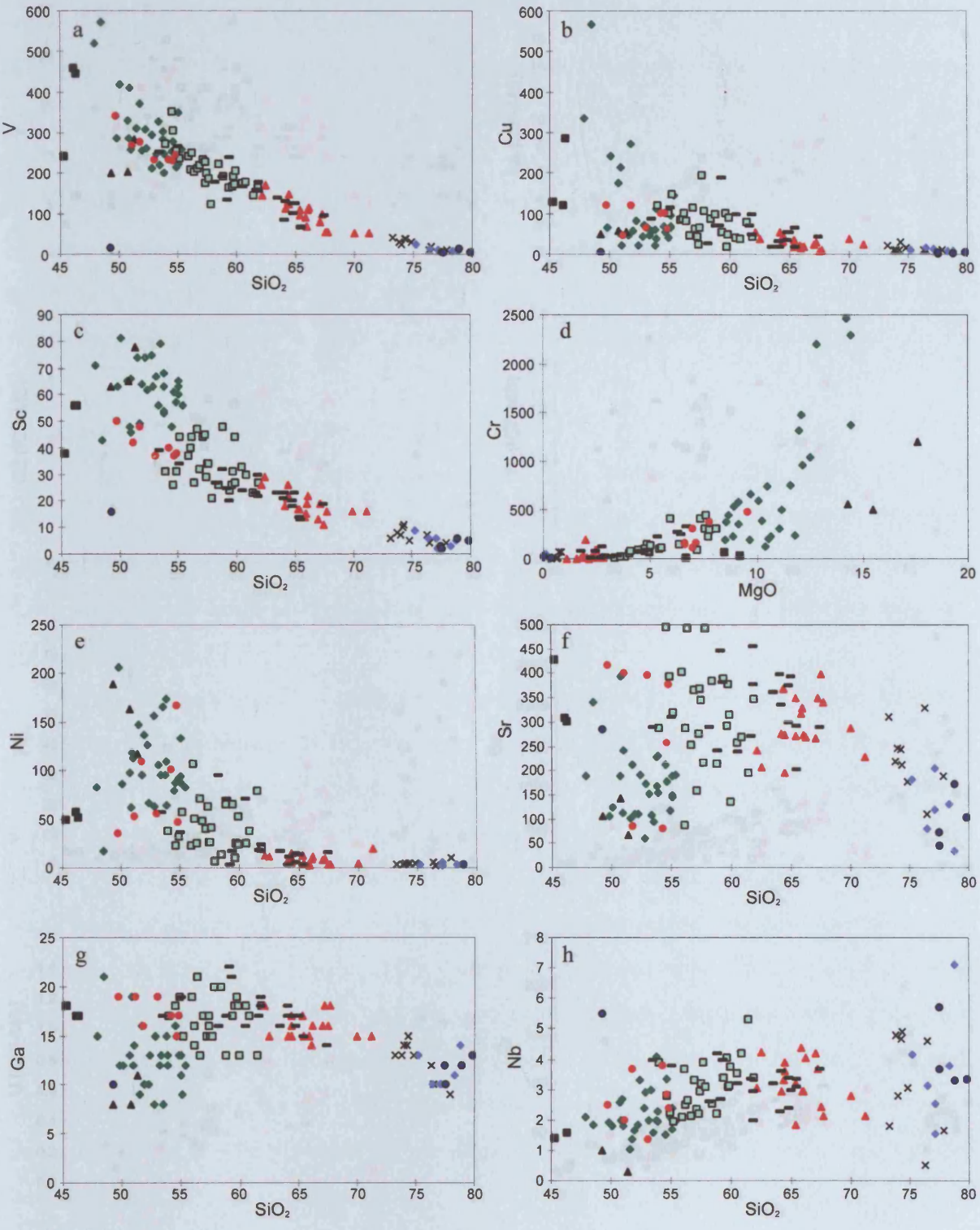

Figs. 8.10 a-h: Plots of trace elements vs. SiO_2 (except Cr, which is plotted against MgO) for the batholith. Figs. 8.10 i-p can be found on the next page. All trace element data in ppm, analysed by XRF.

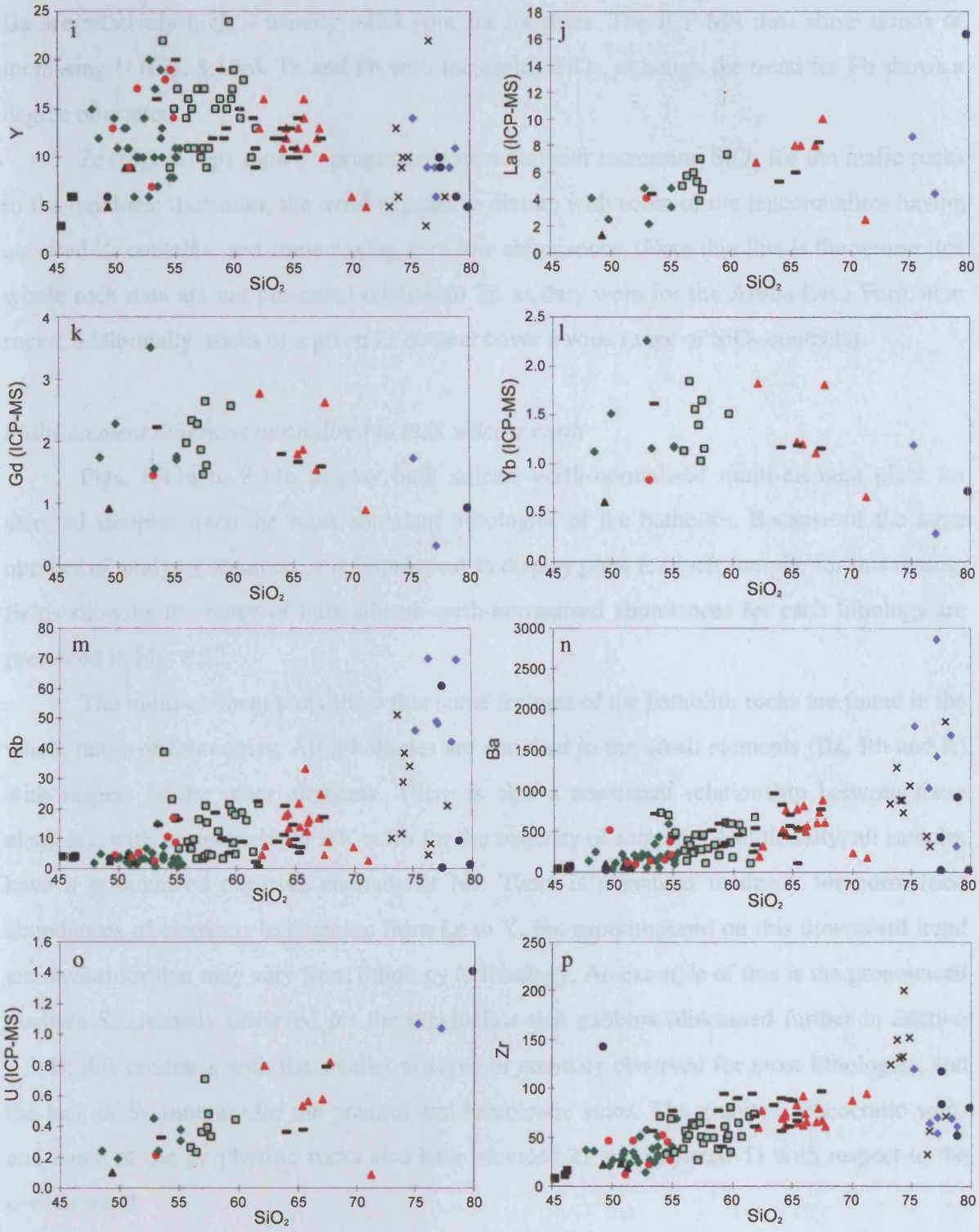

Figs. 8.10 i-p: Plots of trace elements vs. SiO_2 for the batholith. All trace element data in ppm, analysed by XRF except La, Gd, Yb, U, which were analysed by ICP-MS.

Ba are relatively high – usually >400 ppm for tonalites. The ICP-MS data show trends of increasing U (Fig. 8.10o), Th and Pb with increasing SiO_2, although the trend for Pb shows a degree of scatter.

Zr (Fig. 8.10p) shows a progressive increase with increasing SiO_2 for the mafic rocks to the tonalites; thereafter, the trend appears to divide, with some of the leucotonalites having elevated Zr contents, and some having very low abundances. (Note that this is the reason that whole rock data are not presented relative to Zr, as they were for the Aruba Lava Formation rocks; additionally, rocks of a given Zr content cover a wide range of SiO_2 contents).

Multi-element diagrams normalised to bulk silicate earth

Figs. 8.11a to 8.11e display bulk silicate earth-normalised multi-element plots for selected samples from the most abundant lithologies of the batholith. Because of the large number of analyses obtained, it is impractical to display plots for each sample: for this reason, fields showing the range of bulk silicate earth-normalised abundances for each lithology are presented in Fig. 8.12.

The multi-element plots show that some features of the batholith rocks are found in the whole range of lithologies. All lithologies are enriched in the alkali elements (Ba, Rb and K) with respect to the other elements. There is also a consistent relationship between these elements, with normalised Ba > K > Rb for the majority of samples. Additionally, all samples have a pronounced negative anomaly at Nb. There is a general tendency for normalised abundances of elements to decrease from La to Y, but superimposed on this downward trend are deviations that may vary from lithology to lithology. An example of this is the pronounced positive Sr anomaly observed for the plagioclase-rich gabbros (discussed further in Section 8.3.3); this contrasts with the smaller positive Sr anomaly observed for most lithologies, and the lack of Sr anomaly for the granites and leucocratic veins. The granites, leucocratic veins and some of the porphyritic rocks also have elevated Zr and depleted Ti with respect to the overall trend.

The normalised Y contents of these rocks do not vary significantly between lithologies, and are between ~1 and 5 times bulk silicate earth. The main differences between the patterns for the different lithologies arise from the varying degree of enrichment of the alkali and rare earth elements. For the mafic rocks, this relative enrichment is very small, such that the observed patterns are almost flat. For the silicic rocks, the relative enrichment of these elements compared to Y is very conspicuous, and results in steeper patterns.

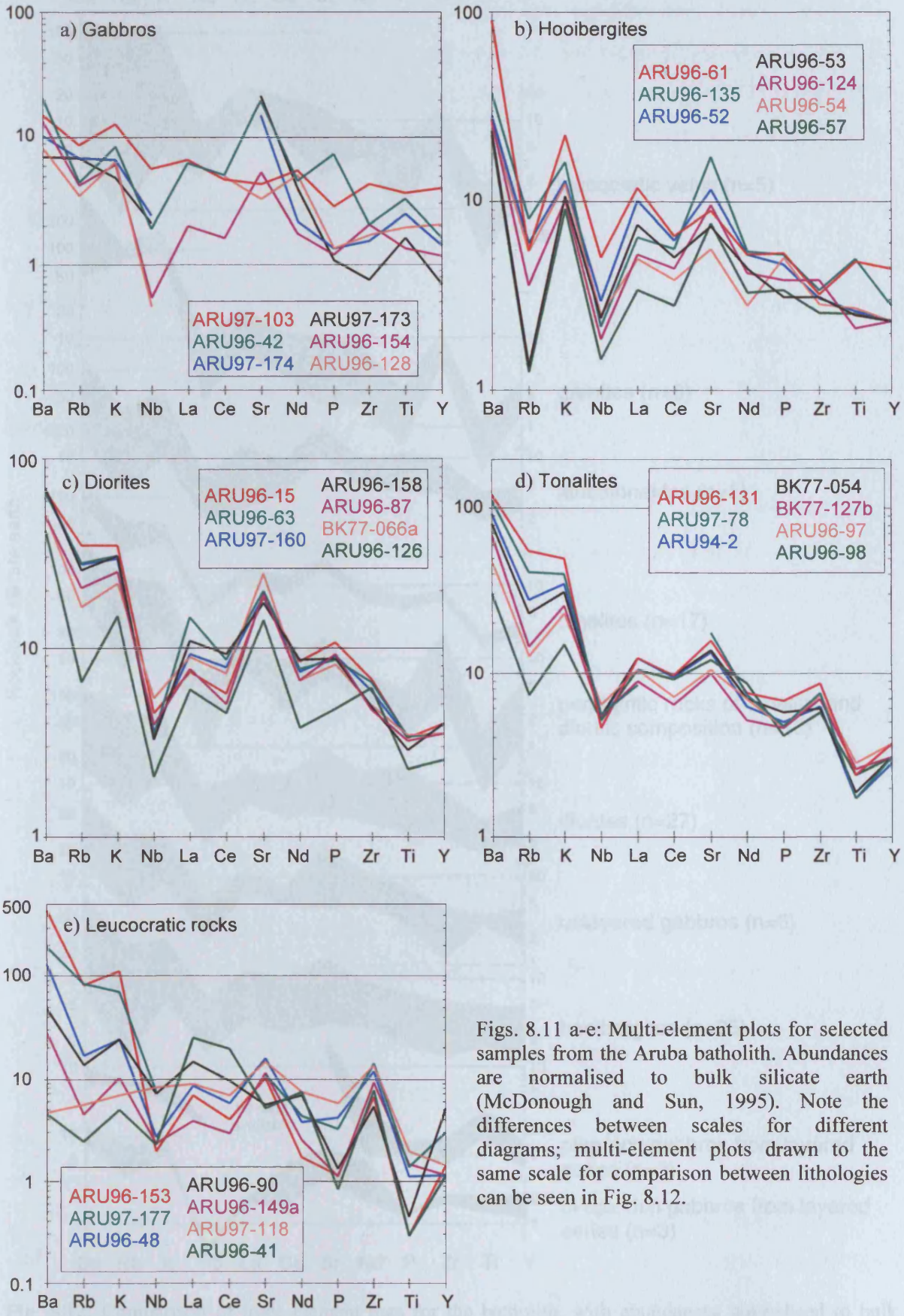

Figs. 8.11 a-e: Multi-element plots for selected samples from the Aruba batholith. Abundances are normalised to bulk silicate earth (McDonough and Sun, 1995). Note the differences between scales for different diagrams; multi-element plots drawn to the same scale for comparison between lithologies can be seen in Fig. 8.12.

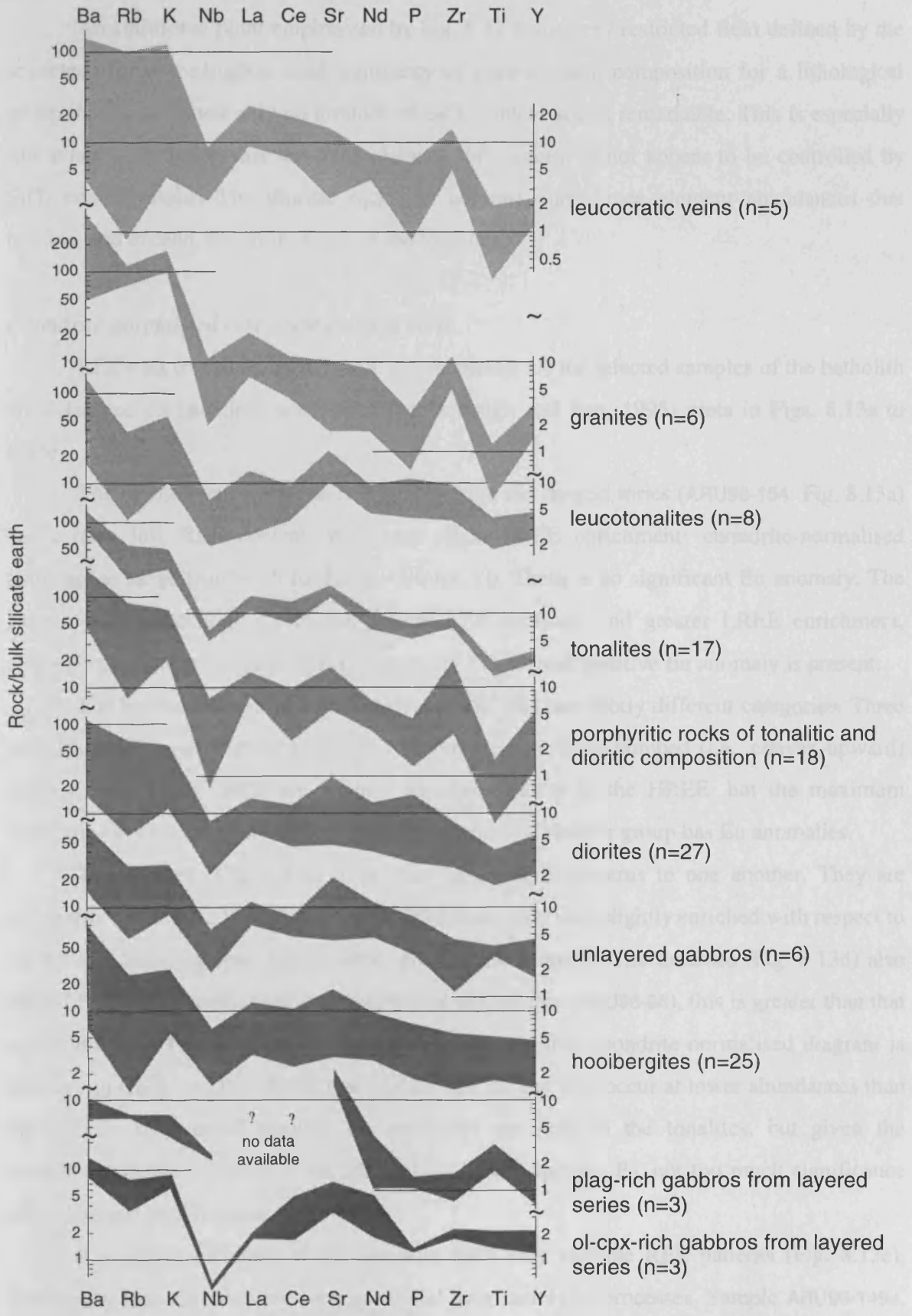

Fig. 8.12: Comparison of trace element data for the batholith, with abundances normalised to bulk silicate earth (McDonough and Sun, 1995). All are drawn to the same scale, and the number of analyses (n) included in each field is stated. Lithologies approximately arranged in order of decreasing MgO towards the top of the page.

An additional point emphasised by Fig. 8.12 is the very restricted field defined by the seventeen tonalite samples. Such constancy of trace element composition for a lithological group that was defined only on grounds of SiO_2 content seems remarkable. This is especially true when considering that the trace element abundances do not appear to be controlled by SiO_2 content alone. The dioritic rocks, in contrast, have trace element abundances that include, and exceed, the entire range of the tonalites.

Chondrite-normalised rare earth element plots

REE data (obtained by ICP-MS: see Appendix D) for selected samples of the batholith are displayed on chondrite-normalised (McDonough and Sun, 1995) plots in Figs. 8.13a to 8.13e.

The olivine- and pyroxene-rich gabbro from the layered series (ARU96-154: Fig. 8.13a) has a very low REE content, with very slight LREE enrichment: chondrite-normalised abundances range from ~5.5 for La to ~3.6 for Yb. There is no significant Eu anomaly. The gabbro (ARU96-42: Fig. 8.13a) has greater REE contents, and greater LREE enrichment, although the pattern for the HREE is essentially flat; a small positive Eu anomaly is present.

The hooibergites (Fig. 8.13b) appear to fall into two subtly different categories. Three samples show small degrees of LREE enrichment; three have humped (i.e., convex-upward) patterns, where the LREE are slightly enriched relative to the HREE, but the maximum chondrite-normalised abundances occur for Nd and Sm. Neither group has Eu anomalies.

The diorites (Fig. 8.13c) have very similar REE patterns to one another. They are noticeably enriched in the LREE, but the MREE are only very slightly enriched with respect to the HREE. Some samples have a small positive Eu anomaly. The tonalites (Fig. 8.13d) also show LREE enrichment: with the exception of one sample (ARU96-98), this is greater than that of the diorites. The MREE-HREE segment of the tonalite chondrite-normalised diagram is concave-upward, i.e., the MREE (particularly Ho, Er and Tm) occur at lower abundances than the HREE. Very small positive Eu anomalies are seen in the tonalites, but given the uncertainty in the accuracy of the Eu analyses (see Appendix E), not too much significance should be assigned to these.

The silicic members of the batholith have very variable REE patterns (Fig. 8.13e), which may indicate that they were generated by a variety of processes. Sample ARU96-149a, which is officially classed as a tonalite due to it having $SiO_2 < 72$ wt.%, is actually a silicic vein hand-picked (during crushing) from an amphibolite of the Aruba Lava Formation. It has

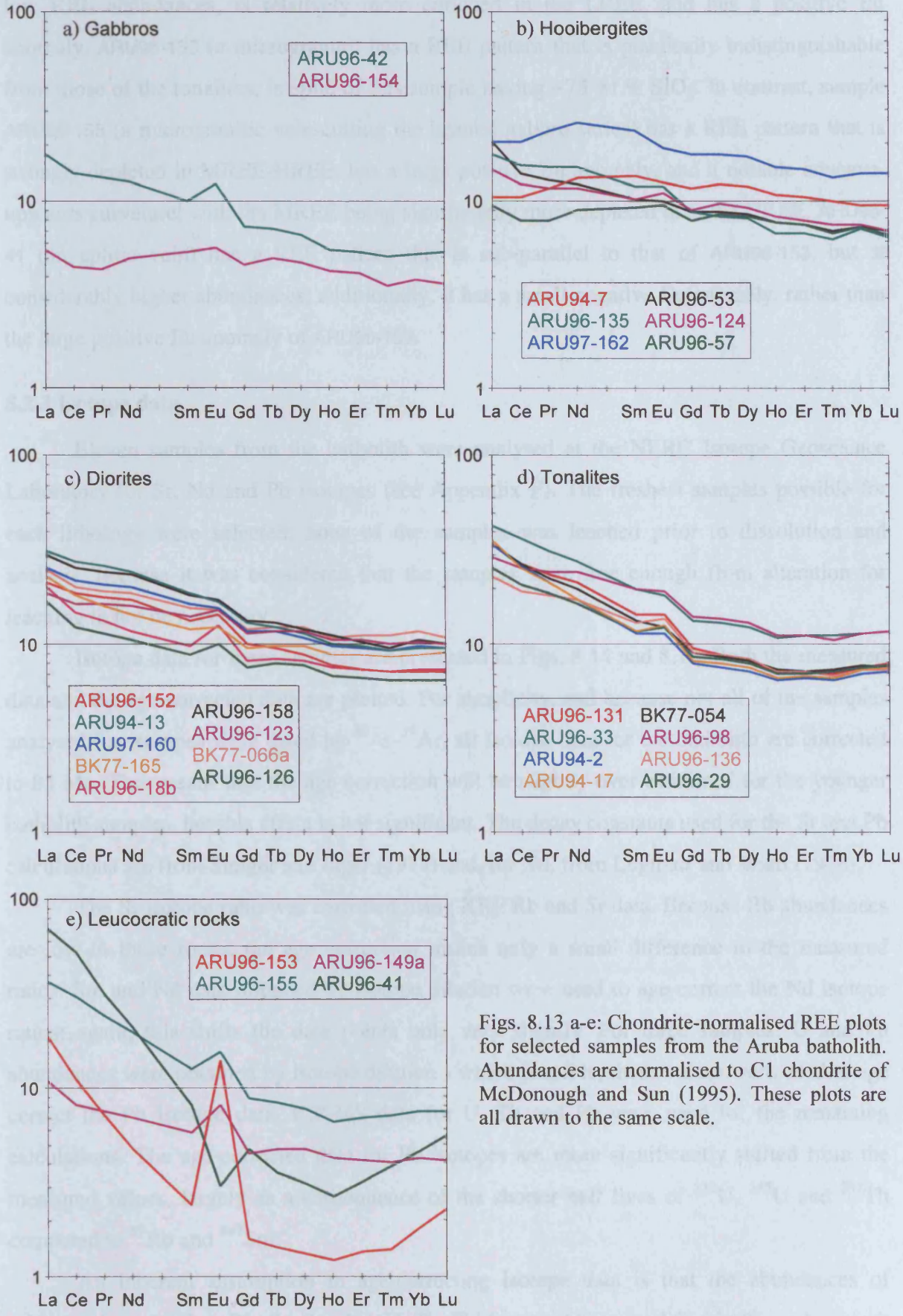

Figs. 8.13 a-e: Chondrite-normalised REE plots for selected samples from the Aruba batholith. Abundances are normalised to C1 chondrite of McDonough and Sun (1995). These plots are all drawn to the same scale.

low REE abundances, is relatively more enriched in the LREE, and has a positive Eu anomaly. ARU96-155 (a microgranite) has a REE pattern that is practically indistinguishable from those of the tonalites, in spite of this sample having ~75 wt.% SiO_2. In contrast, sample ARU96-153 (a microgranitic vein cutting the layered gabbro series) has a REE pattern that is strongly depleted in MREE-HREE, has a large positive Eu anomaly, and a notable concave-upwards curvature, with the MREE being significantly more depleted than the HREE. ARU96-41 (an aplitic vein) has a REE pattern that is sub-parallel to that of ARU96-153, but at considerably higher abundances; additionally, it has a small negative Eu anomaly, rather than the large positive Eu anomaly of ARU96-153.

8.2.3 Isotope data

Eleven samples from the batholith were analysed at the NERC Isotope Geoscience Laboratory for Sr, Nd and Pb isotopes (see Appendix F). The freshest samples possible for each lithology were selected; none of the samples was leached prior to dissolution and analysis, because it was considered that the samples were free enough from alteration for leaching to not be necessary.

Isotope data for these samples are presented in Figs. 8.14 and 8.15. Both the measured data and the age corrected data are plotted. For simplicity, and because not all of the samples analysed for isotopes were dated by ^{40}Ar-^{39}Ar, all isotope data for the batholith are corrected to 85 Ma. This means that the age correction will be slightly over-estimated for the younger batholith samples, but this effect is not significant. The decay constants used for the Sr and Pb calculations are from Steiger and Jäger (1977) and, for Nd, from Lugmair and Marti (1978).

The Sr isotope ratio was corrected using XRF Rb and Sr data. Because Rb abundances are low in these rocks, the age correction makes only a small difference to the measured ratios. Sm and Nd data obtained by isotope dilution were used to age-correct the Nd isotope ratios; again, this shifts the data points only very slightly. For three samples, U and Pb abundances were obtained by isotope dilution - where possible, these values were used to age correct the Pb isotope data. ICP-MS data for U, Th and Pb were used for the remaining calculations. The age-corrected data for Pb isotopes are more significantly shifted from the measured values, largely as a consequence of the shorter half lives of ^{238}U, ^{235}U and ^{232}Th compared to ^{87}Rb and ^{147}Sm.

An inherent assumption in age-correcting isotope data is that the abundances of relevant elements (i.e., Rb, Sr, Sm, Nd, U, Th, Pb) have not been modified in the rock since it cooled through its closure temperature. The smoothness of the REE patterns obtained for

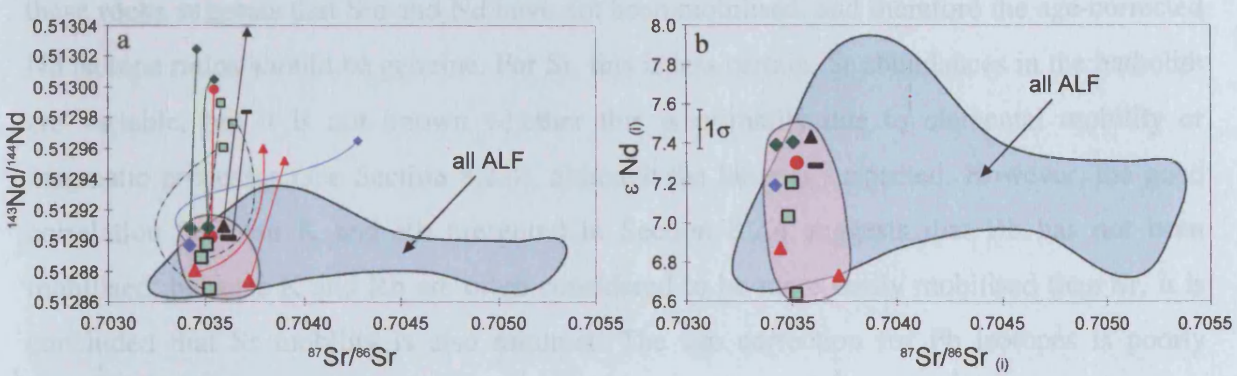

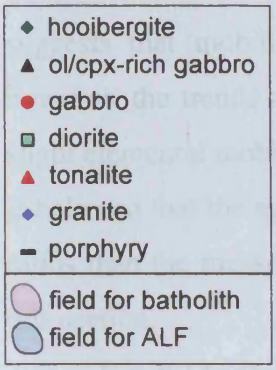

Fig. 8.14a: Measured Sr and Nd isotope ratios for the Aruba batholith (small symbols) compared to data age-corrected to 85Ma (large symbols). Data for individual samples are joined with a line. The age-corrected (to 88Ma) field of the Aruba Lava Formation (ALF) samples is included for comparison.

Fig. 8.14b: Age-corrected (85 Ma) Sr isotope ratios and $\varepsilon Nd_{(t=85\ Ma)}$ for the batholith, compared with equivalent data for the Aruba Lava Formation (t=88Ma), shown as a field. 1σ analytical error bars for εNd are indicated; the analytical error for $^{87}Sr/^{86}Sr$ is within the size of the symbol. This does not include errors arising from uncertainty in the age used for correction.

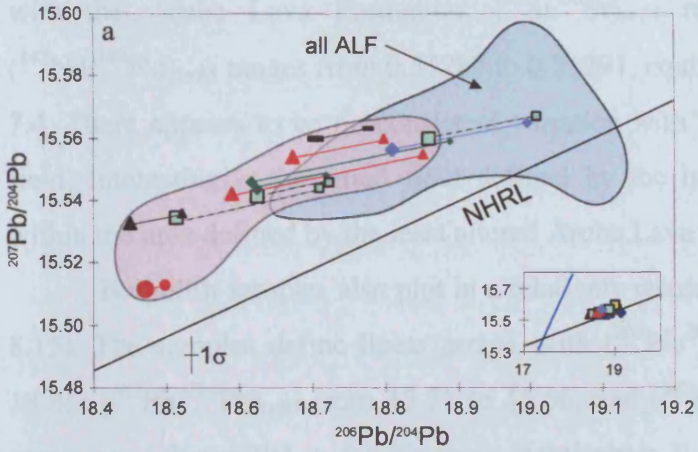

Fig. 8.15a: Measured $^{207}Pb/^{204}Pb$ vs. $^{206}Pb/^{204}Pb$ for the Aruba batholith (small symbols) compared to data age-corrected to 85Ma (large symbols). The age-corrected (88Ma) field of the ALF samples is included for comparison. The small inset shows the location of these Pb isotope ratios compared with the Northern Hemisphere Reference Line (NHRL: black) and the geochron (blue). 1σ errors given by the external reproducibility on the standards are indicated; these do not include uncertainties arising from the age correction.

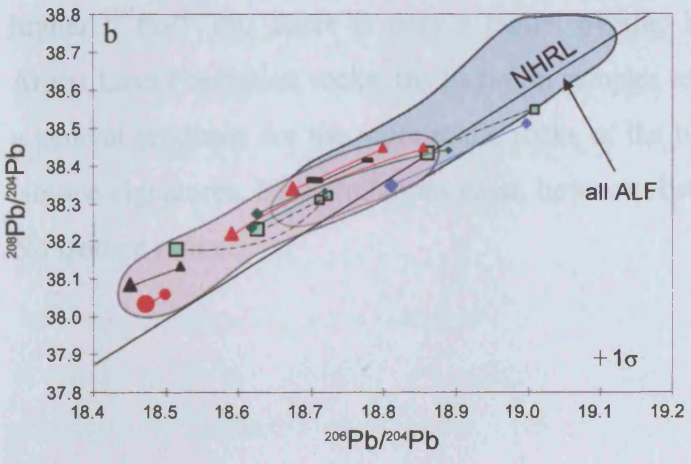

Fig. 8.15b: Measured $^{208}Pb/^{204}Pb$ vs. $^{206}Pb/^{204}Pb$ for the Aruba batholith compared to data age-corrected to 85Ma (symbols as above). The age-corrected (88Ma) field of the ALF samples is included for comparison. 1σ errors given by the external reproducibility on the standards are indicated; these do not include uncertainties arising from the age correction.

these rocks suggests that Sm and Nd have not been mobilised, and therefore the age-corrected Nd isotope ratios should be genuine. For Sr, this is less certain. Sr abundances in the batholith are variable, but it is not known whether this is primarily due to elemental mobility or magmatic processes (see Section 8.2.4), although the latter is suspected. However, the good correlation between K and Rb presented in Section 8.2.4 suggests that Rb has not been mobilised; because K and Rb are often considered to be more easily mobilised than Sr, it is concluded that Sr mobility is also minimal. The age correction for Pb isotopes is poorly constrained. There is a detectable positive correlation between U, Th, Pb and SiO_2, which suggests that mobility has not obliterated the magmatic abundances of these elements; however, the trends are poorly defined. This may be a result of poor analytical precision, or slight elemental mobility: either way, it leads to an error in the age correction. Nevertheless, it is believed that the age corrected data are a more representative indicator of magmatic isotope ratios than the measured data, and it is therefore the age corrected data that are discussed in this section.

Fig. 8.14a shows measured and age corrected Sr and Nd isotope data for the batholith, and Fig. 8.14b displays only the age corrected data ($\varepsilon Nd_{t=85}$ and $(^{87}Sr/^{86}Sr)_{t=85}$) for comparison with the Aruba Lava Formation. $(^{87}Sr/^{86}Sr)_{t=85}$ ranges from 0.7034 to 0.7037, and $(^{143}Nd/^{144}Nd)_{t=85}$ ranges from 0.51287 to 0.51291, equivalent to a range of $\varepsilon Nd_{t=85}$ from 6.6 to 7.4. There appears to be no consistent variation with lithology – all samples plot in a small field. Interestingly, the small field defined by the batholith samples is entirely contained within the area defined by the least altered Aruba Lava Formation basalts and dolerites.

Batholith samples also plot in a relatively restricted range in terms of Pb isotopes (Fig. 8.15). The samples define linear arrays, with $(^{206}Pb/^{204}Pb)_{t=85}$ values ranging from 18.45 to 18.86; $(^{207}Pb/^{204}Pb)_{t=85}$ from 15.51 to 15.56; and $(^{208}Pb/^{204}Pb)_{t=85}$ from 38.03 to 38.43. The arrays are sub-parallel to the Northern Hemisphere Reference Line, but slightly displaced to higher $^{207}Pb/^{204}Pb$. There is only a partial overlap between the batholith samples and the Aruba Lava Formation rocks: the batholith samples extend to less radiogenic values. There is a general tendency for the more mafic rocks of the batholith to have the least radiogenic Pb isotope signatures. No correlations exist, however, between Pb isotope ratios and either Sr or Nd isotope ratios.

8.2.4 Uncertainty in batholith geochemical analyses: sampling and alteration

It was noted in the previous sections that a number of the plots of geochemical data show a degree of scatter from the main trend: this must be evaluated and considered before interpreting the geochemical data petrogenetically. There are a number of potential causes for these scattered trends, but unfortunately, owing to the complexity of plutonic rock environments, it is extremely difficult to evaluate the true cause of this variation. In a complex system such as this, there is no *a priori* reason, for example, to suspect that a particular element should behave in a coherent fashion with respect to SiO_2, MgO or Zr, and so the approach used to determine elemental mobility in the Aruba Lava Formation rocks is not valid. Potential causes for deviation from main trends include:

- genuine differences in melt compositions.
- differences in proportions of minerals between different samples, arising from the accumulative nature of some of the rocks.
- elemental mobility during alteration of the rocks, either during hydrothermal alteration, or subsequent weathering.
- collection of samples that were not large enough to be representative.
- analytical uncertainty (see Appendix E).

Fig. 8.16 demonstrates that the rocks of the batholith are not heavily altered, and is in agreement with the petrographic studies. Loss-on-ignition (LOI) values are mainly less than 1.2 wt.% for all lithologies except the porphyritic rocks, which have higher LOI, possibly due to higher degrees of alteration in their finer-grained groundmass. There is a crude decrease in LOI from the hooibergites to the silicic rocks, which may indicate that the dehydration of hornblende is an important factor influencing LOI values. (This contribution to LOI from hornblende more than compensates for the expected weight increase on heating for the iron-rich lithologies.) An alternative explanation is that the more mafic lithologies (which happen to have a higher hornblende content) have more mafic minerals that are prone to alteration to clays, and the trend of decreasing LOI with increasing SiO_2 is controlled by bulk composition, rather than specifically the amount of hornblende present.

It was shown in Section 7.3 that the alteration suffered by minerals of the batholith is not severe. Ferromagnesian minerals are slightly altered, but it is not known to what extent different components were added to, or removed from, the system. In general, the most common secondary minerals are chlorite and epidote; additionally, SiO_2 has clearly been mobilised by hydrothermal fluids, resulting in late stage quartz veins. Plagioclase also appears

to be prone to alteration. This suggests that elemental mobility should be suspected for SiO_2, CaO, NaO, K_2O, $Fe_2O_{3(t)}$, Al_2O_3, Sr, and Ba, and this can be evaluated further by reconsideration of the element-element plots presented in Section 8.2.

The porphyries, tonalites and more acidic rocks define tight trends for most elements vs. SiO_2: these include MgO, TiO_2, Al_2O_3, $Fe_2O_{3(t)}$, MnO, CaO, Zr, Sc, V, Cr, Co, Ni, Zn, and Ga. This suggests that these elements have not been significantly mobile in these lithologies. The smoothness of the REE patterns, and good correlations between different REE suggest that these elements have been relatively immobile, although they do not necessarily show a good correlation with SiO_2. In contrast, the trends for these immobile elements are more scattered in the diorites and hooibergites. This could mean either that these lithologies are more prone to alteration and elemental mobility, or that the variable compositions are genuine igneous features. Because the majority of the rocks are relatively fresh in thin section, and that the degree of scatter is similar for a wide range of elements (including those considered to be immobile, e.g., Ti, and those considered to be mobile, e.g., Na_2O), it is inferred that this variation is an original feature of these lithologies.

The plagioclase-rich gabbroic rocks from the layered series consistently plot away from the main trends. This is, therefore, unlikely to be a consequence of alteration, which should have an essentially random effect on the compositions of rocks; instead, it is concluded that the compositions of these rocks represent primary igneous variation.

Na_2O, K_2O, Rb and Ba appear to show more scatter over the whole range of lithologies than is observed for the majority of the major elements. Because these elements are present in plagioclase (which is observed to be altered in some samples), and because they tend to be soluble in aqueous (e.g., hydrothermal) fluids, they may be more prone to mobility during alteration. However, plots of Ba and Rb vs. K_2O (Fig. 8.17) demonstrate that these elements have good correlations with one another. This means, firstly, that these elements behave similarly in the processes that have contributed to generation and evolution of the batholith, and secondly, that the ratios of these elements have not been significantly modified by secondary processes, such as alteration. These good correlations do not extend to the very silicic rocks of the batholith, but this is unsurprising given the large variability in trace element compositions already reported for these lithologies: this is more likely to be an original composition feature, and is not necessarily related to elemental mobility during alteration.

P_2O_5 is also rather variable: because P is a high field strength element, and is therefore considered to be relatively immobile, it appears that this scatter is unlikely to be due to alteration. It could, however, result from samples containing unrepresentative proportions of apatite. Nb, Y, U, Th and Pb also show relatively large amounts of scatter. Although some of this scatter arises from analytical uncertainty (these elements occur at low abundances in these rocks: see Appendix E), genuine compositional variation cannot be ruled out. Cu contents are also variable, due to the mobility of Cu in the batholith's hydrothermal circulation system: Cu abundances are, therefore, not used for any of the petrogenetic interpretations in this study.

Sr shows the most variability of any of the major or trace elements when plotted against SiO_2. However, a plot of Sr vs. Al_2O_3 (Fig. 8.18) shows that there is a systematic relationship between these two elements, indicating that the Sr contents are certainly not random and, therefore, that the large variability in Sr is not purely a function of alteration. Because those samples with the highest Sr also have the highest Al_2O_3, a more likely explanation is that the abundances of both elements are controlled by the behaviour of plagioclase in the system.

8.3 Mineralogical controls on whole-rock compositions

It was demonstrated in Chapter 7 that many of the rocks of the batholith, particularly the mafic rocks, have petrographic characteristics consistent with them having originated by crystal accumulation processes. Any accumulation of a particular phase during crystallisation of a magma body, whether in an open or closed magma system, can have profound effects on the compositions of the resultant whole rock. It is particularly important, in a petrogenetic study such as this one, to account for these mineralogical controls on whole rock composition, because petrogenetic interpretations of geochemical data commonly assume that a whole-rock composition is representative of a melt composition. If this assumption is not true, any petrogenetic modelling will be invalid. The aim of this section is, therefore, to use geochemical data to evaluate to what extent the rocks of the batholith represent accumulated crystals, or whether they preserve genuine liquid compositions.

The lithological groups that are considered in this section are the gabbros of the layered series and the hooibergites, because these are the lithologies that show the strongest evidence for crystal accumulation in thin section. It should be noted, however, that mineralogical controls on whole rock composition may also operate on a more subtle level: delicate shifts, for example, in the proportion of plagioclase present in diorites and tonalites

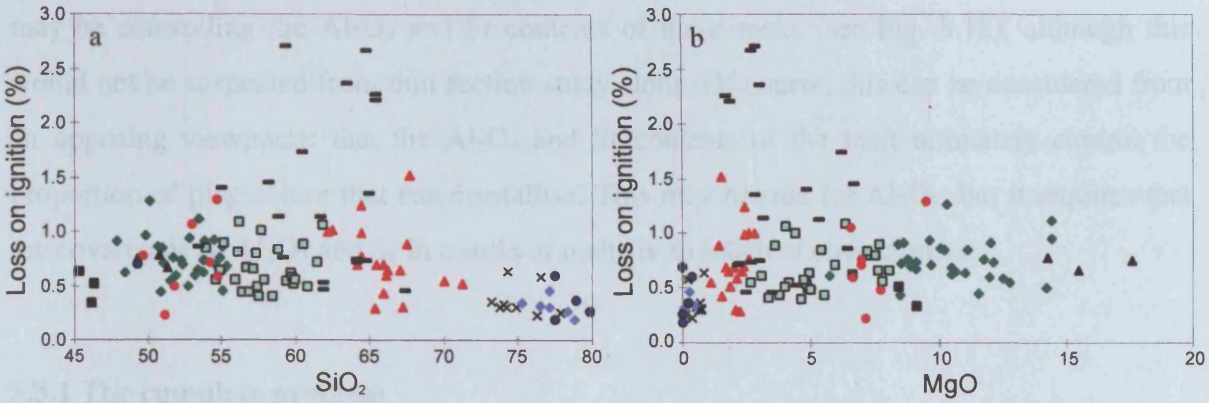

Figs. 8.16a and b: Plots of loss on ignition vs. SiO_2 and MgO for rocks of the batholith.

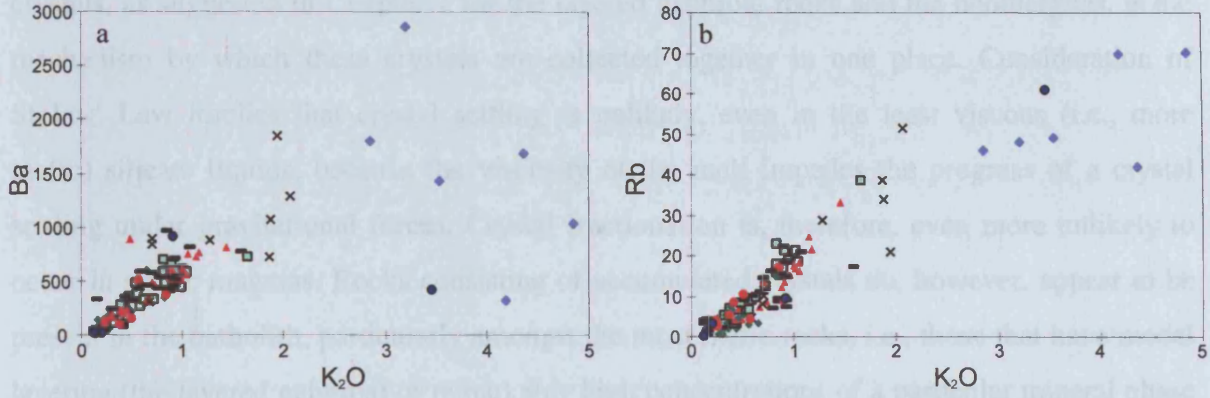

Figs. 8.17a and b: Plots of Ba and Rb vs. K_2O, demonstrating that there is a consistent relationship between these elements for most lithologies of the batholith.

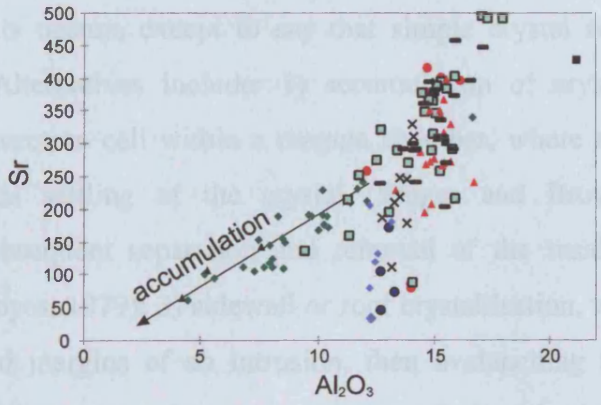

Figs. 8.18: Sr vs. Al_2O_3 for rocks of the batholith; one anorthite-rich leucocratic vein sample plots off this scale, at ~290 ppm Sr and 30.5 wt.% Al_2O_3. This demonstrates that accumulation of minerals in the hooibergites and gabbros does not control the compositions of other members of the batholith: any residual liquids derived by this method would plot on a trend pointing to the upper right. The presence of some residual liquids from gabbro/hooibergite existing within the batholith is not precluded, providing that the proportion of cumulate:residual liquid is low.

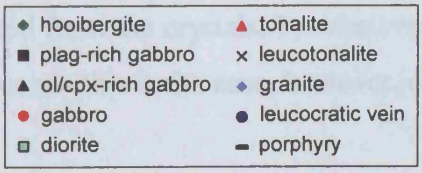

may be controlling the Al_2O_3 and Sr contents of these rocks (see Fig. 8.18), although this would not be suspected from thin section study alone. Of course, this can be considered from an opposing viewpoint: that the Al_2O_3 and Sr contents of the melt ultimately control the proportion of plagioclase that can crystallise. This may be true for Al_2O_3, but it requires that the covariance of Al_2O_3 and Sr in a suite of melts is an inherent characteristic.

8.3.1 The cumulate problem

One difficulty with the formulation of rocks consisting almost entirely of accumulated crystals, as suggested in Chapter 7 for the layered gabbroic rocks and the hooibergites, is the mechanism by which these crystals are collected together in one place. Consideration of Stokes' Law implies that crystal settling is unlikely, even in the least viscous (i.e., more mafic) silicate liquids, because the viscosity of the melt impedes the progress of a crystal settling under gravitational forces. Crystal fractionation is, therefore, even more unlikely to occur in silicic magmas. Rocks consisting of accumulated crystals do, however, appear to be present in the batholith, particularly amongst the most mafic rocks, i.e., those that have modal layering (the layered gabbros) or remarkably high concentrations of a particular mineral phase (some of the hooibergites).

It is beyond the scope of the thesis to debate in detail the mechanism(s) by which this accumulation of crystals occurs, except to say that simple crystal settling is not the only possible mechanism. Alternatives include: 1) accumulation of crystals at the base of a downward-moving convection cell within a magma chamber, where the downwards motion assists the gravitational settling of the crystal (Wager and Brown, 1968); 2) in-situ crystallisation, with subsequent separation and removal of the residual liquid (Campbell, 1978; McBirney and Noyes, 1979); 3) sidewall or roof crystallisation, with crystals forming at the most rapidly-cooled margins of an intrusion, then avalanching to the base in density currents (Irvine, 1980); and 4) random accumulation of phenocrysts during flowage of a crystal-rich magma to form glomerocrysts (Williams *et al.*, 1954), which would then be large enough to overcome the resistance to settling provided by the viscosity of the liquid.

For the purposes of this thesis, therefore, a cumulate rock is defined as any rock that does not represent a true liquid composition, i.e., a rock where the residual liquid from crystallisation has been separated from the crystals, by whatever mechanism. In practice, it is difficult to determine whether or not this is the case; however, comparison of whole-rock data

with compositions of individual phases will at least give some information on whether the rock is likely to have been formed by crystal accumulation.

A further question to be addressed when considering crystal accumulation processes is the nature of the magmatic system: for example, whether the magma chamber was filled by a single magma influx, and developed as a closed system, or whether it was periodically replenished and tapped as it fractionated (i.e., an open system; O'Hara, 1977). This is potentially important, because it may be necessary (later) to evaluate whether the silicic members of the batholith can be derived via fractional crystallisation of the more mafic members: if not, a number of considerations arise. Firstly, if the residual liquids are no longer present in the batholith, they must have been extracted from the system, i.e., erupted, or emplaced into higher level magma chambers that have been subsequently eroded off. Secondly, if the silicic members of the batholith cannot be generated by fractional crystallisation of the mafic members, they must have been generated by some other mechanism.

8.3.2 Comparison of whole-rock compositions with phase compositions

In theory, if a rock crystallises in a closed system, and the crystallising minerals re-equilibrate with the liquid throughout the crystallisation process, it would be expected that in the end product of crystallisation (the whole rock), all the phases present are in equilibrium both with one another and with the whole rock; for example, any relatively high Mg# phases (e.g., olivine, clinopyroxene) are compensated for by low Mg# phases (e.g., magnetite) to make up a rock with intermediate Mg#. If it can be shown that the constituent phases are not in equilibrium with the whole-rock composition, it must be suspected that components have been added to, or removed from, the system.

Olivine- and pyroxene-rich gabbros from the layered series

This lithology is the most MgO-rich analysed in this study: the three samples analysed have whole-rock Mg#s between 74 and 78. It should be noted here that these Mg#s are higher than those predicted for a primary mantle melt, which suggests that these rocks do not represent realistic liquid compositions. If this whole-rock composition *did* represent a liquid composition, the first phase to crystallise from this melt would be forsteritic olivine (Fo_{93}: TRACE3; Nielsen, 1988). The actual olivine compositions measured in this rock are homogeneous, and range from $Fo_{75.4}$ to $Fo_{76.5}$: these must have been derived from a liquid with a significantly lower MgO/FeO. In fact, using a Fe^{2+}-Mg exchange distribution

coefficient of 0.3 for olivine and melt (Roeder and Emslie, 1970), these olivines grew from a melt having Mg# ≈ 50. This result is broadly consistent with the pyroxene compositions: orthopyroxene Mg# averages 78, in equilibrium with liquid having Mg# ≈ 49 if $K_D^{Fe^{2+}\text{-}Mg}{}_{opx\text{-}liq}$=0.28; clinopyroxene Mg# averages 83, in equilibrium with liquid having Mg# ≈ 50 if $K_D^{Fe^{2+}\text{-}Mg}{}_{cpx\text{-}liq}$=0.23. Neither olivine, clinopyroxene nor orthopyroxene are magnesian enough to have grown from a liquid having Mg# > 70: it is therefore concluded that the high Mg# of the rock is a consequence of accumulation of Mg-rich phases.

Plagioclase-rich gabbros from the layered series

The plagioclase-rich gabbros have Mg#s between 61 and 63. Clinopyroxene in this rock has an average Mg# of 80. Using the same exchange coefficient as above, this clinopyroxene crystallised from a liquid having Mg# ≈ 47. Again, because the clinopyroxene cannot have crystallised from a liquid having the same composition of the bulk rock, it must be concluded that the rock formed via crystal accumulation. Another way of viewing this is that a low Mg# component (presumably the residual liquid) was removed from the system. This rock therefore fits the definition of a cumulate rock adopted for this thesis, i.e., one that is not representative of a liquid composition.

Hooibergites

The clinopyroxenes from hooibergites that have been analysed by electron microprobe have Mg#s of 79 to 73. These crystals would have grown in equilibrium with a melt having a Mg# of approximately 45. The hooibergite whole-rock Mg#s range from 62 to 82, indicating that the whole-rock Mg# is controlled by the Mg-rich ferromagnesian phases, and that the Mg-poor residual liquid has been (at least partially) lost from the system, i.e., that the hooibergites also represent accumulative rocks. Independent confirmation of this conclusion using other ferromagnesian phases is not possible, because the only other ferromagnesian phase in the hooibergites is magnesiohornblende, and $K_D^{Fe^{2+}\text{-}Mg}{}_{hbl\text{-}liq}$ reported in or derived from literature (e.g., Sen and Dunn, 1994; Klein *et al.*, 1997) is too variable to be particularly instructive.

8.3.3 Verification of cumulate characteristics using whole rock data

If the lithologies described above are truly cumulate rocks, it follows that it should be possible to account for their whole-rock compositional features by mixtures of the observed cumulus phases, with a minimal contribution from other phases (i.e., crystallised intercumulus liquids). This approach is used in Figs. 8.19 and 8.20: whole-rock compositions are plotted, together with compositions of the proposed cumulus phases, in order to verify that the

compositions of the whole rocks are indeed dominated by these phases. In this way, the proportions of other phases present can be estimated.

Gabbros from the layered series

Figs. 8.19a, 8.19c, 8.20a and 8.20b show that the olivine and pyroxene rich gabbros do not fall within the triangle defined by olivine, orthopyroxene and clinopyroxene. The observed compositions require the presence of a lower MgO, higher Al_2O_3 component. This may have been an intercumulus liquid phase, and is represented on the diagrams by the composition of the intercumulus plagioclase that is present in these rocks. Because the compositions of the ol-px gabbros lie very close to the ol-cpx-opx triangle, only a small proportion of intercumulus plagioclase is required to account for the observations. Additionally, even though petrographic evidence demonstrates that olivine is locally very abundant in this lithology, the whole-rock data, which are in effect compositions averaged over the scale of a large hand specimen, demonstrate that olivine is not a volumetrically important constituent. In Fig. 8.19b, the whole-rock compositions do lie within the ol-opx-cpx triangle, an observation that implies that the presence of intercumulus liquid is not required. This apparent contradiction may have arisen because opaque oxide phases are also present in this lithology: Fe-oxides (magnetite) will increase the $FeO_{(t)}$ abundances in the whole rock, moving the whole-rock data into the ol-opx-cpx triangle, even if intercumulus plagioclase *is* present. This hypothesis is verified by Fig. 8.20c: the whole-rock compositions cannot be explained entirely by any combination of olivine, orthopyroxene, clinopyroxene and plagioclase, because they require a high-TiO_2 component. This is also likely to be provided by a Fe-Ti oxide phase.

In Fig. 8.19a, 8.20a and 8.20b, the plagioclase-rich gabbros fall into the triangle defined by clinopyroxene, plagioclase and olivine. However, olivine was not observed in the thin sections of these rocks. Minor orthopyroxene, though, is present, but the whole-rock compositions do not fall within the cpx-plag-opx triangle on Figs. 8.19a, 8.19b, 8.19c and 8.20c There are two possible explanations of why the observed compositions cannot be explained by plagioclase, clinopyroxene and orthopyroxene alone: either the analysed rock aliquot *did* contain minor olivine, but the thin section did not (this is perfectly possible, because modal variations in this rock type occur over a range of only a few cm); or a low-MgO, low-SiO_2 phase is also present in these rocks. Again, opaque oxide phases (magnetite and ilmenite) were common in this lithology, so the latter explanation is preferred. This conclusion is verified by Fig. 8.19b, which implies that, if the deviation from the plag-cpx join

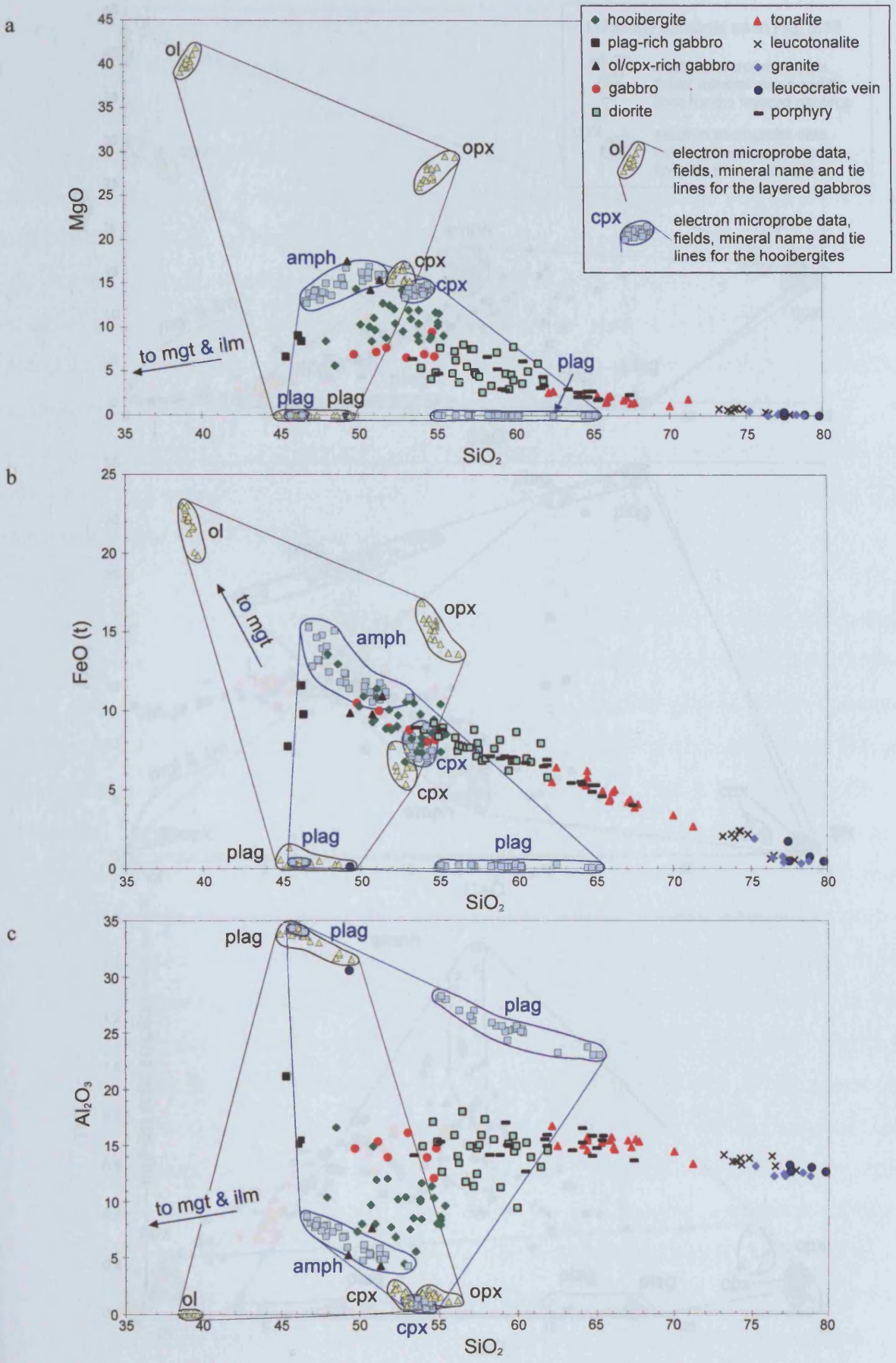

Figs. 8.19 a-c: Plots of major elements vs. SiO_2 for the batholith, and electron microprobe analyses of minerals from the layered ol-, cpx-, and plag-rich gabbros from the layered sequence. See text for discussion.

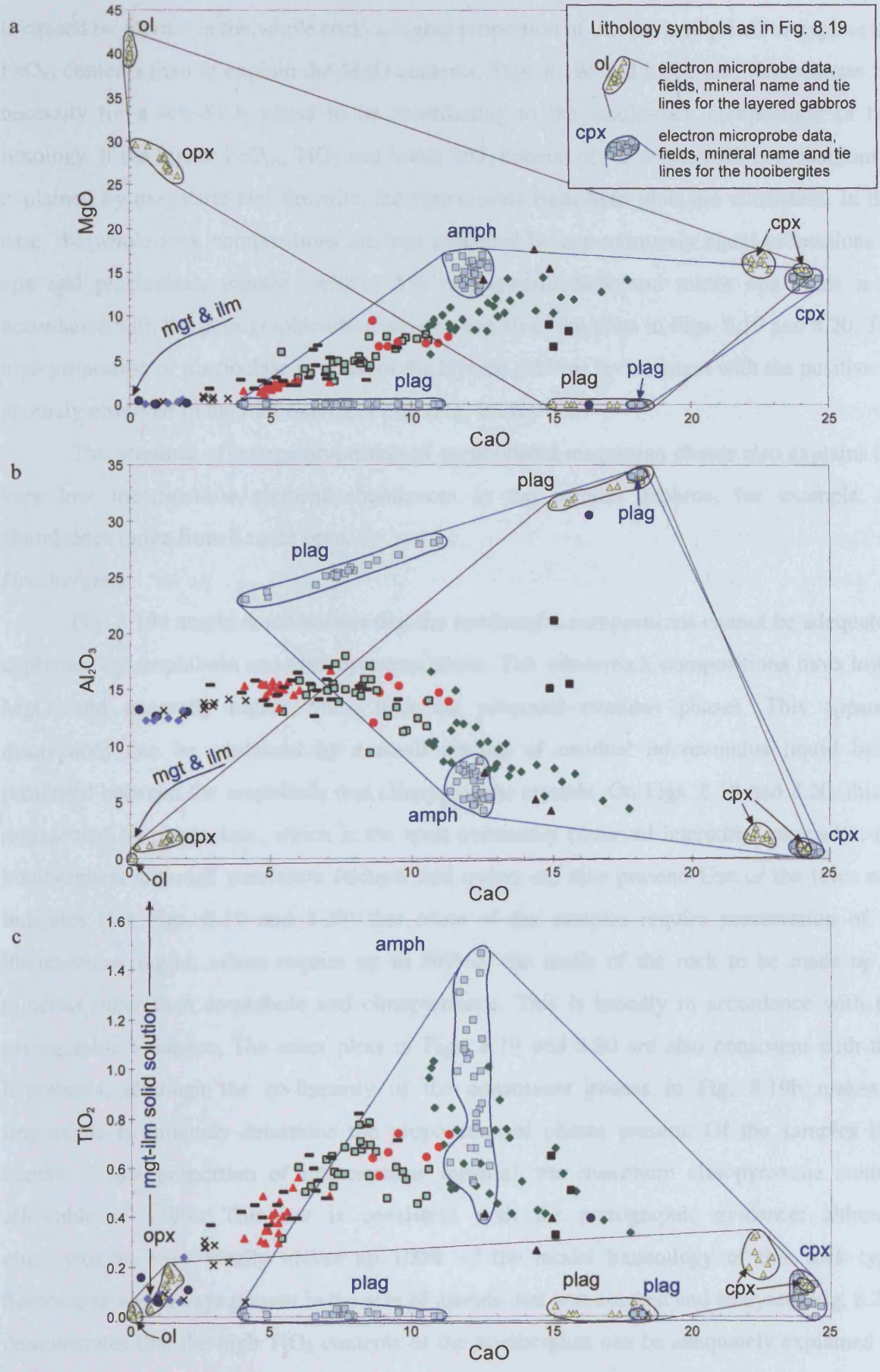

Figs. 8.20 a-c: Plots of major elements vs. CaO for the batholith, and electron microprobe analyses of minerals from the layered ol-, cpx-, and plag-rich gabbros from the layered sequence. See text for discussion.

is caused by olivine in the whole rock, a higher proportion of olivine is required to explain the $FeO_{(t)}$ contents than to explain the MgO contents. Figs. 8.19c and 8.20c also demonstrate the necessity for a low-SiO_2 phase to be contributing to the whole-rock composition of this lithology. If the higher $FeO_{(t)}$, TiO_2 and lower SiO_2 content of the whole-rock compositions is explained by magnetite and ilmenite, the conclusions from both plots are consistent. In this case, the whole-rock compositions are best modelled by approximately equal proportions of cpx and plagioclase, together with ~ 5% magnetite/ilmenite and minor opx. This is in accordance with the petrographic observations, and all of the plots in Figs. 8.19 and 8.20. The high proportion of plagioclase in some of the layered gabbros is consistent with the positive Sr anomaly observed in the multi-element plot (Fig. 8.11a).

The presence of a large proportion of accumulated magnesian phases also explains the very low incompatible element abundances in the layered gabbros, for example, Zr abundances range from 8 to 23 ppm.

Hooibergites

Fig. 8.19a amply demonstrates that the hooibergite compositions cannot be adequately explained by amphibole and clinopyroxene alone. The whole-rock compositions have lower MgO, and generally higher SiO_2, than the proposed cumulus phases. This apparent discrepancy can be explained by a small amount of residual intercumulus liquid being preserved between the amphibole and clinopyroxene crystals. On Figs. 8.19 and 8.20, this is represented by plagioclase, which is the most commonly observed interstitial mineral in the hooibergites, although potassium feldspar and quartz are also present. Use of the lever rule indicates (for Figs. 8.19 and 8.20) that some of the samples require preservation of no intercumulus liquid; others require up to 50% of the mode of the rock to be made up of minerals other than amphibole and clinopyroxene. This is broadly in accordance with the petrographic evidence. The other plots in Figs. 8.19 and 8.20 are also consistent with this hypothesis, although the co-linearity of the constituent phases in Fig. 8.19b makes it impossible to uniquely determine the proportions of phases present. Of the samples that contain a low proportion of intercumulus material, the maximum clinopyroxene content allowable is ~50%. This too is consistent with the petrographic evidence: although clinopyroxene very locally makes up 100% of the modal mineralogy of this rock type, hornblende was always present in the size of sample that was crushed and analysed. Fig. 8.20c demonstrates that the high TiO_2 contents of the hooibergites can be adequately explained by

the amphibole contents, although the presence of other Ti-bearing phases (especially titanite) was noted in the petrographic studies.

Minor and trace element data can also give a useful indication of which phases are controlling the composition of a whole rock. Sc, for example occurs at high abundances in the hooibergites: from 43 to 81 ppm (compared to values of ~40 to 45 ppm in MORB: Saunders, pers. comm.). Sc is relatively compatible in clinopyroxene (D_{Sc} values quoted by Green (1994) range from 0.5 to 4) and amphibole (D_{Sc} ~ 10: Gill, 1981). The high Sc abundances, coupled with the high clinopyroxene and amphibole content of the hooibergites are, therefore, unsurprising.

The existence of cumulate rocks that are so rich in clinopyroxene is somewhat unusual, as olivine is more commonly a liquidus phase for mafic, and even intermediate rocks. Clinopyroxene (rather than olivine) crystallisation is more likely to occur if the magma has a high silica activity: this is likely for the hooibergites, because the clinopyroxenes crystallised from a melt having an Mg# of only ~45, corresponding to a dioritic composition. Additionally, the presence of volatile species is likely to have an important effect. It has already been shown (in Chapter 7) that hornblende is also a liquidus phase in the hooibergite rocks, suggesting that these magmas had a high water content. However, in hydrous liquids, the olivine phase-field is expanded (Nicholls and Ringwood, 1973), meaning that olivine is more likely to be a crystallising phase. (This issue can be resolved if it is hypothesised that any olivine crystallisation occurred at greater depths, where $P_{(H_2O)}$ was even higher). However, the water content may not be the only controlling factor: according to Mysen and Kushiro (1974) whether olivine or pyroxene crystallises also depends on the oxygen fugacity of the magma. At the Ni-NiO oxygen fugacity buffer, olivine will not crystallise, whereas at the magnetite-wüstite buffer (i.e., lower oxygen fugacity), it may. There have also been suggestions that clinopyroxene crystallisation is more likely to occur at higher pressure (e.g., Bender *et al.*, 1978). This demonstrates that clinopyroxene crystallisation (rather than olivine) is controlled by a variety of factors, any of which might be responsible for the high clinopyroxene contents of the hooibergites.

The REE patterns of the hooibergites can also be explained by accumulation of clinopyroxene and hornblende from a dioritic liquid. Fig. 8.21 shows the results of modelling the REE chemistry of cumulus phases in hooibergites. For simplicity, it is assumed that the proportion of cumulates to liquid is extremely small, i.e., an open system that is continually fluxed with dioritic-tonalitic magmas. In this case, the abundance of (e.g.) La in a crystal is

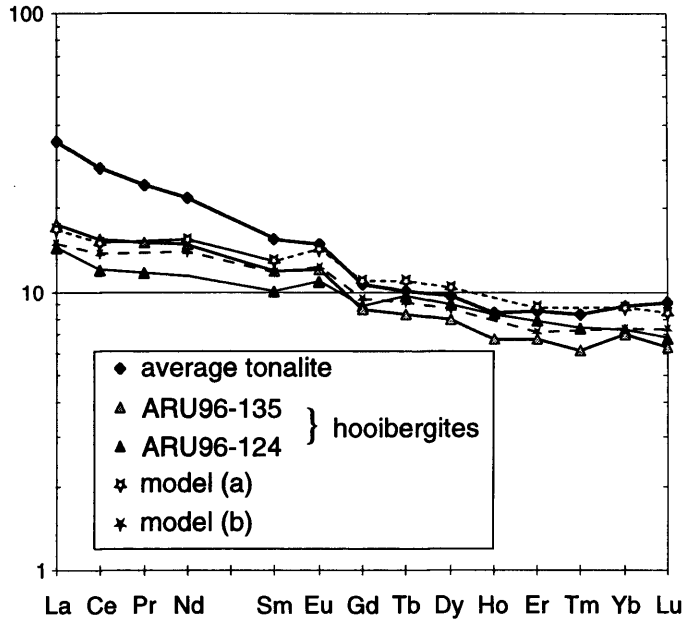

Model (a):
Accumulation of:
25% hornblende
25% clinopyroxene
10% plagioclase
with 40% tonalitic residual liquid

Model (b):
Accumulation of:
10% hornblende
50% clinopyroxene
5% plagioclase
with 35% tonalitic residual liquid

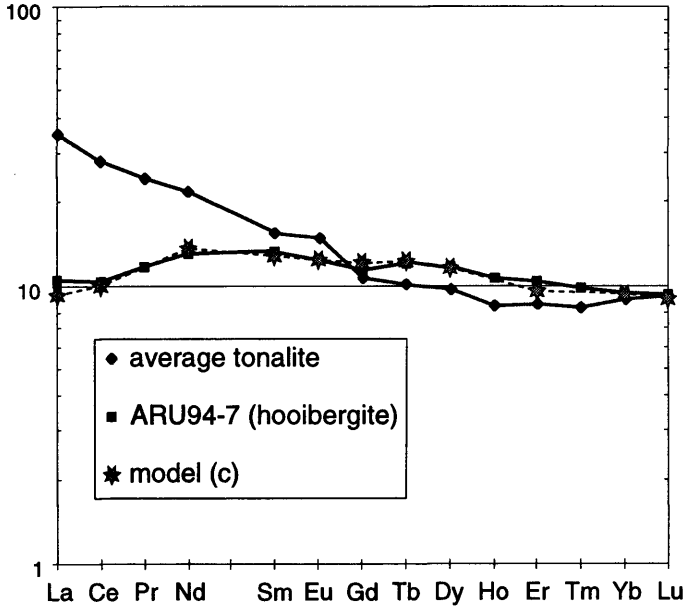

Model (c):
Accumulation of:
35% hornblende
50% clinopyroxene
with 15% tonalitic residual liquid

Figs. 8.21: Chondrite-normalised (McDonough and Sun, 1995) REE plots showing results of modelling the compositions of hooibergites via crystal accumulation. The partition coefficients used are from a compilation of Martin (1987). The modelling assumes that the system is an open system, i.e., that the volume of cumulate rock is negligible compared to the volume of still-liquid, well-mixed tonalitic magma: in this case, the abundance of trace element in a crystallising mineral is equal to the abundance in the liquid multiplied by the partition coefficient. A tonalitic liquid was used as the starting composition, because it has been demonstrated that the clinopyroxenes in the hooibergites were in equilibrium with a melt having Mg# ~ 45, which is equivalent to a diorite or tonalite of the Aruba batholith.

given by $D_{La} \times X_{La}$, where D_{La} is the partition coefficient for La between liquid and crystal, and X_{La} is the abundance of La in the melt phase. Using the assumption of a open system, the hooibergites with the convex-upward pattern can be modelled by mixtures of ~50% clinopyroxene, ~35% hornblende and ~15% residual liquid, whereas the hooibergites that are more LREE-enriched are better explained by a higher proportion of residual liquid (up to ~40%).

8.3.4 Implications of cumulates for the evolution of the batholith

Inflections in curves for some of the figures (e.g., Fig. 8.18) indicate that if the more silicic members of the batholith were generated via accumulation of the gabbros and hooibergites, then either the ratio of cumulus material to residual liquid was small (otherwise the resultant residual liquid compositions would be much more depleted in CaO, and enriched in Al_2O_3), or the residual liquids that were produced were lost from the batholith system. This latter explanation seems unlikely, considering that silicic magmas were clearly present in the batholith. It is inferred, therefore, that the separation of gabbroic and hooibergitic cumulus material from the batholith magma was volumetrically minor, such that there was little overall effect on the residual magma composition.

It was shown in Section 8.3.2 that the phases in the gabbros and hooibergites crystallised in equilibrium with a liquid having MgO $\approx$ 45 to 50, which corresponds to a dioritic composition. It should be noted that the tonalites of the batholith *cannot* be derived from the diorites by the removal of cumulates of gabbroic or hooibergitic composition. If this were the case, the tonalites should have higher Al_2O_3 than the diorites, which they clearly do not. The only way that the tonalites could be related to the diorites by fractional crystallisation is if a cumulus assemblage richer in Al_2O_3 (i.e., rich in plagioclase) was separated from the dioritic magma. Although occasional plagioclase-rich cumulate rocks are present in the batholith, they are volumetrically minor, and it is difficult to see how the diorites could have produced the tonalitic, and more silicic rocks, in this manner. Additionally, fractional crystallisation involving removal of plagioclase would be expected to impart a negative Eu signature to the derived tonalites, which is not observed.

8.4 Dykes cross-cutting the batholith

Both silicic (hornblende-plagioclase porphyries) and mafic dykes cross-cut both the batholith and the Aruba Lava Formation. The porphyritic rocks share geochemical similarities with the tonalites and diorites, and have been discussed, together with those lithologies, earlier

in this chapter. A thorough geochemical and petrogenetic discussion of the later (more mafic) dykes, which tend to be either aphyric or amphibole-phyric, is beyond the scope of this study. Nevertheless, because the dykes provide important constraints on the magmatic evolution of the region subsequent to the emplacement of the batholith, a brief discussion of their geochemical features is presented in this section.

Sixteen late dyke samples from Aruba were analysed; the majority range in composition from basaltic to basaltic andesite (50 to 56 wt.% SiO_2). The dykes were classified into three groups, according to their content of alkalis. Ranges for major and trace element compositions of the dykes are reported in Table 8.1.

One of the most interesting features of these rocks is that they have high Mg#; however, because they are essentially aphyric, this cannot be due to accumulation of Mg-rich phases, as suggested for many of the mafic rocks of the batholith. The cross-cutting dykes may, therefore, represent mantle-derived liquids that have suffered little modification during ascent. There is no correlation between Mg# and SiO_2 content: the six samples with Mg# > 70 have SiO_2 contents ranging from 50 - 55 wt.%. This implies that these relatively silicic magmas may be derived directly from the mantle.

Major & minor elements	(wt.%)	Trace elements	(ppm)
TiO_2	0.3 - 0.9	Rb	up to 50
Al_2O_3	9 - 18	Sr	200 - 400
$Fe_2O_{3(t)}$	8 - 12	Ba	< 600
MnO	0.07 - 0.24	Zr	30 - 80
MgO	4.5 - 12	Nb	1 - 4.5
CaO	8-12	Y	10 - 20
Na_2O	1.5 - 3.5	Cr	up to 1000
K_2O	0.2 - 1.3	Ni	up to 320
P_2O_5	0.11 - 0.33	V	200-350
Mg#	50 - 75	La	3 - 8

Table 8.1: Chemical characteristics of late mafic dykes

The second notable feature about these rocks is their large negative Nb anomalies (Fig. 8.22a), implying that the mantle source region was metasomatised by subduction-related fluids. It should be cautioned that some of the chemical characteristics of these dykes may result from contamination from the batholith, as xenocrystic minerals were observed in the

dykes at some localities (see Section 3.3.1.7). The high Mg# of the dykes, however, suggests that any contamination was not likely to have been volumetrically significant.

The dyke rocks have positive Sr anomalies, suggesting either that Sr abundances in the source region were anomalously high, or that plagioclase may not have been a stable phase in the mantle source region. The low abundances of Y are in agreement with the latter option: they suggest residual garnet in the melting region. Additionally, the HREE are depleted with respect to the LREE (Fig. 8.22b), a feature also consistent with garnet in the source region. Some of the REE patterns show a convex-upward curvature (Fig. 8.22b), with La and Ce being slightly depleted relative to Pr and Nd. Because the La and Ce are the most incompatible REE during mantle melting, this depletion cannot arise from partial melting processes; instead their relative depletion must have been inherited from the mantle source region, i.e., the mantle source had suffered a prior melt extraction event.

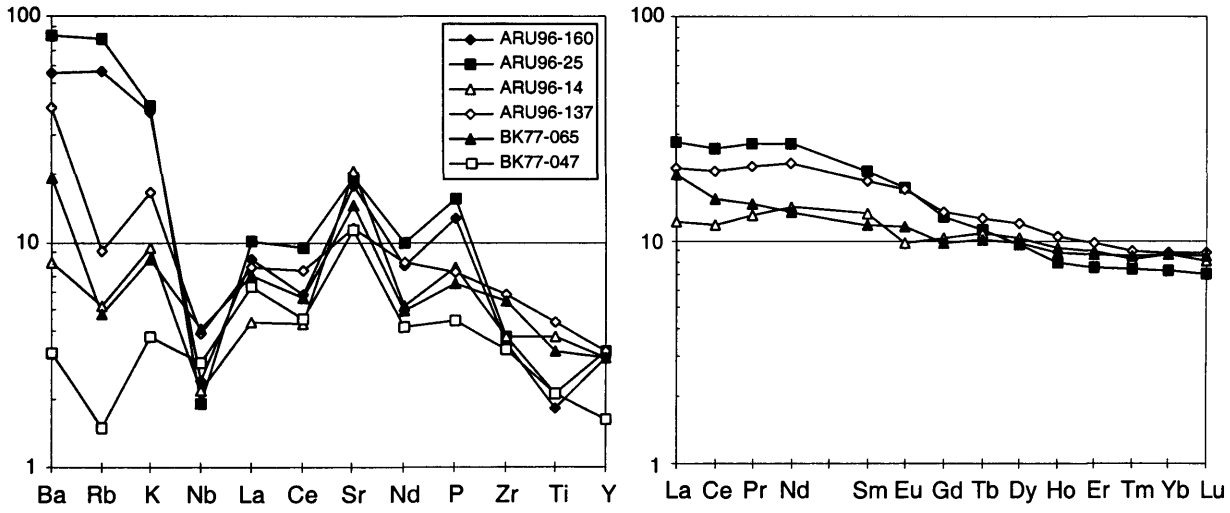

Fig. 8.22: (a) Trace element plot for the late mafic dykes, normalised to bulk silicate earth of McDonough and Sun (1995); (b) Chondrite-normalised (McDonough and Sun, 1995) REE plot for the late mafic dykes.

8.5 Summary

- Classification of the complete batholith suite is non-trivial: depending on the classification scheme used, the data show either tholeiitic and calc-alkaline attributes. The mixed characteristics appear to arise from the batholith having low K_2O contents, superimposed on essentially calc-alkaline characteristics. It is suggested, therefore, that the batholith as a whole should be considered to be low-K calc-alkaline.
- In very few cases is the variability in elemental composition of the batholith rocks attributed to elemental mobility. Many of the elements that show scatter on plots vs. SiO_2

have good correlations with other elements that have similar behaviour in magmatic systems (e.g., K_2O correlates well with Rb and Ba). This demonstrates that the controls on composition are chiefly original igneous features. Mineralogical controls also appear to be important: for example, the Sr contents of these rocks appear to be (at least partially) determined by their plagioclase content (although it should be noted that all lithologies have positive Sr anomalies, indicating that this is an inherent compositional feature of this suite of magmas).

- With increasing SiO_2 content, the rocks of the batholith define trends of increasing Na_2O, K_2O; abundances of MgO, Mg#, $Fe_2O_{3(t)}$, MnO, CaO, and TiO_2 decrease. Al_2O_3 and P_2O_5 increase and then decrease, with the maximum abundances observed in the diorites.
- V, Co, Zn, Cu, Sc, Cr and Ni decrease as SiO_2 increases; Rb, Ba, Th, U and Pb increase. Sr, Ga and the middle-heavy REE show an initial increase as SiO_2 increases, reaching maximum abundances in the diorites, and then decreasing in the more silicic rocks. Nb, Y and the LREE show more complex behaviour, with an initial increase in abundance from the mafic rocks to the diorites, followed by a decrease from the diorites to the leucotonalites, followed by increased abundances for the very silicic rocks. Zr increases throughout the suite as far as tonalite; the more silicic rocks may have either higher or lower Zr contents than the tonalites.
- All rocks of the batholith show negative Nb anomalies on bulk silicate earth-normalised multi-element plots, as well as enrichment in Ba, K and Rb, and, to an extent, the LREE. The degree of this enrichment is dependent on lithology, with the more silicic rocks having the highest abundances of these elements. In contrast, Y and Nb contents only vary slightly throughout the suite.
- The REE patterns of the batholith depict very slight LREE enrichments for the mafic rocks, with increasing LREE enrichment for the diorites and tonalites. Abundances of the HREE do not vary as significantly as the LREE, but do show a general increase from mafic rocks to diorites, then a decrease to the tonalitic values. REE patterns for the tonalites are concave-upwards for the MREE-HREE. None of the volumetrically important lithologies of the batholith has a significant Eu anomaly, although most samples do have a small positive anomaly.
- The tonalites show marked homogeneity in their whole rock and trace element compositions; in contrast, the diorites and hooibergites are more variable.

- The silicic rocks of the batholith are extremely variable in their trace element compositions, particularly the REE. This suggests that they may have formed by a variety of mechanisms.
- The batholith samples span a restricted range in Sr and Nd isotope compositions, and all plot within the field for the least altered Aruba Lava Formation basalts and dolerites. Pb isotope ratios for the batholith are slightly more variable, and only partially overlap with the Aruba Lava Formation field: some samples, particularly the most mafic, extend to less radiogenic values.
- Several lines of evidence suggest that the layered gabbros and hooibergites formed via crystal accumulation: many of the whole rocks have Mg# > 70 (the value expected for a primary mantle melt); the individual phases present are not in equilibrium with the whole-rock composition; and petrographic evidence shows that the some of the rocks are locally monomineralic. Additionally, the layering observed in the field is strong evidence for crystal accumulation. It must, therefore, be borne in mind when considering the petrogenesis of the batholith (Chapter 9) that the whole rock compositions presented here are not necessarily liquid compositions, particularly for the mafic rocks of the batholith.

Chapter 9

Petrogenesis of the Aruba batholith and implications for the generation of continental crust

9.1 Crustal growth via plateau accretion

One of the major theories of continental crustal growth, as reviewed in Chapter 1, involves the accretion of oceanic plateau material at convergent plate margins (e.g., Abbott and Mooney, 1995). It is generally accepted that oceanic plateaux are constructed by voluminous magmatism occurring above mantle plumes (e.g., Campbell and Griffiths, 1990), and so the plateau accretion theory provides a useful link between the episodicity of crustal growth (e.g., McCulloch and Bennett, 1994; Condie, 1997), and the episodicity of mantle plume behaviour (e.g., Stein and Hofmann, 1994). It is clear that oceanic plateaux, with their enormous volumes (Coffin and Eldholm, 1993), could be important contributors to continental growth, and may be able to explain periods of rapid continental growth better than, for example, the volcanic arc accretion model (Taylor, 1977), which implies a more steady-state growth. In order to be preserved in the continental record, however, oceanic plateaux must be able to resist subduction: this buoyancy could be achieved via a combination of the thickness of the plateau crust and a depleted low-density mantle root, especially if the plateau is young and still hot (Saunders *et al.*, 1996).

The disparity between the abundance of oceanic plateaux in the modern oceans and their relative paucity in the continental geological record suggests that, if the rate of production of plateaux has not been anomalously high in the last 150 m.y., either plateaux are eventually subducted, or they are processed and converted into material that is no longer easily recognisable as oceanic plateau crust (Stein and Goldstein, 1996; Saunders *et al.*, 1996). This latter point may be an important one: it was pointed out in Section 1.2 that neither the plateau nor the arc accretion model can adequately account for the silicic composition of the continental crust. This chapter, therefore, incorporates the new data from Aruba and the existing oceanic plateau accretion theory into a new paradigm of crustal growth where the modification of oceanic plateau material via the addition of silicic (tonalitic) magmas results in the generation of a stable nucleus of new continental crust.

9.1.1 Summary of key constraints from earlier chapters

This section summarises the salient conclusions from earlier chapters of this thesis. The aim of this is to remind the reader of the background information required for a full discussion of the mode of generation of the Aruba batholith.

The Aruba Lava Formation consists of a series of basaltic lava flows with interbedded volcaniclastic sedimentary rocks and intrusive dolerites. It is chemically and isotopically similar to other rocks from sequences belonging to the Caribbean oceanic plateau (Donnelly *et al.*, 1990; Kerr *et al.*, 1997b), which is thought to have formed above a mantle plume, and entered the Caribbean region from the Pacific (e.g., Duncan and Hargraves, 1984). Rocks from the Caribbean oceanic plateau have ages clustering around 91 - 88 Ma (Sinton *et al.*, 1998); these dates are in agreement with a biostratigraphic age of Turonian (90.4 - 88.5 Ma) determined from studies of ammonites in sediments intercalated within the Aruba Lava Formation.

Field relationships demonstrate that the Aruba batholith is intrusive into the Aruba Lava Formation. The intrusion appears to be temporally associated with movement along shear zones cutting the lava sequence. Reliable ^{40}Ar-^{39}Ar dates for the batholith range from 85.4 ± 0.5 Ma to 82.2 ± 0.5 Ma. This demonstrates that the intrusion of the Aruba batholith post-dated the emplacement of the Aruba lavas by only a few (~3 to ~9) million years.

The Aruba batholith is geochemically extremely different from the Aruba Lava Formation: it consists of gabbros to silicic rocks, with a predominance of tonalite and diorite. The batholith is low-K calc-alkaline, and has trace element characteristics (e.g., negative Nb anomalies) that are typically associated with subduction zones. Petrogenetic studies of the batholith are complicated by the fact that many of the rocks sampled have some cumulate characteristics, and therefore do not represent liquid compositions. The rocks of the batholith are similar to the Aruba Lava Formation in terms of Sr and Nd isotope ratios, but some of the batholith rocks (particularly the more mafic lithologies) have less radiogenic Pb isotope ratios.

The main questions to be addressed in this chapter concern the sources and processes contributing to the generation of the batholith. The relationship (if any) of the batholith to the Aruba Lava Formation rocks that it intrudes is also a matter for debate. The similarity in age and Sr-Nd isotope ratios of the batholith and the lavas suggests that the two suites are somehow petrogenetically connected, but the less radiogenic Pb isotopes of the batholith suggest that the batholith magmas have an extra component in their petrogenesis that is absent from the Aruba Lava Formation magmas.

9.2 Overview of model for silicic magmas associated with oceanic plateaux

This section describes the basic features of a model to explain the generation of silicic magmas associated with oceanic plateaux. It is hoped that the presentation of the preferred model at this point in the chapter will give the reader a clearer impression of the viewpoint taken throughout Sections 9.3 to 9.7, where the evidence in support of the model is presented. It is appreciated, however, that alternative hypotheses do exist: these will be discussed as they arise in the appropriate sections. The preferred hypothesis that is tested in the succeeding sections is a multi-stage petrogenetic model, involving both conventional subduction zone magmatism and remelting of metabasalt.

The basaltic lavas making up the Caribbean oceanic plateau were extruded in a submarine environment; they would have become hydrated immediately following their emplacement. The Caribbean plateau (containing the Aruba Lava Formation) moved eastwards towards the present Caribbean region; because of its buoyancy it resisted subduction, causing a subduction polarity reversal from eastward-dipping (consuming Farallon oceanic crust) to westward-dipping (consuming Atlantic or Proto-Caribbean) crust (Burke *et al.*, 1984). The hypothesis to be tested is that the Aruba batholith was generated as a consequence of this subduction polarity reversal.

The newly-subducting oceanic crust dehydrated, resulting in a transfer of fluid-mobile elements into the mantle wedge region. Because of the influence of the mantle plume that had generated the Aruba Lava Formation magmas only a few million years earlier, the mantle wedge region was hotter than normal. Addition of a hydrous fluid from the subducting oceanic crust lowered the solidus of this anomalously hot mantle wedge material, creating basaltic partial melts with trace element signatures typical of subduction zone magmas. These were emplaced within the overlying oceanic plateau crust, where they may have been modified by processes such as fractional crystallisation, and assimilation of the oceanic plateau crust.

The most important consequence of the emplacement of these basaltic, subduction-derived magmas within the plateau was that they provided a heat source that resulted in partial melting of the basaltic plateau crust. This was more likely to have occurred in the upper, hydrated, parts of the plateau sequence. Partial melts of metabasalt are tonalitic in composition, and this is the mechanism that is investigated for generation of the Aruba tonalites. The dioritic magmas formed either from mixing of these tonalitic magmas with the basaltic subduction-derived magma, or by fractional crystallisation of the basaltic subduction-derived magma combined with assimilation of plateau material (and/or partial melts thereof).

9.3 Isotopic constraints on the generation of the Aruba batholith suite

The isotopic constraints on the generation of the Aruba batholith suite will be described and discussed in this section, because they are pertinent to many of the arguments presented later in various sections of this chapter.

9.3.1 Sr and Nd isotope constraints

The Sr and Nd isotope ratios of the batholith rocks do not show a great deal of variation: they plot within the field defined by the basalts and dolerites of the Aruba Lava Formation (Fig. 9.1). There appears to be no consistent variation in Sr and Nd isotope ratios with lithology. This provides an important constraint on the petrogenesis of the batholith: any process invoked to explain the generation of the batholith must result in the batholith and the Aruba Lava Formation having similar ratios. The similarities between the isotope ratios of the batholith and the Aruba Lava Formation can be explained by a variety of processes. The most straightforward is to suggest that both suites have similar, or related, source regions. An alternative explanation is that the observed Sr and Nd isotope ratios could be explained by, for example, mixing of depleted mantle and sediment endmembers. However, the proportions of these endmembers would fortuitously have to be exactly those required so that a mixture would result in the same final isotopic composition as the plume source of the Aruba lavas, and this second explanation is therefore considered to be unlikely.

9.3.2 Pb isotope constraints

The Pb isotope compositions of the batholith are more variable then their Sr and Nd isotope compositions (Fig. 9.2). The batholith tends to have less radiogenic Pb isotope ratios than the Aruba Lava Formation, although the most radiogenic batholith samples overlap with the range of the Aruba Lava Formation samples. The more mafic rocks of the batholith have the least radiogenic Pb isotope signatures. The remainder of this section focuses on the compositional characteristics of the unradiogenic-Pb endmember, and discusses possible locations for its input. For convenience, in the following sections, the other endmember (with Sr, Nd and Pb compositions the same as the Aruba Lava Formation) is referred to as the "ALF endmember".

9.3.2.1 Characteristics and composition of the unradiogenic-Pb endmember

The observation that the rocks with the least radiogenic Pb isotope ratios have similar Sr and Nd isotopes to the Aruba Lava Formation and the rest of the batholith suggests that

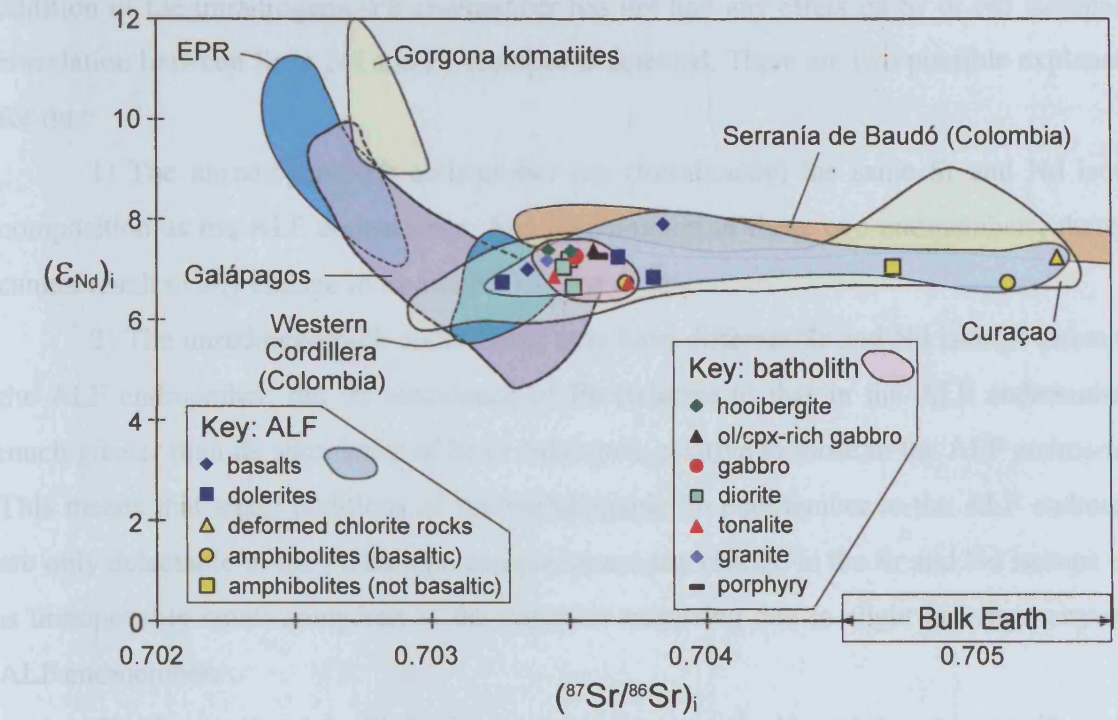

Fig. 9.1: Initial εNd and $^{87}Sr/^{86}Sr$ for the batholith compared with the Aruba Lava Formation (ALF) and other suites from the Caribbean/Pacific region. The samples from the batholith plot within a restricted field that overlaps with the compositions of the ALF basalts and dolerites. Batholith samples are age-corrected to 85 Ma, and ALF samples to 88 Ma. See Fig. 6.10 for data sources.

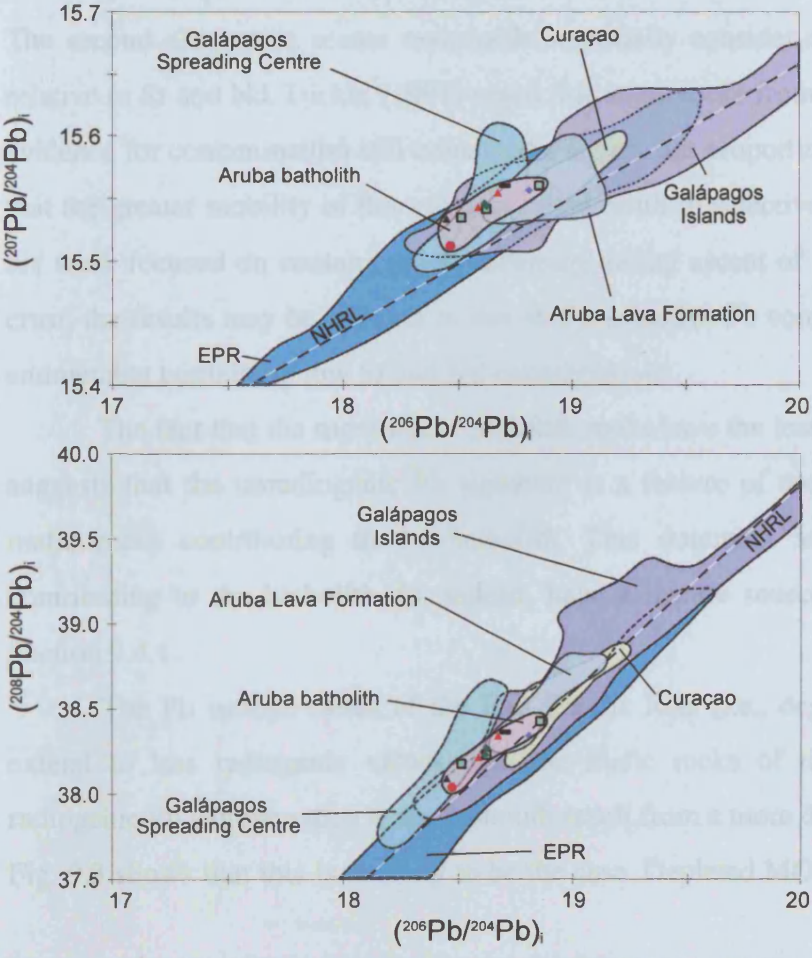

Fig. 9.2: Pb isotope data for the batholith, age corrected to 85 Ma (see Fig. 8.15 for comparison of age-corrected and non-age-corrected data) compared with fields for the Aruba Lava Formation (this study: age corrected to 88 Ma) and other suites from the Caribbean and Pacific regions. See Fig. 6.10 for data sources.

addition of the unradiogenic-Pb endmember has not had any effect on Sr or Nd isotopes: no correlation between Sr or Nd and Pb isotopes is detected. There are two possible explanations for this:

1) The unradiogenic-Pb endmember has (fortuitously) the same Sr and Nd isotopic composition as the ALF endmember. Any combination of these two endmembers, therefore, cannot result in any change in Sr and Nd isotope ratios.

2) The unradiogenic-Pb endmember may have different Sr and Nd isotope ratios from the ALF endmember, but its abundance of Pb (relative to that in the ALF endmember) is much greater than its abundance of Sr or Nd (again, relative to those in the ALF endmember). This means that small additions of the unradiogenic-Pb endmember to the ALF endmember are only detectable in the Pb isotope compositions; any change in the Sr and Nd isotope ratios is unnoticeably small compared to the variation occurring due to slight heterogeneity of the ALF endmember.

The first option is unlikely: it appears to be too coincidental that the unradiogenic-Pb endmember has the same Sr and Nd isotopic composition as the ALF endmember, because any compositional difference that has been prevalent in a reservoir for long enough to affect Pb isotope compositions is also likely to result in a shift in Sr and Nd isotope compositions. The second alternative seems reasonable, especially considering the greater mobility of Pb relative to Sr and Nd. Dickin (1981) noted that some rocks from Skye which showed no other evidence for contamination still contained a significant proportion of crustal Pb, and proposed that the greater mobility of this element could result in selective Pb contamination. Although his work focused on contamination occurring during ascent of a magma through continental crust, the results may be relevant to this study: selective Pb contamination is equivalent to an endmember containing low Sr and Nd concentrations.

The fact that the more mafic batholith rocks have the least radiogenic Pb isotope ratios suggests that the unradiogenic Pb signature is a feature of the mantle source region of the mafic rocks contributing to the batholith. This statement assumes that the mafic melts contributing to the batholith do, indeed, have a mantle source region: this is discussed in Section 9.4.1.

The Pb isotope ratios of the East Pacific Rise (i.e., depleted MORB mantle) source extend to less radiogenic values than the mafic rocks of the batholith: could the least radiogenic Pb isotope ratios in the batholith result from a more depleted mantle source region? Fig. 9.3 shows that this is unlikely to be the case. Depleted MORB mantle has higher Nd and

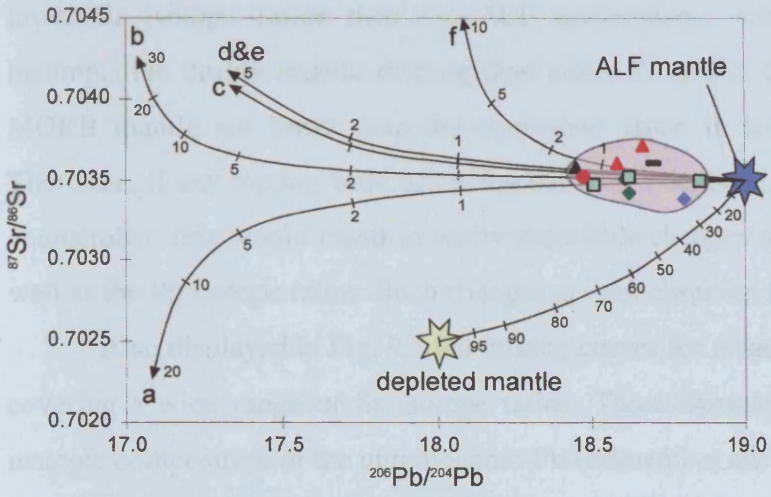

Mantle endmembers	ALF	depleted mantle
Pb (ppm)	0.15	0.1
Sr (ppm)	19.9	18
$^{87}Sr/^{86}Sr$	0.7035	0.7025
$^{206}Pb/^{204}Pb$	19.0	18.0

Hypothesised sedimentary endmembers	a	b	c	d	e	f
Pb (ppm)	13	13	13	13	13	13
Sr (ppm)	40	40	8	15	40	30
$^{87}Sr/^{86}Sr$	0.7000	0.7050	0.7300	0.7200	0.7100	0.7100
$^{206}Pb/^{204}Pb$	17.0	17.0	17.0	17.0	17.0	18.0

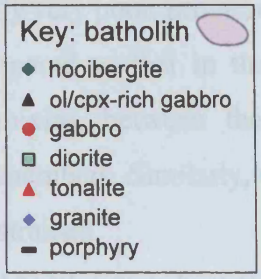

Fig. 9.3: Results of calculations for admixtures of various sources (in the mantle, prior to melting). Small numbers indicate percentages of the unradiogenic-Pb endmember in the mixture. The ALF endmember has isotope ratios determined in this study, and abundances of Pb and Sr from the primitive mantle of McDonough and Sun (1995). Values for the abundances of Pb and Sr in depleted mantle are poorly known, so have been estimated at lower than primitive mantle; the difference is greater for Pb, as it is more incompatible than Sr. Using realistic values for a variety of metasedimentary endmembers, the Pb isotope compositions of the batholith can be explained by a small (< 2%) contribution of sediment to the mantle source region. If this diagram were to be applied to contamination of *magmas* (rather than a mantle source), which may be more appropriate for the batholith, more contaminant is required to account for the observed Pb isotope ratios.

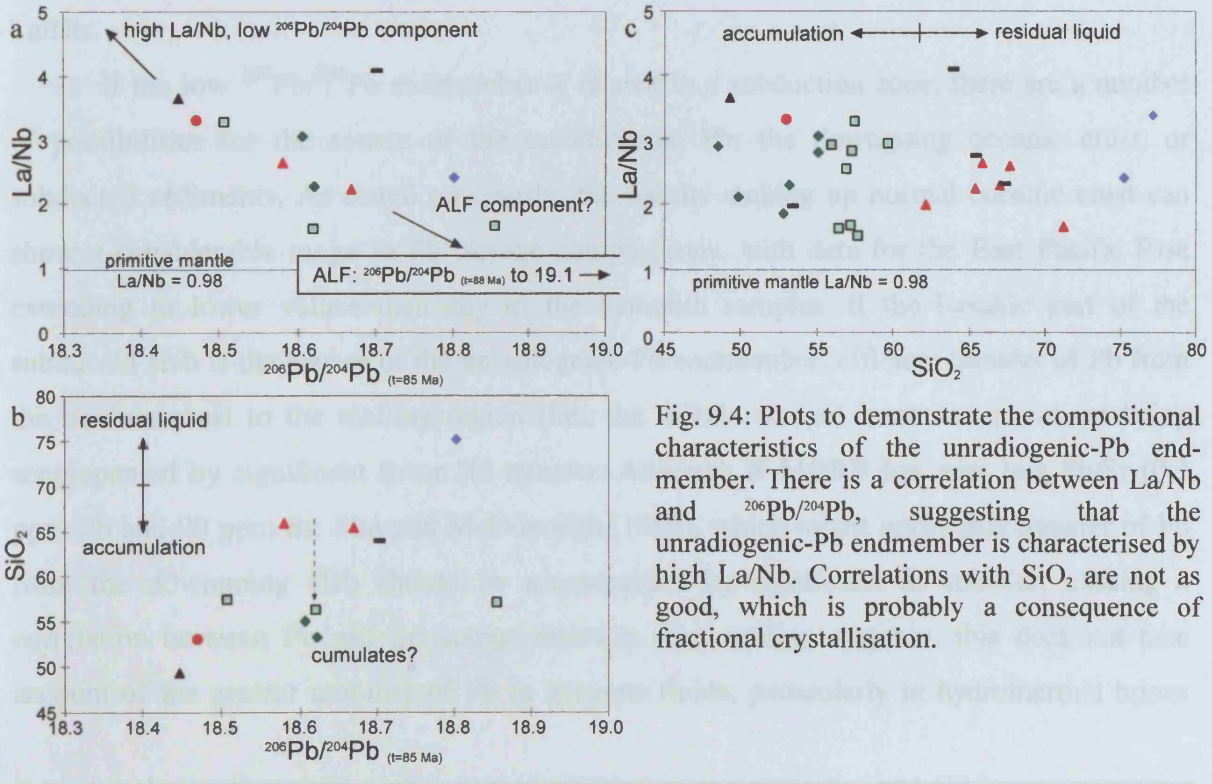

Fig. 9.4: Plots to demonstrate the compositional characteristics of the unradiogenic-Pb endmember. There is a correlation between La/Nb and $^{206}Pb/^{204}Pb$, suggesting that the unradiogenic-Pb endmember is characterised by high La/Nb. Correlations with SiO_2 are not as good, which is probably a consequence of fractional crystallisation.

lower Sr isotope ratios than the ALF endmember. Additionally, because Pb is more incompatible during mantle melting than either Sr or Nd, the Pb/Sr and Pb/Nd of depleted MORB mantle are lower than the equivalent ratios in less depleted or primitive mantle. Therefore, if any mixing were occurring between a depleted mantle endmember and the ALF endmember, this would result in easily detectable changes in the Sr and Nd isotope ratios as well as the Pb isotope ratios. Such changes are not observed for the rocks of the batholith.

Also displayed in Fig. 9.3 are mixing curves for a variety of hypothetical endmembers, covering a wide range of Sr isotope ratios. These demonstrate that the constraints on the isotopic composition of the unradiogenic-Pb endmember are actually very poor: providing that the Pb/Sr ratio in the unradiogenic-Pb endmember is high compared to that in the ALF endmember, the data can be explained by two-component mixing between the ALF endmember and a wide range of hypothetical unradiogenic-Pb endmembers. Similarly, the Nd isotope ratio of the unradiogenic-Pb endmember is also poorly constrained.

Further clues as to the nature of the unradiogenic-Pb endmember can be gained by studying some of its other compositional characteristics. Fig. 9.4a demonstrates that $(^{206}Pb/^{204}Pb)_i$ shows a good correlation with La/Nb, suggesting that the unradiogenic-Pb endmember also has high La/Nb. High La/Nb is a feature commonly associated with melts generated in subduction zones (e.g., Saunders *et al.*, 1980); additionally, because much of the continental crust is thought to have been generated in subduction zone environments (e.g., Taylor, 1977), the bulk continental crust (and sediments derived therefrom) also have high La/Nb.

If the low $^{206}Pb/^{204}Pb$ endmember is related to a subduction zone, there are a number of possibilities for the source of the unradiogenic Pb: the downgoing oceanic crust, or subducted sediments. As stated previously, the basalts making up normal oceanic crust can show a considerable range in Pb isotope compositions, with data for the East Pacific Rise extending to lower values than any of the batholith samples. If the basaltic part of the subducted slab is the source of the unradiogenic-Pb endmember, efficient transfer of Pb from the oceanic crust to the melting region (i.e., the mantle wedge) must occur without being accompanied by significant Sr or Nd transfer. Although N-MORB has very low Pb/Sr (0.3 ppm Pb and 90 ppm Sr: Sun and McDonough, 1989), which might imply that transfer of Pb from the downgoing slab should be accompanied by significant Sr transfer, causing a correlation between Pb and Sr isotope ratios in the resulting magmas, this does not take account of the greater mobility of Pb in aqueous fluids, particularly in hydrothermal brines

(Khitarov and Moskalyuk, 1955). The basaltic part of the subducting slab may, therefore, be a candidate for the source of the unradiogenic-Pb endmember.

The second group of candidates for the unradiogenic-Pb endmember are sedimentary rocks, which tend to have considerably higher Pb abundances than any mantle source region or mafic igneous rock. Chow and Patterson (1962) measured abundances of (acid-soluble) Pb in pelagic sediments, with 19 ppm being recorded for rapidly-deposited oozes, 35 ppm for clays deposited at medium rates, 84 ppm for slowly-deposited clay and 980 ppm for manganese nodules. However, many of these sediment types also have high Sr, particularly those containing significant quantities of carbonate: Hole *et al.* (1984) reported Sr abundances in excess of 1100 ppm for nannofossil oozes and 600 ppm for ferruginous clays. These pelagic sediments would only have high enough Pb/Sr ratios to be representative of the unradiogenic-Pb endmember if they had a very low carbonate (and therefore Sr) content. Moreover, many Pacific and Atlantic pelagic sediments have Pb isotope ratios that are higher than the batholith (e.g., Barreiro, 1983; Ben Othman *et al.*, 1989): admixtures of these sediments cannot be responsible. Others, however, are less radiogenic (e.g., some Nazca plate metalliferous sediments: Dasch *et al.*, 1981) and could conceivably have contributed to the petrogenesis of the batholith gabbros.

Terrigenous sediments, on the other hand, have Pb isotope ratios that reflect their source regions, and can vary dramatically with location. White *et al.* (1985), for example, reported "unusually radiogenic" terrigenous sediments (turbidites) derived from the Archaean Guiana Shield, which contribute to the high Pb isotope ratios of Lesser Antillean island arc magmas. (It should be noted here that, although terrigenous sediments emulate the isotope ratios of their source, they will not necessarily have the same abundances of Pb, Sr and Nd).

Detailed Pb isotopic maps of basement domains in the Andean Altiplano (Aitcheson *et al.*, 1995) show that the basement is isotopically heterogeneous on a scale of ~200km; one domain in particular (the "Northern Altiplano") has unradiogenic Pb isotope ratios that are similar to the hypothesised unradiogenic component in the batholith, although they have slightly higher $^{207}Pb/^{204}Pb$. Archaean and Proterozoic granulitic terranes in various locations also have unradiogenic Pb isotope compositions (e.g., N. Scotland: Halliday *et al.*, 1993; E. Australia: Rudnick and Goldstein, 1990), which probably arise from long-term depletion in U and Th, for example, after extraction of an incompatible-element-rich partial melt.

For terrigenous sediment to become involved in the petrogenesis of the gabbros of the batholith, however, it must have been in geographical proximity with the Caribbean region,

i.e., in northern South America. Unfortunately, Pb isotope data for the northern part of the Andean basement are scarce, probably because the accretion of part of the Caribbean oceanic plateau onto the Colombian continental margin, and later continental arc volcanism, have rendered the basement inaccessible. Some Pb isotope data exist for Colombian lower crustal xenoliths (Weber, 1998), but these are all more radiogenic than the required endmember. However, given the ~200 km scale heterogeneities reported for the central Andes (Aitcheson *et al.*, 1995), the presence of exposed basement rocks (i.e., lower crustal granulite facies gneisses with unradiogenic Pb isotope compositions) contributing to terrigenous sedimentation in the Pacific/Caribbean region is certainly not impossible.

9.3.2.2 Incorporation of the unradiogenic-Pb endmember into the batholith magmas

The above discussion demonstrated that the unradiogenic-Pb endmember is likely to be either some sort of terrigenous sediment derived from ancient granulite, or a fluid derived from the basaltic part of a subducting slab. For the fluid derived from the basaltic part of the subducting slab, the locus of its input into the batholith gabbros is implicit; however, if terrigenous sediment were contributing to the petrogenesis of the batholith, it could do so in a number of ways. There are three main hypotheses (Fig. 9.5):

1) assimilation of terrigenous sediment intercalated in the plateau crust;

2) subduction of terrigenous sediment, and the transferral of its Pb isotope signature into the overlying mantle wedge; and,

3) an ancient recycled sedimentary heterogeneity in the mantle source region of the mafic melts contributing to the batholith.

These hypotheses will be discussed briefly in this section, although during the considerations on individual lithologies in the following sections, it is hoped that the mechanism will become better constrained. The important observations mentioned so far that constrain the location of the unradiogenic-Pb endmember input are:

1) there is a good correlation between $(^{206}Pb/^{204}Pb)_i$ and La/Nb in the batholith rocks, with the lowest $(^{206}Pb/^{204}Pb)_i$ samples having the highest La/Nb; and,

2) any mechanism for incorporation of the unradiogenic-Pb endmember must account for the fact that the more mafic rocks have the highest amount of this component.

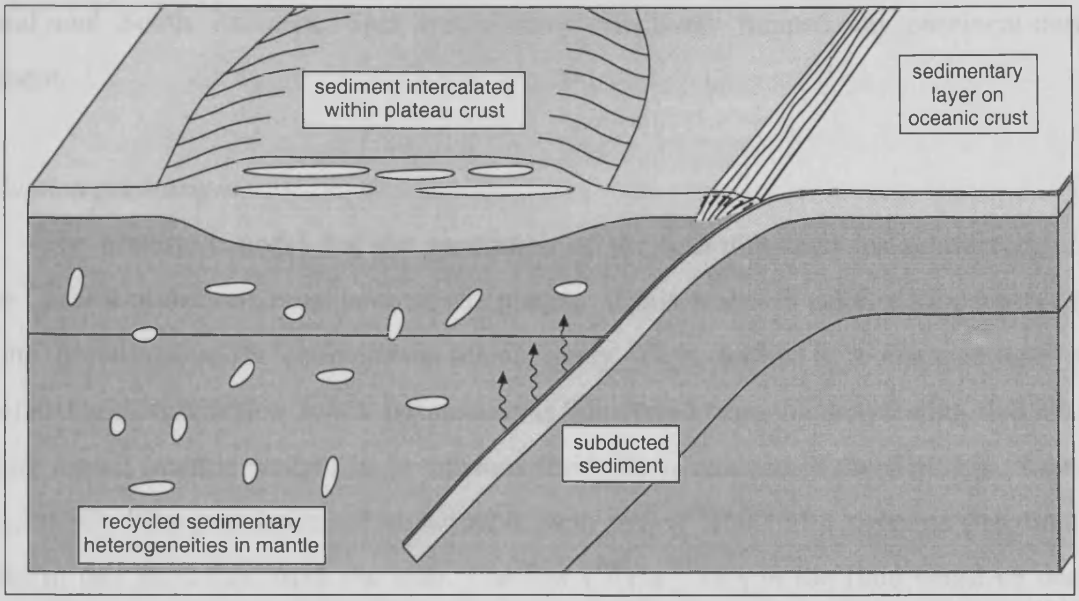

Fig. 9.5: Possible locations for the involvement of a sedimentary unradiogenic-Pb endmember in the petrogenesis of the batholith, notably the more mafic rocks.

Sediments intercalated within the (upper) plateau crust

It is conceivable that terrigenous sediments intercalated within the plateau crust could have contaminated the mafic batholith magmas during ascent through the plateau. These are more likely to be intercalated in the upper parts of the plateau crust, since studies of exhumed portions of oceanic plateaux suggest that the lower parts consist predominantly of intrusive mafic rocks (e.g., Nivia, 1996).

If it is assumed that all magmas of the batholith originally had similar Pb isotope ratios, the gabbros need to incorporate more of the intercalated sediments. Magmas with higher emplacement temperatures have a higher potential for melting adjacent country rocks, and can end up being more contaminated than lower-temperature magmas (Kerr, 1993). This contamination with terrigenous sediment would have resulted in higher La/Nb, as well as lower $(^{206}Pb/^{204}Pb)_i$.

A major argument against terrigenous sediments within the plateau crust being the cause of the low $(^{206}Pb/^{204}Pb)_i$ and high La/Nb of the mafic batholith rocks is that terrigenous sediments are not observed within the plateau sequence. Although sedimentary rocks are present within the Aruba Lava Formation, all those studied in thin section are rich in plagioclase, and likely to be volcaniclastic, rather than terrigenous. Furthermore, consideration of the plate tectonic reconstructions of the area suggests that, at the time of plateau formation, there would have been a subduction zone to the east of the plateau, dipping eastwards beneath

Central and South America. This would have effectively trapped any continent-derived sediment.

Subduction zone origin

The preferred model for the generation of the batholith involves subduction of the Proto-Caribbean oceanic crust beneath the plateau. If this model is valid, a subduction origin for the unradiogenic-Pb endmember seems likely. High La/Nb is a characteristic often associated with subduction zones, because La is transferred from the dehydrating slab into the melting region (mantle wedge) in an aqueous fluid; Nb is retained in the slab (e.g., Saunders *et al.*, 1980). The correlation of high La/Nb with low $(^{206}Pb/^{204}Pb)_i$ suggests that both are related to this fluid flux from the slab. The low $(^{206}Pb/^{204}Pb)_i$ in the fluid could be derived from subducted terrigenous sediment, originating from continental South America and deposited on the Proto-Caribbean oceanic crust. Alternatively, it could be derived from the dehydrating basaltic part of the slab, as suggested in Section 9.3.2.1.

If this is indeed the mechanism by which the unradiogenic-Pb endmember was incorporated into the batholith magmas, it does not simply explain why the gabbros have the highest amount of this component. This point will be returned to in Section 9.5.

Mantle heterogeneity

A further possibility for the source of the unradiogenic-Pb endmember is mantle heterogeneity, perhaps located within the mantle plume, resulting from ancient recycled subducted sediment. This would be difficult to distinguish, on geochemical grounds, from subduction of sediment immediately prior to generation of the batholith magmas. However, there is no evidence for this degree of heterogeneity in the Aruba Lava Formation basalts and dolerites. If mantle heterogeneity were the correct explanation, it requires that the mantle beneath Aruba changed in composition between the eruption of the Aruba Lava Formation and the emplacement of the batholith: a period of only ~3 to 9 m.y.; moreover, this change in Pb isotope composition was not accompanied by any change in Sr or Nd isotope compositions. Of course, it could be argued that the magmas that gave rise to the Aruba Lava Formation basalts and dolerites were more effectively homogenised prior to emplacement, either during the melting process, or in sub-crustal magma chambers, and this is why the unradiogenic-Pb endmember is not detectable in these rocks. The mafic rocks of the batholith, however, are not particularly enriched in incompatible elements (for example, the highest Zr

content of any of the (non-accumulative) gabbros analysed is 52 ppm, compared with 74 ppm for normal MORB: Sun and McDonough, 1989), implying that they originated from reasonably high degree melting in their source regions: this would have resulted in effective homogenisation of any Pb isotope heterogeneities.

It is therefore considered that, even though it is difficult to unequivocally rule out the existence of isotopic heterogeneities in the sub-Aruban mantle, such a scenario requires special pleading. Additionally, mantle heterogeneity alone cannot explain the high La/Nb of the mafic batholith rocks, unless an extremely unusual compositional heterogeneity is invoked. Another argument against mantle heterogeneity being the primary control on the compositions of batholith rocks is presented in Section 9.5.3.1.

9.4 Generation of the gabbros of the batholith

9.4.1 The most primitive liquid of the batholith

It was demonstrated in Section 8.3 that many of the mafic rocks of the batholith (for example, the gabbros from the layered series and the hooibergites) contain cumulus phases with high Mg# that are not in equilibrium with the whole-rock. Indeed, the layered gabbros and the hooibergites are in equilibrium with a melt having Mg#s of ~50 and ~45, respectively. Modelling the petrogenetic history of rocks using compositions that are not representative of liquids is not very instructive unless reasonably accurate estimates can be made of the geochemical effects of crystal accumulation. If this is not taken into account, and the whole rock compositions are taken as melt compositions, serious errors in interpretation could result: for example, rocks containing cumulus ferromagnesian phases have low abundances of incompatible elements, which could be misinterpreted as arising from melting of a highly depleted source, or very high degrees of melting. In order to consider the petrogenetic origin of the batholith, it is vital to have compositional constraints on the most primitive liquid contributing to it, as it is the composition of these liquids that can potentially yield the most information about, for example, source chemistry and melting processes. In this section, potential candidates for the most primitive liquid present in the batholith are considered.

The most magnesian rocks in the batholith are the olivine- and pyroxene-rich gabbros (e.g., sample ARU96-154: MgO = 17.6 wt.%; Mg# ≈ 78; SiO_2 = 49.3 wt.%) from the layered gabbro body at Wariruri. However, these rocks have some of the clearest cumulate characteristics, both texturally and geochemically. Nevertheless, these could still be cumulates

from the most primitive liquid to be present in the batholith. The calculations presented in Section 8.3 that suggest that the layered gabbro sequences crystallised from a melt having Mg# ≈ 50 may not appear to impart very much more information about the liquid. If, however, it is assumed that at least *some* of the batholith rocks represent liquid compositions, the approximate composition of the melt from which these layered gabbros formed can be estimated using the abundance for a particular element where the suite as a whole has Mg# = 50. Fig. 8.9f demonstrates that at Mg# = 50, the suite has MgO ≈ 4 wt.% and SiO_2 = 54 to 60 wt.%. A similar analysis for other elements (plots vs. Mg# not shown, but these figures can be derived from Figs. 8.9 and 8.10 at MgO ≈ 4wt.%) yields the following as a likely composition for the liquid: Zr ≈ 60 ppm; Nb ≈ 2.5 to 4 ppm; Y ≈ 15 ppm; Ni ≈ 25 ppm; Cr ≈ 100 ppm. This hypothesised melt composition can be verified using trace elements, for example, Ni, where the distribution coefficients are relatively well-known. The Ni content from olivines in the gabbros (average of 15 electron microprobe analyses from ARU96-154 and ARU97-111) is 0.074 wt.%, equivalent to 580 ppm. D_{Ni} varies with MgO content, and has a value of approximately 30 at 4 wt.% MgO (Hart and Davis, 1978). This olivine was, therefore, in equilibrium with a liquid having 19 ppm (i.e., $581/D_{Ni}$), which is in reasonable agreement with the 25 ppm value derived from the previous method.

The liquid from which these gabbroic cumulates were derived was *not* basaltic in composition. These rocks formed by crystal accumulation from a melt of basaltic andesite composition. Extrusive rocks of a very similar composition to this postulated liquid have been reported from Tonga (Ewart *et al.*, 1973), and have the similar phenocryst assemblages to the cumulus assemblage observed in the Warirui gabbros.

The hooibergites crystallised from a melt having Mg# ≈ 45 (Section 8.3.2). Using the same technique as for the layered gabbros, this corresponds to a liquid of andesitic composition, with < 3 wt.% MgO and ~ 60% SiO_2. This is less primitive than the liquid from which the layered gabbros formed.

The remaining candidates for the most primitive liquids of the Aruba batholith are the non-layered gabbros, such as those found in the Matividiri massif (and elsewhere). These have no obvious signs of modal layering; indeed, two samples are microgabbros, and are therefore considerably more likely to represent liquid compositions. The most primitive of these microgabbros (ARU97-103) has the following composition: MgO = 7.8 wt.%; SiO_2 = 51.8 wt.%; Zr = 46 ppm; Nb = 3.7 ppm; Y = 17 ppm; Ni = 109 ppm; Cr = 383 ppm; Mg# = 63. Unfortunately, this was not one of the samples analysed by ICP-MS for high precision Nb and

REEs. However, it does show that the magmatic environment responsible for generation of the batholith was capable of producing relatively primitive basaltic melts.

The most likely origin of these basaltic melts is from partial melting of the mantle, although it should be stressed that a magma with a Mg# of 63 is not in equilibrium with mantle olivine (see Section 6.4.1). The most primitive liquid contributing to the batholith is, therefore, not an *unmodified* (i.e., primary) magma. Fractionation of a MgO-rich phase, probably olivine, is a likely candidate for lowering of the Mg#, and MgO content of this magma between extraction from the mantle and emplacement into the batholith. In order to understand the genesis of the batholith as a whole, it is vital to decipher the nature of the mantle from which these gabbros were derived.

9.4.2 Subduction zone origin for the batholith gabbros?

The relative enrichment of large ion lithophile elements (LILE) and, to a lesser extent, light rare earth elements (LREE), with respect to the high field strength elements (HFSE) is a characteristic feature commonly associated with arc magmas – so much so that it has become generally known as the "arc signature" (Pearce, 1982). The enrichment is most noticeable for those elements that are soluble in aqueous fluids, i.e., LILE and LREE (Boettcher and Wyllie, 1968; Nakamura and Kushiro, 1974; Tatsumi *et al.*, 1986) which has led to the interpretation that arc magmas are derived from the mantle wedge, to which a slab-derived component has been added (e.g., Saunders *et al.*, 1991).

In contrast, HFSE and heavy REE are relatively immobile in aqueous fluids (Mysen, 1979), and no enrichment of these elements is seen in subduction zone magmas. In fact, considerable debate has focused on the depletion in HFSE observed in subduction-related magmas: some authors consider it to be only an apparent depletion relative to the LILE, arising because the HFSE are retained in the subducting slab, rather than being transferred into the mantle wedge in slab-derived fluids (e.g., Saunders *et al.*, 1980); others believe that the depletion in HFSE is a genuine depletion (rather than a lack of enrichment) that arises from the presence of phases having a high affinity for HFSE being residual during melting of the mantle wedge (e.g., Green, 1981; Foley and Wheller, 1990). The phases in which the HFSE are relatively compatible are often Ti-bearing minerals such as rutile, titanite and amphibole. It has been pointed out, however, that these titaniferous phases are unlikely to remain residual during the high degrees of melting (up to ~30%) proposed for island arc magmas (e.g., Woodhead *et al.*, 1993). Instead, it has been suggested that the low absolute abundances of the

HFSE in island arc magmas are a consequence of the mantle source having been previously depleted in these elements by an earlier melting event, coupled with a dilution effect due to the large degrees of melting in the mantle wedge (Woodhead *et al.*, 1993).

Fig. 9.6 demonstrates that the gabbros of the Aruba batholith have all the characteristics commonly associated with subduction-related magmas. They are enriched in fluid-mobile elements such as Ba, Rb, K, La and Sr, and relatively depleted in Nb, Zr, Ti and Y. This is true both of the gabbros that have no obvious cumulate characteristics, and those that do; the main difference between the types of gabbro is that those with cumulate characteristics have generally lower abundances of most elements. (There are notable exceptions; for example, the plagioclase-rich gabbros have high Sr, which is relatively compatible in plagioclase, and high Ti, which is relatively compatible in Fe-oxides, and a major component of ilmenite.)

The isotopic constraints discussed in Section 9.3 are all consistent with the gabbros having been derived from melting of the mantle wedge above a subduction zone. The unradiogenic-Pb endmember could have been incorporated into the mantle wedge via a fluid flux from the subducting slab (with contributions from the basaltic part of the slab and/or subducted terrigenous sediment). This explains the correlation between $(^{206}Pb/^{204}Pb)_i$ and La/Nb. Assimilation of terrigenous sediment intercalated within the plateau crust during ascent of the batholith magmas cannot, at this stage, be ruled out: the degree of contamination required to explain the shift in Pb isotope composition need not be unrealistically large if the high La/Nb was derived primarily from the subduction zone fluid flux.

There is, however, a further possible explanation for the isotope ratios of the gabbros. The gabbros plot in a similar location to many subduction-related volcanic rocks (e.g., DePaolo and Wasserburg, 1977; Kay *et al.*, 1978; DePaolo and Johnson, 1979). The Sr, Nd and Pb isotope ratios of these types of rocks are commonly explained by melting of *depleted* mantle in a subduction zone with an additional slab-derived fluid component with higher Sr and Pb isotope ratios, and lower Nd isotope ratios (e.g., Perfit *et al.*, 1980). In Section 9.3.1., however, it was concluded that fortuitous mixing of depleted mantle and sedimentary endmembers in exactly the correct proportions to replicate the Sr and Nd isotope ratios of the Aruba Lava Formation seemed somewhat unlikely.

Two further lines of evidence may also be used to argue against the batholith gabbros being derived from a mixture of depleted mantle and sediment. The first is an empirical argument based on the evidence already presented for this region: the batholith was emplaced

only a few million years after eruption of the Aruba Lava Formation, and consequently, the predominant mantle source region beneath is unlikely to have changed its characteristics so profoundly in such a short time.

The second argument is based on the relative abundances of the incompatible elements Y, Nb and Zr in the batholith gabbros. These are displayed in Fig. 9.7 (Fitton *et al.*, 1997). Because $D_{Nb} < D_{Zr} << D_Y$, if the mantle has suffered a previous melt extraction event, the residue displaced to significantly lower Nb/Y and slightly lower Zr/Y. When this residue remelts, the resultant magma plots below at lower Nb/Y than bulk silicate earth. According to Fitton *et al.* (1997), this displacement of an analysed sample with respect to the lower tramline (their "ΔNb") is a "fundamental source characteristic and is insensitive to the effects of variable degrees of mantle melting, source depletion through melt extraction, crustal contamination of the magmas, or subsequent alteration". In a subduction zone environment, Y, Nb and Zr behave in a similar fashion to one another: they are thought to be preferentially retained in the subducting slab, rather than being transferred in a fluid phase to the mantle wedge (Saunders *et al.*, 1980). Their relative abundances are changed little by high degree partial melting, or by olivine, clinopyroxene and plagioclase fractionation. Fig. 9.7 shows that the mafic batholith magmas lie close to bulk silicate earth and the loci of the Aruba Lava Formation samples: this demonstrates that the mafic batholith magmas and the Aruba Lava Formation were derived from a source with similar characteristics in terms of incompatible high field strength elements. This rules out derivation from a subduction zone mantle wedge having depleted MORB characteristics.

To summarise, the gabbros of the batholith have many geochemical characteristics commonly associated with subduction zone magmas, for example, high LIL/HFSE ratios. However, their isotope and fluid-immobile trace element compositions are consistent with derivation from a plume-type mantle that is enriched (relative to the N-MORB source) in terms of isotope ratios and HFSE abundances. However, a subduction-derived (high LIL/HFSE) component appears to be necessary, in addition to a component with unradiogenic Pb. The high LIL/HFSE and unradiogenic Pb signatures could both be derived from one source, i.e., a fluid derived from a subducting slab, but this need not necessarily be the case.

No primary mantle melts have been sampled from the Aruba batholith: any primary mantle-derived melts probably stalled within the plateau crust and underwent fractional crystallisation, decreasing their MgO contents. Some of the evolved derivative magmas continued their ascent towards the surface, and were eventually emplaced into the batholith.

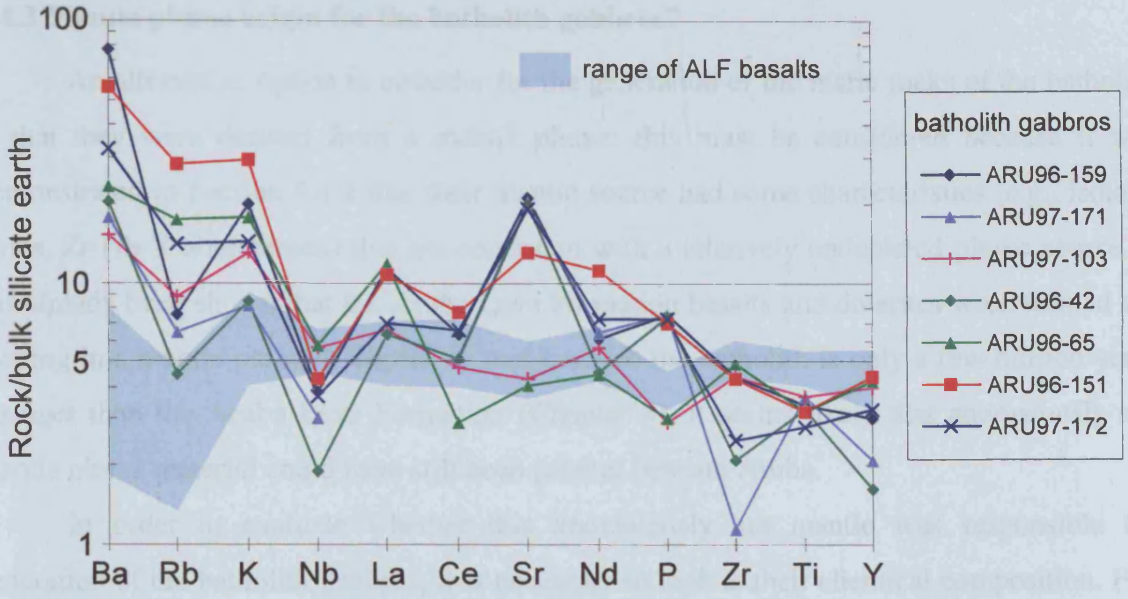

Fig. 9.6: Range of compositions of the *non-layered* gabbros from the batholith, i.e., those that are more likely to represent liquid compositions. These are compared with the range of the ALF basalts. Note that some of these gabbros, even though they show no obvious layering in the field, have geochemical characteristics (high Sr, low Zr) consistent with them containing accumulated plagioclase. Abundances normalised to bulk silicate earth of McDonough and Sun (1995).

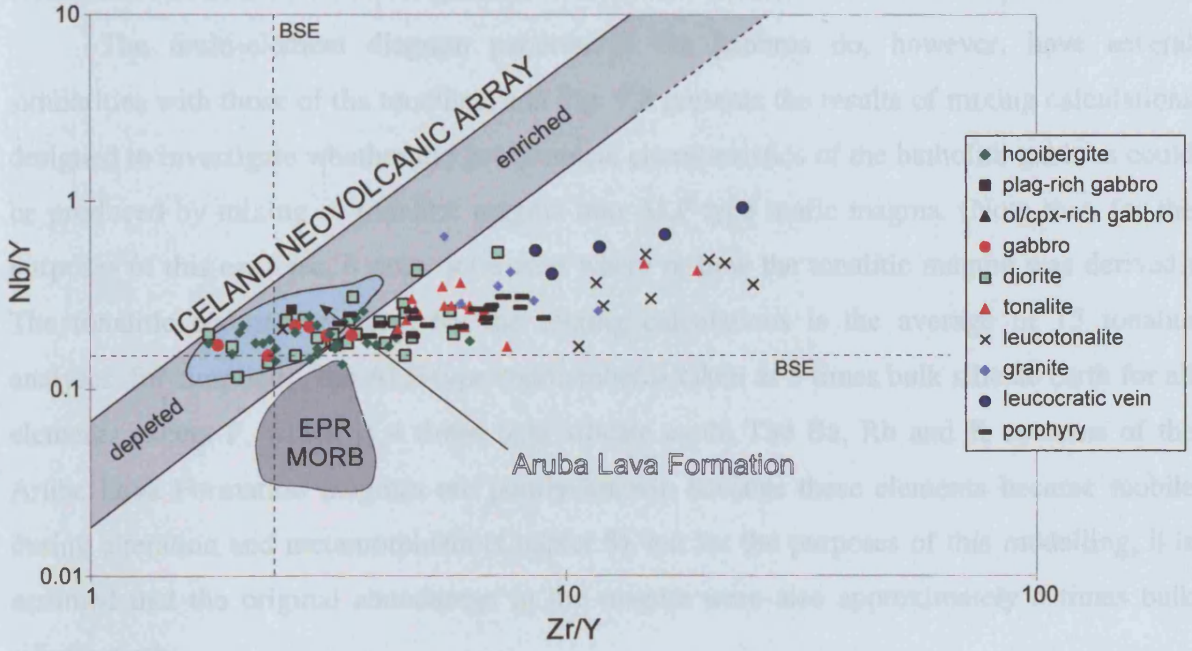

Fig. 9.7: Nb/Y vs. Zr/Y plot for samples from the Aruba batholith, after Fitton *et al.*, 1997, showing the plume-related Iceland neovolcanic array. The relative abundances of Nb, Y and Zr are changed little by partial melting or fractionation processes involving olivine, clinopyroxene or plagioclase (see text); consequently the location of samples on this plot indicates the trace element characteristics of the mantle source of the mafic rocks. Data for the batholith do not plot in the MORB field (EPR: unpublished East Pacific Rise data from A.D. Saunders); instead, the data show that the mafic members of the Aruba batholith were derived from a mantle source resembling that of the Aruba Lava Formation in terms of these incompatible elements. BSE: bulk silicate earth of McDonough and Sun (1995).

9.4.3 Mantle plume origin for the batholith gabbros?

An alternative option to consider for the generation of the mafic rocks of the batholith is that they were derived from a mantle plume: this must be considered because it was demonstrated in Section 9.4.2 that their mantle source had some characteristics (e.g., isotope ratios, Zr-Nb-Y abundances) that are consistent with a relatively undepleted plume source. It has already been shown that the Aruba Lava Formation basalts and dolerites were formed via melting in a mantle plume (Chapter 6), and because the batholith is only a few million years younger than the Aruba Lava Formation (Chapter 4), it seems likely that anomalously hot mantle plume material could have still been present beneath Aruba.

In order to evaluate whether this anomalously hot mantle was responsible for generation of the batholith gabbros, it is necessary to look at their chemical composition. Fig. 9.6 displays a multi-element diagram of the unlayered gabbros from the batholith, compared with the basalts and dolerites of the Aruba Lava Formation. With respect to the basalts and dolerites, the batholith gabbros are enriched in Ba, Rb, K, La, Ce, Sr, and Nd, and depleted in Nb, Zr, Ti and Y. It appears, therefore, that the gabbros cannot be melts from the plume that created the Aruba Lava Formation, unless considerable modification has taken place.

The multi-element diagram patterns of the gabbros do, however, have several similarities with those of the tonalites, and Fig. 9.8 presents the results of mixing calculations designed to investigate whether the geochemical characteristics of the batholith gabbros could be produced by mixing of tonalitic magma into ALF-type mafic magma. (Note that, for the purposes of this exercise, it does not matter where or how the tonalitic magma was derived.) The tonalitic endmember used for the mixing calculations is the average of 15 tonalite analyses; for simplicity, the ALF-type endmember is taken as 5 times bulk silicate earth for all elements except P, which is 4 times bulk silicate earth. The Ba, Rb and K contents of the Aruba Lava Formation magmas are poorly known, because these elements became mobile during alteration and metamorphism (Chapter 5), but for the purposes of this modelling, it is assumed that the original abundances in the magma were also approximately 5 times bulk silicate earth.

Fig. 9.8 shows that the range of compositions of the gabbros cannot be explained by simple mixing between Aruba Lava Formation basaltic magma and tonalite. For some elements, particularly Nb and Zr, the abundances in the gabbros are lower than those found in either the basalts or the tonalites. The Rb, Ba and K contents of the gabbros range to values as high as those found in the tonalites, and could only be explained by very high proportions of

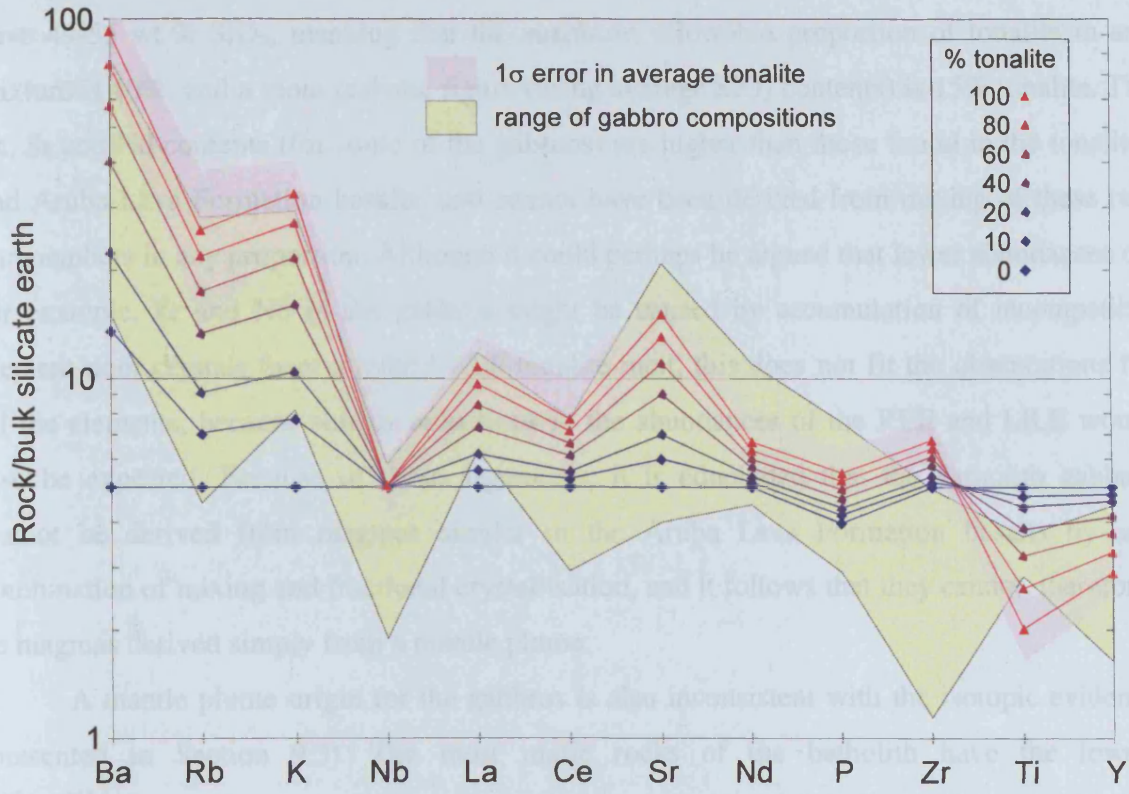

Fig. 9.8: Results of calculations designed to show whether the trace element abundances in the gabbros can be explained via mixing of a tonalitic melt (red triangles) and an Aruba Lava Formation-type mafic melt (blue diamonds). The diagram clearly demonstrates that this mechanism is not feasible: for example, to explain the Ba, Rb and K contents of some of the gabbros, the mixture would require a high proportion of tonalite, which would be easily detectable in the major elements. Abundances normalised to bulk silicate earth of McDonough and Sun (1995).

tonalite contributing to the mixture. Extremely high proportions of tonalite are not permitted by the major element composition of the magmas in question: for example, most Aruba Lava Formation basalts have 49-52 wt.% SiO_2; the tonalites have 64-68 wt.% SiO_2, and the gabbros have 49-55 wt.% SiO_2, meaning that the *maximum* allowable proportion of tonalite in any mixture is 40%, and a more realistic figure (using average SiO_2 contents) is 15% tonalite. The La, Sr and Nd contents (for some of the gabbros) are higher than those found in the tonalites and Aruba Lava Formation basalts, and cannot have been derived from mixing of these two endmembers in any proportion. Although it could perhaps be argued that lower abundances of, for example, Zr and Nb in the gabbros might be caused by accumulation of incompatible element-poor crystals from a hybrid ALF-tonalite melt, this does not fit the observations for all the elements, because similar reductions in the abundances of the REE and LILE would also be expected. Because of these arguments, it is concluded that the batholith gabbros cannot be derived from magmas similar to the Aruba Lava Formation basalts by any combination of mixing and fractional crystallisation, and it follows that they cannot, therefore, be magmas derived simply from a mantle plume.

A mantle plume origin for the gabbros is also inconsistent with the isotopic evidence (presented in Section 9.3). The most mafic rocks of the batholith have the lowest $(^{206}Pb/^{204}Pb)_i$, i.e., the most different from the plume-derived Aruba Lava Formation basalts and dolerites. This certainly does not support the idea of a similar mantle plume source region. The only conceivable way to impart an unradiogenic Pb signature to any plume-derived batholith gabbros is to have them being contaminated by terrigenous sediments intercalated within the plateau crust. Apart from the fact that no terrigenous sediments were observed, this is also inconsistent with the trace element data: an unrealistically high amount of sedimentary contamination would be required to generate the high La/Nb of the gabbros. Additionally, if terrigenous sediments within the plateau were available for contamination of magmas, it seems strange that none of the Aruba Lava Formation basalts or dolerites appear to have suffered a similar fate.

9.4.4 Generation of the gabbros: summary

The arguments presented in Sections 9.4.2 and 9.4.3 appear to yield a paradox: the high La/Nb of the gabbros requires a subduction-derived component in their petrogenesis, whereas the Sr and Nd isotope ratios and the Zr-Nb-Y abundances imply that the mantle source region was plume-like. This paradox can be resolved by envisaging a scenario where

the mantle material located in the wedge above the subducting slab originally had a mantle plume origin. This is likely to be the case for Aruba: the area was clearly overlying anomalously hot (plume) mantle at the time of formation of the Aruba Lava Formation. Subduction beneath this region would result in magmas that had both plume-like and subduction-like characteristics, depending on the properties of the particular trace element or isotopic system under scrutiny.

9.5 Generation of the tonalites of the batholith

9.5.1 Fractionation from the gabbros

Perhaps one of the simplest ways to derive a silicic melt is via fractionation from a mafic parent. Several data, however, suggest that the tonalites cannot be derived from the more primitive members of the batholith by simple fractional crystallisation. The most convincing argument against this mechanism is the Pb isotope ratios: the gabbros have the least radiogenic Pb isotopes, whereas the tonalites have a more radiogenic Pb isotope signature, similar to that of the Aruba Lava Formation basalts and dolerites.

The La/Nb ratios of the gabbros and tonalites also suggest that the two lithologies are not related by fractional crystallisation. The gabbros have, on the whole, higher La/Nb than the tonalites (Fig. 9.4a and c). If these rock types were related by fractional crystallisation of olivine and clinopyroxene, La/Nb would be expected to remain approximately constant throughout the suite. If they were related by fractional crystallisation of amphibole, La/Nb would increase with increasing SiO_2, because Nb is more compatible than La in amphibole (Pearce and Norry, 1979; Martin, 1987).

As stated previously, the correlation between La/Nb and Pb isotope ratio (Fig. 9.4a) suggests that the subduction zone component is contributing both of these signatures. If this is true, the gabbros have a higher subduction zone component than the tonalites. The correlation between Pb isotope ratio and lithology is, however, not perfect. There is a correlation between Pb isotope ratio and SiO_2 (Fig. 9.4b), but it is poorly defined. Similarly, the correlation between La/Nb and SiO_2 is poor (Fig. 9.4c). A possible reason for this is that SiO_2 contents are very susceptible to changes arising from crystal accumulation and fractional crystallisation; conversely, the good correlation between Pb isotopes and La/Nb probably arises because these do not change significantly during fractionation, although La/Nb may show very small changes.

A further argument against the gabbros and tonalites of the batholith being related by fractional crystallisation is the inflections in the trends observed for many of the major elements (see, for example, Fig. 8.19c). The unlayered gabbros are located approximately at the locus of this inflection. The only way to derive the tonalites from magmas of a similar composition to the unlayered gabbros would be to have fractionation involving a high Al_2O_3 phase, i.e., plagioclase. However, most of the cumulate rocks, even those accumulating from more evolved melts than the gabbros, do not have a high proportion of plagioclase in the cumulus assemblage. Moreover, plagioclase-rich cumulate rocks, if they existed, would impart a negative Eu anomaly to the residual liquid: this is not observed in the tonalites (Fig. 8.13d).

9.5.2 Direct melts of a metasomatised mantle wedge

It has been suggested by various authors (e.g., Mysen *et al.*, 1974) that silicic magmas can, in certain circumstances, be generated via direct melting of the mantle wedge, particularly if the mantle has been heavily metasomatised by, for example, slab-derived fluids in a subduction zone. These arguments, however, do not appear to be appropriate for the derivation of magmas resembling the Aruba tonalites. Firstly, any magma derived from the mantle without any subsequent modification would be in equilibrium with mantle olivine, and should consequently have a high Mg#, regardless of its silica content. High Mg# tonalites are not observed in the Aruba batholith. Additionally, the experimental work (e.g., Mysen *et al.*, 1974) has demonstrated that the most silicic rocks that can be generated from direct partial melting of the mantle (under a range of conditions) are andesitic; the tonalites of the batholith correspond to dacitic compositions, mainly having > 63 wt.% SiO_2.

A second argument against the tonalites being derived by this method is their La/Nb and $(^{206}Pb/^{204}Pb)_i$ contents. If these signatures are indeed derived from the fluid flux from the subducting slab, it follows that the tonalites would be generated from the most heavily metasomatised parts of the mantle wedge: these should have the highest La/Nb and the lowest Pb isotopes. This is the opposite to what is observed.

9.5.3 Melting of metabasalt

An origin for silicic calc-alkaline rocks by partial melting of metabasalt was first proposed by Green and Ringwood (1968) for the bimodal trondhjemite-basalt suites that occur in Archaean grey gneisses. This idea has gained a lot of support, particularly with the advent of more recent experimental studies, which have shown that tonalites and trondhjemites can

be generated via partial melting of metabasalt over a wide range of P (0.1 - 3.2 GPa), T (800 - 1100°C) and $P(H_2O)$ conditions (e.g., Beard and Lofgren, 1991; Rapp *et al.*, 1991; Winther and Newton, 1991; Wolf and Wyllie, 1994; Rapp, 1995; Rapp and Watson, 1995; Winther, 1996).

The principal reactions for generation of silicic magmas from an amphibolite precursor (at 1.5 and 2.0 GPa) are stated by Sen and Dunn (1994). These include:

amph (+ quartz) ⇒ melt + cpx

amph + plag (+ quartz) ⇒ melt + cpx + garnet

cpx + garnet ⇒ melt

In these experiments, quartz was the first phase to be exhausted, followed by plagioclase, then amphibole. The clinopyroxene and garnet created during the early stages of melting then reacted together to form melt; clinopyroxene became exhausted at approximately 60% melting, leaving a garnet restite. These equations are, however, not applicable to dehydration melting of amphibolite at lower pressures: Sen and Dunn (1994) place the garnet-in curve at approximately 1 GPa; below this pressure, garnet is not a stable residual phase.

Many of these experimental studies have focused on the generation of Archaean tonalite-trondhjemite-granodiorite (TTG) suites. One of the salient characteristics of TTGs is their extreme depletion in heavy rare earth elements (Fig. 9.9a). This is thought to arise by partial melting of metabasalt at appropriate depths for garnet to be a stable residual phase (e.g., Rapp *et al.*, 1991). A garnet-bearing (i.e., eclogitic) residue resulting from TTG magmatism is also consistent with the complementary geochemical nature of the continental crust and kimberlite-hosted eclogite xenoliths in the West African craton (Rollinson, 1997).

An extreme depletion in HREE is not observed in the Aruba tonalites. In fact, simple modal batch melting modelling (Fig. 9.9a) demonstrates that the Aruba tonalites could be derived from a 17% modal batch melt of an average Aruba Lava Formation basalt with 80% amphibole, 18% plagioclase and 2% garnet in the residue. Fig. 9.9b is designed to distinguish between residual garnet and amphibole (or clinopyroxene) in the source region. Residual garnet results in HREE depletion, and a steep overall REE pattern (i.e., high chondrite-normalised Ce/Yb); residual amphibole (or clinopyroxene) yield a depletion in the MREE, and low Gd/Yb. This modelling demonstrates that the REE contents of the range of Aruba tonalite compositions can be explained by partial melting of metabasalt, provided that the residual garnet in the source does not exceed ~ 3%.

Sensitivity analysis of this modelling demonstrates that the degree of melting and the proportions of phases obtained are actually rather sensitive to the particular basalt-tonalite

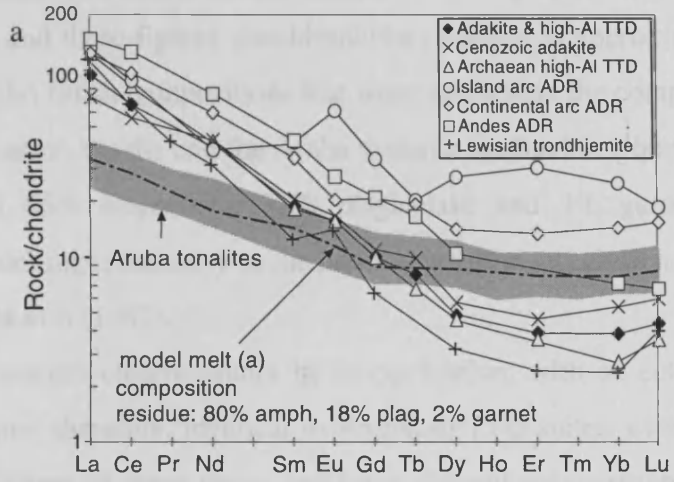

Fig. 9.9a: Chondrite-normalised (McDonough and Sun, 1995) REE plots for the Aruba tonalites and a 17% modal batch melt of ALF; these are compared with data from Drummond *et al.* (1996) and Rollinson and Fowler (1987). Partition coefficients from Martin (1987).

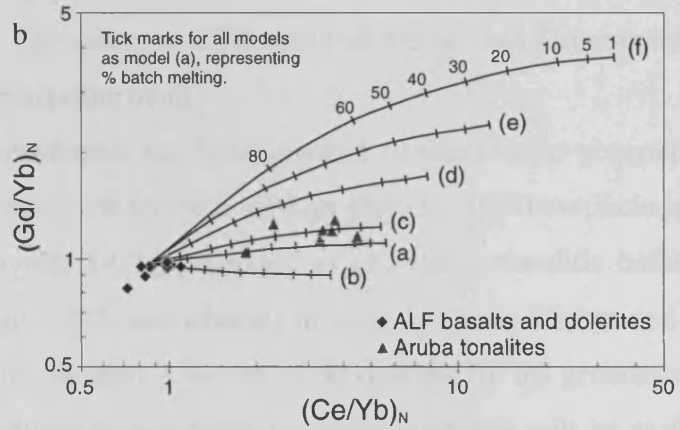

Fig. 9.9b: Results of REE modelling: Ce/Yb represents the steepness of the pattern (due to residual garnet); Gd/Yb represents the curvature (due to residual amph/cpx). All values chondrite-normalised (McDonough and Sun, 1995). Partition coefficients from Martin (1987).

(a) residue has 80% amph, 18% plag, 2% gt
(b) 50% amph, 50% plag
(c) 48% amph, 50% plag, 2% gt
(d) 45% amph, 50% plag, 5% gt
(e) 40% amph, 50% plag, 10% gt
(f) 35% amph, 35% plag, 30% gt

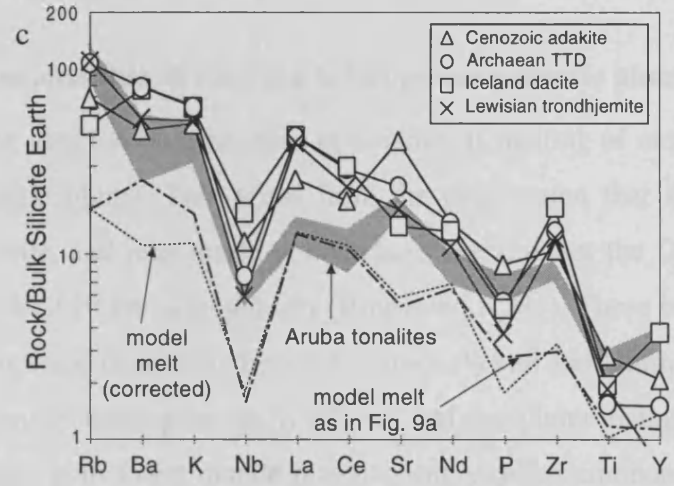

Fig. 9.9c: Trace element plot, normalised to bulk silicate earth (McDonough and Sun, 1995), for the Aruba tonalites, the same model melt as Fig. 9a, and model melt (arbitrarily) corrected for major phases and fluids. Iceland data from Jónasson *et al.* (1992). Partition coefficients from compilations of Rollinson (1993) and Green (1994). Data sources as for Fig. 9.9a.

combination chosen, and these figures should only be regarded as approximate. For example, another pair of start and finish compositions that were still within the compositional ranges of the Aruba Lava Formation basalts and the Aruba tonalites resulted in a best fit for 42% modal batch melting, with 65% amphibole, 32% plagioclase and 3% garnet in the residue. Additionally, the modelling is sensitive to the partition coefficients chosen: those used for this modelling are from Martin (1987).

The Aruba tonalites clearly cannot be in equilibrium with an eclogitic residue. The Aruba tonalites are not, therefore, identical to Archaean TTG suites, even though they have some similarities in terms of other major and trace element compositions, and may still be derived from partial melting of metabasalt at shallower (non-garnetiferous) depths. On a Ca-Na-K plot (Fig. 8.8), for example, the Aruba tonalites trend towards the TTD (tonalite-trondhjemite-dacite; equivalent to TTG) field of Defant and Drummond (1993) rather than having a normal calc-alkaline trend.

Melting of metabasalt has been invoked to explain the generation of tonalites and related rocks in a variety of tectonic settings (Fig. 9.10). These include dacites in Iceland (O'Nions and Grönvold, 1973; Óskarsson *et al.*, 1982), tonalitic batholiths in the Andes (Atherton and Petford, 1993) and adakites in many locations (Defant and Drummond, 1990). In the remainder of this section, a variety of possibilities for the generation of the tonalites by partial melting of metabasalt in a range of different settings will be explored. It is accepted that it is difficult to distinguish these settings by geochemical means alone, and it is possible that any, or all, of the mechanisms outlined below could be contributing to the Aruba tonalites; however, the main aim of this section is to determine the dominant mechanism for generation of the Aruba tonalites.

9.5.3.1 Melting of metabasaltic streaks in a heterogeneous mantle plume

One intriguing idea for the generation of tonalites is melting of metabasaltic streaks in a heterogeneous mantle plume. This arises from the observation that subducted slabs are recycled into the mantle, and may reside at boundary layers, either the D" layer at the core-mantle boundary, or the 670 km discontinuity (Ringwood, 1985). These boundary layers may also be the source for some deep-rooted mantle plumes (White and Hofmann, 1982). If these layers are compositionally heterogeneous, it follows that any plume rising therefrom also has the potential to contain both lower mantle material and recycled components (oceanic crust, oceanic sediments and oceanic lithosphere). As the plume ascends to shallow levels in the

upper mantle, the less refractory components would preferentially melt: this could give rise to a wide range of magma types.

Any recycled metabasaltic component in a plume rising from deep within the mantle would be at eclogite facies. It is doubtful whether the metabasaltic component could be hydrous, because downgoing oceanic slabs are thought to be extensively dehydrated during the early stages of their descent, as they convert to eclogitic (anhydrous) assemblages. (This release of water into the overlying mantle is, of course, the primary driving force for subduction zone magmatism.) It is known that tonalitic melts can be derived from partial melting of metabasalt, and there was undoubtedly a mantle plume beneath this area at ~ 88 Ma (to generate the Aruba Lava Formation): could the Aruba tonalites have been extracted from metabasalt streaks within a mantle plume?

There are several arguments against generation of the Aruba tonalites in this manner. The most serious is their lack of strong HREE depletion (Fig. 9.9a). The 2% residual garnet modelled for the Aruba batholith (Fig. 9.9b) is not compatible with derivation of the tonalites from an eclogite facies metabasaltic source region. It should be recalled here that the 2 GPa melting experiments of Sen and Dunn (1994) predict the existence of a purely garnetiferous restite: consequently, the Aruba tonalites cannot have been extracted from eclogites at these depths, no matter what the degree of melting.

Other geochemical arguments also suggest that the Aruba tonalites were not generated by this mechanism:

1) When oceanic crust is subducted, as it dehydrates, it tends to become depleted in fluid-mobile phases (e.g., La, Ba, K) relative to the HFSE (Saunders *et al.*, 1980). Thus, if this material is recycled in a mantle plume, it would have elevated levels of Nb compared to the other (fluid-mobile) incompatible trace elements. This is thought to be the origin of the positive Nb anomaly described from some ocean island basalts (e.g., Saunders *et al.*, 1988). Melting of a recycled oceanic crust component in a mantle plume should yield magmas that show evidence of this relative enrichment in Nb. The Aruba tonalites, however, have distinct negative Nb anomalies. In order to create magmas with negative Nb anomalies from a recycled basaltic component, Nb-bearing phases (e.g., rutile, sphene) would have to remain residual. The stability of these minor phases is doubtful at high enough degrees of melt (c. 20 - 30%: Winther, 1996) to generate tonalites; even if they did remain residual, it is unlikely that they would be volumetrically important enough to generate negative Nb anomalies from a source having positive Nb anomalies.

2) The degree of melting predicted in an upwelling mantle plume is also a cause for concern. The plume that generated the Aruba Lava Formation had a high enough potential temperature to cause ~30% melting of the mantle source (Chapter 6). If the same plume were responsible for generation of the tonalites, the less refractory recycled component would be expected to melt more extensively: this means that the melt extracted would be more mafic than tonalite. It is also dubious whether any melts generated from metabasaltic streaks within a mantle plume could be extracted from the source region without equilibration with mantle peridotite: this would result in silicic rocks with high Mg#. High Mg# is not a feature of the Aruba tonalites. Additionally, the generation of the Aruba tonalites in a plume-only environment cannot explain the field evidence for deformation observed in the Aruba Lava Formation prior to (and during) intrusion of the tonalites.

3) Finally, there are also good isotopic arguments against generation of the tonalites by melting of plume-hosted metabasalt. Where heterogeneous streaks in plumes have been proposed (e.g., Gorgona: Kerr *et al.*, 1996a; Iceland: Hémond *et al.*, 1993), this is based on isotopic (as well as trace element) differences. This implies that disequilibrium between streaks and host mantle must exist. The tonalites are isotopically very similar to the Aruba Lava Formation in terms of Sr and Nd isotopes; their Pb isotope ratios are only slightly less radiogenic. If the plume were heterogeneous, the largest isotopic differences would be expected to exist between the metabasalt streaks and the Aruba Lava Formation source material. This is not observed: the tonalites are the members of the batholith that are the most similar to the Aruba Lava Formation; it is the gabbros that are the furthest removed. An inherent implication of the suggestion that the tonalites are plume-derived is that the mafic rocks of the batholith are also plume-derived. In this case, it should be the mafic rocks of the batholith that are the most isotopically similar to the Aruba Lava Formation.

It is, of course, possible that the origin of the unradiogenic Pb signature within the batholith is a recycled sedimentary component within the plume. However, any sedimentary component within a plume is likely to be spatially associated with the recycled oceanic crust component. Therefore, melts of the recycled oceanic crust (i.e., tonalites) are the most likely to interact with this sedimentary component. This would again mean that the tonalites would be predicted to have the lowest Pb isotope ratios

It is therefore concluded that, although the mantle plume that generated the Aruba Lava Formation may well have been heterogeneous, it cannot have been the dominant source of the tonalites of the batholith. Moreover, it was shown in Section 9.4.2 that the gabbros of the batholith were also not derived directly from a mantle plume.

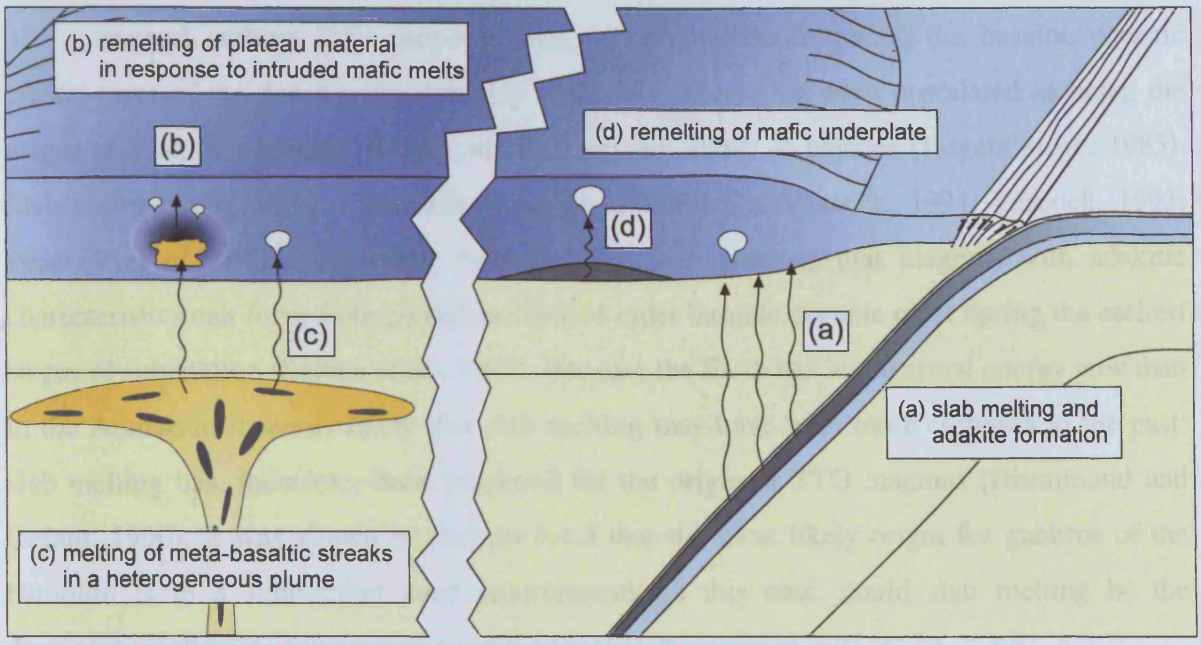

Fig. 9.10: Possible tectonic and thermal regimes where melting of meta-basalt could occur, resulting in:
(a) adakites from slab melting (Defant and Drummond, 1990)
(b) re-melting of ocean plateau crust in response to intrusion of plume-derived mafic melts (Iceland: Óskarsson *et al.*, 1982)
(c) melting of meta-basaltic streaks in a mantle plume to create andesites (Takahahshi *et al.*, 1998)
(d) re-melting of basaltic underplated material (Andes: Atherton and Petford, 1993)

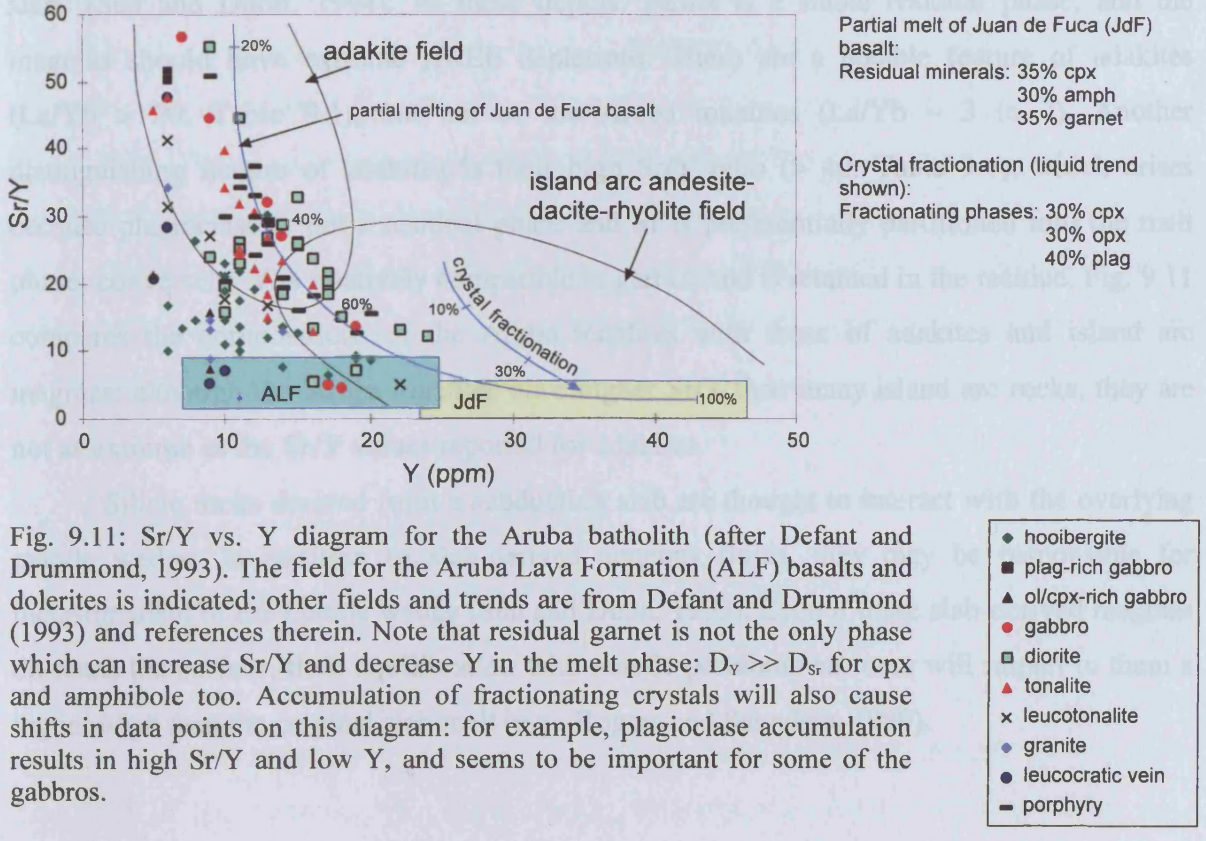

Fig. 9.11: Sr/Y vs. Y diagram for the Aruba batholith (after Defant and Drummond, 1993). The field for the Aruba Lava Formation (ALF) basalts and dolerites is indicated; other fields and trends are from Defant and Drummond (1993) and references therein. Note that residual garnet is not the only phase which can increase Sr/Y and decrease Y in the melt phase: $D_Y >> D_{Sr}$ for cpx and amphibole too. Accumulation of fractionating crystals will also cause shifts in data points on this diagram: for example, plagioclase accumulation results in high Sr/Y and low Y, and seems to be important for some of the gabbros.

9.5.3.2 Melting of the downgoing slab in a subduction zone

Several authors have proposed that, in certain circumstances, the basaltic oceanic crustal layer of the downgoing slab may melt: this process has been postulated as being the origin of adakitic magmas (Defant and Drummond, 1990) or bajaites (Rogers *et al.*, 1985). Slab melting may occur if the slab is young and still hot (Peacock, 1991; Peacock, 1993; Peacock *et al.*, 1994), and there have also been suggestions that magmas with adakitic characteristics can form from partial melting of older basaltic oceanic crust during the earliest stages of subduction (Sajona *et al.*, 1993). Because the Earth has less thermal energy now than in the Archaean, it seems likely that slab melting may have been more common in the past: slab melting has, therefore, been proposed for the origin of TTG magmas (Drummond and Defant, 1990). It was shown in Section 9.4.3 that the most likely origin for gabbros of the batholith is in a subduction zone environment: in this case, could slab melting be the dominant mechanism for generation of the tonalites?

Several lines of evidence argue against slab melting as being the primary contributor to the tonalites of the batholith. Again, although the major element constraints are perfectly compatible with generation of tonalite via partial melting of metabasalt, some of the trace elements are not. Slab melting will only occur where the slab geotherm intersects the wet basalt solidus: this is estimated to occur at depths greater than 50 km, even for young, hot slabs (Sen and Dunn, 1994). At these depths, garnet is a stable residual phase, and the magmas should have extreme HREE depletions. These are a notable feature of adakites (La/Yb > 20: Table 9.1), but not of the Aruba tonalites (La/Yb ~ 3 to 7). Another distinguishing feature of adakites is their high Sr/Y ratio (> 40: Table 9.1), which arises because plagioclase is not a residual phase and Sr is preferentially partitioned into the melt phase; conversely, Y is relatively compatible in garnet, and is retained in the residue. Fig. 9.11 compares the compositions of the Aruba tonalites with those of adakites and island arc magmas: although the Aruba tonalites have higher Sr/Y than many island arc rocks, they are not as extreme as the Sr/Y values reported for adakites.

Silicic melts derived from a subducting slab are thought to interact with the overlying mantle wedge; in addition to slab-derived aqueous fluids, they may be responsible for metasomatism of the mantle wedge (Sen and Dunn, 1993). Even if these slab-derived magmas do reach the surface, their equilibration with mantle peridotite en route will impart to them a higher Mg# than the original slab melt (e.g., Rogers and Saunders, 1989).

Table 9.1: Comparison of Aruba tonalite with adakites (Drummond and Defant, 1990)

Characteristic	Adakite	Aruba tonalite
SiO_2 (wt.%)	>56	62-73
Al_2O_3 (wt.%)	>15	14-16
MgO (wt.%)	<3	<3
Sr (ppm)	>300	200-400
Sr anomaly	positive	positive
$^{87}Sr/^{86}Sr$	<0.7040	~0.7036
Sr/Y	>40	10-40
La/Yb	>20	3-7
Yb (ppm)	<1.9	1.1-1.9
Y (ppm)	<18	10-17
Nb (ppm)	<10	<4
mineralogy	plag + amph ± cpx ± bi ± opaques	plag + amph + bi + qtz + opaques

An origin of the tonalite by slab melting alone is also inconsistent with the isotopic composition of the tonalites: if the predominant source material was subducted N-MORB, the tonalites should have higher ε_{Nd} and lower $(^{87}Sr/^{86}Sr)_i$ than is observed. To explain the ALF-like Nd and Sr isotope signatures, a fortuitous mixture of N-MORB and a subducted sediment component would be required. However, any sedimentary input into the tonalites must have had little effect on the Pb isotopes, and this method of generating the observed isotopic signatures seems unlikely. Additionally, it appears that the gabbros (rather than the tonalites) of the batholith have the most prominent subduction zone signature: the opposite would be expected if the tonalites were derived from slab melting.

On balance, the evidence suggests that an origin of the tonalites by slab melting *alone* is impossible. A small component of melt derived from the downgoing slab cannot, however, be completely ruled out.

9.5.3.3 Melting of metabasalt of the plateau

Several authors have suggested that some of the silicic volcanic rocks on Iceland have formed by remelting of the Icelandic mafic crust (e.g., O'Nions and Grönvold, 1973; Óskarsson *et al.*, 1982, Gunnarsson *et al.*, 1998) or remelting of pre-existing silicic segregations within that crust (Marsh *et al.*, 1991). A major constraint on these models is the low-$\delta^{18}O$ of the some of the silicic rocks, implying involvement of isotopically light

(meteoric) water in their petrogenesis. Additionally, the Icelandic lavas are strongly bimodal, comprising approximately 85% basalts, 12% rhyolites and only 3% intermediate rocks (Walker, 1966; Sigurdsson, 1977), which is more consistent with most being derived by partial melting rather than fractional crystallisation (although the latter process may be responsible for some of the silicic magmas (e.g., MacDonald *et al.*, 1990)). It is now widely accepted that partial anatexis of rocks of basaltic composition can create melts resembling Icelandic dacites and rhyolites (Thy *et al.*, 1990). These magmas also have some geochemical similarities with the Aruba tonalites. The dacites of the Króksfjördur Volcano (Jónasson *et al.*, 1992) in Iceland are calc-alkaline in character, and have depletions in high-field-strength elements (e.g., Nb) normally associated with subduction-related volcanic suites, although a subduction zone component clearly cannot be contributing to these young Icelandic volcanics, located at a spreading ridge.

It is possible that remelting of metabasalt within an oceanic plateau sequence could create melts with similar characteristics to the Aruba tonalites. The prominent difference between these silicic magmas formed by intra-crustal melting, and those formed by partial melting of subducting oceanic crust, is the amount of garnet in the residue. This demonstrates that, if the Aruba tonalites did form by partial melting of the plateau sequence, it must have been at a relatively shallow depth, where residual garnet was not an important phase. Constraints on the actual depth of melting are poor; the garnet-in curve has been placed at about 1 GPa (30 km) by Sen and Dunn (1994), so the melting must have occurred at depths less than this. Of course, if it is postulated that melting is occurring within the plateau sequence, it is obvious that it cannot occur at greater depths than the thickness of the plateau. Seismic studies (Edgar *et al.*, 1971) suggest a thickness of 8 to 20 km for the Caribbean crust: in theory, this thickness could be increased by tectonic thickening (imbrication), particularly at the margins of the plateau.

Fig. 9.9c shows the predicted composition of a 17% (modal) batch melt of an average Aruba Lava Formation basalt with the same residual phases (80% amph, 18% plag, 2% garnet) as for the REE modelling. Although the correspondence is not perfect, the predicted melt composition mimics the relative elemental abundances for the average tonalite. A modal batch melt was chosen as the simplest model, and fits the observations by Sen and Dunn (1994) that the melting proportions of amphibole and plagioclase in their experiments were *approximately* modal. The correspondence of the model with the average tonalite composition is considerably improved if a correction is made for an aqueous fluid phase and minor phases.

It is noted that the K/Rb and Ba/Rb of the model melt are lower than observed in the average tonalite. This could be due to the loss of Rb into a co-existing metamorphic fluid. K would also be liable to become partitioned into this fluid. Similarly, the P and Ti contents of a melt coexisting with amphibolite are likely to be affected by the presence of minor phases remaining residual in the amphibolite: if, for example, ilmenite and apatite remained residual, the Ti and P contents of the coexisting melt would be lower. (Note that both ilmenite and apatite are present in the amphibolites at Andicuri that are interpreted to have begun to partially melt.)

This modelling merely illustrates that it is possible to derive a melt with a trace element composition approximately similar to the Aruba tonalites via partial melting of an ALF-type metabasalt. This modelling, like the REE modelling, is sensitive to relatively small variations in the chosen starting composition: this makes the degree of melting and the proportions of residual phases poorly constrained. The starting composition is particularly ill-defined for Ba, Rb and K, elements that are highly mobile in the Aruba Lava Formation basalts. Another limitation in this modelling is the assumption of modal melting. Although this is likely to be approximately valid, it is undoubtedly a simplification. Experimental studies (Sen and Dunn, 1994) report the progressive exhaustion of quartz, then plagioclase, then amphibole with increasing temperature and degrees of melting, meaning that the melting cannot be truly modal. This may explain the discrepancy in Fig 9.9c between the Sr abundance of the model and observed tonalite: if the proportion of plagioclase entering the melt was greater than its modal proportion, this would result in a higher Sr content, closer to the observed data. Models are also severely limited by poorly constrained partition coefficients - for example, the partition coefficients reported for the REEs in hornblende for silicic magmas vary by almost an order of magnitude between authors (e.g., Arth and Barker, 1976; Henderson, 1984; Martin, 1987; Klein *et al.*, 1997).

One requirement for partial melting of a mafic protolith at geologically reasonable temperatures is that the protolith should be hydrated. On Iceland, this is achieved because the plateau is being constructed at a spreading centre: hydrated basalts sink to deeper levels as the crust rotates and subsides (Palmáson, 1986). Although it was suggested in Chapter 6 that many features of the Aruba Lava Formation are consistent with it having erupted in a near-ridge environment, there is no clear evidence whether or not the Caribbean Plateau was actually formed *at* a spreading centre, so this mechanism of moving hydrated material into the crust is not necessarily appropriate. A tectonically distinct alternative is imbrication of the

plateau as it begins to interact with a subduction zone (sheared rocks at amphibolite facies are found on Aruba). A further possibility is that no external mechanism is required to hydrate an oceanic plateau, because the large thicknesses of extrusive material undergo hydration during the construction of the plateau; submarine volcaniclastic sediments are also present within the plateau, and could act as a water source to assist melting. The evidence for only a small amount of garnet in the melting residue suggests that the melting occurred at shallow depths: this is the most likely horizon of the plateau to be hydrated.

Hydration of the plateau rocks might be expected to leave an isotopic signature that would be inherited by the products of partial melting. The Sr, Nd and Pb isotope ratios of the tonalites are, however, very similar to those of the Aruba Lava Formation, implying that if the tonalites were generated by this mechanism, hydration of the Aruba Lava Formation did not result in any significant isotopic changes. The $^{87}Sr/^{86}Sr$ values obtained in this study show that, although the deformed and altered members of the Aruba Lava Formation tend to be shifted to higher $^{87}Sr/^{86}Sr$ than the undeformed basalts, this must be a very late signature, because one deformed sample has isotopic ratios identical to the undeformed basalts. Instead, these high values are interpreted as secondary alteration (Chapter 6). Consequently, hydrated, altered members of the Caribbean oceanic plateau cannot be precluded as a source material for the Aruba batholith. Future studies using other isotopic systems (e.g., oxygen isotopes) are needed to try and fingerprint any hydrothermal fluid. It should be noted, however, that the Pb isotope ratios of one of the analysed tonalites are very slightly lower than the least radiogenic Aruba Lava Formation sample: this indicates that simple partial melting of the plateau sequence may not be the only process occurring.

Although the genesis of the Aruba batholith can be explained by melting within the plateau sequence (with an additional mantle-derived component: see Section 9.6), tonalites of batholithic proportions are not a commonly observed feature of oceanic plateaux. Aruba may be anomalous in this respect because the intrusion of the tonalite is penecontemporaneous with deformation – the development of shear zones within the plateau sequence may have provided a means by which these silicic melts could segregate, coalesce, and rise to higher levels within the crust (Rushmer, 1995). However, a great deal of thermal energy is required to create the observed volumes of tonalite by partial melting of metabasalt, and this may be the reason why Aruba has these voluminous tonalites: the thermal energy required could potentially be provided via addition of subduction-derived mafic melts to the plateau crust. If these mafic magmas were derived from the underlying plume, the plateau remelting model

predicts a smaller time interval between basaltic and tonalitic magmatism than is observed; if they originated in a subduction zone beneath the plateau, the period of time between plateau basalt and tonalitic magmatism would be longer.

If this method of generating the tonalites is correct, it provides important constraints on the location of the unradiogenic-Pb endmember contributing to the batholith. If this component was, as suggested in Section 9.3.2.2, terrigenous sediment intercalated in the plateau crust, the tonalites should have a higher proportion of this component, because sedimentary intercalations in the plateau should melt concomitantly with their basaltic hosts. One method of avoiding melting of any sediment would be to have the subduction-derived mafic melts stalling in the lower (sediment-free) plateau crust, transferring heat to the hydrated plateau rocks, causing partial melting and formation of tonalites with isotope ratios similar to those of the plateau sequence. In order for this to work, no tonalites could become contaminated with terrigenous sediment during their ascent into the upper part of the plateau; conversely, the gabbros would have to be contaminated with the unradiogenic-Pb endmember, but would not be permitted to cause any melting of the surrounding basaltic material and sediment to generate tonalites. This argument is very contrived. Additionally it requires generation of the tonalites in a sediment-free part of the plateau sequence; this is likely to be the lower parts of the plateau. Generation of the tonalites in the lower plateau crust would be more likely to result in a higher proportion of residual garnet in the metabasaltic source.

It is therefore concluded that the unradiogenic-Pb endmember is located in the mantle wedge region, and was probably derived from the subducting slab. This provides the simplest mechanism for the mantle-wedge-derived batholith gabbros to have the lowest $(^{206}Pb/^{204}Pb)_i$; the tonalites are derived primarily from the plateau sequence, and have isotopic signatures similar to those of the Aruba Lava Formation.

9.6 Clues from the diorites: a combination of processes?

Although partial melting of the upper part of the plateau appears to best explain the generation of the tonalites, the model is still not perfect. In particular, the Pb isotope ratios of one of the tonalites are slightly less radiogenic than any of the analysed Aruba Lava Formation magmas. This might suggest that the tonalites too have a small amount of the subduction zone component. A model where the tonalites are explained by melting within the plateau and the gabbros are generated in the subduction zone predicts that the resulting rock suite should be bimodal: this is not the case, because there are also significant quantities of diorite within the batholith.

An origin for the diorites as direct melts of a metasomatised mantle wedge can be ruled out on the grounds that the diorites do not have high enough Mg#s, (with the exception of those samples that are clearly not representative of liquid compositions, e.g., the hooibergites). Formation of the diorites by partial melting of metabasalt in the plateau is also extremely unlikely, as unreasonably high degrees of melting would be required to generate a melt with a dioritic bulk composition: it is difficult to envisage a realistic heat source for such high degree of melts. Inspection of Fig. 9.4a shows that one of the diorites falls between the tonalites and the gabbros in terms of La/Nb and $(^{206}Pb/^{204}Pb)_i$. Another is similar to the tonalites. This implies that simple fractional crystallisation from the gabbros also cannot account for the compositions of the diorites.

This leaves two main options for the genesis of the diorites, both of which are consistent with the major element compositions and the La/Nb and Pb isotope constraints: 1) fractional crystallisation of the gabbro with concomitant assimilation of plateau material; and 2) mixing between gabbroic and tonalitic liquids. These processes are not mutually exclusive, and there are, in fact, a number of variants that could have occurred, but these would not be easily distinguishable from one another using the geochemical data. For example, the assimilation of plateau material could include wholesale assimilation of basaltic xenoliths that fell into the gabbroic melt. In this case, the low La/Nb and high $(^{206}Pb/^{204}Pb)_i$ characteristics would be contributed by the assimilant, and the major element compositions would be controlled by the fractional crystallisation. Wholesale assimilation of basaltic material (derived from the plateau sequence) on a large scale seems rather unlikely, however, on thermal grounds. For each volume of plateau material that becomes elevated in temperature enough to melt completely, it is logical that there should be an even greater volume that becomes hot enough to only melt partially. Thus, assimilation of partial melts of plateau material seems a more likely alternative to wholesale plateau assimilation.

This process is effectively the same as mixing between gabbroic and tonalitic liquids: in this case, both the bulk compositions and the trace element and isotopic ratios are controlled by the compositions and proportions of the different endmembers, and not by fractional crystallisation. Fig. 9.12 shows mixing lines between a hypothesised gabbroic endmember and either a silicic melt (derived from the plateau, and having the same isotope ratios as the plateau material, but having higher La/Nb) or an Aruba Lava Formation basalt. Given the scatter in the data, either mixing with a plateau-derived silicic melt or wholesale assimilation of Aruba Lava Formation rocks is acceptable to explain the observations.

However, the poorly constrained composition of the gabbroic endmember, and the fact that the plateau (or plateau melt) endmember could have $(^{206}Pb/^{204}Pb)_i$ anywhere between 18.65 and 19.1, mean that Fig. 9.12 should not be viewed as quantitative.

Fig. 9.12 does show, however, that some degree of mixing between an endmember having a slab component and a plateau-derived endmember is necessary to explain the observed compositions, not only of the diorites, but also of the tonalites. The most radiogenic tonalite sample could, conceivably, be a direct partial melt of a relatively unradiogenic part of the plateau sequence; the other tonalite sample has lower $(^{206}Pb/^{204}Pb)_i$ than any of the analysed Aruba Lava Formation rocks, which requires that it has *at least* a small subduction-derived component in its genesis. The field observations also indicate clearly that magma mixing has been an important process in the evolution of the batholith.

Fig. 9.12 does not give any information about fractional crystallisation, because this process does not alter Pb isotope ratios, and has little effect on La/Nb. Although it appears from the preceding arguments that fractional crystallisation does not appear to be *necessary* to explain the range of compositions observed in the batholith, the data certainly do not preclude its occurrence. In fact, the presence of cumulate rocks within the batholith suggests that it may have been important. It seems, therefore that both fractional crystallisation and magma mixing have played important roles in the evolution of the batholith magmas. In practise, it is not possible to judge, using the available data, whether the compositions observed have been controlled more by assimilation of plateau material with concomitant fractional crystallisation (AFC) or by magma mixing.

The discussions above are, of course, oversimplified. In reality, different batches of magma could have different original trace element and isotopic ratios; they will also have undergone differing degrees of mixing and fractional crystallisation. Adopting a more realistic scenario helps to explain some of the scattered data points plotted in Fig. 9.12. Realistic compositional variables that can be introduced into the arguments are:

- subduction-derived gabbro endmembers with varying La/Nb and Pb isotope ratios;
- plateau-derived partial melts with a range of Pb isotope ratios reflecting the range observed in the Aruba Lava Formation rocks;
- different degrees of partial melts of the plateau resulting in different La/Nb and different bulk compositions;
- fractional crystallisation or crystal accumulation from any of the melts, resulting in elevated or decreased SiO_2 content for the same Pb isotope ratio and similar La/Nb.

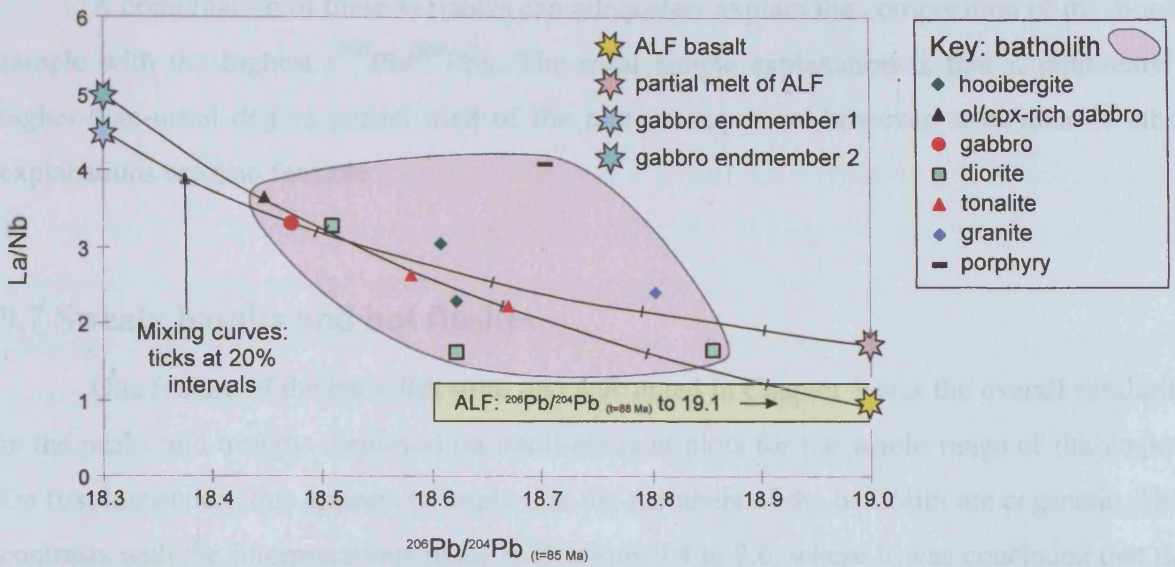

Fig. 9.12: La/Nb vs. $^{206}Pb/^{204}Pb$ plot, showing mixing lines between Aruba Lava Formation (ALF) basalt, partial melt of ALF basalt and hypothesised gabbro endmembers with a subduction zone signature (high La/Nb, low $^{206}Pb/^{204}Pb$). This plot demonstrates that the compositions of the batholith magmas can be explained by contamination of gabbro endmembers with either ALF basalt, or partial melts therefrom. The actual compositions of the endmembers are very poorly constrained (see, for example, range in $^{206}Pb/^{204}Pb$ of ALF), so this diagram should not be considered quantitative.

Compositions of endmembers:	$^{206}Pb/^{204}Pb$	Pb (ppm)	La (ppm)	Nb (ppm)
ALF basalt	19.0	3.2	2.8	3.1
ALF partial melt	19.0	3.0	6.0	3.5
gabbro 1	18.3	2.0	4.5	1.0
gabbro 2	18.3	2.0	5.0	1.0

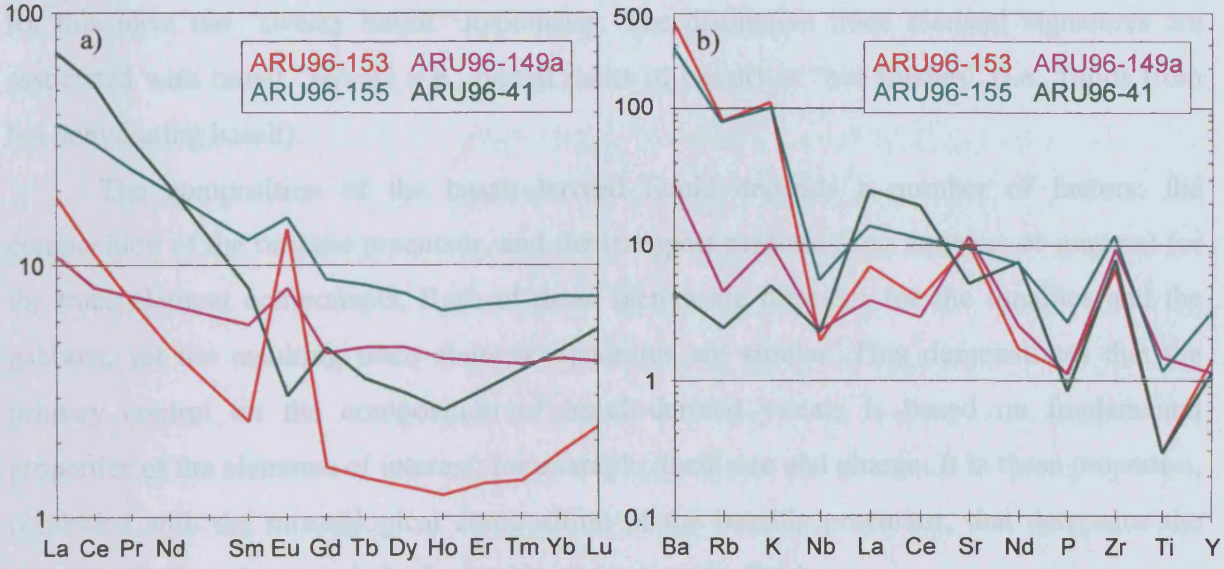

Fig. 9.13: Trace element and REE data for the most leucocratic members of the batholith. In spite of the large differences in REE patterns, the trace element patterns show a number of similarities.
a) normalised to C1 chondrite of McDonough and Sun (1995)
b) normalised to bulk silicate earth of McDonough and Sun (1995)

A combination of these variables can adequately explain the composition of the diorite sample with the highest $(^{206}Pb/^{204}Pb)_i$. The most simple explanation is that it represents a higher-than-usual degree partial melt of the plateau sequence; however, a number of other explanations are also feasible.

9.7 Sweaty basalts and hot flushes

One feature of the batholith suite that was noted in Chapter 8 was the overall similarity in the peaks and troughs displayed on multi-element plots for the whole range of lithologies. On first inspection, this appears to imply that the members of the batholith are cogenetic. This contrasts with the interpretations made in Sections 9.4 to 9.6, where it was concluded that the mafic rocks of the batholith are predominantly subduction-derived, and the silicic rocks arise by partial melting of the plateau sequence. If the two lithological endmembers found in the batholith (i.e., gabbro and tonalite) really do have such different origins, surely this similarity in their trace element compositions is too coincidental?

This is not necessarily true. The trace element compositions in both the gabbros and the tonalites of the batholith may merely be similar because they are caused by similar processes. The basic premise behind this is that the petrogenesis of both the gabbros and the tonalites involves, at some point, pre-existing basaltic rocks getting very hot: hence my phrase for this idea: the "sweaty basalt" hypothesis. The distinctive trace element signatures are associated with basalt "sweat" (i.e., partial melts of basalt) or "hot flushes" (i.e., fluids from hot dehydrating basalt).

The composition of the basalt-derived liquid depends a number of factors: the composition of the basaltic precursor, and the transport medium (i.e., aqueous or magma) for the trace element components. Both of these factors are different for the tonalites and the gabbros, yet the resulting trace element signatures are similar. This demonstrates that the primary control on the composition of basalt-derived sweats is based on fundamental properties of the elements of interest; for example, their size and charge. It is these properties, combined with the mineralogical composition of the basaltic precursor, that determine the mobility of these elements in both aqueous and magmatic fluids.

Let us take first the example of the gabbro. The major element composition suggested that this was derived from the mantle, but an additional component with high La/Nb was required to explain its petrogenesis. Because this high La/Nb component correlated with $(^{206}Pb/^{204}Pb)_i$, it was hypothesised that this component was derived from a subducting slab. In

addition to terrigenous sediments, which may have contributed some of the low $(^{206}Pb/^{204}Pb)_i$ and possibly some of the La/Nb signature, the subducting slab consists of hydrothermally altered basaltic oceanic crust. The trace element characteristics of subduction zone magmas are commonly attributed to slab-derived fluids, a significant component of which could be derived from the basaltic part of the slab. As the slab descends into the subduction zone, it progressively increases in temperature (due mainly to conduction, but possibly also to frictional heating). This results in the progressive destabilisation of hydrous phases, for example, clay minerals, and culminates in the breakdown of amphibole at the amphibolite-eclogite transition zone. Any elements that are mobile in the aqueous fluids leaving the slab, especially those that are incompatible in the newly-forming phases, are liable to be flushed into the mantle wedge. This results in an enrichment of fluid-mobile elements such as Ba, K and La in the mantle wedge; conversely, elements that are compatible in the newly forming phases (e.g., Y) or are not mobile in aqueous fluids (e.g., Nb) are retained in the slab. Thus, an aqueous-fluid-hosted "hot flush" in a subduction zone results in enrichments of Ba, K, Sr, Rb and LREE relative to Y, the HREE and HFSE.

The tonalites, however, are made up almost entirely of magmatic "sweats" from plateau basalt, which was heated following intrusion of subduction-derived magmas. The trace element composition of these sweats is controlled by the partitioning of elements between the residue and the melt, and also the proportions of phases contributing to the melt. It has already been shown (Figs. 9.a and 9.c) that a partial melt of Aruba Lava Formation basalt has enriched Ba, Rb, K, La, Ce and Sr compared to Zr, Y, Nb and HREE. This is controlled primarily by the relative compatibility of the HFSE and HREE in amphibole.

These two types of basalt-derived fluid are remarkably similar in composition, even though they formed in different environments. The reason for their similarity is that both incompatibility in major phases and solubility in aqueous phases are controlled by the ionic potential of the element (i.e., the charge:size ratio for an ion of the element). Those elements with lower ionic potential (e.g., Rb, K, Ba, Sr, La) tend to be both incompatible during melting, and mobile in aqueous fluid phases. Conversely, the elements with smaller ionic radius and/or higher charge are more compatible during melting, and less mobile in aqueous fluids. One element that appears not to perfectly fit this hypothesis is Rb: according to the sweaty basalt hypothesis, Rb, with its large ionic radius and low (1+) charge, should be highly enriched in basalt-derived fluids. However, the abundances of Rb in both the gabbros and the tonalites are lower than would be predicted by this model. This could arise because Rb has

such a low ionic potential that it is, along with Cs, one of the most easily sweated elements. It could, therefore, be partially lost from a system before the temperature rises high enough to cause the other elements to be sweated out. Possible mechanisms for loss of Rb in the particular environments discussed above include: 1) incorporation of Rb from plateau basalts into metamorphic fluids before the onset of melting; 2) loss of Rb in the earliest stages of subduction, with the fluids being transferred into the fore-arc region, rather than the region of significant melt generation.

9.7.1 Generation of the most silicic material in the batholith

The most silicic rocks of the batholith (granites and leucocratic veins) have similar multi-element patterns to the rest of the batholith, except that they tend have steeper negative slopes, and have larger negative anomalies for P and Ti. Analyses of the four silicic rocks that were described in Section 8.2.2 are shown in Figs. 9.13a and b. The REE patterns for these rocks are very different, indicating different processes in their petrogenesis. However, the multi-element plots have a lot of similarities. This indicates, once again, that a variety of processes can generate trace element signatures similar to those observed in the tonalites - are these too variations on the sweaty basalt theme?

ARU96-153 and ARU96-155 have bulk silicate earth-normalised multi-element diagrams that have similar characteristics to the majority of the batholith rocks; however, their REE patterns show that only ARU96-155 is truly similar to the tonalites. This sample was probably generated in a similar fashion to the tonalites, but is richer in Ba, Rb, K and Eu, perhaps reflecting a higher feldspar content. ARU96-153 can be modelled reasonably by a small degree (< 10%) batch melt of Aruba Lava Formation amphibolite, leaving only amphibole in the residue, if partition coefficients for hornblende and rhyolitic liquid are used (Arth, 1976). The increased compatibility of REE in hornblende when in equilibrium with a rhyolitic (rather than dacitic) liquid results in the low absolute REE abundances in this lithology. This model predicts a lower Eu content for this rock than the observed value; this might be because partition coefficients for Eu vary with oxygen fugacity, and the value used may not be appropriate.

The other two rocks have bulk silicate earth-normalised multi-element diagrams that are different from the tonalites in that they have lower abundances of Ba, Rb and K. ARU96-149a is an example of a sweat from a basaltic amphibolite. Even though it has lower abundances of all the REEs than the amphibolite it was veining, its composition can still be

broadly explained by partial melting of this amphibolite, using Arth's (1976) partition coefficients for rhyolitic liquids.

Sample ARU96-41 is completely different: it has the lowest abundances of Ba, Rb and K, but the highest REE contents. Of the four highly silicic samples analysed for REE, this one alone cannot be explained by partial melting of metabasalt. The only residual phase capable of generating a negative Eu anomaly during partial melting is plagioclase, which would have to be present in any residue in considerable proportions: this is at odds with the melting reactions reported in Sen and Dunn (1994; see also Section 9.5.3). Additionally, plagioclase does not discriminate greatly between the LREE and the HREE, and would not be capable of generating the steep REE pattern observed. If anything, plagioclase shows a preference for the LREE (e.g., Arth and Barker, 1976), and this would impart a relative LREE depletion to the melt, that is not observed. The geochemical characteristics of this rock are, however, roughly consistent with it being derived from a tonalitic melt via extraction of amphibole and plagioclase as crystallising phases. Interestingly, this rock, which is not a direct product of a basaltic sweat, has the bulk silicate earth-normalised multi-element diagram that is the most different from the tonalites, and the hypothesised sweat compositions.

9.8 Detailed model for silicic magmatism associated with oceanic plateaux

9.8.1 Key constraints on the model

The association of a sequence of tholeiitic mafic rocks with a dominantly tonalitic batholith raises several important issues: how and why does this association occur? These issues may have relevance to the generation of silicic material (TTGs) associated with Archaean greenstone belts, and the generation of the Earth's earliest continental crust. It has been shown that the Aruba Lava Formation has many geochemical similarities with other members of the Caribbean oceanic plateau, and can therefore be considered a part of this province. The Aruba batholith, on the other hand, is geochemically distinct from the mafic lava sequence, having characteristics typically associated with subduction-related rocks (e.g., negative Nb anomalies, tonalitic composition), although it is possible to derive these chemical characteristics by hydrous melting or dehydration of basalt in a variety of tectonic settings.

Any model which attempts to explain the petrogenesis of this silicic material associated with an oceanic plateau sequence must account for the following observations:

1) The members of the batholith have a wide lithological variation, ranging from gabbroic rocks to tonalites and trondhjemites. These have similar incompatible element ratios and Sr and Nd isotope ratios, and are comagmatic.

2) The ~85 - 82 Ma batholith was intruded into the Aruba Lava Formation shortly after formation of the latter. There is, therefore, only a limited time period (~3 - 9 m.y.) during which the magmatic environment has to change from one producing voluminous mafic tholeiites to one producing a tonalitic series.

3) The intrusion of the batholith is penecontemporaneous with deformation of the Aruba Lava Formation.

4) The Aruba Lava Formation and the batholith overlap in isotopic composition for Sr and Nd. The batholith rocks have slightly less radiogenic Pb isotope ratios; this is most noticeable for the more mafic rocks of the batholith.

9.8.2 Description of the model, and its relation to Caribbean tectonics

In Section 9.2, a basic model was presented for the generation of the Aruba batholith and its tectonic setting. The data in support of this model have now been discussed in Sections 9.3 to 9.7, and a more detailed description of the final, complex, multi-stage petrogenetic model will be the subject of this section. The petrogenetic model will be considered together with the tectonic setting of the region (Fig. 9.14).

Stage 1: Mantle plume activity and the building of the Caribbean plateau (91-88 Ma)

At ~ 91 Ma (Sinton *et al.*, 1998), a mantle plume had its first impact upon a region in the eastern Pacific Ocean: this may have been the starting phase of the Galápagos plume (Duncan and Hargraves, 1984), although this is by no means certain. The volcanic activity arising from the impact of this mantle plume was voluminous, and constructed an oceanic plateau with an area of at least 6×10^5 km^2, and an estimated thickness of 8 to 20 km (Edgar *et al.*, 1971). This stage of magmatism, which produced voluminous tholeiitic basalts, as well as picrites (Curaçao: Klaver, 1987; Kerr *et al.*, 1996b) and komatiites (Gorgona: Echeverría, 1980; Kerr *et al.*, 1996a), lasted until approximately 88 Ma (Sinton *et al.*, 1998).

The Aruba Lava Formation is a part of this magmatic province: the Caribbean oceanic plateau. It consists of predominantly basaltic low-K tholeiitic rocks that are remarkably homogeneous in terms of major and trace element compositions and isotope ratios. The basalts are intercalated with volcaniclastic sediments, and dolerite bodies intrude the

sequence. The trace element and isotope ratios of the basalts and dolerites are all consistent with derivation from a mantle source that was slightly depleted relative to bulk silicate earth, but not as depleted as the N-MORB source. An estimate of 30% partial melting to generate the basalts is proposed: because there is little evidence of significant garnet in the residue, it is inferred that the melt column extended to shallow depths, i.e., the Aruba Lava Formation was erupted in a near-ridge environment. None of the basalts or dolerites is a primary mantle-derived melt – all have undergone some degree of fractionation (probably of olivine) prior to emplacement. This fractionation probably occurred at low pressures.

Stage 2: Initiation of subduction beneath the plateau (88-85 Ma)

Soon after the deposition of the Aruba Lava Formation, a new subduction zone was initiated, dipping westwards beneath the plateau (Burke *et al.*, 1984). This was probably a consequence of the young, hot, buoyant plateau clogging the pre-existing eastward-dipping subduction zone adjacent to the Americas. The collision between the plateau and the subduction zone was presumably the cause of the folding and deformation of the Aruba Lava Formation.

After the reversal of subduction polarity, the oceanic crust in the area between North and South America (the Proto-Caribbean crust) was consumed beneath the plateau. At this time, the mantle beneath the plateau was still the mantle-plume material, which would have been unusually hot, compared to normal mantle. The Proto-Caribbean crust that was subducted beneath the plateau may have had a veneer of terrigenous sediment; when the downgoing oceanic crust dehydrated, it flushed the mantle wedge with fluid containing La, Ce, Ba, K, Rb, Sr and unradiogenic Pb (derived either from the basaltic part of the slab or the subducted sediment). This addition of a hydrous fluid caused the already-hot mantle wedge material to partially melt, creating basaltic melts with a strong subduction zone signature, but with ratios of HFSE representative of the plume-related mantle source region.

Stage 3: Interaction between subduction-derived melts and plateau rocks (85-82 Ma)

None of the magmas of the batholith are primary mantle-derived magmas, indicating that even the most primitive must have undergone some crystal fractionation, probably of olivine, between source and emplacement. This would have required the stalling of the subduction-derived basaltic melts, probably within the oceanic plateau crust. This resulted in a considerable transfer of heat to the adjacent country rock, i.e., the basaltic material of the

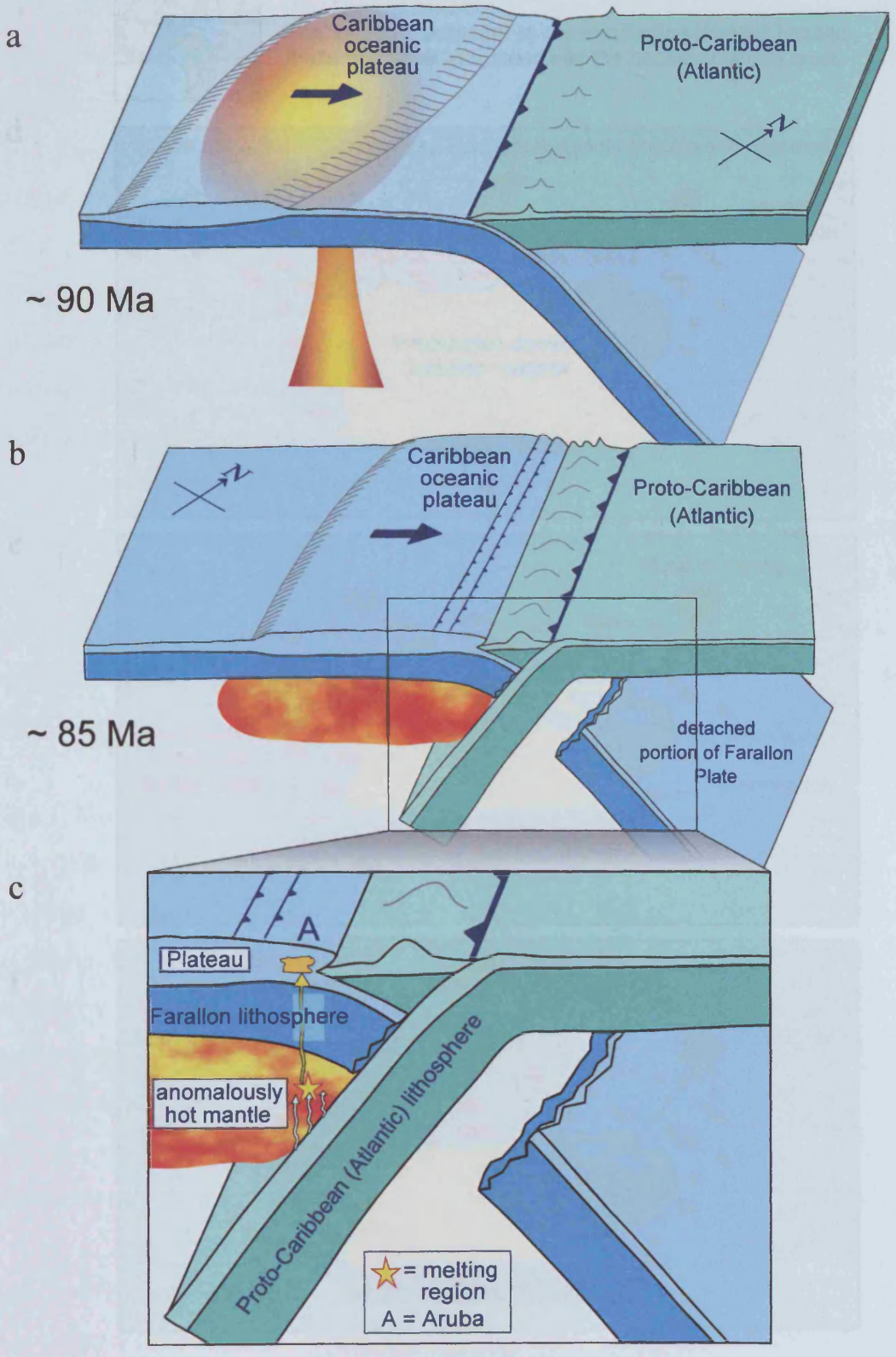

Fig. 9.14: Model for tectonic evolution of the Caribbean region in relation to the petrogenesis of the Aruba batholith (continued on next page)
a) Mantle plume activity and the building of the Caribbean plateau
b) Initiation of subduction beneath the plateau
c) Dehydration of the subducting slab. A high La/Nb and low $^{206}Pb/^{204}Pb$ component derived from the slab and subducted terrigenous sediment is transferred into the anomalously hot mantle wedge, which partially melts; these basaltic melts are emplaced into the plateau crust, and may undergo olivine-dominated fractionation.

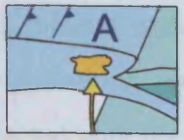

The location: adjacent to the subduction-derived basaltic melts that were emplaced into the oceanic plateau crust.

d

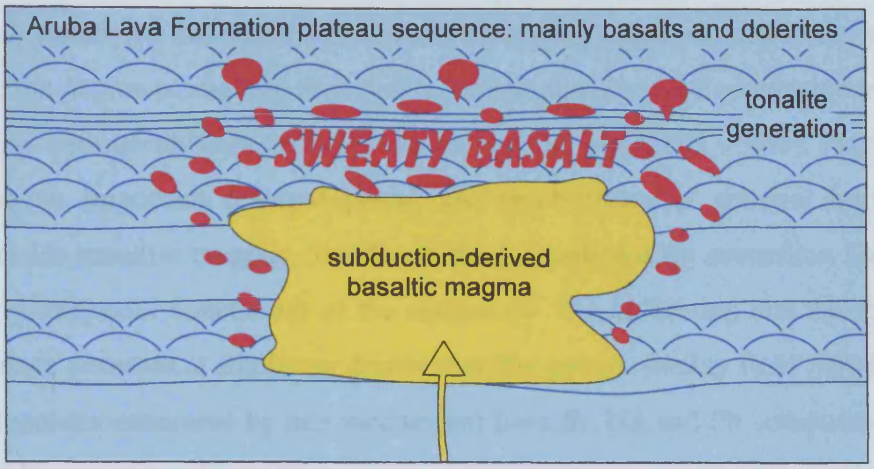

e

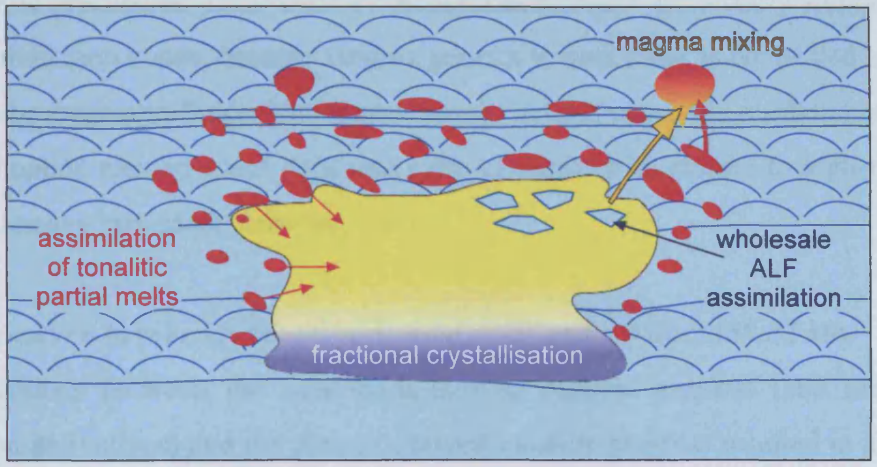

f

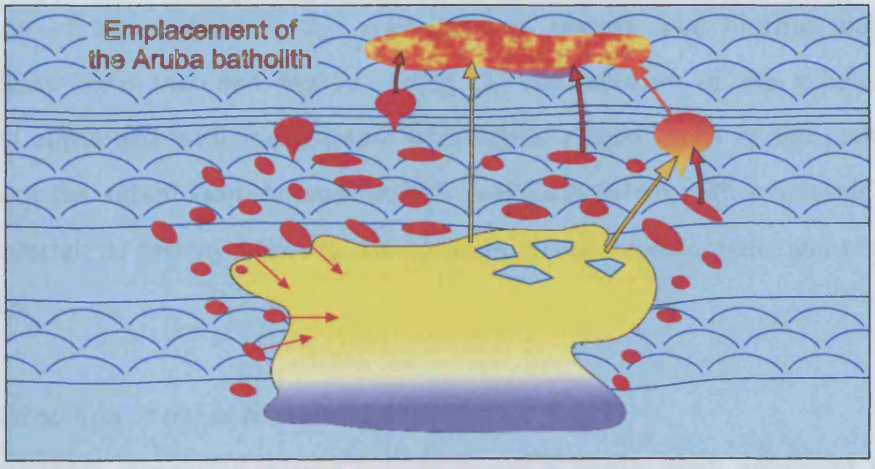

Fig. 9.14 : Model for the petrogenesis of the Aruba batholith (continued from previous page):
d) Emplacement of subduction-derived basaltic melts into the plateau sequence causes the hydrated basaltic country rock (the Aruba Lava Formation) to partially melt, generating tonalites.
e) A number of factors can influence the evolution of the magmas. These include: fractional crystallisation, assimilation of tonalitic partial melts into the subduction-derived basaltic melt, wholesale assimilation of ALF rocks into the subduction-derived basaltic melt and magma mixing.
f) Emplacement of the Aruba batholith, comprising magmas from any of the above processes. Magma mixing and fractional crystallisation continue within the batholith.

plateau. This plateau material may have been hydrous, with the hydration occurring either immediately following eruption of the basalts, or during later tectonic movements as the plateau interacted with the subduction zone.

Partial melting of the metabasaltic material in the plateau resulted in the generation of the tonalites: the degree of melting required to explain the observed compositions varies from ~ 15% to 45%, with hornblende as the dominant residual phase (65 - 80%). Plagioclase (18 - 32%) is also an important residual phase; the combination of residual hornblende and plagioclase yields tonalitic magmas that do not have significant Eu anomalies. Garnet is not a volumetrically important constituent of the residue (< 5%), indicating that the melting of the plateau sequence occurred at shallower depths than the garnet stability field (<30 km).

The tonalites generated by this mechanism have Sr, Nd and Pb compositions identical to their basaltic precursors. Their trace element characteristics are broadly similar to magmas derived in subduction zones, because magma genesis in both cases is controlled by the loss of aqueous and/or magmatic fluids from heated basalt: in both cases this results in enrichment of large-ion-lithophile elements and light rare earth elements with respect to high-field-strength elements and heavy rare earth elements.

Stage 4: Interaction between subduction-derived melts and tonalites (85-82 Ma)

Interactions between the subduction-derived basaltic magmas (and their fractional crystallisation derivatives) and the plateau-derived tonalitic magmas resulted in a reduction in the bimodality of the suite, i.e., the generation of intermediate dioritic magmas. These interactions may have included the following: 1) fractionation of the subduction-derived basaltic melts combined with assimilation of tonalitic partial melts of the plateau crust; 2) fractionation of the subduction-derived basaltic melts combined with wholesale assimilation of plateau material; 3) mixing between subduction-derived basaltic melts and plateau-derived tonalitic melts.

Stage 5: Construction of the batholith (85-82 Ma)

The magmas generated during Stages 3 and 4 above were emplaced to create the Aruba batholith, which is presumably at a higher structural level than the main zone of tonalite generation and magma interaction. The first magmas to be emplaced into the batholith were basaltic to andesitic in composition: these formed the gabbro massif at Matividiri and cumulate rocks (the hooibergites and layered gabbros). The residual liquids from formation of

these cumulates may have either been lost from the system (i.e., erupted), or became assimilated by the voluminous incoming tonalitic and dioritic magmas that formed the bulk of the batholith. Interactions between these magmas continued throughout the construction of the batholith: magma mixing textures are ubiquitous in the tonalitic rocks.

Stage 6: The last gasps: late mafic dykes (~76 Ma)

The final magmatic event to affect Aruba was the emplacement of mafic to intermediate dykes, cutting both the batholith and the Aruba Lava Formation. These have distinct subduction zone signatures, and indicate the continuation of subduction beneath the plateau at this time. There is no evidence of magmatism on Aruba subsequent to this, which raises the question of why the cessation occurred. One explanation could be that, subsequent to 76 Ma, the part of the Caribbean plateau containing Aruba collided with the South American continent, and Aruba became stranded in the Caribbean-South America Plate Boundary Zone. The active subduction zone, however, continued its passage to the east, with the result that Aruba became located further and further from the locus of active magmatism.

9.8.3 Implications for Caribbean tectonics and magmatism

In addition to having implications for the generation of continental crustal material, the model for Aruba presented above has implications for the tectonic evolution of the Caribbean region, and the resulting magmatic evolution. Two aspects of this are discussing in the following sections.

9.8.3.1 Reversal in subduction polarity

One potential difficulty with generation of the Aruba batholith in a subduction regime, as detailed in Section 9.8.2, is the relatively short time period (~ 3 to 9 m.y.) in which the magmatic environment changes from one dominated by plume-derived mafic tholeiites to one dominated by subduction-related magmas and re-melts of the plateau. Is it possible for renewed melt generation to occur so rapidly after a change in tectonic configuration?

The data obtained in this study, however, show clearly that the subduction polarity reversal event must have been complete by ~85 Ma. In normal thermal circumstances, the downgoing oceanic plate must reach a depth of 80 - 100 km before it dehydrates and triggers melting in the overlying mantle wedge (Gill, 1981); the time taken for this is of the order 2 m.y. (using arbitrary figures of 7 cm/yr for the subduction rate at an angle of 45°). This

constrains the subduction polarity reversal event in the Caribbean to have happened swiftly after extrusion of the plateau sequence (91 - 88 Ma). This does indeed appear to be remarkably rapid; however, neither the mechanisms by which subduction zones switch polarity, nor the timescales this occurs on, is known. Two factors may alleviate the apparent problem of this rapid subduction polarity reversal:

1) The mantle wedge overlying the new subduction zone is certainly not thermally "normal". It consists of plume-mantle remaining from the plateau-building event, which would still be anomalously hot; indeed, it may be possible that new, less depleted plume material was transported into the mantle wedge by induced convection. Anomalously hot mantle adjacent to the subducting slab would result in more rapid dehydration of the downgoing oceanic crust, and possibly melt generation at depths less than the 80 - 100 km proposed by Gill (1981).

2) The subduction polarity reversal is unlikely to have occurred at exactly the same time along the whole length of the colliding plateau. A different part of the plateau could have collided with the subduction zone at a slightly earlier time, initiating the polarity reversal. Propagation of the subduction zone having the new polarity would be energetically easier than its initiation, meaning that a subduction flip event in a particular location could occur rapidly. This is illustrated diagramatically in Fig. 9.15.

Until now, the timing of the subduction polarity reversal in the Caribbean has not been well constrained, with estimates ranging from 100 Ma to 60 Ma (Burke, 1988; Draper *et al.*, 1996), and although the consensus is that the reversal was caused by the arrival of the 91-88 Ma phase of the Caribbean oceanic plateau (Burke *et al.*, 1984; Duncan and Hargraves, 1984; Pindell and Barrett, 1990), a number of authors insist that the reversal must have occurred prior to this (e.g., Lebron and Perfit, 1993). However, a polarity reversal prior to formation of the plateau in the Pacific leaves no mechanism for the plateau to ever move into its present location; instead, some of these earlier events (e.g., exhumation of blueschists: Smith *et al.*, submitted) may result from subduction stepping back, rather than reversing.

The data from Aruba provide the best constraints so far on the timing of the subduction polarity reversal in this region: it occurred after eruption of the plateau sequence, and prior to the earliest subduction-derived magmas on Aruba, i.e., between 88 and 85 Ma. Aruba's present location in the South Caribbean plate boundary zone suggests that the area must have originally been located on the leading edge of the advancing plateau before it became (geographically) part of the South American continent. This means that the change in

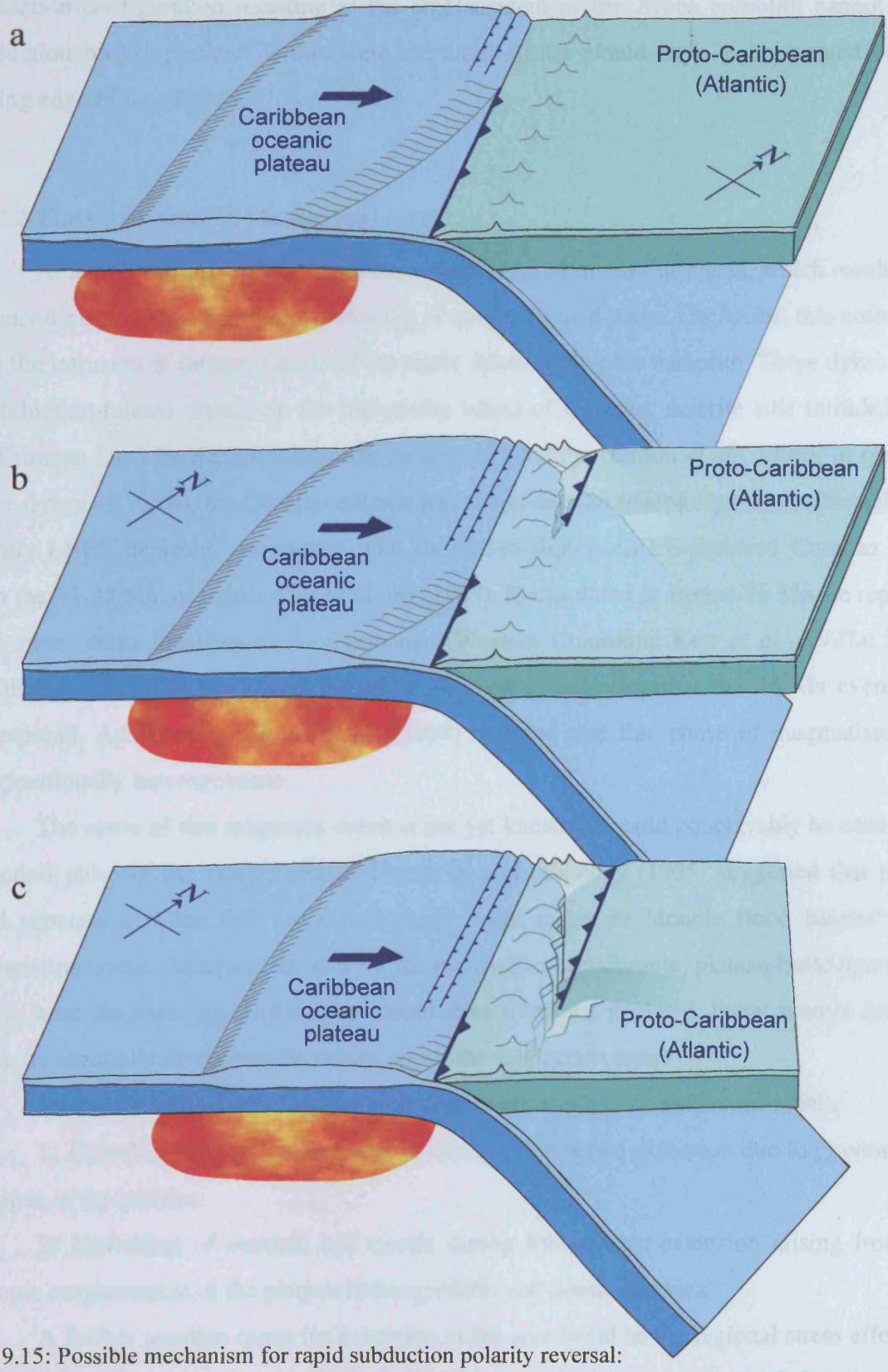

Fig. 9.15: Possible mechanism for rapid subduction polarity reversal:
a) Part of the plateau interacts with a subduction zone, resists subduction, and begins to imbricate.
b) A new subduction zone is initiated, dipping in the opposite direction. In order for this to occur, the original downgoing slab must physically get out of the way. A "rip" initiates (perhaps at a transform fault?), allowing the commencement of subduction of teh Proto-Caribbean plate.
c) Once formed, this "rip" propagates relatively easily and rapidly; consequently, the subduction polarity reversal in locations removed from the original "rip" occurs more quickly.

subduction configuration resulting in the emplacement of the Aruba batholith cannot be a subduction backstep event: if this were the case, Aruba would have to be located on the trailing edge of the plateau.

9.8.3.2 The Caribbean 76 Ma thermal event

At approximately 76 Ma, a thermal event occurred in the Caribbean, which resulted in enhanced magmatism and isotopic resetting of earlier-formed rocks. On Aruba, this coincided with the intrusion of (at least) some of the mafic dykes cutting the batholith. These dykes have a subduction-related chemistry. On the nearby island of Curaçao, dolerite sills intruded into the Curaçao Lava Formation (plateau sequence) at this time (Sinton *et al.*, 1998); in contrast to the dykes on Aruba, the Curaçao dolerite has no subduction related signature, although it is slightly LREE depleted, contrasting with the flat-to-slightly-LREE-enriched Curaçao lavas from the 91-88 Ma magmatic phase (Klaver, 1987). Rocks dated at around 76 Ma are reported from many other localities in the Caribbean (Western Colombia: Kerr *et al.*, 1997a; Haiti, DSDP Site 152/ODP Site 1001: Sinton *et al.*, 1998), indicating that the 76 Ma event was widespread. Additionally, Sinton *et al.* (1998) reported that this phase of magmatism was compositionally heterogeneous.

The cause of this magmatic event is not yet known. It could conceivably be caused by a second pulse of the mantle plume. Bercovici and Mahoney (1995) suggested that plume head separation at the 660 km discontinuity could result in "double flood basalts": this explanation could, therefore, account for the two, apparently discrete, plateau-building events. If this were the case, the Aruba dykes could arise from less depleted, hotter mantle material being transported into the mantle wedge above the subduction zone.

Other explanations for the 76 Ma thermal event include (Sinton *et al.*, 1998):

1) Upwelling of residual hot mantle during lithospheric extension due to gravitational collapse of the plateau;

2) Upwelling of residual hot mantle during lithospheric extension arising from the tectonic emplacement of the plateau between North and South America.

A further possible cause for extension in the area could be the regional stress effects of subduction zones: a westward dipping subduction zone existed at the eastern side of the plateau (the present Lesser Antilles subduction zone), and at some point, an eastward-dipping subduction zone developed along the plateau's western margin (the present Central American

subduction zone). The combined effect of these two subduction zones could have resulted in a back-arc extension on a regional scale, but this is pure speculation.

9.9 Implications for crustal growth models

The data reported in this thesis suggest that the generation of silicic material (with a composition not dissimilar to that of the bulk continental crust) is not just limited to continental active margins. The multi-stage petrogenetic model presented in this chapter indicates that tonalitic material can be generated by partial melting of the metabasaltic crust of plume-derived oceanic plateaux. Silicic magmas generated by this mechanism are found on Iceland, but are volumetrically minor; this indicates that the thermal conditions within an oceanic plateau are normally not sufficiently hot to allow partial re-melting on a grand scale. If, however, an additional thermal input is provided, the potential for melt generation within a plateau is increased dramatically. The mechanism proposed in this study for providing the extra thermal impetus to assist partial re-melting is the addition of subduction-derived basaltic melts to the plateau crust.

This study has showed that creation of batholithic suites consisting primarily of tonalites *can* occur entirely within the oceanic domain, i.e., without any interference or influence from pre-existing continental material. Moreover, the time interval required to modify oceanic plateau crust by addition of tonalitic material can be relatively short. This purely oceanic environment contrasts with the generation of the majority of Phanerozoic tonalites, which are predominantly associated with continental active margins. Therefore, the processes that created the Aruba tonalites may be analogous to the processes that formed the first continental nuclei.

This model has important implications for models of crustal growth. It indicates that crustal growth via plateau accretion is a viable model for addition of mass to the continental crust. One reason why extensive tracts of accreted plateau material may not be recognised in the geological record is that they become modified into material resembling continental crust: this study has demonstrated that this "ripening" of oceanic plateaux may begin at a much earlier stage than was previously suspected.

The mechanism of generating tonalite in a setting involving subduction beneath an oceanic plateau highlights several characteristics of this planet that have had profound effects on its ability to generate continental crust. Firstly, mantle plumes are extremely important, because they provide a spatially-focused source of thermal energy, resulting in locally-

enhanced melting, and the creation of thick oceanic crust. This thick crust (i.e., an oceanic plateau) is more buoyant than normal oceanic crust, and has a greater potential for being accreted, rather than subducted. Additionally, in the Phanerozoic, mantle plume activity has tended to be episodic (for example, the Cretaceous superplume activity: Larson, 1991); if mantle plume episodicity were also a feature of the Precambrian Earth, this temporal control on the production of oceanic large igneous provinces may have been responsible for the apparent episodicity in generation of new continental crust.

A second feature of the Earth that is rather unusual (compared to the other terrestrial planets in this solar system) is the presence of large volumes of free water at the surface. Without this, neither the oceanic crust nor the plateau crust could be hydrated; there would be no mechanism for lowering the mantle solidus to trigger melting in subduction zones; and melting within an oceanic plateau would require more thermal energy, because the dry basalt solidus (rather than the wet amphibolite solidus) would have to be exceeded. Thirdly, in order to transport the Earth's water into locations in which it can assist melting, the motion of lithospheric plates is a prerequisite.

Finally, it should be noted that the model presented in Section 9.8 is capable of generating tonalites associated with voluminous mafic tholeiitic rocks; however, the tonalites generated in this case are *not* identical to Archaean TTGs. This indicates that the mechanism discussed during this thesis cannot be identical to that responsible for generation of the Archaean TTGs. However, the only significant geochemical differences between the Aruba tonalites and the Archaean TTGs are those that are dependent on the amount of garnet in the residue, i.e., the depth of melting: for example, the extent of HREE depletion. The possibility remains, therefore, that a mechanism analogous to the one presented herein is a potential candidate for Archaean TTG generation, providing that the depth of melting for the Archaean TTGs was greater. This may reflect the difference in thermal regime between the Phanerozoic and the Archaean: in the Archaean, the hotter mantle would have produced hotter plumes, resulting in thicker oceanic plateaux, in which remelting could occur at greater depths.

9.10 Scope for further research

The work presented in this study offers considerable opportunities for further research, combining different disciplines, different geographical areas, and different periods in Earth history.

The main conclusion from this study, that silicic material can be generated within oceanic plateaux as a consequence of addition of subduction-derived mafic magmas, is only strictly applicable to those silicic magmas without extensive HREE depletion. However, it was speculated above that an analogous mechanism, with melting occurring at greater depths, may have been responsible for the generation of Archaean TTGs. An interesting further study would be to compare the Caribbean scenario with Archaean greenstone belts that contain TTG-type magmas, to determine whether these TTGs could have been derived from melting within the greenstone sequence. This would require an estimate of the thickness of the greenstone crust. For the purposes of this kind of study, it does not matter whether greenstone belts represent accreted oceanic plateau material, or accreted island arc: both contain hydrated basaltic material that could be a protolith for tonalite generation. The geochemical signatures of the tonalites generated by partial melting of these two different precursors should, however, be different, and distinguishable.

Another unanswered question in this thesis is the mechanism by which subduction polarity reversals occur: it was stated in Section 9.8.3.1 that the subduction polarity reversal in the Caribbean must have occurred quickly, but it remains unclear exactly how this could occur. The 3 - 9 m.y. gap in magmatism proposed for Aruba (this study) is significantly less than the 8 - 12 m.y. suggested for the Solomon Islands subduction polarity reversal event (a consequence of the docking of the Ontong Java Plateau: Petterson *et al.*, 1999). Nevertheless, initiation of new subduction zones must be a relatively common occurrence, when viewed over the whole of Earth history. What features do subduction polarity reversals impart to the geological record? In the Caribbean region, considerable confusion has arisen because a number of geological features (e.g., unconformities, exhumed blueschists) have been cited as evidence for the subduction polarity reversal; but how many of these features can be unequivocally related to reversals, rather than other changes in subduction zone configurations, such as back-step, or accretion of minor seamounts? If a feature was identified that could be unequivocally related to subduction polarity reversal, this could prove a useful tool in the unravelling of geological histories of accreted terranes.

A third potential avenue for research is to look at a modern example of an oceanic plateau (e.g., Iceland) to examine how much of the plateau material geochemically resembles continental crust. Care would have to be taken to distinguish those silicic magmas derived from fractional crystallisation and those from re-melting of the plateau crust. A study such as this would enable an estimate to be made of the volumes of continent-like magmas that are an

inherent part of oceanic plateaux; the relative importance of subduction-derived melts being intruded into the plateau to provide the extra thermal impetus for melting could then be determined. One possibility is that silicic magmas within plateaux are more common than has been realised: on Aruba, the silicic melts generated within the plateau formed a batholith, rather than being extruded: is there any geophysical evidence for relatively low density rock bodies within the Iceland crust?

Finally, it is acknowledged that both mantle plumes and subduction zones have an important role to play in the generation of continental crustal material; a less obvious consideration is that their presence continues to influence the composition of that crust for billions of years after its initial formation. In order for a complete picture to be gained of crustal *evolution* (rather than generation), it is vital to assess the processes by which continental material is "ripened" by addition of further melts, and reworking within the crust.

Appendices

Appendix A: Sample information

Appendix B: ^{40}Ar-^{39}Ar geochronology

Appendix C: XRF analyses

Appendix D: Rare Earth Element analyses

Appendix E: Data Quality for XRF and REE analyses

Appendix F: Radiogenic isotope analyses

Appendix G: Electron microprobe analyses

Appendix H: Presentation and Publication of this study

Appendix A

Sample information

A.1 Location Map (in pocket inside back cover)

Map of Aruba showing locations of samples taken for this study. Sample names of rocks collected by the author in 1996 and 1997 are abbreviated on this map, e.g., sample ARU96-100 is denoted 96-100. Samples donated by Gerard Klaver and colleagues retain their full sample name. A particular sample can be located with reference to Appendix A.2.

A.2 Sample location and lithological information

This appendix consists of a comprehensive list of samples used during this study, sorted according to sample number order.

The location is given as the name of the most appropriate Aruban settlement or topographic feature, and a six-figure grid reference, to be used in conjunction with the map (Appendix A.1), is also reported. Note that grid references can be converted into latitude and longitude (degrees) *for the map area* via the following method:

Northings (N): Degrees = 0.0090393N + 12.3844908

Eastings (E): Degrees = -0.0091991E + 70.0849443

N should be expressed as a number between 3 and 27, and E between 0 and 24, for example, a six figure grid reference 165096 has E = 16.5 and N = 9.6, and corresponds to a location of:

$(0.0090393 \times 9.6) + 12.3844908$	= 12.471268	= 12° 28'16.6" N
$(-0.0091991 \times 16.5) + 70.0849443$	= 69.93315915	= 69° 55'59.4" W

Brief lithological information about samples is also included. For those samples which have been analysed geochemically, a lithology code is assigned. Data reported in Appendices

C to G are organised by lithology according to this classification, and geochemical diagrams in the main body of the thesis also use these groupings. Samples for which the analysis is sub-standard (either for geological or analytical reasons) are not allocated a lithology code.

Table A.2.1: Lithological groups (and their codes) used for Aruba samples throughout this study.

Code	Lithology
	A: Aruba Lava Formation
A1	basalts
A2	dolerites
A3	chlorite schists
A4	amphibolites (basaltic)
A5	amphibolites and schists (non-basaltic)
A6	basaltic volcaniclastic rocks
A7	volcaniclastic rocks (not basaltic)
	B: Aruba batholith
B1	hooibergites
B2	layered gabbro series
B2a	plagioclase-rich gabbros
B2b	olivine- and clinopyroxene-rich gabbros
B3	gabbro and hornblende-gabbros
B4	diorites
B5	tonalites
B6	leucotonalites
B7	granites
B8	leucocratic veins
B9	porphyritic rocks (mainly hbl-plag-phyric)
	C: Cross-cutting dykes (categorised somewhat arbitrarily according to trace element characteristics)
C1	Group 1 dykes (high alkalis)
C2	Group 2 dykes (intermediate alkalis)
C3	Group 3 dykes (low alkalis)

Table A.2.2: Location and lithological sample information

Sample	Locality	Grid ref.	Lithology	code
Samples collected by R. V. White in January-February, 1996				
ARU96-1	Miralamar Pass	155128	fine-grained basalt	A1
ARU96-2	Miralamar Pass	155128	medium-grained basalt	A1
ARU96-3	Miralamar Pass	155129	vesicular basalt	
ARU96-4	S. of Rooi Tambe	174129	hornblende-plagioclase porphyry	B9
ARU96-5	nr Boca Prins	192129	plagioclase-quartz porphyry	B9
ARU96-6	nr Boca Prins	192129	dolerite	A2
ARU96-7	nr Boca Prins	192129	v. coarse dolerite (max. 5 mm)	A2
ARU96-8	nr Boca Prins	193130	pyroxene-plagioclase porphyry	B9
ARU96-9	nr Boca Prins	193130	coarse dolerite	A2
ARU96-10	nr Boca Druif	191133	coarse hornblende-plagioclase porphyry	B9
ARU96-11	nr Boca Druif	191133	tough basalt	A1
ARU96-12	nr Boca Druif	191135	pillow basalt	A1
ARU96-13	Dos Playa	183135	coarse silicic tuff with eutaxitic texture	A7
ARU96-14	Bushiribana	121190	basic dyke cross-cutting gabbro	C2
ARU96-15	Bushiribana	121190	medium-grained meladiorite	B4
ARU96-16	Andicuri (Natural Bridge)	139175	amphibolite (cut by silicic vein)	A4
ARU96-17	Andicuri (Natural Bridge)	139175	amphibolite	
ARU96-18a	Andicuri (Natural Bridge)	139175	amphibolite (cut by silicic vein ARU96-18b))	A4
ARU96-18b	Andicuri (Natural Bridge)	139175	silicic vein intruded parallel to foliation in amphibolite	B4
ARU96-19	Andicuri (Natural Bridge)	139175	amphibolite with fine silicic veining	
ARU96-20	Jamanota Gold mine	152122	amphibolite	A4
ARU96-21	Rooi Taki	143110	basalt	A1
ARU96-22	Rooi Taki	143110	basaltic volcaniclastic rock	A6
ARU96-23	Seroe Colorado	239103	coarse weathered hornblende-tonalite (discarded)	
ARU96-24	Weg Fontein (Vader Piet)	212103	greenish-coloured mafic dyke	C1
ARU96-25	Weg Fontein (Vader Piet)	212103	greenish-coloured mafic dyke	C1
ARU96-26	Weg Fontein (Vader Piet)	212103	greenish-coloured mafic dyke	C1
ARU96-27	Weg Fontein (Vader Piet)	212103	basalt	A1
ARU96-28	Weg Fontein (Vader Piet)	212103	(discarded)	
ARU96-29	Daimari	159161	hornblende-plagioclase-quartz porphyry	B9
ARU96-30	Daimari	159160	dolerite	A2
ARU96-31	Daimari	159160	basalt	A1
ARU96-32	Daimari	160160	plagioclase porphyry	
ARU96-33	Daimari	161158	slightly porphyritic tonalite	B5
ARU96-34	Daimari	161158	chilled margin of ARU96-33: hbl-plag porphyry	
ARU96-35	Daimari	161158	dolerite	A2
ARU96-36	Daimari (Rooi Fluit)	162157	hornblende-plagioclase porphyry	B9
ARU96-37	Daimari (Rooi Fluit)	162157	dolerite	A2
ARU96-38	Daimari at coast	171159	plagioclase-rich dolerite	A2
ARU96-39	Daimari at coast	171157	leucocratic dyke cutting ARU96-40	B8
ARU96-40	Daimari at coast	171157	plagioclase-rich dolerite	A2
ARU96-41	Rooi Awa Marga	134166	aplitic vein cutting gabbro	B8
ARU96-42	Rooi Awa Marga	134166	gabbro (showing no layering)	B3
ARU96-43	Andicuri (Natural Bridge)	140172	weathered amphibole-chorite rock	A3
ARU96-44	Andicuri (Natural Bridge)	139173	hbl-plag-qtz porphyritic enclave in tonalite	
ARU96-45	Hooiberg (loose at base)	101153	sample of contact between hooibergite and diorite	
ARU96-46	Hooiberg (loose at base)	101153	coarse hornblende-poor hooibergite	B1
ARU96-47	Hooiberg (loose at base)	101153	leucotonalite	B6
ARU96-48	Hooiberg (loose at base)	101153	micro-leucotonalite	B6
ARU96-49	Hooiberg (loose at base)	101153	micro-leucotonalite	B6
ARU96-50	Hooiberg (loose at base)	101153	diorite	B4
ARU96-51	Hooiberg (loose at base)	101153	coarse dioritic hooibergite	B1
ARU96-52	Hooiberg (loose at base)	101153	dioritic hooibergite	B1
ARU96-53	Hooiberg (loose at base)	101153	hooibergite	B1
ARU96-54	Hooiberg (loose at base)	101153	hooibergite	B1
ARU96-55	Hooiberg (loose at base)	101153	hooibergite	B1
ARU96-56	Hooiberg (loose at base)	101153	hooibergite	B1
ARU96-57	Hooiberg (loose at base)	101153	hooibergite	B1
ARU96-58	Hooiberg (loose at base)	101153	hooibergite	B1
ARU96-59	Ayo Rock Formations	123167	hornblende-biotite tonalite	B5
ARU96-60	Warawara (90m Hooiberg)	130134	hooibergite	B1
ARU96-61	Warawara (90m Hooiberg)	130134	hooibergite	B1
ARU96-62	California	035259	hornblende-biotite tonalite	B5

Table A.2.2: Location and lithological sample information

Sample	Locality	Grid ref.	Lithology	code
ARU96-63	Sero Muskita	062246	diorite	B4
ARU96-64	Sero Muskita	062246	diorite (cut by cpx-plag-phyric mafic dyke)	B4
ARU96-65	Sero Muskita	062246	microgabbro	B3
ARU96-66	Sero Muskita	062246	foliated amphibolite	
ARU96-67	Hooiberg	100150	silicic vein in hooibergite with hbl-rich rim	
ARU96-68	Hooiberg	100150	silicic vein in hooibergite with hbl-rich rim	
ARU96-69	Warirurí	111193	gabbro with poilikilitic hornblende overgrowth	
ARU96-70	Warirurí	111193	gabbro	
ARU96-71	Warirurí	111193	gabbro with silicic vein	
ARU96-72	Arikok hill	155138	dolerite	A2
ARU96-73	Arikok hill	159139	basalt	A1
ARU96-74	Arikok hill	159139	quartz vein	
ARU96-75	Dos Playa - Boca Prins	189133	?very damaged ammonite fragment (discarded)	
ARU96-76	Dos Playa - Boca Prins	189133	basaltic volcaniclastic rock	
ARU96-77	Dos Playa - Boca Prins	189133	bedded sedimentary rock	
ARU96-78	Alto Vista	081212	mafic dyke	
ARU96-79	Alto Vista	081212	mafic dyke	C2
ARU96-80	Alto Vista	081212	inequigranular hornblende-tonalite	B5
ARU96-81	Sero Blanco	137115	weathered foliated ?hornblende-plagioclase porphyry	
ARU96-82	Jamanota	157125	dolerite	A2
ARU96-83	Jaburibari	094188	aplite vein in tonalite	B8
ARU96-84	Bushiribana - Matividiri	122184	microdioritic enclave in tonalite	B4
ARU96-85	Bushiribana - Matividiri	122184	tonalite with gabbro xenolith and dioritic enclave	
ARU96-86	Bushiribana - Matividiri	124184	coarse hornblende at contact between gabbro and tonalite	
ARU96-87	Bushiribana - Matividiri	127174	medium grained meladiorite	B4
ARU96-88	Wela	136114	crenulated chlorite schist	
ARU96-89	Wela	136114	basaltic volcaniclastic rock (not deformed)	A6
ARU96-90	Hooiberg	101151	leucotonalitic material cutting hooibergite	B6
ARU96-91	Hooiberg	101151	coarse hooibergite	B1
ARU96-92	Hooiberg	101151	coarse hooibergite	B1
ARU96-93	Warirurí	110193	silicic vein in hooibergite with hbl-rich rim	
ARU96-94	Andicuri (Natural Bridge)	137174	foliated tonalite	
ARU96-95	Andicuri (Natural Bridge)	140172	schist	
ARU96-96	Weg Fontein	201082	hornblende tonalite	B5
ARU96-97	Weg Fontein (Sero Cadushi)	212090	tonalite	B5
ARU96-98	Weg Fontein (Sero Cadushi)	212090	tonalite	B5
ARU96-99	Weg Fontein (Sero Cadushi)	212090	microdioritic enclave in tonalite	
ARU96-100	Wela	134116	weathered dolerite	A2
ARU96-101	Wela	134116	undeformed basalt	A1
ARU96-102	Wela	134116	basaltic volcaniclastic rock (not deformed)	A6
ARU96-103	Wela	135115	foliated ?hornblende-plagioclase porphyry	
ARU96-104	Wela	135115	foliated ?hornblende-plagioclase porphyry	
ARU96-105	Wela	136115	chlorite-schist: deformed ?basalt	A3
ARU96-106	Wela	136115	chlorite-schist: deformed ?basalt	A3
ARU96-107	Wela	136115	soft chlorite-schist: deformed ?ultramafic	A3
ARU96-108	Jamanota	155122	soft green chlorite-schist	A3
ARU96-109	Jamanota	155122	chlorite-schist: deformed ?basalt	A3
ARU96-110	Jamanota	155122	?amphibolite	A4
ARU96-111	Warawara (90m Hooiberg)	130134	fine hooibergite	B1
ARU96-112	Dos Playa (S rooi)	178135	bedded basaltic tuff	A6
ARU96-113	Dos Playa (S rooi)	177134	dolerite	
ARU96-114	Dos Playa (hill)	182140	loose dolerite	
ARU96-115	Dos Playa	181141	?intermediate or mafic dyke	C3
ARU96-116	Dos Playa	181142	loose basaltic conglomerate	
ARU96-117	Dos Playa	180140	dolerite	A2
ARU96-118	Dos Playa	179142	graded bed in sediment	
ARU96-119	Dos Playa	182141	glassy basalt	A1
ARU96-120	Dos Playa	183134	volcaniclastic sediment with calcite patches	A7
ARU96-121	Dos Playa	183134	mica on an alteration plane in volcaniclastic sediment	
ARU96-122	Dos Playa	183134	coarse bedded volcaniclastic rock	A7
ARU96-123	Ayo Rock Formations	126166	hornblende-plagioclase porphyry dyke cutting tonalite	B9
ARU96-124	Sero Pita, near Ayo	114162	normal hooibergite	B1
ARU96-125	Sero Pita, near Ayo	114162	fine hooibergite	B1
ARU96-126	Sero Pita, near Ayo	114162	coarse diorite	B4

Table A.2.2: Location and lithological sample information

Sample	Locality	Grid ref.	Lithology	code
ARU96-127	Sero Pita, near Ayo	114162	medium-grained diorite	B4
ARU96-128	Sero Biento, near Hooiberg	098143	very dark mafic rock - mainly hornblende? (altered)	B2b
ARU96-129	California	036261	tonalite	B5
ARU96-130	Druif	057247	amphibolite	A4
ARU96-131	Alto Vista	082218	tonalite	B5
ARU96-132	Alto Vista	084217	diorite	B4
ARU96-133	Alto Vista	084217	microgranite vein	B7
ARU96-134	Alto Vista	083219	microdiorite enclave	B4
ARU96-135	Alto Vista	080213	hooibergitic diorite	B1
ARU96-136	Alto Vista	082216	plagioclase-hornblende porphyry	B9
ARU96-137	Alto Vista	085220	mafic dyke	C2
ARU96-138	Alto Vista	082217	porphyritic hornblende-plagioclase-phyric mafic dyke	B9
ARU96-139	Alto Vista	082217	greenish-coloured mafic dyke cutting tonalite	C2
ARU96-140	Andicuri (Natural Bridge)	140172	amphibolitic schist (basaltic)	A4
ARU96-141	Andicuri (Natural Bridge)	140172	pale-coloured schistose rock	
ARU96-142	Andicuri (Natural Bridge)	140172	pale-coloured schistose rock	A5
ARU96-143	Andicuri (Natural Bridge)	140172	pale-coloured schistose rock	A5
ARU96-144	Andicuri (Natural Bridge)	140173	amphibolite	A4
ARU96-145	Andicuri (Natural Bridge)	140173	amphibolite	A4
ARU96-146	Andicuri (Natural Bridge)	140173	amphibolite	A4
ARU96-147	Andicuri (Natural Bridge)	140174	amphibolite	A4
ARU96-148	Andicuri (Natural Bridge)	140174	amphibolite	A4
ARU96-149a	Andicuri (Natural Bridge)	140174	acidic "sweat" in amphibolite ARU96-149b	B5
ARU96-149b	Andicuri (Natural Bridge)	140174	amphibolite segregated into light and dark bands	A4
ARU96-150a	Andicuri (Natural Bridge)	140175	quartz-rich vein in amphibolite ARU96-150b	
ARU96-150b	Andicuri (Natural Bridge)	140175	amphibolite segregated into light and dark bands	A4
ARU96-151	Andicuri (Natural Bridge)	138174	gabbro from next to amphibolite	B3
ARU96-152	Matividiri	132181	meladiorite	B4
ARU96-153	Wariruri	111192	microgabbro vein invading gabbro	B7
ARU96-154	Wariruri	111192	very dark mafic rock - olivine- and px-rich	B2b
ARU96-155	Wariruri	111192	microgranite	B7
ARU96-156	Wariruri	111192	very dark mafic rock - olivine- and px-rich	B2b
ARU96-157	Wariruri	111192	hooibergitic diorite	B1
ARU96-158	Wariruri	111192	diorite	B4
ARU96-159	Wariruri	109194	microgabbro	B3
ARU96-160	Seroe Cristal	106187	green mafic dyke intrusive into tonalite	C1
ARU96-161	Andicuri (Natural Bridge)	140173	amphibolite with agmatitic texture	
ARU96-162	nr Daimari Plantation	152161	pegmatitic quartz with iridescent ore mineral	
	Samples collected by R. V. White in January-March, 1997			
ARU97-1	Jamanota	159118	basaltic conglomerate	A6
ARU97-2	Ser'i Pos di Noord	092207	dioritic hooibergite	
ARU97-3	N of Alto Vista	082220	hornblende-plagioclase porphyry	B9
ARU97-4	Dos Playa	173135	sandstone bed in basaltic conglomerate	
ARU97-5	Matividiri	131177	hornblende-plagioclase porphyry	B9
ARU97-6	Matividiri	131177	hbl-plag-qtz porphyritic enclave in tonalite	
ARU97-7	Matividiri	132178	gabbro	
ARU97-8	Arikok Park	149136	amphibolite from close to contact with tonalite	
ARU97-9	Andicuri (Natural Bridge)	140172	bedded tuff - hornfelsed?	
ARU97-10	Andicuri (Natural Bridge)	143171	diorite	B4
ARU97-11	Andicuri (Natural Bridge)	143171	small fresh basalt chip	
ARU97-12	Andicuri (Natural Bridge)	140175	anomalous layer in amphibolite	
ARU97-13	Hooiberg	100152	microdiorite dyke	B4
ARU97-14	Hooiberg	101153	coarse acicular tonalite	
ARU97-15	Hooiberg	100151	epidotised fine hooibergite	
ARU97-16	Hooiberg	100151	silicic vein in fine hooibergite; hbl-rich rim	
ARU97-17	Hooiberg	100151	pyroxene-rich hooibergite	
ARU97-18	Hooiberg	100151	coarse hooibergite with plagioclase-rich matrix	
ARU97-19	Sero Blanco	137115	oriented sample of foliated porphyry	
ARU97-20	Sero Blanco	137115	oriented sample of foliated porphyry	
ARU97-21	Sero Blanco	137115	oriented sample of foliated porphyry	
ARU97-22	Wariruri	111193	layered gabbro - hand specimen	
ARU97-23	Wariruri	111191	greenish-coloured mafic dyke	
ARU97-24	Wariruri	110190	acid material disaggregating gabbro	

Table A.2.2: Location and lithological sample information

Sample	Locality	Grid ref.	Lithology	code
ARU97-25	Jamanota stream	154122	deformed green chlorite-schist	A3
ARU97-26	Jamanota stream	154122	deformed green chlorite-schist	A3
ARU97-27	Warawara (90m Hooiberg)	130134	coarse hooibergite	
ARU97-28	Warawara (90m Hooiberg)	130134	hooibergite with hbl crystals occurring in clusters	
ARU97-29	Warawara (90m Hooiberg)	130134	fine hooibergite	
ARU97-30	Warawara (90m Hooiberg)	130134	coarse hooibergite with plagioclase rims around hbl	
ARU97-31	Warawara (90m Hooiberg)	130134	very coarse hooibergite	
ARU97-32	N of Warawara	130137	hooibergite	
ARU97-33	Jamanota mine hill	155125	amphibolitised vesicular basalt	
ARU97-34	Jamanota mine hill	155125	amphibolite from close to contact with tonalite	A5
ARU97-35	Matividiri	136175	mafic dyke	C2
ARU97-36	Andicuri (Natural Bridge)	139175	amphibolite containing green mineral	
ARU97-37	Andicuri (Natural Bridge)	139175	amphibolite with hbl-rich segregations	
ARU97-38	Andicuri (Natural Bridge)	139175	amphibolite with green mineral and hbl-rich segregations	
ARU97-39	Andicuri (Natural Bridge)	139175	amphibolite with porphyroblasts	
ARU97-40	Andicuri (Natural Bridge)	140174	fresh amphibolite	A4
ARU97-41	Andicuri (Natural Bridge)	140174	banded amphibolite	
ARU97-42	Andicuri (Natural Bridge)	140174	amph with coarse green mineral	
ARU97-43	Andicuri (Natural Bridge)	140174	amphibolite sample rich in acid veins	
ARU97-44	Andicuri (Natural Bridge)	140173	oriented amphibolite sample	
ARU97-45	Andicuri (Natural Bridge)	140173	oriented amphibolite sample	
ARU97-46	Andicuri (Natural Bridge)	140173	oriented amphibolite sample	
ARU97-47	Andicuri (Natural Bridge)	140172	oriented pale amphibolite sample	
ARU97-48	Andicuri (Natural Bridge)	140172	interesting textured amphibolite	
ARU97-49	Andicuri (Natural Bridge)	140172	interesting textured amphibolite	
ARU97-50	Andicuri (Natural Bridge)	140172	interesting textured amphibolite	
ARU97-51	California	037260	aplite cross-cutting tonalite	B8
ARU97-52	Alto Vista	080215	micro-leucotonalite	B6
ARU97-53	Alto Vista	080215	diorite	B4
ARU97-54	Alto Vista	080215	enclaves in tonalite	
ARU97-55	Alto Vista	080215	enclaves in tonalite	
ARU97-56	Alto Vista	080215	enclaves in tonalite	
ARU97-57	Alto Vista	080215	enclaves in tonalite	
ARU97-58	Alto Vista	080215	enclaves in tonalite	
ARU97-59	Alto Vista	080215	enclaves in tonalite	
ARU97-60	Alto Vista	080215	enclaves in tonalite	
ARU97-61	Hooiberg	099149	dioritic hooibergite	B1
ARU97-62	Hooiberg	099149	acid-veined hooibergite breccia	
ARU97-63	Hooiberg	099149	loose block of fine hooibergite	B1
ARU97-64	Jamanota - Juditi	168119	clast from basaltic conglomerate	A6
ARU97-65	Jamanota - Juditi	168119	clast from basaltic conglomerate	A6
ARU97-66	Jamanota - Juditi	168119	basalt	A1
ARU97-67	Jamanota - Juditi	168119	light grey fine grained tuff	A6
ARU97-68	Jamanota - Juditi	169118	flattened lapilli tuff	
ARU97-69	Jamanota - Juditi	169118	fine lapilli tuff	
ARU97-70	Jamanota - Juditi	169118	crystal/lithic tuff	
ARU97-71	Jamanota - Juditi	168121	sheared chlorite schist	A3
ARU97-72	Jamanota - Juditi	168121	sheared chlorite schist	A3
ARU97-73	Ser'i Pos di Noord	093208	microdiorite enclave	B4
ARU97-74	Ser'i Pos di Noord	093208	microdiorite dyke	
ARU97-75	Ser'i Pos di Noord	091207	fine dark diorite with equant hornblendes	
ARU97-76	Ser'i Pos di Noord	091207	pyroxene-rich fine hooibergite	B1
ARU97-77	Ser'i Pos di Noord	091207	pyroxene-rich medium-grained hooibergite	B1
ARU97-78	Ayo Rock Formations	125166	tonalite	B5
ARU97-79	Ser'i Padua, near Ayo	121165	fine-grained diorite with equant hornblendes	B4
ARU97-80	Ser'i Padua, near Ayo	121163	pyroxene-rich hooibergite	B1
ARU97-81	Dos Playa	179142	bedded sediment showing cleavage refraction	
ARU97-82	Dos Playa	179142	hornblende-plagioclase porphyry	B9
ARU97-83	Dos Playa	177144	porphyritic dyke	B9
ARU97-84	Dos Playa	183135	grey silicic volcaniclastic rock with eutaxitic texture	
ARU97-85	Dos Playa	183135	grey silicic volcaniclastic rock with eutaxitic texture	
ARU97-86	Dos Playa	183135	grey silicic volcaniclastic rock with eutaxitic texture	
ARU97-87	Dos Playa	183135	grey silicic volcaniclastic rock with eutaxitic texture	
ARU97-88	Dos Playa	183135	grey silicic volcaniclastic rock with eutaxitic texture	

Table A.2.2: Location and lithological sample information

Sample	Locality	Grid ref.	Lithology	code
ARU97-89	Shidiharaca	146104	tonalite	
ARU97-90	Shidiharaca	146104	pinkish-coloured ?weathered tonalite	
ARU97-91	Sero Largo	150114	basalt	A1
ARU97-92	Alto Vista	081217	coarse hornblende-plagioclase porphyry	
ARU97-93	Alto Vista	081217	fine porphyry	
ARU97-94	Alto Vista	081217	phenocryst-rich hbl-plag porphyry with spherulites	
ARU97-95	Alto Vista	082218	mafic dyke with tonalite xenoliths	
ARU97-96	Alto Vista	084218	black dyke	
ARU97-97	Alto Vista	084218	greenish dyke	
ARU97-98	Druif	057246	amphibolite	A4
ARU97-99	Druif	057246	banded amphibolite	
ARU97-100	Druif	057246	amphibolite with dark and light irregular patches	
ARU97-101	Druif	057246	amphibolite segregated into mafic and felsic bands	
ARU97-102	Druif	057246	amphibolite segregated into mafic and felsic bands	
ARU97-103	Sero Muskita (NW)	062245	microgabbro	B3
ARU97-104	Sero Muskita (NW)	062245	microdiorite	B4
ARU97-105	Sero Muskita (NW)	062245	microdiorite with ?microgabbro inclusion	
ARU97-106	Sero Muskita (SE)	066242	mafic porphyritic dyke	C1
ARU97-107	Sero Muskita (SE)	066242	micro-leucotonalite	B6
ARU97-108	Sero Muskita (SE)	066242	coarse hornblende-plagioclase porphyry	
ARU97-109	Sero Muskita (SE)	067238	mafic dyke	C1
ARU97-110	Sero Tres Cabés	067232	fine hooibergite	
ARU97-111	Wariruri	111193	layered gabbro	
ARU97-112	Wariruri	111193	layered gabbro	
ARU97-113	Wariruri	111193	gabbro	
ARU97-114	Wariruri	107195	epidote vein	
ARU97-115	Wariruri	107195	layered diorite	
ARU97-116	Gabilán	100202	melanocratic hornblende-plagioclase porphyry	
ARU97-117	Gabilán	100202	hornblende-plagioclase porphyry	B9
ARU97-118	Urataca	130141	aplitic vein	B8
ARU97-119	Urataca	132142	hooibergite	B1
ARU97-120	Sero Biento (near Hooiberg)	097143	fine diorite with equant hornblendes	
ARU97-121	Gabilán	098206	hornblende-plagioclase porphyry	B9
ARU97-122	Gabilán	097206	mafic dyke	
ARU97-123	Gabilán	097206	melanocratic hornblende-plagioclase porphyry	B9
ARU97-124	Gabilán	099205	banded mafic dyke	
ARU97-125	Gabilán	099205	banded mafic dyke	
ARU97-126	Gabilán	099205	banded mafic dyke	C1
ARU97-127	Gabilán	097203	coarse diorite with equant hornblendes	
ARU97-128	Gabilán	097203	fine diorite with equant hornblendes	
ARU97-129	Gabilán	097203	hooibergitic diorite	
ARU97-130	Gabilán	097203	very coarse diorite with equant hornblendes	
ARU97-131	Gabilán	097203	dioritic hooibergite	
ARU97-132	Hooiberg	101151	micro-leucotonalite	B6
ARU97-133	Hooiberg	101151	very pyroxene-rich hooibergite	B1
ARU97-134	Hooiberg (loose at base)	101153	hooibergite disaggregated by silicic material	
ARU97-135	Hooiberg (loose at base)	101153	hooibergite disaggregated by silicic material	
ARU97-136	Hooiberg (loose at base)	101153	coarse acicular diorite	
ARU97-137	Hooiberg (loose at base)	101153	fine acicular diorite	
ARU97-138	Dos Playa	175134	basaltic conglomerate - relatively fine-grained	
ARU97-139	Dos Playa	175134	sandstone layer in basaltic conglomerate	
ARU97-140	Dos Playa	175134	volcaniclastic sandstone	
ARU97-141	Dos Playa	175134	thinly-bedded sediment	
ARU97-142	Dos Playa	175134	laminated sediment	
ARU97-143	Dos Playa	181134	basalt	A1
ARU97-144	Dos Playa	185135	pillow basalt	A1
ARU97-145	Dos Playa	182139	deformed sediment	
ARU97-146	Dos Playa	182139	irregular angular volcaniclastic rock	
ARU97-147	Dos Playa	183134	thinly-bedded sediment	
ARU97-148	Dos Playa	183134	sediment with ripple cross-lamination and convoluted beds	
ARU97-149	Dos Playa	183134	sediment with convoluted beds	
ARU97-150	Dos Playa	183134	finely laminated sediment	
ARU97-151	Dos Playa	183134	sediment with ripple cross-lamination	
ARU97-152	Dos Playa	183134	convolute layer in sediment	

Table A.2.2: Location and lithological sample information

Sample	Locality	Grid ref.	Lithology	code
ARU97-153	Dos Playa	183135	tuff with eutaxitic texture and adjacent mafic dyke	
ARU97-154	Dos Playa	183135	tuff with eutaxitic texture and adjacent mafic dyke	
ARU97-155	Dos Playa	183135	pale clast from tuff with eutaxitic texture	
ARU97-156	Dos Playa	183135	fresh sample of tuff with eutaxitic texture	
ARU97-157	Wela	135114	deformed chlorite-schist	
ARU97-158	Wela	135114	crenulated chlorite-schist	A3
ARU97-159	Jamanota	156122	chlorite-schist	A3
ARU97-160	Ser'i Pos di Noord	093208	diorite	B4
ARU97-161	Ser'i Pos di Noord	093207	diorite	B4
ARU97-162	Ser'i Pos di Noord	091207	fine hooibergitic diorite	B1
ARU97-163	Ser'i Pos di Noord	091207	coarse hooibergitic diorite	
ARU97-164	N of Warawara hooiberg	130137	hooibergite	B1
ARU97-165	Arikok Park	148136	tonalite	B5
ARU97-166	Arikok Park	148136	granitic vein	B7
ARU97-167	Arikok Park	148136	fine tonalite	B5
ARU97-168	Arikok Park	149136	amphibolite from close to contact with tonalite	A4
ARU97-169	Arikok Park	149136	strange textured amphibolite	
ARU97-170	Dos Playa	188132	tuff with eutaxitic texture	A7
ARU97-171	Matividiti	176138	gabbro	B3
ARU97-172	Matividiti	177137	meladiorite	B3
ARU97-173	Wariruri	111193	gabbro from layered series	B2a
ARU97-174	Wariruri	111193	plagioclase-rich gabbro from layered series	B2a
ARU97-175	Wariruri	108195	coarse plagioclase-rich gabbro from layered series	B2a
ARU97-176	Wariruri	108194	microdiorite	B4
ARU97-177	Alto Vista	083217	micro-leucotonalite	B6
ARU97-178	Alto Vista	083217	hornblende-plagioclase porphyry	B9
ARU97-179	Druif	057246	thin undulating quartz vein in amphibolite	
ARU97-180	Shidiharaca	147107	amphibolite from close to contact with tonalite	
	Samples collected by A. C. Kerr and J. Tarney in January, 1994.			
ARU94-1	batholith	not known	tonalite	B5
ARU94-2	Casibari	accurately	tonalite	B5
ARU94-3	Hooiberg	enough -	leucotonalitic vein in hooibergite	B6
ARU94-4	Hooiberg	place	hooibergite	B1
ARU94-4a	Hooiberg	names	hooibergite	B1
ARU94-5	Hooiberg	are	leucotonalite	B6
ARU94-6	Hooiberg	included	hooibergite	B1
ARU94-7	Hooiberg	on map	hooibergite	B1
ARU94-8	Hooiberg		hooibergite	B1
ARU94-9	Hooiberg		hooibergite	B1
ARU94-10	SW of Hooiberg		granite	B7
ARU94-11	"Rock Fms." (Ayo?)		tonalite	B5
ARU94-12	"House foundations"		hornblende-plagioclase porphyry	B9
ARU94-13	nr. Budui		diorite	B4
ARU94-14	nr. Budui		mafic dyke	C2
ARU94-15	nr. Budui		glassy fragment	C2
ARU94-16	Bushiribana		late dyke	C1
ARU94-17	Bushiribana		porphyritic late dyke (hbl-plag-phyric)	B9
ARU94-18	Bushiribana		tonalite	B5
ARU94-19	Alto Vista		dyke	C2
ARU94-20	Daimari		hornblende-plagioclase-quartz porphyry	B9
ARU94-21	Daimari		agglomerate	
ARU94-22	Daimari		dolerite	A2
ARU94-23	Daimari		basalt	A1
ARU94-24	Daimari		basaltic volcaniclastic rock	A6
ARU94-25	Daimari		dolerite block	A2
ARU94-26	Daimari		mafic dyke	C2
ARU94-27	Daimari		hornblende-plagioclase-quartz porphyry	B9
ARU94-28	Daimari		basalt	A1
ARU94-29	nr. Arikok		basalt pillow	A1
ARU94-30	nr. Arikok		basalt	A1
ARU94-31	nr. Arikok		tuff	A6
ARU94-32	nr. Arikok		crystal tuff	A6
ARU94-33	nr. Arikok		agglomerate	A6

Table A.2.2: Location and lithological sample information

Sample	Locality	Grid ref.	Lithology	code
ARU94-34	nr. Andicuri		basalt	A1
ARU94-35	nr. Andicuri		Cu mineralisation	
ARU94-36	nr. Andicuri		massive basalt	A1
	Samples collected by G. T. Klaver, F. Beunk and the Dutch Army in 1977.			
77AR3b	not known	not known	tonalite	B5
BK77-042	Basiruti	053217	fine hooibergite	B1
BK77-043	Basiruti	052219	porphyritic intermediate/mafic dyke	C2
BK77-047	Ser'i Janchi	072193	mafic dyke	C3
BK77-048	Ser'i Janchi	072193	quite fine granite	B7
BK77-054	Paraguaná	070184	hb-bi tonalite	B5
BK77-065	Sero Muerto	104187	fine mafic dyke	C2
BK77-066a	Sero Plat	102187	dark tonalite (diorite)	B4
BK77-067	Sero Plat	102187	biotite-bearing leucotonalite	B6
BK77-068	Sero Plat	102187	fine granitic aplite	B7
BK77-109b	Piedra Plat	103160	diorite	B4
BK77-127b	Baranca Cora	164105	coarse hb tonalite	B5
BK77-148	Boton	133126	aphyric mafic dyke	C3
BK77-165	S of Sero Canashito	089152	fine diorite with equant hornblendes	B4
BK77-173a	W of Hooiberg	101136	diorite	B4
BK77-180	Montaña	066194	hb-bi tonalite	B5

A.3 Information sources by sample

Table A.3.1 shows the range of analytical, and other, information available for all Aruba samples used in this study, organised by sample number order. Additionally, hand specimens are available for all samples listed. All material will be archived, and stored in the Leicester University Geology Department.

XRF major	• analysed by X-ray fluorescence for major elements • Leicester University Geology Dept. fusion bead reference number listed
XRF trace	• analysed by X-ray fluorescence for trace elements • Leicester University Geology Dept. powder pellet reference number listed
Sr-Nd-Pb	• analysed for Sr, Nd and Pb isotopes at NIGL • number (1 or 2) refers to dissolution batch
Ar-Ar	• dated by ^{40}Ar-^{39}Ar techniques at SURRC
ICP-MS	• analysed by inductively-coupled plasma mass spectrometry at Haarlem • Letter (A to J) refers to dissolution batch • * means that the sample was re-run at Cardiff University Geology Department (courtesy of L. Coogan)
ICP-AES	• analysed by inductively-coupled plasma atomic emission spectrometry at Leicester
INAA	• analysed by instrumental neutron activation analysis at Leicester
EMP	• analysed by Electron Microprobe at Leicester • number refers to run number (also file name)
Section	• a thin section exists for this sample, either glass-covered, or polished • "ORIENT" means that the thin section is from an oriented specimen
code	• refers to lithology code (see Table A.2.1 on page A.2)

Table A.3.1: Sample information sources

Sample	XRF major	XRF trace	Sr-Nd-Pb	Ar-Ar	ICP-MS	ICP-AES	INAA	EMP	Section	code
Samples collected by R. V. White in January-February, 1996										
ARU96-1	LF8697	L29667			YES A				YES	A1
ARU96-2	LF8698	L29668	YES 2	YES	YES J	YES	YES		YES	A1
ARU96-3									YES	
ARU96-4	LF8699	L29669							YES	B9
ARU96-5	LF8700	L29670							YES	B9
ARU96-6	LF8701	L29671							YES	A2
ARU96-7	LF8702	L29672							YES	A2
ARU96-8	LF8703	L29673							YES	B9
ARU96-9	LF8704	L29674							YES	A2
ARU96-10	LF8705	L29675							YES	B9
ARU96-11	LF8706	L29676			YES A				YES	A1
ARU96-12	LF8707	L29677							YES	A1
ARU96-13	LF8708	L29678							YES	A7
ARU96-14	LF8709	L29679	YES 2		YES F				YES	C2
ARU96-15	LF8710	L29680							YES	B4
ARU96-16	LF8711	L29681							YES	A4
ARU96-17									YES	
ARU96-18a	LF8712	L29682							YES	A4
ARU96-18b	LF8713	L29683			YES J				YES	B4
ARU96-19									YES	
ARU96-20	LF8714	L29684							YES	A4
ARU96-21	LF8715	L29685	YES 2		YES A	YES	YES		YES	A1
ARU96-22	LF8716	L29686						YES 13	YES	A6
ARU96-23										
ARU96-24	LF8717	L29687							YES	C1
ARU96-25	LF8718	L29688	YES 2		YES F				YES	C1
ARU96-26	LF8719	L29689							YES	C1
ARU96-27	LF8720	L29690							YES	A1
ARU96-28									YES	
ARU96-29	LF8721	L29691			YES H				YES	B9
ARU96-30	LF8722	L29692	YES 1	YES	YES J	YES	YES	YES 2	YES	A2
ARU96-31	LF8723	L29693		YES	YES A				YES	A1
ARU96-32										
ARU96-33	LF8724	L29694			YES C				YES	B5
ARU96-34									YES	
ARU96-35	LF8726	L29696							YES	A2
ARU96-36	LF8727	L29697							YES	B9
ARU96-37	LF8728	L29698	YES 2		YES B	YES	YES	YES 13	YES	A2
ARU96-38	LF8729	L29699	YES 2		*YES B	YES		YES 13	YES	A2
ARU96-39	LF8730	L29700							YES	B8
ARU96-40	LF8731	L29701							YES	A2
ARU96-41	LF8732	L29702			*YES H				YES	B8
ARU96-42	LF8733	L29703	YES 2		*YES E	YES			YES	B3
ARU96-43	LF8734	L29704			YES G				YES	A3
ARU96-44									YES	
ARU96-45									YES	
ARU96-46	LF8735	L29705							YES	B1
ARU96-47	LF8736	L29706							YES	B6
ARU96-48	LF8737	L29707							YES	B6
ARU96-49	LF8738	L29708							YES	B6
ARU96-50	LF8739	L29709							YES	B4
ARU96-51	LF8740	L29710							YES	B1
ARU96-52	LF8741	L29711							YES	B1
ARU96-53	LF8742	L29712	YES 1		YES D			YES 4	YES	B1
ARU96-54	LF8743	L29713							YES	B1
ARU96-55	LF8744	L29714							YES	B1
ARU96-56	LF8745	L29715							YES	B1
ARU96-57	LF8746	L29716	YES 2		YES D	YES		YES 12	YES	B1
ARU96-58	LF8747	L29717							YES	B1
ARU96-59	LF8748	L29718							YES	B5
ARU96-60	LF8749	L29719							YES	B1
ARU96-61	LF8750	L29720							YES	B1
ARU96-62	LF8751	L29721							YES	B5

Table A.3.1: Sample information sources

Sample	Fusion no	Pellet no	isotopes	Ar-Ar	ICP-MS	ICP-AES	INAA	Section	code
ARU96-63	LF8752	L29722						YES	B4
ARU96-64	LF8753	L29723						YES	B4
ARU96-65	LF8754	L29724						YES	B3
ARU96-66								YES	
ARU96-67								YES	
ARU96-68									
ARU96-69									
ARU96-70									
ARU96-71								YES	
ARU96-72	LF8755	L29725						YES	A2
ARU96-73	LF8756	L29726						YES	A1
ARU96-74									
ARU96-75									
ARU96-76								YES	
ARU96-77								YES	
ARU96-78								YES	
ARU96-79	LF8758	L29728						YES	C2
ARU96-80	LF8759	L29729						YES	B5
ARU96-81								YES	
ARU96-82	LF8760	L29730						YES	A2
ARU96-83	LF8761	L29731						YES	B8
ARU96-84	LF8762	L29732						YES	B4
ARU96-85								YES	
ARU96-86									
ARU96-87	LF8763	L29733						YES	B4
ARU96-88								YES	
ARU96-89	LF8764	L29734						YES	A6
ARU96-90	LF8765	L29735						YES	B6
ARU96-91	LF8766	L29736						YES	B1
ARU96-92	LF8767	L29737						YES	B1
ARU96-93								YES	
ARU96-94								YES	
ARU96-95								YES	
ARU96-96	LF8768	L29738						YES	B5
ARU96-97	LF8769	L29739						YES	B5
ARU96-98	LF8770	L29740			YES C			YES	B5
ARU96-99								YES	
ARU96-100	LF8771	L29741						YES	A2
ARU96-101	LF8772	L29742						YES	A1
ARU96-102	LF8773	L29743						YES	A6
ARU96-103								YES	
ARU96-104								YES	
ARU96-105	LF8776	L29746						YES	A3
ARU96-106	LF8777	L29747						YES	A3
ARU96-107	LF8778	L29748			YES J			YES	A3
ARU96-108	LF8779	L29749	YES 2		YES G			YES	A3
ARU96-109	LF8780	L29750						YES	A3
ARU96-110	LF8781	L29751						YES	A4
ARU96-111	LF8782	L29752						YES	B1
ARU96-112	LF8783	L29753			YES B			YES	A6
ARU96-113								YES	
ARU96-114								YES	
ARU96-115	LF8786	L29756						YES	C3
ARU96-116								YES	
ARU96-117	LF8787	L29757			YES F			YES	A2
ARU96-118								YES	
ARU96-119	LF8788	L29758						YES	A1
ARU96-120	LF8789	L29759						YES	A7
ARU96-121								YES	
ARU96-122	LF8790	L29760						YES	A7
ARU96-123	LF8791	L29761		YES	YES H			YES	B9
ARU96-124	LF8792	L29762			YES J			YES	B1
ARU96-125	LF8793	L29763						YES	B1
ARU96-126	LF8794	L29764			YES J			YES	B4

Table A.3.1: Sample information sources

Sample	Fusion no	Pellet no	isotopes	Ar-Ar	ICP-MS	ICP-AES	INAA	Section	code
ARU96-127	LF8795	L29765						YES	B4
ARU96-128	LF8796	L29766						YES	B2b
ARU96-129	LF8797	L29767						YES	B5
ARU96-130	LF8798	L29768						YES	A4
ARU96-131	LF8799	L29769	YES 1	YES	*YES C	YES	YES 7	YES	B5
ARU96-132	LF8800	L29770						YES	B4
ARU96-133	LF8801	L29771						YES	B7
ARU96-134	LF8802	L29772						YES	B4
ARU96-135	LF8803	L29773			YES D			YES	B1
ARU96-136	LF8804	L29774	YES 2		YES H	YES		YES	B9
ARU96-137	LF8805	L29775			YES F			YES	C2
ARU96-138	LF8806	L29776						YES	B9
ARU96-139	LF8807	L29777						YES	C2
ARU96-140	LF8808	L29778						YES	A4
ARU96-141								YES	
ARU96-142	LF8809	L29779	YES 1		YES G		YES 4	YES	A5
ARU96-143	LF8810	L29780						YES	A5
ARU96-144	LF8811	L29781						YES	A4
ARU96-145	LF8812	L29782	YES 1		YES G		YES 7	YES	A4
ARU96-146	LF8813	L29783						YES	A4
ARU96-147	LF8814	L29784	YES 1	YES	YES G	YES		YES	A4
ARU96-148	LF8815	L29785						YES	A4
ARU96-149a	LF8816	L29786			YES H			YES	B5
ARU96-149b	LF8828	L29798			YES G			YES	A4
ARU96-150a								YES	
ARU96-150b	LF8829	L29799						YES	A4
ARU96-151	LF8818	L29788						YES	B3
ARU96-152	LF8819	L29789		YES	YES E			YES	B4
ARU96-153	LF8820	L29790			*YES J				B7
ARU96-154	LF8821	L29791	YES 2		*YES D	YES	YES 8	YES	B2b
ARU96-155	LF8822	L29792	YES 2		YES H			YES	B7
ARU96-156	LF8823	L29793						YES	B2b
ARU96-157	LF8824	L29794					YES 12	YES	B1
ARU96-158	LF8825	L29795	YES 1	YES	YES E	YES		YES	B4
ARU96-159	LF8826	L29796						YES	B3
ARU96-160	LF8827	L29797						YES	C1
ARU96-161									
ARU96-162									
		Samples collected by R. V. White in January-March, 1997							
ARU97-1	LF10405	L31252							A6
ARU97-2								YES	
ARU97-3	LF10406	L31253						YES	B9
ARU97-4								YES	
ARU97-5	LF10407	L31254						YES	B9
ARU97-6								YES	
ARU97-7								YES	
ARU97-8								YES	
ARU97-9								YES	
ARU97-10	LF10408	L31255						YES	B4
ARU97-11								YES	
ARU97-12								YES	
ARU97-13	LF10409	L31256						YES	B4
ARU97-14								YES	
ARU97-15								YES	
ARU97-16								YES	
ARU97-17								YES	
ARU97-18								YES	
ARU97-19								ORIENT	
ARU97-20								ORIENT	
ARU97-21								ORIENT	
ARU97-22									
ARU97-23								YES	
ARU97-24								YES	

Table A.3.1: Sample information sources

Sample	Fusion no	Pellet no	isotopes	Ar-Ar	ICP-MS	ICP-AES	INAA		Section	code
ARU97-25	LF10410	L31257								A3
ARU97-26	LF10411	L31258								A3
ARU97-27									YES	
ARU97-28									YES	
ARU97-29									YES	
ARU97-30									YES	
ARU97-31										
ARU97-32									YES	
ARU97-33									YES	
ARU97-34	LF10412	L31259								A5
ARU97-35	LF10413	L31260								C2
ARU97-36									YES	
ARU97-37								YES 6	YES	
ARU97-38									YES	
ARU97-39									YES	
ARU97-40	LF10414	L31261							YES	A4
ARU97-41									YES	
ARU97-42									YES	
ARU97-43									YES	
ARU97-44									ORIENT	
ARU97-45									ORIENT	
ARU97-46									ORIENT	
ARU97-47									ORIENT	
ARU97-48									YES	
ARU97-49									YES	
ARU97-50									YES	
ARU97-51	LF10415	L31262							YES	B8
ARU97-52	LF10416	L31263							YES	B6
ARU97-53	LF10417	L31264							YES	B4
ARU97-54									YES	
ARU97-55									YES	
ARU97-56									YES	
ARU97-57									YES	
ARU97-58									YES	
ARU97-59									YES	
ARU97-60									YES	
ARU97-61	LF10418	L31265							YES	B1
ARU97-62									YES	
ARU97-63	LF10419	L31266							YES	B1
ARU97-64	LF10420	L31267								A6
ARU97-65	LF10421	L31268								A6
ARU97-66	LF10422	L31269								A1
ARU97-67	LF10423	L31270								A6
ARU97-68									YES	
ARU97-69									YES	
ARU97-70									YES	
ARU97-71	LF10424	L31271								A3
ARU97-72	LF10425	L31272							YES	A3
ARU97-73	LF10426	L31273						YES 5	YES	B4
ARU97-74									YES	
ARU97-75									YES	
ARU97-76	LF10427	L31274							YES	B1
ARU97-77	LF10428	L31275						YES 8	YES	B1
ARU97-78	LF10429	L31276						YES 2/3	YES	B5
ARU97-79	LF10430	L31277							YES	B4
ARU97-80	LF10431	L31278							YES	B1
ARU97-81									YES	
ARU97-82	LF10432	L31279							YES	B9
ARU97-83	LF10433	L31280								B9
ARU97-84									YES	
ARU97-85									YES	
ARU97-86										
ARU97-87									YES	
ARU97-88									YES	

Table A.3.1: Sample information sources

Sample	Fusion no	Pellet no	isotopes	Ar-Ar	ICP-MS	ICP-AES	INAA		Section	code
ARU97-89									YES	
ARU97-90									YES	
ARU97-91	LF10434	L31281								A1
ARU97-92									YES	
ARU97-93									YES	
ARU97-94									YES	
ARU97-95									YES	
ARU97-96									YES	
ARU97-97									YES	
ARU97-98	LF10435	L31282								A4
ARU97-99									YES	
ARU97-100									YES	
ARU97-101									YES	
ARU97-102									YES	
ARU97-103	LF10436	L31283								B3
ARU97-104	LF10437	L31284								B4
ARU97-105									YES	
ARU97-106	LF10438	L31285								C1
ARU97-107	LF10439	L31286								B6
ARU97-108									YES	
ARU97-109	LF10440	L31287							YES	C1
ARU97-110									YES	
ARU97-111								YES 1/2	YES	
ARU97-112									YES	
ARU97-113										
ARU97-114									YES	
ARU97-115										
ARU97-116									YES	
ARU97-117	LF10441	L31288							YES	B9
ARU97-118	LF10442	L31289							YES	B8
ARU97-119	LF10443	L31290							YES	B1
ARU97-120									YES	
ARU97-121	LF10444	L31291							YES	B9
ARU97-122									YES	
ARU97-123	LF10445	L31292							YES	B9
ARU97-124									YES	
ARU97-125										
ARU97-126	LF10446	L31293								C1
ARU97-127									YES	
ARU97-128									YES	
ARU97-129									YES	
ARU97-130									YES	
ARU97-131									YES	
ARU97-132	LF10447	L31294							YES	B6
ARU97-133	LF10448	L31295							YES	B1
ARU97-134									YES	
ARU97-135									YES	
ARU97-136									YES	
ARU97-137										
ARU97-138									YES	
ARU97-139									YES	
ARU97-140									YES	
ARU97-141										
ARU97-142										
ARU97-143	LF10449	L31296								A1
ARU97-144	LF10450	L31297								A1
ARU97-145										
ARU97-146									YES	
ARU97-147									YES	
ARU97-148									YES	
ARU97-149										
ARU97-150									YES	
ARU97-151									YES	
ARU97-152									YES	

Table A.3.1: Sample information sources

Sample	Fusion no	Pellet no	isotopes	Ar-Ar	ICP-MS	ICP-AES	INAA		Section	code
ARU97-153									YES	
ARU97-154									YES	
ARU97-155										
ARU97-156									YES	
ARU97-157									YES	
ARU97-158	LF10451	L31298							YES	A3
ARU97-159	LF10452	L31299								A3
ARU97-160	LF10453	L31300			YES E		YES 10		YES	B4
ARU97-161	LF10454	L31301							YES	B4
ARU97-162	LF10455	L31302			YES E		YES 11		YES	B1
ARU97-163							YES 11		YES	
ARU97-164	LF10456	L31303					YES 12		YES	B1
ARU97-165	LF10457	L31304							YES	B5
ARU97-166	LF10458	L31305							YES	B7
ARU97-167	LF10459	L31306								B5
ARU97-168	LF10460	L31307								A4
ARU97-169									YES	
ARU97-170	LF10461	L31308								A7
ARU97-171	LF10462	L31309							YES	B3
ARU97-172	LF10463	L31310							YES	B3
ARU97-173	LF10464	L31311							YES	B2a
ARU97-174	LF10465	L31312							YES	B2a
ARU97-175	LF10466	L31313					YES 6,7		YES	B2a
ARU97-176	LF10467	L31314							YES	B4
ARU97-177	LF10468	L31315							YES	B6
ARU97-178	LF10469	L31316							YES	B9
ARU97-179									YES	
ARU97-180									YES	
	Samples collected by A. C. Kerr and J. Tarney in January, 1994.									
ARU94-1	LF03862	L20938							YES	B5
ARU94-2	LF8830	L29800			YES C,I				YES	B5
ARU94-3	LF03864	L20940							YES	B6
ARU94-4	LF03865	L20941							YES	B1
ARU94-4a	LF03866	L20942							YES	B1
ARU94-5	LF03867	L20943							YES	B6
ARU94-6	LF03868	L20944							YES	B1
ARU94-7	LF8831	L29801			YES D,I				YES	B1
ARU94-8	LF03870	L20946							YES	B1
ARU94-9	LF03871	L20947							YES	B1
ARU94-10	LF03872	L20948							YES	B7
ARU94-11	LF03873	L20949							YES	B5
ARU94-12	LF03874	L20950							YES	B9
ARU94-13	LF8832	L29802			YES E,I				YES	B4
ARU94-14	LF03876	L20952							YES	C2
ARU94-15	LF03877	L20953							YES	C2
ARU94-16	LF03878	L20954							YES	C1
ARU94-17	LF8833	L29999			YES F,I				YES	B9
ARU94-18	LF03880	L20956							YES	B5
ARU94-19	LF03881	L20957							YES	C2
ARU94-20	LF03882	L20958							YES	B9
ARU94-21									YES	
ARU94-22	LF8834	L30000			YES B,I				YES	A2
ARU94-23	LF03884	L20960							YES	A1
ARU94-24	LF03885	L20961							YES	A6
ARU94-25	LF03886	L20962							YES	A2
ARU94-26	LF03887	L20963							YES	C2
ARU94-27	LF03888	L20964							YES	B9
ARU94-28	LF03889	L20965								A1
ARU94-29	LF8835	L30001			YES A,I				YES	A1
ARU94-30	LF03891	L20967							YES	A1
ARU94-31	LF03892	L20968							YES	A6
ARU94-32	LF03893	L20969							YES	A6
ARU94-33	LF03894	L20970							YES	A6

Table A.3.1: Sample information sources

Sample	Fusion no	Pellet no	isotopes	Ar-Ar	ICP-MS	ICP-AES	INAA	Section	code
ARU94-34	LF03895	L20971						YES	A1
ARU94-35									
ARU94-36	LF03896	L20972						YES	A1
	Samples collected by G. T. Klaver, F. Beunk and the Dutch Army in 1977.								
77AR3b	LF8681	L29651						YES	B5
BK77-042	LF8682	L29652						YES	B1
BK77-043	LF8683	L29653						YES	C2
BK77-047	LF8684	L29654						YES	C3
BK77-048	LF8685	L29655						YES	B7
BK77-054	LF8686	L29656	YES 2		YES C			YES	B5
BK77-065	LF8687	L29657			YES F			YES	C2
BK77-066a	LF8688	L29658	YES 2		YES C			YES	B4
BK77-067	LF8689	L29659						YES	B6
BK77-068	LF8690	L29660						YES	B7
BK77-109b	LF8691	L29661						YES	B4
BK77-127b	LF8692	L29662						YES	B5
BK77-148	LF8693	L29663						YES	C3
BK77-165	LF8694	L29664	YES 2	YES	*YES D			YES	B4
BK77-173a	LF8695	L29665						YES	B4
BK77-180	LF8696	L29666						YES	B5

Appendix B

^{40}Ar-^{39}Ar geochronology

B.1 Principles of the ^{40}Ar-^{39}Ar method of dating

The ^{40}Ar-^{39}Ar method of dating, first described by Merrihue and Turner (1966), is a variant of the conventional K-Ar dating method, and overcomes some of the limitations of the latter. It is based on the radioactive decay of ^{40}K in natural systems (i.e., rocks and minerals). The half life for decay of ^{40}K is 1.25×10^9 years (Steiger and Jäger, 1977), but decay occurs both by electron capture (1) and β decay (2). This is shown diagramatically in Fig. B.1, and decay constants are given below.

$^{40}K + e^- \Rightarrow {}^{40}Ar^*$	11% of ^{40}K	$\lambda_e = 0.581 \times 10^{-10}\ y^{-1}$
$^{40}K \Rightarrow {}^{40}Ca + e^-$	89% of ^{40}K	$\lambda_\beta = 4.962 \times 10^{-10}\ y^{-1}$
	Total decay constant:	$\lambda = \lambda_e + \lambda_\beta = 5.543 \times 10^{-10}\ y^{-1}$

For conventional K-Ar dating, it is assumed that all the ^{40}Ar in the rock is derived from this radioactive decay of ^{40}K, and that none has subsequently escaped. Similarly, it assumes that no K has been added to or removed from the system. If the concentrations of ^{40}Ar and K can be accurately determined, the age of the mineral or rock can be calculated. These concentrations are determined on separate aliquots of sample, for example, K by XRF and ^{40}Ar by isotope dilution.

In many cases, particularly for weathered rocks, or those which have been subject to secondary heating after their initial crystallisation, the above assumptions are not valid. Because Ar is a gaseous non-reactive element, it diffuses relatively easily at low temperatures, and K-Ar ages frequently represent thermal resetting events, when the system was heated above the Ar closure temperature. Likewise, during weathering, addition of K and loss of radiogenic ^{40}Ar (hereafter: $^{40}Ar^*$) may lower the apparent age. In contrast, if the sample contains excess ^{40}Ar, the dates obtained are too old. It can be very difficult to evaluate whether or not any of these factors have affected a particular sample, and whether the resulting K-Ar date is accurate.

Making radiogenic argon ($^{40}Ar^*$) in the rock:

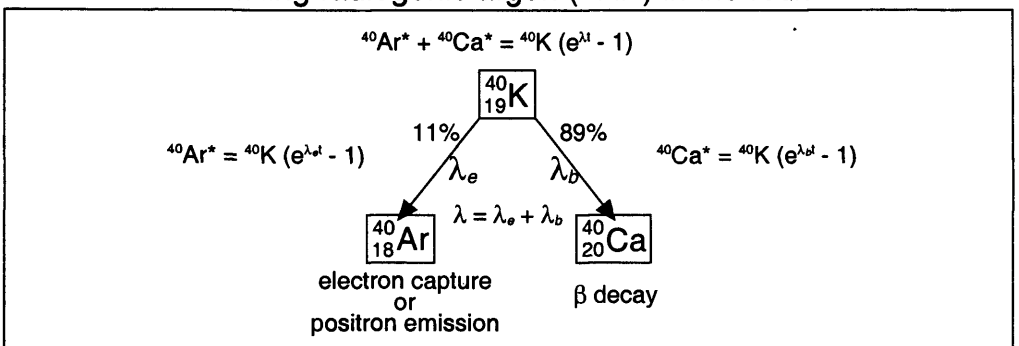

The equation for production of $^{40}Ar^*$ in the rock can also be written:

$$^{40}Ar^* = \frac{\lambda_e}{\lambda} \times {}^{40}K\,(e^{\lambda t} - 1) \qquad \text{(equation 1)}$$

Making argon ($^{39}Ar_K$) from potassium in the reactor:

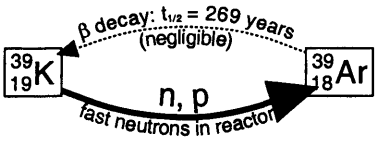

$$^{39}Ar_K = {}^{39}K \times \text{irradiation time} \times \int_0^{\varepsilon} \text{neutron flux}(\varepsilon).\ \text{capture cross-section}(\varepsilon)\ d\varepsilon$$

where terms within the integral are expressed as a function of energy (ε)

This simplifies to:

$$^{39}Ar_K = {}^{39}K \times \text{reactor factors} \qquad \text{(equation 2)}$$

Combining equations (1) and (2):

$$\frac{^{40}Ar^*}{^{39}Ar_K} = \frac{\lambda_e}{\lambda} \times \frac{^{40}K}{^{39}K} \times \frac{(e^{\lambda t} - 1)}{\text{reactor factors}}$$

and defining a value, J, as: $J = \frac{\lambda}{\lambda_e} \times \frac{^{39}K}{^{40}K} \times \text{reactor factors}$

this simplifies to:

$$\frac{^{40}Ar^*}{^{39}Ar_K} = \frac{(e^{\lambda t} - 1)}{J} \qquad \text{(equation 3)}$$

J is determined experimentally from monitor samples of a known age (see text).

The ratio of radiogenic $^{40}Ar^*$ to reactor-derived $^{39}Ar_K$ is calculated from isotopic ratios of Ar measured:

$$\frac{^{40}Ar^*}{^{39}Ar_K} = \left(\frac{^{40}Ar}{^{39}Ar}\right)_m - \left[\left(\frac{^{40}Ar}{^{36}Ar}\right)_{atm.} \times \left(\frac{^{36}Ar}{^{39}Ar}\right)_m\right] \qquad \text{(equation 4)}$$

and corrected for undesirable interfering reactions (see text),

then equation 3 can be solved to find t, the age of the rock/mineral.

Fig. B.1: Principles of the ^{40}Ar-^{39}Ar method of dating, and equations relevant to the calculation of age determinations from measured isotopic values.

^{40}Ar-^{39}Ar dating overcomes some of these problems by converting ^{39}K to ^{39}Ar via bombardment with fast neutrons in a nuclear reactor (Fig. B.1). (Note that the reverse reaction also occurs, but has a long half-life (269 years) compared with the duration of the analytical process; it may be either be corrected for or ignored.) The ^{40}Ar-^{39}Ar technique dispenses with the need to analyse separate aliquots of samples by different methods, eliminating both errors due to sample inhomogeneity and the use of different analytical methods, and reducing laboratory time. Instead, only measurements of *isotopic ratios* of Ar are required - this is more accurate than measurements of absolute abundances, and can be carried out using conventional mass spectrometry techniques. The gases on which the isotopic ratios are determined can be derived from the sample by a number of methods: *total fusion*, where the sample is heated to its melting temperature, either in a furnace or by a laser, driving off all the Ar in one stage; and *incremental* or *step heating*, where the sample is progressively heated in a controlled furnace and the gas is collected and analysed a portion at a time, allowing the construction of an *age spectrum* showing the apparent age of the gas evolved at each temperature step.

Total fusion ^{40}Ar-^{39}Ar dating gives better results than K-Ar, because some of the ^{39}Ar derived from ^{39}K in the reactor (hereafter: $^{39}Ar_K$) is lost from the sample during irradiation - this is termed *recoil loss* (discussed further in Section B.2.1). This $^{39}Ar_K$ loss, arising from the high kinetic energy of sub-atomic particles involved in the nuclear reactions, often occurs from the same sites as those from which $^{40}Ar^*$ was lost during alteration - the two losses balance each other to some extent, and the age obtained is more accurate. This is not always the case - sometimes alteration phases that do not retain $^{39}Ar_K$ may still retain some $^{40}Ar^*$, causing anomalously old apparent ages (Walker and McDougall, 1982); conversely, alteration can result in loss of $^{40}Ar^*$ from certain crystallographic sites that do not suffer from $^{39}Ar_K$ recoil loss.

The incremental heating technique enables identification of radiogenic or reactor-derived argon loss from these sites, because an age is calculated for each increment of gas collected. The lowest temperature fractions contain the most loosely-bound argon, derived from the same sites (e.g., crystal rims or alteration phases) that are prone to loss of $^{40}Ar^*$ over geological time and $^{39}Ar_K$ during irradiation. Conversely, the sites from which Ar is evolved only at high temperatures (e.g., cores of crystals of original igneous or metamorphic mineralogy) are likely to have been resistant to Ar loss over geological time and during

irradiation, and thus the high temperature gas fractions are more likely to give a geologically meaningful age.

In addition to the construction of an age spectrum for determining the apparent age of each increment of gas analysed, an isotope correlation diagram (Merrihue and Turner, 1966) is used to evaluate the contribution from atmospheric $^{40}Ar/^{36}Ar$, because the measured ratios include both an inherited and radiogenic component. The data for each increment are plotted on a diagram in co-ordinates of $[^{40}Ar/^{36}Ar]_{measured}$ (y axis) and $[^{39}Ar/^{36}Ar]_{measured}$ (x axis), which should result in a straight line where the gradient, $[^{40}Ar^{*}/^{39}Ar]_{K}$, is related to the sample age, and the intercept is $[^{40}Ar/^{36}Ar]_{inherited}$, which should theoretically be within error of the atmospheric value (295.5).

Using the incremental heating ^{40}Ar-^{39}Ar dating method, crystallisation ages can be differentiated from unreliable ages using a set of internal statistical tests for each experiment. It may not be possible to differentiate why a particular experiment is unreliable, i.e. because of geological factors or experimental artefact or both. However, it is critical to use these internal tests (discussed in section 4.3.2) to determine whether the K-Ar system of a particular sample is too disturbed to reveal a meaningful geological age. This is particularly important for altered rocks.

The equations relevant to the calculation of a ^{40}Ar-^{39}Ar date are shown in Fig. B.1. In order to obtain a date, it is vital to know what proportion of the ^{39}K originally present in the sample was converted into $^{39}Ar_K$ in the nuclear reactor. This depends on the duration of the sample irradiation and the energy distribution of the fast neutrons incident on the sample. The best way to quantify this is to insert monitor samples of a known age at regular intervals in the irradiation vial, between the samples of unknown age. From the isotopic composition of the Ar derived from the monitor sample and equation 3 (in Fig. B.1), a value known as the J-value can be determined. The J-value not only varies with overall reactor conditions, but also with location within the irradiation vial. Thus, J-values are derived for a number of monitor samples, and J-values for the unknown samples are obtained by extrapolation. The J-value for each unknown sample can then be used, together with the measured Ar isotopic ratios, to calculate the apparent age of the gas evolved (equations 3 and 4).

The process by which the $^{40}Ar^{*}/^{39}Ar_K$ ratio is calculated from the measured Ar isotopic ratios is non-trivial, because several corrections are required in order to account for non-desirable reactions during irradiation. These corrections are discussed further in section B.2.1.

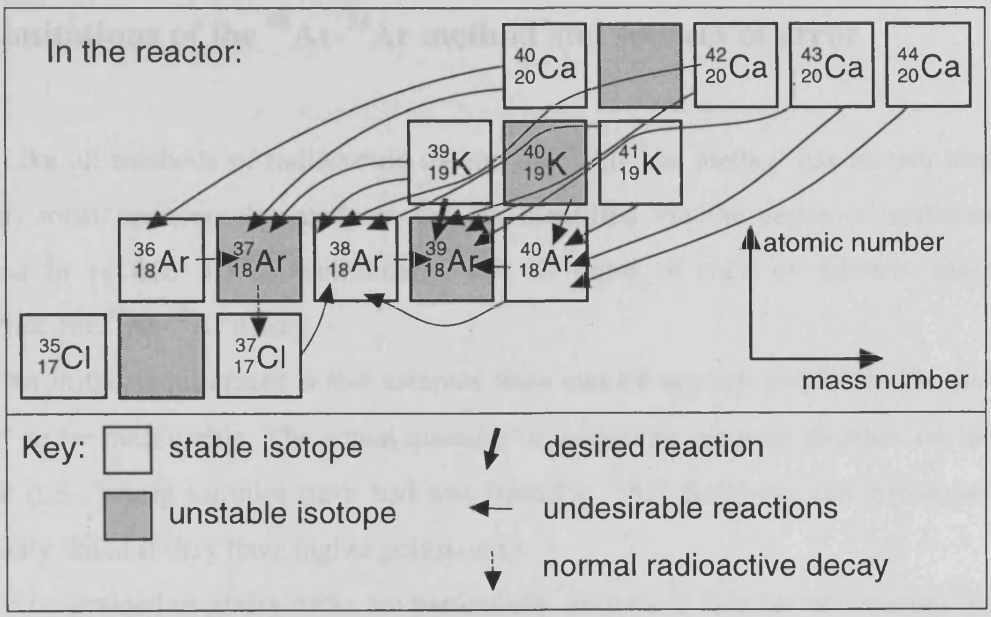

Fig. B.2a: Summary diagram of reactions involving isotopes of Ca, K, Ar and Cl that occur during irradiation of a rock sample in a nuclear reactor (after Brereton, 1970).

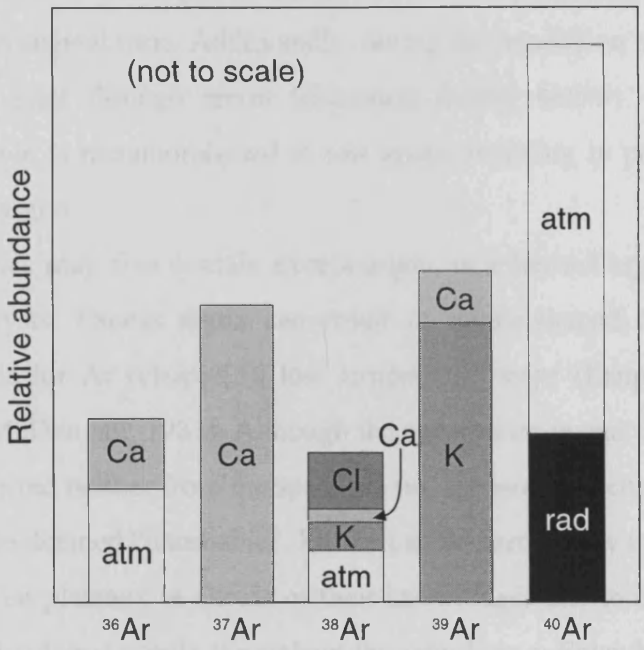

Fig. B.2b: Schematic diagram showing relative abundances of Ar isotopes derived from various sources:

rad: radiogenic Ar derived from radioactive decay of ^{40}K within the rock
Ca: derived from calcium
K: derived from potassium
Cl: derived from chlorine
atm: derived from the atmosphere

B.2 Limitations of the ^{40}Ar-^{39}Ar method and sources of error

Like all methods of radiometric dating, the ^{40}Ar-^{39}Ar method has certain limitations; however, most unsuccessful analyses can be identified via the series of statistical tests, described in section 4.3.2. Additionally, not all types of rock or mineral samples are appropriate for ^{40}Ar-^{39}Ar dating.

An initial requirement is that samples must contain enough potassium for the amount of $^{40}Ar^*$ to be measurable. The actual quantity of potassium required depends on the age of the rock (i.e., young samples have had less time for $^{40}Ar^*$ build-up, and consequently, are more easily dated if they have higher potassium.)

Fine-grained or glassy rocks are particularly difficult to date for two reasons: they have a low argon retentivity, and are prone to argon redistribution during secondary alteration or devitrification (Fleck et al., 1977; McDougall and Harrison, 1988, pp. 29-30) and irradiation. The low argon retentivity results from the relatively high proportion of sites (e.g., grain boundaries, grain rims) in which argon is loosely bound. Consequently, $^{40}Ar^*$ may diffuse out of the sample over geological time. Additionally, during the irradiation process, $^{39}Ar_K$ may be lost from the same sites through recoil (discussed further below). These problems are amplified if the sample is metamorphosed at low grade, resulting in partial recrystallisation and redistribution of argon.

Certain samples may also contain excess argon, or inherited argon contained within, for example, xenocrysts. Excess argon can result in saddle-shaped age spectra, showing anomalously old ages for Ar released in low temperature steps (Lanphere and Dalrymple, 1976; Harrison and McDougall, 1981). Although the age spectra reveal the presence of excess ^{40}Ar, ages can be inferred neither from the spectrum nor the isochron correlation diagram, and the date can merely be deemed "unreliable". Biotite can be particularly misleading: some have been found to have flat plateaux in excess of their known ages due to excess argon, because the excess argon is distributed evenly throughout the sample (e.g. Foland, 1983).

Errors commonly quoted for ^{40}Ar-^{39}Ar dates are only the errors in analytical uncertainty. In addition to these errors, and those inherent to the sample, there is also a degree of uncertainty in the age of the neutron flux monitor standards used. All ages are reported relative to the particular laboratory's preferred neutron flux monitor; in turn, these are calibrated relative to a hornblende standard MMhb-1. Reported ages for this standard range

from 513.9 ± 1.0 Ma (e.g. Pringle, 1992) to 523.1 ± 4.6 Ma (Renne et al., 1998). This uncertainty in the age of the standard leads to a systematic error in the determined ages of the unknown samples: this could be as high as 2%.

B.2.1 Reactor processes

Unavoidable processes occurring in the reactor are responsible for some of the uncertainty in ^{40}Ar-^{39}Ar age determinations. These include undesirable interfering reactions and recoil losses of certain isotopes.

Figure B.2a shows that, in addition to the important $^{39}K(n, p)^{39}Ar$ reaction, numerous other nuclear reactions may occur, that must be corrected for before a realistic values for $^{39}Ar_K$ and $^{40}Ar^*$ can be obtained. These corrections are particularly important if the sample is young (<1 Ma) because it contains less $^{40}Ar^*$, and therefore the amount of ^{40}Ar measured can be significantly increased by ^{40}Ar made by interfering reaction. This is exacerbated if the sample has a low K/Ca ratio, for example, a plagioclase separate. The correction ratios are calibrated for the particular reactor used for irradiation, using an optical grade fluorite, which contains Ca but no K. Additionally, a correction must be made for mass fractionation due to the higher mobility of the lighter isotopes.

The stages involved in the correction are complex, but can be summarised as follows: (see also Fig. B.2b).

- The production of ^{37}Ar in the reactor is dominated by the contribution from ^{40}Ca, and therefore the abundance of ^{37}Ar can be used as a tracer to evaluate Ca interference on other Ar isotopes. However, ^{37}Ar is not a stable isotope, and undergoes β decay to ^{37}Cl with a half life of 35.1 days. This must be corrected for before the Ca interference can be quantified.
- The amount of Ca interference on ^{37}Ar is used to estimate the importance of the reactions $^{40}Ca(n, n\alpha)^{36}Ar$, $^{42}Ca(n, n\alpha)^{38}Ar$ and $^{42}Ca(n, \alpha)^{39}Ar$.
- The amount of atmospheric ^{36}Ar can now be calculated by subtracting the Ca-derived ^{36}Ar from the measured amount. The normal atmospheric ratios are used to derive the quantity of atmospheric ^{40}Ar and ^{38}Ar present in the gas increment.
- The quantity of $^{39}Ar_K$ is calculated from the measured amount minus the Ca-derived component (all corrected for decay of ^{39}Ar: half life = 269 years).

- ^{40}Ar and ^{38}Ar derived from K in the reactor can be quantified because they are proportional to the amount of $^{39}Ar_K$: the correction constant is determined experimentally for each reactor.
- $^{40}Ar^*$ is obtained by subtracting $^{40}Ar_K$ and $^{40}Ar_{atm}$ from the measured ^{40}Ar value.
- Cl-derived ^{38}Ar is given by the total measured ^{38}Ar minus the atmospheric, K-derived and Ca-derived components.

Loss or redistribution of different argon isotopes may occur as a consequence of the high kinetic energy of neutrons during the irradiation process - for example, during the $^{39}K(n, p)^{39}Ar$ reaction, the proton emitted from the nucleus may cause the nucleus to recoil, resulting either in loss of the atom from the sample, or it becoming embedded in the surface of a neighbouring crystal. This may occur either during or after irradiation, and is known as recoil loss. This occurs particularly for atoms that are close to grain boundaries (within ~0.08 μm; Turner and Cadogan, 1974), hence the problems for fine-grained or highly fractured samples. Recoil of $^{39}Ar_K$ tends to be more significant out of high-K low-T steps into low-K high-T steps (e.g. into pyroxenes, which tend to be more retentive) (Huneke and Smith, 1976).

^{39}Ar is not the only isotope to suffer recoil loss: recoil of Ca-derived ^{37}Ar out of high-Ca high-T steps produces too small a correction for Ca-derived ^{36}Ar and results in calculated ages which are too young (Baksi, 1990). The combined effect of these recoil processes is for the age to be over-estimated for low-T argon fractions and under-estimated at high-T.

In general, loss of $^{39}Ar_K$ from a sample results in too old an age being obtained, although for fine-grained samples, this effect is somewhat counterbalanced by diffusional loss of $^{40}Ar^*$ over geological time. The difficulty in quantifying the relative importance of these movements means that the ^{40}Ar-^{39}Ar method of dating is not well suited for fine grained samples.

B.3 Sample preparation techniques

After sample selection, thin section studies were carried out to evaluate the most appropriate size fraction of the relevant mineral for separation. Samples were then crushed using the University of Leicester fly press. Following sieving to select the required size fraction (shown in Table B.1), samples were prepared as follows:

Table B.1: Sample preparation information for Aruba samples

Sample	Lithology	mineral or whole rock	size fraction (μm)	treatment
Aruba Lava Formation				
ARU96-2	coarse basalt	whole rock	125-250	leached in warm 3N HCl
ARU96-30	dolerite	whole rock	125-250	leached in warm 3N HCl
ARU96-31	basalt	whole rock	125-250	leached in warm 3N HCl
ARU96-147	amphibolite	hornblende	125-212	leached in HCl
Aruba batholith				
ARU96-131a	tonalite	biotite	300-500	none
ARU96-131b	tonalite	biotite	300-500	none
ARU96-158	diorite	biotite	212-300	none
BK77-165	diorite	hornblende	212-300	leached in HCl
ARU96-152	meladiorite	hornblende	212-300	leached in HCl
ARU96-123	late mafic dyke	hornblende	125-212	leached in HCl

Whole rock samples of the basalts and dolerite were considered to be too altered for analyses to be carried out on the unprocessed rock: however, acid cleaning with warm 3 to 6N HCl can be quite useful in dissolving altered plagioclase, carbonates, zeolites and phosphates. A grain size range of 125-250 μm, smaller than the original crystals, allows the acid to reach and clean a higher proportion of cleavage surfaces, but without incurring sample handling and recoil problems. HCl cleaning assists in removal of material that is usually degassed in the low-temperature steps of incremental heating experiments. Consequently, samples were placed in beakers with 3N HCl and placed on a warm hot-plate to leach for 30 minutes. The sample was separated from the acid by filtration. The residue (sample) was rinsed in de-ionised water and dried.

Similarly, thin section evaluation of hornblende revealed the presence of minor amounts of alteration products. These samples were leached in cold 3N HCl for 30 minutes, then filtered, rinsed in de-ionised water, and dried. 20 mg samples of hornblende crystals were hand picked from the bulk leached sample using a binocular microscope.

Biotites were free of alteration products, and required no leaching. 5 mg samples were hand picked under a binocular microscope.

B.4 Analytical techniques

After preparation as described above, samples were placed into 99.99% copper foil packets and sealed in air in quartz vials. Neutron flux monitor grains were loaded into copper packets that were placed every ~ 7 mm in the 80 mm vial. The monitor mineral used was sanidine 85G003 from the Taylor Creek rhyolite (Dalrymple and Duffield, 1988). The age of this standard, 27.92 Ma, has been determined by intercalibration against SB-3 biotite (162.9 Ma: c.f., Duffield and Dalrymple, 1990; Dalrymple et al., 1993). Relative to the 27.92 age of the Taylor Creek sanidine, the interlaboratory hornblende standard MMhb-1 gives a K-Ar age of 513.9 ± 2.3 Ma (Dalrymple et al., 1993) and a ^{40}Ar-^{39}Ar age of 513.9 ± 1.0 Ma (Pringle, 1992). Uncertainly in the age of interlaboratory standards used to calibrate minerals used as neutron fluence monitors in various laboratories introduces an uncertainty of ~ 1% into the absolute ages calculated from the data in this study (e.g., Dalrymple et al., 1993; Renne et al., 1994), although the relative ages of the samples are not affected by this uncertainty. Samples were irradiated for 1 hour at the Oregon State University Triga reactor in the cadmium shielded CLICIT facility, where they received a total fast neutron dose of ~ 9×10^{16} n/cm^2. Based on previous analyses of optical grade CaF_2 and Fe-doped K-silicate glass irradiated at Oregon State (Wijbrans et al., 1995), corrections for undesirable neutron-induced reactions on ^{40}K and ^{40}Ca are as follows: $[^{40}Ar/^{39}Ar]_K = 0.00086$; $[^{36}Ar/^{37}Ar]_{Ca} = 0.000264$; $[^{39}Ar/^{37}Ar]_{Ca} = 0.000673$.

At the Scottish Universities Research and Reactor Centre (SURRC), samples were loaded into a glass sidearm over a double vacuum resistance furnace attached to a 225 cm^3 gas clean-up system that employed one SAES AP10-GP Zr-Al getter pump operated at room temperature and one at ~ 400°C. Samples were degassed at 600-750°C to remove undesirably large quantities of atmospheric argon. Incremental heating experiments consisted of 5 to 18 individual steps. Following 10-12 minute heating intervals and an additional 5 minutes of clean-up with a third AP10-GP getter at 400°C, the purified gas was let into an ultrasensitive rare gas mass spectrometer (Mass Analyzer Products 216 with Bauer-Signer ion source). For each analysis, eight sets of peaks over the mass range 40-36 were measured statically on a Johnston secondary electron multiplier and linearly regressed to the height at the time of inlet. The instrument was operated at a sensitivity of 8×10^{-15} mole $^{40}Ar/V$. Each analysis was corrected for mass discrimination and a total system blank that comprised two parts, including a small non-atmospheric component contributed by the mass spectrometer plus an atmospheric component from the furnace and clean-up system. These blanks were measured

prior to degassing each sample. Total system blanks were typically less than 2.4×10^{-15} mole ^{40}Ar and 3.0×10^{-17} mole ^{36}Ar at temperatures below 1200°C; the spectrometer backgrounds were less than 2.0×10^{-18} mole ^{40}Ar and 8.0×10^{-18} mole ^{36}Ar.

Both age spectra and isochron ages were calculated from ^{40}Ar-^{39}Ar incremental heating experiments. Plateau ages were calculated as weighted means. Isochron ages are calculated for both the $^{40}Ar/^{36}Ar$ versus $^{39}Ar/^{36}Ar$ and $^{36}Ar/^{40}Ar$ versus $^{39}Ar/^{40}Ar$ correlation diagrams using the York2 least-squared cubic fit with correlated errors (York, 1969), although the difference between the two correlation methods has previously been found to be negligible (Pringle, 1993).

All errors in this study are reported at the 1 σ (67% confidence) level. For each analysis errors include estimates of the standard deviation of analytical precision on the peak signals, the blank, spectrometer mass discrimination, plus reactor corrections. For plateau ages, inverse-variance weighted mean ages and standard errors were calculated according to Taylor (1982). This weighting allows data with different analytical errors to be combined without the poorer quality data having a disproportionate effect on the result. MSWD calculations were also made to test for scatter about the mean. J values were determined from the mean of 7-13 plateau measurements collected from each monitor packet. Precision estimates for each monitor point along the J curves suggest that errors in J are between 0.3 % and 0.4 %; this error was propagated into the final plateau and isochron ages for each analysis. Ages were calculated using the decay constants of Steiger and Jäger (1977).

Table B.2: ^{40}Ar-^{39}Ar incremental-heating data for samples from the Aruba Lava Formation

Step °C	$^{40}Ar/^{39}Ar$ a	$^{37}Ar/^{39}Ar$ a	$^{36}Ar/^{39}Ar$ a	^{40}Ar (1σ) (%)	^{39}Ar (1σ) (%)	^{37}Ar (1σ) (%)	^{36}Ar (1σ) (%)	$^{40}Ar^*$ (mol)	$^{40}Ar^*$ (%) b	$^{40}Ar_K$ (%) b	$^{39}Ar_{Ca}$ (%) b	$^{36}Ar_{Ca}$ (%) b	K/Ca (%)	^{39}Ar (%)	Apparent Age (Ma) c
ARU96-2	leached whole rock: 125-250μm					J = 0.00277 ± 0 (1σ)			Exp. No.: rw7f0231.IHD				Total gas age =		74.00 ± 0.23
495	78.87	17.35	0.23350	0.06	0.53	9.04	1.32	6.70E-15	14.2	0	1.17	1.96	0.028	0.4	55.97 ± 5.04
540	38.01	23.33	0.11137	0.07	0.26	4.11	1.54	6.80E-15	18.2	0	1.57	5.53	0.021	0.6	34.82 ± 2.43
590	27.72	23.29	0.07893	0.21	0.51	2.07	1.29	1.30E-14	22.4	0	1.57	7.79	0.021	1.3	31.28 ± 1.66
630	23.57	26.14	0.06292	0.15	0.27	1.97	1.40	1.30E-14	29.8	0	1.76	10.97	0.018	1.1	35.37 ± 1.21
675	23.85	24.68	0.06675	0.74	0.47	3.52	2.03	6.40E-15	25.4	0	1.66	9.76	0.020	0.7	30.50 ± 2.10
720	26.73	25.23	0.05248	0.17	0.39	2.66	1.51	1.90E-14	49.4	0	1.70	12.69	0.019	0.9	65.92 ± 1.17
765	28.64	21.11	0.06755	0.12	0.26	2.40	1.36	2.00E-14	36.1	0	1.42	8.25	0.023	1.2	51.67 ± 1.29
815	26.01	15.79	0.05258	0.14	0.28	2.50	1.23	2.80E-14	45.0	0	1.06	7.93	0.031	1.5	58.25 ± 0.96
850	22.84	14.19	0.04127	0.09	0.13	2.26	1.01	3.60E-14	51.4	0	0.95	9.07	0.034	1.9	58.37 ± 0.58
920	20.69	15.79	0.03142	0.04	0.14	1.50	0.90	6.60E-14	61.1	0	1.06	13.27	0.031	3.2	62.81 ± 0.39
975	19.09	16.98	0.02316	0.06	0.14	0.71	0.61	1.30E-13	71.1	0	1.14	19.36	0.029	6.0	67.40 ± 0.23
1025	20.21	20.95	0.02323	0.34	0.30	1.30	2.51	3.90E-13	74.1	0	1.41	23.81	0.023	16.3	74.45 ± 0.77
1070	19.19	16.02	0.01586	0.08	0.20	0.96	1.92	6.50E-13	82.1	0	1.08	26.67	0.030	25.6	77.96 ± 0.38
1110	21.59	21.27	0.02868	0.21	0.26	1.70	2.04	3.10E-13	68.4	0	1.43	19.58	0.023	12.9	73.43 ± 0.76
1150	22.39	26.05	0.03232	0.35	0.36	1.75	2.29	2.20E-13	66.4	0	1.75	21.27	0.019	9.2	74.17 ± 1.01
1200	28.82	30.07	0.04709	0.06	0.18	1.17	0.98	4.10E-13	59.9	0	2.02	16.86	0.016	14.6	86.01 ± 0.63
1300	40.30	42.25	0.08495	0.03	0.12	0.61	0.93	6.80E-14	45.9	0	2.84	13.13	0.011	2.3	92.80 ± 1.03
1400	125.07	46.55	0.38850	0.05	0.74	4.66	0.66	6.10E-15	11.1	0	3.13	3.16	0.010	0.3	70.42 ± 6.97
ARU96-30	leached whole rock: 125-250μm					J = 0.002775 ± 5.6E-06 (1σ)			Exp. No.: rw7f0232.IHD				Total gas age =		53.70 ± 0.43
520	43.42	26.05	0.12710	0.06	0.15	1.55	0.37	1.80E-14	18.2	0	1.75	5.41	0.019	3.5	39.79 ± 0.82
565	30.21	41.58	0.10113	0.19	0.51	3.13	1.84	2.70E-15	11.8	0	2.80	10.86	0.012	1.1	18.28 ± 2.69
610	23.89	40.76	0.07387	0.14	0.86	0.65	0.79	1.20E-14	21.9	0	2.74	14.57	0.012	3.4	26.79 ± 1.57
655	25.66	40.13	0.08235	0.36	0.55	1.85	1.41	6.70E-15	17.4	0	2.70	12.86	0.012	2.2	22.79 ± 1.83
700	26.96	40.55	0.07784	0.30	0.22	1.31	1.05	1.50E-14	26.4	0	2.73	13.75	0.012	3.1	36.25 ± 1.18
750	25.95	34.99	0.06900	0.30	0.16	1.06	1.02	2.40E-14	31.9	0	2.35	13.39	0.014	4.3	41.98 ± 1.01
800	23.73	32.53	0.06197	0.15	0.18	0.99	0.75	2.70E-14	33.5	0	2.19	13.86	0.015	5.1	40.25 ± 0.68
850	22.60	28.55	0.05795	0.25	0.24	1.05	0.82	2.50E-14	34.1	0	1.92	13.01	0.017	4.8	38.88 ± 0.75
905	22.46	24.36	0.05605	0.15	0.61	1.35	1.02	2.50E-14	34.7	0	1.64	11.47	0.020	4.9	39.24 ± 1.13
960	21.62	35.48	0.04785	0.07	0.07	0.52	0.56	6.50E-14	47.4	0	2.39	19.57	0.014	9.5	51.81 ± 0.35
1010	22.14	57.78	0.05072	0.03	0.20	0.35	0.71	9.30E-14	52.7	0	3.89	30.07	0.008	11.8	59.75 ± 0.47
1055	22.41	56.48	0.05329	0.11	0.17	0.38	0.96	5.40E-14	49.4	0	3.80	27.98	0.008	7.2	56.72 ± 0.61
1100	24.86	65.00	0.06516	0.05	0.29	0.55	1.22	3.50E-14	43.0	0	4.37	26.34	0.007	4.8	55.06 ± 0.98
1150	30.99	76.81	0.07992	0.18	0.27	0.47	0.99	7.80E-14	43.1	0	5.17	25.37	0.006	8.5	69.22 ± 1.06
1200	38.48	146.23	0.12843	0.09	0.22	0.36	1.19	1.80E-13	31.0	0	9.84	30.06	0.003	21.1	65.11 ± 1.79
1300	41.93	210.70	0.15248	0.04	0.15	0.18	0.67	4.80E-14	31.7	0	14.18	36.47	0.002	4.7	76.00 ± 1.21
ARU96-31	leached whole rock: 125-250μm					J = 0.002777 ± 5.6E-06 (1σ)			Exp. No.: rw7f0279.IHD				Total gas age =		87.76 ± 0.31
495	51.44	37.49	0.13899	0.13	0.14	1.41	0.39	3.30E-14	25.8	0	2.52	7.12	0.013	4.7	67.06 ± 0.97
545	41.61	37.28	0.09821	0.11	0.14	1.91	0.61	3.10E-14	37.2	0	2.51	10.02	0.013	3.8	77.91 ± 0.89
590	36.16	33.41	0.07837	0.08	0.27	5.02	1.65	1.10E-14	43.2	0	2.25	11.26	0.014	1.4	78.27 ± 1.75
655	36.22	36.77	0.07871	0.20	0.22	3.00	1.25	2.60E-14	43.7	0	2.47	12.33	0.013	3.2	79.55 ± 1.37
710	33.68	34.17	0.07240	0.09	0.09	1.70	0.62	3.30E-14	44.4	0	2.30	12.46	0.014	4.2	75.08 ± 0.63
785	32.56	29.49	0.06670	0.09	0.15	2.44	1.11	2.70E-14	46.5	0	1.98	11.67	0.016	3.4	75.81 ± 1.00
865	27.72	29.57	0.05059	0.10	0.18	1.10	0.72	6.30E-14	54.4	0	1.99	15.43	0.016	8.0	75.45 ± 0.55
935	26.44	51.39	0.04970	0.26	0.49	0.50	1.01	1.20E-13	59.6	0	3.46	27.30	0.009	15.0	79.97 ± 0.96
985	27.47	57.22	0.05452	0.21	0.21	0.73	0.84	5.30E-14	57.6	0	3.85	27.71	0.008	6.3	80.62 ± 0.66
1035	29.91	63.81	0.06559	0.06	0.15	0.74	0.67	5.50E-14	51.8	0	4.29	25.68	0.007	6.7	79.41 ± 0.58
1080	32.81	62.46	0.06917	0.02	0.11	0.77	0.71	5.70E-14	52.6	0	4.20	23.84	0.008	6.2	88.00 ± 0.60
1130	51.08	76.55	0.12492	0.04	0.07	0.19	0.25	3.00E-13	39.4	0	5.15	16.18	0.006	27.6	103.33 ± 0.54
1200	62.61	141.99	0.18409	0.13	0.10	0.29	0.32	1.00E-13	30.8	0	9.56	20.36	0.003	9.2	103.80 ± 1.01
1300	138.76	228.30	0.47440	0.14	1.52	2.76	2.71	2.00E-15	11.8	0	15.36	12.70	0.002	0.2	94.50 ± 22.7

continued on next page

Table B.2: ^{40}Ar-^{39}Ar incremental-heating data for samples from the Aruba Lava Formation

Step °C	^{40}Ar/^{39}Ar [a]	^{37}Ar/^{39}Ar [a]	^{36}Ar/^{39}Ar [a]	^{40}Ar (1σ) (%)	^{39}Ar (1σ) (%)	^{37}Ar (1σ) (%)	^{36}Ar (1σ) (%)	^{40}Ar* (mol)	^{40}Ar* (%) [b]	^{40}Ar$_K$ (%) [b]	^{39}Ar$_{Ca}$ (%) [b]	^{36}Ar$_{Ca}$ (%) [b]	K/Ca (%)	^{39}Ar (%)	Apparent Age (Ma) [c]
ARU96-147 leached hornblende: 125-212μm						J = 0.002789 ± 5.6E-06 (1σ)		Exp. No.: rw7f0236.IHD					Total gas age =		77.68 ± 0.33
635	156.87	5.88	0.50940	0.13	0.90	39.14	1.20	1.20E-15	4.3	0	0.40	0.30	0.083	0.5	33.96 ± 12.9
750	88.97	11.50	0.27090	0.14	0.75	13.98	1.25	2.50E-15	11.0	0	0.77	1.12	0.042	0.7	49.08 ± 6.46
850	74.65	17.98	0.23240	0.24	0.80	9.41	2.10	1.90E-15	9.9	0	1.21	2.04	0.027	0.7	37.16 ± 7.97
935	63.20	17.48	0.20370	0.11	0.44	7.13	1.83	1.70E-15	6.9	0	1.18	2.26	0.028	1.0	22.06 ± 5.59
1000	34.97	24.90	0.09134	0.19	0.34	3.40	1.56	5.70E-15	28.4	0	1.68	7.20	0.019	1.5	50.07 ± 2.07
1025	25.97	27.44	0.05405	0.32	0.43	1.66	2.97	1.10E-14	46.7	0	1.85	13.40	0.018	2.3	61.16 ± 2.12
1045	20.54	28.98	0.02219	0.20	0.21	0.53	1.20	1.60E-13	79.1	0	1.95	34.48	0.017	24.6	81.48 ± 0.39
1055	19.81	27.89	0.02309	0.15	0.35	0.49	4.54	7.10E-14	76.5	0	1.88	31.89	0.017	12.1	76.10 ± 1.08
1070	19.70	28.51	0.02047	0.19	0.14	0.88	6.54	7.40E-14	80.6	0	1.92	36.77	0.017	12.0	79.64 ± 1.22
1085	22.24	27.76	0.03278	0.44	0.49	2.07	5.34	2.30E-14	66.2	0	1.87	22.36	0.017	4.0	73.95 ± 2.06
1105	21.29	28.00	0.02503	0.16	0.13	1.49	7.01	3.10E-14	75.5	0	1.88	29.54	0.017	5.0	80.61 ± 1.76
1130	21.32	29.28	0.02535	0.08	0.20	0.90	3.24	4.70E-14	75.6	0	1.97	30.50	0.016	7.4	80.88 ± 0.84
1150	19.47	29.36	0.01972	0.06	0.19	0.61	2.96	5.70E-14	81.8	0	1.98	39.31	0.016	9.1	79.98 ± 0.54
1170	20.26	29.16	0.02230	0.08	0.10	0.67	3.16	4.20E-14	78.7	0	1.96	34.52	0.017	6.8	80.02 ± 0.67
1200	20.64	29.44	0.02310	0.05	0.12	0.78	3.51	4.20E-14	78.0	0	1.98	33.64	0.016	6.7	80.86 ± 0.77
1250	21.92	30.43	0.02769	0.04	0.15	0.86	2.55	3.60E-14	73.5	0	2.05	29.02	0.016	5.8	80.91 ± 0.73

Notes

a Corrected for ^{37}Ar and ^{39}Ar decay, half-lives 35.1 days and 269 years, respectively.

b Radiogenic (R), calcium-derived (Ca), and potassium-derived (K) argon, respectively (percent).

c Ages calculated relative to 85G003 TCR Sanidine at 27.92 Ma with λ_e = 0.581E-10/yr and λ_β = 4.692E-10/yr.

Table B.3: ^{40}Ar-^{39}Ar incremental-heating data for samples from the Aruba batholith

Step °C a	$^{40}Ar/^{39}Ar$ b	$^{37}Ar/^{39}Ar$ b	$^{36}Ar/^{39}Ar$ b	^{40}Ar (1σ) (%)	^{39}Ar (1σ) (%)	^{37}Ar (1σ) (%)	^{36}Ar (1σ) (%)	$^{40}Ar^*$ (mol)	$^{40}Ar^*$ (%) c	$^{40}Ar_K$ (%) c	$^{39}Ar_{Ca}$ (%) c	$^{36}Ar_{Ca}$ (%) c	K/Ca (%)	^{39}Ar (%)	Apparent Age (Ma) d
ARU96-131a biotite: 300-500µm					J = 0.002789 ± 5.6E-06 (1σ)			Exp. No.: rw7f0228.IHD				Total gas age :			82.69 ± 0.20
1055	18.11	0.13	0.00431	0.08	0.13	11.18	1.41	3.00E-12	93.0	0	0.01	0.78	3.860	57.0	82.81 ± 0.16
1100	17.58	0.31	0.00374	0.14	0.14	33.65	4.66	7.60E-13	93.9	0	0.02	2.20	1.575	14.5	81.20 ± 0.29
1150	17.59	0.21	0.00242	0.07	0.12	33.51	3.63	1.20E-12	96.0	0	0.01	2.26	2.360	22.3	83.03 ± 0.17
1200	17.98	0.22	0.00302	0.11	0.17	21.97	3.21	2.50E-13	95.1	0	0.01	1.93	2.220	4.6	84.06 ± 0.22
1300	52.38	0.64	0.12025	0.14	0.12	21.73	0.36	8.60E-14	32.3	0	0.04	0.14	0.767	1.6	83.09 ± 0.84
ARU96-131b biotite: 300-500µm					J = 0.002789 ± 5.6E-06 (1σ)			Exp. No.: rw7f0229.IHD				Total gas age :			82.29 ± 0.18
495	30.80	0.67	0.09093	0.07	0.30	84.02	0.83	4.60E-15	12.9	0	0.05	0.19	0.729	0.3	19.94 ± 1.27
545	27.26	0.85	0.06243	0.05	0.29	70.04	2.45	1.00E-14	32.6	0	0.06	0.36	0.575	0.3	44.17 ± 2.21
600	26.30	0.07	0.04053	0.06	0.21	400.00	1.38	3.50E-14	54.5	0	0.00	0.04	7.100	0.6	70.67 ± 0.84
655	20.93	0.06	0.01478	0.15	0.24	102.47	0.72	1.90E-13	79.1	0	0.00	0.10	8.460	2.7	81.47 ± 0.33
700	18.87	0.11	0.00681	0.12	0.25	70.74	1.83	1.50E-13	89.4	0	0.01	0.43	4.390	2.1	82.93 ± 0.31
755	18.27	0.11	0.00394	0.14	0.23	57.47	2.94	1.80E-13	93.7	0	0.01	0.71	4.640	2.6	84.10 ± 0.28
800	17.93	0.25	0.00401	0.07	0.17	49.21	5.06	6.10E-13	93.5	0	0.02	1.66	1.942	8.8	82.43 ± 0.32
845	17.75	0.12	0.00221	0.13	0.22	47.45	3.36	1.90E-13	96.4	0	0.01	1.45	4.040	2.7	84.05 ± 0.24
945	17.96	0.16	0.00514	0.13	0.14	175.44	9.39	2.80E-13	91.6	0	0.01	0.80	3.130	4.1	80.92 ± 0.69
985	17.74	0.04	0.00269	0.05	0.14	242.19	3.59	9.30E-13	95.5	0	0.00	0.35	13.880	13.2	83.33 ± 0.19
1025	17.73	0.18	0.00389	0.14	0.14	72.23	5.08	6.50E-13	93.6	0	0.01	1.20	2.780	9.5	81.61 ± 0.32
1055	17.67	0.02	0.00357	0.09	0.15	543.60	5.12	6.00E-13	94.0	0	0.00	0.17	20.850	8.8	81.72 ± 0.30
1090	17.57	0.29	0.00304	0.06	0.18	36.29	3.90	7.30E-13	95.0	0	0.02	2.48	1.717	10.6	82.11 ± 0.23
1120	17.54	0.14	0.00190	0.09	0.16	44.54	5.74	1.30E-12	96.9	0	0.01	1.88	3.620	18.2	83.52 ± 0.22
1150	17.57	0.24	0.00293	0.04	0.18	41.62	7.71	7.70E-13	95.2	0	0.02	2.13	2.070	11.1	82.24 ± 0.34
1200	17.70	0.17	0.00177	0.12	0.18	27.38	3.76	2.40E-13	97.1	0	0.01	2.59	2.810	3.3	84.46 ± 0.21
1300	21.67	0.56	0.01668	0.08	0.15	27.65	1.43	7.20E-14	77.5	0	0.04	0.88	0.877	1.0	82.54 ± 0.38
ARU96-158 biotite: 212-300µm					J = 0.002789 ± 5.6E-06 (1σ)			Exp. No.: rw7f0230.IHD				Total gas age :			84.29 ± 0.20
545	34.39	2.96	0.10921	0.13	0.28	20.47	2.22	9.30E-16	6.8	0	0.20	0.72	0.165	0.1	11.82 ± 3.54
610	29.80	0.44	0.06255	0.15	0.26	18.75	0.31	4.00E-14	38.1	0	0.03	0.19	1.117	1.2	56.25 ± 0.58
695	21.33	0.16	0.01505	0.17	0.21	12.42	0.69	2.10E-13	79.2	0	0.01	0.27	3.160	4.3	83.04 ± 0.32
750	18.64	0.24	0.00580	0.06	0.18	29.13	6.67	4.40E-13	90.9	0	0.02	1.10	2.030	9.0	83.28 ± 0.56
800	18.08	0.09	0.00299	0.08	0.15	56.61	5.00	6.40E-13	95.1	0	0.01	0.76	5.670	12.6	84.52 ± 0.26
850	17.97	0.05	0.00247	0.09	0.20	98.37	8.30	6.30E-13	96.0	0	0.00	0.53	9.950	12.6	84.75 ± 0.34
895	17.99	0.12	0.00177	0.08	0.21	100.00	12.27	4.40E-13	97.1	0	0.01	1.80	4.080	8.7	85.88 ± 0.35
935	18.03	0.16	0.00147	0.14	0.16	100.00	31.64	3.40E-13	97.7	0	0.01	2.81	3.130	6.7	86.48 ± 0.65
975	18.08	0.16	0.00229	0.20	0.18	13.51	3.28	2.50E-13	96.3	0	0.01	1.84	3.070	4.9	85.58 ± 0.26
1010	18.10	0.18	0.00247	0.17	0.22	11.47	3.58	2.40E-13	96.0	0	0.01	1.96	2.660	4.6	85.39 ± 0.27
1055	18.01	0.31	0.00325	0.04	0.14	26.47	7.62	4.00E-13	94.8	0	0.02	2.52	1.580	7.9	83.92 ± 0.36
1090	17.81	0.16	0.00166	0.11	0.19	22.75	6.20	9.70E-13	97.3	0	0.01	2.56	3.050	19.2	85.18 ± 0.23
1120	18.05	0.37	0.00363	0.10	0.13	26.57	10.78	3.20E-13	94.2	0	0.02	2.67	1.338	6.5	83.60 ± 0.54
1150	18.75	0.57	0.00516	0.13	0.19	17.53	6.53	5.60E-14	92.1	0	0.04	2.94	0.853	1.1	84.87 ± 0.50
1200	21.57	2.10	0.01609	0.09	0.23	18.66	6.31	1.40E-14	78.7	0	0.14	3.44	0.233	0.3	83.59 ± 1.38
1300	31.97	1.07	0.05531	0.09	0.13	37.56	2.90	9.50E-15	49.1	0	0.07	0.51	0.457	0.2	77.42 ± 2.23

continued on next page

Table B.3: ^{40}Ar-^{39}Ar incremental-heating data for samples from the Aruba batholith

Step °C a	^{40}Ar/^{39}Ar b	^{37}Ar/^{39}Ar b	^{36}Ar/^{39}Ar b	^{40}Ar (1σ) (%)	^{39}Ar (1σ) (%)	^{37}Ar (1σ) (%)	^{36}Ar (1σ) (%)	^{40}Ar* (mol)	^{40}Ar* (%) c	^{40}Ar$_K$ (%) c	^{39}Ar$_{Ca}$ (%) c	^{36}Ar$_{Ca}$ (%) c	K/Ca (%)	^{39}Ar (%)	Apparent Age (Ma) d
BK77-165 leached hornblende: 212-300μm						J = 0.002789 ± 5.6E-06 (1σ)		Exp. No.: rw7f0234.IHD				Total gas age:			81.09 ± 0.39
635	93.05	4.87	0.24780	0.05	0.23	5.66	1.19	1.60E-14	21.7	0	0.33	0.52	0.100	0.7	99.24 ± 4.27
750	40.05	6.06	0.09935	0.06	0.38	7.15	2.80	7.70E-15	27.9	0	0.41	1.61	0.081	0.6	55.55 ± 3.97
850	41.00	4.96	0.09796	0.14	0.19	5.46	2.02	9.30E-15	30.3	0	0.33	1.34	0.098	0.7	61.73 ± 2.79
935	32.11	7.38	0.07164	0.09	0.33	3.36	1.65	1.40E-14	35.9	0	0.50	2.72	0.066	1.1	57.31 ± 1.74
1000	24.16	14.78	0.04122	0.06	0.20	1.54	2.30	2.10E-14	54.4	0	0.99	9.47	0.033	1.5	65.53 ± 1.24
1010	24.25	20.35	0.03638	0.03	0.23	1.81	2.77	2.40E-14	62.2	0	1.37	14.77	0.024	1.4	75.38 ± 1.25
1025	23.94	16.18	0.03015	0.04	0.17	0.89	1.61	5.20E-14	68.1	0	1.09	14.17	0.030	2.9	81.04 ± 0.63
1035	20.91	14.49	0.01890	0.04	0.19	0.66	1.23	1.30E-13	78.7	0	0.98	20.24	0.033	7.0	81.73 ± 0.33
1045	20.41	15.00	0.01836	0.30	0.12	2.11	7.90	3.00E-13	79.1	0	1.01	21.56	0.032	16.6	80.27 ± 1.62
1050	18.66	13.17	0.01055	0.10	0.10	0.34	3.08	2.50E-13	88.8	0	0.89	32.98	0.037	13.8	82.21 ± 0.33
1055	18.47	12.42	0.00998	0.11	0.09	0.45	4.61	2.30E-13	89.3	0	0.84	32.84	0.039	12.6	81.77 ± 0.45
1065	19.02	12.83	0.01220	0.08	0.14	0.73	4.29	1.10E-13	86.3	0	0.86	27.77	0.038	5.9	81.45 ± 0.55
1080	19.67	13.83	0.01614	0.07	0.18	1.78	6.68	4.90E-14	81.2	0	0.93	22.63	0.035	2.8	79.38 ± 1.18
1100	20.22	14.36	0.01558	0.04	0.20	0.96	6.81	6.00E-14	82.8	0	0.97	24.33	0.034	3.2	83.07 ± 1.14
1120	21.11	15.07	0.02028	0.06	0.12	1.38	5.14	4.90E-14	77.2	0	1.01	19.62	0.032	2.7	80.96 ± 1.18
1140	20.43	14.56	0.01642	0.05	0.20	0.71	4.04	6.90E-14	81.8	0	0.98	23.41	0.033	3.7	83.00 ± 0.74
1160	20.60	12.20	0.01404	0.12	0.15	0.55	4.01	1.50E-13	84.5	0	0.82	22.94	0.040	7.6	86.19 ± 0.63
1210	20.21	13.38	0.01625	0.14	0.54	0.73	6.58	2.70E-13	81.4	0	0.90	21.74	0.036	15.1	81.67 ± 1.29
ARU96-152 leached hornblende: 125-212μm						J = 0.002789 ± 5.6E-06 (1σ)		Exp. No.: rw7f0233.IHD				Total gas age:			84.58 ± 0.27
545	109.16	4.28	0.30000	0.15	0.41	16.09	0.60	1.70E-14	19.1	0	0.29	0.38	0.114	0.8	102.27 ± 3.82
635	50.32	2.46	0.12259	0.11	0.21	19.19	0.99	1.40E-14	28.4	0	0.17	0.53	0.199	0.9	70.61 ± 1.83
715	60.01	3.33	0.13904	0.06	0.13	14.29	1.09	2.20E-14	32.0	0	0.22	0.63	0.147	1.1	94.21 ± 2.15
785	62.90	3.96	0.14808	0.03	0.17	10.60	0.71	2.30E-14	30.9	0	0.27	0.71	0.124	1.1	95.52 ± 1.60
850	48.27	3.92	0.11148	0.06	0.33	11.16	0.95	1.90E-14	32.4	0	0.26	0.93	0.125	1.2	77.17 ± 1.74
905	39.12	3.52	0.07763	0.05	0.25	10.64	1.39	2.30E-14	42.1	0	0.24	1.20	0.139	1.3	81.14 ± 1.59
950	31.31	5.20	0.05262	0.08	0.23	8.67	2.19	1.90E-14	51.6	0	0.35	2.61	0.094	1.1	79.83 ± 1.62
985	32.24	9.51	0.04851	0.03	0.15	1.23	0.64	8.10E-14	57.8	0	0.64	5.17	0.051	4.1	92.01 ± 0.50
1025	26.13	10.13	0.02737	0.05	0.15	1.24	0.86	7.80E-14	72.1	0	0.68	9.77	0.048	3.9	92.96 ± 0.37
1055	20.33	8.89	0.01467	0.15	0.24	1.67	1.90	6.50E-13	82.1	0	0.60	16.01	0.055	36.8	82.58 ± 0.43
1080	19.24	8.27	0.01211	0.13	0.14	2.13	3.60	3.80E-13	84.7	0	0.56	18.03	0.059	21.9	80.67 ± 0.53
1100	22.58	7.80	0.02189	0.06	0.15	2.37	2.29	6.20E-14	74.0	0	0.52	9.40	0.063	3.5	82.62 ± 0.66
1120	20.93	8.42	0.01582	0.02	0.13	1.48	1.99	7.80E-14	80.8	0	0.57	14.05	0.058	4.3	83.61 ± 0.40
1150	21.08	9.62	0.01443	0.02	0.07	0.65	2.50	1.60E-13	83.3	0	0.65	17.60	0.051	8.5	86.84 ± 0.42
1180	23.35	14.53	0.02122	0.02	0.12	0.43	1.43	1.70E-13	78.0	0	0.98	18.08	0.033	8.6	90.26 ± 0.38
1210	73.35	127.79	0.19730	0.07	0.28	0.59	0.81	2.30E-14	34.1	0	8.60	17.10	0.004	0.8	132.72 ± 2.37
1300	192.21	126.29	0.65190	0.09	1.33	2.30	1.06	1.70E-15	4.9	0	8.50	5.11	0.004	0.2	51.09 ± 20.1
ARU96-123 leached hornblende: 125-212μm						J = 0.002789 ± 5.6E-06 (1σ)		Exp. No.: rw7f0235.IHD				Total gas age:			75.57 ± 0.24
635	106.17	4.66	0.32360	0.07	0.27	8.67	0.74	6.70E-15	10.3	0	0.31	0.38	0.105	1.0	54.29 ± 3.89
750	35.31	6.76	0.06881	0.17	0.50	6.43	3.07	2.10E-14	43.9	0	0.46	2.59	0.072	2.3	76.72 ± 3.04
850	24.26	3.14	0.04094	0.07	0.16	5.40	1.58	2.70E-14	51.1	0	0.21	2.03	0.155	3.7	61.49 ± 0.92
935	20.66	2.26	0.02939	0.07	0.15	4.42	0.85	4.30E-14	58.8	0	0.15	2.03	0.216	6.1	60.19 ± 0.40
960	17.05	3.32	0.01731	0.09	0.20	4.92	3.76	2.10E-14	71.5	0	0.22	5.07	0.147	2.9	60.45 ± 0.89
1000	17.95	5.41	0.01724	0.08	0.12	1.76	2.50	4.20E-14	74.0	0	0.36	8.28	0.090	5.4	65.81 ± 0.57
1010	19.07	10.18	0.02224	0.11	0.07	2.52	3.31	2.40E-14	69.7	0	0.69	12.09	0.048	3.1	66.09 ± 0.92
1030	20.93	14.37	0.02144	0.07	0.10	1.06	3.76	4.80E-14	75.1	0	0.97	17.69	0.034	5.1	78.13 ± 0.94
1035	20.40	13.86	0.01947	0.12	0.18	1.47	3.82	5.30E-14	77.1	0	0.93	18.79	0.035	5.7	78.15 ± 0.87
1045	19.84	12.10	0.01562	0.09	0.12	0.40	2.86	9.10E-14	81.5	0	0.81	20.45	0.040	9.5	80.22 ± 0.52
1055	19.22	11.71	0.01389	0.05	0.09	0.41	2.65	1.00E-13	83.4	0	0.79	22.25	0.042	11.0	79.53 ± 0.42
1060	19.34	11.74	0.01529	0.06	0.12	1.29	2.61	6.60E-14	81.4	0	0.79	20.28	0.041	7.1	78.09 ± 0.47
1080	19.70	12.40	0.01868	0.02	0.35	3.47	5.05	4.80E-14	76.9	0	0.83	17.53	0.039	5.4	75.24 ± 1.14
1110	20.64	11.49	0.02035	0.07	0.16	0.79	3.14	5.50E-14	75.2	0	0.77	14.91	0.042	6.0	77.04 ± 0.78
1140	21.43	11.16	0.02109	0.05	0.19	0.63	1.71	7.20E-14	75.0	0	0.75	13.97	0.044	7.6	79.67 ± 0.49
1170	22.30	11.52	0.02193	0.20	0.20	0.47	1.20	1.40E-13	75.0	0	0.78	13.87	0.042	14.5	82.83 ± 0.45
1210	27.36	15.30	0.04282	0.08	0.19	0.66	1.85	3.40E-14	58.1	0	1.03	9.43	0.032	3.6	79.05 ± 1.05

Notes

a Corrected for ^{37}Ar and ^{39}Ar decay, half-lives 35.1 days and 269 years, respectively.

b Radiogenic (R), calcium-derived (Ca), and potassium-derived (K) argon, respectively (percent).

c Ages calculated relative to 85G003 TCR Sanidine at 27.92 Ma with λ_e = 0.581E-10/yr and λ_β = 4.692E-10/yr.

Appendix C

XRF analyses

C.1 Selection of samples for analysis

Samples chosen for XRF analyses were the freshest samples that could be collected. Every effort was made to ensure that samples were large enough to be statistically representative, although this was logistically impossible for some of the coarsest grained rocks.

C.2 Sample preparation

All rocks were prepared for XRF analysis in the Leicester University Geology Department. The rocks were split into ~ 3 cm pieces using the hydraulic and/or hand splitters, and the fly-press was used to split off any remaining weathered surfaces. These pieces were crushed to a fine grit in the fly-press, before being ground in an agate Tema® swing mill for approximately 15 minutes, resulting in a finely-powdered sample.

Major elements were analysed using fused glass beads. To make these, small (~ 5 g) aliquots of the rock powders were dried overnight in an oven at ~ 120°C. A known amount of sample was weighed into a fused Al_2O_3 ceramic crucible (also of known weight), which was placed in a muffle furnace at 950°C for 1½ hours; the furnace door was opened at least twice during this period to prevent build-up of gases that could buffer the assemblage and inhibit full volatile loss. The crucibles were cooled in a dessicator before re-weighing, and the loss on ignition (LOI) was calculated thus:

$$\%\ \text{weight loss on ignition} = 100 \times \frac{(\text{crucible} + \text{sample})_{\text{before}} - (\text{crucible} + \text{sample})_{\text{after}}}{(\text{crucible} + \text{sample})_{\text{before}} - (\text{crucible})}$$

The ignited samples were stored in the 120°C oven, in order to prevent any re-absorption of volatiles. To make the glass bead, 0.8000g of ignited powder was thoroughly mixed with (4.0000 + x) g of lithium tetraborate-metaborate flux, where x represents the correction required to account for the loss on ignition of the flux, which was routinely

determined for every day that fusion beads were made. The mixture, in a Pt-Au crucible, was placed over a burner to melt and homogenise: this took ~ 15 minutes at a temperature of approximately 1200°C. Homogenisation was ensured by swirling the crucible at intervals during heating. The Pt casting dish was heated to 1100°C, and the molten mixture poured into it. The bead was cooled using jets of air, before being ejected into a refractory ceramic dish for further cooling to room temperature. Beads were labelled with stickers on the non-flat side, and stored in individual polythene bags.

Trace element determinations used pressed powder pellets, which were made by thoroughly mixing ~ 7 grams of dry (but *not* ignited) powder with 8 - 15 drops of Moviol 88 binding agent. The mixture was placed into a holder between two polished stainless tool steel dies, and a force of 10 tons was applied using the electrically-powered hydraulic press. Pellets were carefully removed from the dies, and dried overnight at room temperature before being labelled with pencil on the side, and stored in individual polythene bags.

C.3 XRF machine conditions

Samples were analysed for major elements and selected trace elements in the University of Leicester Geology Department on either a Philips PW1400 or an ARL 8420+ wavelength-dispersive XRF spectrometer. The X-ray source was a 3 kW Rh tube. Minimum count times for all data reported in this thesis are reported in Table C.1, together with lower limits of detection. Further information on machine operating conditions can be found in Babbs (1997).

C.4 Results of XRF analyses

The results of the XRF analyses are presented in the following pages (Table C.2), organised in order of lithology code, and, within each lithology, SiO_2 content. The lithologies are presented in the same order as they are listed in Table A.2.1 in Appendix A. CIPW normative mineralogies have been appended to the analyses. Major element totals of between 98 and 102 % are deemed acceptable, although the majority of analyses have totals between 99 and 101%. All major element analyses in Table C.2 have been recalculated to include the loss-on-ignition.

Data accuracy and precision are considered in Appendix E, where results of analyses for international, in-house and personal reference materials are presented.

Table C.1: Lower limits of detection and minimum counting times for XRF analyses

Element	Detection limit	No. of cycles	Counting time on peak (seconds)	Total counting time on background (seconds)
Major elements	(wt.%)			
SiO_2	0.015	1	20	12
TiO_2	0.003	1	20	20
Al_2O_3	0.015	1	40	20
Fe_2O_3	0.015	1	10	8
MnO	0.015	1	40	20
MgO	0.02	1	50	40
CaO	0.015	1	10	8
Na_2O	0.02	1	50	20
K_2O	0.005	1	20	20
P_2O_5	0.005	1	80	80
Trace elements	(p.p.m)			
Rb	1	1	20	8
Sr	1	1	20	16
Ba	8	1	80	40
Zr	3	1	50	40
Nb	1	1	50	40
Y	1	1	40	40
Sc	1	1	80	80
V	2	1	40	20
Cr	3	1	40	20
Co	3	1	40	32
Ni	2	1	40	20
Cu	1	1	20	10
Zn	3	1	20	10
Ga	1	1	40	20
La	4	4	80	80
Ce	7	4	100	100
Nd	1	4	100	n.c.

Notes:
n.c. : not counted
detection limits for trace elements from T. S. Brewer (pers. comm.)
detection limits for major elements from N. G. Marsh (pers. comm.) for a single counting cycle on NIM-G.

Aruba Lava Formation: basalts

Sample	ARU96 -021	ARU94 -029	ARU97 -091	ARU96 -001	ARU96 -101	ARU96 -027	ARU96 -002	ARU96 -119	ARU96 -031	ARU96 -011	ARU97 -144	ARU96 -012
Lith.	A1	A1	A1	A1	A1	A1	A1	A1	A1	A1	A1	A1
major												
SiO_2	49.18	49.20	49.78	49.85	50.03	50.12	50.29	50.48	50.53	50.57	51.00	51.59
TiO_2	0.87	0.87	0.81	1.09	0.85	1.09	1.06	1.00	1.06	1.18	1.14	1.11
Al_2O_3	13.47	14.50	13.20	14.21	13.32	13.82	13.99	14.62	13.76	13.15	13.39	13.25
$Fe_2O_{3(t)}$	11.24	11.25	10.74	12.01	10.92	13.09	11.65	12.54	11.76	13.41	13.07	13.34
MnO	0.17	0.16	0.17	0.18	0.17	0.19	0.16	0.12	0.18	0.19	0.19	0.18
MgO	10.47	8.54	8.78	7.66	9.36	7.14	7.52	7.48	7.70	6.94	6.82	6.77
CaO	11.56	12.56	12.76	11.95	11.08	11.09	11.43	5.87	11.30	8.59	8.58	7.83
Na_2O	1.87	1.88	1.86	2.03	2.18	1.86	2.17	4.12	2.47	3.60	3.64	3.71
K_2O	0.16	0.12	0.12	0.15	0.14	0.15	0.26	0.44	0.13	0.33	0.18	0.16
P_2O_5	0.07	0.07	0.07	0.09	0.07	0.09	0.09	0.08	0.09	0.09	0.09	0.09
LOI	0.88	0.59	0.69	0.86	1.43	0.61	0.96	2.34	0.66	1.68	1.93	1.55
Total	99.94	99.75	98.98	100.08	99.55	99.27	99.57	99.09	99.65	99.74	100.02	99.59
Mg no.	66.4	61.7	63.4	57.5	64.5	53.6	57.8	55.8	58.1	52.3	52.5	51.8
trace												
Rb	0.9	2.8	2.6	2.1	1.0	0.8	2.9	3.9	1.2	4.1	4.0	1.3
Sr	73	86	118	97	76	72	78	203	92	108	125	102
Ba	19	28	12	17	29	53	30	67	16	138	101	56
Zr	46	47	49	63	46	56	63	60	55	61	62	58
Nb	3.8	3.6	4.4	4.6	3.9	4.1	4.5	4.7	4.7	4.6	4.7	4.2
Y	14	18	17	20	15	24	21	18	18	22	23	22
Sc	46	49	49	50	48	53	50	50	46	43	49	46
V	288	309	292	347	295	381	344	307	344	370	364	362
Cr	681	401	485	272	591	162	291	380	256	129	127	241
Co	49	48	47	51	49	53	51	49	47	51	50	54
Ni	228	117	160	101	179	89	106	138	101	84	82	80
Cu	47	75	65	95	121	145	147	378	164	176	182	177
Zn	76	80	80	98	77	96	87	49	72	97	101	102
Ga	15	17	17	20	17	20	16	17	19	19	18	20
La	4	3	n.d.	5	5	3	3	4	6	5	n.d.	4
Ce	6	8	12	9	8	13	7	11	12	6	10	5
Nd	6	6	8	10	5	8	6	8	8	6	10	7
norm												
Q	0.0	0.0	0.2	0.7	0.0	3.2	1.3	0.0	0.3	0.0	0.0	0.0
C	0.0	0.0	0.0	0.0	0.0	0.0	0.0	0.0	0.0	0.0	0.0	0.0
or	1.0	0.7	0.7	0.9	0.8	0.9	1.6	2.7	0.8	2.0	1.1	0.9
ab	16.0	16.0	15.8	17.3	18.7	15.8	18.5	35.7	21.1	31.0	31.4	31.9
an	28.1	31.0	27.5	29.4	26.5	29.1	27.9	20.6	26.2	19.1	20.0	19.3
di	23.8	25.5	29.1	24.4	23.4	21.2	23.6	7.2	24.3	19.5	18.8	16.1
hy	19.8	18.8	20.6	21.2	23.8	22.8	20.9	17.1	21.1	15.4	18.7	24.4
ol	6.0	2.5	0.0	0.0	1.1	0.0	0.0	9.7	0.0	6.1	3.5	0.4
mt	2.5	2.5	2.4	2.7	2.5	2.9	2.6	2.8	2.6	3.0	2.9	3.0
il	1.7	1.7	1.6	2.1	1.6	2.1	2.0	1.9	2.0	2.3	2.2	2.1
ap	0.2	0.2	0.2	0.2	0.2	0.2	0.2	0.2	0.2	0.2	0.2	0.2
sum	99.0	98.8	98.1	99.1	98.6	98.2	98.6	98.0	98.7	98.6	98.9	98.5

Aruba Lava Formation: basalts (cont.) and dolerites

Sample	ARU97 -066	ARU97 -143	ARU96 -073	ARU96 -030	ARU96 -040	ARU96 -117	ARU96 -072	ARU96 -038	ARU96 -100	ARU94 -022	ARU96 -035	ARU96 -009
Lith.	A1	A1	A1	A2	A2	A2	A2	A2	A2	A2	A2	A2
major												
SiO_2	51.99	53.58	54.86	48.94	48.97	48.98	49.10	49.48	49.51	49.54	50.32	50.41
TiO_2	1.14	0.72	0.78	0.75	0.39	0.55	0.40	0.37	0.95	0.78	1.37	1.02
Al_2O_3	13.70	13.13	12.73	14.44	14.17	15.57	12.97	12.81	13.95	14.50	13.33	13.34
$Fe_2O_{3(t)}$	11.73	8.56	7.38	9.74	8.14	8.37	8.24	8.00	11.09	10.54	13.73	12.91
MnO	0.15	0.07	0.09	0.14	0.13	0.14	0.14	0.13	0.17	0.17	0.20	0.20
MgO	7.39	8.39	7.17	9.56	10.90	8.80	11.31	11.73	7.98	9.86	7.03	6.41
CaO	10.71	9.41	11.71	12.82	14.45	13.58	15.08	14.88	11.76	10.92	9.77	10.39
Na_2O	2.27	3.99	4.16	1.68	1.16	1.91	1.02	1.01	1.99	1.98	2.64	2.66
K_2O	0.15	0.14	0.09	0.12	0.09	0.35	0.09	0.08	0.15	0.12	0.30	0.37
P_2O_5	0.10	0.06	0.08	0.06	0.03	0.04	0.03	0.03	0.08	0.06	0.10	0.08
LOI	1.04	1.66	0.41	1.24	1.85	1.72	0.87	1.80	1.37	1.71	1.31	1.97
Total	100.35	99.72	99.47	99.49	100.27	100.02	99.24	100.30	99.01	100.17	100.13	99.76
Mg no.	57.2	67.5	67.3	67.5	73.9	69.0	74.4	75.6	60.4	66.5	52.0	51.3
trace												
Rb	3.8	1.8	0.5	2.0	0.8	5.2	0.4	0.6	2.5	2.5	3.8	5.2
Sr	95	72	121	77	58	82	64	49	88	68	101	136
Ba	31	21	22	11	12	57	9	9	13	28	50	60
Zr	65	40	45	38	23	26	23	15	53	35	66	57
Nb	5.4	3.1	3.6	3.2	1.5	2.2	1.3	1.1	4.0	3.4	5.6	4.0
Y	22	15	17	12	8	15	8	9	17	13	22	23
Sc	43	42	40	48	39	44	50	48	48	42	50	40
V	343	255	294	282	197	235	216	214	335	273	419	332
Cr	272	380	330	685	1232	298	634	1194	412	390	19	5
Co	49	35	28	42	40	36	38	40	46	45	52	51
Ni	99	112	72	175	212	128	191	191	118	139	72	61
Cu	87	14	20	91	113	86	102	97	78	111	151	144
Zn	98	25	30	67	45	53	51	51	77	65	123	91
Ga	18	14	11	17	14	16	11	10	15	18	20	17
La	n.d.	n.d.	4	5	4	4	4	3	6	4	4	5
Ce	23	11	8	3	1	2	3	1	9	5	7	7
Nd	10	10	9	3	3	3	5	5	8	5	6	5
norm												
Q	4.0	0.0	0.5	0.0	0.0	0.0	0.0	0.0	0.9	0.0	0.8	1.0
C	0.0	0.0	0.0	0.0	0.0	0.0	0.0	0.0	0.0	0.0	0.0	0.0
or	0.9	0.8	0.6	0.7	0.5	2.1	0.5	0.5	0.9	0.8	1.8	2.2
ab	19.4	34.4	35.4	14.4	10.0	16.4	8.7	8.7	17.1	17.0	22.7	22.9
an	27.0	17.8	15.8	31.9	33.8	33.4	30.8	30.7	29.1	30.9	23.9	23.9
di	21.3	23.6	33.8	26.0	31.3	28.1	35.7	35.5	24.2	19.4	20.2	23.3
hy	21.6	17.2	8.9	18.7	17.3	8.8	16.6	18.8	21.4	24.6	23.6	20.2
ol	0.0	1.0	0.0	3.2	3.9	7.3	3.5	2.9	0.0	2.6	0.0	0.0
mt	2.6	2.7	2.3	2.2	1.8	1.9	1.8	1.8	2.5	2.4	3.1	2.9
il	2.2	1.4	1.5	1.4	0.8	1.1	0.8	0.7	1.8	1.5	2.6	2.0
ap	0.2	0.1	0.2	0.1	0.1	0.1	0.1	0.1	0.2	0.1	0.3	0.2
sum	99.4	99.0	98.9	98.7	99.6	99.3	98.5	99.6	98.1	99.3	99.0	98.7

Aruba Lava Formation: dolerites (cont.) and deformed rocks

Sample	ARU96 -082	ARU96 -037	ARU96 -007	ARU96 -006	ARU96 -108	ARU96 -107	ARU97 -158	ARU97 -159	ARU96 -105	ARU96 -106	ARU97 -071	ARU97 -072
Lith.	A2	A2	A2	A2	A3	A3	A3	A3	A3	A3	A3	A3
major												
SiO_2	50.48	51.05	51.07	51.12	46.15	48.39	48.75	48.94	48.98	49.06	49.74	50.03
TiO_2	0.90	1.05	1.27	0.68	0.77	0.83	0.85	0.76	0.84	0.87	0.22	0.40
Al_2O_3	14.12	13.14	12.99	14.29	11.22	12.80	12.89	11.21	13.16	13.16	6.51	4.06
$Fe_2O_{3(t)}$	10.61	11.62	15.97	11.13	11.72	11.07	11.01	11.28	10.90	11.09	11.91	11.87
MnO	0.16	0.18	0.21	0.18	0.19	0.17	0.16	0.16	0.17	0.17	0.18	0.22
MgO	7.28	8.12	5.42	6.83	16.98	10.39	10.28	14.21	10.27	10.30	19.27	15.02
CaO	11.94	10.83	7.72	11.26	5.52	11.45	11.33	5.65	10.59	10.52	8.01	14.60
Na_2O	2.35	2.16	3.74	2.35	1.51	1.77	1.78	1.75	2.17	2.04	0.40	0.65
K_2O	0.18	0.12	0.33	0.13	0.11	0.12	0.12	0.10	0.12	0.16	0.08	0.18
P_2O_5	0.08	0.09	0.09	0.05	0.05	0.07	0.07	0.06	0.07	0.07	0.03	0.03
LOI	0.72	1.16	1.61	1.61	5.15	2.45	2.15	3.97	2.18	1.49	4.49	3.17
Total	98.82	99.52	100.43	99.63	99.35	99.50	99.39	98.10	99.45	98.92	100.85	100.21
Mg no.	59.2	59.7	41.8	56.5	75.4	66.5	66.4	72.7	66.6	66.3	77.4	72.8
trace												
Rb	2.1	0.8	4.1	2.0	0.6	0.9	2.4	1.7	0.8	0.6	2.0	1.7
Sr	92	93	100	82	16	90	78	24	76	55	5	110
Ba	35	23	56	12	13	24	10	20	16	25	11	27
Zr	49	60	56	31	39	49	48	40	49	49	23	46
Nb	4.0	4.6	4.0	2.2	3.1	4.1	4.0	3.5	3.6	3.5	2.0	4.2
Y	18	19	23	13	13	16	14	13	15	15	2	15
Sc	51	41	54	46	41	42	50	44	45	46	33	48
V	321	325	414	280	262	286	286	249	285	300	140	290
Cr	160	242	9	132	1372	717	755	1498	699	749	3927	689
Co	45	44	66	45	57	48	47	52	47	50	65	45
Ni	92	102	36	57	351	262	242	335	238	248	586	251
Cu	162	160	48	252	139	73	111	117	114	88	52	50
Zn	84	81	87	68	80	84	83	76	83	81	87	77
Ga	17	18	21	17	15	15	15	13	15	16	9	16
La	4	7	5	5	4	4	n.d.	n.d.	3	3	n.d.	n.d.
Ce	10	11	9	7	1	5	n.d.	8	2	7	13	n.d.
Nd	6	8	6	4	4	5	4	8	4	7	3	5
norm												
Q	1.0	2.7	0.0	2.7	0.0	0.0	0.0	0.3	0.0	0.0	0.0	0.0
C	0.0	0.0	0.0	0.0	0.0	0.0	0.0	0.0	0.0	0.0	0.0	0.0
or	1.0	0.7	2.0	0.8	0.7	0.7	0.7	0.6	0.7	1.0	0.5	1.1
ab	20.1	18.5	32.2	20.2	13.5	15.3	15.4	15.4	18.8	17.5	3.6	5.7
an	27.6	26.1	18.0	28.5	24.8	27.3	27.4	23.4	26.4	26.7	16.5	7.9
di	25.8	22.7	17.1	22.9	3.0	24.7	24.0	4.4	21.8	21.0	20.0	53.7
hy	18.1	23.0	22.1	19.6	36.7	21.7	23.6	48.8	20.9	23.4	54.8	24.9
ol	0.0	0.0	1.5	0.0	15.3	4.6	3.0	0.0	5.6	4.2	1.3	2.3
mt	2.4	2.6	3.6	2.5	2.7	2.5	2.5	2.6	2.5	2.5	2.8	2.7
il	1.7	2.0	2.5	1.3	1.5	1.6	1.7	1.5	1.6	1.7	0.4	0.8
ap	0.2	0.2	0.2	0.1	0.1	0.2	0.2	0.1	0.2	0.2	0.1	0.1
sum	97.9	98.5	99.1	98.7	98.3	98.6	98.5	97.1	98.5	98.0	99.8	99.2

Aruba Lava Formation: deformed rocks (cont.) and basaltic amphibolites

Sample	ARU97-026	ARU96-109	ARU97-025	ARU96-043	ARU96-016	ARU96-145	ARU96-018a	ARU96-148	ARU97-168	ARU97-040	ARU97-098	ARU96-020
Lith.	A3	A3	A3	A3	A4	A4	A4	A4	A4	A4	A4	A4
major												
SiO_2	50.58	51.28	54.69	54.85	46.96	48.25	48.76	48.88	49.77	50.01	50.07	50.42
TiO_2	0.26	0.64	0.95	0.20	1.14	0.82	0.82	0.82	0.90	0.83	0.92	0.88
Al_2O_3	5.54	8.69	13.62	6.32	13.98	14.28	14.10	14.30	12.97	14.17	14.46	13.00
$Fe_2O_{3(t)}$	11.76	11.30	10.81	10.80	14.31	11.20	11.14	11.14	13.20	10.37	12.01	11.07
MnO	0.16	0.18	0.19	0.14	0.19	0.13	0.14	0.14	0.16	0.10	0.16	0.18
MgO	21.80	15.45	7.66	20.14	7.44	8.37	7.91	8.12	8.81	8.36	8.74	9.51
CaO	4.37	6.66	4.96	2.85	12.56	13.44	11.58	12.17	8.86	12.76	9.55	9.55
Na_2O	0.41	1.13	4.65	0.98	1.80	1.87	2.27	2.26	3.09	2.38	3.29	3.29
K_2O	0.10	0.09	0.14	0.33	0.27	0.21	0.36	0.32	0.26	0.25	0.20	0.16
P_2O_5	0.02	0.06	0.07	0.03	0.09	0.07	0.07	0.07	0.08	0.07	0.09	0.08
LOI	4.47	3.41	2.32	2.35	0.52	0.38	1.17	0.64	1.13	0.47	0.61	0.94
Total	99.48	98.87	100.05	98.97	99.27	99.02	98.33	98.85	99.22	99.77	100.08	99.06
Mg no.	79.7	74.3	60.0	79.8	52.4	61.3	60.1	60.7	58.6	63.1	60.7	64.5
trace												
Rb	2.3	1.1	2.1	7.3	5.8	1.8	2.5	2.4	3.2	4.0	3.4	1.5
Sr	4	13	105	88	85	86	96	107	93	95	182	81
Ba	23	12	62	54	69	40	44	154	42	48	56	26
Zr	24	40	50	37	37	42	41	38	46	41	49	50
Nb	1.9	3.3	4.1	1.9	3.7	3.2	3.1	3.8	4.9	3.6	5.3	3.6
Y	4	12	17	8	22	17	17	18	17	18	20	16
Sc	29	36	49	25	54	49	51	57	46	52	51	46
V	114	193	317	97	419	332	309	336	293	325	344	299
Cr	3773	1073	356	2761	183	369	338	364	436	358	458	653
Co	61	55	45	54	54	45	45	44	51	43	48	47
Ni	549	316	104	503	93	125	130	131	164	122	144	181
Cu	17	80	96	48	173	109	166	292	126	57	69	123
Zn	62	76	85	75	77	45	53	65	91	37	77	83
Ga	9	11	16	7	19	18	16	18	18	17	18	15
La	n.d.	4	n.d.	5	5	3	6	3	n.d.	n.d.	n.d.	4
Ce	13	4	8	1	3	8	6	11	19	14	14	5
Nd	2	4	6	1	4	8	7	8	7	8	6	6
norm												
Q	1.1	4.2	2.1	6.9	0.0	0.0	0.0	0.0	0.0	0.0	0.0	0.0
C	0.0	0.0	0.0	0.0	0.0	0.0	0.0	0.0	0.0	0.0	0.0	0.0
or	0.6	0.6	0.8	2.0	1.6	1.2	2.1	1.9	1.5	1.5	1.2	0.9
ab	3.6	9.9	40.3	8.5	15.3	15.9	19.5	19.2	26.5	20.2	28.0	28.1
an	13.6	19.0	16.3	12.2	29.4	30.1	27.5	28.1	21.0	27.4	24.3	20.4
di	7.2	11.9	6.9	1.7	27.0	29.7	24.7	26.3	18.8	29.1	18.7	21.9
hy	69.0	48.3	27.4	63.0	11.1	9.7	14.5	11.3	16.3	10.8	9.9	12.0
ol	0.0	0.0	0.0	0.0	8.1	7.2	4.9	6.8	9.1	5.9	12.4	10.5
mt	2.7	2.6	3.4	3.4	3.2	2.5	2.5	2.5	3.0	2.3	2.7	2.5
il	0.5	1.3	1.8	0.4	2.2	1.6	1.6	1.6	1.7	1.6	1.8	1.7
ap	0.1	0.1	0.2	0.1	0.2	0.2	0.2	0.2	0.2	0.2	0.2	0.2
sum	98.4	97.9	99.2	98.1	98.1	98.1	97.4	97.9	98.1	98.9	99.1	98.1

Aruba Lava Formation: basaltic amphibolites (cont.) and non-basaltic amphibolites

Sample	ARU96 -146	ARU96 -140	ARU96 -110	ARU96 -150b	ARU96 -149b	ARU96 -130	ARU96 -144	ARU96 -147	ARU96 -142	ARU97 -034	ARU96 -143
Lith.	A4	A4	A4	A4	A4	A4	A4	A4	A5	A5	A5
major											
SiO_2	51.12	51.77	51.79	52.33	52.87	53.76	54.24	54.49	54.69	57.90	64.18
TiO_2	0.67	0.93	0.96	0.73	0.78	0.72	0.73	0.31	0.61	0.63	0.31
Al_2O_3	14.52	13.74	13.44	13.71	13.87	14.08	13.55	12.33	10.94	13.46	12.47
$Fe_2O_{3(t)}$	9.83	11.26	11.18	10.33	10.39	9.72	9.91	11.03	11.26	8.40	8.27
MnO	0.15	0.17	0.19	0.15	0.16	0.15	0.15	0.16	0.17	0.14	0.09
MgO	8.56	9.91	8.84	7.38	7.61	7.51	6.90	9.01	13.39	6.30	5.55
CaO	11.30	6.56	8.90	10.94	10.24	11.02	10.26	8.15	5.74	8.24	4.30
Na_2O	2.34	3.16	3.65	2.41	2.64	2.29	2.61	2.78	2.33	3.07	4.06
K_2O	0.40	0.26	0.14	0.37	0.37	0.45	0.40	0.24	0.17	0.42	0.19
P_2O_5	0.06	0.07	0.07	0.06	0.06	0.06	0.06	0.04	0.05	0.16	0.06
LOI	0.67	1.41	0.84	0.89	0.95	0.44	0.61	0.55	1.10	1.28	0.87
Total	99.62	99.24	100.00	99.29	99.94	100.18	99.41	99.10	100.45	100.00	100.36
Mg no.	64.9	65.1	62.6	61.6	62.1	63.4	60.9	64.7	72.7	63.1	60.8
trace											
Rb	2.4	3.7	1.5	4.1	3.5	5.4	3.9	0.2	0.8	6.9	2.1
Sr	90	64	103	130	145	88	136	130	90	286	135
Ba	92	62	35	83	103	126	112	55	44	203	65
Zr	46	54	50	46	45	50	50	29	51	78	67
Nb	3.4	4.1	4.6	3.1	3.7	3.8	3.5	2.9	2.5	3.7	4.4
Y	14	18	19	17	16	16	15	5	10	17	7
Sc	44	46	52	47	47	45	46	46	42	32	21
V	252	291	307	274	285	262	272	188	214	216	134
Cr	390	298	418	320	315	345	284	579	1176	177	356
Co	42	47	47	45	43	37	41	45	48	34	31
Ni	155	115	148	121	105	99	109	129	239	53	70
Cu	125	118	183	131	87	98	80	48	38	126	61
Zn	69	84	84	57	73	71	55	82	75	68	61
Ga	15	19	17	13	18	15	14	13	14	16	13
La	4	3	4	4	4	6	5	6	1	10	7
Ce	7	3	7	8	9	8	6	5	5	17	14
Nd	5	5	6	5	5	6	5	3	2	11	8
norm											
Q	0.0	0.0	0.0	3.9	3.6	5.5	6.5	5.3	5.0	12.2	20.3
C	0.0	0.0	0.0	0.0	0.0	0.0	0.0	0.0	0.0	0.0	0.0
or	2.4	1.5	0.9	2.2	2.2	2.6	2.4	1.4	1.0	2.5	1.1
ab	20.0	27.2	31.1	20.6	22.6	19.5	22.3	23.7	20.0	26.3	34.7
an	28.1	22.9	20.0	25.7	25.1	26.9	24.2	20.6	19.1	22.0	15.4
di	22.7	7.9	19.6	23.3	21.0	22.4	21.7	16.1	7.5	15.0	4.7
hy	21.5	33.9	15.4	18.0	19.7	18.0	17.0	27.0	42.2	16.8	19.6
ol	0.5	0.5	7.6	0.0	0.0	0.0	0.0	0.0	0.0	0.0	0.0
mt	2.2	2.5	2.5	3.2	3.2	3.0	3.1	3.4	3.5	3.0	3.2
il	1.3	1.8	1.8	1.4	1.5	1.4	1.4	0.6	1.2	1.2	0.6
ap	0.1	0.2	0.2	0.1	0.1	0.1	0.2	0.1	0.1	0.4	0.2
sum	98.8	98.3	99.1	98.5	99.1	99.4	98.6	98.2	99.6	99.4	99.8

Aruba Lava Formation: volcaniclastic rocks

Sample	ARU96-022	ARU96-102	ARU97-065	ARU96-089	ARU97-001	ARU97-067	ARU97-064	ARU96-112	ARU96-120	ARU96-122	ARU97-170	ARU96-013
Lith.	A6	A6	A6	A6	A6	A6	A6	A6	A7	A7	A7	A7
major												
SiO_2	48.33	49.14	49.47	50.11	50.39	50.58	51.33	51.76	55.48	58.85	65.67	66.00
TiO_2	0.82	0.84	1.16	0.82	1.14	0.96	1.14	1.04	0.54	0.62	0.54	0.52
Al_2O_3	13.40	13.43	14.80	13.32	14.14	13.04	14.41	15.11	13.66	13.57	12.82	12.37
$Fe_2O_{3(t)}$	11.22	11.02	11.59	11.06	12.37	11.79	11.29	11.72	10.43	10.15	6.49	6.15
MnO	0.16	0.16	0.18	0.18	0.19	0.17	0.17	0.11	0.15	0.11	0.16	0.14
MgO	10.70	9.10	8.70	9.05	7.47	9.44	7.81	6.78	4.96	3.41	3.31	2.74
CaO	12.16	10.50	10.10	11.23	11.29	11.88	9.71	6.39	6.41	3.70	4.92	5.72
Na_2O	1.31	2.33	2.77	2.17	1.72	0.68	3.07	2.11	3.85	3.75	4.14	3.89
K_2O	0.12	0.14	0.16	0.14	0.16	0.07	0.14	0.25	0.35	0.56	0.14	0.12
P_2O_5	0.07	0.07	0.09	0.07	0.09	0.08	0.09	0.10	0.07	0.08	0.09	0.10
LOI	0.81	1.60	1.60	1.32	1.84	2.66	1.37	4.80	3.43	4.95	1.71	1.67
Total	99.10	98.31	100.62	99.45	100.79	101.33	100.54	100.18	99.34	99.75	99.99	99.43
Mg no.	66.9	63.6	61.4	63.4	56.1	62.9	59.4	55.1	51.6	43.3	54.1	50.7
trace												
Rb	0.8	n.d.	3.1	0.7	3.4	2.3	2.3	3.1	3.3	4.5	1.1	0.7
Sr	71	86	120	77	95	97	145	110	159	162	146	59
Ba	13	26	41	22	40	20	29	77	113	120	22	24
Zr	46	50	67	50	63	47	63	60	44	55	105	115
Nb	3.6	3.8	5.1	3.7	5.3	3.8	5.1	4.9	3.9	4.9	7.6	7.6
Y	16	14	24	16	20	17	23	19	12	14	15	16
Sc	45	43	54	48	54	42	58	45	38	42	27	24
V	290	292	356	294	331	282	356	254	181	197	107	93
Cr	719	555	276	520	275	604	275	422	192	61	147	106
Co	49	49	49	48	48	48	49	47	41	33	23	21
Ni	253	173	110	167	107	172	104	135	46	24	42	34
Cu	77	129	237	121	190	111	287	167	85	94	165	88
Zn	70	77	95	79	91	86	91	96	79	77	57	60
Ga	18	16	19	15	19	17	17	19	12	15	14	11
La	5	5	n.d.	4	7	n.d.	n.d.	4	5	6	8	8
Ce	7	4	8	3	18	n.d.	18	8	4	6	14	13
Nd	5	6	5	4	8	2	9	8	5	4	9	10
norm												
Q	0.0	0.0	0.0	0.0	3.7	6.6	0.0	9.3	8.7	18.4	25.3	27.3
C	0.0	0.0	0.0	0.0	0.0	0.0	0.0	0.0	0.0	0.2	0.0	0.0
or	0.7	0.8	1.0	0.8	1.0	0.4	0.9	1.6	2.2	3.5	0.8	0.7
ab	11.2	20.1	23.8	18.6	14.8	5.9	26.3	18.8	33.8	33.4	35.6	33.5
an	30.6	26.2	27.9	26.6	30.9	33.2	25.5	32.6	19.6	18.8	16.3	16.2
di	24.2	21.4	18.2	24.0	21.0	21.8	18.6	0.1	10.6	0.0	6.6	9.9
hy	24.0	21.5	15.9	24.1	23.2	27.6	22.7	31.8	19.1	19.4	11.1	7.7
ol	3.3	3.1	7.8	0.2	0.0	0.0	0.7	0.0	0.0	0.0	0.0	0.0
mt	2.5	2.5	2.6	2.5	2.8	2.7	2.5	2.7	3.3	3.7	2.5	2.4
il	1.6	1.6	2.2	1.6	2.2	1.9	2.2	2.1	1.1	1.2	1.0	1.0
ap	0.2	0.2	0.2	0.2	0.2	0.2	0.2	0.2	0.2	0.2	0.2	0.2
sum	98.2	97.4	99.6	98.5	99.7	100.3	99.6	99.2	98.5	99.0	99.5	99.0

Aruba batholith: hooibergites

Sample	ARU96 -060	ARU96 -135	ARU94 -007	ARU97 -164	ARU96 -046	ARU96 -157	ARU96 -056	BK77 -042	ARU96 -092	ARU96 -055	ARU96 -054	ARU96 -058
Lith.	B1	B1	B1	B1	B1	B1	B1	B1	B1	B1	B1	B1
major												
SiO_2	47.89	48.49	49.83	50.11	50.71	50.85	50.96	51.02	51.53	51.76	51.95	52.25
TiO_2	1.01	1.00	0.72	0.68	0.87	0.52	0.75	0.62	0.39	0.75	0.55	0.58
Al_2O_3	10.39	16.66	7.30	8.05	9.73	14.96	8.05	11.93	5.13	12.08	7.71	6.82
$Fe_2O_{3(t)}$	15.08	14.43	11.40	12.16	10.35	10.49	12.71	12.06	9.83	11.20	9.76	10.02
MnO	0.23	0.16	0.17	0.20	0.16	0.18	0.21	0.21	0.17	0.18	0.19	0.16
MgO	8.43	5.72	14.41	10.37	10.07	8.48	11.14	9.69	12.80	8.83	12.51	12.15
CaO	12.69	10.66	13.45	15.07	13.08	11.55	12.91	11.81	16.81	11.57	13.86	15.33
Na_2O	1.45	2.22	1.18	1.41	2.00	2.07	1.48	0.89	1.13	2.26	1.66	1.31
K_2O	0.36	0.47	0.25	0.26	0.44	0.33	0.29	0.16	0.19	0.43	0.36	0.34
P_2O_5	0.08	0.11	0.06	0.07	0.08	0.06	0.07	0.14	0.07	0.07	0.10	0.07
LOI	0.91	0.62	0.96	1.27	0.86	0.44	0.85	0.71	0.55	0.76	0.59	0.74
Total	98.51	100.54	99.74	99.64	98.36	99.94	99.42	99.27	98.59	99.90	99.24	99.77
Mg no.	54.5	46.0	73.1	64.6	67.6	63.4	65.3	63.3	73.6	62.8	73.3	72.9
trace												
Rb	2.0	4.8	3.3	3.8	2.2	5.4	2.3	1.4	1.7	2.7	3.3	3.4
Sr	190	340	106	124	189	394	112	241	101	212	111	111
Ba	137	249	42	105	215	155	59	144	57	207	169	178
Zr	37	36	21	27	27	26	32	36	23	34	30	24
Nb	2.1	1.9	1.9	1.8	2.6	2.0	2.7	1.8	1.1	1.4	1.7	1.9
Y	15	12	14	11	13	13	11	11	6	10	10	10
Sc	71	43	63	81	65	48	66	46	74	49	64	74
V	519	573	285	418	331	286	409	258	311	372	256	309
Cr	66	n.d.	1373	122	595	198	507	661	2200	232	1047	960
Co	63	53	53	50	42	43	55	48	48	47	45	45
Ni	83	17	206	86	98	62	119	113	148	96	137	127
Cu	337	566	66	241	176	51	215	23	46	273	59	83
Zn	108	87	85	74	76	76	90	91	66	80	81	68
Ga	15	21	12	12	13	19	12	14	9	16	10	10
La	1	5	3	n.d.	4	2	5	2	n.d.	3	3	4
Ce	8	13	8	17	13	2	5	14	12	4	6	7
Nd	8	7	6	8	6	6	4	8	4	5	4	6
norm												
Q	0.0	0.0	0.0	0.0	0.0	0.2	0.8	5.5	0.0	0.7	0.0	1.5
C	0.0	0.0	0.0	0.0	0.0	0.0	0.0	0.0	0.0	0.0	0.0	0.0
or	2.1	2.8	1.5	1.6	2.6	1.9	1.7	1.0	1.1	2.6	2.1	2.0
ab	12.4	18.9	10.1	12.1	17.1	17.6	12.6	7.6	9.6	19.3	14.1	11.2
an	21.0	34.3	14.0	15.0	16.4	30.7	14.6	28.3	8.4	21.7	12.6	11.8
di	34.6	15.2	42.6	49.0	39.3	21.5	40.3	24.4	60.3	29.1	45.0	51.6
hy	19.8	19.5	18.6	15.3	16.4	23.6	23.9	27.3	14.8	21.5	19.6	16.4
ol	1.8	3.3	7.9	1.4	1.5	0.0	0.0	0.0	0.4	0.0	1.5	0.0
mt	3.4	3.2	2.5	2.7	2.3	2.3	2.8	2.7	2.2	2.5	2.2	3.1
il	1.9	1.9	1.4	1.3	1.7	1.0	1.4	1.2	0.7	1.4	1.0	1.1
ap	0.2	0.3	0.1	0.2	0.2	0.2	0.2	0.3	0.2	0.2	0.2	0.2
sum	97.2	99.3	98.8	98.6	97.5	99.0	98.3	98.3	97.8	99.0	98.4	99.0

Aruba batholith: hooibergites (cont.)

Sample	ARU97 -077	ARU97 -133	ARU97 -162	ARU96 -057	ARU97 -076	ARU96 -091	ARU96 -111	ARU97 -080	ARU97 -119	ARU96 -052	ARU96 -051	ARU96 -061
Lith.	B1	B1	B1	B1	B1	B1	B1	B1	B1	B1	B1	B1
major												
SiO_2	52.36	52.78	52.86	53.19	53.36	53.52	53.78	53.81	53.86	53.86	54.51	54.63
TiO_2	0.62	0.34	0.84	0.51	0.84	0.42	1.03	0.76	0.46	0.53	0.52	0.96
Al_2O_3	10.21	4.44	10.41	7.49	8.52	5.56	10.02	10.23	8.45	11.65	11.39	10.27
$Fe_2O_{3(t)}$	10.80	7.52	11.77	9.15	11.66	8.18	10.86	9.23	8.12	8.76	9.53	10.50
MnO	0.20	0.15	0.21	0.17	0.19	0.18	0.20	0.17	0.16	0.16	0.19	0.20
MgO	10.51	14.24	9.66	11.98	11.03	14.44	9.10	10.48	12.07	8.53	8.67	8.93
CaO	12.38	17.73	10.76	15.80	11.39	14.68	10.75	13.33	13.01	12.24	11.38	10.57
Na_2O	1.66	0.95	1.68	1.52	1.35	1.19	1.93	1.71	1.61	2.03	2.43	1.93
K_2O	0.40	0.18	0.50	0.26	0.83	0.22	0.55	0.27	0.38	0.37	0.30	0.65
P_2O_5	0.11	0.04	0.11	0.07	0.08	0.39	0.10	0.08	0.09	0.10	0.07	0.11
LOI	0.69	0.50	0.94	0.60	0.65	1.12	0.74	0.62	0.91	0.73	0.92	0.70
Total	99.94	98.84	99.74	100.72	99.90	99.89	99.06	100.70	99.14	98.95	99.91	99.42
Mg no.	68.3	80.8	64.5	74.4	67.7	79.6	65.0	71.6	76.7	68.3	66.8	65.3
trace												
Rb	6.7	2.8	5.3	0.8	15.0	n.d.	2.9	4.4	7.4	3.6	1.4	3.3
Sr	192	60	173	153	109	94	169	229	155	231	211	177
Ba	226	58	211	146	345	138	426	60	176	189	223	597
Zr	51	14	58	27	38	24	40	51	30	32	35	34
Nb	3.3	2.4	2.9	2.0	3.0	1.6	4.1	2.0	2.3	2.0	1.5	3.4
Y	14	6	20	10	17	7	19	12	13	10	8	19
Sc	62	75	63	67	56	79	63	68	53	54	48	61
V	261	212	294	247	327	219	302	284	202	247	252	278
Cr	210	2469	192	1322	315	2296	584	746	1477	381	452	539
Co	46	37	48	37	50	40	44	41	36	41	40	41
Ni	67	157	63	106	96	166	96	109	174	64	80	88
Cu	23	45	72	67	48	57	61	22	38	114	70	56
Zn	73	55	88	59	87	71	106	80	72	76	85	97
Ga	13	8	15	12	13	8	15	15	12	13	16	15
La	n.d.	n.d.	n.d.	3	n.d.	4	3	n.d.	5	7	8	8
Ce	n.d.	12	13	8	16	10	10	n.d.	13	10	7	11
Nd	8	5	12	3	11	2	8	9	7	7	4	7
norm												
Q	3.0	1.1	5.6	1.4	5.1	3.0	6.9	4.5	4.1	6.1	5.4	7.9
C	0.0	0.0	0.0	0.0	0.0	0.0	0.0	0.0	0.0	0.0	0.0	0.0
or	2.4	1.0	3.0	1.6	4.9	1.3	3.3	1.6	2.3	2.2	1.8	3.9
ab	14.1	8.0	14.4	12.9	11.5	10.2	16.4	14.6	13.8	17.3	20.7	16.4
an	19.4	7.4	19.5	12.9	14.9	9.3	17.2	19.5	14.8	21.7	19.5	17.6
di	33.8	64.3	27.3	52.5	33.5	49.4	29.1	37.3	39.8	31.4	30.0	27.9
hy	21.7	13.3	23.4	14.7	23.7	21.8	19.7	17.9	20.1	15.6	17.6	19.5
ol	0.0	0.0	0.0	0.0	0.0	0.0	0.0	0.0	0.0	0.0	0.0	0.0
mt	3.4	2.3	3.7	2.8	3.6	2.5	3.4	2.9	2.5	2.7	3.0	3.3
il	1.2	0.6	1.6	1.0	1.6	0.8	2.0	1.4	0.9	1.0	1.0	1.8
ap	0.3	0.1	0.3	0.2	0.2	0.9	0.2	0.2	0.2	0.2	0.2	0.3
sum	99.1	98.3	98.8	100.0	99.0	99.3	98.2	100.0	98.5	98.3	99.2	98.6

Aruba batholith: hooibergites (cont.) and layered gabbros

Sample	ARU97 -063	ARU97 -061	ARU96 -124	ARU96 -053	ARU96 -125	ARU97 -173	ARU97 -175	ARU97 -174	ARU96 -154	ARU96 -156	ARU96 -128
Lith.	B1	B1	B1	B1	B1	B2a	B2a	B2a	B2b	B2b	B2b
major											
SiO_2	54.88	55.06	55.07	55.09	55.41	45.31	46.13	46.32	49.30	50.75	51.35
TiO_2	0.42	0.69	0.43	0.50	0.54	0.33	0.65	0.51	0.27	0.42	0.40
Al_2O_3	7.96	8.58	8.29	7.94	9.58	21.17	15.12	15.49	5.26	7.62	4.21
$Fe_2O_{3(t)}$	9.87	11.60	8.20	9.28	9.43	8.62	12.95	10.85	10.97	10.85	12.11
MnO	0.18	0.19	0.17	0.17	0.18	0.11	0.16	0.13	0.19	0.19	0.22
MgO	11.78	10.22	10.65	11.58	9.11	6.65	9.15	8.42	17.62	14.25	15.47
CaO	13.53	11.08	14.41	12.72	11.33	15.07	14.91	15.60	14.40	12.56	14.94
Na_2O	1.62	1.66	1.75	1.77	2.00	1.15	1.03	1.22	0.66	1.02	0.74
K_2O	0.26	0.26	0.29	0.31	0.31	0.14	0.11	0.19	0.18	0.25	0.19
P_2O_5	0.10	0.05	0.08	0.06	0.09	0.02	0.03	0.03	0.02	0.02	0.03
LOI	0.76	0.86	0.65	0.45	0.68	0.63	0.34	0.52	0.75	0.78	0.67
Total	101.36	100.26	99.99	99.87	98.66	99.20	100.57	99.27	99.60	98.71	100.32
Mg no.	72.6	66.1	74.2	73.4	68.1	62.3	60.2	62.4	77.5	73.8	73.3
trace											
Rb	2.6	3.4	2.2	0.8	1.7	4.1	3.7	4.1	2.5	4.7	2.1
Sr	118	150	189	146	192	428	309	302	107	143	66
Ba	161	93	177	155	231	47	41	69	90	66	55
Zr	30	33	40	33	69	8	11	16	22	23	18
Nb	2.1	2.4	1.7	1.7	2.0	1.4	n.d.	1.6	1.0	n.d.	0.3
Y	8	11	10	10	11	3	6	6	5	9	9
Sc	57	63	65	60	56	38	56	56	63	65	78
V	214	350	224	255	259	243	461	445	202	205	283
Cr	243	395	227	761	356	12	40	70	1202	557	500
Co	43	51	35	45	40	37	50	45	57	53	63
Ni	92	87	94	134	83	49	58	52	189	164	118
Cu	42	69	66	95	146	129	121	286	50	57	56
Zn	68	93	67	66	80	47	61	52	65	71	69
Ga	13	11	13	9	12	18	17	17	8	8	11
La	4	n.d.	4	3	1	n.d.	n.d.	n.d.	n.d.	1	n.d.
Ce	10	13	11	9	9	n.d.	n.d.	n.d.	6	7	8
Nd	8	9	8	6	5	5	1	3	3	5	6
norm											
Q	4.7	8.6	5.6	5.5	9.0	0.0	0.0	0.0	0.0	0.0	0.0
C	0.0	0.0	0.0	0.0	0.0	0.0	0.0	0.0	0.0	0.0	0.0
or	1.5	1.6	1.7	1.8	1.9	0.8	0.7	1.1	1.1	1.5	1.1
ab	13.8	14.1	14.9	15.1	17.0	9.8	8.7	10.4	5.6	8.7	6.3
an	13.8	15.3	14.0	12.9	16.4	52.5	36.4	36.4	11.0	15.6	7.7
di	42.7	32.2	46.1	40.2	32.0	18.4	30.7	33.6	48.7	37.8	53.7
hy	19.9	22.5	13.5	19.7	17.5	3.2	5.6	0.9	15.1	30.0	23.8
ol	0.0	0.0	0.0	0.0	0.0	11.0	13.2	12.4	14.2	0.8	3.2
mt	3.1	3.6	2.5	2.9	2.9	1.9	2.9	2.4	2.4	2.4	2.7
il	0.8	1.3	0.8	0.9	1.0	0.6	1.2	1.0	0.5	0.8	0.8
ap	0.2	0.1	0.2	0.2	0.2	0.1	0.1	0.1	0.1	0.1	0.1
sum	100.6	99.3	99.3	99.1	97.9	98.5	99.5	98.4	98.7	97.8	99.3

Aruba batholith: gabbros and diorites

Sample	ARU96 -159	ARU97 -171	ARU97 -103	ARU96 -042	ARU96 -065	ARU96 -151	ARU97 -172	ARU96 -064	ARU97 -073	ARU96 -063	BK77 -109b	ARU96 -152
Lith.	B3	B3	B3	B3	B3	B3	B3	B4	B4	B4	B4	B4
major												
SiO_2	49.71	51.12	51.77	53.03	54.22	54.66	54.82	53.96	54.59	54.89	55.19	55.94
TiO_2	0.68	0.74	0.74	0.66	0.65	0.64	0.57	0.77	0.79	0.68	0.48	0.70
Al_2O_3	14.72	15.29	13.97	16.14	13.97	12.08	14.70	14.90	17.10	15.28	12.68	15.91
$Fe_2O_{3(t)}$	11.65	11.12	9.91	9.82	8.93	9.10	9.62	9.81	10.21	9.33	9.97	9.22
MnO	0.16	0.16	0.16	0.14	0.14	0.15	0.15	0.15	0.16	0.13	0.18	0.14
MgO	7.00	7.15	7.76	6.59	6.98	9.52	6.64	5.40	4.14	4.94	7.71	4.75
CaO	10.95	9.53	11.27	9.17	10.51	8.61	8.85	8.11	8.46	8.21	9.11	8.28
Na_2O	2.78	2.93	2.18	3.16	2.11	2.24	2.90	2.81	3.61	3.19	2.57	3.32
K_2O	0.58	0.24	0.37	0.25	0.51	0.85	0.41	1.64	0.82	0.89	0.54	0.58
P_2O_5	0.16	0.16	0.06	0.15	0.06	0.14	0.15	0.19	0.21	0.18	0.10	0.21
LOI	0.77	0.23	0.49	1.06	0.71	1.29	0.60	0.85	0.55	0.64	0.90	0.56
Total	99.16	98.68	98.68	100.16	98.79	99.28	99.41	98.60	100.64	98.33	99.43	99.62
Mg no.	56.3	58.0	62.7	59.8	63.4	69.9	60.5	55.0	47.3	54.0	63.2	53.3
trace												
Rb	4.6	3.9	5.3	2.7	10.4	16.9	8.5	38.8	23.0	16.8	6.8	9.1
Sr	417	402	86	397	80	258	378	289	496	394	321	403
Ba	513	117	100	134	154	367	213	727	700	436	481	263
Zr	46	12	46	22	52	45	26	71	32	69	35	38
Nb	2.5	2.0	3.7	1.4	3.8	2.9	2.4	3.9	2.8	2.3	2.0	2.1
Y	13	9	17	7	18	19	14	22	9	15	17	14
Sc	50	42	48	37	40	37	38	31	26	31	44	37
V	340	269	278	233	233	231	245	272	305	255	238	243
Cr	110	156	383	162	311	476	150	106	n.d.	69	232	78
Co	46	41	43	37	36	37	35	39	34	32	38	34
Ni	36	53	109	57	101	167	47	38	23	32	58	23
Cu	120	47	121	66	101	102	62	120	1278	103	150	84
Zn	84	84	68	77	66	76	72	81	88	70	90	76
Ga	19	19	16	19	17	15	17	17	18	19	15	19
La	7	n.d.	4	4	8	7	5	5	n.d.	9	4	4
Ce	11	9	8	3	5	13	11	7	10	14	13	11
Nd	8	8	7	5	6	14	9	8	5	10	12	8
norm												
Q	0.0	0.4	2.9	3.4	8.4	6.5	7.0	5.3	4.7	7.3	7.6	8.6
C	0.0	0.0	0.0	0.0	0.0	0.0	0.0	0.0	0.0	0.0	0.0	0.0
or	3.4	1.4	2.2	1.5	3.0	5.1	2.5	9.8	4.9	5.3	3.2	3.5
ab	23.7	24.9	18.5	27.0	18.0	19.2	24.7	23.9	30.7	27.2	21.9	28.3
an	26.2	27.9	27.4	29.5	27.3	20.7	26.0	23.4	28.2	24.9	21.7	26.9
di	22.7	15.2	23.2	12.7	20.2	17.5	14.0	13.1	10.6	12.3	18.9	10.8
hy	10.6	23.7	19.9	20.7	17.0	25.2	20.0	17.3	15.7	16.0	21.1	16.1
ol	7.2	0.0	0.0	0.0	0.0	0.0	0.0	0.0	0.0	0.0	0.0	0.0
mt	2.6	2.5	2.2	3.1	2.8	2.8	3.0	3.1	3.2	2.9	3.1	2.9
il	1.3	1.4	1.4	1.3	1.2	1.2	1.1	1.5	1.5	1.3	0.9	1.3
ap	0.4	0.4	0.1	0.4	0.1	0.3	0.4	0.5	0.5	0.4	0.2	0.5
sum	98.2	97.8	97.9	99.4	98.1	98.6	98.7	97.9	99.9	97.6	98.6	98.9

Aruba batholith: diorites (cont.)

Sample	ARU97 -104	ARU97 -079	BK77 -066a	ARU96 -127	ARU97 -160	BK77 -165	ARU96 -126	ARU96 -015	ARU96 -158	ARU96 -018b	ARU97 -013	ARU96 -087
Lith.	B4	B4	B4	B4	B4	B4	B4	B4	B4	B4	B4	B4
major												
SiO_2	56.14	56.20	56.40	56.68	56.90	57.17	57.35	57.38	57.49	57.65	57.86	58.46
TiO_2	0.60	0.60	0.69	0.49	0.67	0.56	0.46	0.67	0.58	0.69	0.59	0.65
Al_2O_3	14.07	13.42	17.97	11.74	14.94	11.32	12.49	14.75	15.05	15.92	17.30	15.57
$Fe_2O_{3(t)}$	8.26	8.69	8.64	8.52	8.54	9.77	7.89	8.83	8.36	7.59	7.74	8.43
MnO	0.13	0.14	0.13	0.17	0.15	0.17	0.15	0.14	0.14	0.11	0.13	0.13
MgO	7.34	6.36	3.78	8.06	5.51	7.62	7.55	4.91	4.63	4.40	2.67	3.36
CaO	10.58	9.42	7.62	10.50	8.73	9.77	10.18	7.95	7.60	8.50	7.27	7.18
Na_2O	2.22	2.62	3.89	2.37	2.91	2.27	2.59	3.54	3.45	3.34	4.39	3.53
K_2O	0.37	0.55	0.63	0.44	0.85	0.41	0.42	1.00	0.88	0.43	0.40	0.72
P_2O_5	0.06	0.14	0.17	0.09	0.19	0.11	0.10	0.22	0.18	0.15	0.33	0.19
LOI	0.81	1.09	0.44	0.67	0.44	0.66	0.80	0.50	0.40	1.01	0.55	0.41
Total	100.57	99.24	100.34	99.75	99.82	99.82	99.97	99.87	98.76	99.79	99.23	98.61
Mg no.	66.3	61.9	49.2	67.7	58.8	63.7	68.3	55.6	55.5	56.6	43.7	47.2
trace												
Rb	7.2	6.8	9.8	3.4	16.5	3.4	4.0	20.8	15.4	4.9	4.5	12.5
Sr	88	289	492	253	366	159	276	368	346	217	492	384
Ba	137	388	335	241	452	281	275	448	463	104	287	331
Zr	56	48	52	64	62	26	64	71	51	44	50	49
Nb	3.7	2.5	2.7	2.2	3.3	2.4	2.2	3.0	3.2	3.9	3.1	2.6
Y	16	11	15	11	17	10	11	17	17	9	11	15
Sc	40	44	27	47	32	44	45	29	34	34	21	26
V	209	250	205	212	219	234	177	229	201	187	123	223
Cr	415	150	23	310	118	450	305	85	93	96	n.d.	16
Co	32	34	29	35	30	37	32	29	31	26	24	30
Ni	107	51	25	71	48	40	63	27	26	42	7	14
Cu	88	102	83	46	116	62	45	24	67	195	107	87
Zn	66	75	74	73	70	73	72	74	76	43	80	73
Ga	16	14	21	13	17	15	16	17	15	15	20	20
La	n.d.	n.d.	7	7	n.d.	2	5	5	11	5	6	5
Ce	n.d.	n.d.	13	10	21	2	8	10	7	9	13	8
Nd	7	6	9	5	12	3	7	11	11	6	16	8
norm												
Q	9.9	10.4	7.4	9.6	10.0	12.1	10.6	9.0	10.6	12.1	10.5	13.8
C	0.0	0.0	0.0	0.0	0.0	0.0	0.0	0.0	0.0	0.0	0.0	0.0
or	2.2	3.3	3.7	2.6	5.0	2.4	2.5	5.9	5.2	2.5	2.4	4.3
ab	19.0	22.4	33.1	20.2	24.7	19.4	22.1	30.1	29.3	28.5	37.3	30.0
an	27.5	23.5	29.8	20.2	25.3	19.6	21.4	21.5	23.1	27.5	26.5	24.6
di	20.2	18.6	5.9	25.6	13.9	23.1	23.3	13.8	11.2	11.6	6.5	8.3
hy	17.3	16.1	15.4	17.0	15.8	17.7	15.7	14.1	14.3	12.6	11.0	12.4
ol	0.0	0.0	0.0	0.0	0.0	0.0	0.0	0.0	0.0	0.0	0.0	0.0
mt	2.6	2.7	2.7	2.6	2.6	3.4	2.8	3.1	2.9	2.7	2.7	2.9
il	1.1	1.2	1.3	0.9	1.3	1.1	0.9	1.3	1.1	1.3	1.1	1.2
ap	0.1	0.3	0.4	0.2	0.4	0.3	0.2	0.5	0.4	0.4	0.8	0.5
sum	99.9	98.6	99.7	99.1	99.2	99.1	99.4	99.2	98.1	99.2	98.7	98.0

Aruba batholith: diorites (cont.) and tonalites

Sample	BK77 -173a	ARU97 -161	ARU96 -134	ARU94 -013	ARU96 -132	ARU96 -050	ARU96 -084	ARU97 -053	ARU97 -010	ARU97 -176	ARU96 -098	ARU96 -097
Lith.	B4	B4	B4	B4	B4	B4	B4	B4	B4	B4	B5	B5
major												
SiO_2	58.82	59.37	59.61	59.71	59.86	59.90	60.49	60.80	61.43	61.84	62.14	62.46
TiO_2	0.59	0.53	0.61	0.71	0.64	0.57	0.53	0.58	0.32	0.50	0.49	0.56
Al_2O_3	11.29	15.13	15.77	14.47	14.95	9.44	15.23	13.89	13.05	14.56	16.74	14.91
$Fe_2O_{3(t)}$	9.04	6.86	7.56	7.67	7.62	9.61	7.71	7.51	8.83	6.42	6.13	7.13
MnO	0.20	0.14	0.19	0.10	0.15	0.20	0.11	0.17	0.10	0.12	0.10	0.12
MgO	7.21	4.84	3.05	4.72	3.99	7.78	3.61	5.00	5.96	4.05	2.60	2.79
CaO	9.67	7.20	5.98	8.16	6.97	8.47	6.41	7.36	5.40	6.23	7.11	5.97
Na_2O	2.24	3.36	4.48	3.73	3.78	2.18	3.47	3.30	3.64	3.64	3.38	3.35
K_2O	0.33	1.01	0.94	0.47	0.82	0.46	1.04	0.83	0.32	0.90	0.43	0.67
P_2O_5	0.11	0.17	0.14	0.21	0.17	0.07	0.08	0.13	0.06	0.13	0.08	0.10
LOI	0.84	0.54	0.62	0.58	0.52	0.56	0.89	0.49	0.72	1.07	1.00	1.01
Total	100.36	99.15	98.96	100.54	99.49	99.23	99.57	100.05	99.82	99.47	100.20	99.05
Mg no.	64.2	61.4	47.6	58.1	54.1	64.6	51.3	59.9	60.3	58.6	48.9	46.9
trace												
Rb	3.4	21.4	19.0	8.6	18.1	4.9	18.7	16.0	5.5	21.5	4.4	7.6
Sr	215	389	292	379	315	137	258	270	196	348	241	207
Ba	214	607	596	363	591	175	584	491	113	678	200	322
Zr	38	61	48	52	81	34	64	51	72	74	60	77
Nb	2.2	3.4	4.1	3.1	3.2	3.8	3.6	4.2	5.3	3.4	3.1	4.3
Y	16	15	24	16	17	19	14	18	10	13	13	16
Sc	48	24	26	31	27	44	33	30	23	27	26	29
V	193	166	169	193	173	206	175	179	145	165	145	170
Cr	96	153	n.d.	101	60	296	25	138	410	82	26	13
Co	36	27	23	27	26	40	27	26	36	22	21	25
Ni	66	66	10	25	24	53	25	38	80	21	13	12
Cu	98	54	103	20	50	90	40	39	79	43	54	39
Zn	86	66	70	47	70	113	55	75	81	60	56	62
Ga	13	17	18	19	18	13	18	17	13	18	18	15
La	5	7	9	8	8	7	6	6	9	7	6	7
Ce	14	n.d.	11	16	15	18	11	21	11	17	10	12
Nd	11	11	14	11	10	13	7	16	6	14	9	9
norm												
Q	15.3	13.3	11.5	12.9	13.7	17.5	15.9	15.5	16.5	17.6	20.7	22.0
C	0.0	0.0	0.0	0.0	0.0	0.0	0.0	0.0	0.0	0.0	0.0	0.0
or	2.0	6.0	5.6	2.8	4.9	2.7	6.2	4.9	1.9	5.4	2.5	4.0
ab	19.1	28.6	38.2	31.7	32.2	18.5	29.6	28.1	31.1	31.1	28.9	28.6
an	20.0	23.3	20.3	21.5	21.5	14.7	23.1	20.7	18.4	21.0	29.6	23.9
di	22.5	9.4	7.3	14.7	10.0	22.0	7.0	12.4	6.7	7.8	4.6	4.5
hy	16.3	14.3	11.5	11.9	12.4	18.5	13.2	13.8	20.8	12.7	10.2	11.7
ol	0.0	0.0	0.0	0.0	0.0	0.0	0.0	0.0	0.0	0.0	0.0	0.0
mt	3.2	2.4	2.6	2.7	2.7	3.4	2.7	2.6	3.1	2.3	2.1	2.5
il	1.1	1.0	1.2	1.3	1.2	1.1	1.0	1.1	0.6	1.0	0.9	1.1
ap	0.3	0.4	0.3	0.5	0.4	0.2	0.2	0.3	0.1	0.3	0.2	0.2
sum	99.7	98.7	98.4	100.0	98.9	98.5	99.0	99.5	99.2	99.0	99.7	98.5

Aruba batholith: tonalites

Sample	ARU96 -062	ARU97 -165	BK77 -127b	ARU97 -167	ARU96 -059	BK77 -054	ARU96 -131	BK77 -180	BK77 -AR3b	ARU96 -129	ARU94 -002	ARU97 -078
Lith.	B5	B5	B5	B5	B5	B5	B5	B5	B5	B5	B5	B5
major												
SiO_2	64.13	64.38	64.40	64.41	65.34	65.41	65.87	65.92	66.06	66.18	67.03	67.23
TiO_2	0.41	0.47	0.52	0.43	0.41	0.38	0.49	0.38	0.34	0.42	0.35	0.35
Al_2O_3	14.99	15.44	14.58	15.69	15.23	15.39	15.43	15.73	14.80	14.65	15.38	14.84
$Fe_2O_{3(t)}$	6.04	5.85	6.86	6.39	5.26	5.47	4.75	4.96	5.39	5.59	4.71	4.89
MnO	0.11	0.09	0.12	0.12	0.09	0.11	0.09	0.11	0.10	0.10	0.10	0.08
MgO	2.36	2.59	2.46	2.47	2.22	2.00	1.56	1.69	2.13	2.32	1.78	2.04
CaO	5.41	5.33	5.77	5.57	5.03	5.26	4.73	5.03	5.27	5.17	4.81	4.92
Na_2O	3.72	3.80	3.22	3.71	4.03	3.81	3.89	3.91	3.73	3.71	3.88	4.06
K_2O	1.00	1.05	0.74	0.71	1.17	0.90	1.44	0.88	0.96	1.05	1.01	1.15
P_2O_5	0.10	0.12	0.10	0.12	0.11	0.12	0.14	0.13	0.09	0.10	0.10	0.10
LOI	0.70	0.77	1.24	0.99	0.29	0.69	0.43	0.69	0.59	0.65	0.65	0.31
Total	98.96	99.89	100.01	100.60	99.19	99.55	98.83	99.43	99.44	99.93	99.81	99.97
Mg no.	47.2	50.2	45.0	46.8	49.1	45.4	42.9	43.8	47.4	48.7	46.3	48.9
trace												
Rb	17.6	18.3	8.8	13.4	21.6	13.7	33.3	12.3	15.4	16.4	16.9	24.7
Sr	277	368	196	274	351	271	317	330	274	269	267	350
Ba	528	759	460	482	770	542	811	542	491	568	612	733
Zr	69	75	72	62	83	64	92	62	74	66	66	79
Nb	3.0	3.3	3.6	3.9	1.9	3.2	4.4	3.0	3.0	4.1	4.2	3.7
Y	11	12	13	13	11	13	16	14	11	11	12	13
Sc	18	21	26	22	17	17	14	15	19	22	13	19
V	112	129	148	123	111	95	91	69	110	115	80	100
Cr	23	20	94	13	10	198	n.d.	n.d.	4	11	6	13
Co	19	21	23	20	16	18	15	13	16	17	12	14
Ni	8	15	9	6	13	5	3	2	9	11	8	9
Cu	55	31	32	48	19	37	21	16	18	20	24	29
Zn	58	51	61	64	55	58	40	59	46	51	55	52
Ga	15	17	15	16	17	15	15	15	14	16	16	18
La	8	4	6	5	6	6	7	8	7	8	6	6
Ce	8	n.d.	11	10	11	11	16	10	12	10	10	n.d.
Nd	8	9	6	10	6	7	8	6	7	7	7	9
norm												
Q	22.5	21.9	25.6	22.9	22.5	24.4	24.3	25.2	25.4	25.2	26.5	25.0
C	0.0	0.0	0.0	0.0	0.0	0.0	0.0	0.0	0.0	0.0	0.0	0.0
or	5.9	6.3	4.4	4.2	6.9	5.3	8.6	5.2	5.7	6.2	6.0	6.8
ab	31.7	32.4	27.6	31.7	34.2	32.5	33.1	33.3	31.7	31.6	33.1	34.4
an	21.4	22.1	23.4	24.3	20.1	22.4	20.5	22.9	21.0	20.4	21.7	19.0
di	4.2	3.1	4.1	2.4	3.5	2.7	1.9	1.2	4.0	4.0	1.4	4.1
hy	9.4	10.2	10.4	10.9	8.6	8.8	7.1	8.2	8.4	9.0	8.1	7.6
ol	0.0	0.0	0.0	0.0	0.0	0.0	0.0	0.0	0.0	0.0	0.0	0.0
mt	2.3	2.3	2.7	2.5	2.0	2.1	1.8	1.9	2.1	2.2	1.8	1.9
il	0.8	0.9	1.0	0.8	0.8	0.7	0.9	0.7	0.6	0.8	0.7	0.7
ap	0.2	0.3	0.2	0.3	0.3	0.3	0.3	0.3	0.2	0.2	0.2	0.2
sum	98.5	99.5	99.5	100.2	98.8	99.2	98.5	99.1	99.1	99.5	99.5	99.6

Aruba batholith: tonalites and leucotonalites

Sample	ARU96 -080	ARU96 -033	ARU96 -096	ARU96 -149a	ARU96 -048	ARU97 -177	ARU97 -132	ARU97 -052	ARU97 -107	ARU96 -049	ARU96 -047	ARU96 -090
Lith.	B5	B5	B5	B5	B6	B6	B6	B6	B6	B6	B6	B6
major												
SiO_2	67.50	67.72	69.99	71.23	73.20	73.78	73.98	74.22	74.33	74.83	76.30	76.51
TiO_2	0.31	0.32	0.30	0.30	0.22	0.28	0.21	0.29	0.31	0.28	0.06	0.09
Al_2O_3	15.54	15.33	14.40	13.37	14.12	13.55	13.54	13.82	13.27	13.84	14.06	13.15
$Fe_2O_{3(t)}$	4.29	4.52	3.73	2.97	2.23	2.43	2.16	2.63	2.66	2.40	0.71	0.90
MnO	0.06	0.11	0.08	0.05	0.02	0.06	0.03	0.04	0.03	0.04	0.02	0.02
MgO	1.44	1.56	1.11	1.88	0.70	0.65	0.53	0.74	0.83	0.73	0.38	0.23
CaO	4.65	4.03	4.81	5.27	3.48	2.64	2.94	2.99	2.60	2.60	4.09	1.18
Na_2O	4.19	4.54	3.60	3.60	4.29	3.90	4.38	4.03	3.85	4.06	4.33	6.05
K_2O	0.49	0.89	0.47	0.30	0.70	2.06	0.71	1.27	1.87	1.87	0.59	0.69
P_2O_5	0.16	0.13	0.07	0.02	0.09	0.07	0.07	0.08	0.07	0.09	0.06	0.03
LOI	0.89	1.52	0.55	0.52	0.36	0.30	0.33	0.31	0.64	0.30	0.23	0.58
Total	99.51	100.65	99.12	99.50	99.42	99.72	98.88	100.41	100.46	101.04	100.81	99.42
Mg no.	43.3	44.0	40.5	59.1	42.3	38.4	36.4	39.7	42.4	41.5	55.7	37.2
trace												
Rb	4.5	9.1	7.1	2.7	10.2	51.4	11.5	28.8	38.6	34.0	4.7	8.3
Sr	399	342	287	229	311	218	247	245	211	178	330	111
Ba	890	610	233	184	844	1288	888	881	733	1070	449	312
Zr	67	61	88	95	125	150	131	133	201	152	32	56
Nb	2.5	2.2	2.8	2.2	1.8	4.8	2.8	4.7	4.9	3.1	0.5	4.6
Y	10	10	6	5	5	13	6	9	10	10	3	22
Sc	11	16	16	16	6	8	7	10	11	5	7	4
V	54	55	53	51	40	30	26	39	38	30	12	18
Cr	n.d.	3	3	40	6	4	n.d.	n.d.	74	66	4	n.d.
Co	10	12	10	10	3	5	4	5	7	4	n.d.	n.d.
Ni	3	4	5	20	4	3	5	5	5	5	6	2
Cu	8	11	38	26	23	11	11	10	29	16	11	12
Zn	24	52	34	25	24	32	25	30	25	33	16	15
Ga	16	18	15	15	13	13	14	14	15	13	12	10
La	7	4	4	4	6	n.d.	7	8	5	6	6	9
Ce	13	10	7	4	10	n.d.	n.d.	n.d.	n.d.	10	4	16
Nd	8	8	5	4	5	5	7	5	4	4	4	9
norm												
Q	28.0	25.8	34.5	35.5	36.6	36.0	38.3	37.9	37.6	37.0	40.1	35.8
C	0.0	0.0	0.0	0.0	0.2	0.2	0.4	0.6	0.3	0.6	0.0	0.4
or	2.9	5.3	2.8	1.8	4.2	12.2	4.2	7.5	11.1	11.1	3.5	4.1
ab	35.8	39.0	30.6	30.6	36.5	33.1	37.1	34.2	32.7	34.4	36.7	51.5
an	22.3	19.1	21.9	19.5	16.8	12.7	14.2	14.4	12.6	12.4	17.2	5.7
di	0.0	0.4	1.5	5.4	0.0	0.0	0.0	0.0	0.0	0.0	2.3	0.0
hy	7.5	8.0	5.5	4.7	3.4	3.4	2.9	3.8	4.0	3.6	0.4	1.3
ol	0.0	0.0	0.0	0.0	0.0	0.0	0.0	0.0	0.0	0.0	0.0	0.0
mt	1.7	1.8	1.4	1.1	1.0	1.1	1.0	1.2	1.2	1.1	0.3	0.4
il	0.6	0.6	0.6	0.6	0.4	0.5	0.4	0.6	0.6	0.5	0.1	0.2
ap	0.4	0.3	0.2	0.1	0.2	0.2	0.2	0.2	0.2	0.2	0.1	0.1
sum	99.2	100.3	98.8	99.3	99.3	99.6	98.7	100.2	100.3	100.9	100.8	99.4

Aruba batholith: leucotonalites (cont.), granites and leucocratic veins

Sample	BK77 -067	ARU96 -155	ARU96 -133	BK77 -048	ARU96 -153	BK77 -068	ARU97 -166	ARU97 -118	ARU96 -039	ARU96 -083	ARU97 -051	ARU96 -041
Lith.	B6	B7	B7	B7	B7	B7	B7	B8	B8	B8	B8	B8
major												
SiO_2	77.87	75.21	76.44	77.09	77.13	78.29	78.80	49.27	77.47	77.50	78.83	79.77
TiO_2	0.07	0.24	0.06	0.07	0.06	0.09	0.07	0.40	0.16	0.07	0.11	0.06
Al_2O_3	12.73	13.14	12.22	12.47	12.23	12.58	12.25	30.54	13.26	12.69	13.06	12.67
$Fe_2O_{3(t)}$	0.65	2.12	0.76	0.90	0.49	0.40	0.53	0.13	1.92	0.57	0.88	0.52
MnO	0.01	0.03	0.01	0.03	0.01	0.01	0.01	0.01	0.06	0.02	0.02	0.01
MgO	0.12	0.49	0.05	0.13	0.29	0.07	0.00	0.00	0.37	0.02	0.19	0.01
CaO	1.86	1.87	0.85	1.37	1.72	0.95	0.56	16.31	0.30	0.92	2.03	0.95
Na_2O	4.26	3.71	3.49	3.62	3.38	3.57	3.81	1.10	7.51	4.40	4.92	6.95
K_2O	1.94	2.85	4.85	3.53	3.20	4.37	4.18	0.20	0.12	3.45	0.91	0.14
P_2O_5	0.04	0.06	0.02	0.03	0.02	0.02	0.01	0.12	0.06	0.02	0.02	0.02
LOI	0.25	0.34	0.32	0.30	0.46	0.27	0.19	0.69	0.60	0.19	0.37	0.26
Total	99.80	100.07	99.06	99.53	99.00	100.60	100.41	98.76	101.82	99.84	101.34	101.36
Mg no.	30.2	35.0	13.4	25.3	58.1	29.1			31.0	7.6	33.6	4.3
trace												
Rb	20.9	46.1	70.1	49.1	48.3	42.1	69.7	3.3	0.5	61.1	9.4	1.5
Sr	188	181	80	119	206	132	34	286	73	47	172	104
Ba	1854	1797	1038	1424	2862	1681	317	31	25	422	921	30
Zr	72	120	65	54	70	69	61	143	118	84	52	81
Nb	1.7	4.2	3.2	2.6	1.6	3.8	7.1	5.5	5.7	3.7	3.3	3.4
Y	6	14	9	9	6	9	11	6	10	9	6	5
Sc	4	9	6	6	2	3	5	16	3	2	6	5
V	10	26	13	11	9	9	8	16	6	5	13	6
Cr	n.d.	n.d.	n.d.	41	4	n.d.	14	20	7	n.d.	n.d.	n.d.
Co	n.d.	5	n.d.	n.d.	n.d.	n.d.	n.d.	n.d.	5	n.d.	n.d.	n.d.
Ni	10	4	n.d.	2	6	3	n.d.	n.d.	n.d.	n.d.	4	n.d.
Cu	10	12	16	n.d.	13	7	7	6	4	5	4	5
Zn	14	25	13	19	13	13	13	10	37	10	18	10
Ga	9	13	10	10	10	11	14	10	12	10	12	13
La	7	8	7	13	5	6	14	6	8	14	9	15
Ce	0	13	9	14	n.d.	10	19	11	11	19	n.d.	18
Nd	1	8	5	4	1	4	10	9	9	7	5	10
norm												
Q	41.5	37.6	35.7	39.2	41.2	38.7	39.3	8.0	31.8	36.6	42.0	37.1
C	0.3	0.7	0.0	0.3	0.1	0.3	0.5	0.0	0.4	0.1	0.3	0.0
or	11.5	16.9	28.8	21.0	19.0	25.9	24.8	1.2	0.7	20.4	5.4	0.8
ab	36.1	31.5	29.6	30.7	28.8	30.3	32.3	9.4	63.9	37.3	41.8	59.0
an	9.0	9.0	3.4	6.6	8.4	4.6	2.7	78.4	1.2	4.5	10.0	2.9
di	0.0	0.0	0.6	0.0	0.0	0.0	0.0	0.0	0.0	0.0	0.0	0.8
hy	0.8	2.8	0.4	1.1	1.1	0.4	0.4	0.0	2.5	0.5	1.1	0.0
ol	0.0	0.0	0.0	0.0	0.0	0.0	0.0	0.0	0.0	0.0	0.0	0.0
mt	0.3	1.0	0.3	0.4	0.2	0.2	0.2	0.0	0.9	0.3	0.4	0.2
il	0.1	0.5	0.1	0.1	0.1	0.2	0.1	0.2	0.3	0.1	0.2	0.1
ap	0.1	0.1	0.0	0.1	0.1	0.0	0.0	0.3	0.1	0.0	0.1	0.0
sum	99.8	99.9	99.0	99.5	99.0	100.6	100.4	98.8	101.7	99.8	101.3	101.3

Aruba batholith: porphyritic rocks

Sample	ARU96 -123	ARU97 -003	ARU97 -123	ARU97 -121	ARU97 -005	ARU97 -083	ARU96 -008	ARU96 -036	ARU96 -138	ARU97 -082	ARU96 -136	ARU97 -178
Lith.	B9	B9	B9	B9	B9	B9	B9	B9	B9	B9	B9	B9
major												
SiO_2	53.39	55.02	58.16	58.80	59.11	59.30	60.43	61.59	61.77	63.39	64.01	64.06
TiO_2	0.71	0.82	0.55	0.64	0.48	0.77	0.60	0.65	0.51	0.45	0.40	0.51
Al_2O_3	14.19	15.37	14.14	14.18	17.05	15.03	12.65	15.49	14.95	14.53	16.52	15.27
$Fe_2O_{3(t)}$	9.92	9.77	7.90	7.78	7.87	7.84	7.41	7.18	7.25	6.01	6.12	5.93
MnO	0.15	0.15	0.12	0.12	0.14	0.11	0.12	0.11	0.14	0.09	0.11	0.10
MgO	6.42	4.81	6.69	5.31	2.98	2.86	6.23	3.10	4.41	3.02	2.11	2.65
CaO	9.49	8.07	6.66	7.11	6.96	8.35	6.51	6.35	6.59	5.20	5.92	5.41
Na_2O	2.63	3.32	3.09	2.96	3.40	2.15	3.34	3.87	3.46	4.14	3.87	4.03
K_2O	0.92	0.77	0.92	0.58	0.50	0.44	0.91	0.30	0.89	0.84	0.66	1.07
P_2O_5	0.16	0.21	0.12	0.15	0.18	0.23	0.16	0.11	0.09	0.12	0.19	0.12
LOI	0.86	1.40	1.46	1.13	0.76	2.71	1.74	1.14	0.53	2.36	0.72	0.74
Total	98.84	99.71	99.82	98.75	99.41	99.79	100.09	99.88	100.59	100.15	100.64	99.88
Mg no.	58.9	52.2	65.6	60.6	46.0	45.1	65.4	49.3	57.8	53.4	44.1	50.5
trace												
Rb	14.8	16.4	18.7	10.2	9.2	5.1	9.2	2.4	22.3	8.9	11.3	20.9
Sr	291	311	290	242	448	383	240	272	377	361	398	337
Ba	721	431	518	591	318	356	459	242	537	969	456	823
Zr	56	77	61	77	40	95	90	95	71	83	57	90
Nb	4.0	3.8	2.6	4.2	2.7	4.0	3.2	3.4	3.0	3.2	2.3	3.6
Y	16	20	12	19	12	13	15	14	11	12	12	13
Sc	39	34	27	32	25	20	24	23	30	23	21	23
V	253	267	180	193	134	240	168	160	180	140	84	132
Cr	248	95	327	227	n.d.	30	276	21	78	20	n.d.	15
Co	40	38	31	30	25	27	29	22	26	20	19	20
Ni	58	37	96	71	4	17	72	18	24	17	4	11
Cu	87	116	28	72	72	191	100	72	49	19	34	20
Zn	69	83	54	69	70	75	71	62	57	51	55	43
Ga	17	19	16	17	22	21	16	17	19	16	18	17
La	4	5	n.d.	n.d.	n.d.	9	6	6	2	8	7	6
Ce	13	13	n.d.	n.d.	n.d.	7	10	15	6	n.d.	12	n.d.
Nd	6	9	7	8	9	12	9	9	6	6	8	9
norm												
Q	5.2	7.4	11.6	15.7	15.9	23.0	14.8	18.6	16.7	20.2	21.7	20.3
C	0.0	0.0	0.0	0.0	0.0	0.0	0.0	0.0	0.0	0.0	0.0	0.0
or	5.5	4.6	5.5	3.5	3.0	2.7	5.5	1.8	5.3	5.1	3.9	6.4
ab	22.4	28.5	26.6	25.3	29.0	18.7	28.8	33.1	29.4	35.9	33.0	34.4
an	24.4	25.1	22.3	24.0	30.0	30.9	17.1	24.3	22.7	19.0	25.9	20.6
di	18.0	11.7	8.5	8.8	3.1	8.5	12.0	5.7	7.8	5.5	2.1	4.8
hy	17.7	16.5	20.6	16.6	13.8	10.5	17.2	11.8	14.4	10.6	10.0	9.6
ol	0.0	0.0	0.0	0.0	0.0	0.0	0.0	0.0	0.0	0.0	0.0	0.0
mt	3.1	3.1	2.8	2.7	2.8	2.8	2.6	2.5	2.5	2.4	2.4	2.3
il	1.4	1.6	1.1	1.2	0.9	1.5	1.2	1.3	1.0	0.9	0.8	1.0
ap	0.4	0.5	0.3	0.4	0.4	0.5	0.4	0.3	0.2	0.3	0.5	0.3
sum	98.1	99.0	99.2	98.2	98.8	99.2	99.6	99.4	100.1	99.7	100.2	99.5

Aruba batholith: porphyritic rocks (cont.); Cross-cutting dykes

Sample	ARU97 -117	ARU96 -004	ARU96 -010	ARU96 -005	ARU96 -029	ARU94 -017	ARU97 -126	ARU96 -026	ARU96 -160	ARU96 -024	ARU96 -025	ARU97 -109
Lith.	B9	B9	B9	B9	B9	B9	C1	C1	C1	C1	C1	C1
major												
SiO_2	64.70	64.70	64.92	65.34	65.37	67.35	51.33	53.10	53.21	53.45	54.15	54.19
TiO_2	0.40	0.40	0.42	0.37	0.45	0.37	0.63	0.41	0.36	0.44	0.42	0.66
Al_2O_3	15.82	14.04	14.78	15.39	15.80	13.67	12.94	9.30	9.15	10.55	10.16	14.48
$Fe_2O_{3(t)}$	5.87	5.36	5.83	5.06	5.12	4.43	11.56	9.34	8.97	9.38	9.29	9.21
MnO	0.11	0.08	0.09	0.09	0.11	0.07	0.23	0.16	0.16	0.16	0.15	0.15
MgO	2.17	2.72	2.81	1.72	1.84	2.42	7.72	11.38	11.54	10.39	10.95	7.22
CaO	5.69	4.67	3.92	2.80	4.38	4.87	10.31	11.22	10.86	10.58	11.56	7.91
Na_2O	3.73	3.96	5.61	6.03	4.65	3.69	1.95	1.56	1.60	1.86	1.68	2.84
K_2O	0.69	0.91	0.84	0.40	0.78	1.57	0.63	1.23	1.08	1.31	1.16	1.08
P_2O_5	0.15	0.10	0.10	0.08	0.13	0.09	0.18	0.27	0.26	0.32	0.32	0.16
LOI	0.73	2.67	1.35	2.26	2.21	0.46	1.46	1.18	1.86	1.44	1.18	1.14
Total	100.06	99.63	100.70	99.55	100.84	98.98	98.93	99.15	99.08	99.87	101.04	99.03
Mg no.	45.8	53.7	52.4	43.7	45.1	55.5	58.9	73.0	74.0	71.0	72.3	63.5
trace												
Rb	14.6	7.6	9.6	5.1	7.1	17.2	19.0	43.4	33.9	27.3	47.6	27.6
Sr	375	300	395	203	293	291	328	334	352	373	381	242
Ba	573	700	432	108	539	779	291	391	371	570	538	379
Zr	61	89	88	74	67	97	33	36	37	38	40	53
Nb	3.4	2.4	3.0	3.1	3.4	3.7	2.4	1.3	1.6	1.0	2.4	2.9
Y	13	10	11	10	14	12	17	12	13	16	14	16
Sc	18	20	23	14	13	19	51	52	52	52	45	34
V	102	126	127	68	66	96	247	212	202	203	223	206
Cr	7	122	28	84	n.d.	75	347	813	941	749	714	265
Co	17	19	17	17	15	14	48	40	39	40	39	36
Ni	6	15	14	4	3	16	65	100	114	89	90	99
Cu	54	37	54	67	20	44	157	75	78	87	94	98
Zn	45	53	91	59	57	35	155	71	73	74	72	82
Ga	17	16	17	15	15	14	15	12	10	9	12	14
La	4	5	5	4	6	7	n.d.	7	5	7	5	n.d.
Ce	n.d.	7	11	9	11	8	9	13	10	14	15	12
Nd	7	8	8	10	7	7	8	11	10	12	12	9
norm												
Q	23.6	23.8	15.9	18.7	22.2	26.0	3.5	2.9	3.7	3.0	3.5	5.1
C	0.0	0.0	0.0	0.1	0.0	0.0	0.0	0.0	0.0	0.0	0.0	0.0
or	4.1	5.5	5.0	2.4	4.7	9.3	3.8	7.4	6.5	7.9	7.0	6.4
ab	31.8	34.4	48.1	52.2	40.2	31.4	16.8	13.4	13.8	16.0	14.4	24.3
an	24.6	18.3	12.8	13.7	20.4	16.2	25.1	14.9	14.9	16.8	16.9	23.9
di	2.5	4.0	5.1	0.0	0.8	6.2	21.1	32.0	30.8	27.8	31.5	12.0
hy	9.7	10.0	9.9	9.1	8.9	7.0	23.5	23.6	24.5	23.2	22.6	22.0
ol	0.0	0.0	0.0	0.0	0.0	0.0	0.0	0.0	0.0	0.0	0.0	0.0
mt	2.3	2.1	2.3	2.0	2.0	1.7	2.6	2.9	2.8	2.9	2.9	2.9
il	0.8	0.8	0.8	0.7	0.9	0.7	1.2	0.8	0.7	0.9	0.8	1.3
ap	0.4	0.2	0.2	0.2	0.3	0.2	0.4	0.7	0.6	0.8	0.8	0.4
sum	99.7	99.2	100.3	99.2	100.5	98.7	98.0	98.5	98.4	99.2	100.4	98.3

	Cross-cutting dykes										
Sample	ARU97 -106	ARU96 -139	ARU96 -079	ARU96 -014	ARU96 -137	ARU97 -035	BK77 -065	BK77 -043	BK77 -148	BK77 -47	ARU96 -115
Lith.	C1	C2	C2	C2	C2	C2	C2	C2	C3	C3	C3
major											
SiO_2	55.14	50.49	51.78	52.17	54.06	54.77	55.72	61.79	53.77	58.71	60.26
TiO_2	0.77	0.83	0.70	0.76	0.88	0.56	0.65	0.48	0.85	0.43	0.72
Al_2O_3	14.95	11.31	14.39	17.12	14.02	11.38	13.30	15.92	13.33	14.92	14.38
$Fe_2O_{3(t)}$	9.79	10.24	11.73	9.54	10.36	9.34	8.47	7.64	10.61	6.60	7.96
MnO	0.15	0.21	0.19	0.07	0.16	0.14	0.14	0.09	0.16	0.15	0.11
MgO	5.00	11.38	5.66	4.82	6.55	11.52	7.53	3.43	7.08	6.29	3.78
CaO	8.40	9.74	9.65	11.85	9.73	8.75	9.72	6.94	10.76	11.78	6.61
Na_2O	3.19	2.29	2.45	1.83	2.65	2.20	2.81	3.52	1.13	0.52	3.88
K_2O	1.14	0.40	0.31	0.27	0.48	0.34	0.24	0.15	0.11	0.11	0.11
P_2O_5	0.21	0.20	0.21	0.16	0.15	0.12	0.13	0.11	0.06	0.09	0.21
LOI	0.79	1.75	0.12	0.65	0.56	1.82	0.86	0.47	1.09	0.80	2.07
Total	99.54	98.83	98.01	99.24	99.62	100.94	99.58	100.55	98.96	100.38	100.10
Mg no.	53.1	70.5	50.9	52.8	58.4	73.2	66.4	50.3	59.7	68.2	51.7
trace											
Rb	29.3	4.0	3.3	3.1	5.5	5.2	2.9	0.8	1.2	0.9	0.8
Sr	298	236	400	407	230	204	287	457	50	226	313
Ba	400	159	1020	54	260	252	128	331	20	21	23
Zr	74	73	34	40	61	58	57	61	51	35	99
Nb	4.2	2.7	1.7	2.1	3.2	2.7	3.6	2.0	4.4	1.9	3.6
Y	21	18	13	13	14	11	13	9	18	7	13
Sc	34	40	43	32	43	37	34	22	46	35	28
V	267	246	285	334	263	208	221	158	288	179	201
Cr	94	733	119	n.d.	133	1005	479	37	357	186	81
Co	36	47	47	33	38	41	33	27	42	25	30
Ni	32	227	36	12	36	311	91	17	105	47	23
Cu	115	85	132	23	78	17	33	100	154	17	124
Zn	78	109	96	75	76	69	55	41	75	48	67
Ga	18	16	17	19	18	16	14	18	16	13	18
La	6	7	n.d.	4	5	6	5	4	3	4	8
Ce	9	19	8	7	10	13	12	9	11	8	19
Nd	11	18	6	6	9	7	8	8	7	5	14
norm											
Q	6.5	0.0	5.6	8.3	6.6	5.5	8.1	19.1	13.3	22.4	17.2
C	0.0	0.0	0.0	0.0	0.0	0.0	0.0	0.0	0.0	0.0	0.0
or	6.8	2.4	1.8	1.6	2.9	2.1	1.4	0.9	0.7	0.7	0.6
ab	27.2	19.7	20.9	15.6	22.6	19.0	23.9	30.0	9.6	4.4	33.5
an	23.3	19.8	27.7	37.9	25.1	20.5	23.2	27.3	31.3	38.4	22.0
di	14.4	22.8	16.1	16.7	18.5	18.4	19.9	5.5	18.2	16.1	8.4
hy	15.6	25.8	20.6	13.6	18.0	30.4	18.1	13.4	19.9	14.6	13.1
ol	0.0	3.2	0.0	0.0	0.0	0.0	0.0	0.0	0.0	0.0	0.0
mt	3.0	2.3	2.6	3.0	3.2	2.9	2.6	2.7	3.3	2.3	2.8
il	1.5	1.6	1.3	1.5	1.7	1.1	1.3	0.9	1.6	0.8	1.4
ap	0.5	0.5	0.5	0.4	0.4	0.3	0.3	0.3	0.1	0.2	0.5
sum	98.8	98.0	97.0	98.5	98.8	100.2	98.9	100.0	98.1	99.9	99.5

Appendix D

Rare Earth Element Analyses

D.1 Introduction

REE analyses were made on a selection of samples taken during this study. The majority of data obtained were ICP-MS analyses (Section D.2), but a few samples were cross-checked using the ICP-OES (Section D.3) and INAA (Section D.4) facilities at Leicester. This verification was considered necessary because of discrepancies between the ICP-MS Eu values compared to the accepted values for international standards (see Appendix E). Additionally, a comparison between different facilities was of interest to those in charge of the respective laboratories.

All sample powders used for REE analysis were aliquots of the same powders used for XRF analysis (i.e., crushed in agate); the powders were dried overnight in an oven at 120°C prior to weighing for ICP-MS and INAA analyses; dried ignited powders were used for ICP-OES analyses.

D.2 Inductively Coupled Plasma Mass Spectrometry (ICP-MS) analyses

D.2.1 Sample selection and preparation

Samples were selected to cover the range of lithologies sampled, although the timing of the ICP-MS analytical work meant that the samples analysed were almost exclusively those sampled during (or before) the 1996 field season.

0.250 grams of dry powder were accurately weighed out, and 10ml 48% HF and 4 ml 16M HNO_3 (both analytical grade) were added. The samples were digested using a microwave system: each dissolution batch consisted of six samples, one standard (either JG-1a or JB-1) and a blank. Six samples were dissolved and analysed twice, to assess the reproducibility of the dissolution procedure. The dissolved samples were dried down in a fume cupboard, then a further 4 ml of 16M HNO_3 was added to ensure complete removal of fluoride. After being dried down again, the samples were taken up in 3.5 ml 60% HNO_3, and diluted with water to a

final volume of 50 ml. (This is equivalent to a 200× dilution factor). Immediately prior to analysis, these solutions were diluted by a further factor of 5, making the final dissolution factor ~ 1000×.

D.2.2 ICP-MS analysis

ICP-MS analysis was carried out under the instruction of Bertil van Os at the Rijks Geologische Dienst in Haarlem, using a Fisons Plasmaquad PQ 2+ ICP-MS in dual detector mode. The method used was peak jumping, with three points per peak and a 10 μs dwell time per point. There were fourteen sweeps per run, and four runs per sample. The cool gasbox was set at 14 and the auxiliary gasbox at 3; the DeGalan V-groove nebuliser was set at 1 litre per minute, and the Gilson minipulse peristaltic pump operated at 1 ml per minute.

^{115}In was used as an internal standard: this was automatically added by the second channel on the peristaltic pump. Before each experiment, a mass calibration was performed. The ICP-MS was optimised at ^{115}In (intensity > 40 million counts per ppm). The standard deviation of a 25 ppb solution was checked to ensure that it was < 2%. The cones and nebuliser were checked after every experiment, and cleaned (if necessary) in an ultrasonic bath. External calibration was achieved using three multi element standards ("major", "high" and "low") prepared freshly each week from 1000 ppm stock solutions from Merck, Alfa and Aldrich. A blank was run every 12 samples, and the "low" standard was used as a drift monitor every 6 samples.

The concentrations were calculated by taking the mean value from 4 runs per sample. The data were corrected for drift assuming linear variation between the values obtained for the "low" standard. If the internal standard (^{115}In) still deviated between samples and standards, the data were also corrected for the variation in internal standard. Calibration took place every 12 samples with use of the synthetic standards. The concentration of the standards is adapted to natural abundances. In addition to the blank, three standards were used for calibration: the major elements standard (containing Fe, Al, Mg, Ca, K, Na and Mn); a multielement standard containing low abundances (from 0.5 and 50 ppb depending on the element); and a multielement standard containing high abundances (from 5 to 500 ppb). Calibration lines were checked for linearity by calculating regression coefficients and slope changes. Calibration was performed from point to point (blank to low, low to high and high to major). Samples were corrected for variation in slopes assuming linear change with time between two sets of standards. Isobaric interferences from ^{151}(BaO) on ^{151}Eu and ArCl on As were corrected for.

Theoretical detection limits for monoisotopic elements without any isobaric interference are 5 ppt (40×10^6 cps/ppm ≡ 40×10^3 cps/ppb ≡ 40 cps/ppt; detection limit about 200 cps ≡ 5 ppt). Detection limits are dependent on the wearing of cones, interferences, and the abundance of the measured isotope.

D.2.3 ICP-MS results

ICP-MS data are reported in Table D.1, organised in the same way as the data in Table C.2, i.e., by lithology and then SiO_2 content. A correction has been applied to the Eu data (the reason and method for correction are given in Appendix E.2.3). Data for international reference materials are presented in Appendix E (Table E.6).

D.3 Inductively Coupled Plasma Optical Emissions Spectrometry (ICP-OES) analyses

D.3.1 Sample selection and preparation

Six samples from the batholith and six from the Aruba Lava Formation were chosen, to allow comparison between ICP-OES and the other REE determination methods. Samples were prepared for analysis at the University of Leicester by Emma Mansley and Kevin Sharkey.

Microwave digestion

0.3g samples of *ignited* powder were weighed into clean CEM digestion vessels and moistened with a few drops of de-ionised water. 10 ml of 48% HF and 4 ml 16M HNO_3 were added. Rupture membranes were installed in the vent fittings, which were then screwed onto the vessel caps. For each batch of samples, one vessel had a cap attached to the pressure sensing line, to monitor the pressure inside the vessels. Eight samples at a time were placed in a carousel within the CEM MDS-2000 microwave sample preparation system. The fan speed was set to 60% and the pressure inside the vessels ramped to 80 psi over a 20 minute period with the microwave power at 100%. Once the pressure had reached 80 psi it was held at that level for a further 60 minutes, with the power again at 100%. The samples were then allowed to cool before removal from the microwave cavity.

Remaining vapours were vented by hand in a fume cupboard, and the resultant solutions transferred to 50 ml PTFE beakers. The PTFE beakers were then placed on a hot plate at ~200°C and the samples evaporated to incipient dryness. A further 4 ml of 16M HNO_3

was added to each sample, to ensure the complete removal of excess fluoride ions, and the solutions evaporated to complete dryness. The remaining precipitate was then dissolved in 1.7M HCl with gentle heating until a clear solution was obtained.

Separation

The REE emit extremely complex spectra in the ICP, with a large number of strong emission lines being generated for each element, and many examples of spectral overlap. Because there is also potential for interference from major elements, chemical separation methods are used to remove the bulk of the major elements from the solution and to concentrate to REE into a small volume prior to analysis.

Quartz glass columns of 180 mm length and 8 mm internal diameter were used. The columns have a 100 ml reservoir at the top and a plug of quartz glass wool, to act as a sinter, at the bottom. 5g of resin (Dowex AG 50W-8X, 200-400 mesh) was loaded on to the columns in 1.7M HCl and settled at a height of 130 mm. The resin was washed with 50 ml of 6M HCl, followed by 50 ml of de-ionised water and the pH adjusted to match that of the sample solutions with 50 ml of 1.7M HCl. The samples were loaded on to the columns in 30 ml of 1.7M HCl. All the major constituents (including Ca and Fe which are potential spectral interferences in the ICP-OES) and most of the trace elements in the solution were then eluted, by washing the resin with a further 100 ml of 1.7M HCl. This fraction was discarded. The REE, which are quantitatively held on the resin, were then eluted by washing with 80 ml of 6M HCl. This fraction was collected in 100 ml Pyrex beakers and evaporated to dryness on a sand bath at ~110°C. The samples were converted to nitrates by the addition of 4 ml of 16M HNO_3 and then redissolved in 3 ml of 5% HNO_3 and stored in polypropylene tubes prior to analysis.

D.3.2 ICP-OES analysis

Analysis was carried out at the University of Leicester using a Philips PV 8060 ICP-OES and a simultaneous spectrometer. The sample solution is carried in an aerosol in argon to the centre of the plasma flame where it reaches a temperature of about 8000 K. At this extreme temperature atomisation of the analyte solution occurs. The energised atoms or ions will spontaneously revert to a lower energy state and emit a photon of light energy, at a characteristic wavelength. For quantitative analysis it is assumed that the intensity of light emitted is proportional to the concentration of the element in solution. The light emitted is focused into a spectrometer where a diffraction grating resolves the light into its component wavelengths. The intensity of light emitted at each given wavelength is then converted to an

electrical signal by photomultiplier tubes located at specific wavelengths for each element line. Using calibration lines which relate elemental concentration with intensity of light emitted, the electrical signal is converted into a concentration measurement.

Detection limits for the REE are:

Element	det. limit	Element	det. limit	Element	det. limit	Element	det. limit
La	0.8	Nd	0.5	Gd	0.8	Yb	0.14
Ce	0.9	Sm	0.5	Dy	0.7	Lu	0.08
Pr	0.9	Eu	0.15	Er	0.8		

D.3.2 ICP-OES results

Data for the twelve samples analysed by ICP-OES are presented in Table D.2. Data for international reference materials are presented in Appendix E (Table E.6).

D.4 Instrumental Neutron Activation analyses (INAA)

Four samples from the Aruba Lava Formation were analysed by INAA at Leicester for rare earth elements (La, Ce, Nd, Sm, Eu, Gd, Tb, Yb, Lu) and certain trace elements (Ta, Th, Hf, Sc, Co, U).

D.4.1 Sample preparation

0.2 gram aliquots of powder (which had been dried overnight at 120°C) were accurately weighed into plastic capsules, which were sealed by soldering. The capsules were stacked into a polythene tube, interspersed with capsules containing standard powders (international standard JB-1A and internal standard WS-1A); irradiation flux monitors made of iron foil (of known weight) coated with plastic were placed between the capsules in the tube. Irradiation was carried out at Silwood Park (the Imperial College Reactor Centre at Ascot). Samples and iron-foil flux monitors were given a total neutron flux of approximately 6.2×10^{16} n.cm^{-2}, by irradiating in core tube 4, positions 3 and 4, for 2 days (= 2 × 7½ hours). Samples were allowed to "cool" for 6 days before counting, to allow for the decay of short-lived isotopes.

D.4.2 Detection, counting and processing

Each sample was counted three times. Two counts, each of approximately 2000 seconds, were made within one week of irradiation. These counts provide peak spectra for La,

Sm, Sc and Co. The main count, carried out between one and four weeks after irradiation, was for a longer duration, between a half and one day per sample.

Two detectors were used: a high-energy GEM (Li) coaxial detector, with a resolution of 1.67 keV at 1.33 MeV (FWHM), for measuring La at 1596.2 keV, Sc at 889.3 keV, and Co at 1333 KeV; and a LOAX (planar low-energy photon) detector with a resolution of 299 eV at 5.9 keV and 563 eV at 122 keV (FWHM) for Sm (103.2 keV), Nd (91.0 keV), Eu (123.1 keV), Tb (86.8 keV), Tm (84.3 keV), Yb (63.1 keV), Lu (113.0 or 208.4 keV), Ta (67.7 or 100.1 keV), Hf (133.0 keV), and Th (98.4 keV).

The equipment used is EG&G hardware, with an MCA buffer emulator installed on an IBM 30 PC. Data from the two detectors are channelled through a multiplexer prior to storage in the MCA buffer. Spectra are transferred to the VAX for peak stripping peak-area computation using SAMPO software. Peak intensities are compared to those of known reference standards (Ailsa Criag microgranite AC-2 for most elements, JB-1A basalt for Sc and Co) for calculation of element abundances. Interelement corrections are made where necessary (see Potts, 1986) although it was found that Tm data were excessively high and were ignored. Flux corrections were applied using data from the iron foils.

D.4.3 Results

The INAA data for the four basalts from the Aruba Lava Formation are presented in Table D.3. Data for reference materials are presented in Appendix E (Table E.6).

Aruba Lava Formation

Sample	ARU96 -021	ARU94 -029	ARU96 -001	ARU96 -002	ARU96 -031	ARU96 -011	ARU96 -030	ARU96 -117	ARU96 -038	ARU94 -022	ARU96 -037	ARU96 -108	ARU96 -107
Lith.	A1	A1	A1	A1	A1	A1	A2	A2	A2	A2	A2	A3	A3
REE													
La	2.65	2.63	3.59	3.56	3.38	3.35	2.28	1.57	1.22	2.60	3.83	2.23	2.72
Ce	6.65	6.76	8.92	9.20	8.35	8.26	5.89	4.08	2.84	6.29	9.71	5.71	7.07
Pr	1.02	1.06	1.40	1.43	1.28	1.29	0.92	0.65	0.42	0.97	1.42	0.88	1.08
Nd	5.40	5.62	7.25	7.23	6.67	6.91	4.79	3.37	2.18	4.90	7.25	4.53	5.56
Sm	1.69	1.84	2.23	2.36	2.06	2.25	1.67	1.16	0.73	1.57	2.24	1.51	1.82
Eu	0.71	0.72	0.88	0.92	0.82	0.88	0.65	0.51	0.35	0.61	0.87	0.55	0.74
Gd	2.11	2.33	2.72	2.94	2.51	2.85	2.09	1.53	1.02	1.95	2.65	1.88	2.31
Tb	0.42	0.47	0.55	0.60	0.52	0.58	0.43	0.31	0.22	0.39	0.53	0.37	0.48
Dy	2.92	3.29	3.81	4.18	3.58	4.09	2.95	2.12	1.55	2.72	3.76	2.59	3.32
Ho	0.59	0.68	0.77	0.85	0.74	0.85	0.63	0.43	0.32	0.58	0.77	0.54	0.70
Er	1.75	2.00	2.24	2.46	2.18	2.56	1.80	1.32	0.95	1.67	2.28	1.58	2.05
Tm	0.25	0.30	0.33	0.36	0.33	0.38	0.26	0.21	0.15	0.24	0.34	0.23	0.30
Yb	1.77	2.02	2.31	2.43	2.21	2.62	1.80	1.33	1.02	1.67	2.30	1.54	1.98
Lu	0.26	0.30	0.34	0.37	0.33	0.41	0.27	0.20	0.15	0.24	0.35	0.22	0.29
U	0.08	0.07	0.11	0.08	0.11	0.16	0.07	0.04	0.08	0.10	0.15	0.08	0.08
Th	0.25	0.24	0.35	0.30	0.34	0.37	0.21	0.13	0.12	0.40	0.37	0.20	0.23
Pb	1.04	8.31	2.31	3.01	0.94	3.55	3.27	5.61	0.55	4.83	1.58	3.31	3.71
Y	14.05	15.91	18.16	19.66	18.11	20.94	14.03	11.99	8.15	13.85	20.04	13.57	15.78
Nb	3.08	2.92	4.31	4.16	4.15	3.80	2.72	1.74	0.78	2.19	4.57	2.64	2.76
Hf	2.29	1.99	2.39	1.43	2.99	4.03	0.98	0.97	1.93	1.50	3.84	1.05	1.29
Ta	0.28	0.24	0.33	0.30	0.35	0.35	0.29	0.16	0.06	0.11	0.50	0.17	0.16
Ratios	$_N$ denotes chondrite-normalised ratio												
$(La/Yb)_N$	1.02	0.89	1.06	0.99	1.04	0.87	0.86	0.80	0.81	1.06	1.13	0.98	0.93
$(La/Sm)_N$	0.98	0.90	1.01	0.94	1.03	0.93	0.85	0.85	0.88	1.04	1.07	0.92	0.94
$(Sm/Yb)_N$	1.03	0.99	1.05	1.05	1.02	0.93	1.01	0.95	0.90	1.02	1.06	1.07	1.00
$(Ce/Yb)_N$	0.99	0.88	1.02	1.00	1.00	0.83	0.86	0.81	0.73	0.99	1.11	0.98	0.94
$(Nd/Yb)_N$	1.07	0.98	1.11	1.05	1.07	0.93	0.94	0.89	0.75	1.03	1.11	1.04	0.99
$(Th/Nd)_N$	0.74	0.68	0.76	0.65	0.80	0.83	0.68	0.60	0.49	1.29	0.79	0.68	0.66
La/Nb	0.86	0.90	0.83	0.85	0.81	0.88	0.84	0.90	1.57	1.19	0.84	0.84	0.99
Nb/Ta	11.01	12.16	13.08	13.88	11.86	10.82	9.22	10.99	13.86	20.43	9.20	15.69	17.55

	Aruba Lava Formation (cont);						Aruba batholith: mafic rocks						
Sample	ARU96 -043	ARU96 -145	ARU96 -149b	ARU96 -147	ARU96 -142	ARU96 -112	ARU96 -135	ARU94 -007	ARU97 -162	ARU96 -057	ARU96 -124	ARU96 -053	ARU96 -154
Lith.	A3	A4	A4	A4	A5	A6	B1	B1	B1	B1	B1	B1	B2b
REE													
La	3.13	2.36	2.92	3.04	3.01	3.83	4.14	2.49	4.86	2.21	3.41	4.84	1.30
Ce	5.07	6.11	7.30	5.49	6.57	8.89	9.48	6.35	12.50	4.74	7.37	8.52	2.73
Pr	0.61	0.99	1.15	0.67	0.92	1.34	1.39	1.08	2.17	0.73	1.08	1.20	0.39
Nd	2.44	5.18	5.72	2.83	4.49	6.76	6.76	5.96	11.75	4.10	5.24	5.51	2.21
Sm	0.59	1.85	1.89	0.75	1.38	2.09	1.77	1.97	3.41	1.36	1.50	1.50	0.77
Eu	0.24	0.69	0.75	0.35	0.50	0.81	0.67	0.70	1.07	0.53	0.62	0.55	0.32
Gd	0.62	2.30	2.26	0.87	1.66	2.44	1.73	2.28	3.51	1.56	1.76	1.71	0.90
Tb	0.12	0.46	0.47	0.17	0.32	0.49	0.30	0.43	0.63	0.31	0.35	0.31	0.18
Dy	0.78	3.24	3.17	1.15	2.20	3.39	1.95	2.90	4.15	2.03	2.22	2.06	1.14
Ho	0.16	0.68	0.67	0.22	0.46	0.70	0.37	0.58	0.83	0.41	0.45	0.42	0.23
Er	0.46	1.99	1.96	0.66	1.33	2.05	1.08	1.64	2.31	1.17	1.26	1.18	0.65
Tm	0.07	0.30	0.29	0.10	0.20	0.32	0.15	0.24	0.33	0.16	0.18	0.17	0.09
Yb	0.44	2.02	2.00	0.68	1.31	2.09	1.13	1.52	2.25	1.15	1.18	1.17	0.61
Lu	0.07	0.30	0.30	0.10	0.19	0.32	0.15	0.23	0.34	0.16	0.17	0.17	0.09
U	0.12	0.02	0.06	0.12	0.14	0.24	0.24	0.19	0.45	0.24	0.31	0.38	0.10
Th	0.53	0.07	0.13	0.37	0.36	0.39	0.45	0.36	0.87	0.47	0.66	0.68	0.20
Pb	2.38	1.55	2.37	2.20	2.40	1.22	1.99	3.29	2.50	2.16	3.85	1.81	1.19
Y	3.82	17.26	16.41	5.91	11.50	17.61	10.12	14.21	22.10	10.46	9.70	10.97	5.58
Nb	1.45	2.74	2.67	2.02	2.65	3.89	1.43	1.18	2.64	0.96	1.22	1.59	0.36
Hf	0.55	1.24	1.33	0.86	0.91	2.83	2.06	1.33	2.54	1.91	0.86	2.27	1.53
Ta	0.14	0.20	0.19	0.19	0.17	0.30	0.15	0.08	0.35	0.13	0.12	0.15	0.08
Ratios													
$(La/Yb)_N$	4.84	0.80	0.99	3.05	1.56	1.24	2.50	1.12	1.47	1.30	1.96	2.80	1.45
$(La/Sm)_N$	3.34	0.80	0.97	2.55	1.37	1.15	1.47	0.79	0.89	1.02	1.43	2.02	1.05
$(Sm/Yb)_N$	1.45	1.00	1.03	1.20	1.14	1.08	1.70	1.41	1.64	1.28	1.37	1.39	1.38
$(Ce/Yb)_N$	3.04	0.80	0.96	2.14	1.32	1.12	2.21	1.10	1.46	1.08	1.64	1.91	1.18
$(Nd/Yb)_N$	1.96	0.91	1.01	1.47	1.21	1.14	2.12	1.39	1.84	1.25	1.56	1.66	1.29
$(Th/Nd)_N$	3.42	0.22	0.37	2.05	1.28	0.91	1.06	0.94	1.17	1.81	1.98	1.93	1.44
La/Nb	2.16	0.86	1.09	1.50	1.13	0.99	2.89	2.11	1.84	2.29	2.80	3.05	3.65
Nb/Ta	10.56	13.46	14.25	10.89	16.03	13.02	9.59	14.86	7.50	7.32	10.52	10.59	4.28

Aruba batholith (continued): gabbros, diorites and tonalites

Sample	ARU96 -042	ARU96 -152	BK77 -066a	ARU97 -160	BK77 -165	ARU96 -126	ARU96 -158	ARU96b -018b	ARU94 -013	ARU96 -098	BK77 -054	ARU96 -131	ARU94 -002
Lith.	B3	B4	B4	B4	B4	B4	B4	B4	B4	B5	B5	B5	B5
REE													
La	4.09	4.99	5.75	6.01	5.32	3.92	7.06	4.75	7.39	6.74	8.02	8.03	8.03
Ce	8.58	11.26	12.26	13.06	10.99	7.52	15.32	9.05	16.77	15.28	16.26	16.35	15.71
Pr	1.22	1.62	1.77	1.92	1.46	1.04	2.20	1.21	2.40	2.22	2.03	2.18	1.94
Nd	5.73	7.84	8.42	9.22	6.46	4.70	10.67	5.31	10.98	10.95	8.77	9.52	7.81
Sm	1.47	1.97	2.26	2.41	1.73	1.29	2.65	1.42	2.72	2.88	1.92	2.13	1.65
Eu	0.68	0.81	0.85	0.86	0.68	0.56	0.96	0.70	0.94	1.05	0.68	0.80	0.64
Gd	1.45	1.97	2.33	2.28	1.87	1.47	2.65	1.61	2.56	2.78	1.79	1.86	1.54
Tb	0.25	0.34	0.44	0.41	0.35	0.28	0.46	0.30	0.44	0.48	0.30	0.31	0.27
Dy	1.59	2.11	3.00	2.61	2.39	1.86	2.94	1.95	2.77	3.13	1.97	1.97	1.75
Ho	0.30	0.41	0.59	0.53	0.47	0.36	0.60	0.40	0.54	0.60	0.39	0.37	0.34
Er	0.85	1.15	1.76	1.49	1.40	1.03	1.63	1.17	1.53	1.77	1.13	1.13	1.04
Tm	0.12	0.17	0.27	0.22	0.21	0.15	0.23	0.17	0.22	0.26	0.18	0.17	0.16
Yb	0.83	1.13	1.85	1.56	1.40	1.03	1.66	1.15	1.51	1.83	1.23	1.20	1.12
Lu	0.13	0.17	0.26	0.23	0.22	0.15	0.24	0.18	0.23	0.28	0.18	0.19	0.17
U	0.21	0.26	0.23	0.37	0.71	0.40	0.48	0.33	0.45	0.80	0.53	0.57	0.58
Th	0.68	0.55	0.63	0.89	1.65	0.82	0.98	0.83	1.05	1.12	1.37	1.30	1.70
Pb	6.56	3.15	1.98	3.01	4.05	3.60	4.55	3.62	4.64	9.12	3.59	4.12	4.86
Y	8.03	10.95	16.00	14.16	12.50	8.32	14.49	9.35	13.66	16.03	10.71	10.46	9.13
Nb	1.24	1.71	3.57	2.37	3.20	1.38	2.15	3.16	2.51	3.38	3.57	3.04	3.52
Hf	1.51	1.56	2.26	2.03	2.95	0.99	2.34	0.77	1.29	11.34	2.88	2.89	1.10
Ta	0.18	0.19	0.23	1.03	0.52	0.12	0.05	0.27	0.11	0.27	0.27	0.19	0.32
Ratios													
$(La/Yb)_N$	3.33	3.00	2.11	2.62	2.59	2.58	2.89	2.80	3.33	2.51	4.43	4.54	4.88
$(La/Sm)_N$	1.75	1.59	1.59	1.57	1.93	1.90	1.67	2.10	1.70	1.47	2.61	2.37	3.04
$(Sm/Yb)_N$	1.91	1.89	1.33	1.67	1.35	1.36	1.74	1.33	1.96	1.71	1.70	1.92	1.61
$(Ce/Yb)_N$	2.71	2.62	1.74	2.20	2.07	1.92	2.44	2.07	2.93	2.20	3.48	3.58	3.70
$(Nd/Yb)_N$	2.42	2.44	1.60	2.09	1.63	1.60	2.27	1.62	2.57	2.12	2.51	2.79	2.47
$(Th/Nd)_N$	1.86	1.11	1.17	1.52	4.01	2.74	1.45	2.46	1.50	1.60	2.46	2.15	3.43
La/Nb	3.30	2.92	1.61	2.54	1.66	2.83	3.28	1.51	2.95	2.00	2.24	2.64	2.28
Nb/Ta	7.04	8.93	15.72	2.31	6.12	11.48	45.40	11.55	22.25	12.51	13.31	16.30	11.10

Aruba batholith (continued): silicic rocks and porphyries; Cross-cutting dykes

Sample	ARU96 -033	ARU96a -149a	ARU96 -155	ARU96 -153	ARU96 -041	ARU96 -123	ARU96 -136	ARU96 -029	ARU94 -017	ARU96 -025	ARU96 -014	ARU96 -137	BK77 -065
Lith.	B5	B5	B7	B7	B8	B9	B9	B9	B9	C1	C2	C2	C2
REE													
La	10.02	2.52	8.68	4.41	16.29	4.42	5.37	6.03	8.27	6.57	2.85	5.01	4.64
Ce	22.30	4.93	18.59	6.66	32.16	9.83	11.66	12.53	15.34	15.79	7.20	12.45	9.42
Pr	2.86	0.68	2.21	0.66	2.85	1.49	1.66	1.72	1.92	2.53	1.20	1.98	1.36
Nd	12.47	3.11	8.85	2.14	9.28	7.16	7.71	7.34	7.81	12.36	6.44	10.13	6.14
Sm	2.84	0.86	1.87	0.35	1.20	2.06	1.88	1.69	1.69	3.01	1.94	2.73	1.75
Eu	1.01	0.46	0.86	0.78	0.17	0.85	0.77	0.69	0.70	0.97	0.55	0.96	0.65
Gd	2.62	0.88	1.71	0.31	0.93	2.22	1.79	1.66	1.60	2.52	2.04	2.66	1.94
Tb	0.46	0.17	0.30	0.05	0.13	0.42	0.31	0.30	0.28	0.40	0.39	0.45	0.36
Dy	3.00	1.13	1.86	0.32	0.76	2.81	2.03	1.92	1.85	2.34	2.53	2.94	2.39
Ho	0.58	0.23	0.36	0.06	0.14	0.57	0.38	0.38	0.36	0.43	0.51	0.57	0.48
Er	1.73	0.66	1.10	0.21	0.51	1.67	1.12	1.11	1.08	1.22	1.44	1.55	1.39
Tm	0.27	0.10	0.17	0.03	0.09	0.24	0.17	0.17	0.16	0.19	0.20	0.22	0.21
Yb	1.81	0.67	1.19	0.29	0.72	1.62	1.17	1.19	1.16	1.19	1.39	1.41	1.40
Lu	0.29	0.10	0.18	0.06	0.14	0.24	0.18	0.19	0.18	0.18	0.20	0.22	0.21
U	0.82	0.09	1.06	1.04	1.41	0.33	0.37	0.38	0.79	0.45	0.31	0.24	0.44
Th	1.95	0.17	2.83	4.19	7.37	0.75	0.82	1.01	2.12	0.97	0.64	0.43	1.13
Pb	3.85	3.05	4.79	7.46	4.38	2.74	4.54	5.29	4.07	3.23	1.70	2.23	3.97
Y	16.04	5.64	10.25	1.93	4.43	14.13	9.93	9.14	9.37	11.12	12.59	14.10	13.08
Nb	3.87	1.54	3.59	1.30	1.46	2.26	1.31	2.18	3.58	1.26	1.44	2.58	2.69
Hf	6.64	0.80	2.23	1.88	2.64	1.65	1.78	1.75	2.16	1.26	1.23	1.67	1.40
Ta	0.31	0.11	0.28	0.18	0.00	0.11	0.03	0.01	0.29	0.35	0.19	0.30	0.19
Ratios													
$(La/Yb)_N$	3.75	2.57	4.96	10.49	15.33	1.85	3.11	3.45	4.85	3.77	1.40	2.42	2.25
$(La/Sm)_N$	2.21	1.84	2.91	7.93	8.52	1.34	1.79	2.23	3.06	1.37	0.92	1.15	1.66
$(Sm/Yb)_N$	1.70	1.40	1.71	1.33	1.80	1.39	1.74	1.55	1.59	2.76	1.52	2.10	1.36
$(Ce/Yb)_N$	3.24	1.95	4.12	6.15	11.73	1.60	2.62	2.78	3.49	3.51	1.37	2.33	1.77
$(Nd/Yb)_N$	2.43	1.65	2.63	2.65	4.54	1.56	2.32	2.18	2.38	3.68	1.64	2.54	1.55
$(Th/Nd)_N$	2.45	0.87	5.02	30.74	12.50	1.65	1.67	2.16	4.26	1.23	1.55	0.66	2.88
La/Nb	2.59	1.64	2.41	3.39	11.14	1.96	4.09	2.76	2.31	5.20	1.98	1.94	1.73
Nb/Ta	12.63	13.59	12.76	7.24	622	20.72	38.37	161	12.48	3.63	7.81	8.66	14.29

Table D.2: ICP-OES data

Sample	Lith.	La	Ce	Pr	Nd	Sm	Eu	Gd	Dy	Er	Yb	Lu
Aruba Lava Formation												
ARU96-2	A1	3.86	9.51	1.37	7.09	2.44	0.93	3.14	3.81	2.56	2.17	0.34
ARU96-21	A1	2.71	7.22	0.95	5.18	1.63	0.74	2.67	3.43	2.14	1.79	0.29
ARU96-30	A2	3.00	6.81	1.08	5.02	1.77	0.75	2.56	3.16	2.10	1.75	0.28
ARU96-37	A2	3.77	10.06	1.43	7.02	2.09	0.71	3.58	4.34	2.69	2.39	0.42
ARU96-38	A2	1.55	4.00	0.62	3.33	1.20	0.39	1.28	1.43	0.79	0.67	0.10
ARU96-147	A4	3.76	6.92	0.89	3.87	0.75	n.d.	1.22	1.46	0.88	0.79	0.15
Aruba batholith												
ARU96-57	B1	1.96	5.07	0.74	4.51	1.42	0.47	1.55	1.73	0.76	0.65	0.09
ARU96-154	B2b	1.04	2.76	0.44	2.36	0.83	0.19	0.88	0.87	0.50	0.47	0.07
ARU96-42	B3	3.44	7.35	1.03	5.61	1.48	0.52	1.51	1.41	0.82	0.74	0.14
ARU96-158	B4	6.90	16.44	2.20	10.90	2.68	0.83	2.91	2.73	1.53	1.47	0.22
ARU96-131	B5	7.78	16.34	2.00	8.29	2.30	0.75	2.08	2.00	1.10	1.03	0.16
ARU96-136	B9	5.97	12.71	1.69	8.35	1.99	0.69	1.91	1.71	1.07	1.10	0.20

Table D.3: INAA data

a) REE analyses

Sample	Lith.	La	Ce	Nd	Sm	Eu	Gd	Tb	Yb	Lu
Aruba Lava Formation										
ARU96-2	A1	3.4	8.7	7.08	2.22	0.9	2.28	0.59	2.28	0.36
ARU96-21	A1	2.7	7.0	5.20	1.86	0.74	1.88	0.42	1.75	0.28
ARU96-30	A2	2.3	6.0	4.37	1.56	0.66	1.68	0.41	1.77	0.26
ARU96-37	A2	3.5	8.7	7.51	2.27	0.91	2.24	0.55	2.30	0.38

b) other elements

Sample	Lith.	Th	Hf	Sc	Co	U	Ta	Zr[a]	Nb[b]	Zr/Hf	Nb/Ta
Aruba Lava Formation											
ARU96-2	A1	0.37	1.70	51.9	49.3	bdl	0.29	63	4.16	37.1	14.6
ARU96-21	A1	0.50	1.30	46.5	60.0	bdl	0.23	46	3.08	35.4	13.4
ARU96-30	A2	0.23	1.14	50.6	49.6	bdl	0.19	38	2.72	33.3	14.7
ARU96-37	A2	0.37	1.70	49.5	48.1	bdl	0.31	60	4.57	35.3	15.0

Notes: [a] XRF Zr data
[b] ICP-MS Nb data

Appendix E

Data Quality for XRF and REE Analyses

E.1 XRF

E.1.1 Major elements

XRF accuracy and precision was assessed by running international, in-house and personal reference materials with each batch of unknown samples. Data for international and in-house reference materials are presented in Table E.1, together with the recommended values, where appropriate. Accuracy and precision are generally good, although for some runs, the precision for Na_2O was poor; this fault was rectified and none of the data reported in Appendix C is affected by this. Data for the personal reference materials are presented in Table E.2, and can be used as a guide to analytical precision over the two to three year period that samples were analysed by XRF in Leicester. Table E.3 displays analytical data for four samples for which repeat fusion beads were made. This demonstrates that, even with different aliquots of sample, the precision is reasonably good for most elements. The data for Na_2O show more variability; it is not known whether this is due primarily to: 1) loss of Na during fusion (due to its volatility); 2) handling of fusion beads introducing Na contamination from sweat; or 3) poor analytical precision for Na_2O at the time these samples were run.

E.1.2 Trace elements

Precision and accuracy of trace element analyses was also monitored using international, in-house, and personal reference materials. Data for the international and in-house reference materials are presented in Table E.4. For most elements, there is good agreement with the analysed values and the recommended values. However, in the Aruba batholith and the Aruba Lava Formation, some elements (e.g., Nb, La, Ce, Nd) occur at low levels, close to the detection limit for the counting times used. For this reason, ICP-MS data (where available) were used for these elements.

Trace element analyses for personal reference materials are presented in Table E.5.

Appendix E: Table E.1 - XRF major element standards

	SiO_2	TiO_2	Al_2O_3	$Fe_2O_{3(t)}$	MnO	MgO	CaO	Na_2O	K_2O	P_2O_5	Total
406:AGV-1	59.04	1.08	17.61	6.79	0.10	1.41	4.92	5.11	3.06	0.52	99.66
407:AGV-1	59.05	1.07	17.66	6.80	0.10	1.40	4.98	5.19	3.07	0.52	99.87
408:AGV-1	59.18	1.07	17.65	6.84	0.10	1.42	4.99	5.17	3.14	0.53	100.11
AGV-1 rec	**58.79**	**1.05**	**17.14**	**6.76**	**0.09**	**1.53**	**4.94**	**4.26**	**2.91**	**0.49**	**100.00**
406:AN-G	45.89	0.20	30.92	3.38	0.05	1.68	16.06	1.58	0.14	0.02	99.92
407:AN-G	46.12	0.20	30.90	3.35	0.05	1.66	15.99	1.61	0.14	0.02	100.05
408:AN-G	46.19	0.21	30.84	3.36	0.05	1.68	16.07	1.59	0.15	0.02	100.15
AN-G rec	**46.30**	**0.22**	**29.80**	**3.36**	**0.04**	**1.80**	**15.90**	**1.63**	**0.13**	**0.01**	**99.79**
447:$ARSiO_2$	99.91	0.00	0.00	0.02	0.00	0.10	0.00	0.44	0.00	0.01	100.43
448:$ARSiO_2$	99.14	0.00	0.00	0.02	0.01	0.11	0.00	0.45	0.00	0.01	99.69
469:$ARSiO_2$	100.19	0.00	0.00	0.02	0.01	0.09	0.00	0.23	0.00	0.01	100.50
470:$ARSiO_2$	100.51	0.00	0.00	0.02	0.01	0.11	0.00	0.23	0.00	0.01	100.81
502:$ARSiO_2$	99.49	0.01	0.04	0.01	0.01	0.01	0.00	0.56	0.07	0.01	100.20
503:$ARSiO_2$	99.00	0.00	0.05	0.01	0.01	0.01	0.00	0.55	0.07	0.01	99.71
504:$ARSiO_2$	99.24	0.00	0.05	0.01	0.01	0.00	0.00	0.55	0.07	0.01	99.92
505:$ARSiO_2$	99.41	0.00	0.04	0.01	0.01	0.02	0.00	0.54	0.07	0.01	100.11
506:$ARSiO_2$	99.55	0.00	0.04	0.01	0.01	0.01	0.00	0.56	0.07	0.01	100.26
530:$ARSiO_2$	99.63	0.01	0.02	0.01	0.01	0.00	0.00	0.59	0.07	0.01	100.32
$ARSiO_2$ rec	**100.00**										
469:BCS353	21.01	0.11	3.61	4.74	0.18	2.52	64.78	0.42	0.23	0.10	97.70
470:BCS353	20.78	0.11	3.58	4.78	0.18	2.51	64.33	0.40	0.23	0.09	96.99
BCS353 rec	**20.50**	**0.16**	**3.77**	**4.82**	**N/A**	**2.42**	**64.80**	**0.10**	**0.49**	**0.08**	**97.14**
502:BCS372/1	20.68	0.16	5.12	3.36	0.06	1.33	65.49	0.35	0.36	0.08	96.99
530:BCS372/1	20.57	0.15	5.05	3.38	0.06	1.34	66.31	0.31	0.35	0.09	97.59
503:BCS372/1	20.61	0.16	5.17	3.38	0.06	1.35	65.95	0.34	0.36	0.08	97.44
504:BCS372/1	20.66	0.16	5.17	3.36	0.06	1.29	65.86	0.32	0.36	0.08	97.33
505:BCS372/1	20.65	0.16	5.13	3.38	0.06	1.36	65.79	0.32	0.37	0.08	97.30
506:BCS372/1	20.66	0.16	5.13	3.38	0.06	1.29	65.59	0.31	0.36	0.09	97.03
BCS372/1 rec	**20.30**	**0.27**	**5.37**	**3.42**	**N/A**	**1.31**	**65.30**	**0.10**	**0.75**	**0.07**	**96.89**
447:BCS375	67.03	0.41	20.49	0.15	0.01	0.04	0.81	10.49	0.77	0.03	100.23
448:BCS375	66.33	0.40	20.24	0.15	0.01	0.05	0.81	10.43	0.78	0.02	99.23
469:BCS375	67.58	0.40	19.96	0.11	0.01	0.05	0.80	10.46	0.76	0.02	100.17
470:BCS375	67.26	0.40	19.91	0.12	0.01	0.04	0.80	10.52	0.76	0.02	99.82
BCS375 rec	**67.10**	**0.38**	**19.80**	**0.12**	**N/A**	**0.05**	**0.89**	**10.40**	**0.79**	**N/A**	**99.53**
447:BCS376	67.39	0.00	18.42	0.10	0.01	0.03	0.47	2.99	11.29	0.02	100.71
448:BCS376	66.51	0.01	18.03	0.10	0.01	0.06	0.48	2.95	11.23	0.02	99.39
470:BCS376	67.90	0.01	17.88	0.10	0.01	0.05	0.45	2.72	11.19	0.01	100.32
BCS376 rec	**67.10**	**<0.02**	**17.70**	**0.10**	**N/A**	**0.03**	**0.54**	**2.83**	**11.20**	**N/A**	**99.50**
406:BH-1a	68.36	0.42	14.76	5.81	0.14	2.56	3.54	4.32	0.82	0.07	100.81
407:BH-1a	68.33	0.41	14.81	5.80	0.14	2.54	3.34	4.26	0.85	0.07	100.55
408:BH-1a	67.38	0.42	14.60	5.74	0.14	2.55	3.52	4.28	0.83	0.07	99.52
447:BH-1	68.62	0.43	14.68	5.94	0.14	2.77	3.53	3.39	0.86	0.08	100.45
406:BH-1b	67.83	0.41	14.51	5.75	0.13	2.51	3.47	4.24	0.88	0.07	99.81
407:BH-1b	67.85	0.42	14.58	5.74	0.13	2.52	3.37	4.23	0.90	0.07	99.81
408:BH-1b	67.77	0.41	14.50	5.74	0.14	2.52	3.17	4.29	0.92	0.07	99.51
In-house standard for assessment of precision only.											
406:BHVO-1	48.64	3.16	13.81	11.99	0.17	7.10	11.34	3.10	0.54	0.27	100.14
407:BHVO-1	48.54	3.13	13.88	12.00	0.18	7.20	11.35	3.00	0.54	0.27	100.08
408:BHVO-1	48.65	3.22	13.80	11.99	0.18	7.12	11.21	3.21	0.55	0.27	100.20
BHVO-1 rec	**49.94**	**2.71**	**13.80**	**12.23**	**0.17**	**7.23**	**11.40**	**2.26**	**0.52**	**0.27**	**101.73**
406:BOB-1	50.43	1.28	16.98	8.63	0.15	7.56	11.44	3.14	0.34	0.17	100.13
407:BOB-1	50.47	1.28	17.02	8.63	0.15	7.54	11.48	3.11	0.34	0.17	100.19
408:BOB-1	50.35	1.27	17.02	8.64	0.15	7.57	11.34	3.16	0.35	0.17	100.00
BOB-1 rec	**49.83**	**1.27**	**16.42**	**8.55**	**0.14**	**7.51**	**11.13**	**3.06**	**0.35**	**0.17**	**99.16**

Appendix E: Table E.1 - XRF major element standards

	SiO_2	TiO_2	Al_2O_3	$Fe_2O_{3(t)}$	MnO	MgO	CaO	Na_2O	K_2O	P_2O_5	Total
406:GHa	48.52	1.36	16.32	11.05	0.20	9.85	6.64	4.42	1.10	0.44	99.89
407:GHa	48.43	1.36	16.33	11.05	0.20	9.91	6.63	4.52	1.08	0.44	99.97
408:GHa	48.51	1.42	16.32	10.97	0.20	9.87	6.63	4.39	1.07	0.44	99.82
In-house standard for assessment of precision only.											
406:GHb	48.60	1.37	16.38	10.89	0.19	9.76	6.66	4.50	1.10	0.44	99.88
407:GHb	48.74	1.37	16.51	10.90	0.20	9.82	6.68	4.47	1.09	0.43	100.21
408:GHb	48.52	1.34	16.41	10.90	0.20	9.79	6.54	4.54	1.11	0.44	99.79
In-house standard for assessment of precision only.											
502:JGb-1	43.36	1.43	17.67	15.27	0.18	7.55	11.90	1.31	0.28	0.05	99.00
503:JGb-1	43.35	1.44	17.63	15.30	0.18	7.62	11.81	1.34	0.28	0.05	98.99
504:JGb-1	43.47	1.44	17.67	15.23	0.18	7.78	11.87	1.30	0.28	0.06	99.28
505:JGb-1	43.43	1.46	17.68	15.32	0.18	7.57	11.87	1.31	0.29	0.05	99.16
506:JGb-1	43.51	1.44	17.63	15.28	0.18	7.64	11.85	1.34	0.28	0.06	99.21
JGb-1 rec	**43.44**	**1.62**	**17.66**	**15.16**	**0.17**	**7.83**	**11.98**	**1.23**	**0.24**	**0.05**	**99.63**
447:JP-1	44.26	0.01	0.61	8.51	0.13	46.04	0.54	0.13	0.01	0.01	100.25
502:JP-1	44.25	0.01	0.66	8.74	0.13	46.00	0.50	0.00	0.07	0.01	100.29
503:JP-1	44.38	0.01	0.66	8.74	0.12	46.35	0.50	0.00	0.07	0.01	100.78
504:JP-1	44.68	0.01	0.66	8.66	0.12	47.15	0.50	0.00	0.07	0.01	101.79
505:JP-1	44.33	0.01	0.66	8.77	0.12	45.94	0.50	0.00	0.07	0.01	100.30
506:JP-1	44.58	0.01	0.66	8.72	0.12	46.01	0.51	0.01	0.07	0.01	100.70
530:JP-1	44.25	0.01	0.66	8.65	0.12	47.10	0.50	0.02	0.07	0.01	101.39
JP-1 rec	**42.39**	**N/A**	**0.62**	**8.34**	**0.12**	**44.72**	**0.56**	**0.02**	**0.00**	**N/A**	**99.22**
406:JR-1	75.08	0.11	13.15	0.90	0.10	0.07	0.65	5.33	4.94	0.03	100.36
407:JR-1	74.49	0.11	12.99	0.89	0.11	0.06	0.66	5.31	4.91	0.03	99.55
408:JR-1	74.41	0.11	13.04	0.89	0.11	0.07	0.64	5.30	4.94	0.03	99.53
447:JR-1	76.03	0.12	13.09	0.91	0.11	0.18	0.68	4.05	4.48	0.02	99.67
448:JR-1	75.52	0.11	12.94	0.91	0.11	0.17	0.71	4.06	4.47	0.02	99.02
502:JR-1	75.60	0.11	12.51	0.92	0.10	0.08	0.67	3.96	4.19	0.02	98.14
502:JR-1	75.37	0.10	12.46	0.93	0.10	0.08	0.68	4.07	4.38	0.02	98.18
503:JR-1	75.65	0.10	12.48	0.93	0.10	0.08	0.66	4.03	4.23	0.02	98.27
503:JR-1	75.47	0.10	12.45	0.94	0.10	0.08	0.67	4.07	4.38	0.02	98.28
504:JR-1	75.87	0.11	12.49	0.92	0.10	0.09	0.68	3.95	4.21	0.02	98.44
504:JR-1	75.78	0.11	12.43	0.93	0.10	0.08	0.67	4.11	4.38	0.02	98.60
505:JR-1	75.81	0.11	12.53	0.92	0.10	0.07	0.66	4.01	4.22	0.02	98.44
505:JR-1	75.72	0.11	12.46	0.93	0.10	0.06	0.67	4.07	4.38	0.02	98.52
506:JR-1	75.86	0.10	12.52	0.92	0.10	0.06	0.66	4.06	4.22	0.02	98.53
506:JR-1	75.75	0.11	12.46	0.94	0.10	0.05	0.68	4.07	4.42	0.02	98.59
JR-1 rec	**75.41**	**0.10**	**12.89**	**0.96**	**0.10**	**0.09**	**0.63**	**4.10**	**4.41**	**0.02**	**99.83**
406:MRG-1	39.00	4.43	8.78	17.46	0.17	13.81	14.92	1.28	0.20	0.07	100.12
407:MRG-1	38.86	4.41	8.73	17.31	0.18	13.73	14.88	1.28	0.18	0.07	99.62
408:MRG-1	38.92	4.43	8.76	17.36	0.17	13.74	14.76	1.27	0.19	0.07	99.67
447:MRG-1	39.39	3.81	8.55	17.89	0.17	13.59	14.95	1.10	0.19	0.07	99.71
448:MRG-1	39.29	3.83	8.59	17.90	0.18	13.72	15.03	1.07	0.19	0.06	99.86
469:MRG-1	40.05	3.82	8.58	17.87	0.18	13.74	14.85	0.80	0.18	0.07	100.13
470:MRG-1	40.28	3.81	8.70	18.04	0.18	13.84	14.88	0.73	0.18	0.07	100.72
MRG-1 rec	**39.09**	**3.77**	**8.46**	**17.93**	**0.17**	**13.55**	**14.71**	**0.74**	**0.18**	**0.08**	**99.95**
447:NIM-D	39.13	0.02	0.17	16.61	0.22	43.65	0.28	0.09	0.01	0.01	100.20
448:NIM-D	39.09	0.02	0.17	16.63	0.22	43.81	0.27	0.08	0.01	0.01	100.32
NIM-D rec	**39.00**	**0.02**	**0.30**	**17.00**	**0.22**	**43.50**	**0.28**	**0.04**	**0.01**	**0.01**	**100.00**

Appendix E: Table E.1 - XRF major element standards

	SiO_2	TiO_2	Al_2O_3	$Fe_2O_{3(t)}$	MnO	MgO	CaO	Na_2O	K_2O	P_2O_5	Total
406:NIM-G	74.54	0.10	12.29	1.94	0.03	0.00	0.70	4.78	5.43	0.01	99.75
407:NIM-G	74.86	0.09	12.33	1.93	0.02	0.00	0.70	4.74	5.44	0.01	100.07
408:NIM-G	74.88	0.10	12.34	1.94	0.02	0.00	0.71	4.70	5.44	0.01	100.08
447:NIM-G	75.53	0.10	12.17	1.99	0.02	0.09	0.78	3.35	4.97	0.02	99.02
448:NIM-G	75.54	0.10	12.22	1.99	0.02	0.12	0.79	3.65	4.96	0.01	99.40
469:NIM-G	77.26	0.10	12.17	2.06	0.03	0.11	0.78	3.47	4.96	0.01	100.95
470:NIM-G	77.06	0.10	12.07	2.01	0.02	0.09	0.77	3.41	4.91	0.01	100.44
530:NIM-G	76.49	0.09	11.67	2.03	0.02	0.00	0.73	3.44	4.91	0.01	99.36
502:NIM-G	76.88	0.09	11.96	2.04	0.02	0.00	0.73	3.42	4.92	0.01	100.07
503:NIM-G	76.90	0.10	11.94	2.05	0.02	0.00	0.76	3.45	4.94	0.01	100.14
504:NIM-G	76.91	0.09	11.92	2.03	0.02	0.00	0.75	3.49	4.91	0.01	100.15
505:NIM-G	77.02	0.09	11.96	2.04	0.02	0.00	0.74	3.40	4.90	0.01	100.18
506:NIM-G	77.10	0.10	11.97	2.03	0.02	0.00	0.76	3.41	4.94	0.01	100.31
NIM-G rec	**75.70**	**0.09**	**12.08**	**2.02**	**0.02**	**0.06**	**0.78**	**3.36**	**4.99**	**0.01**	**99.11**
406:NIM-N	51.80	0.17	16.88	8.71	0.18	7.45	11.36	3.05	0.24	0.02	99.87
407:NIM-N	51.78	0.18	16.83	8.70	0.17	7.51	11.26	3.02	0.24	0.02	99.70
408:NIM-N	51.63	0.18	16.85	8.69	0.18	7.42	11.28	3.03	0.24	0.02	99.53
447:NIM-N	52.13	0.19	16.60	8.90	0.18	7.59	11.42	2.35	0.24	0.02	99.61
448:NIM-N	52.65	0.19	16.74	9.06	0.18	7.76	11.68	2.30	0.23	0.02	100.81
NIM-N rec	**52.64**	**0.20**	**16.50**	**8.91**	**0.18**	**7.50**	**11.50**	**2.46**	**0.25**	**0.03**	**100.17**
406:QLO-1	64.99	0.66	16.87	4.73	0.10	1.12	3.54	4.80	3.04	0.27	100.14
407:QLO-1	65.01	0.66	16.83	4.75	0.10	1.13	3.57	4.82	3.05	0.27	100.18
408:QLO-1	65.14	0.68	16.85	4.72	0.10	1.13	3.57	4.86	3.04	0.27	100.37
QLO-1 rec	**65.55**	**0.62**	**16.18**	**4.35**	**0.09**	**1.00**	**3.17**	**4.20**	**3.60**	**0.25**	**99.91**
406:W-1	52.37	1.04	15.70	10.90	0.17	6.59	10.95	2.41	0.59	0.14	100.87
407:W-1	52.56	1.06	15.64	10.83	0.17	6.64	10.92	2.36	0.60	0.14	100.91
408:W-1	52.44	1.06	15.62	10.93	0.17	6.67	10.88	2.45	0.61	0.14	100.97
447:W-1	51.99	1.07	15.49	10.91	0.17	6.60	10.79	2.10	0.62	0.14	99.90
448:W-1	52.27	1.10	15.26	11.10	0.17	6.69	10.87	2.19	0.62	0.14	100.41
502:W-1	52.81	0.99	14.97	11.30	0.17	6.43	10.99	2.18	0.57	0.13	100.53
503:W-1	52.92	0.99	14.89	11.31	0.17	6.48	10.94	2.25	0.57	0.14	100.65
504:W-1	53.06	0.99	14.93	11.26	0.17	6.60	10.96	2.21	0.57	0.13	100.87
505:W-1	53.09	0.99	14.98	11.31	0.17	6.46	10.99	2.20	0.56	0.13	100.87
506:W-1	52.99	0.99	14.98	11.30	0.17	6.49	10.96	2.18	0.58	0.13	100.77
530:W-1	52.81	0.93	14.71	11.23	0.16	6.60	10.90	2.24	0.56	0.13	100.29
W-1 rec	**52.46**	**1.07**	**15.00**	**11.11**	**0.17**	**6.62**	**11.00**	**2.16**	**0.64**	**0.13**	**100.36**
406:WS-1a	50.92	2.52	14.25	13.18	0.18	5.26	8.86	2.97	1.36	0.31	99.82
406:WS-1b	51.37	2.54	14.33	13.25	0.18	5.31	8.94	3.00	1.36	0.31	100.59
407:WS-1a	50.91	2.50	14.22	13.21	0.18	5.29	8.87	2.97	1.36	0.31	99.83
407:WS-1b	51.52	2.57	14.39	13.27	0.18	5.36	8.96	3.04	1.37	0.31	100.97
408:WS-1a	51.13	2.55	14.29	13.29	0.18	5.30	8.77	3.05	1.38	0.30	100.24
408:WS-1b	51.35	2.54	14.36	13.26	0.18	5.32	8.82	2.98	1.38	0.30	100.50
447:WS-1	50.92	2.58	14.05	13.63	0.19	5.37	8.88	2.36	1.37	0.30	99.65

In-house standard; but recommended data for WS-e (same rock) due to be published shortly.

Note: RHF run number precedes the name of the standard.

Appendix E: Table E.2 - personal reference materials run with each batch (XRF majors)

Run	SiO_2	TiO_2	Al_2O_3	$Fe_2O_{3(t)}$	MnO	MgO	CaO	Na_2O	K_2O	P_2O_5	Total
	LF8830										
406	67.25	0.36	16.25	4.67	0.10	1.73	4.81	4.54	1.00	0.11	100.82
407	67.17	0.37	16.25	4.70	0.10	1.75	4.86	4.56	1.02	0.11	100.89
408	66.89	0.38	16.15	4.67	0.11	1.72	4.83	4.61	1.01	0.10	100.47
447	66.56	0.39	16.13	4.66	0.10	1.89	4.81	3.37	0.99	0.10	98.99
448	67.51	0.39	16.03	4.81	0.11	1.93	4.94	3.40	1.01	0.11	100.24
469	68.06	0.39	15.63	4.78	0.10	1.96	4.84	3.54	0.99	0.11	100.40
470	67.96	0.40	15.64	4.72	0.11	1.92	4.82	3.46	0.98	0.11	100.12
471a	67.76	0.39	15.66	4.77	0.10	1.96	4.86	3.55	0.99	0.11	100.15
471b	67.59	0.39	15.66	4.84	0.10	1.96	4.80	3.63	0.99	0.12	100.09
471c	68.62	0.41	15.85	4.78	0.10	1.89	4.88	3.51	1.00	0.12	101.15
471d	67.40	0.39	15.58	4.81	0.10	1.95	4.76	3.58	1.00	0.11	99.68
471e	67.80	0.39	15.73	4.82	0.11	1.92	4.81	3.62	1.00	0.12	100.31
471f	68.44	0.40	15.75	4.78	0.10	1.92	4.85	3.49	1.00	0.11	100.84
471g	67.40	0.39	15.54	4.80	0.10	1.95	4.77	3.53	1.01	0.11	99.60
471h	68.42	0.40	15.84	4.82	0.11	1.91	4.83	3.56	1.00	0.11	101.00
	LF8831										
406	50.04	0.77	7.64	11.28	0.18	14.88	13.69	0.98	0.22	0.06	99.74
407	49.92	0.76	7.63	11.27	0.18	14.94	13.67	0.96	0.22	0.06	99.62
408	50.16	0.76	7.66	11.29	0.19	14.94	13.82	0.96	0.23	0.06	100.06
447	50.66	0.80	7.74	11.44	0.18	14.63	13.58	0.87	0.22	0.06	100.20
448	50.62	0.82	7.56	11.58	0.19	14.82	13.78	0.83	0.23	0.06	100.49
469	50.02	0.77	7.27	11.39	0.18	14.55	13.28	0.94	0.22	0.06	98.67
470	49.82	0.79	7.28	11.77	0.18	14.58	13.17	1.02	0.21	0.06	98.89
471a	46.45	0.82	18.96	12.05	0.19	10.31	14.16	1.05	0.23	0.08	104.31
471b	47.07	0.69	12.73	10.27	0.17	11.69	11.46	1.11	0.37	0.14	95.71
471c	47.26	0.65	19.37	10.35	0.16	11.69	10.23	1.05	0.48	0.25	101.50
471d	46.81	0.70	12.18	10.26	0.17	11.04	11.65	1.12	0.35	0.14	94.42
471e	47.23	0.66	19.27	10.32	0.16	11.58	10.24	1.02	0.49	0.26	101.21
471f	47.28	0.71	11.84	10.31	0.17	10.49	11.75	1.09	0.36	0.13	94.11
471g	47.32	0.65	19.52	10.30	0.16	11.47	10.18	1.07	0.48	0.26	101.40
471h	47.36	0.71	12.14	10.40	0.17	11.16	11.79	1.14	0.36	0.13	95.36
	LF8832										
406	59.42	0.75	15.24	7.57	0.11	4.69	8.34	4.10	0.42	0.22	100.86
407	58.84	0.75	15.00	7.45	0.11	4.67	8.17	4.07	0.42	0.22	99.69
408	58.79	0.75	15.01	7.43	0.11	4.57	8.20	4.04	0.42	0.22	99.55
447	59.37	0.78	15.38	7.51	0.10	4.80	8.14	3.08	0.42	0.22	99.80
448	59.56	0.80	14.91	7.69	0.11	4.85	8.32	3.01	0.44	0.22	99.91
469	59.59	0.78	14.59	7.59	0.10	4.84	8.13	3.15	0.42	0.23	99.42
470	59.91	0.79	14.67	7.63	0.11	4.77	8.15	3.22	0.43	0.23	99.90
471a	60.01	0.79	14.65	7.67	0.11	4.78	8.26	3.14	0.43	0.23	100.07
471b	60.01	0.78	14.62	7.64	0.11	4.84	8.17	3.19	0.44	0.23	100.02
471c	59.15	0.78	14.38	7.73	0.10	4.86	8.08	3.29	0.42	0.22	99.01
471d	59.88	0.78	14.61	7.70	0.10	4.76	8.20	3.19	0.44	0.23	99.90
471e	59.88	0.79	14.49	7.62	0.11	4.83	8.16	3.17	0.43	0.23	99.69
471f	59.13	0.77	14.43	7.74	0.10	4.80	8.07	3.27	0.43	0.22	98.98
471g	60.39	0.79	14.66	7.69	0.11	4.74	8.20	3.18	0.43	0.23	100.43
471h	59.64	0.79	14.62	7.67	0.10	4.83	8.14	3.12	0.42	0.23	99.56
	LF8833										
406	67.75	0.38	14.43	4.43	0.08	2.37	4.94	4.36	1.62	0.10	100.46
407	67.63	0.39	14.47	4.44	0.08	2.36	4.97	4.37	1.64	0.10	100.45
408	67.66	0.40	14.48	4.41	0.08	2.32	4.98	4.37	1.63	0.10	100.42
447	68.05	0.40	14.61	4.45	0.08	2.52	4.97	3.24	1.60	0.10	100.02
448	68.42	0.41	14.20	4.57	0.08	2.57	5.07	3.43	1.64	0.11	100.52
469	67.28	0.40	13.70	4.47	0.08	2.50	4.85	3.46	1.58	0.11	98.43
470	69.08	0.42	14.11	4.47	0.08	2.54	4.94	3.41	1.59	0.11	100.74
471a	67.39	0.41	13.77	4.44	0.08	2.52	4.90	3.31	1.60	0.10	98.52
471b	67.51	0.40	13.74	4.48	0.08	2.51	4.84	3.41	1.57	0.10	98.64
471c	67.52	0.40	13.74	4.46	0.08	2.50	4.87	3.36	1.58	0.10	98.61
471d	67.78	0.40	13.87	4.50	0.08	2.53	4.88	3.32	1.59	0.11	99.06
471e	67.38	0.40	13.77	4.46	0.08	2.52	4.84	3.38	1.58	0.10	98.51
471f	68.18	0.41	13.89	4.48	0.08	2.53	4.88	3.34	1.60	0.11	99.50
471g	67.15	0.40	13.69	4.50	0.08	2.50	4.82	3.40	1.59	0.10	98.22
471h	68.43	0.41	13.98	4.47	0.08	2.50	4.89	3.35	1.61	0.11	99.83

continued on next page

Appendix E: Table E.2 - personal reference materials run with each batch (XRF majors)

Run	SiO_2	TiO_2	Al_2O_3	$Fe_2O_{3(t)}$	MnO	MgO	CaO	Na_2O	K_2O	P_2O_5	Total
	LF8834										
406	49.65	0.80	15.46	10.69	0.18	9.86	11.36	1.88	0.07	0.06	100.00
407	49.80	0.80	15.40	10.63	0.18	9.86	11.33	1.86	0.07	0.06	99.99
408	49.71	0.80	15.49	10.63	0.18	9.83	11.33	1.89	0.07	0.06	99.99
447	50.47	0.86	15.72	10.49	0.18	10.17	11.17	1.45	0.06	0.06	100.64
448	49.87	0.88	14.85	10.67	0.19	10.28	11.21	1.47	0.06	0.06	99.53
469	50.27	0.86	14.79	10.61	0.18	10.19	11.01	1.61	0.06	0.06	99.64
470	50.58	0.88	14.85	10.70	0.18	10.31	11.07	1.58	0.07	0.06	100.28
471a	50.67	0.86	14.95	10.63	0.18	10.45	11.18	1.52	0.06	0.06	100.56
471b	50.56	0.86	14.82	10.83	0.18	10.40	11.07	1.60	0.06	0.05	100.44
471c	51.35	0.89	15.05	10.68	0.19	10.30	11.20	1.52	0.06	0.06	101.29
471d	50.74	0.87	14.88	10.64	0.18	10.45	11.11	1.56	0.06	0.05	100.55
471e	50.39	0.87	14.77	10.80	0.18	10.32	11.15	1.60	0.07	0.05	100.20
471f	51.58	0.88	15.04	10.69	0.19	10.29	11.17	1.59	0.07	0.07	101.57
471g	50.76	0.86	14.82	10.65	0.19	10.50	11.10	1.52	0.06	0.07	100.53
471h	51.58	0.88	15.18	10.64	0.19	10.36	11.20	1.55	0.07	0.06	101.70
	LF8835										
406	49.06	0.93	15.19	10.94	0.17	8.72	12.69	1.76	0.06	0.07	99.60
407	49.16	0.92	15.28	10.92	0.17	8.77	12.67	1.76	0.06	0.07	99.78
408	49.26	0.95	15.26	10.93	0.17	8.73	12.69	1.78	0.06	0.07	99.89
447	49.50	0.95	15.49	11.00	0.17	8.61	12.54	1.42	0.06	0.07	99.80
448	49.55	0.98	14.95	11.37	0.17	8.87	12.81	1.39	0.06	0.07	100.24
469	49.65	0.95	14.72	11.08	0.17	8.66	12.55	1.53	0.05	0.07	99.43
470	49.94	0.97	14.79	11.11	0.17	8.69	12.56	1.47	0.06	0.07	99.84
471a	49.87	0.96	14.70	11.15	0.17	8.73	12.63	1.49	0.06	0.07	99.84
471b	49.47	0.96	14.73	11.25	0.17	8.70	12.51	1.46	0.05	0.08	99.39
471c	49.33	0.96	14.63	11.18	0.17	8.79	12.44	1.50	0.06	0.07	99.13
471d	49.81	0.96	14.66	11.16	0.17	8.74	12.59	1.46	0.06	0.08	99.68
471e	49.40	0.96	14.60	11.13	0.17	8.72	12.51	1.47	0.06	0.07	99.10
471f	49.81	0.96	14.68	11.27	0.17	8.61	12.45	1.61	0.05	0.08	99.70
471g	49.43	0.97	14.68	11.17	0.17	8.83	12.49	1.48	0.05	0.07	99.34
471h	50.25	0.97	14.84	11.16	0.17	8.69	12.61	1.44	0.06	0.07	100.26

Table E.3: Comparison of major element data for duplicate fusion beads of the same sample

Run	SiO_2	TiO_2	Al_2O_3	$Fe_2O_{3(t)}$	MnO	MgO	CaO	Na_2O	K_2O	P_2O_5	Total
LF8745											
a	51.86	0.87	8.31	12.77	0.22	11.64	13.24	1.16	0.22	0.06	100.36
b	51.45	0.81	8.47	12.71	0.22	11.33	13.32	1.39	0.23	0.06	99.99
LF8795											
a	57.05	0.55	12.01	8.58	0.18	8.50	10.69	1.99	0.40	0.10	100.05
b	56.52	0.50	12.40	8.61	0.18	8.09	10.69	2.49	0.43	0.10	100.00
LF8793											
a	56.54	0.61	9.91	9.54	0.19	9.67	11.65	1.60	0.26	0.09	100.06
b	57.11	0.56	10.41	8.47	0.18	10.00	10.98	1.98	0.24	0.09	100.02
LF8803											
a	47.83	1.11	16.89	14.53	0.17	5.92	10.85	1.77	0.42	0.12	99.60
b	47.46	1.12	17.18	14.74	0.19	5.90	11.02	2.56	0.44	0.12	100.73

Appendix E: Table E.4 - XRF trace element standards

		Rb	Sr	Ba	Zr	Nb	Y	Sc	V	Cr	Co	Ni	Cu	Zn	Ga	La	Ce	Nd
b	AGV-1			1151		15		14	124	7						38	66	33
c	AGV-1			1198				15	121	7						36	66	35
d	AGV-1			1196				18	126	5	15					39	68	33
m	AGV-1	69	676		245	13	21					17	58	87	21			
p	AGV-1	71	670	1194	233	14	29	14	144	7	12	18	61	85	20			
q	AGV-1	70	670	1213	233	14	25	14	146	16	11	21	61	89	21			
r	AGV-1	70	675	1226	239	15	21	17	126	6	23	17	58	86	20			
	AGV-1	**67**	**662**	**1226**	**227**	**15**	**20**	**12**	**121**	**10**	**15**	**16**	**60**	**88**	**20**	**38**	**67**	**33**
b	AN-G					1										4	6	7
c	AN-G			30				25	73	59						1	0	1
d	AN-G			35				23	72	61	25					6	9	6
m	AN-G	2	80		9	0	10					35	17	21	20			
p	AN-G	2	76	38	17	2	9	18	76	45	9	30	21	20	19			
r	AN-G	2	75	13	12	2	7	19	71	47	19	33	16	21	18			
r	AN-G	0	77	16	17	3	8	22	77	45	18	33	17	25	20			
r	AN-G	0	74	22	15	2	6	20	74	42	19	35	14	25	18			
r	AN-G	0	75	0	13	2	7	19	75	49	19	35	13	24	19			
	AN-G	**1**	**76**	**34**	**15**	**2**	**8**	**10**	**70**	**50**	**25**	**35**	**19**	**20**	**18**	**2**	**5**	**2**
a	BCR-1					13										27	54	32
m	BCR-1	50	344		189	12	41					13	17	134	24			
q	BCR-1	50	332	720	192	12	36	29	455	12	51	18	28	129	23	29	51	31
r	BCR-1	50	340	742	191	13	38	32	396	0	51	12	27	122	23			
	BCR-1	**47**	**330**	**681**	**190**	**14**	**38**	**33**	**407**	**16**	**37**	**13**	**19**	**130**	**22**	**25**	**54**	**29**
a	BE-N					112										89	165	75
b	BE-N					109										83	154	75
c	BE-N			1173				31	266	358						85	160	75
d	BE-N			1190				34	273	361	58					90	155	78
e	BE-N	49	1426	1166	270	114	32	35	272	367	59	275	80	126	18	93	168	77
f	BE-N		1412		265	110												
h	BE-N		1394		267	108												
p	BE-N	51	1371	976	260	101	36	25	305	397	76	266	82	125	18	89	169	71
q	BE-N	50	1345	1006	259	99	30	25	311	341	72	259	75	120	18	92	164	69
r	BE-N	49	1369	1007	267	106	30	25	243	361	62	283	80	124	17			
r	BE-N	49	1373	1006	275	105	30	28	243	367	60	281	81	123	15			
r	BE-N	51	1397	995	276	108	31	28	254	375	62	279	83	128	17			
r	BE-N	48	1367	1006	272	105	30	30	262	366	59	284	82	123	16			
r	BE-N	46	1357	1014	267	106	28	30	249	384	60	277	85	122	18			
	BE-N	**47**	**1370**	**1025**	**265**	**100**	**30**	**22**	**235**	**360**	**60**	**267**	**72**	**120**	**17**	**82**	**152**	**70**
b	BHVO-1			158		19		34	340	282						16	40	26
c	BHVO-1			156				35	336	289						17	41	26
m	BHVO-1	10	409		173	18	30					120	137	105	23			
q	BHVO-1	12	392	151	171	18	24	31	375	271	55	116	134	103	22	17	44	25
r	BHVO-1	11	387	129	172	19	28	30	297	294	48	117	133	98	22			
	BHVO-1	**11**	**403**	**139**	**179**	**19**	**28**	**32**	**317**	**289**	**45**	**121**	**136**	**105**	**21**	**16**	**39**	**25**
b	BIR-1			27		1		39	321	392						1	3	2
c	BIR-1			19				40	306	383						1	2	5
e	BIR-1	1	109	17	15	1	17	39	308	403	49	161	127	66	16	0	2	2
m	BIR-1	1	113		19	0	19					167	128	68	16			
q	BIR-1	3	110	32	21	2	16	39	334	353	53	153	128	68	16	3	0	3
r	BIR-1	3	107	0	19	2	14	42	316	377	49	165	129	69	16			
	BIR-1	**1**	**108**	**8**	**22**	**2**	**16**	**44**	**313**	**382**	**51**	**166**	**126**	**71**	**16**	**1**	**3**	**3**
a	BOB-1					5										6	16	13
b	BOB-1					5										6	15	12
c	BOB-1			45				32	232	276						5	12	11
d	BOB-1			44				43	227	285	57					6	18	11
e	BOB-1	6	199	41	105	4	29	35	235	295	56	113	70	78	15	4	14	11
g	BOB-1		202		102	5												
n	BOB-1	6	204		101	4	30					116	60	80	16			
q	BOB-1	8	192	54	103	5	24	35	247	252	44	103	68	64	16	6	13	11
r	BOB-1	5	193	47	100	5	25	33	222	271	46	107	70	67	15			
r	BOB-1	5	198	35	101	6	27	36	237	277	45	110	72	67	16			

Appendix E: Table E.4 - XRF trace element standards

		Rb	Sr	Ba	Zr	Nb	Y	Sc	V	Cr	Co	Ni	Cu	Zn	Ga	La	Ce	Nd
r	BOB-1	6	197	40	98	5	27	34	228	269	44	110	69	68	14			
r	BOB-1	6	192	38	103	7	27	35	231	280	46	108	68	65	13			
r	BOB-1	8	190	51	98	6	26	37	229	267	43	106	73	69	15			
	BOB-1	**6**	**190**	**44**	**100**	**5**	**26**		**234**	**304**		**115**		**63**	**16**	**6**	**15**	**11**
a	BR					113										81	154	72
i	BR	49	1345		257	104	30					273	74	154	18			
j	BR	47	1389		256	109	34					267	78	126	19			
m	BR	51	1436		268	110	34					286	74	171	18			
n	BR	51	1431		266	111	33					289	69	168	18			
p	BR	52	1361	1021	260	102	35	25	300	375	66	268	85	160	17	84	167	67
r	BR	50	1391	1058	278	110	31	24	248	354	60	287	88	155	18			
r	BR	48	1408	1041	279	111	33	27	247	357	57	285	89	159	17			
r	BR	47	1383	1052	277	107	31	25	241	361	58	281	91	157	16			
r	BR	49	1402	1035	281	110	31	31	239	348	60	292	89	158	16			
r	BR	51	1391	1047	272	110	30	27	252	355	57	288	89	155	15			
	BR	**47**	**1320**	**1050**	**250**	**98**	**30**	**25**	**235**	**380**	**52**	**260**	**72**	**160**	**19**	**82**	**151**	**65**
b	DNC-1			111		2		31	147	275						7	10	6
c	DNC-1			111				30	141	264						5	9	5
r	DNC-1	2	143	100	37	2	15	32	146	272	47	241	89	65	15			
	DNC-1	**5**	**145**	**114**	**41**	**3**	**18**	**31**	**148**	**285**	**55**	**247**	**96**	**66**	**15**	**4**	**11**	**5**
b	DR-N			375		8		27	226	47						21	45	24
c	DR-N			374				27	215	44						19	41	24
h	DR-N		398		128	7												
r	DR-N	71	384	421	125	8	27	29	217	30	39	20	44	143	20			
	DR-N	**73**	**400**	**385**	**125**	**8**	**28**	**28**	**220**	**42**	**35**	**15**	**50**	**145**	**22**	**21**	**46**	**23**
b	DT-N			129		37		2	152	252						82	128	54
	DT-N	**5**	**27**	**130**	**370**	**N/A**	**10**	**2**	**150**	**240**	**15**	**16**	**7**	**28**	**30**	**90**	**134**	**50**
b	DTS-1			8		0		2	6	3878						2	0	0
	DTS-1	**0**	**0**	**2**	**4**	**2**	**0**	**4**	**11**	**3990**	**137**	**2360**	**7**	**46**	**1**	**0**	**0**	**0**
e	FK-N	861	39	214	2	1	7	1	0	13	17	12	4	9	23	1	0	2
	FK-N	**860**	**39**	**200**	**13**	**N/A**	**0**	**0**	**3**	**5**	**14**	**3**	**2**	**10**	**19**	**1**	**1**	**0**
a	G-2					12										87	158	57
b	G-2					12										86	161	54
d	G-2			1806				5	41	2	5					89	165	56
e	G-2	167	488	1805	319	12	13	6	39	4	4	7	12	83	23	91	162	57
h	G-2		466		315	11												
m	G-2	169	482		327	11	13					4	9	85	23			
q	G-2	106	840	733	726	87	119	21	353	435	67	225	60	159	55			
r	G-2	169	473	1882	315	13	12	7	36	8	6	2	10	82	23			
	G-2	**170**	**478**	**1882**	**309**	**12**	**11**	**4**	**36**	**9**	**5**	**5**	**11**	**86**	**23**	**89**	**160**	**55**
a	GA					13										17	32	16
d	GA			784				11	39	23	7					33	57	25
r	GA	170	292	820	134	12	21	11	41	8	6	6	17	70	15			
r	GA	163	301	829	133	12	25	12	39	0	7	5	20	69	14			
r	GA	169	298	829	136	13	22	8	38	0	6	5	20	70	16			
r	GA	170	297	843	134	12	24	12	39	5	7	5	17	72	15			
r	GA	167	293	831	134	12	23	12	42	10	7	4	20	70	15			
	GA	**175**	**310**	**840**	**150**	**12**	**21**	**7**	**38**	**12**	**5**	**7**	**16**	**80**	**16**	**40**	**76**	**27**
a	GH					94										19	45	28
d	GH			21				1	1	23	1					19	47	27
r	GH	391	9	0	145	92	80	2	2	10	0	10	19	61	24			
r	GH	387	8	0	150	92	83	3	7	13	0	8	20	61	23			
r	GH	387	9	9	148	93	83	2	2	7	0	11	21	61	23			
r	GH	392	9	9	148	92	82	4	3	8	0	9	22	61	22			
r	GH	387	8	0	140	92	81	5	0	5	0	11	18	62	22			
	GH	**390**	**10**	**20**	**150**	**85**	**75**	**1**	**5**	**6**	**0**	**3**	**3**	**85**	**23**	**25**	**60**	**29**

Appendix E: Table E.4 - XRF trace element standards

		Rb	Sr	Ba	Zr	Nb	Y	Sc	V	Cr	Co	Ni	Cu	Zn	Ga	La	Ce	Nd
h	GSP-1		227		524	25												
m	GSP-1	248	231		528	25	30					12	31	101	22			
r	GSP-1	253	223	1265	530	26	26	6	48	17	11	14	42	101	22			
	GSP-1	**254**	**234**	**1310**	**530**	**28**	**26**	**6**	**53**	**13**	**7**	**9**	**33**	**104**	**23**	**184**	**399**	**196**
a	JA-1					2										5	15	13
d	JA-1			290				33	103	11	14					6	12	11
e	JA-1	11	263	301	85	1	32	25	104	12	15	5	43	85	17	5	15	11
h	JA-1		258		84	1												
p	JA-1	12	259	331	84	3	32	27	122	3	13	4	46	96	18	0	10	11
q	JA-1	12	257	321	87	2	27	27	127	11	10	7	43	97	18	8	7	9
	JA-1	**12**	**266**	**307**	**87**	**2**	**31**	**28**	**105**	**7**	**12**	**2**	**42**	**91**	**17**	**6**	**13**	**11**
h	JA-2		251		123	9												
	JA-2	**68**	**252**	**317**	**119**	**10**	**18**	**20**	**130**	**465**	**30**	**142**	**29**	**63**	**16**	**16**	**33**	**14**
h	JA-3		284		119	3												
	JA-3	**36**	**294**	**318**	**123**	**3**	**19**	**22**	**172**	**68**	**21**	**36**	**45**	**68**	**17**	**10**	**23**	**12**
a	JB-1A					28										39	68	30
b	JB-1A					27										39	65	28
r	JB-1A	41	447	537	140	28	22	27	189	369	39	134	52	75	15			
	JB-1A	**41**	**443**	**497**	**144**	**27**	**25**	**28**	**220**	**415**	**40**	**140**	**56**	**82**	**18**	**38**	**67**	**N/A**
a	JB-2					1										4	6	6
e	JB-2	7	177	227	47	0	26	40	564	12	33	15	225	109	17	5	9	5
p	JB-2	9	174	243	50	2	26	48	591	30	55	16	221	107	17	5	2	6
q	JB-2	9	176	242	51	2	22	50	595	30	59	15	224	107	17	0	22	9
r	JB-2	6	179	239	50	2	25	55	566	0	53	14	227	107	16			
r	JB-2	7	179	234	48	2	25	49	567	0	51	13	229	106	16			
r	JB-2	8	181	243	55	1	24	53	564	4	50	11	227	103	18			
r	JB-2	5	177	243	52	3	23	50	565	0	54	14	225	107	17			
	JB-2	**6**	**178**	**208**	**52**	**1**	**26**	**54**	**578**	**27**	**40**	**14**	**227**	**110**	**17**	**2**	**7**	**7**
a	JB-3					2										9	23	16
e	JB-3	16	414	256	93	2	28	34	354	50	35	36	199	93	20	11	21	18
i	JB-3	15	411		100	2	29					60	193	95	21			
j	JB-3	15	416		92	2	30					56	203	94	21			
k	JB-3	14	400		92	1	25					56	201	89	26			
m	JB-3	15	424		96	1	29					36	196	94	21			
n	JB-3	15	426		96	1	28					38	193	96	22			
o	JB-3	16	424		95	1	28					37	193	96	21			
p	JB-3	17	411	252	97	3	28	34	379	55	40	32	193	95	20	8	21	18
q	JB-3	17	409	264	96	3	25	33	382	52	37	35	194	94	21	10	38	18
r	JB-3	14	412	249	88	2	28	35	350	40	42	37	199	95	22			
r	JB-3	12	413	264	94	4	27	30	347	35	42	36	200	94	21			
r	JB-3	14	412	265	94	3	28	37	362	38	45	36	198	93	19			
r	JB-3	14	408	266	90	4	27	35	351	27	44	35	196	92	19			
r	JB-3	68	364	478	143	7	18	13	69	14	13	15	6	47	17			
r	JB-3	68	366	480	149	7	18	12	62	20	13	13	5	47	16			
r	JB-3	67	361	485	146	7	17	14	65	14	12	16	5	46	15			
r	JB-3	66	354	478	142	7	17	11	59	19	12	13	5	48	16			
r	JB-3	67	353	483	148	6	18	9	67	16	13	12	4	46	15			
	JB-3	**13**	**395**	**251**	**99**	**2**	**28**	**33**	**383**	**60**	**36**	**39**	**198**	**106**	**21**	**9**	**21**	**17**
h	JF-1		161		34	0												
	JF-1	**264**	**163**	**1680**	**41**	**1**	**4**	**0**	**3**	**6**	**0**	**0**	**0**	**3**	**18**	**3**	**4**	**2**
h	JF-2		188		2	0												
	JF-2	**222**	**193**	**320**	**7**	**0**	**0**	**0**	**1**	**4**	**0**	**0**	**0**	**1**	**18**	**3**	**1**	**0**
c	JG-1			430				9	66	29						13	30	16
	JG-1	**181**	**184**	**462**	**114**	**13**	**29**	**7**	**25**	**65**	**4**	**6**	**2**	**42**	**17**	**22**	**46**	**20**
h	JG-2		19		90	14												
	JG-2	**297**	**16**	**67**	**97**	**15**	**89**	**2**	**3**	**8**	**4**	**2**	**0**	**13**	**19**	**18**	**46**	**24**

Appendix E: Table E.4 - XRF trace element standards

		Rb	Sr	Ba	Zr	Nb	Y	Sc	V	Cr	Co	Ni	Cu	Zn	Ga	La	Ce	Nd
a	JG-3					6										32	57	25
d	JG-3															18	29	14
h	JG-3		363		145	6												
m	JG-3	67	366		147	5	18					16	8	51	16			
p	JG-3	67	355	460	145	6	25	9	78	19	6	13	6	44	16	15	25	14
	JG-3	**66**	**372**	**453**	**137**	**6**	**19**	**9**	**73**	**24**	**11**	**13**	**6**	**45**	**17**	**22**	**42**	**16**
a	JGB-1					3										5	6	4
d	JGB-1			65				48	636	52	58					6	10	7
e	JGB-1	7	333	67	26	2	10	41	652	47	61	24	83	111	19	2	9	4
h	JGB-1		337		26	3												
p	JGB-1	8	325	76	34	3	11	38	691	65	83	23	89	122	19	4	9	6
q	JGB-1	9	325	85	33	3	10	37	683	63	87	25	89	113	20	6	6	5
r	JGB-1	4	323	78	30	4	10	40	622	24	60	29	87	106	19			
	JGB-1	**4**	**321**	**63**	**13**	**3**	**11**	**37**	**640**	**59**	**62**	**25**	**87**	**111**	**19**	**4**	**8**	**6**
h	JH-1		157		49	4												
	JH-1	**12**	**155**	**N/A**	**N/A**	**N/A**	**N/A**	**N/A**	**231**	**630**	**53**	**56**	**9**	**62**	**N/A**	**N/A**	**N/A**	**N/A**
e	JP-1	0	1	17	7	0	1	6	22	2740	104	2388	6	49	0	0	0	0
h	JP-1		4		7	0												
m	JP-1	2	1		4	0	0					2424	9	58	0			
p	JP-1	1	2	16	13	0	1	8	32	2826	99	2433	12	49	2	0	0	1
q	JP-1	1	2	20	15	0	3	7	32	2982	104	2280	11	56	2	0	2	0
r	JP-1	0	0	0	7	2	0	7	20	3032	72	2404	6	47	0			
	JP-1	**N/A**	**N/A**	**17**	**6**	**1**	**1**	**7**	**29**	**2970**	**116**	**2460**	**6**	**30**	**1**	**0**	**N/A**	**N/A**
a	JR-1					16										20	51	27
d	JR-1			51				6	6	15	2					20	51	25
e	JR-1	253	30	49	105	16	50	4	6	13	1	7	3	28	16	24	49	28
g	JR-1		28		104	15												
k	JR-1	254	28		103	15	45					3	0	26	16			
l	JR-1	250	28		101	14	49					3	5	27	16			
n	JR-1	250	28		102	14	48					3	0	28	16			
p	JR-1	253	29	62	100	15	73	5	18	6	0	8	3	39	17	18	38	23
q	JR-1	253	29	51	101	15	61	4	16	29	0	10	3	30	16			
r	JR-1	255	29	43	98	16	45	6	4	22	0	3	0	36	16			
r	JR-1	306	9	11	95	20	50	9	0	0	0	3	0	32	17			
	JR-1	**257**	**30**	**40**	**102**	**16**	**46**	**5**	**N/A**	**2**	**1**	**1**	**1**	**30**	**18**	**21**	**49**	**26**
e	JR-2	301	9	35	101	19	55	4	2	15	1	9	2	25	16	18	39	23
p	JR-2	303	9	35	96	18	84	3	11	5	0	9	3	27	17	14	37	18
q	JR-2	301	9	31	97	18	71	6	12	10	0	13	3	27	17	16	34	20
	JR-2	**297**	**8**	**39**	**99**	**19**	**51**	**6**	**N/A**	**3**	**0**	**1**	**1**	**27**	**18**	**18**	**38**	**25**
e	JR-3	465	9	59	1720	577	185	0	0	15	3	16	0	204	40	159	306	111
p	JR-3	468	10	72	1566	521	222	0	15	0	5	23	3	200	38	156	328	102
q	JR-3	465	10	72	1578	519	184	0	17	12	3	26	3	201	38	169	308	103
	JR-3	**458**	**9**	**N/A**	**N/A**	**N/A**	**N/A**	**N/A**	**N/A**	**3**	**1**	**1**	**2**	**204**	**N/A**	**N/A**	**N/A**	**N/A**
a	MRG-1					21										9	27	19
b	MRG-1			89		20		57	621	490						7	31	21
c	MRG-1			62				59	609	504						12	26	21
d	MRG-1			59				73	600	503	92					10	26	20
e	MRG-1	8	270	61	109	23	14	52	620	509	84	189	129	210	18	11	29	20
h	MRG-1		276		109	21												
i	MRG-1	10	267		100	19	15					186	119	211	18			
j	MRG-1	9	271		104	20	15					190	138	214	17			
k	MRG-1	8	266		98	19	15					189	135	202	20			
l	MRG-1	8	290		103	20	17					204	133	223	19			
m	MRG-1	10	287		104	21	16					203	135	228	20			
n	MRG-1	9	287		103	20	14					205	136	228	21			
o	MRG-1	8	291		106	20	16					206	130	231	21			
p	MRG-1	10	270	87	105	19	15	55	657	550	135	183	140	206	18	11	36	19
q	MRG-1	10	269	73	106	19	14	52	669	490	155	184	139	206	18	10	58	20
r	MRG-1	7	267	55	108	19	15	55	525	523	84	195	133	193	15			

Appendix E: Table E.4 - XRF trace element standards

		Rb	Sr	Ba	Zr	Nb	Y	Sc	V	Cr	Co	Ni	Cu	Zn	Ga	La	Ce	Nd
r	MRG-1	10	263	44	95	20	14	56	526	490	82	189	140	187	16			
r	MRG-1	4	264	45	106	21	13	50	537	507	82	194	136	187	17			
r	MRG-1	7	262	69	104	20	16	54	529	519	84	192	134	189	17			
r	MRG-1	8	261	46	110	21	15	53	530	492	81	192	143	192	18			
	MRG-1	**9**	**266**	**61**	**108**	**20**	**14**	**55**	**526**	**430**	**87**	**193**	**134**	**191**	**17**	**10**	**28**	**19**
a	NIM-G					57										102	194	78
c	NIM-G			102				1	0	24						95	189	76
d	NIM-G			104				1	1	21	1					101	193	79
e	NIM-G	310	12	107	287	56	148	2	0	23	2	14	12	52	28	107	192	76
f	NIM-G		10		303	52												
h	NIM-G		13		300	53												
i	NIM-G	309	12		292	53	147					4	10	49	27			
j	NIM-G	317	12		291	55	150					3	11	51	27			
k	NIM-G	321	12		287	52	136					4	15	50	30			
l	NIM-G	315	12		289	53	144					4	10	52	29			
m	NIM-G	312	12		291	53	143					4	12	52	29			
n	NIM-G	313	11		286	53	143					6	9	52	28			
o	NIM-G	316	12		281	51	143					4	10	52	28			
p	NIM-G	315	12	111	266	51	170	0	9	9	3	18	14	51	28	102	195	67
q	NIM-G	316	12	118	269	51	142	0	11	15	0	21	15	51	28	107	189	67
r	NIM-G	321	10	97	276	53	143	4	5	9	3	6	11	54	28			
r	NIM-G	319	12	108	277	54	146	6	0	13	0	4	14	55	27			
r	NIM-G	324	11	104	280	55	150	3	0	15	3	6	13	54	26			
r	NIM-G	322	11	102	280	55	148	3	0	10	0	6	11	54	28			
r	NIM-G	318	13	94	272	56	147	3	6	11	0	4	11	53	27			
	NIM-G	**320**	**10**	**120**	**300**	**53**	**143**	**1**	**2**	**12**	**4**	**8**	**12**	**50**	**27**	**109**	**195**	**72**
b	NIM-N					1										5	5	4
c	NIM-N			92				36	197	42						3	5	5
	NIM-N	**6**	**260**	**100**	**23**	**2**	**7**	**38**	**220**	**30**	**58**	**120**	**14**	**68**	**16**	**3**	**6**	**3**
a	PCC-1					0										2	0	0
e	PCC-1	1	1	0	1	0	1	5	25	2528	100	2340	9	45	0	0	0	0
m	PCC-1	2	1		2	0	1					2357	10	46	1			
p	PCC-1	0	1	0	9	0	2	10	35	2603	92	2380	14	44	2	0	2	0
q	PCC-1	1	1	0	10	0	2	7	39	2715	101	2235	14	46	2	0	0	0
r	PCC-1	0	0	0	6	1	0	8	30	2730	70	2365	12	48	2			
	PCC-1	**0**	**0**	**1**	**10**	**1**	**0**	**8**	**31**	**2730**	**112**	**2380**	**10**	**42**	**1**	**0**	**0**	**0**
c	QLO-1			1310				10	51	0						22	42	23
d	QLO-1			1319				12	53	0	8					27	47	22
h	QLO-1		335		195	10												
m	QLO-1	72	335		197	9	27					4	27	57	18			
	QLO-1	**74**	**336**	**1370**	**185**	**10**	**24**	**9**	**54**	**3**	**7**	**6**	**29**	**61**	**17**	**27**	**55**	**26**
a	RGM-1					9										21	40	19
p	RGM-1	141	96	826	213	9	39	3	26	0	3	4	7	31	15	20	32	18
q	RGM-1	141	98	842	215	9	33	5	23	8	0	6	8	31	15	20	35	18
	RGM-1	**149**	**108**	**807**	**219**	**9**	**25**	**4**	**13**	**4**	**2**	**4**	**12**	**32**	**15**	**24**	**47**	**19**
a	STM-1					278										123	242	83
d	STM-1			573				1	1	10	2					129	252	86
e	STM-1	116	726	560	1402	273	51	3	0	11	3	8	2	232	38	131	240	81
i	STM-1	117	719		1380	256	50					6	4	235	37			
j	STM-1	114	712		1371	267	53					5	1	235	37			
m	STM-1	118	721		1388	265	50					4	2	244	37			
q	STM-1	119	702	591	1267	242	51	0	13	11	4	8	5	229	35	143	255	80
r	STM-1	116	698	605	1461	255	49	0	0	8	11	5	5	222	35			
	STM-1	**118**	**700**	**560**	**1210**	**268**	**46**	**1**	**9**	**4**	**1**	**3**	**5**	**235**	**36**	**150**	**259**	**79**
d	SY-2			451				13	43	15	11					66	151	78
	SY-2	**217**	**271**	**460**	**280**	**29**	**128**	**7**	**50**	**10**	**9**	**10**	**5**	**248**	**29**	**75**	**175**	**73**
a	TYG					13										32	65	32
	TYG	**67**	**65**	**416**	**198**	**13**	**46**		**15**	**8**		**4**		**70**	**15**	**31**	**65**	**28**

Appendix E: Table E.4 - XRF trace element standards

		Rb	Sr	Ba	Zr	Nb	Y	Sc	V	Cr	Co	Ni	Cu	Zn	Ga	La	Ce	Nd
a	W-1					7										12	21	15
c	W-1			163				34	260	121						11	17	10
e	W-1	22	192	167	96	7	24	36	260	122	42	73	115	84	19	10	25	13
p	W-1	24	187	168	97	7	27	34	283	120	47	67	112	87	18	14	21	14
q	W-1	24	188	179	96	7	22	33	276	110	48	72	106	89	18	13	25	13
r	W-1	23	191	168	99	7	24	36	260	107	48	75	112	90	17			
r	W-1	19	190	178	96	9	25	34	255	101	46	69	116	86	16			
r	W-1	26	191	158	97	8	23	40	266	111	46	72	110	87	16			
r	W-1	21	188	179	96	8	24	37	265	112	44	71	115	87	17			
r	W-1	25	196	172	95	9	22	34	274	114	47	77	116	87	17			
	W-1	**21**	**186**	**162**	**99**	**10**	**26**	**35**	**257**	**119**	**47**	**75**	**113**	**84**	**17**	**11**	**24**	**15**
a	W-2					7										12	22	11
b	W-2			193		7		35	259	92						11	21	15
c	W-2			189				35	255	91						10	29	17
d	W-2			185				42	244	92	45					14	19	11
g	W-2		200		97	7												
g	W-2		199		98	7												
k	W-2	22	195		87	6	22					68	107	72	21			
l	W-2	248	28		102	14	49					2	3	28	16			
m	W-2	22	203		93	6	25					73	107	81	20			
p	W-2	22	196	195	98	8	25	34	278	96	44	65	108	79	19	13	21	13
	W-2	**20**	**194**	**182**	**94**	**8**	**24**	**35**	**262**	**93**	**44**	**70**	**103**	**77**	**20**	**11**	**24**	**14**
a	WS-1					17										30	67	39
e	WS-1	42	496	422	196	17	33	27	337	45	48	49	68	105	25	31	64	40
e	WS-1	43	497	434	196	16	34	28	339	50	45	50	70	107	25	30	65	39
h	WS-1		505		203	17												
i	WS-1	40	480		178	13	34					52	63	104	23			
j	WS-1	44	499		190	16	36					50	76	105	26			
k	WS-1	43	494		188	16	30					47	75	100	27			
l	WS-1	46	519		192	16	35					50	69	110	27			
m	WS-1	45	518		196	17	34					52	69	109	26			
n	WS-1	44	517		190	16	35					49	63	109	26			
o	WS-1	45	523		194	17	35					55	58	110	26			

In-house standard; but recommended data for WS-e (same rock) due to be published shortly.

Notes: letter in left hand column refers to run number as follows:

a	LAK17 and 18
b	LAK19, 20 and 21
c	LAK22 and 23
d	LAK24 and 25
e	LAK28, 29 and 30
f	ARHT50
g	ARHT50a
h	ARHT51
i	ARHT59
j	ARHT60
k	ARHT61
l	ARHT62
m	ARHT63
n	ARHT65
o	ARHT66
p	LRW1, 2 and 3
q	LRW4, 5 and 6
r	LRW13 and 14

Appendix E: Table E.5 - personal reference materials run with each batch (XRF trace elements)

		Rb	Sr	Ba	Zr	Nb	Y	Sc	V	Cr	Co	Ni	Cu	Zn	Ga	La	Ce	Nd
b	L29800					1										7	12	7
c	L29800			567				14	78	15						5	9	8
d	L29800			603				15	75	15	13					6	10	7
e	L29800	16	283	582	62	3	11	14	76	15	10	6	17	53	16	7	10	8
j	L29800	16	289		73	3	12					3	8	53	15			
m	L29800	17	286		70	3	12					5	9	50	14			
o	L29800	17	285		68	3	12					5	6	50	14			
q	L29800	17	283	647	73	4	12	16	85	17	5	4	14	48	15	1	0	6
b	L29801					4										4	0	6
c	L29801			52				56	270	1298						2	7	7
d	L29801			46				80	266	1354	64					3	7	7
e	L29801	2	105	50	19	1	15	49	271	1343	59	193	57	81	11	0	10	7
j	L29801	1	108		23	0	17					197	61	79	9			
m	L29801	2	111		23	1	16					199	48	83	11			
o	L29801	0	112		20	0	16					207	48	82	12			
q	L29801	3	109	67	28	2	14	66	282	1291	64	187	63	79	11	0	4	4
b	L29802					4										8	18	12
c	L29802			358				27	191	111						5	14	8
d	L29802			360				32	193	116	28					9	16	11
e	L29802	7	388	360	52	2	17	25	193	113	26	26	11	41	18	10	15	11
j	L29802	6	399		60	3	19					24	7	41	18			
m	L29802	6	402		64	3	18					26	5	41	16			
q	L29802	9	398	381	65	4	16	29	201	99	16	26	14	39	17	5	3	8
b	L29999					2										7	9	6
c	L29999			707				15	96	84						7	7	5
d	L29999			726				18	92	86	14					9	8	8
e	L29999	17	314	722	106	3	13	16	101	89	15	17	49	29	13	7	11	9
k	L29999	19	299		102	3	11					16	48	27	13			
m	L29999	18	303		105	3	13					17	40	28	13			
q	L29999	17	299	795	105	4	13	18	104	73	5	16	43	29	14	4	0	9
b	L30000					4										5	2	6
c	L30000			18				37	273	395						2	7	6
d	L30000			17				51	271	410	55					5	0	4
k	L30000	1	72		36	3	17					136	104	52	16			
m	L30000	2	75		39	2	18					140	98	59	14			
q	L30000	3	73	39	45	4	16	44	278	363	48	128	102	58	15	1	9	6
b	L30001					5										3	8	5
c	L30001			23				45	300	398						1	4	4
d	L30001			15				59	285	404	49					5	8	6
k	L30001	4	88		51	4	19					113	59	73	15			
m	L30001	1	93		50	2	22					119	60	79	16			
q	L30001	3	90	37	52	4	18	51	315	367	50	110	71	77	15	0	4	7

Codes for run numbers (left-hand column) as for Table E.4.

E.2 REE analyses

E.2.1 Comparison with international reference materials

Analyses of international reference materials were carried out, together with the Aruba samples, for INAA, ICP-MS and ICP-OES REE analyses. The data obtained are compared with the recommended values in Table E.6, and this is illustrated on Page E.17.

For La, Ce, Nd and Nb, the precision at low levels for the ICP-MS analyses is better than for XRF. The same is true for U and Th, which occur at very low abundances in these rocks: these are below the detection limit for XRF (and, consequently, are not reported), but can be measured by ICP-MS. Throughout this thesis, ICP-MS data (where available) are used in preference to XRF data for these elements. Eu, however, appears to be consistently low with respect to the recommended values for JB-2 and JB-1a.

Precision and accuracy for INAA are good, with the exception of Gd, which was problematic for this particular INAA batch (number 44). ICP-OES data are in good agreement with the recommended values for the standards.

E.2.2 Comparison between different analytical methods for REE determination

Samples that were analysed for REE more than once are reported in Table E.7, and illustrated on the following page (Page E.19). Agreement between methods is generally good, which is also a good indication that the dissolution process used for sample preparation was effective. There are, however, a few cases where agreement between methods is less good:

1) The LREE at low abundances: this is a particular problem for the mafic rocks of the batholith that are thought to represent cumulates, and have very low trace element abundances in general.

2) The low INAA Gd – there is a problem with Gd data for the Leicester INAA if a third count for Gd is not obtained. Comparison of the INAA Gd data with the recommended values shows that it *is* the INAA data that is at fault, not the ICP-MS data.

3) Ta data obtained by ICP-MS at Haarlem are not in good agreement with INAA data. The Nb/Ta ratios given by the ICP-MS data are variable, and distinctly sub-chondritic. The $Nb_{ICP\text{-}MS}/Ta_{INAA}$ ratios are more uniform, and closer to the chondritic value, as expected. Thus, it appears that the INAA Ta data are more reliable. However, because only four samples were measured by INAA, Ta has not been used in this study for any petrogenetic interpretations.

4) The Haarlem ICP-MS Eu data is in poor agreement with that obtained by the other methods; it is also in poor agreement with the recommended values for the reference materials. This is discussed further below.

E.2.3 The Eu correction

Because the Haarlem ICP-MS data appeared to be *consistently* low when compared to the international reference materials and the INAA and ICP-OES data, a correction was applied to all Haarlem data reported in Appendix D. The correction was derived using the JB-2 and JG-1a analyses (compared with the recommended values) and INAA data for the four samples that were run by this method. The correction is (expressed in ppm):

$$Eu_{measured} = 0.6949\ Eu_{corrected} - 0.0477$$

This recalibration was then checked using the Cardiff ICP-MS data and the ICP-OES data, and yielded reasonable agreement. It should be noted, however, that the degree of correction is sufficient to turn a small negative Eu anomaly into a small positive anomaly; consequently, not too much significance should be attached to the Eu data reported in this study.

Appendix E: Table E.6 - International standards for REE analyses

ICP-MS

	La	Ce	Pr	Nd	Sm	Eu	Gd	Tb	Dy	Ho	Er	Tm	Yb	Lu
BLANK	0.036	0.055	0.007	0.026	0.007	0.002	0.005	0.001	0.009	0.001	0.004	0.001	0.004	0.001
JB-2	2.6	6.8	1.16	6.4	2.23	0.53	2.73	0.54	3.91	0.81	2.40	0.37	2.52	0.38
JB-2	2.8	7.9	1.32	7.3	2.55	0.62	3.08	0.61	4.43	0.92	2.76	0.41	2.73	0.42
JB-2	2.3	6.5	1.13	6.2	2.21	0.55	2.78	0.56	3.92	0.81	2.46	0.35	2.49	0.38
JB-2	2.4	6.6	1.15	6.4	2.22	0.56	2.75	0.58	4.18	0.88	2.58	0.39	2.58	0.40
JB-2	2.3	6.4	1.15	6.3	2.28	0.58	2.87	0.62	4.29	0.91	2.65	0.40	2.72	0.40
JB-2	**2.37**	**6.77**	**0.96**	**6.70**	**2.25**	**0.86**	**3.28**	**0.62**	**3.66**	**0.81**	**2.63**	**0.45**	**2.51**	**0.39**
JG-1a	17.0	43.6	4.09	15.9	3.52	0.41	3.26	0.60	4.02	0.77	2.33	0.37	2.48	0.37
JG-1a	21.0	50.7	4.99	19.4	4.27	0.49	3.94	0.75	4.95	0.95	2.87	0.44	3.02	0.45
JG-1a	17.5	40.0	4.24	16.2	3.58	0.42	3.38	0.63	4.16	0.80	2.38	0.35	2.43	0.37
JG-1a	19.8	44.4	4.70	18.0	4.15	0.48	3.81	0.73	4.71	0.91	2.70	0.42	2.84	0.42
JG-1a	**21.80**	**45.20**	**6.08**	**21.00**	**4.85**	**0.72**	**3.75**	**0.79**	**4.20**	**0.76**	**2.36**	**0.39**	**2.74**	**0.44**

ICP-MS (continued)

	Y	Nb	Hf	Ta	U	Th	Pb
BLANK	0.030	0.011	0.008	0.001	0.003	0.014	1.451
JB-2	21	0.7	3.47	0.08	0.24	0.39	7.26
JB-2	25	0.6	2.72	0.13	0.19	0.33	6.81
JB-2	21	0.5	1.68	0.12	0.15	0.27	6.45
JB-2	21	0.5	2.09	0.05	0.17	0.30	7.60
JB-2	21	0.4	1.59	0.01	0.16	0.28	10.57
JB-2	**26**	**0.8**	**1.42**	**0.20**	**0.16**	**0.33**	**5.40**
JG-1a	24	11.1	3.04	1.56	4.08	9.89	21.08
JG-1a	30	11.6	3.76	1.43	4.46	11.45	26.23
JG-1a	25	10.2	3.19	1.40	3.94	10.00	22.91
JG-1a	26	6.4	2.36	0.27	3.72	10.77	28.94
JG-1a	**32.1**	**11.4**	**3.84**	**1.70**	**4.7**	**12.10**	**27.00**

INAA

	La	Ce	Nd	Sm	Eu	Gd	Tb	Yb	Lu	Ta	Th	Hf	Sc	Co	U
JB-1a	37.2	63.9	26.5	5.0	1.5	0.8	0.7	2.0	0.3	1.6	9.3	3.6	*29.0*	*39.5*	nd
JB1-a	*36.9*	*64.0*	*25.1*	*5.1*	*1.5*	3.8	*0.7*	*2.1*	*0.3*	*1.6*	*9.3*	*3.6*	*28.9*	*40.7*	*1.9*
JB-1a	**38.0**	**67.0**	**27.0**	**5.0**	**1.5**	**4.7**	**0.7**	**2.1**	**0.3**	**2.0**	**8.8**	**3.4**	**cal**	**cal**	**1.6**
WS-1A	26.0	56.1	31.0	7.1	2.2	6.0	0.9	2.4	0.3	1.0	3.0	5.2	29.9	51.1	-
WS-1A	*26.6*	*56.5*	*32.7*	*7.2*	*2.3*	*6.96*	*1.1*	*2.6*	*0.4*	*1.1*	*3.1*	*5.4*	*29.5*	*49.6*	*0.7*

In-house standard; but recommended data for WS-e (same rock) due to be published shortly.

ICP-OES

	La	Ce	Pr	Nd	Sm	Eu	Gd	Dy	Er	Yb	Lu
DR-N	20.30	44.96	5.49	21.74	4.97	1.38	4.69	4.14	2.39	2.45	0.35
DR-N	**21.5**	**46**	**5.7**	**23.5**	**5.4**	**1.45**	**4.7**	**4.6**	**2.5**	**2.5**	**0.4**
JGb-1	3.71	8.74	1.20	5.91	1.50	0.55	1.75	1.59	1.02	0.81	0.14
JGb-1	**3.6**	**8.17**	**1.13**	**5.47**	**1.49**	**0.62**	**1.61**	**1.56**	**1.04**	**1.06**	**0.15**
JB-2	2.51	6.83	1.19	6.66	2.11	0.78	3.49	4.05	2.50	2.44	0.41
JB-2	**2.37**	**6.77**	**0.96**	**6.7**	**2.25**	**0.86**	**3.28**	**3.66**	**2.63**	**2.51**	**0.39**

Notes: BLANK is the average of the eleven blank samples prepared and run.
Values in bold are the recommended values
Values in italics (INAA) are the average values obtained over the last ten runs

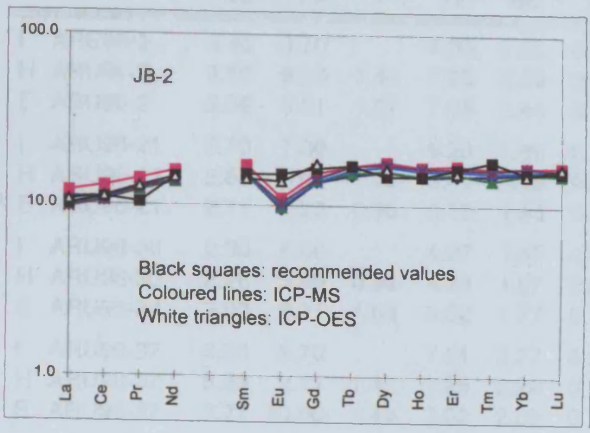

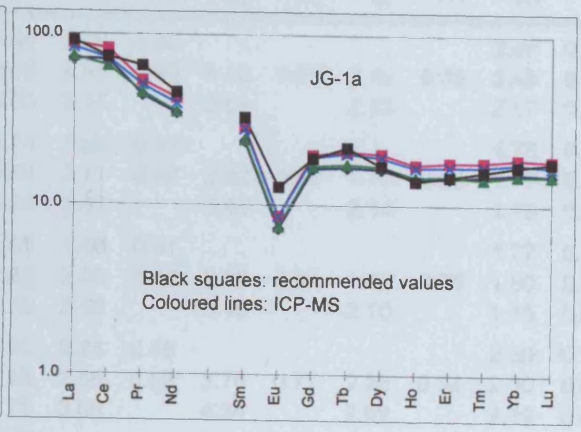

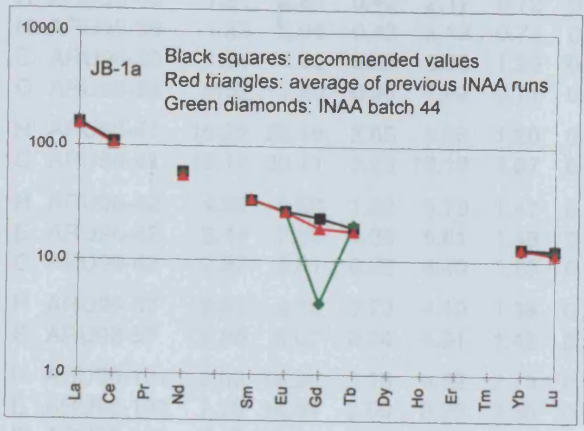

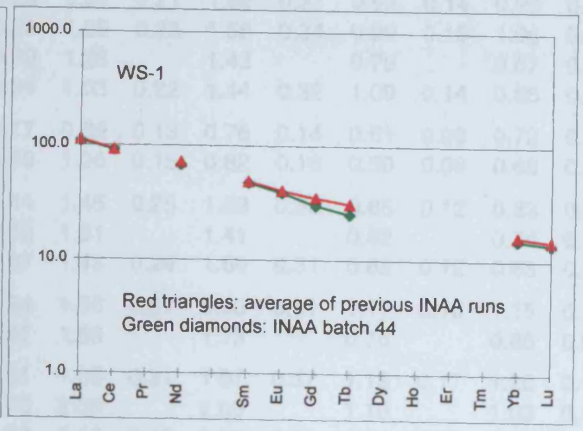

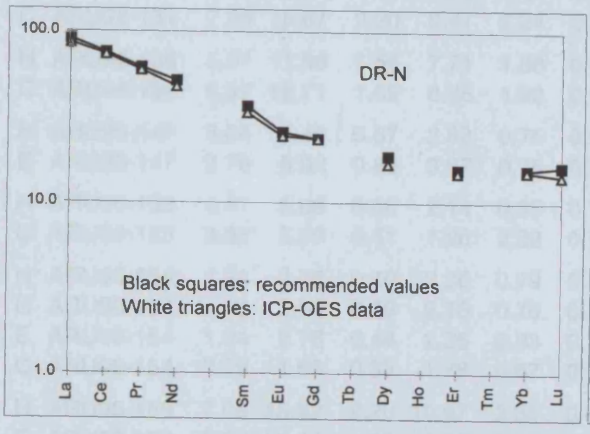

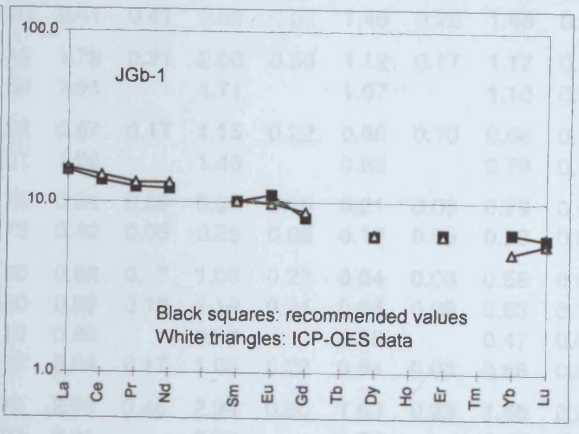

Values normalised to C1 chondrite of McDonough and Sun (1995).

Appendix E: Table E.7 - repeat REE analyses by various methods

		La	Ce	Pr	Nd	Sm	Eu	Gd	Tb	Dy	Ho	Er	Tm	Yb	Lu
I	ARU96-2	3.40	8.70		7.08	2.22	0.90	2.28	0.59					2.28	0.36
H	ARU96-2	3.56	9.20	1.43	7.23	2.36	0.59	2.94	0.60	4.18	0.85	2.46	0.36	2.43	0.37
E	ARU96-2	3.86	9.51	1.37	7.09	2.44	0.93	3.14		3.81		2.56		2.17	0.34
I	ARU96-21	2.70	7.00		5.20	1.86	0.74	1.88	0.42					1.75	0.28
H	ARU96-21	2.65	6.65	1.02	5.40	1.69	0.46	2.11	0.42	2.92	0.59	1.75	0.25	1.77	0.26
E	ARU96-21	2.71	7.22	0.95	5.18	1.63	0.74	2.67		3.43		2.14		1.79	0.29
I	ARU96-30	2.30	6.00		4.37	1.56	0.66	1.68	0.41					1.77	0.26
H	ARU96-30	2.28	5.89	0.92	4.79	1.67	0.42	2.09	0.43	2.95	0.63	1.80	0.26	1.80	0.27
E	ARU96-30	3.00	6.81	1.08	5.02	1.77	0.75	2.56		3.16		2.10		1.75	0.28
I	ARU96-37	3.50	8.70		7.51	2.27	0.91	2.24	0.55					2.30	0.38
H	ARU96-37	3.83	9.71	1.42	7.25	2.24	0.56	2.65	0.53	3.76	0.77	2.28	0.34	2.30	0.35
E	ARU96-37	3.77	10.06	1.43	7.02	2.09	0.71	3.58		4.34		2.69		2.39	0.42
H	ARU96-38	1.21	2.81	0.42	2.17	0.72	0.23	0.99	0.21	1.52	0.31	0.92	0.14	0.99	0.14
H	ARU96-38	1.23	2.86	0.42	2.19	0.74	0.23	1.05	0.23	1.58	0.34	0.99	0.15	1.06	0.15
E	ARU96-38	1.55	4.00	0.62	3.33	1.20	0.39	1.28		1.43		0.79		0.67	0.10
C	ARU96-38	0.82	2.20	0.36	1.82	0.71	0.34	1.03	0.22	1.44	0.32	1.00	0.14	0.86	0.14
H	ARU96-41	16.29	32.16	2.85	9.28	1.20	0.17	0.93	0.13	0.76	0.14	0.51	0.09	0.72	0.14
C	ARU96-41	18.12	30.71	3.23	10.19	1.37	0.19	1.26	0.15	0.82	0.16	0.50	0.09	0.68	0.13
H	ARU96-42	4.09	8.58	1.22	5.73	1.47	0.44	1.45	0.25	1.59	0.30	0.85	0.12	0.83	0.13
E	ARU96-42	3.44	7.35	1.03	5.61	1.48	0.52	1.51		1.41		0.82		0.74	0.14
C	ARU96-42	2.57	5.91	0.92	4.40	1.28	0.67	1.43	0.26	1.50	0.31	0.82	0.12	0.83	0.13
H	ARU96-57	2.21	4.74	0.73	4.10	1.36	0.34	1.56	0.31	2.03	0.41	1.17	0.16	1.15	0.16
E	ARU96-57	1.96	5.07	0.74	4.51	1.42	0.47	1.55		1.73		0.76		0.65	0.09
H	ARU96-131	8.03	16.35	2.18	9.52	2.13	0.51	1.86	0.31	1.97	0.37	1.13	0.17	1.20	0.19
E	ARU96-131	7.78	16.34	2.00	8.29	2.30	0.75	2.08		2.00		1.10		1.03	0.16
C	ARU96-131	7.45	16.27	2.23	9.30	2.20	0.88	2.46	0.40	2.38	0.51	1.44	0.22	1.44	0.21
C	ARU96-131	7.28	15.67	2.20	9.47	2.24	0.90	2.41	0.41	2.52	0.52	1.48	0.22	1.48	0.22
H	ARU96-136	5.37	11.66	1.66	7.71	1.88	0.49	1.79	0.31	2.03	0.38	1.12	0.17	1.17	0.18
E	ARU96-136	5.97	12.71	1.69	8.35	1.99	0.69	1.91		1.71		1.07		1.10	0.20
H	ARU96-147	3.04	5.49	0.67	2.83	0.75	0.22	0.87	0.17	1.15	0.22	0.66	0.10	0.68	0.10
E	ARU96-147	3.76	6.92	0.89	3.87	0.75	0.01	1.22		1.46		0.88		0.79	0.15
H	ARU96-153	4.41	6.66	0.66	2.14	0.35	0.78	0.31	0.05	0.32	0.06	0.21	0.03	0.29	0.06
C	ARU96-153	3.83	5.69	0.61	1.96	0.32	0.73	0.42	0.05	0.29	0.06	0.19	0.03	0.23	0.04
H	ARU96-154	1.31	2.76	0.40	2.26	0.79	0.20	0.88	0.17	1.08	0.22	0.64	0.08	0.58	0.08
H	ARU96-154	1.29	2.69	0.39	2.16	0.75	0.20	0.92	0.19	1.19	0.24	0.66	0.09	0.63	0.10
E	ARU96-154	1.04	2.76	0.44	2.36	0.83	0.19	0.88		0.87		0.50		0.47	0.07
C	ARU96-154	0.79	1.88	0.33	1.78	0.67	0.29	0.84	0.17	1.06	0.22	0.61	0.08	0.58	0.08
H	ARU96-158	7.06	15.32	2.20	10.67	2.65	0.62	2.65	0.46	2.94	0.60	1.63	0.23	1.66	0.24
E	ARU96-158	6.90	16.44	2.20	10.90	2.68	0.83	2.91		2.73		1.53		1.47	0.22
H	BK77-165	5.32	10.99	1.46	6.46	1.73	0.68	1.87	0.35	2.39	0.47	1.40	0.21	1.40	0.22
C	BK77-165	3.94	8.25	1.15	4.97	1.40	0.57	1.65	0.32	1.91	0.45	1.16	0.18	1.23	0.18
H	ARU94-2	6.45	12.99	1.68	6.87	1.55	0.41	1.47	0.27	1.74	0.34	1.02	0.15	1.09	0.16
H	ARU94-2	9.60	18.43	2.20	8.75	1.76	0.40	1.60	0.27	1.77	0.35	1.06	0.16	1.14	0.18
H	ARU94-7	1.99	5.34	0.94	5.15	1.78	0.42	2.11	0.41	2.76	0.56	1.55	0.23	1.42	0.21
H	ARU94-7	3.00	7.35	1.23	6.78	2.16	0.48	2.45	0.46	3.04	0.61	1.74	0.25	1.61	0.24
H	ARU94-13	7.33	16.99	2.44	10.98	2.74	0.62	2.63	0.45	2.93	0.57	1.63	0.24	1.58	0.24
H	ARU94-13	7.45	16.55	2.35	10.98	2.69	0.59	2.50	0.42	2.62	0.50	1.43	0.21	1.44	0.22
H	ARU94-17	7.95	15.18	1.90	7.48	1.65	0.45	1.60	0.28	1.86	0.36	1.08	0.16	1.15	0.18
H	ARU94-17	8.59	15.50	1.95	8.15	1.73	0.45	1.60	0.29	1.84	0.36	1.08	0.16	1.17	0.18
H	ARU94-22	2.15	5.54	0.89	4.61	1.58	0.41	2.02	0.42	2.88	0.62	1.78	0.26	1.77	0.26
H	ARU94-22	3.06	7.04	1.04	5.18	1.55	0.37	1.88	0.36	2.56	0.53	1.56	0.23	1.58	0.23
H	ARU94-29	2.58	6.62	1.10	5.72	1.96	0.49	2.51	0.51	3.54	0.73	2.12	0.32	2.15	0.31
H	ARU94-29	2.68	6.91	1.03	5.52	1.72	0.43	2.16	0.44	3.04	0.63	1.87	0.28	1.89	0.28

I: INAA (Leicester); H: ICP-MS (Haarlem); E: ICP-OES (Leicester); C: ICP-MS (Cardiff)

Data normalised to C1 chondrite of McDonough and Sun (1995).

Notes: I: INAA (Leicester)
H: ICP-MS (Haarlem)
E: ICP-OES (Leicester)
C: ICP-MS (Cardiff)

Appendix F

Radiogenic isotope analyses

F.1 Sample selection and preparation

Samples used for isotopic analysis were selected according to two criteria: firstly, that they should be representative of the range of lithologies sampled, and secondly, that they should be the least altered samples of the chosen lithology. Thin section studies and whole-rock XRF data assisted in the selection of samples. For all samples analysed for isotopes, the fine grit obtained from the fly-press was crushed to a fine powder in a tungsten carbide mill at Leicester University: this is to avoid the potential Pb contamination introduced by agate-milling. After the crushing, all subsequent stages of preparation, and the measurement of isotope ratios, were carried out at the NERC Isotope Geoscience Laboratories (NIGL) under the direction of Pamela Kempton. Full details of the procedures used for isotopic analysis can be found in Kempton (1995) and Royse et al. (1998). The NIGL batch numbers allocated for the Aruba samples were P111 (7 samples) and P123 (15 samples).

It was decided that the powders would not be leached with acid prior to digestion and isotope analysis. Acid-leaching removes easily-dissolved phases, such as clay minerals and alteration products, from the rock powders; this process is commonly used for slightly-altered basaltic rocks, and leaves a residue containing (ideally) only the primary igneous mineralogy, which can then be dissolved and used for isotopic analysis. For the ALF rocks, where, in many cases, it is doubtful whether *any* primary igneous minerals remain, leaching makes interpretation of the results more complex, because it is not known which phases are removed or preserved during leaching, and which phases potentially contain material having original isotope ratios. The batholith samples had suffered less alteration, and it was considered that acid-leaching was not necessary in their preparation.

F.1.1 Weighing and spiking of samples

For each sample, approximately 150 - 200 mg of powder was accurately weighed into a pre-cleaned 7 ml Savillex® beaker (or bomb: see later) that had been treated with an anti-static gun. The amount of powder used depended upon the Pb content of the sample, with

more powder being used for those sample with lower Pb contents. For batch P111, each sample was weighed out twice: one set of samples (+ blank + standard) was spiked for Sr and Sm-Nd; the other set of samples (+ blank + standard) was spiked for U and Pb. For batch P123, U-Pb spiking was not necessary, because it was known that the U and Pb abundances would be obtained by ICP-MS; only Sr and Sm-Nd spikes were added. The eight plutonic samples (+ blank) of batch P123 were weighed into Savillex® bombs rather than beakers, because it was considered that they might be more easily digested if heated to >110°C under slight pressure. The remaining seven samples (+ blank + standard) were weighed into beakers, as usual. The samples were wetted with a small amount of high-purity MILLI-Q (hereafter: MQ) H_2O to avoid loss of sample on re-opening of the beakers/bombs.

F.1.2 Digestion and conversion to bromides

0.5 -1 ml of teflon-distilled (hereafter: TD) 16M HNO_3 and 2 - 3 ml of TD 29M HF were added to the sample in the Savillex® beaker/bomb. This mixture was shaken: the beakers were left (cold) over a weekend to allow digestion of the silicate; the bombs were placed into an oven at 110°C for the same period, with the digested mixture being allowed to cool before being transferred into a Savillex® beaker. The beaker lids were removed, and the solutions evaporated to near-dryness on a hot-plate at ~100°C. 2 - 3 ml of TD 16M HNO_3 were then added, and the beakers sealed and placed in an ultra-sonic bath for ~ ½ hour, before the lids were removed and the beakers returned to the hot-plate. After evaporation to near-dryness, 2 - 3 ml of TD 6M HCl were added, the beakers were sealed, and placed on the hot-plate overnight. Those samples that had dissolved completely were evaporated to near-dryness, before addition of 1 ml 1M HBr.

If samples remained incompletely dissolved at this point, they were placed in the ultra-sonic bath for ~ ½ hour. If complete dissolution was still not achieved, the samples were evaporated to near-dryness, then 2 - 3 ml of TD 16M HNO_3 were added, and the beakers returned to the ultra-sonic bath for ~ 1 hour. After slow evaporation on a warm hot-plate overnight, 2 - 3 ml of TD 6M HCl were added, and the beakers returned to the ultra-sonic bath for ~1 hour. For all samples, complete digestion was achieved at this point, and the HCl was evaporated from the beakers, before addition of 1 ml 1M HBr.

It is necessary to convert the fluoride/nitrate salts arising from the initial digestion stage into bromides in order to allow efficient separation and preconcentration of the Pb. Pb forms stable bromide complexes that are preferentially retained on the ion exchange columns, allowing it to be separated from those elements that do not form stable bromide complexes.

F.2 Ion exchange chromatography column chemistry

The aim of the ion exchange chromatography is to separate the required analytes from one another. Each chromatography procedure outlined below yields a relatively pure, preconcentrated solution of a particular analyte, and the eluted material is then used to separate the subsequent analytes. U separation was only required for the subset of samples that was spiked for U concentrations (i.e., half of batch P111). For all the procedures described below, each addition of acid is allowed to completely drain through the column before the next addition.

F.2.1 Pb separation

The columns used for Pb separation were made of 1 ml polypropylene pipette tips with a 3 mm thick porous (35μm) polyethylene frit in the tip; the columns were cleaned with one column volume (hereafter: CV) of quartz-distilled (hereafter: QD) 6M HCl and 1 CV MQ H_2O before being loaded with 15-25 μl Dowex 1 × 8, 200-400 mesh resin. The resin was washed with 1 CV TD 6M HCl followed by 1 CV MQ H_2O; this washing procedure was then repeated. The columns were preconditioned by adding 0.5 CV 1M HBr.

The first elute of the Pb column process was required for U, Sr and Sm-Nd separation, so beakers were placed beneath the columns to collect this. The samples were transferred onto the columns using clean pipettes, with any solid residue remaining in the dissolution beaker being transferred to the U-Sr-Nd collection vessel. The dissolution beakers were then cleaned in readiness for collection of the Pb fraction. The sample was washed into the column with 0.5 ml 1M HBr, then 1 ml 1M HBr, and the eluent was collected at this stage for U, Sr and Sm-Nd. To this eluent, 2 ml of TD 16M HNO_3 was added (in a fume cupboard) to release excess bromine gas, and then the samples were evaporated to near-dryness.

The Pb was then stripped from the columns by adding 1 CV TD 6M HCl. 3 - 4 drops of HNO_3 were added to the Pb eluent in the beaker, in order to liberate excess bromine, and then the sample was evaporated to near-dryness. The Pb column procedure was then repeated, with the sample being taken up in 0.5 ml 1M HBr before being added to the columns; no collection of the HBr eluent was necessary. The final Pb extracts were collected in 1 ml Savillex® beakers, and 3 μl of 1M H_3PO_4 was added, in addition to the HNO_3, before evaporation to near dryness: the H_3PO_4 does not evaporate at these temperatures, and so the Pb extract can be more easily located in the beaker for loading.

F.2.2 U separation

The columns for U separation contained 0.5 ml of pre-cleaned AG 1 × 8 resin, and were washed through a total of 6 times with 1 ml MQ H_2O into waste beakers. The columns were preconditioned with 1 CV 6M HCl, and the dried down residues (containing U, Sr, Sm and Nd) from the Pb columns were taken up in 1 ml 6M HCl and loaded onto the columns with clean pipettes. The waste beakers were replaced with sample collection beakers for Sr and the REEs. The following were added to the columns and allowed to elute: 0.5 ml 6M HCl; 1 ml 8M HNO_3; 1 ml 8M HNO_3; 1 ml 6M HCl; 1ml 6M HCl. The eluent was collected for use in the Sr and REE columns, and these beakers were replaced with the U collection vessels. The U fraction was collected by addition of: 1 ml MQ H_2O; 1ml MQ H_2O.

This was evaporated to near-dryness, and then the columns were set up again, using 0.5 ml of pre-cleaned AG 1 × 8 resin. The procedure for this second stage is not a simple repeat of the first stage, as it was for the Pb collection. The following reagents were eluted from the column *before* loading of the sample: 1 ml MQ H_2O; 1 ml 1M HCl; 1 ml 1M HCl; 1 ml 1M HCl; 1 ml MQ H_2O; 1 ml MQ H_2O; 1 ml 8M HNO_3; 1 ml 8M HNO_3; 1 ml 8M HNO_3. The samples were then taken up in 1 ml 8M HNO_3, and loaded onto the columns using clean pipettes. Then, the following were allowed to elute: 1 ml 8M HNO_3; 1 ml 8M HNO_3; 1 ml 8M HNO_3. The waste beaker was replaced by the U-collection beaker, and the following added to the column to collect the U: 1 ml MQ H_2O; 1 ml MQ H_2O. 3 µl of H_3PO_4 were added to the U fraction, which was then evaporated to near dryness.

F.2.3 Separation of Sr and REEs from the bulk solution

The eluent from the first pass on the U columns was dried down, and then taken up in 2 ml 2.5M HCl, and transferred to a centrifuge tube: centrifuging for ~ 5 minutes ensured that any solid residue remained at the bottom of the tubes and was not transferred onto the columns. The columns were set up with Dowex AG 50W-X12 resin, and were thoroughly washed with 6M HCl, then preconditioned with 15 ml 2.5M HCl. Clean pipette tips were used to transfer each sample onto the columns, and this was washed in with 1 ml 2.5M HCl followed by 1 ml 2.5M HCl. 39 ml 2.5M HCl were then added to the column, and allowed to elute into the waste beaker. The Sr fraction was then collected using 9 ml of 2.5ml HCl: the beakers containing this fraction were evaporated to dryness on the hot-plate.

The columns were then flushed with 9 ml of 6M HCl, with the eluent collected in waste beakers. The REE fraction was then collected in 11 ml of 6M HCl, and the beakers evaporated to dryness on the hot-plate.

F.2.4 Separation of Sm and Nd from the REE fraction

The dried REE fractions were taken up in 1 ml 0.25M HCl, and pipetted onto the columns, which had been prepared using S-X8 biobeads coated with bis Di-ethylhexyl hydrogen phosphate, rinsed with 5 ml 6M HCl and preconditioned with 5ml 0.25M HCl. The samples were washed into the columns using: 1 ml 0.25M HCl; 1 ml 0.25M HCl; 1 ml 0.25M HCl. 8 ml 0.25M HCl (or 6 ml, depending on which particular column was used) was added to each column, and allowed to elute to waste. The Nd fraction was collected in 4 ml of 0.3M HCl and the sample was evaporated to dryness.

The waste beakers were replaced, and 2 ml 0.6M HCl were allowed to elute. The Sm fraction was collected in 2.5 ml of 0.6M HCl and the sample evaporated to dryness.

F.3 Measurement of isotope ratios

F.3.1 Loading

Pb and U samples were loaded using the silica gel method: single Re filaments were used for Pb and double Re filaments for U. Sr samples were dissolved in 2 - 3 µl of MQ H_2O, and loaded onto single tantalum filaments together with H_3PO_4. For Nd and Sm, double Ta-Re filament assemblies were used: the sample was taken up in 1 - 2 µl of 0.6M HCl, and loaded onto the filament. Full details of sample loading procedures are described in Kempton (1995), Kempton (1997) and Royse et al. (1998).

F.3.2 Analysis

Analysis of Sr, Nd, and Pb isotopes was carried out using a Finnegan MAT 262 multicollector mass spectrometer in static mode. The measurements for Pb were carried out at a fixed temperature of 1125°C where possible. U and Sm were also run on the MAT 262.

F.3.3 Blanks and reference materials

Maximum blanks for Sr, Nd, Sm, U and Pb were 388 pg, 153 pg, 520 pg, 14 pg and 647 pg, respectively. In addition to the international standard BHVO-1, which was prepared in the same way as the unknown samples, reference standards were used to determine the accuracy and precision of the mass spectrometric analysis. Reference standards throughout the

course of analysis averaged values of $^{87}Sr/^{86}Sr$ = 0.710197 ± 14 (1σ) for the NBS 987 standard, $^{143}Nd/^{144}Nd$ = 0.511874 ± 8 (1σ) for the La Jolla Nd standard. $^{87}Sr/^{86}Sr$ was normalised during run time to $^{86}Sr/^{88}Sr$ = 0.1194; $^{143}Nd/^{144}Nd$ was normalised to a value of $^{146}Nd/^{144}Nd$ = 0.7219. Sample data are reported relative to accepted values of NBS 987 of 0.71024 and 0.51186 for La Jolla. Based on repeated runs of NBS 981, the reproducibility of Pb-isotope ratios is better than ± 0.1%. Pb isotope ratios were corrected relative to the average standard Pb isotopic compositions of Todt et al. (1993).

F.4 Age correction

Data for all isotopic systems were age-corrected to the time of emplacement, to enable comparison with published data. The time of emplacement (t) was taken, for simplicity, as 88 Ma for ALF rocks and 85 Ma for rocks of the batholith. The equations and constants used for age correction used were:

Sr isotopes

$$(^{87}Sr/^{86}Sr)_t = (^{87}Sr/^{86}Sr)_{norm.} - (^{87}Rb/^{86}Sr)(e^{\lambda t} - 1) \quad (1)$$

$$\lambda = 1.42 \times 10^{-11}\ yr^{-1}$$

$$^{87}Rb/^{86}Sr = (Rb/Sr)_{meas.\ ppm} \times (2.6929487 + (0.283039 \times (^{87}Sr/^{86}Sr)_{norm})) \quad (2)$$

Nd isotopes

$$(^{143}Nd/^{144}Nd)_t = (^{143}Nd/^{144}Nd)_{norm} - (^{147}Sm/^{144}Nd)(e^{\lambda t} - 1) \quad (3)$$

$$\lambda = 6.54 \times 10^{-12}\ yr^{-1}$$

$$^{147}Sm/^{144}Nd = (Sm/Nd)_{meas.\ ppm} \times (0.5316288 + (0.142556 \times (^{143}Nd/^{144}Nd)_{norm})) \quad (4)$$

Pb isotopes

$$(^{206}Pb/^{204}Pb)_t = (^{206}Pb/^{204}Pb)_{corr} - ^{238}U/^{204}Pb(e^{\lambda t} - 1) \quad (5)$$

$$\lambda = 1.55125 \times 10^{-10}\ yr^{-1}$$

$$^{238}U/^{204}Pb = (U/Pb)_{meas.\ ppm} \times \frac{\text{atomic weight Pb} \times 99.27}{\%\ ^{204}Pb \times 238.03} \quad (6)$$

$$(^{207}Pb/^{204}Pb)_t = (^{207}Pb/^{204}Pb)_{corr} - ^{235}U/^{204}Pb(e^{\lambda t} - 1) \quad (7)$$

$$\lambda = 9.8485 \times 10^{-10}\ yr^{-1}$$

$$^{235}U/^{204}Pb = ^{238}U/^{204}Pb \div 137.88$$

$$(^{208}Pb/^{204}Pb)_t = (^{208}Pb/^{204}Pb)_{corr} - {}^{232}Th/^{206}Pb(e^{\lambda t} - 1) \quad (9)$$

$$\lambda = 4.9475 \times 10^{-11}\ yr^{-1}$$

$$^{232}Th/^{204}Pb = (Th/Pb)_{meas.\ ppm} \times \frac{\text{atomic weight Pb} \times 100}{\%\ ^{204}Pb \times 232.038} \quad (10)$$

Note that equations (2) and (4) take account of the variation in atomic weight of Sr or Nd due to variations in isotopic ratio. For Pb, the isotope ratios were used to calculate proportions of the different isotopes prior to use in these equations, and the atomic weight of Pb was derived individually for each sample. The subscript "norm" refers to isotope ratios of Sr and Nd that have been normalised as described in Section F.3.3; "corr" refers to corrected Pb isotope ratios (see also Section F.3.3).

Table F.1: Sr and Nd isotope data

Sample	Lith.	$^{87}Sr/^{86}Sr$ measured	$^{87}Sr/^{86}Sr$ normalised	$^{87}Sr/^{86}Sr$ initial	$^{143}Nd/^{144}Nd$ measured	$^{143}Nd/^{144}Nd$ normalised	$^{143}Nd/^{144}Nd$ initial	εNd(i)	Nd ppm	Sm ppm
Aruba Lava Formation: initial ratios age corrected to 88 Ma										
ARU96-2	A1	0.703467 ± 9	0.703512	**0.703347**	0.513014 ± 4	0.512997	**0.512884**	**7.01**	6.88	2.23
ARU96-21	A1	0.703882 ± 7	0.703927	**0.703842**	0.513061 ± 4	0.513044	**0.512930**	**7.91**	5.47	1.79
ARU96-30	A2	0.703719 ± 6	0.703760	**0.703672**	0.513023 ± 5	0.513013	**0.512898**	**7.27**	4.86	1.61
ARU96-37	A2	0.703824 ± 5	0.703869	**0.703807**	0.513006 ± 4	0.512989	**0.512876**	**6.86**	7.30	2.36
ARU96-38	A2	0.703299 ± 5	0.703344	**0.703256**	0.513022 ± 5	0.513005	**0.512870**	**6.75**	2.15	0.83
ARU96-108	A3	0.705486 ± 6	0.705531	**0.705294**	0.513028 ± 5	0.513011	**0.512897**	**7.25**	4.49	1.48
ARU96-145	A4	0.703720 ± 7	0.703761	**0.703700**	0.513001 ± 3	0.512991	**0.512872**	**6.78**	5.39	1.84
ARU96-147	A4	0.705083 ± 6	0.705124	**0.705113**	0.512974 ± 5	0.512964	**0.512872**	**6.77**	2.86	0.76
ARU96-142	A5	0.704705 ± 7	0.704746	**0.704691**	0.513004 ± 5	0.512994	**0.512888**	**7.09**	4.57	1.39
Aruba batholith: initial ratios age corrected to 85 Ma										
ARU96-53	B1	0.703506 ± 7	0.703547	**0.703508**	0.513015 ± 5	0.513005	**0.512908**	**7.41**	4.85	1.39
* ARU96-57	B1	0.703411 ± 5	0.703456	**0.703424**	0.513042 ± 5	0.513025	**0.512908**	**7.40**	3.54	1.24
* ARU96-154	B2b	0.703668 ± 6	0.703713	**0.703589**	0.513053 ± 5	0.513036	**0.512910**	**7.44**	1.83	0.69
* ARU96-154	B2b				0.513067 ± 5	0.513050	**0.512924**	**7.71**	1.83	
* ARU96-42	B3	0.703500 ± 5	0.703545	**0.703525**	0.513015 ± 5	0.512998	**0.512903**	**7.30**	4.70	1.33
ARU96-158	B4	0.703600 ± 4	0.703641	**0.703480**	0.512986 ± 4	0.512976	**0.512889**	**7.03**	10.17	2.63
* BK77-066	B4	0.703547 ± 5	0.703592	**0.703517**	0.512978 ± 5	0.512961	**0.512869**	**6.64**	8.15	2.23
* BK77-165	B4	0.703533 ± 6	0.703578	**0.703501**	0.513007 ± 5	0.512990	**0.512898**	**7.20**	5.30	1.45
ARU96-131	B5	0.703749 ± 5	0.703790	**0.703443**	0.512970 ± 3	0.512960	**0.512881**	**6.87**	9.98	2.35
* BK77-054	B5	0.703858 ± 5	0.703903	**0.703722**	0.512969 ± 4	0.512952	**0.512874**	**6.73**	7.19	1.67
* ARU96-155	B7	0.704230 ± 6	0.704275	**0.703418**	0.512982 ± 4	0.512965	**0.512897**	**7.19**	10.04	2.03
ARU96-136	B9	0.703662 ± 5	0.703707	**0.703610**	0.513001 ± 4	0.512984	**0.512902**	**7.29**	7.77	1.89
Cross-cutting dykes: initial ratios age corrected to 76 Ma (best estimate, but poorly constrained)										
ARU96-25	C1	0.703449 ± 7	0.703494	**0.703121**	0.512903 ± 4	0.512886	**0.512814**	**5.34**	11.56	2.78
* ARU96-14	C2	0.703568 ± 6	0.703613	**0.703591**	0.513017 ± 5	0.513000	**0.512907**	**7.16**	6.38	1.97
BHVO-1 standard										
BHVO-1		0.703401 ± 5	0.703442		0.512971 ± 4	0.512961			24.93	6.14
BHVO-1		0.703416 ± 9	0.703461		0.513012 ± 4	0.512995			24.79	6.11
Procedural blanks										
BLANK		270pg							107pg	48pg
* BLANK		388pg			153pg					520pg
BLANK		failed			failed				failed	failed

Notes:

* : initial dissolution in bomb rather than beaker

Errors reported are run-time precision (1σ) in the sixth decimal place; however, a more realistic estimate of the error is given by the external reproducibility on the standards (see Section F.3.3).

Lith. : Lithology code (see Appendix A)

Nd and Sm (ppm) by isotope dilution

Table F.2: Pb isotope data

Sample	Lith.	$^{206}Pb/^{204}Pb$ measured	$^{207}Pb/^{204}Pb$ measured	$^{208}Pb/^{204}Pb$ measured	$^{206/204}Pb$ corr.	$^{207/204}Pb$ corr.	$^{208/204}Pb$ corr.	**$^{206/204}Pb$ inital**	**$^{207/204}Pb$ initial**	**$^{208/204}Pb$ initial**	Pb ppm	U ppm
Aruba Lava Formation: initial ratios age corrected to 88 Ma												
ARU96-2	A1	18.773 ± 5	15.533 ± 4	38.371 ± #	18.795	15.564	38.482	**18.772**	**15.563**	**38.45**		
ARU96-21	A1	19.157 ± 2	15.516 ± 2	38.710 ± 4	19.179	15.546	38.822	**19.111**	**15.543**	**38.75**		
ARU96-30	A2	18.946 ± 2	15.508 ± 2	38.530 ± 5	18.973	15.548	38.679	**18.771**	**15.538**	**38.32**	0.17	0.04
ARU96-37	A2	18.924 ± 2	15.522 ± 2	38.500 ± 5	18.946	15.553	38.612	**18.862**	**15.549**	**38.54**		
ARU96-38	A2	19.105 ± 3	15.569 ± 3	38.719 ± 7	19.127	15.600	38.831	**18.998**	**15.594**	**38.77**		
ARU96-108	A3	18.655 ± 1	15.509 ± 1	38.199 ± 2	18.676	15.539	38.309	**18.655**	**15.538**	**38.29**		
ARU96-145	A4	18.728 ± 2	15.550 ± 2	38.333 ± 1	18.755	15.590	38.481	**18.520**	**15.579**	**38.25**	0.09	0.02
ARU96-147	A4	19.031 ± 2	15.532 ± 1	38.647 ± 4	19.058	15.572	38.796	**18.932**	**15.566**	**38.62**	0.62	0.09
ARU96-142	A5	18.945 ± 1	15.523 ± 1	38.489 ± 3	18.972	15.563	38.637	**18.854**	**15.557**	**38.50**	0.75	0.10
Aruba batholith: initial ratios age corrected to 85 Ma												
ARU96-53	B1	18.862 ± 1	15.519 ± 1	38.293 ± 1	18.889	15.559	38.441	**18.616**	**15.546**	**38.23**	0.91	0.29
*ARU96-57	B1	18.697 ± 1	15.518 ± 1	38.221 ± 3	18.718	15.548	38.331	**18.624**	**15.544**	**38.27**		
*ARU96-154	B2b	18.500 ± 1	15.506 ± 1	38.023 ± 3	18.521	15.536	38.133	**18.450**	**15.533**	**38.09**		
*ARU96-154	B2b											
*ARU96-42	B3	18.478 ± 2	15.482 ± 2	37.951 ± 4	18.499	15.513	38.061	**18.472**	**15.512**	**38.03**		
ARU96-158	B4	18.683 ± 1	15.504 ± 1	38.163 ± 1	18.710	15.544	38.310	**18.515**	**15.535**	**38.18**	2.10	0.49
*BK77-066	B4	18.701 ± 1	15.516 ± 1	38.209 ± 2	18.722	15.546	38.320	**18.624**	**15.541**	**38.23**		
*BK77-165	B4	18.988 ± 1	15.536 ± 1	38.436 ± 1	19.009	15.567	38.547	**18.860**	**15.560**	**38.43**		
ARU96-131	B5	18.826 ± 1	15.514 ± 1	38.299 ± 1	18.853	15.555	38.446	**18.590**	**15.542**	**38.22**	1.61	0.50
*BK77-054	B5	18.777 ± 1	15.530 ± 1	38.334 ± 1	18.798	15.560	38.445	**18.673**	**15.554**	**38.34**		
*ARU96-155	B7	18.975 ± 1	15.534 ± 1	38.400 ± 1	18.997	15.565	38.510	**18.809**	**15.556**	**38.35**		
ARU96-136	B9	18.751 ± 1	15.532 ± 1	38.302 ± 1	18.772	15.563	38.413	**18.703**	**15.560**	**38.36**		
Cross-cutting dykes: initial ratios age corrected to 76 Ma (best estimate, but poorly constrained)												
ARU96-25	C1	18.705 ± 1	15.509 ± 1	38.156 ± 2	18.727	15.539	38.266	**18.622**	**15.534**	**38.19**		
*ARU96-14	C2	20.122 ± 3	15.584 ± 2	39.183 ± 5	20.145	15.614	39.296	**20.003**	**15.607**	**39.20**		
BHVO-1 standard												
BHVO-1		18.632 ± 10	15.498 ± 9	38.102 ± #	18.658	15.539	38.249				1.94	0.42
BHVO-1		18.845 ± 7	15.521 ± 6	38.130 ± #	18.867	15.552	38.240					
Procedural blanks												
BLANK		64pg									647pg	
*BLANK		624pg										
BLANK		70pg										

Notes:

* : initial dissolution in bomb rather than beaker

Errors reported are run-time precision (1σ) in the third decimal place; however, a more realistic estimate of the error is given by the external reproducibility on the standards (see Section F.3.3).

Lith. : Lithology code (see Appendix A)

U and Pb (ppm) by isotope dilution; other U, Th and Pb data used for age correction obtained by ICP-MS (see Appendix D).

ARU96-145 did not yield sufficient Pb for a reliable result

corr. : corrected according to Todt et al. (1993)

Appendix G

Electron microprobe analyses

G.1 Analytical techniques

Samples selected for electron microprobe analysis were prepared in the University of Leicester as polished thin sections. These were sputtered with carbon prior to analysis.

The analyses were carried out using the JEOL JXA-8600 Superprobe at the University of Leicester. A wavelength dispersive system was used, and the elements analysed were: Si, Ti, Al, Cr, Fe, Mn, Mg, Ca, Na, K and Ni. The programme was calibrated using a mixture of synthetic (for Fe, Mg, Cr, Ni) and natural (rhodonite: Mn; wollastonite: Ca, Si; rutile: Ti; jadeite: Na, Al; microcline: K) standards. The probe current was 3×10^{-8} A, and the operating voltage was 15kV. Beam diameters used were 10 μm for feldspars and micas and 5 μm for other minerals; however, when stage positions were preset, and analyses run unattended, the beam diameter was 10 μm for all minerals. Count times for each element analysed were 20 seconds on the peak and 20 seconds (total) on the background. Estimated precision (2σ) for common minerals is ± 0.25% at 50 wt.% oxide (calculated from standard deviations of raw intensity data). Compositional data was corrected using the ZAF procedure.

G.2 Results

Results of electron microprobe analyses are presented in Tables G.1 to G.6. Each table is organised alphabetically by mineral. Tables G.1 and G.2 contain analyses from basalts and dolerites of the Aruba Lava Formation; Tables G.3 and G.4 show amphibolite data. Tables G.5 and G.6 contain results for the batholith. Tables G.1, G.3 and G.5 contain data in wt.% oxide; Tables G.2, G.4 and G.6 contain cation proportion data calculated on the basis of:

Mineral		no. oxygens	Mineral		no. oxygens
olivine	ol	4	magnetite	mag	4
pyroxenes	cpx, opx	6	ilmenite	ilm	6
feldspars	plag, kfsp	8	spinel	sp	32
amphiboles	amph	23	epidote	ep	25
biotite	bi	22	titanite	tit	5
chlorite	chl	28	apatite	ap	N/A

Appendix G: Electron microprobe data: Table G.1

Sample		Lith.	SiO_2	TiO_2	Al_2O_3	Cr_2O_3	FeO	MnO	MgO	CaO	Na_2O	K_2O	NiO	Total
ARU96-22	amph	A1	50.05	0.46	6.79	0.16	12.35	0.18	15.28	11.45	0.80	0.05	0.05	97.62
ARU96-22	amph	A1	50.31	0.47	6.14	0.13	12.44	0.24	15.52	11.48	0.69	0.03	0.02	97.47
ARU96-22	amph	A1	50.46	0.51	6.38	0.11	12.37	0.22	15.45	11.56	0.75	0.05	0.04	97.90
ARU96-22	amph	A1	50.27	0.50	6.41	0.15	12.57	0.21	15.50	11.52	0.77	0.05	0.05	98.00
ARU96-22	amph	A1	50.57	0.36	6.67	0.11	12.31	0.19	15.49	11.58	0.73	0.04	0.03	98.08
ARU96-22	amph	A1	50.31	0.47	6.17	0.09	12.26	0.23	15.68	11.78	0.74	0.05	0.08	97.86
ARU96-30	amph	A2	52.08	0.10	5.13	0.00	13.88	0.21	14.39	12.50	0.49	0.08	0.01	98.87
ARU96-37	amph	A2	48.56	0.15	6.96	0.03	17.91	0.25	11.08	12.27	0.56	0.09	0.04	97.90
ARU96-37	chl	A2	27.48	0.03	18.59	0.02	24.75	0.16	16.07	0.06	0.05	0.05	0.08	87.34
ARU96-30	cpx	A2	52.86	0.33	2.64	0.84	5.40	0.15	17.23	20.93	0.18	0.00	0.04	100.60
ARU96-30	cpx	A2	53.58	0.25	1.82	0.48	6.25	0.18	18.16	19.88	0.18	0.01	0.02	100.81
ARU96-30	cpx	A2	54.01	0.38	1.73	0.05	7.67	0.25	17.70	19.29	0.17	0.00	0.03	101.28
ARU96-38	cpx	A2	52.60	0.33	2.00	0.52	6.46	0.27	17.93	19.38	0.18	0.01	0.09	99.77
ARU96-38	cpx	A2	50.13	0.74	2.12	0.12	10.02	0.29	15.16	19.13	0.20	0.01	0.03	97.95
ARU96-38	cpx	A2	51.08	0.75	1.88	0.27	9.86	0.24	15.76	18.72	0.23	0.01	0.02	98.82
ARU96-38	cpx	A2	51.90	0.63	1.83	0.21	9.85	0.22	16.22	18.41	0.21	0.00	0.03	99.51
ARU96-38	cpx	A2	53.05	0.23	2.21	0.72	5.10	0.18	18.34	20.06	0.14	0.00	0.02	100.05
ARU96-38	cpx	A2	51.56	0.61	1.71	0.17	10.90	0.24	15.39	18.78	0.24	0.01	0.04	99.65
ARU96-38	cpx	A2	51.40	0.78	1.89	0.30	10.79	0.22	14.89	19.36	0.19	0.00	0.02	99.84
ARU96-38	cpx	A2	52.91	0.26	2.11	0.50	6.19	0.20	17.97	19.93	0.20	0.00	0.05	100.32
ARU96-37	cpx	A2	53.86	0.28	1.39	0.23	7.22	0.27	20.78	15.84	0.14	0.00	0.06	100.07
ARU96-37	cpx	A2	52.83	0.48	1.74	0.04	12.01	0.31	19.19	13.60	0.12	0.00	0.03	100.35
ARU96-37	cpx	A2	51.93	0.52	2.39	0.02	9.87	0.34	17.10	17.79	0.19	0.01	0.03	100.19
ARU96-37	cpx	A2	53.49	0.22	1.75	0.61	5.70	0.17	18.61	19.53	0.20	0.01	0.06	100.35
ARU96-37	cpx	A2	52.31	0.33	2.94	0.89	5.60	0.16	18.19	19.63	0.21	0.00	0.05	100.31
ARU96-37	cpx	A2	53.07	0.40	2.66	0.27	7.35	0.25	19.58	16.71	0.16	0.01	0.03	100.49
ARU96-22	ilm	A1	0.97	52.04	0.81	0.12	42.54	1.39	0.81	0.28	0.02	0.01	0.02	99.01
ARU96-22	ilm	A1	1.26	52.05	0.57	0.08	43.32	1.41	0.56	0.50	0.03	0.01	0.01	99.80
ARU96-30	ilm	A2	1.03	50.59	0.13	0.03	43.73	1.99	0.11	0.91	0.00	0.01	0.00	98.53
ARU96-38	ilm	A2	0.08	67.60	0.08	0.68	26.75	0.74	0.03	1.31	0.03	0.01	0.01	97.32
ARU96-38	ilm	A2	6.37	50.40	0.36	0.49	32.57	2.89	0.08	4.65	0.03	0.00	0.02	97.86
ARU96-38	ilm	A2	0.81	55.43	0.06	0.74	34.80	1.73	0.04	2.48	0.02	0.01	0.02	96.14
ARU96-37	mag	A2	2.12	19.29	0.15	0.01	69.79	1.06	0.03	1.97	0.00	0.01	0.00	94.43
ARU96-37	mag	A2	8.42	15.98	0.73	0.04	62.45	0.46	0.04	7.46	0.04	0.01	0.02	95.65
ARU96-37	mag	A2	1.17	1.49	0.33	0.03	85.62	0.06	0.24	0.37	0.03	0.00	0.03	89.37
ARU96-22	plag	A1	47.92	0.01	33.08	0.00	0.14	0.03	0.02	16.70	2.14	0.00	0.03	100.07
ARU96-30	plag	A2	53.08	0.04	29.39	0.04	0.72	0.01	0.18	13.30	4.10	0.03	0.00	100.89
ARU96-30	plag	A2	54.52	0.08	28.11	0.05	0.89	0.01	0.12	11.93	4.91	0.14	0.02	100.78
ARU96-30	plag	A2	47.79	0.02	33.06	0.05	0.69	0.02	0.07	17.27	1.82	0.02	0.01	100.82
ARU96-30	plag	A2	52.04	0.05	28.79	0.02	1.62	0.00	0.78	12.56	4.19	0.06	0.00	100.11
ARU96-38	plag	A2	46.45	0.03	33.11	0.04	0.76	0.03	0.05	17.87	1.47	0.02	0.01	99.84
ARU96-38	plag	A2	50.05	0.06	30.54	0.02	0.82	0.00	0.17	14.78	3.21	0.09	0.00	99.74
ARU96-38	plag	A2	52.24	0.04	29.07	0.04	0.71	0.02	0.08	12.98	4.14	0.20	0.02	99.54
ARU96-38	plag	A2	47.04	0.02	32.50	0.03	0.73	0.01	0.04	17.09	1.80	0.01	0.01	99.28
ARU96-38	plag	A2	45.53	0.02	32.34	0.05	0.73	0.02	0.08	17.44	1.64	0.02	0.03	97.90
ARU96-38	plag	A2	46.58	0.03	33.09	0.01	0.68	0.03	0.04	17.60	1.83	0.03	0.02	99.94
ARU96-37	plag	A2	52.30	0.05	29.24	0.04	0.78	0.01	0.24	13.26	3.98	0.03	0.02	99.95
ARU96-37	plag	A2	56.34	0.09	26.71	0.02	0.84	0.05	0.09	10.27	5.79	0.07	0.04	100.31
ARU96-37	plag	A2	53.10	0.06	28.42	0.03	1.06	0.03	0.15	12.42	4.49	0.05	0.02	99.83
ARU96-37	plag	A2	59.16	0.05	25.22	0.01	0.82	0.01	0.03	8.01	7.15	0.11	0.01	100.58
ARU96-37	plag	A2	52.67	0.04	29.17	0.04	1.07	0.02	0.17	13.23	4.17	0.03	0.02	100.63
ARU96-37	plag	A2	52.61	0.05	28.85	0.04	1.00	0.01	0.20	13.18	4.15	0.02	0.02	100.13
ARU96-37	plag	A2	61.12	0.04	23.89	0.07	0.80	0.02	0.00	6.31	7.77	0.25	0.02	100.29
ARU96-37	plag	A2	52.52	0.06	29.31	0.04	0.83	0.03	0.21	13.36	4.03	0.05	0.05	100.49
ARU96-22	sp	A1	0.00	0.17	14.17	45.24	34.87	0.62	1.00	0.01	0.05	0.00	0.00	96.13
ARU96-22	sp	A1	0.00	2.20	6.76	28.39	54.66	0.74	0.09	0.07	0.00	0.01	0.09	93.01

Appendix G: Electron microprobe data: Table G.2

Sample		Lith.	O	Si	Ti	Al	Cr	Fe^{2+}	Mn	Mg	Ca	Na	K	Ni	Total
ARU96-22	amph	A1	23	7.223	0.050	1.155	0.018	1.491	0.022	3.287	1.771	0.224	0.009	0.006	15.256
ARU96-22	amph	A1	23	7.274	0.051	1.046	0.015	1.504	0.029	3.345	1.778	0.193	0.006	0.002	15.243
ARU96-22	amph	A1	23	7.261	0.055	1.082	0.013	1.489	0.027	3.314	1.782	0.209	0.009	0.005	15.246
ARU96-22	amph	A1	23	7.237	0.054	1.088	0.017	1.513	0.026	3.326	1.777	0.215	0.009	0.006	15.268
ARU96-22	amph	A1	23	7.255	0.039	1.128	0.012	1.477	0.023	3.313	1.780	0.203	0.007	0.003	15.240
ARU96-22	amph	A1	23	7.250	0.051	1.048	0.010	1.478	0.028	3.368	1.819	0.207	0.009	0.010	15.278
ARU96-30	amph	A2	23	7.461	0.011	0.866	0.000	1.663	0.025	3.073	1.919	0.136	0.015	0.001	15.170
ARU96-37	amph	A2	23	7.198	0.017	1.216	0.004	2.220	0.031	2.448	1.949	0.161	0.017	0.005	15.266
ARU96-37	chl	A2	28	5.790	0.005	4.617	0.003	4.361	0.029	5.047	0.014	0.020	0.013	0.014	19.913
ARU96-30	cpx	A2	6	1.924	0.009	0.113	0.024	0.164	0.005	0.935	0.816	0.013	0.000	0.001	4.004
ARU96-30	cpx	A2	6	1.945	0.007	0.078	0.014	0.190	0.006	0.983	0.773	0.013	0.000	0.001	4.010
ARU96-30	cpx	A2	6	1.957	0.010	0.074	0.001	0.232	0.008	0.956	0.749	0.012	0.000	0.001	4.000
ARU96-38	cpx	A2	6	1.933	0.009	0.087	0.015	0.199	0.008	0.982	0.763	0.013	0.000	0.003	4.012
ARU96-38	cpx	A2	6	1.913	0.021	0.095	0.004	0.320	0.009	0.862	0.782	0.015	0.000	0.001	4.022
ARU96-38	cpx	A2	6	1.925	0.021	0.084	0.008	0.311	0.008	0.886	0.756	0.017	0.000	0.001	4.017
ARU96-38	cpx	A2	6	1.937	0.018	0.080	0.006	0.307	0.007	0.902	0.736	0.015	0.000	0.001	4.009
ARU96-38	cpx	A2	6	1.934	0.006	0.095	0.021	0.155	0.006	0.997	0.783	0.010	0.000	0.001	4.008
ARU96-38	cpx	A2	6	1.934	0.017	0.076	0.005	0.342	0.008	0.861	0.755	0.017	0.000	0.001	4.016
ARU96-38	cpx	A2	6	1.927	0.022	0.084	0.009	0.338	0.007	0.832	0.778	0.014	0.000	0.001	4.012
ARU96-38	cpx	A2	6	1.933	0.007	0.091	0.014	0.189	0.006	0.979	0.780	0.014	0.000	0.001	4.014
ARU96-37	cpx	A2	6	1.955	0.008	0.059	0.007	0.219	0.008	1.125	0.616	0.010	0.000	0.002	4.009
ARU96-37	cpx	A2	6	1.943	0.013	0.075	0.001	0.369	0.010	1.052	0.536	0.009	0.000	0.001	4.009
ARU96-37	cpx	A2	6	1.921	0.014	0.104	0.001	0.305	0.011	0.943	0.705	0.014	0.000	0.001	4.019
ARU96-37	cpx	A2	6	1.946	0.006	0.075	0.018	0.173	0.005	1.009	0.761	0.014	0.000	0.002	4.009
ARU96-37	cpx	A2	6	1.907	0.009	0.126	0.026	0.171	0.005	0.989	0.767	0.015	0.000	0.001	4.016
ARU96-37	cpx	A2	6	1.925	0.011	0.114	0.008	0.223	0.008	1.059	0.650	0.011	0.000	0.001	4.010
ARU96-22	ilm	A1	6	0.048	1.956	0.048	0.005	1.778	0.059	0.060	0.015	0.002	0.000	0.002	3.971
ARU96-22	ilm	A1	6	0.063	1.946	0.033	0.003	1.800	0.060	0.042	0.027	0.003	0.000	0.000	3.977
ARU96-30	ilm	A2	6	0.052	1.937	0.008	0.001	1.862	0.086	0.008	0.050	0.000	0.001	0.000	4.005
ARU96-38	ilm	A2	6	0.005	2.397	0.005	0.026	1.055	0.030	0.002	0.066	0.003	0.000	0.000	3.587
ARU96-38	ilm	A2	6	0.306	1.826	0.021	0.018	1.311	0.119	0.006	0.240	0.003	0.000	0.002	3.851
ARU96-38	ilm	A2	6	0.041	2.097	0.003	0.030	1.464	0.074	0.003	0.134	0.002	0.000	0.002	3.848
ARU96-37	mag	A2	4	0.089	0.611	0.007	0.000	2.459	0.038	0.002	0.089	0.000	0.001	0.000	3.296
ARU96-37	mag	A2	4	0.327	0.467	0.033	0.001	2.029	0.015	0.002	0.311	0.003	0.000	0.001	3.189
ARU96-37	mag	A2	4	0.060	0.058	0.020	0.001	3.688	0.003	0.018	0.020	0.003	0.000	0.001	3.872
ARU96-22	plag	A1	8	2.197	0.000	1.787	0.000	0.005	0.001	0.001	0.820	0.190	0.000	0.001	5.002
ARU96-30	plag	A2	8	2.394	0.001	1.563	0.001	0.027	0.000	0.012	0.643	0.359	0.002	0.000	5.002
ARU96-30	plag	A2	8	2.457	0.003	1.493	0.002	0.034	0.000	0.008	0.576	0.429	0.008	0.001	5.011
ARU96-30	plag	A2	8	2.183	0.001	1.780	0.002	0.026	0.001	0.005	0.845	0.161	0.001	0.000	5.005
ARU96-30	plag	A2	8	2.377	0.002	1.550	0.001	0.062	0.000	0.053	0.615	0.371	0.003	0.000	5.034
ARU96-38	plag	A2	8	2.150	0.001	1.806	0.001	0.029	0.001	0.003	0.886	0.132	0.001	0.000	5.010
ARU96-38	plag	A2	8	2.299	0.002	1.654	0.001	0.032	0.000	0.012	0.727	0.286	0.005	0.000	5.018
ARU96-38	plag	A2	8	2.391	0.001	1.568	0.001	0.027	0.001	0.005	0.637	0.367	0.012	0.001	5.011
ARU96-38	plag	A2	8	2.183	0.001	1.778	0.001	0.028	0.000	0.003	0.850	0.162	0.001	0.000	5.007
ARU96-38	plag	A2	8	2.150	0.001	1.800	0.002	0.029	0.001	0.006	0.883	0.150	0.001	0.001	5.024
ARU96-38	plag	A2	8	2.153	0.001	1.803	0.000	0.026	0.001	0.003	0.872	0.164	0.002	0.001	5.026
ARU96-37	plag	A2	8	2.383	0.002	1.571	0.001	0.030	0.000	0.016	0.648	0.352	0.002	0.001	5.006
ARU96-37	plag	A2	8	2.537	0.003	1.418	0.001	0.032	0.002	0.006	0.496	0.506	0.004	0.001	5.006
ARU96-37	plag	A2	8	2.422	0.002	1.528	0.001	0.040	0.001	0.010	0.607	0.397	0.003	0.001	5.012
ARU96-37	plag	A2	8	2.639	0.002	1.326	0.000	0.031	0.000	0.002	0.383	0.618	0.006	0.000	5.007
ARU96-37	plag	A2	8	2.388	0.001	1.559	0.001	0.041	0.001	0.011	0.643	0.367	0.002	0.001	5.015
ARU96-37	plag	A2	8	2.396	0.002	1.549	0.001	0.038	0.000	0.014	0.643	0.366	0.001	0.001	5.011
ARU96-37	plag	A2	8	2.720	0.001	1.253	0.002	0.030	0.001	0.000	0.301	0.670	0.014	0.001	4.993
ARU96-37	plag	A2	8	2.383	0.002	1.567	0.001	0.031	0.001	0.014	0.649	0.355	0.003	0.002	5.008
ARU96-22	sp	A1	32	0.000	0.037	4.850	10.387	8.468	0.152	0.433	0.003	0.028	0.000	0.000	24.358
ARU96-22	sp	A1	32	0.000	0.554	2.668	7.517	15.308	0.210	0.045	0.025	0.000	0.004	0.024	26.355

Sample		Lith.	SiO_2	TiO_2	Al_2O_3	Cr_2O_3	FeO	MnO	MgO	CaO	Na_2O	K_2O	NiO	Total
ARU97-37	amph	A4	45.78	1.62	7.84	0.08	16.50	0.16	11.67	11.39	1.32	0.58	0.02	96.96
ARU97-37	amph	A4	43.95	2.32	8.96	0.09	17.43	0.15	10.66	11.25	1.80	0.56	0.03	97.20
ARU97-37	amph	A4	44.65	1.57	8.33	0.00	17.29	0.19	11.29	11.28	1.53	0.59	0.06	96.78
ARU97-37	amph	A4	44.57	1.66	8.68	0.06	17.39	0.14	10.97	11.28	1.53	0.59	0.02	96.89
ARU97-37	amph	A4	48.22	0.97	5.98	0.00	16.13	0.19	12.66	11.26	1.01	0.39	0.03	96.84
ARU97-37	amph	A4	43.19	1.65	9.67	0.03	17.75	0.10	10.71	11.40	1.67	0.63	0.02	96.82
ARU97-37	amph	A4	43.38	1.62	8.97	0.08	17.33	0.16	10.87	11.36	1.54	0.62	0.04	95.97
ARU96-145	amph	A4	55.73	0.07	0.79	0.02	15.17	0.14	14.23	12.09	0.12	0.01	0.02	98.39
ARU96-145	amph	A4	56.47	0.02	1.08	0.03	14.13	0.14	13.95	11.53	0.11	0.03	0.02	97.51
ARU96-145	amph	A4	47.24	1.52	7.39	0.07	15.14	0.23	13.10	11.47	1.33	0.30	0.01	97.80
ARU96-145	amph	A4	47.84	1.59	7.18	0.06	15.05	0.18	13.21	11.32	1.36	0.28	0.02	98.09
ARU96-145	amph	A4	47.24	1.58	7.41	0.08	14.65	0.21	13.46	11.59	1.36	0.26	0.05	97.89
ARU96-145	amph	A4	48.00	1.48	7.08	0.13	14.44	0.18	13.61	11.34	1.28	0.28	0.02	97.84
ARU96-142	amph	A5	51.95	0.88	5.29	0.30	9.27	0.15	17.76	11.18	0.62	0.09	0.05	97.54
ARU96-142	amph	A5	56.18	0.16	1.06	0.08	15.60	0.29	22.57	1.31	0.11	0.00	0.04	97.40
ARU96-142	amph	A5	56.12	0.15	1.06	0.05	15.71	0.31	22.51	1.31	0.11	0.01	0.03	97.37
ARU96-142	amph	A5	56.54	0.19	1.02	0.07	15.59	0.31	22.75	1.43	0.13	0.01	0.04	98.08
ARU96-142	amph	A5	55.94	0.25	1.71	0.07	14.90	0.24	21.93	2.56	0.17	0.02	0.07	97.86
ARU96-142	amph	A5	56.52	0.14	1.08	0.04	15.82	0.27	22.67	1.32	0.12	0.01	0.10	98.09
ARU96-142	amph	A5	56.26	0.18	1.08	0.06	15.58	0.26	22.46	1.38	0.14	0.01	0.04	97.45
ARU96-142	amph	A5	56.25	0.13	1.07	0.06	15.80	0.33	22.46	1.35	0.11	0.00	0.01	97.57
ARU96-142	amph	A5	51.43	0.77	5.56	0.46	9.04	0.13	17.64	11.40	0.66	0.14	0.07	97.30
ARU96-142	amph	A5	56.47	0.11	0.96	0.04	15.99	0.33	22.52	1.20	0.11	0.00	0.07	97.80
ARU96-142	amph	A5	56.12	0.16	1.20	0.06	15.86	0.31	22.24	2.10	0.16	0.01	0.03	98.25
ARU96-142	amph	A5	56.67	0.16	1.02	0.11	15.86	0.31	22.52	1.39	0.12	0.02	0.08	98.26
ARU96-142	amph	A5	52.90	0.64	4.37	0.52	11.39	0.21	18.80	8.48	0.54	0.09	0.04	97.98
ARU96-142	amph	A5	51.44	0.76	5.81	0.70	9.34	0.11	17.32	11.27	0.77	0.13	0.05	97.70
ARU96-142	amph	A5	52.15	0.80	5.50	0.52	9.56	0.10	17.68	11.26	0.67	0.10	0.06	98.40
ARU97-37	ap	A4	0.01	0.04	0.08	0.00	0.25	0.07	0.02	54.37	0.01	0.00	0.02	54.87
ARU96-145	cpx	A4	52.73	0.21	1.04	0.04	10.35	0.28	13.64	21.90	0.29	0.01	0.02	100.51
ARU97-37	ilm	A4	0.00	48.47	0.03	0.06	46.73	3.11	0.02	0.17	0.00	0.01	0.02	98.62
ARU96-145	ilm	A4	0.00	50.58	0.04	0.10	46.15	1.30	0.08	0.07	0.02	0.00	0.04	98.38
ARU96-142	ilm	A5	0.44	51.26	0.05	0.09	44.68	0.44	5.52	0.15	0.08	0.01	0.01	102.73
ARU96-145	mag	A4	3.81	0.01	0.55	0.01	83.52	0.01	1.60	0.05	0.02	0.03	0.03	89.64
ARU97-37	plag	A4	57.03	0.01	27.12	0.00	0.17	0.00	0.03	9.57	6.42	0.16	0.02	100.53
ARU97-37	plag	A4	56.74	0.03	26.27	0.04	0.12	0.01	0.01	8.90	6.64	0.24	0.01	99.01
ARU97-37	plag	A4	57.43	0.01	26.42	0.04	0.12	0.02	0.00	8.65	6.63	0.19	0.00	99.51
ARU97-37	plag	A4	56.96	0.03	26.42	0.04	0.13	0.02	0.00	8.74	6.70	0.16	0.02	99.22
ARU97-37	plag	A4	56.92	0.01	26.43	0.03	0.18	0.00	0.02	8.76	6.61	0.18	0.02	99.16
ARU97-37	plag	A4	56.96	0.03	26.51	0.04	0.12	0.03	0.01	9.02	6.53	0.13	0.02	99.40
ARU97-37	plag	A4	56.18	0.02	26.70	0.05	0.18	0.03	0.02	9.32	6.31	0.15	0.03	98.99
ARU97-37	plag	A4	56.82	0.01	26.48	0.04	0.17	0.03	0.00	9.16	6.38	0.20	0.02	99.31
ARU97-37	plag	A4	57.35	0.00	26.13	0.02	0.26	0.01	0.00	8.58	6.72	0.12	0.02	99.21
ARU96-145	plag	A4	54.55	0.01	28.66	0.01	0.20	0.01	0.00	11.40	5.07	0.11	0.02	100.04
ARU96-145	plag	A4	50.67	0.01	31.20	0.02	0.18	0.00	0.00	14.25	3.48	0.04	0.03	99.88
ARU96-145	plag	A4	55.39	0.02	28.18	0.04	0.14	0.01	0.01	10.95	5.46	0.10	0.01	100.31
ARU96-142	plag	A5	56.45	0.01	26.80	0.05	0.16	0.02	0.01	9.41	6.41	0.05	0.02	99.39
ARU96-142	plag	A5	57.29	0.01	26.91	0.02	0.30	0.03	0.04	9.56	6.35	0.03	0.03	100.57
ARU96-142	plag	A5	55.58	0.04	27.98	0.04	0.25	0.04	0.02	10.83	5.63	0.02	0.02	100.45
ARU96-142	plag	A5	56.29	0.01	27.64	0.04	0.21	0.03	0.02	10.36	5.88	0.04	0.02	100.54
ARU96-142	plag	A5	55.57	0.01	27.99	0.00	0.17	0.02	0.02	10.91	5.59	0.02	0.02	100.32
ARU96-142	plag	A5	56.39	0.01	27.69	0.01	0.27	0.00	0.00	10.24	5.88	0.03	0.05	100.57
ARU96-142	plag	A5	57.52	0.01	26.87	0.03	0.29	0.02	0.01	9.38	6.42	0.04	0.00	100.59
ARU96-142	plag	A5	54.91	0.00	28.45	0.00	0.12	0.02	0.00	11.52	5.31	0.03	0.02	100.38
ARU96-142	plag	A5	55.04	0.02	28.39	0.00	0.22	0.03	0.00	11.30	5.31	0.05	0.02	100.38
ARU96-142	plag	A5	56.05	0.01	27.81	0.03	0.16	0.01	0.01	10.66	5.66	0.06	0.02	100.48
ARU96-142	sp	A5	0.00	3.19	6.01	28.13	56.46	0.51	0.16	0.02	0.02	0.02	0.06	94.58
ARU96-142	sp	A5	0.00	0.89	5.67	28.04	58.68	0.50	0.08	0.10	0.02	0.01	0.07	94.06
ARU96-142	sp	A5	0.00	1.22	6.14	29.66	56.67	0.69	0.21	0.01	0.05	0.01	0.11	94.77
ARU96-142	sp	A5	0.00	1.21	6.67	35.80	48.89	0.42	0.73	0.01	0.02	0.00	0.02	93.77

Sample		Lith.	O	Si	Ti	Al	Cr	Fe^{2+}	Mn	Mg	Ca	Na	K	Ni	Total
ARU97-37	amph	A4	23	6.875	0.183	1.388	0.009	2.072	0.020	2.613	1.833	0.384	0.111	0.002	15.490
ARU97-37	amph	A4	23	6.645	0.264	1.597	0.011	2.204	0.019	2.403	1.823	0.528	0.108	0.004	15.606
ARU97-37	amph	A4	23	6.764	0.179	1.487	0.000	2.190	0.024	2.549	1.831	0.449	0.114	0.007	15.594
ARU97-37	amph	A4	23	6.743	0.189	1.548	0.007	2.200	0.018	2.474	1.829	0.449	0.114	0.002	15.573
ARU97-37	amph	A4	23	7.187	0.109	1.051	0.000	2.011	0.024	2.813	1.798	0.292	0.074	0.004	15.363
ARU97-37	amph	A4	23	6.572	0.189	1.734	0.004	2.259	0.013	2.430	1.859	0.493	0.122	0.002	15.677
ARU97-37	amph	A4	23	6.648	0.187	1.620	0.010	2.221	0.021	2.483	1.865	0.458	0.121	0.005	15.639
ARU96-145	amph	A4	23	8.006	0.008	0.134	0.002	1.823	0.017	3.047	1.861	0.033	0.002	0.002	14.935
ARU96-145	amph	A4	23	8.110	0.002	0.183	0.003	1.697	0.017	2.987	1.774	0.031	0.005	0.002	14.811
ARU96-145	amph	A4	23	6.961	0.168	1.284	0.008	1.866	0.029	2.878	1.811	0.380	0.056	0.001	15.442
ARU96-145	amph	A4	23	7.012	0.175	1.241	0.007	1.845	0.022	2.886	1.778	0.387	0.052	0.002	15.407
ARU96-145	amph	A4	23	6.943	0.175	1.284	0.009	1.801	0.026	2.949	1.825	0.388	0.049	0.006	15.455
ARU96-145	amph	A4	23	7.032	0.163	1.223	0.015	1.769	0.022	2.972	1.780	0.364	0.052	0.002	15.394
ARU96-142	amph	A5	23	7.377	0.094	0.885	0.034	1.101	0.018	3.760	1.701	0.171	0.016	0.006	15.163
ARU96-142	amph	A5	23	7.925	0.017	0.176	0.009	1.840	0.035	4.746	0.198	0.030	0.000	0.005	14.981
ARU96-142	amph	A5	23	7.924	0.016	0.176	0.006	1.855	0.037	4.738	0.198	0.030	0.002	0.003	14.985
ARU96-142	amph	A5	23	7.922	0.020	0.168	0.008	1.827	0.037	4.751	0.215	0.035	0.002	0.005	14.990
ARU96-142	amph	A5	23	7.860	0.026	0.283	0.008	1.751	0.029	4.593	0.385	0.046	0.004	0.008	14.993
ARU96-142	amph	A5	23	7.923	0.015	0.178	0.004	1.855	0.032	4.737	0.198	0.033	0.002	0.011	14.988
ARU96-142	amph	A5	23	7.931	0.019	0.179	0.007	1.837	0.031	4.720	0.208	0.038	0.002	0.005	14.977
ARU96-142	amph	A5	23	7.928	0.014	0.178	0.007	1.862	0.039	4.719	0.204	0.030	0.000	0.001	14.982
ARU96-142	amph	A5	23	7.331	0.083	0.934	0.052	1.078	0.016	3.748	1.741	0.182	0.025	0.008	15.198
ARU96-142	amph	A5	23	7.943	0.012	0.159	0.004	1.881	0.039	4.722	0.181	0.030	0.000	0.008	14.979
ARU96-142	amph	A5	23	7.881	0.017	0.199	0.007	1.863	0.037	4.656	0.316	0.044	0.002	0.003	15.025
ARU96-142	amph	A5	23	7.933	0.017	0.168	0.012	1.857	0.037	4.700	0.209	0.033	0.004	0.009	14.979
ARU96-142	amph	A5	23	7.486	0.068	0.729	0.058	1.348	0.025	3.966	1.286	0.148	0.016	0.005	15.135
ARU96-142	amph	A5	23	7.312	0.081	0.974	0.079	1.110	0.013	3.670	1.717	0.212	0.024	0.006	15.198
ARU96-142	amph	A5	23	7.354	0.085	0.914	0.058	1.127	0.012	3.716	1.701	0.183	0.018	0.007	15.175
ARU97-37	ap	A4	6	0.001	0.003	0.010	0.000	0.021	0.006	0.003	5.944	0.002	0.000	0.002	5.992
ARU96-145	cpx	A4	6	1.969	0.006	0.046	0.001	0.323	0.009	0.759	0.876	0.021	0.000	0.001	4.011
ARU97-37	ilm	A4	6	0.000	1.902	0.002	0.002	2.039	0.137	0.002	0.010	0.000	0.001	0.001	4.096
ARU96-145	ilm	A4	6	0.000	1.964	0.002	0.004	1.993	0.057	0.006	0.004	0.002	0.000	0.002	4.034
ARU96-142	ilm	A5	6	0.021	1.859	0.003	0.003	1.802	0.018	0.397	0.008	0.007	0.001	0.000	4.119
ARU96-145	mag	A4	4	0.188	0.000	0.032	0.000	3.450	0.000	0.118	0.003	0.002	0.002	0.001	3.796
ARU97-37	plag	A4	8	2.552	0.000	1.430	0.000	0.006	0.000	0.002	0.459	0.557	0.009	0.001	5.016
ARU97-37	plag	A4	8	2.575	0.001	1.405	0.001	0.005	0.000	0.001	0.433	0.584	0.014	0.000	5.019
ARU97-37	plag	A4	8	2.587	0.000	1.403	0.001	0.005	0.001	0.000	0.418	0.579	0.011	0.000	5.005
ARU97-37	plag	A4	8	2.577	0.001	1.409	0.001	0.005	0.001	0.000	0.424	0.588	0.009	0.001	5.016
ARU97-37	plag	A4	8	2.577	0.000	1.410	0.001	0.007	0.000	0.001	0.425	0.580	0.010	0.001	5.012
ARU97-37	plag	A4	8	2.573	0.001	1.411	0.001	0.005	0.001	0.001	0.437	0.572	0.007	0.001	5.010
ARU97-37	plag	A4	8	2.552	0.001	1.430	0.002	0.007	0.001	0.001	0.454	0.556	0.009	0.001	5.014
ARU97-37	plag	A4	8	2.571	0.000	1.412	0.001	0.006	0.001	0.000	0.444	0.560	0.012	0.001	5.008
ARU97-37	plag	A4	8	2.593	0.000	1.392	0.001	0.010	0.000	0.000	0.416	0.589	0.007	0.001	5.009
ARU96-145	plag	A4	8	2.463	0.000	1.525	0.000	0.008	0.000	0.000	0.552	0.444	0.006	0.001	4.999
ARU96-145	plag	A4	8	2.311	0.000	1.677	0.001	0.007	0.000	0.000	0.696	0.308	0.002	0.001	5.003
ARU96-145	plag	A4	8	2.491	0.001	1.494	0.001	0.005	0.000	0.001	0.528	0.476	0.006	0.000	5.003
ARU96-142	plag	A5	8	2.553	0.000	1.429	0.002	0.006	0.001	0.001	0.456	0.562	0.003	0.001	5.014
ARU96-142	plag	A5	8	2.561	0.000	1.418	0.001	0.011	0.001	0.003	0.458	0.550	0.002	0.001	5.006
ARU96-142	plag	A5	8	2.497	0.001	1.481	0.001	0.009	0.002	0.001	0.521	0.490	0.001	0.001	5.005
ARU96-142	plag	A5	8	2.522	0.000	1.459	0.001	0.008	0.001	0.001	0.497	0.511	0.002	0.001	5.003
ARU96-142	plag	A5	8	2.498	0.000	1.483	0.000	0.006	0.001	0.001	0.525	0.487	0.001	0.001	5.003
ARU96-142	plag	A5	8	2.524	0.000	1.461	0.000	0.010	0.000	0.000	0.491	0.510	0.002	0.002	5.000
ARU96-142	plag	A5	8	2.568	0.000	1.414	0.001	0.011	0.001	0.001	0.449	0.556	0.002	0.000	5.003
ARU96-142	plag	A5	8	2.471	0.000	1.509	0.000	0.005	0.001	0.000	0.556	0.463	0.002	0.001	5.008
ARU96-142	plag	A5	8	2.476	0.001	1.506	0.000	0.008	0.001	0.000	0.545	0.463	0.003	0.001	5.004
ARU96-142	plag	A5	8	2.513	0.000	1.470	0.001	0.006	0.000	0.001	0.512	0.492	0.003	0.001	4.999
ARU96-142	sp	A5	32	0.000	0.793	2.342	7.354	15.613	0.143	0.079	0.007	0.013	0.008	0.016	26.368
ARU96-142	sp	A5	32	0.000	0.227	2.265	7.513	16.631	0.144	0.040	0.036	0.013	0.004	0.019	26.892
ARU96-142	sp	A5	32	0.000	0.305	2.405	7.792	15.747	0.194	0.104	0.004	0.032	0.004	0.029	26.616
ARU96-142	sp	A5	32	0.000	0.296	2.555	9.200	13.290	0.116	0.354	0.003	0.013	0.000	0.005	25.832

Sample		Lith.	SiO_2	TiO_2	Al_2O_3	Cr_2O_3	FeO	MnO	MgO	CaO	Na_2O	K_2O	NiO	Total
ARU96-53	amph	B1	51.23	0.84	5.07	0.14	10.67	0.19	15.83	12.38	0.70	0.25	0.03	97.33
ARU96-53	amph	B1	48.98	0.68	6.88	0.19	11.79	0.17	15.06	12.20	1.11	0.28	0.01	97.35
ARU96-53	amph	B1	51.58	0.70	5.23	0.14	10.99	0.20	16.11	12.67	0.71	0.25	0.05	98.63
ARU96-53	amph	B1	49.04	0.99	6.94	0.26	12.34	0.25	14.74	12.40	1.11	0.33	0.01	98.41
ARU96-53	amph	B1	50.26	0.78	5.78	0.15	11.85	0.21	15.51	12.26	0.99	0.27	0.02	98.08
ARU96-53	amph	B1	50.24	0.82	6.14	0.11	11.58	0.21	15.28	12.25	1.12	0.21	0.05	98.01
ARU96-53	amph	B1	51.24	0.75	5.36	0.25	11.03	0.20	16.10	12.52	0.96	0.26	0.01	98.68
ARU96-53	amph	B1	48.65	0.76	7.75	0.36	11.85	0.19	14.89	12.24	1.28	0.27	0.02	98.26
ARU96-53	amph	B1	50.65	0.61	5.43	0.36	11.16	0.21	15.69	12.73	0.85	0.26	0.04	97.99
ARU96-53	amph	B1	51.36	0.55	4.88	0.21	11.50	0.19	15.72	12.14	0.84	0.25	0.05	97.69
ARU96-53	amph	B1	51.53	0.62	4.85	0.18	11.18	0.22	16.02	12.19	0.81	0.23	0.02	97.85
ARU97-77	amph	B1	47.92	1.07	7.90	0.03	12.43	0.24	15.09	11.88	1.26	0.37	0.07	98.26
ARU97-77	amph	B1	47.27	1.10	8.34	0.08	13.17	0.29	14.34	11.81	1.41	0.35	0.00	98.16
ARU97-77	amph	B1	47.53	1.06	7.56	0.03	13.93	0.31	13.95	11.99	1.18	0.45	0.02	98.01
ARU97-77	amph	B1	47.83	0.97	6.96	0.05	14.08	0.28	13.92	12.15	1.07	0.50	0.01	97.82
ARU97-77	amph	B1	47.71	1.04	7.77	0.04	13.50	0.24	14.09	11.91	1.17	0.37	0.03	97.87
ARU96-157	amph	B1	49.22	0.62	5.98	0.03	11.44	0.30	16.83	11.34	0.76	0.50	0.01	97.03
ARU96-157	amph	B1	50.71	1.08	5.26	0.04	10.53	0.21	16.97	11.81	0.77	0.45	0.04	97.87
ARU96-157	amph	B1	48.94	0.99	6.86	0.01	12.42	0.30	15.64	11.58	1.01	0.49	0.04	98.28
ARU96-57	amph	B1	51.24	0.86	5.81	0.25	11.73	0.22	16.08	12.45	1.02	0.24	0.02	99.92
ARU96-57	amph	B1	53.06	0.40	4.28	0.27	10.85	0.23	17.07	12.51	0.77	0.20	0.02	99.66
ARU96-57	amph	B1	50.60	0.68	5.34	0.26	11.18	0.19	16.26	12.04	0.91	0.30	0.04	97.80
ARU96-57	amph	B1	50.20	0.54	4.72	0.23	11.23	0.20	16.34	12.17	0.82	0.33	0.07	96.85
ARU96-57	amph	B1	46.84	1.20	8.08	0.50	12.79	0.20	13.87	12.14	1.41	0.49	0.03	97.55
ARU97-164	amph	B1	47.53	1.16	7.37	0.00	14.76	0.26	13.17	11.89	1.26	0.28	0.02	97.70
ARU97-164	amph	B1	47.13	1.36	7.71	0.02	14.62	0.26	13.54	11.81	1.39	0.27	0.04	98.15
ARU97-164	amph	B1	47.22	1.31	7.90	0.04	13.22	0.19	14.18	11.66	1.43	0.25	0.02	97.42
ARU97-164	amph	B1	46.66	1.39	8.56	0.05	15.32	0.25	12.97	12.35	1.21	0.82	0.01	99.59
ARU97-164	amph	B1	46.67	1.47	8.74	0.06	15.29	0.23	12.82	12.42	1.45	0.35	0.04	99.54
ARU97-164	amph	B1	48.27	1.12	7.34	0.09	15.06	0.27	13.60	12.44	1.21	0.33	0.03	99.76
ARU97-175	amph	B2a	46.11	1.57	9.35	0.03	11.49	0.22	14.90	12.31	1.54	0.38	0.05	97.95
ARU97-175	amph	B2a	46.78	1.46	8.91	0.02	11.54	0.12	14.87	12.27	1.45	0.20	0.02	97.64
ARU97-111	amph	B2b	43.41	2.37	11.69	0.03	10.80	0.19	14.90	11.48	2.22	0.34	0.01	97.43
ARU97-111	amph	B2b	43.67	2.30	11.88	0.05	10.58	0.12	14.48	11.98	2.05	0.38	0.05	97.54
ARU97-111	amph	B2b	48.08	1.44	8.12	0.02	10.98	0.16	15.59	11.72	1.45	0.15	0.04	97.75
ARU96-154	amph	B2b	44.63	0.97	11.05	0.15	10.34	0.09	15.84	12.02	2.06	0.50	0.03	97.68
ARU96-154	amph	B2b	47.14	0.00	11.30	0.00	7.94	0.14	17.69	12.36	1.84	0.15	0.04	98.60
ARU96-154	amph	B2b	43.53	2.10	11.50	0.10	10.92	0.12	15.15	11.75	2.46	0.37	0.02	98.02
ARU97-73	amph	B4	47.58	1.33	7.36	0.04	15.75	0.38	12.41	11.99	0.96	0.80	0.03	98.63
ARU97-73	amph	B4	48.24	1.57	6.96	0.00	14.85	0.52	13.01	11.42	1.26	0.63	0.02	98.48
ARU97-73	amph	B4	48.44	1.51	6.85	0.03	14.70	0.52	13.12	11.65	1.16	0.61	0.02	98.61
ARU97-73	amph	B4	49.94	1.19	6.02	0.01	13.78	0.45	13.94	11.90	0.97	0.53	0.02	98.75
ARU97-73	amph	B4	48.08	1.35	7.25	0.01	15.09	0.45	12.95	11.86	1.05	0.70	0.02	98.81
ARU97-73	amph	B4	48.89	1.31	6.63	0.03	13.58	0.47	13.60	12.19	1.00	0.64	0.04	98.38
ARU97-73	amph	B4	48.71	1.36	6.89	0.01	14.64	0.45	13.56	11.64	1.22	0.63	0.02	99.13
ARU97-73	amph	B4	47.90	1.47	7.04	0.04	14.12	0.39	13.37	12.24	0.94	0.62	0.02	98.15
ARU97-73	amph	B4	48.68	1.52	6.86	0.02	14.29	0.55	13.53	11.62	1.23	0.60	0.03	98.93
ARU97-73	amph	B4	48.49	1.48	6.84	0.02	14.69	0.47	13.25	11.81	1.17	0.64	0.05	98.91
ARU97-160	amph	B4	48.12	1.67	7.27	0.04	12.58	0.27	15.00	11.33	1.37	0.48	0.02	98.15
ARU97-160	amph	B4	47.73	1.62	7.12	0.03	13.06	0.33	14.93	11.37	1.34	0.51	0.03	98.07
ARU97-160	amph	B4	47.00	1.61	7.24	0.02	13.35	0.36	14.12	11.15	1.33	0.50	0.05	96.73
ARU97-163	amph	B4	47.43	1.66	6.87	0.01	12.36	0.27	14.78	11.47	1.40	0.57	0.02	96.84
ARU97-163	amph	B4	55.01	0.63	1.15	0.02	8.84	0.43	19.47	11.52	0.22	0.05	0.06	97.40
ARU97-163	amph	B4	46.74	1.75	7.35	0.02	12.05	0.21	15.01	11.36	1.51	0.53	0.01	96.54
ARU97-162	amph	B4	47.32	1.17	7.53	0.14	13.95	0.31	13.63	12.12	1.06	0.71	0.03	97.97
ARU97-162	amph	B4	47.63	1.28	7.16	0.06	13.54	0.29	13.94	12.15	1.06	0.54	0.03	97.68
ARU96-131	amph	B5	48.93	1.34	6.05	0.08	13.20	0.69	14.69	11.28	1.36	0.18	0.02	97.82
ARU96-131	amph	B5	49.33	1.29	5.90	0.00	13.13	0.66	15.01	11.39	1.23	0.17	0.02	98.13
ARU96-131	amph	B5	49.46	1.31	5.84	0.01	13.55	0.78	14.51	11.45	1.19	0.20	0.04	98.34
ARU96-131	amph	B5	48.53	1.55	6.82	0.01	12.69	0.67	15.20	11.39	1.38	0.19	0.02	98.45
ARU97-78	amph	B5	49.07	1.32	6.49	0.05	12.55	0.33	15.32	11.69	1.46	0.19	0.02	98.49
ARU97-78	amph	B5	51.14	0.56	4.38	0.03	14.06	0.54	14.40	12.09	0.77	0.31	0.02	98.30
ARU97-78	amph	B5	48.93	0.93	5.88	0.03	14.87	0.67	13.26	11.43	1.18	0.28	0.01	97.47
ARU97-78	amph	B5	49.21	1.15	6.54	0.02	12.69	0.36	14.81	11.10	1.44	0.18	0.03	97.53
ARU97-78	amph	B5	50.77	0.79	4.78	0.02	14.11	0.60	14.45	11.94	1.01	0.31	0.06	98.84
ARU97-78	amph	B5	48.04	1.52	7.15	0.01	12.99	0.23	14.71	11.47	1.52	0.22	0.02	97.88

Sample		Lith.	SiO_2	TiO_2	Al_2O_3	Cr_2O_3	FeO	MnO	MgO	CaO	Na_2O	K_2O	NiO	Total
ARU97-164	ap	B1	0.00	0.01	0.00	0.04	0.02	0.09	0.01	54.09	0.01	0.00	0.02	54.29
ARU97-163	ap	B4	0.05	0.01	0.00	0.04	0.17	0.03	0.01	54.67	0.01	0.01	0.02	55.02
ARU97-163	ap	B4	0.04	0.01	0.00	0.02	0.17	0.07	0.02	54.45	0.01	0.01	0.02	54.82
ARU97-163	ap	B4	0.03	0.01	0.01	0.07	0.06	0.09	0.02	53.67	0.01	0.00	0.02	53.99
ARU96-131	ap	B5	0.12	0.00	0.00	0.02	0.25	0.06	0.01	54.17	0.01	0.01	0.02	54.67
ARU96-131	ap	B5	0.10	0.01	0.03	0.02	0.76	0.11	0.02	53.85	0.01	0.00	0.01	54.92
ARU97-73	bi	B4	36.47	5.03	14.44	0.02	19.58	0.27	10.83	0.01	0.15	8.74	0.02	95.56
ARU97-73	bi	B4	36.17	4.87	14.07	0.02	18.48	0.28	11.07	0.00	0.16	9.07	0.03	94.22
ARU97-73	bi	B4	36.51	4.80	14.21	0.02	19.58	0.25	10.41	0.01	0.11	9.44	0.01	95.35
ARU97-73	bi	B4	36.81	5.08	14.19	0.02	18.54	0.21	11.45	0.01	0.17	9.16	0.01	95.65
ARU97-160	bi	B4	36.23	4.03	14.37	0.04	17.85	0.23	11.90	0.01	0.12	9.14	0.04	93.96
ARU96-131	bi	B5	36.92	4.31	13.98	0.00	18.50	0.48	11.79	0.01	0.23	9.48	0.00	95.70
ARU96-131	bi	B5	36.83	4.02	14.17	0.03	18.32	0.46	12.13	0.01	0.17	9.62	0.02	95.78
ARU96-131	bi	B5	36.70	4.42	14.24	0.05	18.25	0.42	11.95	0.02	0.22	9.38	0.03	95.68
ARU96-131	bi	B5	36.71	4.27	13.89	0.03	17.75	0.41	12.18	0.02	0.17	9.26	0.03	94.72
ARU97-78	bi	B5	36.72	4.05	13.77	0.02	18.37	0.32	12.00	0.01	0.17	9.19	0.02	94.64
ARU97-78	bi	B5	37.01	4.09	13.73	0.01	18.21	0.35	11.76	0.02	0.13	9.27	0.01	94.59
ARU97-78	bi	B5	36.94	2.90	14.09	0.01	17.42	0.28	12.32	0.18	0.06	8.46	0.00	92.66
ARU97-160	chl	B4	27.31	0.03	19.01	0.03	24.64	0.72	15.50	0.05	0.02	0.06	0.07	87.44
ARU96-131	chl	B5	26.64	0.04	18.88	0.01	24.98	0.88	15.87	0.09	0.04	0.04	0.02	87.49
ARU96-53	cpx	B1	54.19	0.10	0.80	0.03	6.86	0.21	14.46	24.05	0.32	0.01	0.04	101.07
ARU96-53	cpx	B1	53.68	0.17	1.27	0.05	7.15	0.26	14.18	23.90	0.40	0.01	0.01	101.08
ARU96-53	cpx	B1	54.22	0.04	0.78	0.05	7.00	0.28	14.49	24.06	0.35	0.00	0.03	101.30
ARU96-53	cpx	B1	53.72	0.12	0.83	0.08	7.54	0.23	14.29	23.72	0.38	0.00	0.04	100.95
ARU96-53	cpx	B1	54.51	0.05	0.43	0.06	7.46	0.23	14.28	24.27	0.34	0.00	0.02	101.65
ARU96-53	cpx	B1	54.28	0.05	0.68	0.09	7.20	0.28	14.62	23.90	0.39	0.00	0.01	101.50
ARU96-53	cpx	B1	54.26	0.04	0.65	0.02	7.20	0.35	14.50	24.03	0.32	0.01	0.01	101.39
ARU96-53	cpx	B1	54.14	0.07	0.86	0.05	7.10	0.28	14.67	23.95	0.31	0.01	0.03	101.47
ARU96-53	cpx	B1	54.37	0.05	0.70	0.07	7.36	0.22	14.47	24.08	0.39	0.01	0.02	101.74
ARU96-53	cpx	B1	54.22	0.11	0.67	0.06	7.06	0.27	14.65	23.99	0.32	0.02	0.02	101.39
ARU96-53	cpx	B1	54.16	0.00	0.54	0.08	7.17	0.27	14.04	24.45	0.33	0.01	0.01	101.06
ARU97-77	cpx	B1	53.02	0.04	0.66	0.04	8.14	0.34	14.00	23.96	0.27	0.00	0.02	100.49
ARU97-77	cpx	B1	53.56	0.05	0.67	0.02	8.16	0.32	13.59	24.31	0.31	0.00	0.02	101.01
ARU97-77	cpx	B1	53.20	0.06	0.69	0.03	8.37	0.32	13.71	24.18	0.30	0.00	0.02	100.88
ARU97-77	cpx	B1	53.75	0.04	0.55	0.01	7.46	0.37	14.34	24.63	0.22	0.01	0.00	101.38
ARU96-57	cpx	B1	53.66	0.10	0.69	0.08	7.00	0.22	14.60	23.73	0.35	0.02	0.02	100.47
ARU96-57	cpx	B1	53.23	0.11	0.74	0.03	7.12	0.25	14.51	23.76	0.30	0.01	0.02	100.08
ARU96-57	cpx	B1	53.44	0.07	0.81	0.06	7.30	0.26	14.35	23.71	0.41	0.00	0.01	100.42
ARU96-57	cpx	B1	53.20	0.16	1.21	0.19	7.29	0.22	14.47	23.74	0.34	0.00	0.04	100.86
ARU96-57	cpx	B1	54.40	0.13	1.03	0.09	7.18	0.23	14.87	24.26	0.30	0.01	0.03	102.53
ARU97-164	cpx	B1	53.16	0.12	0.61	0.04	7.76	0.32	13.87	24.10	0.29	0.03	0.02	100.32
ARU97-164	cpx	B1	54.03	0.12	1.04	0.04	8.19	0.33	14.22	24.30	0.36	0.00	0.01	102.64
ARU97-164	cpx	B1	52.94	0.12	0.94	0.03	8.30	0.28	13.36	23.86	0.33	0.01	0.04	100.21
ARU97-164	cpx	B1	54.10	0.13	1.10	0.04	9.02	0.30	13.78	24.42	0.39	0.01	0.07	103.36
ARU97-175	cpx	B2a	52.98	0.12	0.73	0.00	6.58	0.22	15.50	24.04	0.18	0.01	0.02	100.38
ARU97-175	cpx	B2a	52.92	0.14	1.25	0.01	6.92	0.26	15.41	23.93	0.17	0.01	0.02	101.04
ARU97-175	cpx	B2a	52.89	0.24	1.54	0.04	7.54	0.25	15.34	22.87	0.27	0.01	0.02	101.01
ARU97-175	cpx	B2a	53.24	0.12	1.03	0.03	6.43	0.25	15.33	24.21	0.16	0.02	0.01	100.83
ARU97-175	cpx	B2a	52.01	0.32	1.85	0.04	7.76	0.24	15.45	22.18	0.29	0.00	0.02	100.16
ARU96-154	cpx	B2b	52.82	0.21	1.84	0.23	5.36	0.15	17.06	22.72	0.19	0.01	0.03	100.62
ARU96-154	cpx	B2b	52.92	0.20	1.97	0.21	6.40	0.19	16.52	22.03	0.27	0.00	0.01	100.72
ARU96-154	cpx	B2b	52.17	0.21	2.14	0.15	6.45	0.18	16.08	22.70	0.29	0.00	0.02	100.39
ARU96-154	cpx	B2b	52.77	0.17	1.75	0.37	5.97	0.19	16.52	22.54	0.26	0.01	0.02	100.57
ARU96-154	cpx	B2b	52.24	0.33	2.76	0.22	6.19	0.15	16.16	22.31	0.21	0.00	0.02	100.59
ARU96-154	cpx	B2b	52.45	0.26	2.28	0.31	5.84	0.14	16.66	22.21	0.23	0.00	0.00	100.38
ARU96-154	cpx	B2b	52.22	0.23	2.13	0.30	6.57	0.20	15.97	22.36	0.35	0.00	0.03	100.36
ARU97-163	cpx	B4	53.23	0.18	0.83	0.02	7.87	0.39	14.91	22.19	0.32	0.01	0.02	99.97
ARU96-53	ep	B1	38.71	0.02	24.74	0.04	9.86	0.05	0.01	24.11	0.00	0.00	0.02	97.56
ARU97-162	ep	B4	38.01	0.11	23.64	0.04	11.30	0.14	0.12	23.55	0.01	0.01	0.03	96.96
ARU97-163	ep	B4	39.78	0.01	29.21	0.02	4.03	0.30	0.03	23.45	0.34	0.04	0.06	97.27
ARU97-162	ep	B4	38.49	0.21	25.75	0.04	8.75	0.13	0.06	23.40	0.01	0.00	0.02	96.86
ARU97-162	ep	B4	37.66	0.24	25.25	0.02	9.74	0.60	0.12	22.74	0.01	0.02	0.02	96.42

Sample		Lith.	SiO_2	TiO_2	Al_2O_3	Cr_2O_3	FeO	MnO	MgO	CaO	Na_2O	K_2O	NiO	Total
ARU97-175	ilm	B2a	0.00	48.22	0.05	0.06	47.11	2.26	0.26	0.01	0.02	0.00	0.02	98.01
ARU97-175	ilm	B2a	0.00	31.87	3.17	0.04	58.68	1.85	0.31	0.00	0.02	0.01	0.04	95.99
ARU96-154	ilm	B2b	0.00	52.82	0.01	0.11	42.30	2.31	3.51	0.00	0.01	0.00	0.02	101.09
ARU97-73	ilm	B4	0.00	49.03	0.04	0.02	44.29	5.23	0.03	0.03	0.00	0.01	0.02	98.70
ARU97-77	kfsp	B1	64.69	0.02	18.26	0.04	0.08	0.03	0.00	0.01	0.70	15.77	0.02	99.62
ARU97-77	kfsp	B1	64.35	0.04	18.21	0.04	0.07	0.03	0.00	0.00	0.66	15.85	0.00	99.25
ARU97-160	kfsp	B4	64.01	0.04	18.09	0.01	0.28	0.03	0.00	0.02	0.33	16.18	0.00	98.99
ARU97-163	kfsp	B4	64.13	0.04	18.27	0.04	0.04	0.00	0.00	0.04	0.68	15.73	0.03	99.00
ARU96-131	kfsp	B5	64.12	0.03	18.08	0.03	0.05	0.03	0.00	0.01	0.52	16.21	0.02	99.10
ARU97-77	mag	B1	0.00	0.04	0.00	0.48	89.93	0.01	0.01	0.00	0.02	0.01	0.01	90.51
ARU96-157	mag	B1	0.53	3.16	0.44	0.99	84.94	0.05	0.16	0.06	0.04	0.02	0.07	90.46
ARU96-157	mag	B1	0.00	0.23	0.24	0.71	90.02	0.03	0.03	0.01	0.00	0.01	0.00	91.28
ARU96-157	mag	B1	0.01	0.09	0.08	0.59	89.74	0.13	0.01	0.06	0.06	0.03	0.03	90.83
ARU96-157	mag	B1	0.00	0.32	0.39	0.58	89.38	0.13	0.04	0.02	0.06	0.01	0.03	90.96
ARU97-164	mag	B1	0.00	0.02	0.04	0.35	89.79	0.05	0.00	0.00	0.01	0.01	0.02	90.29
ARU97-164	mag	B1	0.00	0.08	0.06	0.38	86.56	0.04	0.06	0.01	0.01	0.01	0.07	87.28
ARU97-175	mag	B2a	0.00	2.93	0.75	0.09	86.09	0.16	0.19	0.01	0.02	0.01	0.03	90.28
ARU97-175	mag	B2a	0.00	0.31	2.12	0.07	87.47	0.02	0.08	0.00	0.01	0.01	0.06	90.15
ARU97-111	mag	B2b	0.00	0.76	0.80	0.13	88.43	0.08	0.22	0.00	0.01	0.00	0.06	90.49
ARU96-154	mag	B2b	0.04	0.03	0.50	0.03	89.96	0.14	1.50	0.11	0.02	0.01	0.06	92.40
ARU96-154	mag	B2b	0.00	1.38	0.73	0.06	88.77	0.28	0.65	0.02	0.02	0.01	0.18	92.10
ARU96-154	mag	B2b	0.07	0.80	0.21	1.35	88.65	0.33	0.09	0.06	0.01	0.01	0.02	91.60
ARU96-154	mag	B2b	0.00	4.32	3.55	2.30	80.45	0.34	1.43	0.01	0.02	0.01	0.10	92.53
ARU97-73	mag	B4	0.01	0.07	0.12	0.03	89.08	0.03	0.01	0.02	0.01	0.01	0.02	89.41
ARU97-73	mag	B4	0.00	0.15	0.14	0.01	91.14	0.12	0.05	0.01	0.02	0.00	0.02	91.66
ARU97-73	mag	B4	0.00	0.11	0.10	0.04	91.16	0.08	0.01	0.00	0.00	0.01	0.03	91.54
ARU97-73	mag	B4	0.00	0.04	0.16	0.03	88.86	0.06	0.03	0.01	0.02	0.01	0.02	89.24
ARU97-73	mag	B4	0.02	0.24	0.07	0.05	89.23	0.08	0.01	0.01	0.01	0.01	0.01	89.74
ARU97-160	mag	B4	0.00	0.11	0.03	0.54	89.36	0.05	0.02	0.01	0.02	0.00	0.01	90.15
ARU97-160	mag	B4	0.00	0.15	0.01	0.39	89.63	0.02	0.01	0.05	0.02	0.01	0.03	90.32
ARU97-160	mag	B4	0.00	0.00	0.01	0.45	89.37	0.12	0.01	0.00	0.02	0.01	0.03	90.02
ARU97-160	mag	B4	0.00	0.11	0.02	0.52	89.67	0.05	0.02	0.01	0.02	0.01	0.02	90.45
ARU97-163	mag	B4	0.02	0.21	0.01	0.49	91.39	0.06	0.01	0.05	0.02	0.01	0.01	92.28
ARU97-163	mag	B4	0.00	0.10	0.01	0.50	92.34	0.04	0.01	0.18	0.02	0.01	0.04	93.25
ARU97-162	mag	B4	0.02	0.01	0.01	0.75	89.60	0.06	0.01	0.03	0.01	0.00	0.02	90.52
ARU96-131	mag	B5	0.00	0.10	0.09	0.05	91.72	0.11	0.01	0.00	0.00	0.01	0.02	92.11
ARU96-131	mag	B5	0.00	0.08	0.09	0.01	91.73	0.09	0.01	0.02	0.04	0.00	0.03	92.10
ARU97-78	mag	B5	0.00	1.66	0.01	0.11	89.07	0.69	0.02	0.17	0.02	0.01	0.02	91.78
ARU97-111	ol	B2b	38.61	0.00	0.00	0.00	23.06	0.39	39.01	0.00	0.03	0.01	0.10	101.21
ARU97-111	ol	B2b	39.08	0.01	0.00	0.03	22.04	0.43	39.57	0.01	0.03	0.01	0.05	101.26
ARU97-111	ol	B2b	39.30	0.02	0.00	0.03	21.55	0.47	39.83	0.02	0.02	0.00	0.05	101.29
ARU97-111	ol	B2b	39.06	0.01	0.02	0.01	21.25	0.42	40.28	0.02	0.00	0.01	0.08	101.16
ARU97-111	ol	B2b	39.31	0.01	0.00	0.02	21.67	0.43	40.27	0.03	0.01	0.01	0.04	101.80
ARU97-111	ol	B2b	38.78	0.01	0.00	0.01	22.15	0.44	39.69	0.01	0.01	0.00	0.06	101.16
ARU97-111	ol	B2b	39.41	0.00	0.00	0.01	20.10	0.39	41.10	0.04	0.00	0.00	0.04	101.09
ARU97-111	ol	B2b	39.63	0.04	0.00	0.03	19.83	0.37	41.82	0.00	0.01	0.00	0.06	101.79
ARU96-154	ol	B2b	38.95	0.01	0.01	0.03	22.23	0.38	40.24	0.05	0.01	0.01	0.11	102.03
ARU96-154	ol	B2b	38.89	0.00	0.00	0.01	23.05	0.39	39.74	0.00	0.01	0.00	0.08	102.17
ARU96-154	ol	B2b	38.84	0.03	0.00	0.01	22.57	0.39	39.94	0.00	0.00	0.01	0.10	101.89
ARU96-154	ol	B2b	38.81	0.01	0.00	0.04	22.76	0.37	39.58	0.03	0.01	0.01	0.06	101.68
ARU96-154	ol	B2b	38.99	0.01	0.00	0.03	22.12	0.32	40.13	0.02	0.02	0.01	0.11	101.76
ARU96-154	ol	B2b	39.06	0.01	0.00	0.02	22.29	0.32	40.62	0.01	0.01	0.00	0.10	102.44
ARU96-154	ol	B2b	38.75	0.00	0.01	0.03	22.92	0.41	39.62	0.03	0.03	0.01	0.07	101.88
ARU96-157	opx	B1	53.39	0.23	1.27	0.01	19.64	0.60	24.57	1.05	0.00	0.00	0.02	100.78
ARU96-157	opx	B1	52.97	0.19	0.93	0.01	21.34	0.78	23.42	0.92	0.02	0.01	0.03	100.62
ARU96-157	opx	B1	52.82	0.18	1.02	0.04	20.91	0.66	23.64	1.06	0.05	0.00	0.02	100.40
ARU96-157	opx	B1	53.73	0.21	1.00	0.01	19.83	0.69	24.20	0.89	0.00	0.01	0.03	100.60
ARU96-157	opx	B1	54.46	0.21	1.11	0.02	18.38	0.54	25.69	1.25	0.02	0.02	0.03	101.73
ARU96-157	opx	B1	52.62	0.06	0.85	0.02	20.22	0.71	23.54	0.99	0.04	0.01	0.00	99.06
ARU97-175	opx	B2a	53.88	0.16	1.87	0.04	16.81	0.40	26.01	1.69	0.00	0.01	0.01	100.88
ARU97-111	opx	B2b	53.98	0.15	1.87	0.02	15.85	0.42	26.57	1.39	0.03	0.02	0.04	100.34

Appendix G: Electron microprobe data: Table G.5 (continued)

Sample		Lith.	SiO_2	TiO_2	Al_2O_3	Cr_2O_3	FeO	MnO	MgO	CaO	Na_2O	K_2O	NiO	Total
ARU97-111	opx	B2b	54.79	0.16	1.72	0.01	15.71	0.41	27.10	1.39	0.02	0.01	0.03	101.35
ARU97-111	opx	B2b	54.74	0.17	1.68	0.00	15.47	0.41	26.98	1.41	0.01	0.01	0.02	100.90
ARU97-111	opx	B2b	56.17	0.03	1.22	0.02	13.61	0.46	29.50	0.66	0.00	0.01	0.01	101.69
ARU97-111	opx	B2b	54.79	0.16	1.76	0.03	15.33	0.31	27.35	1.40	0.02	0.00	0.00	101.15
ARU97-111	opx	B2b	54.63	0.17	1.84	0.03	15.43	0.44	27.15	1.35	0.03	0.00	0.08	101.15
ARU97-111	opx	B2b	54.20	0.18	2.04	0.03	15.54	0.39	26.92	1.34	0.01	0.01	0.02	100.68
ARU97-111	opx	B2b	54.35	0.15	2.18	0.00	15.81	0.44	26.81	1.41	0.02	0.00	0.02	101.19
ARU97-111	opx	B2b	54.59	0.20	1.81	0.00	15.06	0.42	27.23	1.32	0.00	0.01	0.03	100.67
ARU97-111	opx	B2b	55.06	0.18	1.51	0.01	14.23	0.39	28.27	1.21	0.03	0.02	0.06	100.97
ARU96-154	opx	B2b	54.39	0.19	1.72	0.08	14.55	0.33	28.45	1.27	0.03	0.00	0.01	101.02
ARU96-154	opx	B2b	55.56	0.01	1.13	0.02	13.67	0.38	29.58	0.23	0.01	0.01	0.00	100.60
ARU96-154	opx	B2b	54.42	0.08	1.36	0.05	15.11	0.39	28.11	1.11	0.00	0.01	0.07	100.71
ARU96-154	opx	B2b	54.70	0.13	1.36	0.03	15.06	0.39	28.00	1.18	0.01	0.00	0.00	100.86
ARU96-154	opx	B2b	54.70	0.12	1.62	0.07	14.51	0.41	28.13	1.26	0.03	0.01	0.00	100.86
ARU96-53	plag	B1	59.88	0.01	25.38	0.02	0.19	0.02	0.02	7.42	7.42	0.09	0.00	100.45
ARU96-53	plag	B1	60.20	0.01	25.30	0.02	0.18	0.02	0.00	7.27	7.59	0.09	0.05	100.73
ARU96-53	plag	B1	59.70	0.03	25.36	0.01	0.17	0.01	0.01	7.62	7.36	0.17	0.02	100.46
ARU96-53	plag	B1	59.81	0.01	25.39	0.04	0.13	0.03	0.00	7.33	7.54	0.08	0.02	100.38
ARU96-53	plag	B1	59.84	0.00	25.57	0.01	0.27	0.00	0.00	7.93	7.29	0.17	0.00	101.08
ARU96-53	plag	B1	60.24	0.01	25.01	0.02	0.06	0.04	0.00	7.30	7.58	0.07	0.05	100.38
ARU96-53	plag	B1	57.15	0.02	26.96	0.01	0.15	0.03	0.00	9.54	5.87	0.77	0.02	100.52
ARU97-77	plag	B1	55.34	0.01	27.98	0.01	0.14	0.03	0.01	10.28	5.68	0.17	0.01	99.66
ARU97-77	plag	B1	58.54	0.01	25.61	0.04	0.20	0.02	0.00	7.76	6.71	0.79	0.03	99.71
ARU97-77	plag	B1	54.96	0.00	28.07	0.02	0.20	0.04	0.00	10.77	5.39	0.26	0.03	99.74
ARU97-77	plag	B1	45.63	0.01	34.34	0.01	0.42	0.00	0.01	18.18	1.21	0.09	0.02	99.92
ARU97-77	plag	B1	55.06	0.00	28.24	0.03	0.22	0.12	0.00	10.96	5.27	0.19	0.02	100.11
ARU97-77	plag	B1	60.15	0.01	25.16	0.01	0.11	0.02	0.02	6.94	7.73	0.19	0.00	100.34
ARU97-77	plag	B1	46.42	0.01	34.00	0.04	0.44	0.03	0.00	17.86	1.41	0.04	0.02	100.27
ARU96-157	plag	B1	53.31	0.01	29.62	0.01	0.31	0.03	0.02	12.38	4.52	0.23	0.00	100.44
ARU96-157	plag	B1	52.81	0.03	29.88	0.04	0.27	0.03	0.01	12.91	3.92	0.18	0.01	100.09
ARU96-157	plag	B1	49.43	0.01	31.50	0.02	0.27	0.03	0.02	15.13	2.98	0.11	0.03	99.53
ARU96-157	plag	B1	54.93	0.01	28.36	0.04	0.18	0.01	0.03	11.20	5.20	0.23	0.02	100.21
ARU96-157	plag	B1	48.89	0.04	31.83	0.04	0.28	0.02	0.00	15.49	2.80	0.08	0.03	99.50
ARU96-157	plag	B1	54.17	0.02	29.19	0.04	0.21	0.03	0.02	11.86	4.93	0.17	0.01	100.65
ARU96-57	plag	B1	59.27	0.00	24.31	0.04	0.10	0.00	0.01	6.58	8.03	0.07	0.02	98.43
ARU96-57	plag	B1	65.19	0.02	23.01	0.04	0.06	0.02	0.00	3.99	9.66	0.07	0.02	102.08
ARU96-57	plag	B1	58.26	0.01	25.88	0.05	0.17	0.02	0.01	7.82	7.10	0.12	0.01	99.45
ARU96-57	plag	B1	59.33	0.01	25.22	0.01	0.17	0.01	0.03	7.23	7.47	0.20	0.01	99.69
ARU96-57	plag	B1	56.21	0.02	27.04	0.01	0.20	0.03	0.00	9.51	6.05	0.17	0.01	99.25
ARU96-57	plag	B1	62.46	0.00	23.28	0.02	0.25	0.00	0.01	4.89	8.99	0.20	0.01	100.11
ARU97-164	plag	B1	59.10	0.03	25.15	0.02	0.16	0.03	0.01	7.32	7.36	0.09	0.01	99.28
ARU97-164	plag	B1	64.42	0.01	23.75	0.02	0.07	0.04	0.00	4.85	9.21	0.10	0.02	102.49
ARU97-164	plag	B1	57.06	0.02	26.06	0.04	0.23	0.01	0.00	8.43	6.65	0.18	0.02	98.70
ARU97-164	plag	B1	56.94	0.01	26.49	0.01	0.21	0.00	0.00	8.76	6.42	0.20	0.01	99.05
ARU97-164	plag	B1	64.74	0.00	23.05	0.01	0.05	0.02	0.00	4.07	9.38	0.33	0.03	101.68
ARU97-164	plag	B1	58.90	0.00	25.57	0.01	0.17	0.04	0.00	7.73	7.01	0.11	0.04	99.58
ARU97-175	plag	B2a	44.89	0.01	33.84	0.04	0.59	0.03	0.00	18.21	1.32	0.02	0.01	98.96
ARU97-175	plag	B2a	45.28	0.01	34.10	0.01	0.21	0.00	0.01	18.09	1.25	0.02	0.01	98.99
ARU97-175	plag	B2a	48.60	0.01	31.97	0.04	0.31	0.03	0.01	15.67	2.74	0.05	0.05	99.48
ARU97-175	plag	B2a	45.61	0.01	34.10	0.00	0.28	0.03	0.01	18.18	1.35	0.02	0.02	99.61
ARU97-175	plag	B2a	48.38	0.01	31.59	0.03	0.28	0.02	0.02	15.54	2.74	0.06	0.00	98.67
ARU97-175	plag	B2a	48.60	0.01	32.10	0.01	0.30	0.03	0.00	15.81	2.64	0.05	0.02	99.57
ARU97-175	plag	B2a	45.63	0.02	33.74	0.04	0.36	0.03	0.00	18.12	1.37	0.02	0.00	99.33
ARU97-175	plag	B2a	49.40	0.04	31.58	0.01	0.19	0.00	0.01	15.06	3.04	0.02	0.02	99.37
ARU97-175	plag	B2a	45.42	0.00	34.63	0.03	1.37	0.03	0.00	18.33	1.17	0.01	0.02	101.01
ARU97-111	plag	B2b	46.09	0.01	34.07	0.03	0.26	0.03	0.01	18.26	1.25	0.02	0.03	100.06
ARU97-111	plag	B2b	46.29	0.02	33.68	0.01	0.34	0.02	0.01	18.21	1.30	0.02	0.00	99.90
ARU97-111	plag	B2b	46.53	0.06	33.83	0.02	0.36	0.03	0.09	17.87	1.41	0.06	0.02	100.28
ARU97-111	plag	B2b	46.23	0.01	34.20	0.02	0.51	0.03	0.08	18.21	1.22	0.01	0.02	100.54
ARU97-111	plag	B2b	45.97	0.00	33.93	0.00	0.30	0.01	0.00	18.21	1.35	0.01	0.00	99.78
ARU97-111	plag	B2b	45.88	0.01	34.36	0.01	0.30	0.00	0.01	18.43	1.18	0.00	0.02	100.20

Sample		Lith.	SiO_2	TiO_2	Al_2O_3	Cr_2O_3	FeO	MnO	MgO	CaO	Na_2O	K_2O	NiO	Total
ARU97-111	plag	B2b	46.26	0.03	33.66	0.02	0.40	0.03	0.08	18.15	1.44	0.04	0.00	100.11
ARU97-111	plag	B2b	46.06	0.01	34.11	0.03	0.36	0.01	0.01	18.16	1.28	0.01	0.01	100.05
ARU97-111	plag	B2b	46.53	0.03	33.76	0.02	0.33	0.03	0.01	17.81	1.39	0.02	0.02	99.95
ARU97-111	plag	B2b	46.29	0.01	33.90	0.04	0.35	0.00	0.01	18.23	1.35	0.03	0.00	100.21
ARU97-111	plag	B2b	46.57	0.03	33.62	0.04	0.40	0.03	0.00	18.10	1.43	0.02	0.02	100.26
ARU97-111	plag	B2b	46.07	0.00	34.34	0.01	0.33	0.00	0.01	18.39	1.12	0.01	0.03	100.31
ARU97-111	plag	B2b	46.19	0.00	33.98	0.01	0.53	0.03	0.03	18.22	1.24	0.01	0.04	100.28
ARU97-111	plag	B2b	46.35	0.01	33.66	0.04	0.40	0.00	0.00	18.23	1.37	0.01	0.02	100.09
ARU96-154	plag	B2b	45.54	0.00	34.22	0.04	0.29	0.03	0.01	18.34	1.15	0.03	0.00	99.65
ARU96-154	plag	B2b	46.81	0.01	33.15	0.02	0.41	0.02	0.03	17.36	1.91	0.01	0.05	99.78
ARU96-154	plag	B2b	47.36	0.01	33.02	0.04	0.51	0.03	0.03	17.06	1.97	0.02	0.05	100.10
ARU97-73	plag	B4	55.93	0.02	28.10	0.00	0.23	0.00	0.00	10.51	5.61	0.22	0.00	100.62
ARU97-73	plag	B4	59.15	0.02	26.16	0.08	0.18	0.03	0.00	8.25	6.96	0.18	0.00	101.01
ARU97-73	plag	B4	59.30	0.00	25.72	0.01	0.18	0.02	0.01	8.10	6.97	0.30	0.01	100.62
ARU97-73	plag	B4	59.56	0.01	26.14	0.02	0.21	0.00	0.00	8.22	6.87	0.33	0.01	101.37
ARU97-73	plag	B4	58.18	0.06	26.89	0.03	0.11	0.03	0.00	9.13	6.47	0.20	0.02	101.12
ARU97-73	plag	B4	58.22	0.01	27.10	0.04	0.17	0.03	0.01	9.35	6.38	0.21	0.02	101.54
ARU97-73	plag	B4	59.65	0.02	25.93	0.00	0.17	0.02	0.01	7.95	6.96	0.30	0.02	101.03
ARU97-73	plag	B4	55.19	0.01	28.44	0.00	0.19	0.02	0.00	11.08	5.20	0.20	0.02	100.35
ARU97-73	plag	B4	57.62	0.01	27.33	0.02	0.20	0.00	0.01	9.74	6.29	0.22	0.00	101.44
ARU97-73	plag	B4	58.96	0.03	26.70	0.01	0.13	0.00	0.00	8.90	6.68	0.18	0.02	101.61
ARU97-160	plag	B4	55.68	0.01	27.18	0.01	0.21	0.02	0.02	10.01	5.78	0.26	0.00	99.18
ARU97-160	plag	B4	56.21	0.01	26.85	0.00	0.45	0.03	0.07	8.75	6.31	0.67	0.02	99.37
ARU97-160	plag	B4	55.71	0.01	27.36	0.04	0.22	0.01	0.02	9.99	5.88	0.33	0.01	99.58
ARU97-160	plag	B4	57.52	0.01	25.92	0.04	0.24	0.00	0.02	8.28	6.75	0.36	0.06	99.20
ARU97-160	plag	B4	55.05	0.00	27.77	0.01	0.27	0.01	0.01	10.69	5.33	0.36	0.02	99.52
ARU97-163	plag	B4	58.71	0.01	25.21	0.04	0.23	0.00	0.00	7.52	7.13	0.40	0.05	99.30
ARU97-163	plag	B4	53.61	0.02	28.40	0.02	0.29	0.01	0.02	11.69	4.85	0.23	0.01	99.15
ARU97-163	plag	B4	54.46	0.02	27.69	0.04	0.23	0.00	0.00	10.74	5.57	0.18	0.07	99.00
ARU97-163	plag	B4	62.06	0.01	24.60	0.01	0.27	0.01	0.01	6.36	8.10	0.22	0.01	101.66
ARU97-163	plag	B4	64.96	0.01	22.51	0.01	0.31	0.02	0.04	2.63	9.76	0.83	0.01	101.09
ARU97-162	plag	B4	53.31	0.01	28.94	0.02	0.14	0.01	0.01	11.95	4.79	0.11	0.02	99.31
ARU97-162	plag	B4	55.69	0.01	29.19	0.05	0.31	0.02	0.01	11.70	5.26	0.17	0.02	102.43
ARU97-162	plag	B4	55.89	0.01	27.43	0.03	0.28	0.02	0.02	10.00	5.77	0.24	0.02	99.71
ARU97-162	plag	B4	57.01	0.01	28.17	0.05	0.36	0.02	0.01	10.34	5.66	0.35	0.02	102.00
ARU96-131	plag	B5	57.69	0.01	26.32	0.04	0.22	0.03	0.01	8.76	6.53	0.27	0.00	99.88
ARU96-131	plag	B5	57.94	0.01	26.36	0.01	0.15	0.00	0.00	8.55	6.57	0.51	0.02	100.12
ARU96-131	plag	B5	57.93	0.01	26.53	0.04	0.19	0.04	0.01	8.70	6.61	0.26	0.01	100.33
ARU96-131	plag	B5	64.63	0.01	22.01	0.01	0.17	0.02	0.01	3.36	9.71	0.42	0.01	100.36
ARU96-131	plag	B5	61.64	0.02	24.30	0.04	0.15	0.02	0.00	6.11	8.01	0.38	0.02	100.69
ARU96-131	plag	B5	63.46	0.01	22.62	0.04	0.14	0.04	0.01	3.94	9.28	0.28	0.04	99.86
ARU97-78	plag	B5	58.03	0.03	26.26	0.00	0.13	0.00	0.01	8.71	6.72	0.13	0.03	100.05
ARU97-78	plag	B5	60.28	0.01	24.44	0.04	0.11	0.02	0.01	6.57	7.81	0.24	0.01	99.54
ARU97-78	plag	B5	60.73	0.01	24.45	0.01	0.15	0.03	0.01	6.62	7.86	0.29	0.01	100.17
ARU97-78	plag	B5	59.62	0.03	24.88	0.04	0.13	0.03	0.03	7.26	7.39	0.26	0.02	99.69
ARU97-78	plag	B5	59.59	0.01	25.41	0.02	0.13	0.04	0.01	7.81	7.07	0.29	0.02	100.40
ARU97-78	plag	B5	59.52	0.02	25.50	0.04	0.20	0.03	0.01	7.75	7.22	0.28	0.01	100.58
ARU97-78	plag	B5	58.84	0.02	26.05	0.02	0.17	0.04	0.00	8.33	6.86	0.27	0.03	100.63
ARU97-78	plag	B5	58.80	0.01	25.97	0.01	0.19	0.00	0.02	8.41	6.80	0.26	0.03	100.50
ARU97-78	plag	B5	58.44	0.01	25.24	0.00	0.20	0.00	0.03	7.85	6.97	0.28	0.02	99.04
ARU97-78	plag	B5	59.92	0.01	25.28	0.00	0.24	0.00	0.03	7.42	7.28	0.32	0.02	100.52
ARU97-78	plag	B5	59.39	0.01	25.25	0.01	0.24	0.03	0.02	7.67	7.05	0.30	0.02	99.99
ARU97-78	plag	B5	58.38	0.01	26.43	0.03	0.19	0.03	0.01	8.76	6.68	0.24	0.02	100.78
ARU97-78	plag	B5	57.88	0.01	26.55	0.01	0.19	0.00	0.01	9.07	6.42	0.24	0.02	100.40
ARU97-78	plag	B5	58.01	0.03	26.27	0.01	0.23	0.03	0.04	8.95	6.53	0.24	0.02	100.36
ARU97-78	plag	B5	58.35	0.00	26.12	0.04	0.24	0.01	0.03	8.58	6.75	0.27	0.02	100.41
ARU97-78	plag	B5	56.76	0.01	27.11	0.04	0.22	0.00	0.00	10.01	5.97	0.18	0.03	100.33
ARU97-78	plag	B5	57.16	0.01	26.82	0.03	0.23	0.03	0.03	9.59	6.20	0.20	0.02	100.32
ARU97-78	plag	B5	60.16	0.02	25.05	0.00	0.26	0.01	0.00	7.31	7.38	0.29	0.03	100.51
ARU97-78	plag	B5	59.96	0.01	25.29	0.04	0.25	0.03	0.01	7.74	7.25	0.27	0.00	100.85
ARU97-78	plag	B5	58.39	0.01	26.35	0.04	0.25	0.03	0.03	8.93	6.65	0.22	0.02	100.92

Sample		Lith.	SiO_2	TiO_2	Al_2O_3	Cr_2O_3	FeO	MnO	MgO	CaO	Na_2O	K_2O	NiO	Total
ARU97-78	plag	B5	57.73	0.00	26.61	0.00	0.25	0.01	0.00	9.20	6.30	0.20	0.03	100.33
ARU97-78	plag	B5	58.05	0.01	26.36	0.01	0.22	0.02	0.02	8.95	6.39	0.19	0.04	100.26
ARU97-78	plag	B5	57.97	0.01	26.55	0.02	0.23	0.01	0.01	9.14	6.47	0.22	0.02	100.65
ARU97-78	plag	B5	58.23	0.00	26.41	0.03	0.26	0.03	0.01	8.89	6.49	0.26	0.02	100.63
ARU97-78	plag	B5	57.33	0.01	26.79	0.04	0.21	0.03	0.02	9.35	6.24	0.21	0.02	100.25
ARU97-78	plag	B5	56.82	0.04	27.21	0.04	0.23	0.05	0.00	9.73	5.95	0.18	0.02	100.27
ARU97-78	plag	B5	57.67	0.00	26.72	0.00	0.23	0.01	0.02	9.33	6.27	0.21	0.02	100.48
ARU97-78	plag	B5	58.30	0.00	26.29	0.00	0.22	0.01	0.01	8.69	6.61	0.22	0.02	100.37
ARU97-78	plag	B5	59.01	0.01	25.91	0.00	0.19	0.02	0.02	8.24	6.88	0.24	0.00	100.52
ARU97-78	plag	B5	58.13	0.01	26.39	0.04	0.23	0.01	0.00	8.94	6.52	0.23	0.02	100.52
ARU97-78	plag	B5	58.20	0.01	26.52	0.04	0.20	0.01	0.01	8.87	6.55	0.19	0.01	100.61
ARU97-78	plag	B5	57.96	0.00	26.72	0.04	0.20	0.01	0.01	9.14	6.57	0.16	0.01	100.82
ARU97-78	plag	B5	59.46	0.01	25.37	0.04	0.11	0.03	0.00	7.76	7.27	0.19	0.02	100.26
ARU97-78	plag	B5	58.27	0.01	25.27	0.03	0.09	0.02	0.01	7.87	6.91	0.16	0.01	98.65
ARU97-78	plag	B5	58.10	0.01	26.54	0.06	0.13	0.03	0.02	8.91	6.47	0.17	0.02	100.46
ARU97-78	plag	B5	56.57	0.03	27.65	0.05	0.21	0.03	0.00	10.30	5.89	0.12	0.00	100.85
ARU97-78	plag	B5	55.13	0.04	27.98	0.04	0.43	0.03	0.05	10.95	5.41	0.32	0.02	100.40
ARU97-78	plag	B5	55.70	0.02	28.06	0.04	0.19	0.03	0.00	10.81	5.36	0.14	0.03	100.38
ARU97-78	plag	B5	55.76	0.02	27.83	0.02	0.26	0.00	0.01	10.64	5.64	0.15	0.02	100.35
ARU97-78	plag	B5	56.89	0.01	27.34	0.04	0.17	0.00	0.00	9.95	6.03	0.17	0.02	100.62
ARU97-78	plag	B5	55.72	0.02	28.31	0.04	0.25	0.01	0.00	11.05	5.37	0.16	0.02	100.95
ARU97-78	plag	B5	55.41	0.03	28.33	0.02	0.21	0.02	0.01	11.15	5.32	0.17	0.01	100.68
ARU97-78	plag	B5	54.04	0.00	29.41	0.00	0.22	0.03	0.02	12.02	4.65	0.12	0.04	100.55
ARU97-78	plag	B5	54.96	0.01	28.39	0.01	0.16	0.00	0.00	11.20	5.13	0.10	0.04	100.00
ARU97-78	plag	B5	55.34	0.02	28.33	0.00	0.20	0.02	0.00	11.12	5.32	0.15	0.03	100.53
ARU97-78	plag	B5	55.44	0.01	28.34	0.04	0.20	0.03	0.00	11.02	5.39	0.17	0.00	100.64
ARU97-78	plag	B5	55.17	0.00	28.46	0.04	0.14	0.02	0.00	11.03	5.29	0.13	0.04	100.32
ARU96-57	tit	B1	30.35	38.54	0.71	0.10	0.60	0.05	0.01	28.59	0.01	0.01	0.03	99.00

Sample		Lith.	O	Si	Ti	Al	Cr	Fe^{2+}	Mn	Mg	Ca	Na	K	Ni	Total
ARU96-53	amph	B1	23	7.380	0.091	0.861	0.016	1.285	0.023	3.399	1.911	0.196	0.046	0.003	15.211
ARU96-53	amph	B1	23	7.123	0.074	1.179	0.022	1.434	0.021	3.265	1.901	0.313	0.052	0.001	15.385
ARU96-53	amph	B1	23	7.347	0.075	0.878	0.016	1.309	0.024	3.421	1.934	0.196	0.045	0.006	15.251
ARU96-53	amph	B1	23	7.083	0.108	1.182	0.030	1.491	0.031	3.174	1.919	0.311	0.061	0.001	15.391
ARU96-53	amph	B1	23	7.244	0.085	0.982	0.017	1.428	0.026	3.332	1.893	0.277	0.050	0.002	15.336
ARU96-53	amph	B1	23	7.234	0.089	1.042	0.013	1.395	0.026	3.280	1.890	0.313	0.039	0.006	15.327
ARU96-53	amph	B1	23	7.307	0.080	0.901	0.028	1.315	0.024	3.422	1.913	0.265	0.047	0.001	15.303
ARU96-53	amph	B1	23	7.020	0.082	1.318	0.041	1.430	0.023	3.203	1.893	0.358	0.050	0.002	15.420
ARU96-53	amph	B1	23	7.290	0.066	0.921	0.041	1.343	0.026	3.366	1.963	0.237	0.048	0.005	15.306
ARU96-53	amph	B1	23	7.399	0.060	0.829	0.024	1.386	0.023	3.376	1.874	0.235	0.046	0.006	15.258
ARU96-53	amph	B1	23	7.398	0.067	0.821	0.020	1.342	0.027	3.428	1.875	0.225	0.042	0.002	15.247
ARU97-77	amph	B1	23	6.941	0.117	1.349	0.003	1.506	0.029	3.258	1.844	0.354	0.068	0.008	15.477
ARU97-77	amph	B1	23	6.885	0.120	1.432	0.009	1.604	0.036	3.113	1.843	0.398	0.065	0.000	15.505
ARU97-77	amph	B1	23	6.960	0.117	1.305	0.003	1.706	0.038	3.045	1.881	0.335	0.084	0.002	15.476
ARU97-77	amph	B1	23	7.023	0.107	1.205	0.006	1.729	0.035	3.047	1.912	0.305	0.094	0.001	15.464
ARU97-77	amph	B1	23	6.971	0.114	1.338	0.005	1.650	0.030	3.069	1.865	0.331	0.069	0.004	15.446
ARU96-157	amph	B1	23	7.160	0.068	1.025	0.003	1.392	0.037	3.650	1.768	0.214	0.093	0.001	15.411
ARU96-157	amph	B1	23	7.272	0.116	0.889	0.005	1.263	0.026	3.628	1.815	0.214	0.082	0.005	15.315
ARU96-157	amph	B1	23	7.071	0.108	1.168	0.001	1.501	0.037	3.368	1.793	0.283	0.090	0.005	15.425
ARU96-57	amph	B1	23	7.239	0.091	0.967	0.028	1.386	0.026	3.386	1.885	0.279	0.043	0.002	15.332
ARU96-57	amph	B1	23	7.459	0.042	0.709	0.030	1.276	0.027	3.577	1.884	0.210	0.036	0.002	15.252
ARU96-57	amph	B1	23	7.286	0.074	0.906	0.030	1.346	0.023	3.490	1.858	0.254	0.055	0.005	15.327
ARU96-57	amph	B1	23	7.314	0.059	0.811	0.026	1.368	0.025	3.549	1.900	0.232	0.061	0.008	15.353
ARU96-57	amph	B1	23	6.879	0.133	1.399	0.058	1.571	0.025	3.036	1.910	0.402	0.092	0.004	15.509
ARU97-164	amph	B1	23	6.999	0.128	1.279	0.000	1.818	0.032	2.891	1.876	0.360	0.053	0.002	15.438
ARU97-164	amph	B1	23	6.913	0.150	1.333	0.002	1.794	0.032	2.961	1.856	0.395	0.051	0.005	15.492
ARU97-164	amph	B1	23	6.925	0.144	1.366	0.005	1.621	0.024	3.100	1.832	0.407	0.047	0.002	15.473
ARU97-164	amph	B1	23	6.797	0.152	1.470	0.006	1.866	0.031	2.816	1.928	0.342	0.152	0.001	15.561
ARU97-164	amph	B1	23	6.788	0.161	1.498	0.007	1.860	0.028	2.780	1.936	0.409	0.065	0.005	15.537
ARU97-164	amph	B1	23	6.976	0.122	1.250	0.010	1.820	0.033	2.930	1.926	0.339	0.061	0.003	15.470
ARU97-175	amph	B2a	23	6.707	0.172	1.603	0.003	1.398	0.027	3.231	1.919	0.434	0.071	0.006	15.571
ARU97-175	amph	B2a	23	6.803	0.160	1.527	0.002	1.404	0.015	3.224	1.912	0.409	0.037	0.002	15.495
ARU97-111	amph	B2b	23	6.353	0.261	2.016	0.003	1.322	0.024	3.251	1.800	0.630	0.063	0.001	15.693
ARU97-111	amph	B2b	23	6.377	0.253	2.045	0.006	1.292	0.015	3.152	1.874	0.580	0.071	0.006	15.671
ARU97-111	amph	B2b	23	6.939	0.156	1.381	0.002	1.325	0.020	3.354	1.813	0.406	0.028	0.005	15.429
ARU96-154	amph	B2b	23	6.497	0.106	1.896	0.017	1.259	0.011	3.437	1.875	0.581	0.093	0.004	15.776
ARU96-154	amph	B2b	23	6.670	0.000	1.885	0.000	0.940	0.017	3.731	1.874	0.505	0.027	0.005	15.654
ARU96-154	amph	B2b	23	6.348	0.230	1.977	0.012	1.332	0.015	3.293	1.836	0.696	0.069	0.002	15.810
ARU97-73	amph	B4	23	6.991	0.147	1.275	0.005	1.936	0.047	2.718	1.888	0.274	0.150	0.004	15.435
ARU97-73	amph	B4	23	7.055	0.173	1.200	0.000	1.816	0.064	2.836	1.789	0.357	0.118	0.002	15.410
ARU97-73	amph	B4	23	7.069	0.166	1.178	0.003	1.794	0.064	2.854	1.822	0.328	0.114	0.002	15.394
ARU97-73	amph	B4	23	7.221	0.129	1.026	0.001	1.666	0.055	3.005	1.844	0.272	0.098	0.002	15.319
ARU97-73	amph	B4	23	7.021	0.148	1.248	0.001	1.843	0.056	2.819	1.856	0.297	0.130	0.002	15.421
ARU97-73	amph	B4	23	7.117	0.143	1.138	0.003	1.653	0.058	2.951	1.901	0.282	0.119	0.005	15.370
ARU97-73	amph	B4	23	7.065	0.148	1.178	0.001	1.776	0.055	2.932	1.809	0.343	0.117	0.002	15.426
ARU97-73	amph	B4	23	7.017	0.162	1.216	0.005	1.730	0.048	2.920	1.921	0.267	0.116	0.002	15.404
ARU97-73	amph	B4	23	7.067	0.166	1.174	0.002	1.735	0.068	2.928	1.807	0.346	0.111	0.004	15.408
ARU97-73	amph	B4	23	7.059	0.162	1.174	0.002	1.788	0.058	2.875	1.842	0.330	0.119	0.006	15.415
ARU97-160	amph	B4	23	6.980	0.182	1.243	0.005	1.526	0.033	3.244	1.761	0.385	0.089	0.002	15.450
ARU97-160	amph	B4	23	6.956	0.178	1.223	0.003	1.592	0.041	3.244	1.776	0.379	0.095	0.004	15.491
ARU97-160	amph	B4	23	6.958	0.179	1.263	0.002	1.653	0.045	3.116	1.769	0.382	0.094	0.006	15.467
ARU97-163	amph	B4	23	6.987	0.184	1.193	0.001	1.523	0.034	3.245	1.810	0.400	0.107	0.002	15.486
ARU97-163	amph	B4	23	7.789	0.067	0.192	0.002	1.047	0.052	4.109	1.748	0.060	0.009	0.007	15.082
ARU97-163	amph	B4	23	6.902	0.194	1.279	0.002	1.488	0.026	3.304	1.798	0.432	0.100	0.001	15.526
ARU97-162	amph	B4	23	6.949	0.129	1.303	0.016	1.713	0.039	2.984	1.907	0.302	0.133	0.004	15.479
ARU97-162	amph	B4	23	6.992	0.141	1.239	0.007	1.662	0.036	3.050	1.911	0.302	0.101	0.004	15.445
ARU96-131	amph	B5	23	7.135	0.147	1.040	0.009	1.610	0.085	3.193	1.763	0.385	0.033	0.002	15.402
ARU96-131	amph	B5	23	7.160	0.141	1.009	0.000	1.594	0.081	3.248	1.771	0.346	0.031	0.002	15.383
ARU96-131	amph	B5	23	7.180	0.143	0.999	0.001	1.645	0.096	3.140	1.781	0.335	0.037	0.005	15.362
ARU96-131	amph	B5	23	7.021	0.169	1.163	0.001	1.535	0.082	3.278	1.766	0.387	0.035	0.002	15.439
ARU97-78	amph	B5	23	7.083	0.143	1.104	0.006	1.515	0.040	3.296	1.808	0.409	0.035	0.002	15.441
ARU97-78	amph	B5	23	7.421	0.061	0.749	0.003	1.706	0.066	3.115	1.880	0.217	0.057	0.002	15.277
ARU97-78	amph	B5	23	7.212	0.103	1.022	0.003	1.833	0.084	2.914	1.805	0.337	0.053	0.001	15.367
ARU97-78	amph	B5	23	7.156	0.126	1.121	0.002	1.543	0.044	3.211	1.730	0.406	0.033	0.004	15.376
ARU97-78	amph	B5	23	7.341	0.086	0.815	0.002	1.706	0.073	3.115	1.850	0.283	0.057	0.007	15.335
ARU97-78	amph	B5	23	6.996	0.166	1.227	0.001	1.582	0.028	3.194	1.790	0.429	0.041	0.002	15.456

Sample		Lith.	O	Si	Ti	Al	Cr	Fe^{2+}	Mn	Mg	Ca	Na	K	Ni	Total
ARU97-164	ap	B1													
ARU97-163	ap	B4													
ARU97-163	ap	B4					recalculation not applicable because P not analysed by electron microprobe								
ARU97-163	ap	B4													
ARU96-131	ap	B5													
ARU96-131	ap	B5													
ARU97-73	bi	B4	22	5.550	0.576	2.590	0.002	2.492	0.035	2.457	0.002	0.044	1.697	0.002	15.447
ARU97-73	bi	B4	22	5.575	0.565	2.556	0.002	2.382	0.037	2.544	0.000	0.048	1.784	0.004	15.497
ARU97-73	bi	B4	22	5.592	0.553	2.565	0.002	2.508	0.032	2.377	0.002	0.033	1.845	0.001	15.510
ARU97-73	bi	B4	22	5.579	0.579	2.535	0.002	2.350	0.027	2.587	0.002	0.050	1.771	0.001	15.483
ARU97-160	bi	B4	22	5.581	0.467	2.609	0.005	2.299	0.030	2.732	0.002	0.036	1.796	0.005	15.562
ARU96-131	bi	B5	22	5.610	0.493	2.504	0.000	2.351	0.062	2.671	0.002	0.068	1.838	0.000	15.599
ARU96-131	bi	B5	22	5.591	0.459	2.536	0.004	2.326	0.059	2.745	0.002	0.050	1.863	0.002	15.637
ARU96-131	bi	B5	22	5.570	0.504	2.547	0.006	2.316	0.054	2.704	0.003	0.065	1.816	0.004	15.589
ARU96-131	bi	B5	22	5.612	0.491	2.503	0.004	2.269	0.053	2.776	0.003	0.050	1.806	0.004	15.571
ARU97-78	bi	B5	22	5.630	0.467	2.489	0.002	2.356	0.042	2.743	0.002	0.051	1.798	0.002	15.582
ARU97-78	bi	B5	22	5.671	0.471	2.480	0.001	2.333	0.045	2.686	0.003	0.039	1.812	0.001	15.542
ARU97-78	bi	B5	22	5.724	0.338	2.573	0.001	2.257	0.037	2.846	0.030	0.018	1.672	0.000	15.496
ARU97-160	chl	B4	28	5.758	0.005	4.724	0.005	4.345	0.129	4.872	0.011	0.008	0.016	0.012	19.885
ARU96-131	chl	B5	28	5.642	0.006	4.713	0.001	4.425	0.158	5.011	0.020	0.017	0.010	0.004	20.007
ARU96-53	cpx	B1	6	1.988	0.003	0.035	0.001	0.210	0.007	0.791	0.945	0.023	0.000	0.001	4.004
ARU96-53	cpx	B1	6	1.973	0.005	0.055	0.001	0.220	0.008	0.777	0.941	0.029	0.000	0.000	4.009
ARU96-53	cpx	B1	6	1.986	0.001	0.034	0.001	0.214	0.009	0.791	0.944	0.025	0.000	0.001	4.006
ARU96-53	cpx	B1	6	1.980	0.003	0.036	0.002	0.232	0.007	0.785	0.937	0.027	0.000	0.001	4.010
ARU96-53	cpx	B1	6	1.994	0.001	0.019	0.002	0.228	0.007	0.779	0.951	0.024	0.000	0.001	4.006
ARU96-53	cpx	B1	6	1.986	0.001	0.029	0.003	0.220	0.009	0.797	0.937	0.028	0.000	0.000	4.010
ARU96-53	cpx	B1	6	1.988	0.001	0.028	0.001	0.221	0.011	0.792	0.943	0.023	0.000	0.000	4.008
ARU96-53	cpx	B1	6	1.981	0.002	0.037	0.001	0.217	0.009	0.800	0.939	0.022	0.000	0.001	4.009
ARU96-53	cpx	B1	6	1.986	0.001	0.030	0.002	0.225	0.007	0.788	0.943	0.028	0.000	0.001	4.011
ARU96-53	cpx	B1	6	1.985	0.003	0.029	0.002	0.216	0.008	0.800	0.941	0.023	0.001	0.001	4.009
ARU96-53	cpx	B1	6	1.993	0.000	0.023	0.002	0.221	0.008	0.770	0.964	0.024	0.000	0.000	4.005
ARU97-77	cpx	B1	6	1.973	0.001	0.029	0.001	0.253	0.011	0.777	0.955	0.019	0.000	0.001	4.020
ARU97-77	cpx	B1	6	1.982	0.001	0.029	0.001	0.253	0.010	0.750	0.964	0.022	0.000	0.001	4.013
ARU97-77	cpx	B1	6	1.974	0.002	0.030	0.001	0.260	0.010	0.758	0.962	0.022	0.000	0.001	4.020
ARU97-77	cpx	B1	6	1.978	0.001	0.024	0.000	0.230	0.012	0.786	0.971	0.016	0.000	0.000	4.018
ARU96-57	cpx	B1	6	1.983	0.003	0.030	0.002	0.216	0.007	0.804	0.940	0.025	0.001	0.001	4.012
ARU96-57	cpx	B1	6	1.977	0.003	0.032	0.001	0.221	0.008	0.803	0.946	0.022	0.000	0.001	4.014
ARU96-57	cpx	B1	6	1.979	0.002	0.035	0.002	0.226	0.008	0.792	0.941	0.029	0.000	0.000	4.014
ARU96-57	cpx	B1	6	1.962	0.004	0.053	0.006	0.225	0.007	0.796	0.938	0.024	0.000	0.001	4.016
ARU96-57	cpx	B1	6	1.971	0.004	0.044	0.003	0.218	0.007	0.803	0.942	0.021	0.000	0.001	4.014
ARU97-164	cpx	B1	6	1.979	0.003	0.027	0.001	0.242	0.010	0.770	0.961	0.021	0.001	0.001	4.016
ARU97-164	cpx	B1	6	1.967	0.003	0.045	0.001	0.249	0.010	0.772	0.948	0.025	0.000	0.000	4.020
ARU97-164	cpx	B1	6	1.976	0.003	0.041	0.001	0.259	0.009	0.743	0.954	0.024	0.000	0.001	4.011
ARU97-164	cpx	B1	6	1.963	0.004	0.047	0.001	0.274	0.009	0.745	0.950	0.027	0.000	0.002	4.022
ARU97-175	cpx	B2a	6	1.960	0.003	0.032	0.000	0.204	0.007	0.855	0.953	0.013	0.000	0.001	4.028
ARU97-175	cpx	B2a	6	1.947	0.004	0.054	0.000	0.213	0.008	0.845	0.943	0.012	0.000	0.001	4.027
ARU97-175	cpx	B2a	6	1.946	0.007	0.067	0.001	0.232	0.008	0.841	0.902	0.019	0.000	0.001	4.024
ARU97-175	cpx	B2a	6	1.959	0.003	0.045	0.001	0.198	0.008	0.841	0.954	0.011	0.001	0.000	4.021
ARU97-175	cpx	B2a	6	1.931	0.009	0.081	0.001	0.241	0.008	0.855	0.882	0.021	0.000	0.001	4.030
ARU96-154	cpx	B2b	6	1.931	0.006	0.079	0.007	0.164	0.005	0.930	0.890	0.013	0.000	0.001	4.026
ARU96-154	cpx	B2b	6	1.937	0.006	0.085	0.006	0.196	0.006	0.902	0.864	0.019	0.000	0.000	4.021
ARU96-154	cpx	B2b	6	1.923	0.006	0.093	0.004	0.199	0.006	0.884	0.897	0.021	0.000	0.001	4.034
ARU96-154	cpx	B2b	6	1.936	0.005	0.076	0.011	0.183	0.006	0.904	0.886	0.018	0.000	0.001	4.026
ARU96-154	cpx	B2b	6	1.915	0.009	0.119	0.006	0.190	0.005	0.883	0.877	0.015	0.000	0.001	4.020
ARU96-154	cpx	B2b	6	1.924	0.007	0.099	0.009	0.179	0.004	0.911	0.873	0.016	0.000	0.000	4.022
ARU96-154	cpx	B2b	6	1.926	0.006	0.093	0.009	0.203	0.006	0.878	0.884	0.025	0.000	0.001	4.031
ARU97-163	cpx	B4	6	1.978	0.005	0.036	0.001	0.245	0.012	0.826	0.884	0.023	0.000	0.001	4.011
ARU96-53	ep	B1	25	6.228	0.002	4.692	0.005	1.327	0.007	0.002	4.156	0.000	0.000	0.003	16.422
ARU97-162	ep	B4	25	6.209	0.014	4.551	0.005	1.544	0.019	0.029	4.122	0.003	0.002	0.004	16.502
ARU97-163	ep	B4	25	6.200	0.000	5.366	0.003	0.525	0.041	0.006	3.916	0.103	0.009	0.006	16.175
ARU97-162	ep	B4	25	6.188	0.025	4.881	0.006	1.178	0.019	0.016	4.031	0.003	0.000	0.003	16.350
ARU97-162	ep	B4	25	6.131	0.028	4.844	0.003	1.325	0.081	0.028	3.966	0.003	0.003	0.003	16.416

Sample		Lith.	O	Si	Ti	Al	Cr	Fe^{2+}	Mn	Mg	Ca	Na	K	Ni	Total
ARU97-175	ilm	B2a	6	0.000	1.901	0.003	0.002	2.066	0.100	0.020	0.001	0.002	0.000	0.001	4.096
ARU97-175	ilm	B2a	6	0.000	1.373	0.214	0.002	2.811	0.090	0.026	0.000	0.002	0.001	0.002	4.521
ARU96-154	ilm	B2b	6	0.000	1.951	0.001	0.004	1.737	0.096	0.257	0.000	0.001	0.000	0.001	4.048
ARU97-73	ilm	B4	6	0.000	1.917	0.002	0.001	1.926	0.230	0.002	0.002	0.000	0.001	0.001	4.082
ARU97-77	kfsp	B1	8	2.998	0.001	0.998	0.001	0.003	0.001	0.000	0.000	0.063	0.933	0.001	4.999
ARU97-77	kfsp	B1	8	2.996	0.001	0.999	0.001	0.003	0.001	0.000	0.000	0.060	0.941	0.000	5.002
ARU97-160	kfsp	B4	8	2.995	0.001	0.998	0.000	0.011	0.001	0.000	0.001	0.030	0.966	0.000	5.003
ARU97-163	kfsp	B4	8	2.992	0.001	1.005	0.001	0.002	0.000	0.000	0.002	0.062	0.936	0.001	5.002
ARU96-131	kfsp	B5	8	2.996	0.001	0.996	0.001	0.002	0.001	0.000	0.001	0.047	0.966	0.001	5.012
ARU97-77	mag	B1	4	0.000	0.002	0.000	0.020	3.964	0.000	0.001	0.000	0.002	0.001	0.000	3.990
ARU96-157	mag	B1	4	0.027	0.120	0.026	0.040	3.585	0.002	0.012	0.003	0.004	0.001	0.003	3.823
ARU96-157	mag	B1	4	0.000	0.009	0.015	0.029	3.912	0.001	0.002	0.001	0.000	0.001	0.000	3.970
ARU96-157	mag	B1	4	0.001	0.004	0.005	0.024	3.933	0.006	0.001	0.003	0.006	0.002	0.001	3.986
ARU96-157	mag	B1	4	0.000	0.013	0.024	0.024	3.889	0.006	0.003	0.001	0.006	0.001	0.001	3.968
ARU97-164	mag	B1	4	0.000	0.001	0.002	0.015	3.969	0.002	0.000	0.000	0.001	0.001	0.001	3.992
ARU97-164	mag	B1	4	0.000	0.003	0.004	0.016	3.952	0.002	0.005	0.001	0.001	0.001	0.003	3.988
ARU97-175	mag	B2a	4	0.000	0.113	0.045	0.004	3.677	0.007	0.014	0.001	0.002	0.001	0.001	3.865
ARU97-175	mag	B2a	4	0.000	0.012	0.129	0.003	3.768	0.001	0.006	0.000	0.001	0.001	0.002	3.923
ARU97-111	mag	B2b	4	0.000	0.030	0.049	0.005	3.836	0.004	0.017	0.000	0.001	0.000	0.003	3.945
ARU96-154	mag	B2b	4	0.002	0.001	0.030	0.001	3.818	0.006	0.113	0.006	0.002	0.001	0.002	3.982
ARU96-154	mag	B2b	4	0.000	0.052	0.044	0.002	3.755	0.012	0.049	0.001	0.002	0.001	0.007	3.925
ARU96-154	mag	B2b	4	0.004	0.031	0.013	0.055	3.804	0.014	0.007	0.003	0.001	0.001	0.001	3.934
ARU96-154	mag	B2b	4	0.000	0.152	0.196	0.085	3.154	0.014	0.100	0.001	0.002	0.001	0.004	3.709
ARU97-73	mag	B4	4	0.001	0.003	0.008	0.001	3.975	0.001	0.001	0.001	0.001	0.001	0.001	3.994
ARU97-73	mag	B4	4	0.000	0.006	0.009	0.000	3.963	0.005	0.004	0.001	0.002	0.000	0.001	3.991
ARU97-73	mag	B4	4	0.000	0.004	0.006	0.002	3.974	0.004	0.001	0.000	0.000	0.001	0.001	3.993
ARU97-73	mag	B4	4	0.000	0.002	0.010	0.001	3.972	0.003	0.002	0.001	0.002	0.001	0.001	3.995
ARU97-73	mag	B4	4	0.001	0.010	0.004	0.002	3.963	0.004	0.001	0.001	0.001	0.001	0.000	3.988
ARU97-160	mag	B4	4	0.000	0.004	0.002	0.023	3.949	0.002	0.002	0.001	0.002	0.000	0.000	3.985
ARU97-160	mag	B4	4	0.000	0.006	0.001	0.016	3.956	0.001	0.001	0.003	0.002	0.001	0.001	3.988
ARU97-160	mag	B4	4	0.000	0.000	0.001	0.019	3.962	0.005	0.001	0.000	0.002	0.001	0.001	3.992
ARU97-160	mag	B4	4	0.000	0.004	0.001	0.022	3.950	0.002	0.002	0.001	0.002	0.001	0.001	3.986
ARU97-163	mag	B4	4	0.001	0.008	0.001	0.020	3.943	0.003	0.001	0.003	0.002	0.001	0.000	3.983
ARU97-163	mag	B4	4	0.000	0.004	0.001	0.020	3.946	0.002	0.001	0.010	0.002	0.001	0.002	3.989
ARU97-162	mag	B4	4	0.001	0.000	0.001	0.031	3.943	0.003	0.001	0.002	0.001	0.000	0.001	3.984
ARU96-131	mag	B5	4	0.000	0.004	0.005	0.002	3.974	0.005	0.001	0.000	0.000	0.001	0.001	3.993
ARU96-131	mag	B5	4	0.000	0.003	0.005	0.000	3.976	0.004	0.001	0.001	0.004	0.000	0.001	3.995
ARU97-78	mag	B5	4	0.000	0.064	0.001	0.004	3.821	0.030	0.002	0.009	0.002	0.001	0.001	3.935
ARU97-111	ol	B2b	4	0.996	0.000	0.000	0.000	0.497	0.009	1.500	0.000	0.002	0.000	0.002	3.006
ARU97-111	ol	B2b	4	1.002	0.000	0.000	0.001	0.472	0.009	1.512	0.000	0.001	0.000	0.001	2.998
ARU97-111	ol	B2b	4	1.004	0.000	0.000	0.001	0.461	0.010	1.517	0.001	0.001	0.000	0.001	2.996
ARU97-111	ol	B2b	4	0.999	0.000	0.001	0.000	0.454	0.009	1.535	0.001	0.000	0.000	0.002	3.001
ARU97-111	ol	B2b	4	1.000	0.000	0.000	0.000	0.461	0.009	1.527	0.001	0.000	0.000	0.001	2.999
ARU97-111	ol	B2b	4	0.996	0.000	0.000	0.000	0.476	0.010	1.520	0.000	0.000	0.000	0.001	3.003
ARU97-111	ol	B2b	4	1.002	0.000	0.000	0.000	0.427	0.008	1.558	0.001	0.000	0.000	0.001	2.997
ARU97-111	ol	B2b	4	0.999	0.001	0.000	0.001	0.418	0.008	1.572	0.000	0.000	0.000	0.001	3.000
ARU96-154	ol	B2b	4	0.992	0.000	0.000	0.001	0.474	0.008	1.528	0.001	0.000	0.000	0.002	3.006
ARU96-154	ol	B2b	4	0.993	0.000	0.000	0.000	0.492	0.008	1.512	0.000	0.000	0.000	0.002	3.007
ARU96-154	ol	B2b	4	0.992	0.001	0.000	0.000	0.482	0.008	1.521	0.000	0.000	0.000	0.002	3.006
ARU96-154	ol	B2b	4	0.994	0.000	0.000	0.001	0.488	0.008	1.512	0.001	0.000	0.000	0.001	3.005
ARU96-154	ol	B2b	4	0.995	0.000	0.000	0.001	0.472	0.007	1.526	0.001	0.001	0.000	0.002	3.005
ARU96-154	ol	B2b	4	0.991	0.000	0.000	0.000	0.473	0.007	1.536	0.000	0.000	0.000	0.002	3.009
ARU96-154	ol	B2b	4	0.992	0.000	0.000	0.001	0.491	0.009	1.512	0.001	0.001	0.000	0.001	3.008
ARU96-157	opx	B1	6	1.952	0.006	0.055	0.000	0.601	0.019	1.339	0.041	0.000	0.000	0.001	4.014
ARU96-157	opx	B1	6	1.958	0.005	0.041	0.000	0.660	0.024	1.290	0.036	0.001	0.000	0.001	4.016
ARU96-157	opx	B1	6	1.953	0.005	0.044	0.001	0.647	0.021	1.303	0.042	0.004	0.000	0.001	4.021
ARU96-157	opx	B1	6	1.968	0.006	0.043	0.000	0.608	0.021	1.322	0.035	0.000	0.000	0.001	4.004
ARU96-157	opx	B1	6	1.960	0.006	0.047	0.001	0.553	0.016	1.378	0.048	0.001	0.001	0.001	4.012
ARU96-157	opx	B1	6	1.966	0.002	0.037	0.001	0.632	0.022	1.311	0.040	0.003	0.000	0.000	4.014
ARU97-175	opx	B2a	6	1.943	0.004	0.080	0.001	0.507	0.012	1.398	0.065	0.000	0.000	0.000	4.010
ARU97-111	opx	B2b	6	1.948	0.004	0.080	0.001	0.478	0.013	1.429	0.054	0.002	0.001	0.001	4.011

Sample		Lith.	O	Si	Ti	Al	Cr	Fe^{2+}	Mn	Mg	Ca	Na	K	Ni	Total
ARU97-111	opx	B2b	6	1.953	0.004	0.072	0.000	0.468	0.012	1.440	0.053	0.001	0.000	0.001	4.004
ARU97-111	opx	B2b	6	1.958	0.005	0.071	0.000	0.463	0.012	1.439	0.054	0.001	0.000	0.001	4.004
ARU97-111	opx	B2b	6	1.970	0.001	0.050	0.001	0.399	0.014	1.543	0.025	0.000	0.000	0.000	4.003
ARU97-111	opx	B2b	6	1.953	0.004	0.074	0.001	0.457	0.009	1.453	0.053	0.001	0.000	0.000	4.005
ARU97-111	opx	B2b	6	1.950	0.005	0.077	0.001	0.461	0.013	1.445	0.052	0.002	0.000	0.002	4.008
ARU97-111	opx	B2b	6	1.945	0.005	0.086	0.001	0.466	0.012	1.440	0.052	0.001	0.000	0.001	4.009
ARU97-111	opx	B2b	6	1.942	0.004	0.092	0.000	0.473	0.013	1.428	0.054	0.001	0.000	0.001	4.008
ARU97-111	opx	B2b	6	1.953	0.005	0.076	0.000	0.451	0.013	1.453	0.051	0.000	0.000	0.001	4.003
ARU97-111	opx	B2b	6	1.957	0.005	0.063	0.000	0.423	0.012	1.498	0.046	0.002	0.001	0.002	4.009
ARU96-154	opx	B2b	6	1.937	0.005	0.072	0.002	0.433	0.010	1.511	0.048	0.002	0.000	0.000	4.020
ARU96-154	opx	B2b	6	1.969	0.000	0.047	0.001	0.405	0.011	1.563	0.009	0.001	0.000	0.000	4.006
ARU96-154	opx	B2b	6	1.949	0.002	0.057	0.001	0.453	0.012	1.501	0.043	0.000	0.000	0.002	4.020
ARU96-154	opx	B2b	6	1.954	0.003	0.057	0.001	0.450	0.012	1.491	0.045	0.001	0.000	0.000	4.014
ARU96-154	opx	B2b	6	1.950	0.003	0.068	0.002	0.433	0.012	1.495	0.048	0.002	0.000	0.000	4.013
ARU96-53	plag	B1	8	2.660	0.000	1.329	0.001	0.007	0.001	0.001	0.353	0.639	0.005	0.000	4.996
ARU96-53	plag	B1	8	2.667	0.000	1.321	0.001	0.007	0.001	0.000	0.345	0.652	0.005	0.002	5.001
ARU96-53	plag	B1	8	2.655	0.001	1.329	0.000	0.006	0.000	0.001	0.363	0.635	0.010	0.001	5.001
ARU96-53	plag	B1	8	2.659	0.000	1.331	0.001	0.005	0.001	0.000	0.349	0.650	0.005	0.001	5.002
ARU96-53	plag	B1	8	2.648	0.000	1.334	0.000	0.010	0.000	0.000	0.376	0.625	0.010	0.000	5.003
ARU96-53	plag	B1	8	2.676	0.000	1.310	0.001	0.002	0.002	0.000	0.347	0.653	0.004	0.002	4.997
ARU96-53	plag	B1	8	2.560	0.001	1.424	0.000	0.006	0.001	0.000	0.458	0.510	0.044	0.001	5.005
ARU97-77	plag	B1	8	2.502	0.000	1.491	0.000	0.005	0.001	0.001	0.498	0.498	0.010	0.000	5.006
ARU97-77	plag	B1	8	2.632	0.000	1.357	0.001	0.008	0.001	0.000	0.374	0.585	0.045	0.001	5.004
ARU97-77	plag	B1	8	2.488	0.000	1.498	0.001	0.008	0.002	0.000	0.522	0.473	0.015	0.001	5.008
ARU97-77	plag	B1	8	2.109	0.000	1.871	0.000	0.016	0.000	0.001	0.900	0.108	0.005	0.001	5.011
ARU97-77	plag	B1	8	2.484	0.000	1.501	0.001	0.008	0.005	0.000	0.530	0.461	0.011	0.001	5.002
ARU97-77	plag	B1	8	2.673	0.000	1.318	0.000	0.004	0.001	0.001	0.330	0.666	0.011	0.000	5.004
ARU97-77	plag	B1	8	2.135	0.000	1.843	0.001	0.017	0.001	0.000	0.880	0.126	0.002	0.001	5.006
ARU96-157	plag	B1	8	2.408	0.000	1.577	0.000	0.012	0.001	0.001	0.599	0.396	0.013	0.000	5.007
ARU96-157	plag	B1	8	2.393	0.001	1.596	0.001	0.010	0.001	0.001	0.627	0.344	0.010	0.000	4.984
ARU96-157	plag	B1	8	2.272	0.000	1.706	0.001	0.010	0.001	0.001	0.745	0.266	0.006	0.001	5.009
ARU96-157	plag	B1	8	2.476	0.000	1.507	0.001	0.007	0.000	0.002	0.541	0.455	0.013	0.001	5.003
ARU96-157	plag	B1	8	2.250	0.001	1.727	0.001	0.011	0.001	0.000	0.764	0.250	0.005	0.001	5.011
ARU96-157	plag	B1	8	2.436	0.001	1.548	0.001	0.008	0.001	0.001	0.572	0.430	0.010	0.000	5.008
ARU96-57	plag	B1	8	2.685	0.000	1.298	0.001	0.004	0.000	0.001	0.319	0.705	0.004	0.001	5.018
ARU96-57	plag	B1	8	2.820	0.001	1.173	0.001	0.002	0.001	0.000	0.185	0.810	0.004	0.001	4.998
ARU96-57	plag	B1	8	2.620	0.000	1.372	0.002	0.006	0.001	0.001	0.377	0.619	0.007	0.000	5.005
ARU96-57	plag	B1	8	2.658	0.000	1.332	0.000	0.006	0.000	0.002	0.347	0.649	0.011	0.000	5.005
ARU96-57	plag	B1	8	2.546	0.001	1.444	0.000	0.008	0.001	0.000	0.462	0.531	0.010	0.000	5.003
ARU96-57	plag	B1	8	2.770	0.000	1.217	0.001	0.009	0.000	0.001	0.232	0.773	0.011	0.000	5.014
ARU97-164	plag	B1	8	2.657	0.001	1.333	0.001	0.006	0.001	0.001	0.353	0.642	0.005	0.000	5.000
ARU97-164	plag	B1	8	2.783	0.000	1.209	0.001	0.003	0.001	0.000	0.225	0.772	0.006	0.001	5.001
ARU97-164	plag	B1	8	2.592	0.001	1.396	0.001	0.009	0.000	0.000	0.410	0.586	0.010	0.001	5.006
ARU97-164	plag	B1	8	2.578	0.000	1.414	0.000	0.008	0.000	0.000	0.425	0.564	0.012	0.000	5.001
ARU97-164	plag	B1	8	2.815	0.000	1.181	0.000	0.002	0.001	0.000	0.190	0.791	0.018	0.001	4.999
ARU97-164	plag	B1	8	2.642	0.000	1.352	0.000	0.006	0.002	0.000	0.371	0.610	0.006	0.001	4.990
ARU97-175	plag	B2a	8	2.100	0.000	1.866	0.001	0.023	0.001	0.000	0.913	0.120	0.001	0.000	5.025
ARU97-175	plag	B2a	8	2.110	0.000	1.873	0.000	0.008	0.000	0.001	0.903	0.113	0.001	0.000	5.009
ARU97-175	plag	B2a	8	2.240	0.000	1.736	0.001	0.012	0.001	0.001	0.774	0.245	0.003	0.002	5.015
ARU97-175	plag	B2a	8	2.114	0.000	1.863	0.000	0.011	0.001	0.001	0.903	0.121	0.001	0.001	5.016
ARU97-175	plag	B2a	8	2.246	0.000	1.729	0.001	0.011	0.001	0.001	0.773	0.247	0.004	0.000	5.013
ARU97-175	plag	B2a	8	2.237	0.000	1.742	0.000	0.012	0.001	0.000	0.780	0.236	0.003	0.001	5.012
ARU97-175	plag	B2a	8	2.121	0.001	1.849	0.001	0.014	0.001	0.000	0.903	0.124	0.001	0.000	5.015
ARU97-175	plag	B2a	8	2.271	0.001	1.711	0.000	0.007	0.000	0.001	0.742	0.271	0.001	0.001	5.006
ARU97-175	plag	B2a	8	2.087	0.000	1.876	0.001	0.053	0.001	0.000	0.903	0.104	0.001	0.001	5.027
ARU97-111	plag	B2b	8	2.125	0.000	1.851	0.001	0.010	0.001	0.001	0.902	0.112	0.001	0.001	5.005
ARU97-111	plag	B2b	8	2.137	0.001	1.833	0.000	0.013	0.001	0.001	0.901	0.116	0.001	0.000	5.004
ARU97-111	plag	B2b	8	2.139	0.002	1.833	0.001	0.014	0.001	0.006	0.880	0.126	0.004	0.001	5.007
ARU97-111	plag	B2b	8	2.122	0.000	1.851	0.001	0.020	0.001	0.005	0.896	0.109	0.001	0.001	5.007
ARU97-111	plag	B2b	8	2.126	0.000	1.849	0.000	0.012	0.000	0.000	0.902	0.121	0.001	0.000	5.011
ARU97-111	plag	B2b	8	2.113	0.000	1.865	0.000	0.012	0.000	0.001	0.909	0.105	0.000	0.001	5.006

Sample		Lith.	O	Si	Ti	Al	Cr	Fe^{2+}	Mn	Mg	Ca	Na	K	Ni	Total
ARU97-111	plag	B2b	8	2.134	0.001	1.830	0.001	0.015	0.001	0.006	0.897	0.129	0.002	0.000	5.016
ARU97-111	plag	B2b	8	2.124	0.000	1.854	0.001	0.014	0.000	0.001	0.897	0.114	0.001	0.000	5.006
ARU97-111	plag	B2b	8	2.144	0.001	1.834	0.001	0.013	0.001	0.001	0.879	0.124	0.001	0.001	5.000
ARU97-111	plag	B2b	8	2.131	0.000	1.840	0.001	0.013	0.000	0.001	0.899	0.121	0.002	0.000	5.008
ARU97-111	plag	B2b	8	2.143	0.001	1.824	0.001	0.015	0.001	0.000	0.892	0.128	0.001	0.001	5.007
ARU97-111	plag	B2b	8	2.118	0.000	1.861	0.000	0.013	0.000	0.001	0.906	0.100	0.001	0.001	5.001
ARU97-111	plag	B2b	8	2.127	0.000	1.844	0.000	0.020	0.001	0.002	0.899	0.111	0.001	0.001	5.006
ARU97-111	plag	B2b	8	2.137	0.000	1.829	0.001	0.015	0.000	0.000	0.901	0.122	0.001	0.001	5.007
ARU96-154	plag	B2b	8	2.110	0.000	1.868	0.001	0.011	0.001	0.001	0.910	0.103	0.002	0.000	5.007
ARU96-154	plag	B2b	8	2.162	0.000	1.805	0.001	0.016	0.001	0.002	0.859	0.171	0.001	0.002	5.020
ARU96-154	plag	B2b	8	2.179	0.000	1.790	0.001	0.020	0.001	0.002	0.841	0.176	0.001	0.002	5.013
ARU97-73	plag	B4	8	2.505	0.001	1.484	0.000	0.009	0.000	0.000	0.504	0.487	0.013	0.000	5.003
ARU97-73	plag	B4	8	2.621	0.001	1.366	0.003	0.007	0.001	0.000	0.392	0.598	0.010	0.000	4.999
ARU97-73	plag	B4	8	2.637	0.000	1.348	0.000	0.007	0.001	0.001	0.386	0.601	0.017	0.000	4.998
ARU97-73	plag	B4	8	2.629	0.000	1.360	0.001	0.008	0.000	0.000	0.389	0.588	0.019	0.000	4.994
ARU97-73	plag	B4	8	2.581	0.002	1.406	0.001	0.004	0.001	0.000	0.434	0.557	0.011	0.001	4.998
ARU97-73	plag	B4	8	2.574	0.000	1.412	0.001	0.006	0.001	0.001	0.443	0.547	0.012	0.001	4.998
ARU97-73	plag	B4	8	2.639	0.001	1.352	0.000	0.006	0.001	0.001	0.377	0.597	0.017	0.001	4.992
ARU97-73	plag	B4	8	2.482	0.000	1.507	0.000	0.007	0.001	0.000	0.534	0.453	0.011	0.001	4.996
ARU97-73	plag	B4	8	2.554	0.000	1.428	0.001	0.007	0.000	0.001	0.463	0.541	0.012	0.000	5.007
ARU97-73	plag	B4	8	2.600	0.001	1.388	0.000	0.005	0.000	0.000	0.420	0.571	0.010	0.001	4.996
ARU97-160	plag	B4	8	2.529	0.000	1.455	0.000	0.008	0.001	0.001	0.487	0.509	0.015	0.000	5.005
ARU97-160	plag	B4	8	2.550	0.000	1.436	0.000	0.017	0.001	0.005	0.425	0.555	0.039	0.001	5.029
ARU97-160	plag	B4	8	2.522	0.000	1.460	0.001	0.008	0.000	0.001	0.485	0.516	0.019	0.000	5.012
ARU97-160	plag	B4	8	2.602	0.000	1.382	0.001	0.009	0.000	0.001	0.401	0.592	0.021	0.002	5.011
ARU97-160	plag	B4	8	2.498	0.000	1.485	0.000	0.010	0.000	0.001	0.520	0.469	0.021	0.001	5.005
ARU97-163	plag	B4	8	2.646	0.000	1.339	0.001	0.009	0.000	0.000	0.363	0.623	0.023	0.002	5.006
ARU97-163	plag	B4	8	2.449	0.001	1.529	0.001	0.011	0.000	0.001	0.572	0.430	0.013	0.000	5.007
ARU97-163	plag	B4	8	2.486	0.001	1.490	0.001	0.009	0.000	0.000	0.525	0.493	0.010	0.003	5.018
ARU97-163	plag	B4	8	2.717	0.000	1.270	0.000	0.010	0.000	0.001	0.298	0.688	0.012	0.000	4.996
ARU97-163	plag	B4	8	2.841	0.000	1.161	0.000	0.011	0.001	0.003	0.123	0.828	0.046	0.000	5.014
ARU97-162	plag	B4	8	2.430	0.000	1.555	0.001	0.005	0.000	0.001	0.584	0.423	0.006	0.001	5.006
ARU97-162	plag	B4	8	2.460	0.000	1.520	0.002	0.011	0.001	0.001	0.554	0.451	0.010	0.001	5.011
ARU97-162	plag	B4	8	2.525	0.000	1.461	0.001	0.011	0.001	0.001	0.484	0.505	0.014	0.001	5.004
ARU97-162	plag	B4	8	2.519	0.000	1.467	0.002	0.013	0.001	0.001	0.490	0.485	0.020	0.001	4.999
ARU96-131	plag	B5	8	2.591	0.000	1.394	0.001	0.008	0.001	0.001	0.422	0.569	0.015	0.000	5.002
ARU96-131	plag	B5	8	2.597	0.000	1.392	0.000	0.006	0.000	0.000	0.411	0.571	0.029	0.001	5.007
ARU96-131	plag	B5	8	2.590	0.000	1.398	0.001	0.007	0.002	0.001	0.417	0.573	0.015	0.000	5.004
ARU96-131	plag	B5	8	2.846	0.000	1.142	0.000	0.006	0.001	0.001	0.159	0.829	0.024	0.000	5.008
ARU96-131	plag	B5	8	2.724	0.001	1.266	0.001	0.006	0.001	0.000	0.289	0.686	0.021	0.001	4.996
ARU96-131	plag	B5	8	2.812	0.000	1.181	0.001	0.005	0.002	0.001	0.187	0.797	0.016	0.001	5.003
ARU97-78	plag	B5	8	2.599	0.001	1.386	0.000	0.005	0.000	0.001	0.418	0.584	0.007	0.001	5.002
ARU97-78	plag	B5	8	2.698	0.000	1.289	0.001	0.004	0.001	0.001	0.315	0.678	0.014	0.000	5.001
ARU97-78	plag	B5	8	2.702	0.000	1.282	0.000	0.006	0.001	0.001	0.316	0.678	0.016	0.000	5.002
ARU97-78	plag	B5	8	2.670	0.001	1.313	0.001	0.005	0.001	0.002	0.348	0.642	0.015	0.001	4.999
ARU97-78	plag	B5	8	2.652	0.000	1.333	0.001	0.005	0.002	0.001	0.372	0.610	0.016	0.001	4.993
ARU97-78	plag	B5	8	2.647	0.001	1.337	0.001	0.007	0.001	0.001	0.369	0.623	0.016	0.000	5.003
ARU97-78	plag	B5	8	2.619	0.001	1.367	0.001	0.006	0.002	0.000	0.397	0.592	0.015	0.001	5.001
ARU97-78	plag	B5	8	2.620	0.000	1.364	0.000	0.007	0.000	0.001	0.402	0.588	0.015	0.001	4.998
ARU97-78	plag	B5	8	2.640	0.000	1.344	0.000	0.008	0.000	0.002	0.380	0.611	0.016	0.001	5.002
ARU97-78	plag	B5	8	2.663	0.000	1.324	0.000	0.009	0.000	0.002	0.353	0.627	0.018	0.001	4.997
ARU97-78	plag	B5	8	2.655	0.000	1.330	0.000	0.009	0.001	0.001	0.367	0.611	0.017	0.001	4.992
ARU97-78	plag	B5	8	2.598	0.000	1.386	0.001	0.007	0.001	0.001	0.418	0.576	0.014	0.001	5.003
ARU97-78	plag	B5	8	2.587	0.000	1.399	0.000	0.007	0.000	0.001	0.434	0.556	0.014	0.001	4.999
ARU97-78	plag	B5	8	2.594	0.001	1.385	0.000	0.009	0.001	0.003	0.429	0.566	0.014	0.001	5.003
ARU97-78	plag	B5	8	2.606	0.000	1.375	0.001	0.009	0.000	0.002	0.411	0.585	0.015	0.001	5.005
ARU97-78	plag	B5	8	2.546	0.000	1.433	0.001	0.008	0.000	0.000	0.481	0.519	0.010	0.001	4.999
ARU97-78	plag	B5	8	2.562	0.000	1.417	0.001	0.009	0.001	0.002	0.461	0.539	0.011	0.001	5.004
ARU97-78	plag	B5	8	2.673	0.001	1.312	0.000	0.010	0.000	0.000	0.348	0.636	0.016	0.001	4.997
ARU97-78	plag	B5	8	2.658	0.000	1.322	0.001	0.009	0.001	0.001	0.368	0.623	0.015	0.000	4.998
ARU97-78	plag	B5	8	2.597	0.000	1.381	0.001	0.009	0.001	0.002	0.426	0.573	0.012	0.001	5.003

Sample		Lith.	O	Si	Ti	Al	Cr	Fe^{2+}	Mn	Mg	Ca	Na	K	Ni	Total
ARU97-78	plag	B5	8	2.582	0.000	1.403	0.000	0.009	0.000	0.000	0.441	0.546	0.011	0.001	4.993
ARU97-78	plag	B5	8	2.596	0.000	1.389	0.000	0.008	0.001	0.001	0.429	0.554	0.011	0.001	4.990
ARU97-78	plag	B5	8	2.586	0.000	1.396	0.001	0.009	0.000	0.001	0.437	0.560	0.013	0.001	5.004
ARU97-78	plag	B5	8	2.596	0.000	1.388	0.001	0.010	0.001	0.001	0.425	0.561	0.015	0.001	4.999
ARU97-78	plag	B5	8	2.569	0.000	1.415	0.001	0.008	0.001	0.001	0.449	0.542	0.012	0.001	4.999
ARU97-78	plag	B5	8	2.548	0.001	1.438	0.001	0.009	0.002	0.000	0.467	0.517	0.010	0.001	4.994
ARU97-78	plag	B5	8	2.577	0.000	1.407	0.000	0.009	0.000	0.001	0.447	0.543	0.012	0.001	4.997
ARU97-78	plag	B5	8	2.603	0.000	1.384	0.000	0.008	0.000	0.001	0.416	0.572	0.013	0.001	4.998
ARU97-78	plag	B5	8	2.627	0.000	1.360	0.000	0.007	0.001	0.001	0.393	0.594	0.014	0.000	4.997
ARU97-78	plag	B5	8	2.594	0.000	1.388	0.001	0.009	0.000	0.000	0.428	0.564	0.013	0.001	4.998
ARU97-78	plag	B5	8	2.594	0.000	1.393	0.001	0.007	0.000	0.001	0.424	0.566	0.011	0.000	4.997
ARU97-78	plag	B5	8	2.581	0.000	1.402	0.001	0.007	0.000	0.001	0.436	0.567	0.009	0.000	5.004
ARU97-78	plag	B5	8	2.651	0.000	1.333	0.001	0.004	0.001	0.000	0.371	0.628	0.011	0.001	5.001
ARU97-78	plag	B5	8	2.639	0.000	1.349	0.001	0.003	0.001	0.001	0.382	0.607	0.009	0.000	4.992
ARU97-78	plag	B5	8	2.592	0.000	1.396	0.002	0.005	0.001	0.001	0.426	0.560	0.010	0.001	4.994
ARU97-78	plag	B5	8	2.526	0.001	1.455	0.002	0.008	0.001	0.000	0.493	0.510	0.007	0.000	5.003
ARU97-78	plag	B5	8	2.485	0.001	1.486	0.001	0.016	0.001	0.003	0.529	0.473	0.018	0.001	5.014
ARU97-78	plag	B5	8	2.501	0.001	1.485	0.001	0.007	0.001	0.000	0.520	0.467	0.008	0.001	4.992
ARU97-78	plag	B5	8	2.506	0.001	1.474	0.001	0.010	0.000	0.001	0.512	0.492	0.009	0.001	5.007
ARU97-78	plag	B5	8	2.543	0.000	1.441	0.001	0.006	0.000	0.000	0.477	0.523	0.010	0.001	5.002
ARU97-78	plag	B5	8	2.491	0.001	1.492	0.001	0.009	0.000	0.000	0.529	0.465	0.009	0.001	4.998
ARU97-78	plag	B5	8	2.485	0.001	1.497	0.001	0.008	0.001	0.001	0.536	0.463	0.010	0.000	5.003
ARU97-78	plag	B5	8	2.431	0.000	1.560	0.000	0.008	0.001	0.001	0.579	0.406	0.007	0.001	4.994
ARU97-78	plag	B5	8	2.479	0.000	1.510	0.000	0.006	0.000	0.000	0.541	0.449	0.006	0.001	4.992
ARU97-78	plag	B5	8	2.485	0.001	1.499	0.000	0.008	0.001	0.000	0.535	0.463	0.009	0.001	5.002
ARU97-78	plag	B5	8	2.486	0.000	1.498	0.001	0.008	0.001	0.000	0.530	0.469	0.010	0.000	5.003
ARU97-78	plag	B5	8	2.481	0.000	1.508	0.001	0.005	0.001	0.000	0.531	0.461	0.007	0.001	4.996
ARU96-57	tit	B1	5	1.003	0.958	0.028	0.003	0.017	0.001	0.000	1.013	0.001	0.000	0.001	3.025

Appendix H

Presentation and Publication of this study

H.1 Publications

WHITE, R. V., TARNEY, J., KERR, A. C., SAUNDERS, A. D., KEMPTON, P. D., PRINGLE, M. S. & KLAVER, G. T., 1999. Modification of an oceanic plateau, Aruba, Dutch Caribbean: Implications for the generation of continental crust. *Lithos* **46**, 43-68. *Reprint located in back pocket of thesis.*

BEETS, D. J., WESTERMANN, J. H., DE BUISONJÉ, P. H., MONEN, H. P., STIENSTRA, J., KLAVER, G. T., RUIZ, A. V., CURET, E. A., **WHITE, R. V.** & FOUKE, B. W., 1996. Geological Map of Aruba, 1:50000. *Publications Foundation for Scientific Research in the Caribbean Region*: **140**.

BEETS, D. J. & **WHITE, R.V.**, in prep. Explanatory notes to the Geological Map of Aruba, 1:50000. *Publications Foundation for Scientific Research in the Caribbean Region:* **X**.

H.2 Oral and poster presentations

WHITE, R. V., TARNEY, J., KLAVER, G. T. & RUIZ, A. V., 1996. Preliminary report on fieldwork investigation of a tonalitic batholith associated with volcanic sequences of the Caribbean oceanic plateau. *Caribbean Plateau Workshop, Rennes*, Apr. 1996.

WHITE, R. V., TARNEY, J., KLAVER, G. T. & RUIZ, A. V., 1996. The genesis of primitive tonalites associated with an accreting Cretaceous oceanic plateau: the Aruba batholith and the Aruba Lava Formation. (extended abs.) *ISAG 1996 volume of abstracts, Sept. 1996*, 661-663.

WHITE, R. V., TARNEY, J. & KEMPTON, P. D., 1997. Petrogenesis of primitive granitoids associated with oceanic plateaux and mantle plumes: new evidence from Cretaceous Caribbean tonalites. (abs.) *IAVCEI '97 General Assembly volume of abstracts*, Jan. 1997, p164. **[invited lecture]**

WHITE, R. V., TARNEY, J., KERR, A. C. & ARNDT, N. T., 1997. The Cretaceous Caribbean-Colombian oceanic plateau: aspects of formation and destruction. (abs.) *IAVCEI '97 General Assembly volume of abstracts*, Jan. 1997, p116.

WHITE, R. V. Session chair for symposium on "Sources and emplacement mechanisms of granitic magmas", *IAVCEI '97 General Assembly*, Jan. 1997.

TARNEY, J., **WHITE, R. V.** & KLAVER, G. T., 1997. Dutch Leeward Antilles: accreted arc or accreted oceanic plateau? *Workshop on the evolution of the Eastern Caribbean - South American Plate Boundary Zone, Rice University, Houston*, Oct. 1997.

WHITE, R. V., TARNEY, J. & KERR, A. C., 1997. Origin of silicic rocks associated with mantle plumes and oceanic plateaux: a Cretaceous Caribbean example. (abs.) *Geol. Soc. Am. Abstracts with Programs*, Oct. 1997, vol. 29 no. 6, p246.

WHITE, R. V., TARNEY, J., KERR, A. C., KEMPTON, P. D. & PRINGLE, M. S., 1998. The origin of tonalites associated with oceanic plateaux: Aruba, Dutch Caribbean. (abs.) *Volcanic and Magmatic Studies Group 1998 volume of abstracts*, Jan. 1998, 48-49.

WHITE, R. V., TARNEY, J., KEMPTON, P. D. & KERR, A. C., 1998. Origin of tonalites associated with oceanic plateaux: Aruba, Dutch Caribbean. (abs.) *IAVCEI '98 volume of abstracts*, Jul. 1998, p68.

References

Abbott, D. & Mooney, W., 1995. The structural and geochemical evolution of the continental crust - support for the oceanic plateau model of crustal growth. *Revs. Geophys.* **33**, 231-242.

Abbott, D. H., 1996. Plumes and hotspots as sources of greenstone belts. *Lithos* **37**, 113-127.

Aggarwal, Y. P., 1983. Seismic gaps and earthquake hazard in Venezuela. *Proceedings of a Symposium on Neotectonics, Seismicity and Geologic Risk in Venezuela and the Caribbean*, Caracas, Venezuela, 26 pp.

Aitcheson, S. J., Harmon, R. S., Moorbath, S., Schneider, A., Soler, P., Soria-Escalante, E., Steele, G., Swainbank, I. & Woerner, G., 1995. Pb isotopes define basement domains of the Altiplano, Central Andes. *Geology* **23**, 555-558.

Allègre, C. J., 1969. Comportement des systèmes U-Th-Pb dans le manteau supérieur et modèle d'évolution de ce dernier au cours des temps géologiques. *Earth Planet. Sci. Lett.* **5**, 261-269.

Allègre, C. J., 1982. Chemical geodynamics. *Tectonophys.* **81**, 109-132.

Andersen, O., 1915. The system anorthite-forsterite-silica. *Amer. J. Sci.* **39**, 407-454.

Annesley, I. R., 1990. Petrochemistry of the Woodburn Lake Group komatiitic suite, Amer Lake, N.W.T., Canada. *Unpubl. Ph.D. Thesis,* University of Ottawa.

Armstrong, R. L., 1981. Radiogenic isotopes: The case for crustal recycling on a near-steady-state no-continental-growth Earth. *Phil. Trans. Roy. Soc. London* **A301**, 443-472.

Armstrong, R. L., 1991. The persistent myth of crustal growth. *Australian J. Earth. Sci.* **38**, 613-630.

Arndt, N. T. & Jenner, G. A., 1986. Crustally contaminated komatiites and basalts from Kambalda, Western Australia. *Chem. Geol.* **56**, 229-255.

Arth, J. G., 1976. Behavior of trace elements during magmatic processes - a summary of theoretical models and their applications. *Jour. Research U.S. Geol. Surv.* **4**, 41-47.

Arth, J. G. & Barker, F., 1976. Rare-earth partitioning between hornblende and dacitic liquid and implications for the genesis of trondhjemitic-tonalitic magmas. *Geology* **4**, 534-536.

Atherton, M. P. & Petford, N., 1993. Generation of sodium-rich magmas from newly underplated basaltic crust. *Nature* **362**, 144-146.

Avé Lallement, H. G., 1997. Transpression, displacement partitioning and exhumation in the eastern Caribbean/South American plate boundary. *Tectonics* **16**, 272-289.

Babbs, T. L., 1997. Geochemical and petrological investigations of the deeper portions of the Ontong Java Plateau: Malaita, Solomon Islands. *Unpubl. Ph.D. Thesis,* University of Leicester.

Baksi, A. K., 1990. $^{40}Ar/^{39}Ar$ incremental heating studies on terrestrial whole-rock basalts: an attempt to unravel the effects of recoil loss of ^{39}Ar and ^{37}Ar (abstract). *Trans. Am. Geophys. Un.* **71**, 653.

Barker, F., 1979. Trondhjemites: definition, environment and hypotheses of origin. *In*: Barker, F., (ed.), *Trondhjemites, Dacites and Related Rocks*. Elsevier, Amsterdam, pp. 1-12.

Barker, F. & Arth, J., 1976. Generation of trondhjemitic-tonalitic liquids and Archean bimodal trondhjemite-basalt suites. *Geology* **4**, 596-600.

Barr, S. R., Temperley, S. & Tarney, J., 1999. Lateral growth of the continental crust through deep level subduction-accretion: a re-evaluation of central Greek Rhodope. *Lithos* **46**, 69-94.

Barreiro, B., 1983. Lead isotopic compositions of South Sandwich island volcanic rocks and their bearing on magma genesis in intra-oceanic island arcs. *Geochim. Cosmochim. Acta* **47**, 817-822.

Beard, J. S. & Lofgren, G. E., 1991. Dehydration melting and water-saturated melting of basaltic and andesitic greenstones and amphibolites at 1, 3 and 6.9 kb. *J. Petrol.* **32**, 365-401.

Beets, D. J., 1977. Cretaceous and Early Tertiary history of Curaçao. *Eighth Caribbean Geological Conference Guide to the Field Excursions on Curaçao, Bonaire and Aruba*: GUA Papers of Geology, **10**, pp. 7-17.

Beets, D. J., Klaver, G. T., Beunk, F. F., Kieft, G. & Maaskant, P., 1982. Picrites as parental magmas of MORB-type tholeiites. *Nature* **296**, 341-343.

Beets, D. J. & MacGillavry, H. J., 1977. Outline of the Cretaceous and early Tertiary history of Curaçao, Bonaire and Aruba. *Eighth Caribbean Geological Conference Guide to the Field Excursions on Curaçao, Bonaire and Aruba*: GUA Papers of Geology, **10**, pp. 1-6.

Beets, D. J., MacGillavry, H. J. & Klaver, G., 1977. Outline of the Cretaceous and Early Tertiary of Bonaire. *Eighth Caribbean Geological Conference Guide to the Field Excursions on Curaçao, Bonaire and Aruba*: GUA Papers of Geology, **10**, pp. 18-28.

Beets, D. J., Maresch, W. V., Klaver, G. T., Mottana, A., Bocchio, R., Beunk, F. F. & Monen, H. P., 1984. Magmatic rock series and high-pressure metamorphism as constraints on the tectonic history of the southern Caribbean. *In*: Bonini, W. E., Hargraves, R. B. & Shagam, R., (eds.), *The Caribbean-South American plate boundary and regional tectonics*: *Geol. Soc. Am. Mem.* **162**, pp. 95-130.

Beets, D. J., Westermann, J. H., De Buisonjé, P. H., Monen, H. P., Stienstra, P., Klaver, G. T., Ruiz, A. V., Curet, E. A., White, R. V. & Fouke, B. W., 1996. Geological Map of Aruba, 1:50 000. *Publications Foundation for Scientific Research in the Caribbean Region*: **140**.

Beets, D. J. & White, R. V., in prep. *Explanatory notes to the Geological Map of Aruba, 1:50 000.* Publications Foundation for Scientific Research in the Caribbean Region, **unknown**.

Ben Othman, D., White, W. M. & Patchett, J., 1989. The geochemistry of marine sediments, island arc magma genesis, and crust-mantle recycling. *Earth Planet. Sci. Lett.* **94**, 1-21.

Ben-Avraham, Z., Nur, A., Jones, D. & Cox, A., 1981. Continental accretion: from oceanic plateaus to allochthonous terranes. *Science* **213**, 47-54.

Bender, J. F., Hodges, F. N. & Bence, A. E., 1978. Petrogenesis of basalts from the Project FAMOUS area: Experimental study from 0 to 15 Kbars. *Earth Planet. Sci. Lett.* **41**, 277-302.

Bercovici, D. & Mahoney, J. J., 1995. Double flood basalts and plume head separation at the 660-kilometer discontinuity. *Science* **266**, 1367-1369.

Bernard-Griffiths, J., Peucat, J. & Menot, R. P., 1991. Isotopic (Rb-Sr, U-Pb and Sm-Nd) and trace element geochemistry of eclogites from the Pan-African belt: a case study of REE fractionation during high-grade metamorphism. *Lithos* **27**, 43-57.

Beswick, A. E., 1982. Some geochemical aspects of alteration and genetic relations in komatiitic suites. *In*: Arndt, N. T. & Nisbet, E. G., (eds.), *Komatiites*. George Allen and Unwin, London, pp. 281-308.

Bickle, M. J., Martin, A. & Nisbet, E. G., 1975. Basaltic and peridotitic komatiites, stromatolites, and a basal unconformity in the Belingwe Greenstone Belt, Rhodesia. *Earth Planet. Sci. Lett.* **27**, 155-162.

Bickle, M. J., Nisbet, E. G. & Martin, A., 1994. Archaean greenstone belts are not oceanic crust. *J. Geol.* **102**, 121-138.

Blundy, J. D. & Holland, T. J. B., 1990. Calcic amphibole equilibria and a new amphibole-plagioclase geothermometer. *Contrib. Mineral. Petrol.* **104**, 208-224.

Blundy, J. D., Robinson, J. A. C. & Wood, B. J., 1998. Heavy REE are compatible in clinopyroxene on the spinel lherzolite solidus. *Earth Planet. Sci. Lett.* **160**, 493-504.

Boettcher, A. L. & Wyllie, P. J., 1968. Jadeite stability measured in the presence of silicate liquids in the system $NaAlSiO_4$-SiO_2-H_2O. *Geochim. Cosmochim. Acta* **32**, 999-1012.

Borsi, L., Petrini, R., Talarico, F. & Palmeri, R., 1995. Geochemistry and Sr-Nd isotopes of amphibolite dykes of northern Victoria Land, Antarctica. *Lithos* **35**, 245-259.

Bott, M. H. P., 1982. *The Interior of the Earth, its Structure, Constitution and Evolution* (2nd edition). Edward Arnold. London.

Bourdon, B., Langmuir, C. H. & Zindler, A., 1996. Ridge-hotspot interaction along the Mid-Atlantic Ridge between 37°30' and 40°30'N: the U-Th disequilibrium evidence. *Earth Planet. Sci. Lett.* **142**, 175-189.

Bowring, S. A. & Housh, T., 1995. The Earth's early evolution. *Science* **269**, 1535-1540.

Bowring, S. A. & Williams, I. S., 1999. Priscoan (4.00 - 4.03 Ga) orthogneisses from Northwestern Canada. *Contrib. Mineral. Petrol.* **134**, 3-16.

Brandl, G. & de Wit, M. J., 1997. The Kaapvaal Craton. *In*: de Wit, M. & Ashwal, L. D., (eds.), *Greenstone Belts*: Oxford Monographs on Geology and Geophysics **35**, pp. 5-29.

Brown, G. C., 1979. The changing pattern of batholith emplacement during earth history. *In*: Atherton, M. P. & Tarney, J., (eds.), *Origin of Granite Batholiths*. Shiva, Nantwich, pp. 106-115.

Burke, K., 1988. Tectonic evolution of the Caribbean. *Ann. Revs. Earth Planet. Sci.* **16**, 201-230.

Burke, K., Cooper, C., Dewey, J. F., Mann, P. & Pindell, J. L., 1984. Caribbean tectonics and relative plate motions. *In*: Bonini, W. E., Hargraves, R. B. & Shagam, R., (eds.), *The Caribbean-South American plate boundary and regional tectonics*: *Geol. Soc. Am. Mem.* **162**, pp. 31-63.

Burke, K., Fox, P. J. & Sengör, M. C., 1978. Buoyant ocean floor and the origin of the Caribbean. *J. Geophys. Res.* **83**, 3949-3954.

Calderone, G. M., Gronvold, K. & Oskarsson, N., 1990. The Welded Air-Fall Tuff Layer At Krafla, Northern Iceland - a Composite Eruption Triggered By Injection of Basaltic Magma. *J. Volc. Geoth. Res.* **44**, 303-314.

Campbell, I. H., 1978. Some problems with the cumulus theory. *Lithos* **11**, 311-323.

Campbell, I. H. & Griffiths, R. W., 1990. Implications of a mantle plume structure for the evolution of flood basalts. *Earth Planet. Sci. Lett.* **99**, 79-93.

Cann, J. R., 1979. Metamorphism in the ocean crust. *In*: Talwani, M., Harrison, C. G. & Hayes, D. E., (eds.), *Deep Drilling Result in the Atlantic Crust*. Am. Geophys. Un., Maurice Ewing Series, pp. 230-238.

Cantrell, K. J. & Byrne, R. H., 1987. Rare earth elements complexation by carbonate and oxalate ions. *Geochim. Cosmochim. Acta* **51**, 597-605.

Card, K. D., 1990. A review of the Superior Province of the Canadian Shield, a product of Archean accretion. *Precambrian Res.* **48**, 99-156.

Cas, R. A. F. & Wright, J. V., 1987. *Volcanic Successions: modern and ancient.* Allen & Unwin. London. 528 pp.

Case, J. E. & Holcomb, T. L., 1980. Geologic-tectonic map of the Caribbean region, 1:2,500,000 (3 sheets). *USGS Series*: **No. 1-1100**.

Case, J. E., Holcomb, T. L. & Martin, R. G., 1984. Map of geologic provinces in the Caribbean region. *In*: Bonini, W. E., Hargraves, R. B. & Shagam, R., (eds.), *The Caribbean-South American plate boundary and regional tectonics*: *Geol. Soc. Am. Mem.* **162**, pp. 1-30.

Castillo, P. R., Carlson, R. W. & Batiza, R., 1991. Origin of Nauru Basin igneous complex: Sr, Nd and Pb isotope and REE constraints. *Earth Planet. Sci. Lett.* **103**, 200-213.

Chauvel, C., Goldstein, S. L. & Hofmann, A. W., 1995. Hydration and dehydration of oceanic crust controls Pb evolution in the mantle. *Chem. Geol.* **126**, pp. 65-75.

Chow, T. J. & Patterson, C. C., 1962. The occurrence and significance of lead isotopes in pelagic sediments. *Geochim. Cosmochim. Acta* **26**, 263-308.

Christensen, N. I. & Mooney, W. D., 1995. Seismic velocity structure and composition of the continental crust: a global view. *J. Geophys. Res.* **100**, 9761-9788.

Cloos, M., 1993. Lithospheric buoyancy and collisional orogenesis: subduction of oceanic plateaus, continental margins, island arcs, spreading ridges, and seamounts. *Geol. Soc. Amer. Bull.* **105**, 715-737.

Coffin, M. F. & Eldholm, O., 1993. Scratching the surface: estimating the dimensions of large igneous provinces. *Geology* **21**, 515-518.

Coffin, M. F. & Eldholm, O., 1994. Large igneous provinces: crustal structure, dimensions and external consequences. *Rev. Geophys.* **32**, 1-36.

Condie, K., 1993. Chemical composition and evolution of the upper continental crust: Contrasting results from surface samples and shales. *Chem. Geol.* **104**, 1-37.

Condie, K., 1997. *Plate tectonics and crustal evolution.* Butterworth-Heinemann. (4th edition). 282 pp.

Cooper, P. A. & Taylor, B., 1985. Polarity reversal in the Solomon Islands arc. *Nature* **314**, 428-430.

Courtney, R. & White, R., 1986. Anomalous heat flow and geoid across the Cape Verde Rise: evidence for dynamic support from a thermal plume in the mantle. *Geophys. J. Roy. Ast. Soc.* **87**, 815-867.

Courtillot, V., Besse, J., Vandamme, D., Montingny, R., Jaegger, J.-J. & Capetta, H., 1986. Deccan flood basalts at the Cretaceous/Tertiary boundary? *Earth Planet. Sci. Lett.* **80**, 361-374.

Dalrymple, G. B. & Duffield, W. A., 1988. High precision $^{40}Ar/^{39}Ar$ dating of Oligocene rhyolites from the Mogollon-Datil volcanic field using a continuous laser system. *Geophys. Res. Lett.* **15**, 463-466.

Dalrymple, G. B., Izett, G. A., Snee, L. W. & Obradovich, J. D., 1993. $^{40}Ar/^{39}Ar$ age spectra and total-fustion ages of tektites from Cretacous-Tertiary boundary sedimentary rocks in the Beloc Formation, Haiti. *US Geol. Surv. Bull.* **2065**.

Dasch, E. J., 1981. Lead isotopic compositions of metalliferous sediments from the Nazca plate. *Geol. Soc. Am. Mem.* **154**, 199-209.

De Buisonjé, P. H., 1964. Marine terraces and sub-aeric sediments on the Netherlands Leeward Islands, Curacao, Aruba, and Bonaire, as indications of Quaternary changes in sea level and climate. *Koninkl. Nederlandse Akad. Wetensch. Proc., ser. B* **67**, 60-79.

De Buisonjé, P. H., 1974. Neogene and Quaternary geology of Aruba, Curaçao and Bonaire (Netherlands Antilles). *Uitgaven Natuurwetenschappelijke Studiekring voor Suriname en de Nederlandse Antillen* **78**, 293 pp.

de Wit, M. & Ashwal, L. D., 1997. *Greenstone Belts*: Oxford Monographs on Geology and Geophysics, **35**. Oxford University Press (1st edition). 809 pp.

de Wit, M. J., 1982. Gliding and overthrust nappe tectonics in the Barberton greenstone belt. *J. Struct. Geol.* **4**, 117-136.

Defant, M. J. & Drummond, M. S., 1990. Derivation of some modern arc magmas by melting of young subducted lithosphere. *Nature* **347**, 662-665.

Defant, M. J. & Drummond, M. S., 1993. Mount St. Helens: Potential example of the partial melting of the subducted lithosphere in a volcanic arc. *Geology* **21**, 547-550.

DePaolo, D. J. & Johnson, D. W., 1979. Magma genesis in the New Britain island-arc: constraints from Nd and Sr isotopes and trace element patterns. *Contrib. Mineral. Petrol.* **70**, 367-379.

DePaolo, D. J. & Wasserburg, G. J., 1977. The sources of island arcs as indicated by Nd and Sr isotopic studies. *Geophys. Res. Lett.* **4**, 465-468.

Desrochers, J.-P., Hubert, C., N., L. J. & Pilote, P., 1993. Accretion of Archaean oceanic plateau fragments in the Abitibi greenstone belt, Canada. *Geology* **21**, 451-454.

Dewey, J. F. & Windley, B. F., 1981. Growth and differentiation of the continental crust. *Phil. Trans. Roy. Soc. London* **A301**, 189-206.

Dickin, A. P., 1981. Isotope geochemistry of Tertiary igneous rocks from the Isle of Skye, N.W. Scotland. *J. Petrol.* **22**, 155-189.

Donnelly, T. W., 1973. Late Cretaceous basalts from the Caribbean, a possible flood basalt province of vast size (abstract). *EOS, Trans. Am. Geophys. Un.* **54**, 1004.

Donnelly, T. W., Beets, D. J., Carr, M. J., Jackson, T., Klaver, G. T., Lewis, J., Maury, R., Schellenkens, H., Smith, A. L., Wadge, G. & Westercamp, D., 1990. History and tectonic setting of Caribbean magmatism. *In*: Dengo, G. & Case, J. E., (eds.), *The Caribbean region*: The Geology of North America, **vol. H**. Geol. Soc. Am., Boulder, Colorado, pp. 339-374.

Donnelly, T. W. & Rogers, J. J. W., 1967. Crust vs. mantle derivation of eastern Antillean igneous rocks (abstract). *EOS, Trans. Am. Geophys. Un.* **48**, 253.

Donnelly, T. W., Rogers, J. J. W., Pushkar, P. & Armstrong, R. L., 1971. Chemical Evolution of the Igneous Rocks of the Eastern West Indies; An Investigation of Thorium, Uranium, and Potassium Distributions, and Lead and Strontium Isotopic Ratios. *Caribbean Geophysical, Tectonic, and Petrologic Studies*: *Geol. Soc. Am. Mem.* **130**, pp. 181-224.

Dostal, J. & Strong, D. F., 1983. Trace-element mobility during low-grade metamorphism and silicification of basaltic rocks from Saint John, New Brunswick. *Can. J. Earth. Sci.* **20**, 431-435.

Draper, G., Guierrez, G. & Lewis, J. F., 1996. Thrust emplacement of the Hispaniola peridotite belt: Orogenic expression of the mid-Cretaceous Caribbean arc polarity reversal? *Geology* **24**, 1143-1146.

Drummond, M. S. & Defant, M. J., 1990. A model for trondhjemite-tonalite-dacite genesis and crustal growth via slab melting: Archean to modern comparisons. *J. Geophys. Res.* **95**, 21503-21521.

Drummond, M. S., Defant, M. J. & Kepezhinskas, P. K., 1996. Petrogenesis of slab-derived trondhjemite-tonalite-dacite/adakite magmas. *Trans. Roy. Soc. Edinburgh: Earth Sci.* **87**, 205-215.

Duffield, W. A. & Dalrymple, G. B., 1990. The Taylor Creek Rhyolite of New Mexico: a rapidly emplaced field of lava domes and flows. *Bull. Volc.* **52**, 475-487.

Duncan, R. A. & Hargraves, R. B., 1984. Plate tectonic evolution of the Caribbean in the mantle reference frame. *In*: Bonini, W. E., Hargraves, R. B. & Shagam, R., (eds.), *The Caribbean-South American plate boundary and regional tectonics*: *Geol. Soc. Am. Mem.* **162**, pp. 31-63.

Echeverría, L. M., 1980. Tertiary or Mesozoic komatiites from Gorgona Island, Colombia: field relations and geochemistry. *Contrib. Mineral. Petrol.* **73**, 253-256.

Edgar, N. T., Ewing, J. I. & Hennion, J., 1971. Seismic refraction and reflection in the Caribbean Sea. *Bull. Amer. Assoc. Petrol. Geol.* **55**, 833-870.

Evans, O. C. & Hanson, G. N., 1997. Late- to post-kinematic Archaean granitoids of the S.W. Superior Province: Derivation through direct mantle melting. *In*: de Wit, M. & Ashwal, L. D., (eds.), *Greenstone Belts*: Oxford Monographs on Geology and Geophysics, **35**, pp. 280-295.

Ewart, A., 1976. Mineralogy and chemistry of modern orogenic lavas - some statistics and implications. *Earth Planet. Sci. Lett.* **31**, 417-432.

Ewart, A., Bryan, W. B. & Gill, J. B., 1973. Mineralogy and petrology of the younger volcanic islands of Tonga, S.W. Pacific. *J. Petrol.* **14**, 429-465.

Faure, G., 1986. *Principles of isotope geology*. John Wiley & Sons (2nd edition). 589 pp.

Fitton, J. G., Saunders, A. D., Norry, M. J., Hardarson, B. S. & Taylor, R. N., 1997. Thermal and chemical structure of the Iceland plume. *Earth Planet. Sci. Lett.* **153**, 197-208.

Fleck, R. J., Sutter, J. F. & Elliot, D. H., 1977. Interpretation of discordant $^{40}Ar/^{39}Ar$ age spectra of Mesozoic tholeiites from Antarctica. *Geochim. Cosmochim. Acta* **41**, 15-32.

Foland, K. A., 1983. $^{40}Ar/^{39}Ar$ incremental heating plateaus for biotites with excess argon. *Isotope Geoscience* **1**, 3-21.

Foley, S. F. & Wheller, G. E., 1990. Parallels in the origin of the geochemical signature of island arc volcanics and continental potassic igneous rocks: the role of residual titanites. *Chem. Geol.* **85**, 1-18.

Fountain, D. M. & Salisbury, M. H., 1981. Exposed cross-sections through the continental crust; implications for crustal structure, petrology, and evolution. *Earth Planet. Sci. Lett.* **56**, 263-277.

Fox, P. J. & Heezen, B. C., 1975. Geology of the Caribbean crust. *In*: Nairn, A. E. M. & Stehli, F. G., (eds.), *The Gulf of Mexico and the Caribbean*: The Ocean Basins and Margins, **vol. 3**. Plenum, New York, pp. 421-465.

Fyfe, W. S., 1978. The evolution of the Earth's crust: Modern plate tectonics to ancient hot spot tectonics? *Chem. Geol.* **23**, 89-114.

Gallahan, W. E. & Nielsen, R. L., 1992. The partitioning of Sc, Y and the rare earth elements between high-Ca pyroxene and natural mafic to intermediate lavas at 1 atmosphere. *Geochim. Cosmochim. Acta* **56**, 2387-2404.

Gass, I. G., 1958. Ultrabasic pillow lavas from Cyprus. *Geol. Mag.* **45**, 241-251.

Gélinas, L., Mellinger, M. & Trudel, P., 1982. Archean mafic metavolcanics from the Rouyn-Noranda District, Abitibi greenstone belt, Quebec; 1, Mobility of the major elements. *Can. J. Earth Sci.* **19**, 2258-2275.

Gill, J. B., 1981. *Orogenic andesites and plate tectonics*. Springer-Verlag. Berlin. 358 pp.

Gladczenko, T. P., Coffin, M. F. & Eldholm, O., 1997. Crustal structure of the Ontong Java Plateau: Modeling of new gravity and existing seismic data. *J. Geophys. Res.* **102**, 22711-22729.

Green, D. H., 1976. Experimental testing of "equilibrium" partial melting of peridotite under water-saturated, high-pressure conditions. *Can. Mineral.* **14**, 255-268.

Green, D. H., Edgar, A. D., Beasley, P., Kiss, E. & Ware, N. G., 1974. Upper mantle source for some hawaiites, mugearites and benmoreites. *Contrib. Mineral. Petrol.* **48**, 33-43.

Green, T. H., 1981. Experimental evidence for the role of accessory phases in magma genesis. *J. Volc. Geoth. Res.* **10**, 405-422.

Green, T. H., 1982. Anatexis of mafic crust and high pressure crystallization of andesite. *In*: Thorpe, R. S., (ed.), *Andesites*. Wiley, pp. 465-487.

Green, T. H., 1994. Experimental studies of trace-element partitioning applicable to igneous petrogenesis – Sedona 16 years later. *Chem. Geol.* **117**, 1-36.

Green, T. H. & Ringwood, A. E., 1968. Genesis of the calc-alkaline igneous rock suite. *Contrib. Mineral. Petrol.* **18**, 105-162.

Gunnarsson, B., Marsh, B. D. & Taylor, H. P., Jr., 1998. Generation of Icelandic rhyolites: silicic lavas from the Torfajökull central volcano. *J. Volc. Geoth. Res.* **83**, 1-45.

Hall, S. A., 1995. Oceanic basement of the Caribbean basements (abstract). *Geol. Soc. Am., Abstracts with Programs* **27**, A153.

Halliday, A. N., Dickin, A. P., Hunter, R. N., Davies, G. R., Dempster, T. J., Hamilton, P. J. & Upton, B. G. J., 1993. Formation and composition of the lower continental crust: evidence from Scottish xenolith suites. *J. Geophys. Res.* **98**, 581-607.

Hanson, G. N. & Langmuir, C. H., 1978. Modelling of major elements in mantle-melt systems using trace element approaches. *Geochim. Cosmochim. Acta* **42**, 725-741.

Harland, W. B., Armstrong, R. L., Cox, A. V., Craig, L. E., Smith, A. G. & Smith, D. G., 1990. *A Geologic Time Scale 1989*. Cambridge University Press. Cambridge. 263 pp.

Harrison, T. M. & McDougall, I., 1981. Excess ^{40}Ar in metamorphic rocks from Broken Hill, New South Wales: Implications for $^{40}Ar/^{39}Ar$ age spectra and the thermal history of the region. *Earth Planet. Sci. Lett.* **55**, 123-149.

Hart, S. R., 1988. Heterogeneous mantle domains: signatures, genesis and mixing chronologies. *Earth Planet. Sci. Lett.* **90**, 273-296.

Hart, S. R. & Davis, K. E., 1978. Nickel partitioning between olivine and silicate melt. *Earth Planet. Sci. Lett.* **40**, 203-219.

Hart, S. R., Erlank, A. J. & Kable, E. J. D., 1974. Seafloor basalt alteration: Some chemical and strontium isotopic effects. *Contrib. Mineral. Petrol.* **44**, 707-725.

Hart, S. R., Hauri, E. H., Oschmann, L. A. & Whitehead, J. A., 1992. Mantle plumes and entrainment: isotopic evidence. *Science* **256**, 517-520.

Hauff, F., Hoernle, K., Tilton, G., Graham, D. & Kerr, A. C., submitted. Large Volume Recycling of Oceanic Lithosphere: Geochemical Evidence from the Caribbean Large Igneous Province. *Earth Planet. Sci. Lett.*

Helmers, H. & Beets, D. J., 1977. Geology of the Cretaceous of Aruba. *Eighth Caribbean Geological Conference Guide to the Field Excursions on Curaçao, Bonaire and Aruba*: GUA Papers of Geology, **10**, pp. 29-35.

Helmstaedt, H., Padgham, W. A. & Brophy, J. A., 1986. Multiple dikes in Lower Kam Group, Yellowknife Greenstone Belt – evidence for Archean sea-floor spreading. *Geology* **14**, 562-566.

Helz, R. T., 1982. Experimental studies of amphibole stability; Phase relations and compositions of amphiboles produced in studies of the melting behavior of rocks. *In*: Veblen, D. R. & Ribbe, P. H., (eds.), *Amphiboles; petrology and experimental phase relations*: Reviews in Mineralogy, **9B**. Min. Soc. Am., Washington, DC, pp. 279-353.

Hémond, C., Arndt, N. T. & Hofmann, A. W., 1993. The heterogeneous Iceland plume: Nd-Sr-O and trace element constraints. *J. Geophys. Res.* **98**, 15833-15850.

Henderson, P., 1984. General geochemical properties and abundances of the rare earth elements. *In*: Henderson, P., (ed.), *Rare Earth Element Geochemistry*: Developments in Geochemistry **2**. Elsevier, Amsterdam, pp. 1-29.

Herweijer, J. P. & Focke, J. W., 1978. Late Pleistocene depositional and denudational history of Aruba, Bonaire and Curaçao. *Geol. Mijn.* **57**, 177-187.

Herzberg, C. T. & Chapman, N. A., 1976. Clinopyroxene geothermometry of spinel lherzolite. *Amer. Mineral.* **61**, 626-637.

Hill, R. I., 1993. Mantle plumes and continental tectonics. *Lithos* **30**, 193-206.

Hole, M. J., Saunders, A. D., Marriner, G. F. & Tarney, J., 1984. Subduction of pelagic sediments: implications for the origin of Ce-anomalous basalts from the Mariana Islands. *J. Geol. Soc. London* **141**, 453-472.

Hollister, L. S., Grissom, G. C., Peters, E. K., Stowell, H. H. & Sisson, V. B., 1987. Confirmation of the empirical correlation of Al in hornblende with pressure of solidification of calc-alkaline plutons. *Amer. Mineral.* **72**, 231-239.

Horsefield, S. J., Whitmarsh, R. B., White, R. S. & Sibuet, J. C., 1994. Crustal structure of the Goban Spur rifted continental margin, NE Atlantic. *Geophys. J. Int.* **119**, 1-19.

Hughes, G. W. & Turner, C. C., 1977. Upraised Pacific Ocean floor, southern Malaita, Solomon Islands. *Geol. Soc. Am. Bull.* **88**, 412-424.

Humphris, S. E., Morrison, M. A. & Thompson, R. N., 1978. Influence of rock crystallisation history upon subsequent lanthanide mobility during hydrothermal alteration of basalts. *Chem. Geol.* **23**, 125-137.

Humphris, S. E. & Thompson, G., 1978. Trace element mobility during hydrothermal alteration of oceanic basalts. *Geochim. Cosmochim. Acta* **42**, 127-136.

Huneke, J. C. & Smith, S. P., 1976. The realities of recoil: ^{39}Ar recoil out of small grains and anomalous patterns in ^{40}Ar/^{39}Ar dating. *Geochim. Cosmochim. Acta Suppl.* **7** (Proceedings of the 7th Lunar Science Conference), 1987-2008.

Hunter, D. R. & Stowe, C. W., 1997. A historical review of the origin, composition and setting of Archaean greenstone belts (pre-1980). *In*: de Wit, M. & Ashwal, L. D., (eds.), *Greenstone Belts*: Oxford Monographs on Geology and Geophysics **35**. Oxford University Press, pp. 5-29.

Hurley, P. M. & Rand, J. R., 1969. Predrift continental nuclei. *Science* **164**, 1229-1242.

Hynes, A., 1980. Carbonization and mobility of Ti, Y, and Zr in Ascot formation, S.E. Quebec. *Contrib. Mineral. Petrol.* **75**, 79-87.

Irvine, T. N., 1980. Magmatic density currents and cumulus processes. *Am. Journal Sci.* **280A**, 1-58.

Irvine, T. N. & Baragar, W. R. A., 1971. A guide to the chemical classification of the common volcanic rocks. *Can. J. Earth Sci.* **8**, 523-548.

Jackson, T. A. & Robinson, E., 1994. The Netherlands and Venezuelan Antilles. *In*: *Caribbean Geology: an introduction*. U. W. I. Publishers' Association, Kingston, Jamaica, pp. 249-263.

Jakes, P. & Gill, J., 1970. Rare earth elements and the island arc tholeiitic series. *Earth Planet. Sci. Lett.* **9**, 17-28.

Johannes, W., 1989. Melting of plagioclase-quartz assemblages of 2 kbar water pressure. *Contrib. Mineral. Petrol.* **103**, 270-276.

Jónasson, K., Holm, P. M. & Pederson, A. K., 1992. Petrogenesis of silicic rocks from the Króksfjördur Central Volcano, NW Iceland. *J. Petrol.* **33**, 1345-1369.

Kay, R. W., Sun, S.-S. & Lee-Hu, C. N., 1978. Pb and Sr isotopes in volcanic rocks from the Aleutians and Pribilof Isalnds, Alaska. *Geochim. Cosmochim. Acta* **42**, 263-273.

Kearey, P. & Vine, F. J., 1996. *Global Tectonics*. Blackwell Science (2nd edition). 333 pp.

Kellogg, J. N. & Bonini, W. E., 1982. Subduction of the Caribbean Plate and basement uplifts in the overriding South America Plate. *Tectonics* **1**, 251-276.

Kempton, P. D., 1995. Common Pb procedures for silicate rocks and minerals, methods of data correction and an assessment of data quality at the NERC Isotope Geosciences Laboratory. *NIGL Report Series* **78**, 26 pp.

Kempton, P. D., 1997. Procedures for the Chemical Analysis of U in Silicate Rocks at the NERC Isotope Geosciences Laboratory. *NIGL Report Series* **117**, 8 pp.

Kempton, P. D. & Casey, J. F., 1997. Petrology and geochemistry of crosscutting diabase dikes, Sites 920 and 921. *In*: Karson, J. A., Cannat, M., Miller, D. J. & Elthon, D., (eds.): *Proc. ODP Sci. Res.* **153**, 363-377.

Kerr, A. C., 1993. The geochemistry and petrogenesis of the Mull and Morvern Tertiary lava succession, Argyll, Scotland. *Unpubl. Ph.D. Thesis,* University of Durham, 357 pp.

Kerr, A. C., Iturralde-Vinent, M. A., Saunders, A. D., Babbs, T. L. & Tarney, J., in press. A new plate tectonic model of the Caribbean: Implications from a geochemical reconnaissance of Cuban Mesozoic volcanic rocks. *Geol. Soc. Am. Bull.* **unknown**, unknown.

Kerr, A. C., Marriner, G. F., Arndt, N. T., Tarney, J., Nivia, A., Saunders, A. D. & Duncan, R. A., 1996a. The petrogenesis of Gorgona komatiites, picrites and basalts: new field, petrographic and geochemical constraints. *Lithos* **37**, 245-260.

Kerr, A. C., Marriner, G. F., Tarney, J., Nivia, A., Saunders, A. D., Thirlwall, M. F. & Sinton, C. W., 1997a. Cretaceous basaltic terranes in Western Colombia: Elemental, Chronological and Sr-Nd isotopic constraints on petrogenesis. *J. Petrol.* **38**, 677-702.

Kerr, A. C., Saunders, A. D., Tarney, J., Berry, N. H. & Hards, V. L., 1995. Depleted mantle plume geochemical signatures; no paradox for plume theories. *Geology* **23**, 843-846.

Kerr, A. C., Tarney, J., Marriner, G. F., Klaver, G. T., Saunders, A. D. & Thirlwall, M. F., 1996b. The geochemistry and petrogenesis of the late-Cretaceous picrites and basalts of Curaçao, Netherlands Antilles: a remnant of an oceanic plateau. *Contrib. Mineral. Petrol.* **124**, 29-43.

Kerr, A. C., Tarney, J., Marriner, G. F., Nivia, A. & Saunders, A. D., 1997b. The Caribbean-Colombian Cretaceous igneous province: the internal anatomy of an oceanic plateau. *In*: Mahoney, J. J. & Coffin, M., (eds.), *Large Igneous Provinces: Continental, Oceanic, and Planetary Flood Volcanism: Geophys. Mon.*, **100**. Am. Geophys. Un., pp. 123-144.

Kerr, A. C., Tarney, J., Marriner, G. F., Nivia, A., Saunders, A. D. & Klaver, G. T., 1996c. The geochemistry and tectonic setting of late Cretaceous Caribbean and Colombian volcanism. *J. South Am. Earth Sci.* **9**, 111-120.

Kerr, A. C., Tarney, J., Nivia, A., Marriner, G. F. & Saunders, A. D., 1998. The internal structure of oceanic plateaus: inferences from obducted Cretaceous terranes in western Colombia and the Caribbean. *Tectonophys.* **292**, 173-188.

Kerrich, R., 1994. Dating of auriferous quartz vein deposits in the Abitibi greenstone belt, Canada: $^{40}Ar/^{39}Ar$ evidence for a 70- to 100-m.y. time gap between plutonism-metamorphism and mineralization - A discussion. *Econ. Geol.* **89**, 679-687.

Khitarov, N. I. & Moskalyuk, A. A., 1955. Experimental data on the problem of genesis of lead mineralisation. *Sovetskaya Geologiya* **43**, 126-136.

Kinny, P. D., 1986. 3820 Ma zircons from a tonalitic Amitsoq Gneiss in the Godthaab District of southern West Greenland. *Earth Planet. Sci. Lett.* **79**, 337-347.

Klaver, G. T., 1987. *The Curacao Lava Formation: an ophiolitic analogue of the anomalous thick layer 2B of the mid-Cretaceous oceanic plateaus in the western Pacific and central Caribbean*, Ph.D. Thesis: *GUA Papers of Geology* **27**, 168 pp.

Klein, E. M. & Langmuir, C. H., 1987. Global correlation of ocean ridge basalt chemistry with axial depth and crustal thickness. *J. Geophys. Res.* **92**, 8089-8115.

Klein, M., Stosch, H. G. & Seck, H. A., 1997. Partitioning of high field-strength and rare-earth elements between amphibole and quartz-dioritic to tonalitic melts; an experimental study. *Chem. Geol.* **138**, 257-271.

Kusky, T. M., 1989. Accretion of the Archean Slave Province. *Geology* **17**, 63-67.

Ladd, J. W., Holcombe, T. L., Westbrook, G. K. & Edgar, N. T., 1990. Caribbean marine geology; Active margins of the plate boundary. *In*: Dengo, G. & Case, J. E., (eds.), *The Caribbean region*: The Geology of North America, **vol. H**. Geol. Soc. Am., Boulder, Colorado, pp. 261-290.

Ladd, J. W. & Watkins, J. S., 1979. Tectonic development of trench-arc complexes on the northern and southern margins of the Venezuela Basin. *In*: Watkins, J. S., Montadert, L. & Dickerson, P. W., (eds.), *Geological and geophysical investigations of continental margins*: *Memoir - American Association of Petroleum Geologists,* **29**, 363-371.

Lahaye, Y., Arndt, N. T., Byerly, G., Chauvel, C., Fourcade, S. & Gruau, G., 1995. The influence of alteration on the trace-element and Nd isotopic compositions of komatiites. *Chem. Geol.*, **126**, pp. 43-64.

Lanphere, M. A. & Dalrymple, G. B., 1971. A test of the $^{40}Ar/^{39}Ar$ age spectrum technique on some terrestrial materials. *Earth Planet. Sci. Lett.* **12**, 359-372.

Lapierre, H., Dupuis, V., deLepinay, B. M., Tardy, M., Ruiz, J., Maury, R. C., Hernandez, J. & Loubet, M., 1997. Is the lower Duarte igneous complex (Hispaniola) a remnant of the Caribbean plume-generated oceanic plateau? *J. Geol.* **105**, 111-120.

Larson, R. L., 1991. Latest pulse of Earth: Evidence for a mid-Cretaceous superplume. *Geology* **19**, 547-550.

Le Maitre, R. W. & others, 1989. *A classification of igneous rocks and glossary of terms*. Blackwell, Oxford.

Leake, B. E. & others, 1997. Nomenclature of amphiboles; report of the Subcommittee on Amphiboles of the International Mineralogical Association Commission on new minerals and mineral names. *Min. Mag.* **61**, 295-321.

Lebron, M. C. & Perfit, M. R., 1993. Stratigraphic and petrochemical data support subduction polarity reversal of the Cretaceous Caribbean island arc. *J. Geol.* **101**, 389-396.

Lebron, M. C. & Perfit, M. R., 1994. Petrochemistry and tectonic significance of Cretaceous island-arc rocks, Cordillera Oriental, Dominican Republic. *Tectonophys.* **229**, 69-100.

Lesher, C. M. & Arndt, N. T., 1995. REE and Nd isotope geochemistry, petrogenesis and volcanic evolution of contaminated komatiites at Kambalda, Western-Australia. *Lithos* **34**, 127-157.

Ludden, J., Gelinas, L. & Trudel, P., 1982. Archean metavolcanics from the Rouyn-Noranda district, Abitibi greenstone belt, Quebec. 2. Mobility of trace elements and petrogenetic constraints. *Can. J. Earth Sci.* **19**, 2276-2287.

Ludden, J. N. & Gelinas, L., 1982. Trace-element characteristics of komatiites and komatiitic basalts from the Abitibi metavolcanic belt of Quebec. *In*: Arndt, N. T. & Nisbet, E. G., (eds.), *Komatiites*. George Allen and Unwin, London, pp. 331-346.

Ludden, J. N. & Thompson, G., 1979. An evaluation of the behavior of the rare earth elements during the weathering of sea-floor basalt. *Earth Planet. Sci. Lett.* **43**, 85-92.

Lugmair, G. W. & Marti, K., 1978. Lunar initial $^{143}Nd/^{144}Nd$; differential evolution of the lunar crust and mantle. *Earth Planet. Sci. Lett.* **39**, 349-357.

Lundberg, N., Reed, D. L., Liu, C.-S. & Lieske, J., Jr., 1997. Forearc-basin closure and arc accretion in the submarine suture south of Taiwan. *Tectonophys.* **274**, 5-23.

Maas, R., Kinny, P. D., Williams, I. S., Froude, D. O. & Compston, W., 1992. The Earth's oldest known crust - a geochronological and geochemical study of 3900-4200 Ma old detrital zircons from Mt Narryer and Jack Hills, Western-Australia. *Geochim. Cosmochim. Acta* **56**, 1281-1300.

MacDonald, R., McGarvie, D. W., Pinkerton, H., Smith, R. L. & Palacz, Z. A., 1990. Petrogenetic evolution of the Torfajökull volcanic complex, Iceland: I. Relationships between the magma types. *J. Petrol.* **31**, 429-459.

MacDonald, W. D., 1968. Communication in: *Status of geological research in the Caribbean* **14**, 40-41.

MacDonald, W. D., Estrada, J. J. & Gonzalez, J., 1997. Paleoplate affiliations of volcanic accretionary terranes of the northern Andes. *Geol. Soc. Am., Abstracts with Programs*, A245.

Mahoney, J. J., 1987. An isotopic survey of Pacific ocean plateaus: implications for their nature and origin. *In*: Keating, B. H., Fryer, P., Batiza, R. & Boehlert, G. W., (eds.), *Seamounts, Islands and Atolls*. Am. Geophys. Un., Washington D.C., pp. 207-220.

Mahoney, J. J. & Spencer, K. J., 1991. Isotopic evidence for the origin of the Manihiki and Ontong Java oceanic plateaus. *Earth Planet. Sci. Lett.* **104**, 196-210.

Mahoney, J. J., Storey, M., Duncan, R. A., Spencer, K. J. & Pringle, M., 1993. Geochemistry and geochronology of Leg 130 basement lavas: nature and origin of the Ontong Java Plateau. *Proc. ODP Sci. Res.* **130**, 3-22.

Mann, P., Schubert., C. & Burke, K., 1990. Review of Caribbean neotectonics. *In*: Dengo, G. & Case, J. E., (eds.), *The Caribbean region*: The Geology of North America, **vol. H**. Geol. Soc. Am., Boulder, Colorado, pp. 307-338.

Maresch, W. V., 1974. Plate tectonic origin of the Caribbean Mountain System of northern South America: Discussion and proposal. *Geol. Soc. Am. Bull.* **85**, 669-682.

Marsh, B. D., Gunnarsson, B., Congdon, R. & Carmody, R., 1991. Hawaiian basalt and Icelandic rhyolite: indicators of differentiation and partial melting. *Geol. Rund.* **80**, 481-510.

Martin, H., 1987. Petrogenesis of Archean trondhjemites, tonalites, and granodiorites from Eastern Finland: major and trace element geochemistry. *J. Petrol.* **28**, 921-953.

Martin, K., 1888. Bericht uber eine Reise nach Niederlandisch West Indien und darauf gegrundete Studien. *Geologie* **2**, 237pp.

Mauffret, A. & Leroy, S., 1997. Seismic stratigraphy and structure of the Caribbean igneous province. *Tectonophys.* **283**, 61-104.

McBirney, A. R. & Noyes, R. M., 1979. Crystallization and layering of the Skaergaard intrusion. *J. Petrol.* **20**, 487-554.

McCann, W. R. & Pennington, W. D., 1990. Seismicity, large earthquakes, and the margin of the Caribbean Plate. *In*: Dengo, G. & Case, J. E., (eds.), *The Caribbean region*: The Geology of North America, **vol. H**. Geol. Soc. Am., Boulder, Colorado, pp. 291-306.

McCulloch, M. T. & Bennett, V. C., 1994. Progressive growth of the Earth's continental crust and depleted mantle - geochemical constraints. *Geochim. Cosmochim. Acta* **58**, 4717-4738.

McDonough, W. F. & Sun, S.-s., 1995. The composition of the Earth. *Chem. Geol.* **120**, 223-253.

McDougall, I. & Harrison, T. M., 1988. *Geochronology and Thermochronology by the $^{40}Ar/^{39}Ar$ Method.* Oxford University Press. 212 pp.

McKenzie, D. & Bickle, M. J., 1988. The volume and composition of melt generated by extension of the lithosphere. *J. Petrol.* **29**, 625-679.

McKenzie, D. & O'Nions, R. K., 1991. Partial Melt Distributions from Inversion of Rare Earth Element Concentrations. *J. Petrol.* **32**, 1021-1091.

McKenzie, D. P., 1989. Some remarks on the movement of small melt fractions in the mantle. *Earth Planet. Sci. Lett.* **95**, 53-72.

McLennan, S. M. & Taylor, S. R., 1982. Geochemical constraints on the growth of the continental crust. *J. Geol.* **90**, 347-361.

Merrihue, C. M. & Turner, G., 1966. Potassium-argon dating by activation with fast neutrons. *J. Geophys. Res.* **71**, 2852-2857.

Middlemost, E. A. K., 1975. The Basalt clan. *Earth Sci. Rev.* **11**, 51-57.

Middlemost, E. A. K., 1989. Iron oxidation ratios, norms and the classification of volcanic rocks. *Chem. Geol.* **77**, 19-26.

Miller, R. G., O'Nions, R. K., Hamilton, P. J. & Welin, E., 1986. Crustal residence ages of clastic sediments, orogeny and continental evolution. *Chem. Geol.* **57**, 87-99.

Millward, D., Marriner, G. F. & Saunders, A. D., 1984. Cretaceous tholeiitic volcanic rocks from the Western Cordillera of Colombia. *J. Geol. Soc. London* **141**, 847-860.

Mitchell, R. H., 1986. *Kimberlites: mineralogy, geochemistry and petrology.* Plenum Press, New York. 442 pp.

Miyashiro, A., 1974. Volcanic rock series in island-arcs and active continental margins. *Amer. Jour. Sci.* **274**, 321-355.

Monen, H. P., 1977. Geological map of the Aruba Lava Formation. *Unpubl. M.Sc. Thesis.*

Morimoto, N., Fabries, J., Ferguson, A. K., Ginzburg, I. V., Ross, M., Seifert, F. A., Zussman, J., Aoki, K. & Gottardi, G., 1988. Nomenclature of pyroxenes (IMA Subcommittee on pyroxenes). *Min. Mag.* **52**, 535-550.

Morrison, M. A., 1979. Igneous and metamorphic geochemistry of Mull lavas. *Unpubl. Ph.D. Thesis,* Univ. London.

Mysen, B. O., 1979. Trace-element partitioning between garnet peridotite minerals and water-rich vapour: experimental data from 5 to 30 kbar. *Amer. Mineral.* **64**, 274-287.

Mysen, B. O. & Kushiro, I., and Nicholls, I. A. & Ringwood, A. E., 1974. A possible mantle origin for andesitic magmas: discussion of a paper by Nicholls and Ringwood. *Earth Planet. Sci. Lett.* **21**, 221-229.

Nakamura, Y. & Kushiro, I., 1974. Composition of the gas phase in Mg_2SiO_4-SiO_2-H_2O at 15 kbar. *Carnegie Inst. Wash., Yearbk.* **73**, 255-258.

Nelson, B. K. & DePaolo, D. J., 1985. Rapid production of continental crust 1.7-1.9 b.y. ago: Nd isotopic evidence from the basement of the North American mid-continent. *Geol. Soc. Am. Bull.* **96**, 746-754.

Nicholls, I. A. & Ringwood, A. E., 1973. Effect of olivine stability in tholeiites and the production of silica undersaturated magmas in the island arc environment. *J.Geol.* **81**, 285-300.

Nielsen, R. L., 1988. A model of the simulation of combined major and trace element liquid lines of descent. *Geochim. Cosmochim. Acta* **52**, 27-38.

Nivia, A., 1996. The Bolivar mafic-ultramafic complex, SW Colombia: the base of an obducted plateau. *J. South Am. Earth Sci.* **9**, 59-68.

Nur, A. & Ben-Avraham, Z., 1982. Oceanic plateaus, the fragmentation of continents, and mountain building. *J. Geophys. Res.* **87**, 3644-3661.

Nutman, A. P., Friend, C. R. L., Kinny, P. D. & McGregor, V. R., 1993. Anatomy of an Early Archean gneiss complex: 3900 to 3600 Ma crustal evolution in southern West Greenland. *Geology* **21**, 415-418.

O'Hara, M. J., 1968. The bearing of phase equilibria studies in synthetic and natural systems and the origin and evolution of basic and ultrabasic rocks. *Earth Planet. Sci. Lett.* **4**, 69-133.

O'Hara, M. J., 1977. Geochemical evolution during fractional crystallization of a periodically refilled magma chamber. *Nature* **266**, 503-507.

Olson, P., 1994. Mechanics of Flood Basalt Magmatism. *In*: Ryan, M. P., (ed.), *Magmatic Systems*. Academic Press, pp. 1-18.

O'Nions, R. K., 1992. The Continents. *In*: Brown, G. C., Hawkesworth, C. J. & Wilson, R. C. L., (eds.), *Understanding the Earth: a new synthesis*. Cambridge University Press, Cambridge, pp. 145-163.

O'Nions, R. K., Evensen, N. M. & Hamilton, P. J., 1979. Geochemical modeling of mantle differentiation and crustal growth. *J. Geophys. Res.* **84**, 6091-6101.

O'Nions, R. K., Evensen, N. M. & Hamilton, P. J., 1980. Differentiation and evolution of the mantle. *Phil. Trans. Roy. Soc. London* **297A**, 479-493.

O'Nions, R. K., Evensen, N. M., Hamilton, P. J. & Carter, S. R., 1978. Melting of the mantle past and present: isotope and trace element evidence. *Phil. Trans. Roy. Soc. London* **288A**, 547-559.

O'Nions, R. K. & Grönvold, K., 1973. Petrogenetic relationships of acid and basic rocks in Iceland: Sr-isotopes and rare-earth elements in late and postglacial volcanics. *Earth Planet. Sci. Lett.* **19**, 397-409.

O'Nions, R. K. & McKenzie, D. P., 1988. Melting and continent generation. *Earth Planet. Sci. Lett.* **90**, 449-456.

Osborn, E. F. & Tait, D. B., 1952. The system diopside-forsterite-anorthite. *Amer. J. Sci.* **40** (Bowen Volume), 413-433.

Óskarsson, N., Sigvaldason, G. E. & Steinthórsson, S., 1982. A dynamic model of rift zone petrogenesis and the regional petrology of Iceland. *J. Petrol.* **23**, 28-74.

Palmason, G., 1986. Model of crustal formation in Iceland and application to submarine mid-ocean ridges. *In*: Vogt, P. R. & Tulcholke, B. E., (eds.), *The Western N. Atlantic Region*: The Geology of North America, **vol. M**. Geol. Soc. Am., Boulder, Colorado, pp. 87-97.

Parsons, B. & McKenzie, D. P., 1978. Mantle convection and the thermal structure of the plates. *J. Geophys. Res.* **83**, 4485-4496.

Patchett, P. J. & Arndt, N. T., 1986. Nd isotopes and tectonics of 1.9-1.7 Ga crustal genesis. *Earth Planet. Sci. Lett.* **78**, 329-338.

Peacock, M. A., 1931. Classification of igneous rock series. *J. Geol.* **39**, 54-67.

Peacock, S. M., 1991. Numerical-Simulation of Subduction Zone Pressure Temperature Time Paths - Constraints On Fluid Production and Arc Magmatism. *Phil. Trans. Roy. Soc. London* **335A**, 341-353.

Peacock, S. M., 1993. The Importance of Blueschist - Eclogite Dehydration Reactions in Subducting Oceanic-Crust. *Geol. Soc. Am. Bull.* **105**, 684-694.

Peacock, S. M., Rushmer, T. & Thompson, A. B., 1994. Partial Melting of Subducting Oceanic-Crust. *Earth Planet. Sci. Lett.* **121**, 227-244.

Pearce, J. A., 1982. Trace element characteristics of lavas from destructive plate boundaries. *In*: Thorpe, R. S., (ed.), *Andesites: orogenic andesites and related rocks*. Wiley, Chichester, pp. 525-548.

Pearce, J. A. & Norry, M. J., 1979. Petrogenetic implications of Ti, Zr, Y and Nb variations in volcanic rocks. *Contrib. Mineral. Petrol.* **69**, 33-47.

Pearce, J. A. & Parkinson, I. J., 1993. Trace element models for mantle melting; application to volcanic arc petrogenesis. *In*: Prichard, H. M., Alabaster, T., Harris, N. B. W. & Neary, C. R., (eds.), *Magmatic processes and plate tectonics*: *Geol. Soc. London Spec. Publ.* **76**, 373-403.

Pearce, T. H., 1968. A contribution to the theory of variation diagrams. *Contrib. Mineral. Petrol.* **19**, 142-157.

Perfit, M. R., Gust, D. A., Bence, A. E., Arculus, R. J. & Taylor, S. R., 1980. Chemical characteristics of island-arc basalts: implications for mantle sources. *Chem. Geol.* **30**, 227-256.

Petterson, M. G., Babbs, T. L., Neal, C. R., Mahoney, J. J., Saunders, A. D., Duncan, R. A., Tolia, D., Magu, R., Qopoto, C., Mahoa, H. & Natogga, D., 1999. Geological-tectonic framework of Solomon Islands, SW Pacific: crustal accretion and growth within an intra-oceanic setting. *Tectonophys.* **201**, 35-60.

Pindell, J. L., 1993. Regional synopsis of Gulf of Mexico and Caribbean evolution. *In*: Pindell, J. L. & Perkins, B. F., (eds.), *Mesozoic and early Cenozoic development of the Gulf of Mexico and Caribbean region: A context for hydrocarbon exploration*. Gulf Coast Section of Society for Economic Palaeontologists and Mineralogists Foundation 13th Annual Research Conference: Houston, Texas, SEPM foundation, pp. 251-274.

Pindell, J. L. & Barrett, S. F., 1990. Geologic evolution of the Caribbean region: a plate tectonic perspective. *In*: Dengo, G. & Case, J. E., (eds.), *The Caribbean region*: The Geology of North America, **vol. H**. Geol. Soc. Am., Boulder, Colorado, pp. 405-432.

Pindell, J. L., Cande, S. C., Pitman, W. C., Rowley, D. B., Dewey, J. F., Labrecque, J. & Haxby, W., 1988. A plate-kinematic framework for models of Caribbean evolution. *Tectonophys.* **155**, 121-138.

Polet, J. & Anderson, D. L., 1995. Depth extent of cratons as inferred from tomographic studies. *Geology* **23**, 205-208.

Potts, P. J., 1986. *A Handbook of Silicate Analysis: Chapter 12*. Blackie. Glasgow & London.

Priem, H. N. A., Andriessen, P. A. M., Beets, D. J., Boelrijk, N. A. I. M., Hebeda, E. A., Verdurmen, E. A. T. & Verschure, R. H., 1979. K-Ar and Rb-Sr dating in the Cretaceous island-arc succession of Bonaire, Netherlands Antilles. *Geol. Mijn.* **58**, 367-373.

Priem, H. N. A., Beets, D. J., Boelrijk, N. A. I. M. & Hebeda, E. H., 1986a. On the age of the late Cretaceous tonalitic/gabbroic batholith on Aruba, Netherlands Antilles (southern Caribbean borderland). *Geol. Mijn.* **65**, 247-265.

Priem, H. N. A., Beets, D. J., Boelrijk, N. A. I. M., Hebeda, E. H., Verdurmen, E. A. T. & Verschure, R. H., 1977. Isotopic dating of the quartz diorite batholith on Aruba, Netherlands Antilles - a progress report. *Abs. 8th Carib. Geol. Conf. (Curaçao)*, 149-150.

Priem, H. N. A., Beets, D. J., Boelrijk, N. A. I. M., Hebeda, E. H., Verdurmen, E. A. T. & Verschure, R. H., 1978. Rb-Sr evidence for episodic intrusion of the late Cretaceous tonalitic batholith of Aruba, Netherlands Antilles. *Geol. Mijn.* **57**, 293-296.

Priem, H. N. A., Beets, D. J. & Verdurmen, E. A. T., 1986b. Precambrian rocks in an Early Tertiary conglomerate on Bonaire, Netherlands Antilles (southern Caribbean borderland): evidence for a 300 km eastward displacement relative to the South American mainland? *Geol. Mijn.* **65**, 35-40.

Priem, H. N. A., Boelrijk, N. A. I. M., Verschure, R. H., Hebeda, E. H. & Lagaay, R. A., 1966. Isotopic age of the quartz diorite batholith on the island of Aruba, Netherlands Antilles. *Geol. Mijn.* **45**, 188-190.

Pringle, M. S., 1992. Radiometric ages of basaltic basement recovered at sites 800, 801 and 802, ODP Leg 129, Western Pacific Ocean. *Proc. ODP Sci. Res.* **129**, 389-404.

Pringle, M. S., 1993. Age progressive volcanism in the Musicians seamounts: a test of the hot spot hypothesis for the late Cretaceous Pacific. *In*: Pringle, M. S., Sager, W. W., Sliter, W. V. & Stein, S., (eds.), *The Mesozoic Pacific: Geology, Tectonics and Volcanism*: *Geophys. Mon.*, **77**. Am. Geophys. Un., pp. 187-215.

Rapp, R. P., 1995. Amphibole-out phase boundary in partially melted metabasalt, its control over liquid fraction and composition, and source permeability. *J. Geophys. Res.* **100**, 15601-15610.

Rapp, R. P. & Watson, E. B., 1995. Dehydration melting of metabasalt at 8-32 kbar - implications for continental growth and crust-mantle recycling. *J. Petrol.* **36**, 891-931.

Rapp, R. P., Watson, E. B. & Miller, C. F., 1991. Partial melting of amphibolite/eclogite and the origins of Archaean trondhjemites and tonalites. *Precambrian Res.* **51**, 1-25.

Ratcliff, J. T., Bercovici, D., Schubert, G. & Kroenke, L. W., 1998. Mantle plume heads and the initiation of plate tectonic reorganizations. *Earth Planet. Sci. Lett.* **156**, 195-207.

Read, H. H., 1948. Granites and granites. *Geol. Soc. Am. Mem.* **28**.

Renne, P. R., Deino, A. L., Walter, R. C., Turrin, B. D., Swisher, C. C., III, Becker, T. A., Curtis, G. H., Sharp, W. D. & Jaouni, A.-R., 1994. Intercalibration of astronomical and radioisotopic time. *Geology* **22**, 783-786.

Renne, P. R., Swisher, C. C., Deino, A. L., Karner, D. B., Owens, T. L. & DePaolo, D. J., 1998. Intercalibration of standards, absolute ages and uncertainties in $^{40}Ar/^{39}Ar$ dating. *Chem. Geol.* **145**, 117-152.

Reymer, A. & Schubert, G., 1984. Phanerozoic addition rates to the continental crust and crustal growth. *Tectonics* **3**, 63-77.

Reymer, A. & Schubert, G., 1986. Rapid growth of some segments of continental crust. *Geology* **14**, 299-302.

Rickwood, P. C., 1989. Boundary lines within petrologic diagrams which use oxides of major and minor elements. *Lithos* **22**, 247-263.

Ringwood, A. E., 1985. Mantle dynamics and basalt petrogenesis. *Tectonophys.* **112**, 17-34.

Roeder, P. L. & Emslie, R. F., 1970. Olivine-liquid equilibrium. *Contrib. Mineral. Petrol.* **29**, 275-282.

Rogers, G. & Saunders, A. D., 1989. Magnesian andesites from Mexico, Chile and the Aleutian Islands: implications for magmatism associated with ridge-trench collision. *In*: Crawford, A. J., (ed.), *Boninites and related rocks*. Unwin Hyman, London, pp. 416-445.

Rogers, G., Saunders, A. D., Terrell, D. J., Verma, S. P. & Marriner, G. F., 1985. Geochemistry of Holocene Volcanic-Rocks Associated With Ridge Subduction in Baja-California, Mexico. *Nature* **315**, 389-392.

Rollinson, H., 1997. Eclogite xenoliths in west African kimberlites as residues from Archaean granitoid crust formation. *Nature* **389**, 173-176.

Rollinson, H. R., 1993. *Using Geochemical Data: Evaluation, Presentation, Interpretation.* Longman. 352 pp.

Rollinson, H. R. & Fowler, M. B., 1987. The magmatic evolution of the Scourian complex at Gruinard Bay. *In*: Park, R. G. & Tarney, J., (eds.), *Evolution of the Lewisian and Comparable High Grade Terrains*: *Geol. Soc. London Spec. Publ.* **27**, 57-71.

Rollinson, H. R. & Roberts, C. R., 1986. Ratio correlations and major element mobility in altered basalts and komatiites. *Contrib. Mineral. Petrol.* **93**, 89-97.

Royse, K. R., Kempton, P. D. & Darbyshire, P. D. F., 1998. Procedure for the analysis for Rubidium-Strontium and Samarium-Neodymium Isotopes at the NERC Isotope Geosciences Laboratory. *NIGL Report Series* **121**. 28 pp.

Rudnick, R. L., 1995. Making continental crust. *Nature* **378**, 571-578.

Rudnick, R. L. & Fountain, D. M., 1995. Nature and composition of the continental crust: A lower crustal perspective. *Revs. Gephys. Space Phys.* **33**, 267-309.

Rudnick, R. L. & Goldstein, S. L., 1990. The Pb isotopic composition of lower crustal xenoliths and the evolution of lower crustal Pb. *Earth Planet. Sci. Lett.* **98**, 192-207.

Rudnick, R. L. & Taylor, S. R., 1987. The composition and petrogenesis of the lower crust: a xenolith study. *J. Geophys. Res.* **92**, 13981-14005.

Rushmer, T., 1995. An experimental deformation study of partially molten amphibolite: Application to low-melt fraction segregation. *J. Geophys. Res.* **100**, 15681-15695.

Sajona, F. Z., Maury, R. C., Bellon, H., Cotten, J., Defant, M. J. & Pubellier, M., 1993. Initiation of subduction and the generation of slab melts in western and eastern Mindanao, Philippines. *Geology* **21**, 1007-1010.

Santamaría, F. & Schubert, C., 1974. Geochemistry and geochronology of the Southern Caribbean-North Venezuela plate boundary. *Geol. Soc. Am. Bull.* **85**, 1085-1098.

Saunders, A. D., 1985. Geochemistry of basalts from the Nauru Basin, Deep Sea Drilling Project Legs 61 and 89: implications for the origin of oceanic flood basalts. *In*: Moberly, R., Schlanger, S. O. & al., e., (eds.), *Init. Rep. DSDP* **89**, 499-517.

Saunders, A. D., Norry, M. J. & Tarney, J., 1988. Origin of MORB and chemically-depleted mantle reservoirs: trace element constraints. *In*: Menzies, M. A. & Cox, K. G., (eds.), *Oceanic and Continental Lithosphere: Similarities and Differences: J. Petrol. Special Lithosphere Issue*, 415-445.

Saunders, A. D., Norry, M. J. & Tarney, J., 1991. Fluid influence on the trace element compositions of subduction zone magmas. *Phil. Trans. Roy. Soc. London* **A335**, 377-392.

Saunders, A. D., Storey, M., Kent, R. W. & Norry, M. J., 1992. Consequences of plume-lithosphere interactions. *In*: Storey, B. C., Alabaster, T. & Pankhurst, R. J., (eds.), *Magmatism and the causes of continental breakup*. Geological Society of London, pp. 41-60.

Saunders, A. D., Tarney, J., Kerr, A. C. & Kent, R. W., 1996. The formation and fate of large oceanic igneous provinces. *Lithos* **37**, 81-95.

Saunders, A. D., Tarney, J. & Weaver, S. D., 1980. Transvserse geochemical variations across the Antarctic Peninsula: implications for the genesis of calc-alkaline magmas. *Earth Planet. Sci. Lett.* **46**, 344-360.

Schiano, P., Dupré, B. & Lewin, E., 1993. Application of element concentration variability to the study of basalt alteration (Fangataufa Atoll, French Polynesia). *Chem. Geol.* **104**, 99-124.

Schubert, G. & Sandwell, D., 1989. Crustal volumes of the continents and of oceanic and continental submarine plateaus. *Earth Planet. Sci. Lett.* **92**, 234-246.

Seewald, J. S. & Seyfried, W. E., Jr., 1990. The effect of temperature on metal mobility in subseafloor hydrothermal systems; constraints from basalt alteration experiments. *Earth Planet. Sci. Lett.* **101**, 388-403.

Sen, C. & Dunn, T., 1994. Dehydration melting of a basaltic composition amphibolite at 1.5 and 2.0 Gpa - implications for the origin of adakites. *Contrib. Mineral. Petrol.* **117**, 394-409.

Shaw, D. M., Cramer, J. J., Higgins, M. D. & Truscott, M. G., 1986. Composition of the Canadian Precambrian shield and the continental crust of the Earth. *Geol. Soc. London Spec. Publ.* **24**, 275-282.

Shaw, D. M., Reilly, G. A., Muysson, J. R., Pattenden, G. E. & Campbell, F. E., 1967. An estimate of the chemical composition of the Canadian Precambrian Shield. *Can. J. Earth Sci.* **4**, 829-853.

Sheraton, J. W., Oliver, R. L. & Stuwe, K., 1989. Geochemistry of Proterozoic amphibolite dykes in Commonwealth Bay, Antarctica, and possible correlations wth mafic dyke swarms elsewhere in Gondwanaland. *Precambrian Res.* **44**, 353-361.

Sigurdsson, H., 1977. Generation of Icelandic rhyolites by melting of plagiogranites in the oceanic layer. *Nature* **269**, 25-28.

Silver, E. A., Case, J. E. & MacGillavry, H. J., 1975. Geophysical study of the Venezuelan Borderland. *Geol. Soc. Am. Bull.* **86**, 213-226.

Singer, B. S. & Pringle, M. S., 1996. Age and duration of the Matuyama-Brunhes geomagnetic polarity reversal from Ar-40/Ar-39 incremental heating analyses of lavas. *Earth Planet. Sci. Lett.* **139**, 47-61.

Sinton, C. W., Duncan, R. A. & Denyer, P., 1997. Nicoya Peninsula, Costa Rica: A single suite of Caribbean oceanic plateau magmas. *J. Geophys. Res.* **102**, 15507-15520.

Sinton, C. W., Duncan, R. A., Storey, M., Lewis, J. & Estrada, J. J., 1998. An oceanic flood basalt province within the Caribbean plate. *Earth Planet. Sci. Lett.* **155**, 221-235.

Smith, C. A., Sisson, V. B., Avé Lallement, H. G. & Copeland, P., submitted. Two contrasting P-T-t paths in the Villa de Cura blueschist velt, Venezuela: a record of ~97 Ma subduction in the Caribbean. *Geol. Soc. Am. Bull.*

Sparks, R. S. J., Meyer, P. & Sigurdsson, H., 1980. Density variations amongst mid-ocean ridge basalts: implications for magma mixing and the scarcity of primitive lavas. *Earth Planet. Sci. Lett.* **46**, 419-430.

Staudigel, H., Muehlenbachs, K., Richardson, S. H. & Hart, S. R., 1981. Agents of low temperature ocean crust alteration. *Contrib. Mineral. Petrol.* **77**, 150-157.

Stearns, C., Mauk, F. J. & Van der Voo, R., 1982. Late Cretaceous to early Tertiary palaeomagnetism of Aruba and Bonaire, Netherlands Antilles. *J. Geophys. Res.* **87**, 1127-1141.

Steiger, R. H. & Jäger, E., 1977. Subcommission on geochronology: convention on the use of decay constants in geo- and cosmochronology. *Earth Planet. Sci. Lett.* **36**, 359-362.

Stein, M. & Goldstein, S. L., 1996. From plume head to continental lithosphere in the Arabian-Nubian shield. *Nature* **382**, 773-778.

Stein, M. & Hofmann, A. W., 1994. Mantle plumes and episodic crustal growth. *Nature* **372**, 63-68.

Storey, M., Kent, R., Saunders, A. D., Salters, V. J., Hergt, J., Whitechurch, H., Sevigny, J. H., Thirlwall, M. F., Leat, P., Ghose, N. C. & Gifford, M., 1992. Lower Cretaceous volcanic rocks on continental margins and their relationship to the Kerguelen Plateau. *In*: Wise, S. W., Schlich, R. et al., (ed.), *Proc. ODP Sci. Res.* **120**, 33-53.

Streckeisen, A., 1976. To each plutonic rock its proper name. *Earth. Sci. Revs.* **12**, 1-33.

Sun, S.-s. & McDonough, W. F., 1989. Chemical and isotopic systematics of oceanic basalts: implications for mantle composition and processes. *In*: Saunders, A. D. & Norry, M. J., (eds.), *Magmatism in the ocean basins*: Geol. Soc. London Spec. Pub., **42**. Blackwell, Oxford, pp. 313-345.

Sun, S.-S. & Nesbitt, R. W., 1979. Geochemical characteristics of mid-ocean ridge basalts. *Earth Planet. Sci. Lett.* **44**, 119-138.

Sykes, L. R., McCann, W. R. & Kafka, A. L., 1982. Motion of the Caribbean plate during the last 7 million years and implications for earlier Cenozoic movements. *J. Geophys. Res.* **87**, 10656-10676.

Sylvester, P. J., Campbell, I. H. & Bowyer, D. A., 1997. Niobium/Uranium Evidence for Early Formation of the Continental Crust. *Science* **275**, 521-523.

Takahahshi, E., Nakajima, K. & Wright, T., 1998. Origin of the Columbia River basalts: melting model of a heterogeneous plume head. *Earth Planet. Sci. Lett.* **162**, 63-80.

Tarduno, J. A., Sliter, W. V., Kroenke, L., Leckie, M., Mayer, H., Mahoney, J. J., Musgrave, R., Storey, M. & Winterer, E. L., 1991. Rapid formation of the Ontong Java Plateau by Aptian mantle plume volcanism. *Science* **254**, 399-403.

Tarney, J., Dalziel, I. & de Wit, M., 1976. Marginal basin "Rocas Verdes" complex from S. Chile: a model for Archaean greenstone belt formation. *In*: Windley, B. F., (ed.), *The Early History of the Earth*. Wiley, pp. 131-146.

Tarney, J. & Windley, B. F., 1977. Chemistry, thermal gradients and evolution of the lower continental crust. *J. Geol. Soc. London* **134**, 153-172.

Tatsumi, Y., Hamilton, D. L. & Nesbitt, R. W., 1986. Chemical characteristics of fluid phase released from a subducted lithosphere and origin of arc magmas: evidence from high pressure experiments and natural rocks. *J. Volc. Geoth. Res.* **29**, 293-309.

Taylor, J. R., 1982. *An Introduction to Error Analysis*. University Science Books. Mill Valley, CA. 270 pp.

Taylor, S. R., 1967. The origin and growth of continents. *Tectonophys.* **4**, 17-34.

Taylor, S. R., 1977. Island arc models and the composition of the continental crust. *AGU Ewing Series* **I**, 325-335.

Taylor, S. R. & McLennan, S. M., 1985. *The Continental Crust: Its Composition and Evolution*. Blackwell. Oxford. 312 pp.

Taylor, S. R. & McLennan, S. M., 1995. The geochemical evolution of the continental crust. *Rev. Geophys.* **33**, 241-265.

Tejada, M. L. G., Mahoney, J. J., Duncan, R. A. & Hawkins, M. P., 1996. Age and geochemistry of basement and alkali rocks of Malaita and Santa Isabel, Solomon Islands, southern margin of Ontong Java Plateau. *J. Petrol.* **37**, 361-394.

Thompson, R. N., 1972. The one-atmosphere melting patterns of some basaltic volcanic series. *Amer. J. Sci.* **272**, 901-932.

Thompson, R. N., 1973. One-atmosphere melting behaviour and nomenclature of basaltic lavas. *Contrib. Mineral. Petrol.* **41**, 197-204.

Thompson, R. N., 1974. Primary basalts and magma genesis. *Contrib. Mineral. Petrol.* **45**, 317-341.

Thy, P., 1991. High and low pressure phase equilibria of a mildly alkali lava from the 1965 Surtsey eruption: Experimental results. *Lithos* **26**, 223-243.

Thy, P., Beard, J. S. & Lofgren, G. E., 1990. Experimental constraints on the origin of Icelandic rhyolites. *J. Geol.* **98**, 417-421.

Todt, W., Cliff, R. A., Hanser, A. & Hofmann, A. W., 1993. Re-calibration of NBS lead standards using a $^{202}Pb + ^{205}Pb$ double spike. *Terra abstracts* **5**, 396.

Turner, G. & Cadogan, P. H., 1974. Possible effects of ^{39}Ar recoil in ^{40}Ar-^{39}Ar dating. *Proceedings of the Fifth Lunar Science Conference* **2**, 1601-1615.

Ulmer, P., 1989. Partitioning of high-field strength elements among olivine, pyroxene, garnet and calc-alkaline picrobasalt: experimental results and application. *Carnegie Inst. Wash. Yearbook, 1988-1989*, 42-47.

Veizer, J. & Jansen, S. L., 1979. Basement and sedimentary recycling and continental evolution. *J. Geol.* **87**, 341-370.

Veizer, J. & Jansen, S. L., 1985. Basement and sedimentary recycling - 2: time dimension to global tectonics. *J. Geol.* **93**, 625-643.

Wager, L. R. & Brown, G. M., 1968. *Layered Igneous Rocks*. Oliver and Boyd (1st edition). 588 pp.

Walker, D. A. & McDougall, I., 1982. $^{40}Ar/^{39}Ar$ and K-Ar dating of altered glassy volcanic rocks: the Dabi volcanics, P. N. G. *Geochim. Cosmochim. Acta* **46**, 2181-2190.

Walker, G. P. L., 1966. Acid rock in Iceland. *Bull. Volc.* **29**, 375-402.

Walker, R. J., Storey, M., Kerr, A. C., Tarney, J. & Arndt, N. T., in press. Implications of ^{187}Os isotopic heterogeneities in a mantle plume: evidence from Gorgona Island and Curaçao. *Geochim. Cosmochim. Acta* **unknown**, unknown.

Weaver, B. L. & Tarney, J., 1981. Chemical changes during dyke metamorphism in high-grade basement terrains. *Nature* **289**, 47-49.

Weaver, B. L. & Tarney, J., 1981. Geochemistry of Archean Crustal Components. *Geophys. J. Roy. Ast. Soc.* **65**, 246.

Weaver, B. L. & Tarney, J., 1984. Empirical approach to estimating the composition of the continental crust. *Nature* **310**, 575-577.

Weber, M. B. I., 1998. The Mercaderes-Río Mayo xenoliths, Colombia: Their bearing on mantle and crustal processes in the Northern Andes. *Unpubl. Ph.D. Thesis,* Univ. Leicester.

Westermann, J. H., 1932. The geology of Aruba. *Ph.D. Thesis: Geographische en Geologische Mededeelingen, Physiographisch-Geologische Reeks* **7**. University of Utrecht, 129 pp.

White, R. S. & McKenzie, D. P., 1989. Magmatism at rift zones: the generation of volcanic continental margins and flood basalts. *J. Geophys. Res.* **94**, 7685-7729.

White, R. S., Spence, G. D., Fowler, S. R., McKenzie, D. P., Westbrook, G. K. & Bowen, A. N., 1987. Magmatism at rifted continental margins. *Nature* **330**, 439-444.

White, R. V., Tarney, J., Kerr, A. C., Saunders, A. D., Kempton, P. D., Pringle, M. S. & Klaver, G. T., 1999. Modification of an oceanic plateau, Aruba, Dutch Caribbean: Implications for the generation of continental crust. *Lithos* **46**, 43-68.

White, W. M., Dupré, B. & Vidal, P., 1985. Isotope and trace element geochemistry of sediments from the Barbados Ridge-Demerara Plain region, Atlantic Ocean. *Geochim. Cosmochim. Acta* **49**, 1875-1886.

White, W. M. & Hofmann, A. W., 1982. Sr and Nd isotope geochemistry of oceanic basalts and mantle evolution. *Nature* **296**, 821-825.

Williams, H., Turner, F. J. & Gilbert, C. M., 1954. *Petrography; an introduction to the study of rocks in thin sections*. Freeman and Co. San Francisco. 406 pp.

Wilson, J. T., 1966. Are the structures of the Caribbean and Scotia Arc regions analogous to ice rafting? *Earth Planet. Sci. Lett.* **1**, 335-338.

Windley, B. F., 1995. *The Evolving Continents*. Wiley (3rd edition). 526 pp.

Winther, K. T., 1996. An experimentally based model for the origin of tonalitic and trondhjemitic melts. *Chem. Geol.* **127**, 43-59.

Winther, K. T. & Newton, R. C., 1991. Experimental melting of hydrous low-K tholeiite: evidence on the origin of Archean cratons. *Bull. Geol. Soc. Den.* **39**, 213-228.

Wolf, M. B. & Wyllie, P. J., 1994. Dehydration-melting of amphibolite at 10 kbar: the effects of temperature and time. *Contrib. Mineral. Petrol.* **115**, 369-383.

Wolfe, C. J., Bjarnason, I. T., VanDecar, J. C. & Solomon, S. C., 1997. Seismic structure of the Iceland mantle plume. *Nature* **385**, 285-247.

Wood, D. A., Gibson, I. L. & Thompson, R. N., 1976. Elemental mobility during the zeolite facies metamorphism of the Tertiary Basalts of Eastern Iceland. *Contrib. Mineral. Petrol.* **55**, 241-254.

Woodhead, J. D., Eggins, S. E. & Gamble, J. G., 1993. High field strength and transition element systematics in island arc and back-arc basin basalts: evidence for multi-phase extraction and a depleted mantle wedge. *Earth Planet. Sci. Lett.* **114**, 491-504.

Yoder, H. S., Jr., Stewart, D. B. & Smith, J. R., 1957. Ab-Or-An-H_2O at 5000 bars. *Geol. Soc. Am. Bull.* **68**, 1815-1816.

York, D., 1969. Least squares fitting of a straight line with correlated errors. *Earth Planet. Sci. Lett.* **5**, 320-324.

Zhao, L. S., Helmberger, D. V. & Harkrider, D. G., 1991. Shear velocity structure of the crust and upper mantle beneath the Tibetan Plateau and South-eastern China. *Geophys. J. Int.* **105**, 713-730.

This copy belongs to the Ph.D. thesis of Rosalind White, 1999.

Reprinted from

LITHOS

Lithos 46 (1999) 43–68

Modification of an oceanic plateau, Aruba, Dutch Caribbean: Implications for the generation of continental crust

R.V. White [a,*], J. Tarney [a], A.C. Kerr [a], A.D. Saunders [a], P.D. Kempton [b], M.S. Pringle [c], G.T. Klaver [d]

[a] *Department of Geology, University of Leicester, Leicester, LE1 7RH, UK*
[b] *NERC Isotope Geoscience Laboratory, Keyworth, Nottingham, NG12 5GG, UK*
[c] *SURRC, Scottish Enterprise Technology Park, Rankine Av., East Kilbride, G75 0QF, UK*
[d] *Rijks Geologische Dienst, Postbus 157, 2000 AD Haarlem, Netherlands*

ELSEVIER

LITHOS

An International Journal of Mineralogy, Petrology and Geochemistry

ELSEVIER

Editor-in-Chief
S. Foley
Universität Göttingen, Mineralogisch-Petrologisches Inst., Goldschmidtstr. 1, D-37077 Göttingen, Germany

Editorial Board
T. Andersen (Oslo)
H. Austrheim (Oslo)
K. Bell (Ottawa, Ont.)
D.A. Carswell (Sheffield)
S. Claesson (Stockholm)
H. Downes (London)
J.-C. Duchesne (Liège)
G.L. Farmer (Boulder, CO)
S.J.G. Galer (Mainz)
R. Gorbatchev (Lund)
T.H. Green (North Ryde, N.S.W.)
W.L. Griffin (North Ryde, N.S.W.)
W.M. Lamb (College Station, TX)
L.M. Larsen (Copenhagen)
J.P. Lorand (Paris)
R.H. Mitchell (Thunder Bay, Ont.)
J.-M. Montel (Clermont-Ferrand)
A. Mottana (Rome)
P. O'Brien (Bayreuth)
S.Y. O'Reilly (North Ryde, N.S.W.)
O.T. Rämö (Helsinki)
M. Roden (Athens, GA)
Z.D. Sharp (Lausanne)
J. Touret (Amsterdam)
R. Vannucci (Pavia, Italy)
M.J. Whitehouse (Stockholm)
J.R. Wilson (Aarhus)

Scope of the Journal
Lithos accepts articles of international interest in the field of mineralogy, petrology and geochemistry. A paper submitted for consideration should be concise, original material, not previously published in any major language. Types of contributions to be published are: (1) scholastic papers, (2) reviews, (3) discussions, and (4) book reviews.

Publication Information
Lithos (ISSN 0024-4937). For 1998 volumes 43–45 are scheduled for publication. Subscription prices are available upon request from the publisher. Subscriptions are accepted on a prepaid basis only and are entered on a calendar year basis. Issues are sent by surface mail except to the following countries where air delivery via SAL is ensured: Argentina, Australia, Brazil, Canada, Hong Kong, India, Israel, Japan, Malaysia, Mexico, New Zealand, Pakistan, PR China, Singapore, South Africa, South Korea, Taiwan, Thailand, USA. For all other countries airmail rates are available upon request. Claims for missing issues must be made within six months of our publication (mailing) date. Please address all your requests regarding orders and subscription queries to: Elsevier Science, Customer Support Department, P.O. Box 211, 1000 AE Amsterdam, The Netherlands. Fax: 31-20-4853432.

Advertising information
Advertising orders and enquiries may be sent to: Elsevier Science, Advertising Department, The Boulevard, Langford Lane, Kidlington, Oxford, OX5 1GB, UK, tel.: (+44) (0) 1865 843565, fax: (+44) (0) 1865 843976. *In the USA and Canada*: Weston Media Associates, attn. Dan Lipner, P.O. Box 1110, Greens Farms, CT 06436-1110, USA, tel: (203) 261 2500, fax: (203) 261 0101. *In Japan:* Elsevier Science Japan, Marketing Services, 1-9-15 Higashi Azabu, Minato-ku, Tokyo 106; Tel. +81 5 5561 5033; Fax +81 5 5561 5047.

Publication of abstracts and contents
Abstracts or contents of this Journal are published in AGI's Bibliography and Index of Geology, Bulletin Signalétique, Chemical Abstracts, Current Contents, Geo Abstracts, and Mineralogical Abstracts.

Copyright © 1998 Elsevier Science B.V. All rights reserved.

0024-4937/98/$19.00

This journal and the individual contributions contained in it are protected by the copyright of Elsevier Science B.V., and the following terms and conditions apply to their use:

Photocopying
Single photocopies of single articles may be made for personal use as allowed by national copyright laws. Permission of the Publisher and payment of a fee is required for all other photocopying, including multiple or systematic copying, copying for advertising or promotional purposes, resale, and all forms of document delivery. Special rates are available for educational institutions that wish to make photocopies for non-profit educational classroom use.
In the USA, users may clear permissions and make payment through the Copyright Clearance Center Inc., 222 Rosewood Drive, Danvers, MA 01923, USA. In the UK, users may clear permissions and make payment through the Copyright Licensing Agency Rapid Clearance Service (CLARCS), 90 Tottenham Court Road, London W1P 0LP, UK. In other countries where a local copyright clearance centre exists, please contact it for information on required permissions and payments.

Derivative works
Subscribers may reproduce tables of contents or prepare lists of articles including abstracts for internal circulation within their institutions. Permission of the Publisher is required for resale or distribution outside the institution.
Permission of the Publisher is required for all other derivative works, including compilations and translations.

Electronic storage
Permission of the Publisher is required to store electronically any material contained in this journal, including any article or part of an article. Contact the Publisher at the address indicated.
Except as outlined above, no part of this publication may be reproduced, stored in a retrieval system or transmitted in any form or by any means, electronic, mechanical, photocopying, recording or otherwise, without prior written permission of the Publisher.

Notice
No responsibility is assumed by the Publisher for any injury and/or damage to persons or property as a matter of products liability, negligence or otherwise, or from any use or operation of any methods, products, instructions or ideas contained in the material herein.

♾ The paper used in this publication meets the requirements of ANSI/NISO Z39.48-1992 (Permanence of Paper).

PRINTED IN THE NETHERLANDS

Modific
In

R.V. W

Abstract

The generation
the processes invo
material and assoc
particularly in anci
island of Aruba in
tonalitic batholith
komatiitic rocks th
plume-related ocea
the Pacific region.
and Y) with Archa
plateau sequence,
batholith. New inci
the batholith occur
uniform ($^{87}Sr/^{86}S$
18.6–19.1, $^{207}Pb/$
$^{204}Pb = 15.51–15.$
source region of th
subduction-related
of the plateau seq
Elsevier Science B

Keywords: Tonalit

* Corresponding a

0024-4937/99/$ - s
PII: S0024-4937(

1. Introduction

The question of how continental crust was (and is) generated is of fundamental importance to geologists and planetary scientists. Several authors have proposed that the growth of the continental crust may be connected to the presence of mantle plumes and oceanic plateaux (e.g., Stein and Hofmann, 1994; Abbott and Mooney, 1995; Stein and Goldstein, 1996), although the nature of this link is not well-constrained and many questions remain unanswered. Growth of the continental crust can arise directly from a plume ascending beneath continental lithosphere, particularly if accompanied by rifting (e.g., White et al., 1987); additionally, plumes which rise beneath oceanic lithosphere can result in the formation of thick oceanic plateaux, which because of their buoyancy may resist subduction (Saunders et al., 1996), becoming accreted to the edges of continents. A major difficulty is unequivocally identifying examples of oceanic plateaux in the ancient geological record. Modern plateaux are recognised by their crustal thickness, composition, and sedimentary record (e.g., Coffin and Eldholm, 1994), but even when all these criteria are used to evaluate an environment of formation, the interpretation is rarely irrefutable. The disparity between the abundance of oceanic plateaux in the modern oceans and their relative paucity in the continental geological record suggests that, if the rate of production of plateaux has not been anomalously high in the last 150 m.y., either plateaux are eventually subducted, or they are processed and converted into material which is no longer easily recognisable as oceanic plateau crust (Stein and Goldstein, 1996; Saunders et al., 1996).

Several important comparisons can be made between the two generally accepted models of continental growth: volcanic arc accretion and oceanic plateau accretion. Firstly, oceanic plateaux represent enormous volumes of material (Schubert and Sandwell, 1989). The crust of the Ontong Java plateau (OJP), for example, occupies a volume of 44 to 56 million km^3 (Gladczenko et al., 1997), which could potentially be accreted to make continental lithosphere. The oceanic plateau model may therefore be able to explain periods of *rapid* continental growth better than the volcanic arc accretion model; additionally, as evidence mounts for episodic crustal growth (e.g., McCulloch and Bennett, 1994), it has been suggested that the sporadic nature of mantle plume activity and oceanic plateau magmatism is responsible for this episodicity (e.g., Condie, 1997). Secondly, neither oceanic plateau nor oceanic arc accretion can, on their own, explain the geochemical characteristics of the bulk continental crust, because both are too mafic in composition (Tarney and Windley, 1977). Differentiation and modification of primitive mantle-derived arcs or plateaux must therefore be an important process in creating the enrichment of silica and various incompatible trace elements observed in continental crust. We need to know how these enrichment processes operate, and on what timescale. Finally, it must be stressed that there are unambiguous examples of accretion of both oceanic plateaux (e.g., the Caribbean plateau in Colombia: Millward et al., 1984; Kerr et al., 1997a) and oceanic arcs (Soja, 1996) to pre-existing continents. Accordingly, our task should now be to constrain the means by which conversion of oceanic plateau or arc into continental crust occurs, by considering both modern and ancient examples.

Some fragments of oceanic plateau crust have been identified as accreted members of greenstone belts (e.g., Kusky and Kidd, 1992; Desrochers et al., 1993), although other greenstone belts are interpreted as accreted volcanic arc terranes (e.g., the Slave Province, Canada: Kusky, 1989; Davis and Hegner, 1992) or autochthonous eruptive sequences (Bickle et al., 1994). In spite of this dissent, however, it seems that studies of Phanerozoic oceanic plateaux and their subsequent histories may provide useful constraints on Archaean processes.

The island of Aruba, located in the complex southern plate boundary zone of the Caribbean region, may provide the answers to some of these controversies. Here, a predominantly tonalitic batholith dated as ~ 85–82 Ma intrudes a sequence of mafic lavas, volcaniclastic sediments and intrusive rocks belonging to the predominantly 88 to 91 Ma Caribbean–Colombian Cretaceous Igneous Province (CCCIP; Fig. 1) (Kerr et al., 1997b; Sinton et al., 1998). The association of mafic rocks that are thought to be plume-related members of the CCCIP and tonalites that share some characteristics with Archaean tonalites means that Aruba is an ideal place to study the relationships between initial material

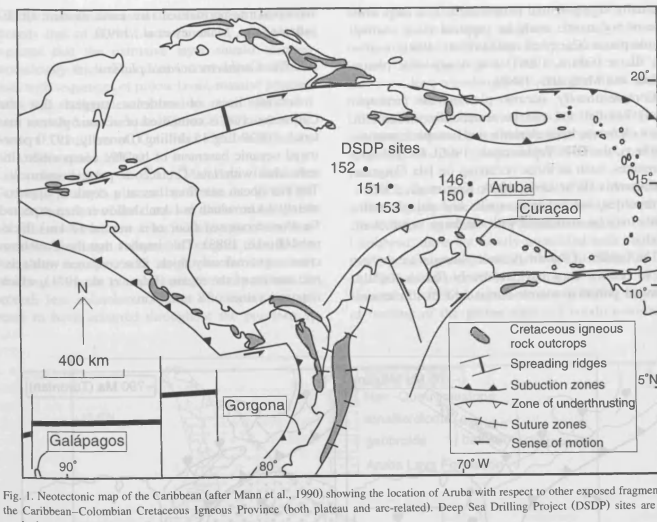

Fig. 1. Neotectonic map of the Caribbean (after Mann et al., 1990) showing the location of Aruba with respect to other exposed fragments of the Caribbean–Colombian Cretaceous Igneous Province (both plateau and arc-related). Deep Sea Drilling Project (DSDP) sites are also marked.

extracted from the mantle and the silicic material intimately associated with it in both space and time. The swift transmutation in magmatic environment observed on Aruba suggests that conversion of plateau material into continental crust may begin at a much earlier stage than has been previously suspected (e.g., Stein and Goldstein, 1996).

2. Characteristics of modern oceanic plateaux

The region covered by the Caribbean Sea is the site of an oceanic large igneous province (LIP) of late Cretaceous age (Donnelly et al., 1990). LIPs may be divided into two categories: continental flood basalts and oceanic plateaux. Continental flood basalt provinces clearly have a better preservation potential in the geological record, and will not be considered further here, but the fate of oceanic plateaux is much less certain.

The formation of oceanic plateaux can be extremely rapid, with enormous volumes of magma being extruded (and intruded) in timescales of the order of a few m.y. (e.g., Tarduno et al., 1991). The crust produced is considerably thicker than normal oceanic crust, with thicknesses of ≈ 32 km being proposed for the OJP (Gladczenko et al., 1997), although the majority of plateaux are 10–20 km thick (Coffin and Eldholm, 1993, 1994). The anomalously high rates of magma production associated with oceanic plateaux can best be explained by the presence of large volumes of mantle material with an

unusually high potential temperature. This large volume of hot mantle could be supplied via a starting mantle plume (Campbell and Griffiths, 1990), a solitary diapir (Olson, 1994) or a steady state plume (White and McKenzie, 1989).

Compositionally, oceanic plateaux are predominantly basaltic and can be remarkably uniform in major elements, trace elements and isotopic composition (e.g., the OJP: Tejada et al., 1996). Picrites and komatiites, such as those occurring on Isla Gorgona in Colombia (Echeverría, 1980; Kerr et al., 1996a), or rhyolites, volcaniclastic rocks and pelagic sediments may be associated with the large volumes of basalts.

The basalts of Pacific oceanic plateaux are tholeiitic in nature. They have relatively flat to slightly enriched primitive mantle-normalised multi-element and chondrite-normalised rare earth element (REE) patterns (e.g., Mahoney et al., 1993).

2.1. The Caribbean oceanic plateau

Several lines of evidence suggest that the Caribbean crust is composed of oceanic plateau material. DSDP Leg 15 drilling (Donnelly, 1973) penetrated oceanic basement of basaltic composition, interbedded with late Cretaceous pelagic sediments. The Caribbean sea floor lies at a depth of approximately 4 km, which is 1 km shallower than expected for Cretaceous sea floor of a normal (7 km) thickness (Burke, 1988). This implies that the Caribbean crust is anomalously thick, in accordance with seismic studies of the region (Edgar et al., 1971), which obtained values of 8 to 20 km.

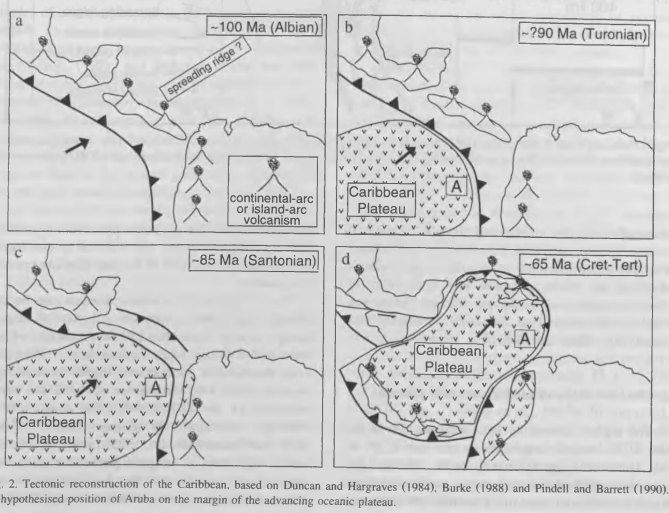

Fig. 2. Tectonic reconstruction of the Caribbean, based on Duncan and Hargraves (1984), Burke (1988) and Pindell and Barrett (1990). A: hypothesised position of Aruba on the margin of the advancing oceanic plateau.

If the total thickness of the crust in the Caribbean exceeds that of normal oceanic crust, it might be expected that the extrusive layer should also be anomalously thick. This does indeed seem to be the case, with sequences of pillow lavas, massive basaltic flows and shallow level intrusives more than 5 km thick recorded on Curaçao (Klaver, 1987) and in the Western Cordillera of Colombia (Millward et al., 1984; Kerr et al., 1997a).

A compilation of $^{40}Ar/^{39}Ar$ data from the Caribbean oceanic plateau by Sinton et al. (1998) reveals that most of the dates are clustered at 91–88 Ma. These dates come from widely spaced on-land sections. The large volumes of magma extruded in this short timespan add weight to the arguments invoking a mantle plume origin for the province. A second, less voluminous, phase of magmatism appears to have occurred throughout the province at about 78–72 Ma (Sinton et al., 1998; Kerr et al., 1997a). No convincing magnetic anomaly patterns indicating normal spreading oceanic crust are present in the Caribbean region (Fox and Heezen, 1975). However, long wavelength NE–SW and E–W linear magnetic anomalies over the Venezuelan and Colombian basins are interpreted by Hall (1995) as resulting from an Early Cretaceous phase of seafloor spreading at the Farallon–Pacific–Phoenix triple junction.

The composition of the rocks is also consistent with melting in a decompressing hot mantle plume to create large quantities of tholeiitic magma. In the Caribbean, these are locally associated with komatiites (e.g., Gorgona Island: Echeverría, 1980; Kerr et al., 1996a) and picrites (e.g., Curaçao: Klaver, 1987; Kerr et al., 1996b), which represent higher degrees of melting of the plume source. Chondrite-normal-

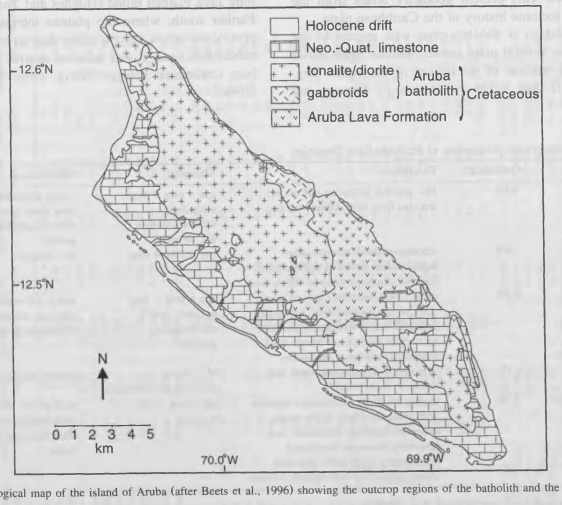

Fig. 3. Geological map of the island of Aruba (after Beets et al., 1996) showing the outcrop regions of the batholith and the Aruba Lava Formation.

ised REE patterns are variable, ranging from moderately LREE enriched through flat to moderately depleted (e.g., Kerr et al., 1996b).

2.2. Caribbean plate tectonics

Detailed studies of the Caribbean oceanic plateau have relied on the fact that portions of it have been uplifted at the margins of the Caribbean plate, and now crop out subaerially. Fig. 1 shows obducted fragments of Cretaceous igneous rocks (either parts of the plateau or arc material accreted with it) together with present plate boundaries. To the north and south the Caribbean plate is bounded by complex broad zones of strike–slip movement, along which the Caribbean is moving eastwards relative to North and South America at a rate of 2 to 4 cm/yr (Sykes et al., 1982). Subduction zones dipping beneath the plateau form the eastern and western boundaries. This present geometry arises from the complex tectonic history of the Caribbean plate.

The plateau is allochthonous with respect to the Americas. Several plate reconstructions agree about the major features of the history of the region (Fig. 2) even if they differ in detail (e.g., Duncan and Hargraves, 1984; Burke, 1988; Pindell and Barrett, 1990). The plateau formed in the eastern Pacific region, as part of the Farallon plate, although it is unknown whether it was extruded onto pre-existing oceanic crust, or formed at a spreading ridge (e.g., Iceland). Duncan and Hargraves (1984) suggest that the plateau was formed above the starting Galápagos mantle plume.

At this time, east- or north-eastward-directed subduction was occurring beneath the Proto-Caribbean region and continental North and South America, consuming the Farallon plate and carrying the newly formed Caribbean plateau towards the Americas. As the thick, possibly still hot, oceanic plateau approached these subduction zones, its buoyancy meant that it was reluctant to subduct (Burke et al., 1978). In the Caribbean region, a reversal in subduction polarity ensued, possibly analogous to that in the Solomon Islands where attempts to subduct the Ontong Java Plateau failed (Hughes and Turner, 1977). Farther south, where the plateau interacted with a continental active margin rather than an intra-oceanic subduction zone, it was accreted against the Colombian continental margin (Nivia, 1996; Kerr et al., 1996c).

Table 1
Field and petrographic observations of the Aruba Lava Formation

Lithology	Abundance[a]	Description	Mineralogy	Deformation
Basalt	41%	fine-grained, aphanitic; pillows or massive flow units; often vesicular	cpx + plag + mag; secondary minerals include hbl, ep, chl	rarely deformed except near shear zones, where slight foliation present
Dolerite	24%	medium-grained, homogeneous, equigranular; occurs as sill-like thick sheets in successions up to 400 m thick	cpx + plag + mag	not observed
Basaltic breccio-conglomerate	~ 2%	up to 15 cm diameter clasts of basalt, dolerite and volcaniclastic sandstone; restricted to one stratigraphic horizon up to 50 m thick; some interbedded graded volcaniclastic sandstones	cpx + plag + mag in clasts; matrix occasionally silicified	rarely deformed; cleavage sometimes developed in matrix
Chlorite schist	< 1%	very soft, pale green coloured; only occurs in shear zones	Mg-chlorite + magnesium-hornblende	always well-foliated
Volcaniclastic sediment	33%	mainly reworked sedimentary deposits with graded bedding, ripple marks, convolute bedding; chemically and texturally immature; occasional accretionary lapilli tuffs; silicified coarse ignimbrite with eutaxitic texture	qtz + plag + clay minerals	axial planar cleavage often well-developed; shear cleavage in shear zones

[a]Taken from geological map of Beets et al. (1996).

Table 2
Representative major element, trace element and isotopic data for the Aruba Lava Formation

Sample	ARU96-1	ARU96-2	ARU96-11	ARU96-21	ARU96-31	ARU96-30	ARU96-37	ARU96-112	ARU96-145	ARU96-147	ARU96-107	ARU96-108	ARU96-142	JB-2	BHVO-1
Rock type	basalt	basalt	basalt	basalt	basalt	dolerite	dolerite	tuff	amphibolite	amphibolite	chl-schist	chl-schist	schist	standard	standard
SiO_2	49.0	50.2	49.3	48.8	50.5	48.9	50.7	51.8	48.2	54.1	48.1	46.2	53.6	–	48.6
TiO_2	1.18	1.17	1.24	0.93	1.14	0.80	1.16	1.04	0.89	0.33	0.93	0.82	0.63	–	3.16

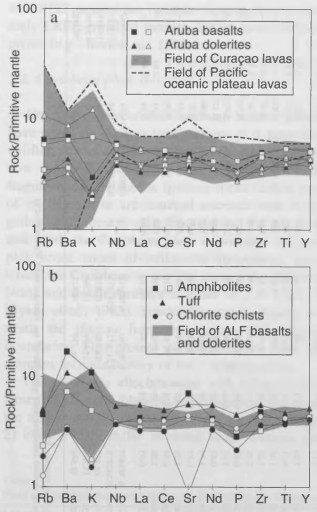

Fig. 4. a: Multi-element diagram for the Aruba Lava Formation (ALF), normalised to primitive mantle of Sun and McDonough (1989), compared with ranges for Curaçao and Pacific plateau lavas taken from Kerr et al. (1996b) and references therein. b: Range of Aruba basalts and dolerites (grey) compared with other members of the Aruba Lava Formation.

As subduction resumed, Proto-Caribbean oceanic crust was now subducted westwards beneath the plateau, which moved northwards and eastwards into the Caribbean region. The Antilles arc was built up on the leading edge of the advancing plateau, and a north-east directed subduction zone formed beneath the trailing edge of the plateau (the present day Central American arc system). As the Caribbean plateau moved past the Americas on its way to its present location, fragments of it were obducted and accreted along the margins. The study area, Aruba, is one such accreted fragment, now located within an uplifted fault block that is part of the complex southern Caribbean plate boundary zone (Silver et al., 1975; Ladd et al., 1990).

3. The Aruba Lava Formation—a part of the Caribbean oceanic plateau?

3.1. Field observations and interpretations

The rocks of the Aruba Lava Formation (ALF) cover an area of approximately 20 km^2 in central Aruba (Fig. 3). The ALF comprises a sequence of basaltic lavas interbedded with volcaniclastic rocks, and intruded by dolerites. The main lithological observations are summarised in Table 1. According to Monen (1977), the structure of the ALF consists of, from south to north, a faulted syncline and anticline. The majority of the outcrop area represents the northward-dipping northern limb of the anticline. The ALF is variably metamorphosed from prehnite facies to amphibolite-hornfels facies towards the batholith. It is cut by a number of ductile shear zones, one of which is at amphibolite facies and contains small silicic melt segregations. Many of the rocks in the sheared regions are highly altered, and contain low-grade metamorphic minerals. One lithology of particular interest is a pale green chlorite schist, which may have had an ultramafic or picritic protolith.

Three points must be emphasised about the stratigraphy of the ALF—firstly the dominance of

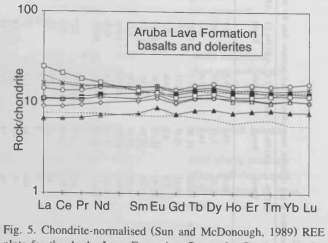

Fig. 5. Chondrite-normalised (Sun and McDonough, 1989) REE plots for the Aruba Lava Formation. Range for Curaçao samples (Kerr et al., 1996b) shown as dashed lines.

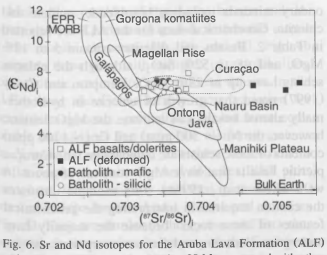

Fig. 6. Sr and Nd isotopes for the Aruba Lava Formation (ALF) and Aruba batholith, age-corrected to 88 Ma, compared with other Pacific plateaux and Galápagos (data from references in Kerr et al., 1997b). Range of Bulk Earth estimates for Sr isotopes from Faure (1986). EPR: East Pacific Rise.

material of a mafic composition; secondly, the absence of any sedimentary material of an obviously continental provenance; and finally, the high abundance of volcaniclastic deposits. These observations provide constraints on the environment of formation of the ALF.

The absence of continental-derived sediments implies that the ALF was deposited a significant distance from any continental source. Given that Aruba is currently located only 40 km from the South American mainland, credibility is given to models (e.g., Pindell and Barrett, 1990) suggesting that the whole Caribbean plate, including Aruba, is allochthonous. The abundance of pillowed basaltic material is also consistent with an oceanic association for the ALF; however, the sequence cannot represent normal ocean floor material, because there is evidence for substantial erosion (to derive clasts for basaltic conglomerate) and subaerial or shallow submarine eruption (accretionary lapilli tuff and ignimbrite). The presence of abundant vesicles in pillows also points to a relatively shallow sub-aqueous environment, with hydrostatic pressure being insufficient to inhibit degassing of the magma. Sedimentological features of the volcaniclastic rocks also suggest reworking in relatively shallow water, above the storm wave-base (ripple cross-lamination) and deposition on a slope (convolute bedding).

The association of uniformly mafic extrusive and intrusive magmas with a large volume of volcaniclastic material supports the interpretation of a shallow submarine environment. Basaltic magma tends not to be involved in explosive volcanic activity unless it interacts with water; the presence of accretionary lapilli indicates the existence of moist eruption clouds and suggests that hydromagmatic processes have been important. It is also possible that some of the volcaniclastic material is derived from explosive eruptions of more evolved magmas ($SiO_2 \approx 55$–65%).

The lithological association of submarine basalts, dolerites and volcaniclastic rocks found in the ALF, together with the presence of metamorphosed mag-

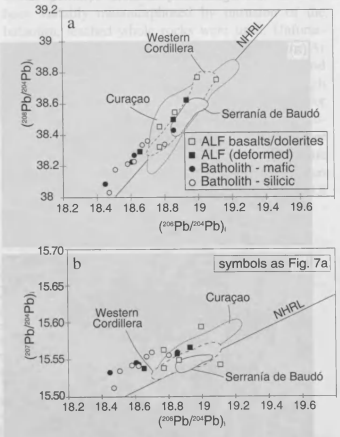

Fig. 7. a and b: Lead isotope data for the Aruba Lava Formation (ALF) and the batholith, age-corrected to 88 Ma, compared with data from elsewhere in the Caribbean (contaminated or hydrothermally altered samples excluded: Hauff et al., 1998). Note that some Aruba batholith samples have lower radiogenic Pb than the ALF. Most samples plot above the Northern Hemisphere Reference Line (NHRL).

nesian rocks (now found as chlorite schists), is consistent with an origin as part of an oceanic plateau. This link is strengthened by the existence of rocks which show evidence of subaerial and shallow submarine reworking, which would be expected on the flanks of an emergent oceanic plateau volcano, but never in a normal mid-ocean ridge environment.

Although both an oceanic arc environment and an oceanic plateau environment are broadly compatible with the lithological and stratigraphic observations, the dominance of mafic material is in better agreement with the oceanic plateau scenario. Geochemical means must be used to distinguish between the two.

3.2. Whole-rock compositions

Most of the rocks of the tholeiitic Aruba Lava Formation are significantly altered, common secondary minerals including hornblende, epidote and chlorite. Geochemical data for the ALF are reported in Table 2. Basalts and dolerites contain 5 to 12% MgO, and 48 to 52% SiO_2, although the chlorite schists have up to 22% MgO. Kempton and Casey (1997) noted that growth of chlorite in hydrothermally altered basalts can increase the MgO content; however, the Ni (~ 300 ppm) and Cr (~ 1200 ppm) contents of these schists are comparable with Curaçao picritic basalts that have MgO contents of about 16 wt.% (Kerr et al., 1996b). This example illustrates the caution required in interpreting the geochemical features of these rocks: because the majority have undergone alteration and/or metamorphism, the potential mobility of elements such as Sr, Rb, K, Na and Ba must be considered. In contrast, elements such as Zr, Nb, Y, Ti, Cr and the REE are believed to be relatively immobile (e.g., Ludden et al., 1982).

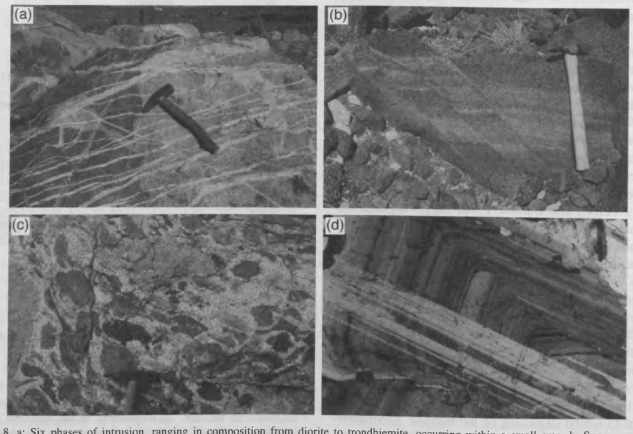

Fig. 8. a: Six phases of intrusion, ranging in composition from diorite to trondhjemite, occurring within a small area. b: Syn-magmatic faulting in a layered noritic gabbro. c: High abundance of microdiorite and porphyry inclusions within a tonalite, showing evidence for ductile deformation, indicating that they were not completely solidified before they became included. d: Oscillatory zoning (An_{58} to An_{31}) in plagioclase, suggesting that magma-mixing may have been an important process in the petrogenesis of the batholith (field of view is 2 mm).

Multi-element plots of the Aruba basalts and dolerites show flat patterns (Fig. 4a), with some scatter in the mobile elements (Ba, Rb and K). Fig. 4b compares these data with samples of amphibolites, volcaniclastic sediments and chlorite schists in the ALF—these show considerably more variation for the mobile elements, particularly Sr, but have comparable abundances for immobile elements such as Zr, Y and Nb, suggesting that these rocks have a similar origin to the basalts and dolerites. REE plots also show flat to slightly enriched patterns at 10 times chondrite for the Aruba basalts and dolerites (Fig. 5). They are similar to those observed for other localities documented as belonging to the Caribbean plateau (e.g., Kerr et al., 1996c).

The ALF is also isotopically very similar to other members of the Caribbean plateau. The data cluster tightly at $^{87}Sr/^{86}Sr_{t=88\ Ma} \approx 0.7035$ and $\varepsilon Nd_{t=88\ Ma} \approx +7$ (Fig. 6). The higher $^{87}Sr/^{86}Sr$ values (up to 0.7053) are interpreted as being due to alteration, because only the deformed basalts and amphibolites are affected. Pb isotope data are also similar to those from Curaçao and Colombia (Fig. 7a and b).

The lack of significant volumes of evolved material within the sequence suggests that an island arc origin is unlikely, and this observation is supplemented by the geochemical data, in particular the lack of a negative Nb anomaly. The ALF rocks have compositions typical of an oceanic plateau sequence, and very similar to other formations generally accepted as belonging to the Caribbean oceanic plateau (e.g., Curaçao: Kerr et al., 1996b).

3.3. Age of the ALF

No palaeontological evidence for the age of the ALF was found during this study; however, imprints of ammonites have previously been recovered from a sedimentary intercalation in the ALF. None has been formally described or identified, but MacDonald (1968) and Wiedmann (reported in Beets et al., 1984) independently concluded that the fauna are Turonian in age (90.4–88.5 Ma: Harland et al., 1990).

Three of the freshest samples from the ALF were dated by $^{40}Ar/^{39}Ar$ methods. Because the ALF has been variably metamorphosed by intrusion of the batholith, leached whole rocks were used. Unfortunately, the results were inconclusive because the Ar systematics of the samples were too disturbed, and none reached an acceptable age plateau. Even though reliable radiometric dates could not be obtained for the Aruba Lava Formation, its geochemical and isotopic similarity with rocks from Curaçao (and other acknowledged members of the Caribbean oceanic plateau) and its geographic proximity to Curaçao suggest that it may have a similar age (88.9 ± 0.8

Table 3
Field and petrographic observations of the Aruba batholith

Lithology	Abundance[a]	Mineralogy	Texture	Colour index (C.I.)
Tonalite	70%	hbl + qz + plag + bi + mag	grain size ≈ 3 mm; hbl up to 10 mm; finer-grained varieties present; elongate hbl may show crucifix twinning	10–30; some trondhjemites with C.I. < 10
Diorite	20%	hbl + qz + plag + mag	grain size ≈ 2–3 mm; equigranular; fine grained varieties present	30–55
Hbl-gabbro	< 5%	hbl + qz + plag + mag ± cpx ± opx	grain size ≈ 2–4 mm; equigranular	55–80
Norite	< 5%	ol + plag + opx ± secondary hbl	grain size ≈ 3–4 mm; equigranular; magmatic layering present	55–80
Hooibergite[b]	< 5%	cpx + hbl + plag ± qz	large (up to 20 mm) euhedral, equant hbl in matrix of cpx + plag; magmatic layering sometimes present	55–100
Acid material	< 1%	qz ± plag ± kfeld	coarse-grained or aplitic	< 1

[a] Estimated from this study.
[b] Defined by Westermann (1932) as a "dark-coloured igneous rock in which many large hornblende crystals are particularly striking"; technically a mela-diorite.

Table 4
Representative major element, trace element and isotopic data for the Aruba batholith

Sample	ARU96-154	ARU96-42	ARU96-57	ARU96-53	BK77-165	BK77-066a	ARU96-158	ARU96-123	ARU96-136	ARU96-29	ARU96-98	BK77-054	ARU96-131	ARU96-33	ARU96-155
Rock type	norite	gabbro	hooibergite	hooibergite	hooibergite	diorite	diorite	late mafic porphyry	hbl-plag-porphyry	hbl-plag-porphyry	tonalite	tonalite	tonalite	tonalite	microgranite
SiO_2	48.7	52.6	53.0	55.0	57.3	55.3	56.9	53.9	62.1	63.7	61.3	65.0	65.2	66.7	74.1
TiO_2	0.29	0.69	0.54	0.54	0.59	0.73	0.63	0.76	0.41	0.46	0.50	0.40	0.52	0.33	0.25
Al_2O_3	5.4	16.9	7.8	8.2	11.9	18.5	15.7	15.1	16.9	16.2	17.4	16.1	16.2	16.0	13.7
Fe_2O_3 (tot)	10.67	9.52	8.92	9.02	9.57	8.27	8.16	9.82	5.91	4.95	6.00	5.35	4.66	4.43	2.11
MnO	0.19	0.15	0.17	0.17	0.18	0.13	0.15	0.17	0.12	0.11	0.10	0.11	0.09	0.11	0.03
MgO	18.1	6.7	12.3	11.9	8.0	3.7	4.6	6.7	2.0	1.6	2.5	2.0	1.5	1.4	0.4
CaO	14.47	9.32	15.95	12.92	9.77	7.47	7.66	9.60	5.80	4.26	7.17	5.20	4.63	3.94	1.79
Na_2O	0.45	3.26	1.36	1.65	2.36	4.28	3.86	2.70	4.34	5.40	3.68	4.42	4.62	5.39	4.40
K_2O	0.12	0.18	0.21	0.25	0.37	0.57	0.85	0.90	0.62	0.74	0.38	0.89	1.47	0.87	3.00
P_2O_5	0.026	0.153	0.069	0.064	0.109	0.173	0.186	0.174	0.192	0.141	0.088	0.120	0.143	0.129	0.057
LOI%	0.75	1.06	0.60	0.45	0.56	0.44	0.40	0.86	0.72	2.21	1.00	0.69	0.43	1.52	0.34
Total	99.23	100.57	100.85	100.26	100.73	99.61	99.01	100.66	99.06	99.83	100.17	100.26	99.57	100.79	100.18
Ni	193	57	111	135	42	27	28	59	3	2	12	5	4	2	2
Cr	1156	172	1325	742	454	33	106	260	8	10	33	215	6	9	0
Ba	97	132	189	161	269	313	448	680	450	458	188	495	723	529	1752
Rb	4	2	2	2	4	11	17	15	12	8	5	14	33	9	46
Sr	113	414	166	143	173	495	362	296	420	308	254	277	329	354	188
Nb	1.0	0.7	2.0	0.4	1.7	2.3	2.4	3.0	1.6	2.9	2.1	2.4	2.8	1.3	3.3
Zr	13	23	24	29	30	51	54	54	60	72	59	61	96	62	129
Y	7	9	13	13	13	13	18	17	13	12	17	12	18	10	14
Th	0.20	0.68	0.47	0.68	1.65	0.63	0.98	0.75	0.82	1.01	1.12	1.37	1.30	1.95	2.83
U	0.10	0.21	0.24	0.38	0.71	0.23	0.48	0.33	0.37	0.38	0.80	0.53	0.57	0.82	1.06
La	1.30	4.09	2.21	4.84	5.32	5.75	7.06	4.42	5.37	6.03	6.74	8.02	8.03	10.02	8.68
Ce	2.73	8.58	4.74	8.52	10.99	12.26	15.32	9.83	11.66	12.53	15.28	16.26	16.35	22.30	18.59
Pr	0.39	1.22	0.73	1.20	1.46	1.77	2.20	1.49	1.66	1.72	2.22	2.03	2.18	2.86	2.21
Nd	2.21	5.73	4.10	5.51	6.46	8.42	10.67	7.16	7.71	7.34	10.95	8.77	9.52	12.47	8.85
Sm	0.77	1.47	1.36	1.50	1.73	2.26	2.65	2.06	1.88	1.69	2.88	1.92	2.13	2.84	1.87
Eu	0.32	0.68	0.53	0.56	0.68	0.85	0.96	0.85	0.77	0.69	1.06	0.68	0.80	1.01	0.86
Gd	0.90	1.45	1.56	1.71	1.87	2.33	2.65	2.22	1.79	1.66	2.78	1.79	1.86	2.62	1.71
Tb	0.18	0.25	0.31	0.31	0.35	0.44	0.46	0.42	0.31	0.30	0.48	0.30	0.31	0.46	0.30
Dy	1.14	1.59	2.03	2.06	2.39	3.00	2.94	2.81	2.03	1.92	3.13	1.97	1.97	3.00	1.86
Ho	0.23	0.30	0.41	0.42	0.47	0.59	0.60	0.57	0.38	0.38	0.60	0.39	0.37	0.58	0.36
Er	0.65	0.85	1.17	1.18	1.40	1.76	1.63	1.67	1.12	1.11	1.71	1.13	1.13	1.73	1.10
Tm	0.09	0.12	0.16	0.17	0.21	0.27	0.23	0.24	0.17	0.17	0.26	0.18	0.17	0.27	0.17
Yb	0.61	0.83	1.15	1.17	1.40	1.85	1.66	1.62	1.17	1.19	1.83	1.23	1.20	1.81	1.19
Lu	0.09	0.13	0.16	0.17	0.22	0.26	0.24	0.24	0.18	0.19	0.28	0.18	0.19	0.29	0.18
$(^{87}Sr/^{86}Sr)_i$	0.703585	0.703524	0.703423	0.703507	0.703498	0.703515	0.703474	–	0.703607	–	–	0.703715	0.703611	–	0.703387
$(^{143}Nd/^{144}Nd)_i$	0.512905	0.512900	0.512904	0.512905	0.512894	0.512866	0.512886	–	0.512899	–	–	0.512871	0.512878	–	0.512895
$(^{206}Pb/^{204}Pb)_i$	18.448	18.471	18.621	18.606	18.855	18.620	18.508	–	18.701	–	–	18.668	18.581	–	18.802
$(^{207}Pb/^{204}Pb)_i$	15.533	15.512	15.543	15.546	15.560	15.541	15.534	–	15.560	–	–	15.554	15.542	–	15.556
$(^{208}Pb/^{204}Pb)_i$	38.085	38.031	38.269	38.227	38.429	38.229	38.176	–	38.361	–	–	38.335	38.213	–	38.339

Major elements (in wt.%) recalculated to include LOI. Fe_2O_3 (tot) = total Fe as Fe_2O_3; trace elements in p.p.m.
Major elements and Ni, Cr, Ba, Rb, Sr, Zr, Y by XRF; others by ICP-MS. Isotopic data by thermal ionisation mass spectrometry, age corrected to 88 Ma (denoted i).
(See Appendix A for summary of analytical techniques and Table 2 for standard measurements.)

Ma weighted mean of two Curaçao samples: Sinton et al., 1998) to the Curaçao Lava Formation. In view of this, it seems that the Turonian assignation of the ammonites is correct.

4. The Aruba batholith

4.1. Field and petrological observations and interpretations

The Aruba batholith has two main outcrops (Fig. 3), totalling 80 km^2 in area. Although predominantly tonalitic, the batholith consists of a wide range of lithological types, which coexist on a range of scales, from a few centimetres (Fig. 8a) to hundreds of metres. Field and petrological observations for the batholith are summarised in Table 3. The batholith displays considerably less alteration than the Aruba Lava Formation, although some samples show sericitisation of plagioclase and replacement of biotite by chlorite. Thin epidote veins cutting the batholith are witnesses to a late phase of hydrothermal alteration, and the batholith is cross-cut by late mafic dykes. One important general observation is that chilled margins between different members of the batholith are extremely rare, suggesting either that the bulk of the magmas were intruded within a short time-frame, or that the batholith was emplaced at a depth where temperatures remained high. The only pronounced chilling observed is at the margins of the late mafic dykes.

Fig. 9. Plot showing normative data for Aruba tonalites and diorites with > 10% normative quartz, after Barker (1979).

Fig. 10. Total alkali vs. silica plot for the batholith reveals its subalkaline character. Dividing line from Irvine and Baragar (1971). Field for the Aruba Lava Formation (ALF) is indicated.

Fig. 11. a: Fe_2O_3 (tot) decreases as silica increases. b: Fe_2O_3 (tot)/MgO ratio increases with increasing silica. Fields for the Aruba Lava Formation (ALF) are indicated.

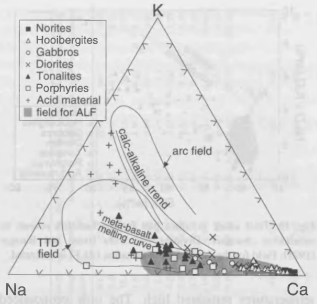

Fig. 12. K–Ca–Na plot for the Aruba batholith (after Defant and Drummond, 1993) showing that samples of the Aruba batholith trend into the trondhjemite–tonalite–dacite (TTD) field rather than following a typical calc–alkaline trend. Field for the Aruba Lava Formation (ALF) is indicated.

The mafic members of the batholith are transitional to the diorites, and frequently exhibit magmatic layering, which is interpreted as being of cumulus origin. In some cases, this layering shows spectacular structures, such as syn-magmatic faulting (Fig. 8b). Mafic members include gabbros, norites and texturally distinctive hornblende-rich mela-diorites known locally as 'hooibergites' (Westermann, 1932). Thin sections of the norites contain olivine (Fo_{79}) poikilitically enclosed by orthopyroxene, with interstitial anorthitic plagioclase (An_{89}). The 'hooibergites' contain diopside, poikilitically enclosed by plagioclase and large (frequently up to 2 cm) euhedral hornblende crystals.

The tonalites commonly contain numerous inclusions, ranging from a few percent to about 80% of the rock volume. Tonalite-hosted inclusions cover a vast range of lithologies and morphologies, ranging in size from 1 cm to 3 metres, with the majority falling in the 5–30 cm range. By far the most abundant included lithologies are microdiorite and tonalitic hornblende-plagioclase porphyry. These have diffuse contacts with the host rock, and irregular, globular shapes. Sometimes they are highly flattened and aligned. Two observations point to this type of inclusion being at least partially liquid when incorporated into the tonalite: 1) extreme flattening of some inclusions; and 2) clear evidence of ductile deformation in some examples (Fig. 8c). The presence of large plagioclase crystals in the tonalite (Fig. 8d) showing oscillatory zoning from An_{58} to An_{31}, together with the field observations, suggests that magma mixing has been a very important process.

Other common inclusions are diorites and gabbroic rocks. These mainly occur close to localities where tonalite intrudes these rocks, and are commonly much more angular, appearing to have been derived from fracturing of the wall rock by tonalite. The lack of chilled margins, however, suggests that even though the diorite failed in a brittle manner, it was still hot.

An overall sequence of more mafic to more felsic was determined from field relationships: The first rocks to crystallise were mafic cumulates (i.e., norites, gabbros and 'hooibergites'). These may have crystallised at the same time, with the textural differences reflecting different volatile contents in the magma, but no direct evidence for their relative age was found. Rocks of a dioritic composition are the next in the sequence. These are in places transitional from the gabbroic rocks. A voluminous phase of tonalitic magmatism followed. This magma locally stoped xenoliths from its wall rocks, and entrained magmas of a slightly different, more dioritic composition. Some of these magmas may have been completely mixed into the tonalite, whereas others are preserved as deformed enclaves. Phases of veining by magmas of progressively more silicic compositions occurred next; these magmas may represent late-stage differentiates of the tonalite. Finally, suites of mafic dykes intruded the whole complex, which was by then cool enough for the dykes to chill, but hot enough for hydrothermal circulation and epidote mineralisation to continue.

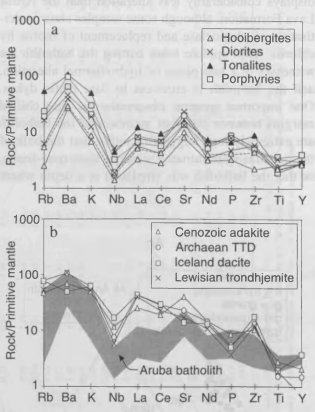

Fig. 13. a: Primitive mantle-normalised (after Sun and McDonough, 1989) multi-element plot showing samples of the Aruba batholith; in b these are compared with adakites, dacites, and tonalite–trondhjemite–granodiorite suites. Adakite and tonalite–trondhjemite–dacite (TTD) from Drummond et al. (1996); Iceland dacite from Jónasson et al. (1992); Lewisian trondhjemite from Rollinson and Fowler (1987).

Table 5
Comparison of Aruba tonalite with adakites (Drummond and Defant, 1990)

Characteristic	Adakite	Aruba tonalite
SiO_2 (wt.%)	> 56	62–73
Al_2O_3 (wt.%)	> 15	14–16
MgO (wt.%)	< 3	< 3
Sr (ppm)	> 300	200–400
Sr anomaly	positive	positive
$^{87}Sr/^{86}Sr$	< 0.7040	~ 0.7036
Sr/Y	> 40	10–40
La/Yb	> 20	3–7
Yb	< 1.9	1.1–1.9
Y	< 18	15–17
Nb	< 10	< 4
Mineralogy	plag + amph ± cpx ± bi ± opaques	plag + amph + bi + qz

4.2. Whole rock geochemistry

Geochemical data for the batholith are presented in Table 4. The members of the batholith range in SiO_2 content from 48% for the norites and hooibergites to 77% for some trondhjemitic veins. MgO content varies from 18% to < 0.1%. The majority of samples are low in potassium, and are classified as tonalites (Fig. 9).

On a total alkali versus silica plot (Fig. 10), the batholith is classified as sub-alkaline. Although samples appear to follow calc–alkaline trends, with decreasing $Fe_2O_3(tot)$ and increasing $Fe_2O_3(tot)/MgO$ as silica increases (Fig. 11a and b), a K–Ca–Na plot (Fig. 12) shows that the samples of the Aruba batholith do not follow a trend typical of calc–alkaline arc rocks: rather, they fall into the tonalite–trondhjemite–dacite field. Multi-element diagrams for the batholith (Fig. 13a) show that all members have similar relative abundances of incompatible elements, suggesting that all members of the batholith are closely related. The notable characteristics of this rock suite are high Sr and Ba, negative Nb anoma-

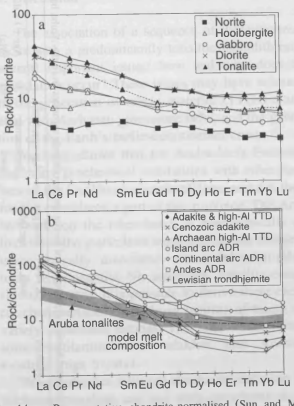

Fig. 14. a: Representative chondrite-normalised (Sun and McDonough, 1989) REE plots of representative members of the Aruba batholith. b: Aruba tonalites compared with average values for other rock suites (Rollinson and Fowler, 1987; Drummond et al., 1996) and a model 17% modal batch melt of an average ALF basalt with 80% amphibole, 18% plagioclase and 2% garnet in the residue (partition coefficients from compilation by Martin (1987)). TTD: tonalite–trondhjemite–dacite; ADR: andesite–dacite–rhyolite.

Table 6
Summary of $^{40}Ar/^{39}Ar$ incremental heating experiments of biotite and hornblende separates from the Aruba batholith and a cross-cutting mafic dyke

Sample	Material	Lithology	K/Ca total	Total gas age (Ma)	Age spectrum				Isochron analysis		
					Increments used	^{39}Ar (%)	Age ± 1 s.d. (Ma)	MSWD	SUMS (N-2)	$^{40}Ar/^{39}Ar$ ± 1 s.d. intercept	Age ± 1 s.d. (Ma)
ARU96-131	biotite	tonalite	2.8	82.75 ± 0.20	5 of 5	100.0	82.95 ± 0.31	7.61	11.45	295.8 ± 4.4	82.84 ± 0.36
ARU96-131	biotite	tonalite	3.3	82.27 ± 0.18	14 of 17	98.9	82.94 ± 0.31	12.82	13.11	276.5 ± 12.6	83.09 ± 0.40
ARU96-158	biotite	diorite	3.4	84.20 ± 0.21	13 of 16	94.3	84.91 ± 0.23	2.21	2.77	278.5 ± 20	84.99 ± 0.35
BK77-165	hornblende	diorite	0.037	81.09 ± 0.39	10 of 18	71.3	81.80 ± 0.26	1.43	1.49	287.4 ± 7.7	82.20 ± 0.51
ARU96-152	hornblende	hbl-gabbro	0.059	84.58 ± 0.27	8 of 17	91.5	87.21 ± 1.67	113	54.5	365.7 ± 25.2	79.92 ± 2.76
ARU96-123	hornblende	late mafic dyke	0.063	75.57 ± 0.24	10 of 17	75.5	79.59 ± 0.62	10.5	11.4	320.8 ± 25.7	77.46 ± 2.09

Analytical methods and data reduction after Singer and Pringle (1996).
All ages calculated relative to 27.92 Ma for TCR sanidine; all errors reported as 1 s.d. of analytical precision.

lies, and moderate
of these characte
tonalites (tonalite-
suites) and Cenoz
eral, the adakites
values, in particul
(Fig. 13b). REE p
in Fig. 14a, and co
andesite–dacite–ri
and a model mel
members of the t
REE (LREE) enr
pleted middle-to
whereas the maf
showing only slig
of the Aruba ba
LREE enrichmen
the adakites and
garnet control is l
Aruba batholith.

Fig. 6 shows t
the Aruba batholi
Formation, havin
+7.0 The Pb is
overlap with thos
Colombian and
although the Pb
from the batholit
the ALF. Note th
relationship betw
composition for t

4.3. Age of the A

The Aruba t
evidence to be y
of the contacts
the ALF are in
batholith has not
the ALF. Prefer
shear zones wi
deformation, ind
occurred penec
along shear zon

Radiometric
reported by Sa
obtained a K/
analyses of Prie

komatiites of greenstone belts and Gorgona Island (Echeverría, 1980; Kerr et al., 1996a) and the picrites of Curaçao (Klaver, 1987; Kerr et al., 1996b). Both Archaean tonalites and the Aruba tonalites are associated with trondhjemites; additionally, both contain populations of more mafic inclusions.

Any model which attempts to explain the petrogenesis of this silicic material associated with an oceanic plateau sequence must account for the following observations:

1) The members of the batholith have a wide lithological variation, ranging from gabbroic rocks to tonalites and trondhjemites. These are closely related to one another—they have similar incompatible trace element ratios and isotopic signatures and are comagmatic.

2) The ~85–82 Ma batholith was intruded into the Aruba Lava Formation shortly after the formation of the latter; the Turonian (90.4–88.5 Ma) age of the ALF reported by Beets et al. (1984) and the 88–91 Ma range of ages for the whole Caribbean plateau (Sinton et al., 1998) mean that there is only a limited time period (approximately 3–9 m.y.) during which the magmatic environment has to change from one producing voluminous mafic tholeiites to one producing a tonalitic series.

3) The ALF and the batholith overlap in isotopic composition for Sr and Nd, and their Pb isotopic compositions also partially overlap. This is intriguing for suites of rocks which are otherwise very different.

4) The intrusion of the batholith is penecontemporaneous with deformation of the Aruba Lava Formation.

5.1. Models for generation of silicic melts associated with oceanic plateaux

5.1.1. Remelting of plateau material

Several authors have suggested that some of the silicic volcanic rocks on Iceland have formed by remelting of the Icelandic mafic crust (e.g., O'Nions and Grönvold, 1973; Óskarsson et al., 1982) or remelting of pre-existing silicic segregations within that crust (Marsh et al., 1991). It is now widely accepted that partial anatexis of rocks of basaltic composition can create melts resembling Icelandic dacites and rhyolites (Thy et al., 1990), as well as tonalites and trondhjemites (Drummond and Defant, 1990; Rapp et al., 1991).

The geochemistry of melts created by partial melting of mafic protoliths is also broadly consistent with the geochemistry of the tonalites of the Aruba batholith. The dacites of the Króksfjördur Volcano (Jónasson et al., 1992) in Iceland are calc–alkaline in character, and have depletions in high-field-strength elements (e.g., Nb) normally associated with subduction-related volcanic suites, although there can be no subduction zone contribution to the petrogenesis of young Icelandic volcanics. The Aruba tonalites also share some characteristics with adakitic rocks (Table 5), thought to be formed from partial melting of mafic material at the amphibolite–eclogite transition zone, either in a hot subduction environment (Defant and Drummond, 1990) or beneath thickened continental arcs (e.g., Atherton and Petford, 1993). Remelting at deep levels within an oceanic plateau sequence could create melts with similar characteristics. The major difference between the Aruba tonalites and adakites is that the HREE depletions seen in the Aruba rocks are less extreme than those seen in adakites (Fig. 14b). This could be explained by partial melting of an oceanic plateau sequence at a shallower depth (i.e., not in the garnet stability field) than either environment proposed for true adakites. Preliminary geochemical modelling of rare earth elements is consistent with derivation of Aruba tonalites from partial (batch) melting of an average ALF basalt with $< 5\%$ garnet in the melting residue, contrasting with the large amount of residual garnet proposed for true adakites (35%: Defant and Drummond, 1993).

One requirement for partial melting of a mafic protolith at geologically reasonable temperatures is that the protolith should be hydrated. On Iceland, this is achieved because the plateau is being constructed at a spreading centre: hydrated basalts sink to deeper levels as the crust rotates and subsides (Palmáson, 1986). There is no clear evidence whether or not the Caribbean Plateau was formed at a spreading centre, so this mechanism of moving hydrated material into the crust is not necessarily appropriate. A tectonically distinct alternative is imbrication of the plateau as it begins to interact with a subduction zone (sheared rocks at amphibolite facies are found on Aruba). A further possibility is that no external

mechanism is requ
because the large
undergo hydrother
ing the constructic

Hydrothermal
leave an isotopic
by the products
values obtained in
deformed member
higher $^{87}Sr/^{86}Sr$ t
unlikely to be a
deformed sample
undeformed basal
interpreted as se
hydrothermally al
oceanic plateau
material for the A
other isotopic sy
needed to try and

The enormous
the Aruba batholi
partial melting o
hydrated basalt ur
tions (Winther, 1
tent of ~62.5%,
have SiO_2 values
does not necessar
position, because
have shown that
batholith have cur
presence of olivin
indicates that the
ably more mafic t
partial melting of
liquid composition
istics of the tona
could be explaine
tonalitic liquid in
mantle. Mixing b
and tonalites, inf
and petrography,
process, and fits
the K–Ca–Na dia
tion diagrams. H
yet been quantitat

Although the
be explained by r
with an additic

Sr–Nd isotopic characteristics of the batholith are primitive, with $^{87}Sr/^{86}Sr_i \approx 0.7035$ and $\varepsilon Nd_i \approx +7$: identical to the isotopic ratios of the plateau basalts into which the batholith intrudes. If subduction of hydrothermally altered Proto-Caribbean crust (and associated sediments) was responsible for triggering melting of the mantle wedge and creation of the Aruba batholith melts, it might be expected that this would be seen in the isotopic signature of the melts produced. This does not appear to be the case for Sr and Nd isotopes although the Pb isotope ratios of some samples from the batholith are displaced to lower values with respect to the ALF. This may reflect some sedimentary contamination of the batholithic magmas, and could have occurred either due to subducted sediment in the source region or assimilation of sediments intercalated in the oceanic plateau crust into which the batholith intruded. The former explanation is preferred, because field studies have shown that sediment intercalated in the plateau crust is primarily volcanogenic (rather than terrigenous), and is therefore likely to have the same Pb isotope composition as the plateau sequence itself. Pb isotopes are more sensitive than Sr and Nd to the addition of a small sedimentary component, because sediments have high Pb contents (~ 20 ppm: Taylor and McLennan, 1985) compared to the Aruba magmas (< 5 ppm). The sedimentary contaminant, characterised by low radiogenic Pb, could have been derived from the South American continent. The amount of sedimentary contaminant is likely to be small, because it has not affected the Sr and Nd isotopes (and it is extremely unlikely that the contaminant has identical Sr and Nd isotopes to the Aruba batholith).

The second difficulty with creation of the Aruba batholith in a subduction regime is the timing: the magmatic environment on Aruba has changed quickly (within 3–9 m.y.) from one creating voluminous mafic tholeiites to one creating a tonalitic suite. In normal thermal circumstances, the downgoing oceanic plate must reach a depth of 80–100 km before it dehydrates and triggers melting in the mantle wedge above (Gill, 1981); the time taken for this is of the order 2 m.y. (using arbitrary figures of 7 cm/yr for the subduction rate at an angle of 45°). If the Aruba batholith (~ 85 to ~ 82 Ma) is subduction-related, this constrains the subduction polarity reversal event in the Caribbean to have happened swiftly after extrusion of the plateau sequence (~ 91 to ~ 88 Ma).

The timing of the subduction polarity reversal in the Caribbean is not yet well-constrained, with estimates ranging from 100 Ma to 60 Ma (Burke, 1988; Draper et al., 1996). This uncertainty has led to considerable debate over the cause of the reversal. The general consensus (Burke et al., 1984; Duncan and Hargraves, 1984; Pindell and Barrett, 1990) is that the arrival of the 88–91 Ma phase of the Caribbean plateau and its collision with the Proto-Greater Antilles Arc clogged the subduction zone and caused the polarity reversal. Alternative explanations include: 1) there being an earlier phase of plateau magmatism (Lapierre et al., 1997) which blocked the subduction zone, triggering subduction 'flip'; and 2) significantly increased spreading rates in the Atlantic at around 100 Ma initiating a new subduction zone with the opposite polarity (Pindell, 1993). A possible reason for this dissent is that a subduction polarity reversal is likely to be an extremely complex event occurring over a protracted period of time that may involve backstep of the trench and accretion of plateau fragments in addition to the polarity reversal itself.

Whatever the cause and timing of the subduction polarity reversal, it seems that the anomalously hot plume mantle responsible for the generation of the Caribbean oceanic plateau (and Aruba Lava Formation) at 88–91 Ma must have spread out laterally from its source in order to create the large volumes of magma over a wide area. As the Caribbean Plateau moved towards the easterly-dipping subduction zone (Fig. 15a), the residual mantle, depleted by the plateau-building event, would have been carried with it. This anomalously hot mantle would have therefore become located within the mantle wedge region after the subduction zone reversed its polarity (Fig. 15b).

The magmas that form the batholith could ultimately originate in the mantle wedge above the incipient subduction zone. These wedge-derived magmas may also provide the thermal impetus leading to melting of the young, hydrated plateau crust. A component derived from melting of the downgoing slab may help to explain the partial adakitic characteristics of the melts. The age of the subducting Proto-Caribbean crust is not known, but in addition to melting of young subducting oceanic lithosphere (Drummond and Defant, 1990), it has been suggested that magmas with adakitic characteristics can form from partial melting of basaltic oceanic crust during the earliest stages of subduction (Sajona et al., 1993) into hot mantle. In the plume-affected case of the Caribbean, this mantle could have been more-than-usually hot.

In summary, the Aruba batholith could have formed by melting in a subduction zone, with contributions from both the mantle wedge, the newly-subducting slab, and the overlying plateau crust. The ~ 85 Ma age of the batholith suggests that the

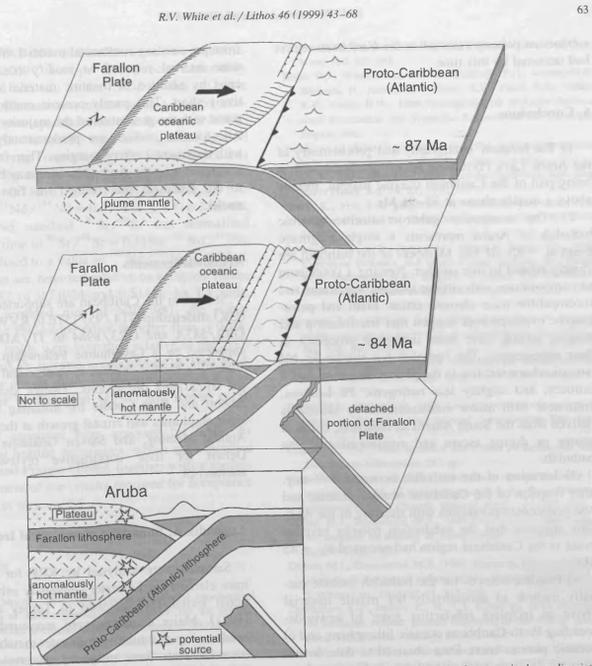

Fig. 15. Model for the tectonic environment in which the Aruba batholith formed. A newly-formed subduction zone is descending into anomalously hot mantle remaining from the 88–91 Ma plateau-building event. Potential sources for the Aruba batholith are indicated in the enlarged part of the figure.

subduction polarity reversal in the Caribbean region had occurred by this time.

6. Conclusions

1) The location, stratigraphy and geochemistry of the Aruba Lava Formation are all consistent with it being part of the Caribbean oceanic plateau, formed above a mantle plume at 88–91 Ma.

2) The composite gabbroic–dioritic–tonalitic batholith of Aruba represents a single magmatic event at ~ 85–82 Ma. Members of the batholith are closely related to one another, forming a continuum of compositions with similar isotopic signatures and incompatible trace element ratios. Field and petrographic evidence both suggest that fractionation and magma mixing have been important processes in their petrogenesis. The batholith has similar Sr–Nd isotopic characteristics to the plateau sequence that it intrudes, and slightly less radiogenic Pb isotopes, consistent with minor contamination by sediments derived from the South American continent, either at source or during ascent and emplacement of the batholith.

3) Intrusion of the batholith occurred 3–9 m.y. after eruption of the Caribbean oceanic plateau, and was penecontemporaneous with shearing in the ALF. This suggests that the subduction polarity reversal event in the Caribbean region had occurred by ~ 85 Ma.

4) Possible sources for the batholith include partially melted: a) anomalously hot mantle material above an incipient subduction zone; b) newly-descending Proto-Caribbean oceanic lithosphere; and c) oceanic plateau crust. Data obtained to date do not allow us to distinguish unequivocally between these sources, although our preliminary interpretations favour an origin in an incipient subduction zone setting: mafic melts derived predominantly from the anomalously hot mantle wedge (with a small contribution from the subducting slab and associated sediments) enter the oceanic plateau crust, locally triggering partial remelting of the still-hot hydrated basaltic lava pile.

5) Creation of batholithic suites consisting primarily of tonalites *can* occur entirely within the oceanic domain, i.e., without any interference or influence from pre-existing continental material. Moreover, the time interval required to modify oceanic plateau crust by addition of tonalitic material can be relatively short. This purely oceanic environment contrasts with the generation of the majority of Phanerozoic tonalites, which are predominantly associated with continental active margins. Therefore, the processes creating the Aruba tonalites may be analogous to the processes that formed the first continental nuclei.

Acknowledgements

Studies in the Caribbean are supported by NERC (UK) studentship GT4/95/157E to RVW and grants GR9/583A and GR3/8984 to JT/ADS; ACK is supported by a Leverhulme Fellowship. We thank Vivi Ruiz for her support in Aruba, and Dirk Beets for stimulating discussions. Thanks also to Dallas Abbott and Kent Condie for initiating the symposium on plumes and crustal growth at the 1997 GSA Annual Meeting, and Steven Goldstein and Marc Defant for their constructive reviews of this manuscript.

Appendix A. Summary of analytical techniques

Samples were analysed by XRF for major and trace elements at Leicester University using conventional techniques described in Tarney and Marsh (1991). Major elements were measured on fused beads using a lithium tetraborate–metaborate flux; trace elements were measured on pressed powder pellets using a Mowiol binding agent. Major element totals of 99–101% were deemed acceptable.

ICP-MS analyses were carried out on selected samples at the Rijks Geologische Dienst, Haarlem, using a Fisons PlasmaQuad PQ 2 + Mass Spectrometer with an ^{115}In internal standard, and calibrated with synthetic standard solutions. Samples were digested in a $HF–HNO_3$ mixture before being dried down, converted to nitrates, and diluted by a factor of 1000 before being introduced into the nebuliser.

Sr and Pb were run as the metal species on single Ta and single Re filaments, respectively, using a

Finnegan MA1
ter at the NE
(NIGL); Nd w
Ta–Re–Ta fila
ticollector mas
Blanks for Sr,
pg and 600 p
throughout the
$^{87}Sr/^{86}Sr = 0.$
standard, ^{143}Nd
La Jolla Nd
during run time
was normalised
Sample data ar
of NBS 987 o
Based on repe
ducibility of Pl
Pb isotope rati
age standard P
(1993). For det
dures, refer to
(1998).

Mineral sep
incremental he
in Singer and I
cal assessment
of an age as m

References

Abbott, D., Moon
evolution of t
plateau model
Atherton, M.P., I
magmas from
144–146.
Barker, F., 1979.
potheses of ori
and Related R
Beets, D.J., MacC
and early Ter
Eighth Caribb
Excursions on
Geology 10, 1
Beets, D.J., Mares
R., Beunk, F.F
high-pressure
history of the
graves, R.B., S

slab melting: Archean to modern comparisons. J. Geophys. Res. 95, 21503–21521.

Drummond, M.S., Defant, M.J., Kepezhinskas, P.K., 1996. Petrogenesis of slab-derived trondhjemite–tonalite–dacite/adakite magmas. Trans. Roy. Soc. Edinburgh: Earth Sci. 87, 205–215.

Duncan, R.A., Hargraves, R.B., 1984. Plate tectonic evolution of the Caribbean in the mantle reference frame. In: Bonini, W.E., Hargraves, R.B., Shagam, R. (Eds.), The Caribbean–South American Plate Boundary and Regional Tectonics. Geol. Soc. Am., Mem. 162, 31–63.

Echeverría, L.M., 1980. Tertiary or Mesozoic komatiites from Gorgona Island, Colombia: field relations and geochemistry. Contrib. Mineral. Petrol. 73, 253–256.

Edgar, N.T., Ewing, J.I., Hennion, J., 1971. Seismic refraction and reflection in the Caribbean Sea. Bull. Amer. Assoc. Petrol. Geol. 55, 833–870.

Faure, G., 1986. Principles of Isotope Geology, 2nd edn., Wiley, 589 pp.

Fox, P.J., Heezen, B.C., 1975. Geology of the Caribbean crust. In: Nairn, A.E.M., Stehli, F.G. (Eds.), The Gulf of Mexico and the Caribbean. The Ocean Basins and Margins, Vol. 3, Plenum, New York, pp. 421–465.

Gill, J.B., 1981. Orogenic Andesites and Plate Tectonics. Springer, Berlin, 358 pp.

Gladczenko, T.P., Coffin, M.F., Eldholm, O., 1997. Crustal structure of the Ontong Java Plateau: modeling of new gravity and existing seismic data. J. Geophys. Res. 102, 22711–22729.

Hall, S.A., 1995. Oceanic basement of the Caribbean basements. Geol. Soc. Am. Abstracts with Programs 27, A153, abstract.

Harland, W.B., Armstrong, R.L., Cox, A.V., Craig, L.E., Smith, A.G., Smith, D.G., 1990. A Geologic Time Scale 1989. Cambridge University Press, Cambridge, 263 pp.

Hauff, F., Hoernle, K., Tilton, G., Graham, D., Kerr, A.C., 1998, submitted. Large volume recycling of oceanic lithosphere: geochemical evidence from the Caribbean Large Igneous Province. Earth Planet. Sci. Lett.

Hughes, G.W., Turner, C.C., 1977. Upraised Pacific Ocean floor, southern Malaita. Solomon Islands. Geol. Soc. Am. Bull. 88, 412–424.

Irvine, T.N., Baragar, W.R.A., 1971. A guide to the chemical classification of the common volcanic rocks. Can. J. Earth Sci. 8, 523–548.

Jónasson, K., Holm, P.M., Pederson, A.K., 1992. Petrogenesis of silicic rocks from the Króksfjördur Central Volcano NW Iceland. J. Petrol. 33, 1345–1369.

Kempton, P.D., 1995. Common Pb procedures for silicate rocks and minerals, methods of data correction and an assessment of data quality at the NERC Isotope Geosciences Laboratory. NIGL Report Series, 78, 26 pp.

Kempton, P.D., Casey, J.F., 1997. Petrology and geochemistry of crosscutting diabase dikes, sites 920 and 921. Proc. Ocean Drill. Progr., Sci. Res. 153, 363–377.

Kerr, A.C., Marriner, G.F., Arndt, N.T., Tarney, J., Nivia, A., Saunders, A.D., Duncan, R.A., 1996a. The petrogenesis of Gorgona komatiites, picrites and basalts: new field, petrographic and geochemical constraints. Lithos 37, 245–260.

Kerr, A.C., Tarney, J., Marriner, G.F., Klaver, G.T., Saunders, A.D., Thirlwall, M.F., 1996b. The geochemistry and petrogenesis of the late-Cretaceous picrites and basalts of Curaçao, Netherlands Antilles: a remnant of an oceanic plateau. Contrib. Mineral. Petrol. 124, 29–43.

Kerr, A.C., Tarney, J., Marriner, G.F., Nivia, A., Saunders, A.D., Klaver, G.T., 1996c. The geochemistry and tectonic setting of late Cretaceous Caribbean and Colombian volcanism. J. South Am. Earth Sci. 9, 111–120.

Kerr, A.C., Marriner, G.F., Tarney, J., Nivia, A., Saunders, A.D., Thirlwall, M.F., Sinton, C.W., 1997a. Cretaceous basaltic terranes in Western Colombia: elemental, chronological and Sr–Nd isotopic constraints on petrogenesis. J. Petrol. 38, 677–702.

Kerr, A.C., Tarney, J., Marriner, G.F., Nivia, A., Saunders, A.D., 1997b. The Caribbean–Colombian Cretaceous igneous province: the internal anatomy of an oceanic plateau. In: Mahoney, J.J., Coffin, M. (Eds.), Large Igneous Provinces: Continental, Oceanic, and Planetary Flood Volcanism. AGU Geophys. Monogr. 100, 123–144.

Klaver, G.T., 1987. The Curaçao Lava Formation: an ophiolitic analogue of the anomalous thick layer 2B of the mid-Cretaceous oceanic plateaus in the western Pacific and central Caribbean. PhD thesis, University of Amsterdam. GUA Papers of Geology, 27, 168 pp.

Kusky, T.M., 1989. Accretion of the Archean Slave Province. Geology 17, 63–67.

Kusky, T.M., Kidd, W.S.F., 1992. Remnants of an Archean oceanic plateau Belingwe greenstone belt, Zimbabwe. Geology 20, 43–46.

Ladd, J.W., Holcombe, T.L., Westbrook, G.K., Edgar, N.T., 1990. Caribbean marine geology; Active margins of the plate boundary. In: Dengo, G., Case, J.E. (Eds.), The Caribbean region. The Geology of North America: Vol. H. Geological Society of America, Boulder, CO, pp. 261–290.

Lapierre, H., Dupuis, V., de Lepinay, B.M., Tardy, M., Ruiz, J., Maury, R.C., Hernandez, J., Loubet, M., 1997. Is the lower Duarte igneous complex (Hispaniola) a remnant of the Caribbean plume-generated oceanic plateau?. J. Geol. 105, 111–120.

Ludden, J., Gelinas, L., Trudel, P., 1982. Archean metavolcanics from the Rouyn-Noranda district, Abitibi greenstone belt, Quebec: 2. Mobility of trace elements and petrogenetic constraints. Can. J. Earth Sci. 19, 2276–2287.

MacDonald, W.D., 1968. Communication in: Status of geological research in the Caribbean, University of Puerto Rico 14, 40-1.

Mahoney, J.J., Storey, M., Duncan, R.A., Spencer, K.J., Pringle, M., 1993. Geochemistry and geochronology of Leg 130 basement lavas: nature and origin of the Ontong Java Plateau. Proc. Ocean Drill. Progr., Sci. Res. 130, 3–22.

Mann, P., Schubert., C., Burke, K., 1990. Review of Caribbean neotectonics. In: Dengo, G., Case, J.E. (Eds.), The Caribbean region. The Geology of North America: Vol. H. Geol. Soc. Am., Boulder, CO, pp. 307–338.

Marsh, B.D., Gunnarsson, B., Congdon, R., Carmody, R., 1991. Hawaiian basalt and Icelandic rhyolite: indicators of differentiation and partial melting. Geol. Rundsch. 80, 481–510.

Martin, H., 1987. Petrogenesis of Archean trondhjemites, tonalites,

and granodiori
ment geochem
McCulloch, M.T.,
Earth's contin
constraints. Ge
Millward, D., Ma
tholeiitic volc
Colombia. J. C
Monen, H.P., 197
Unpubl. M.Sc.
Nivia, A., 1996.
Colombia: the
Sci. 9, 59–68.
Olson, P., 1994. M
M.P. (Ed.), Ma
O'Nions, R.K., G
acid and basi
elements in la
Lett. 19, 397–
Óskarsson, N., S
dynamic mod
petrology of Ic
Palmáson, G., 19
application to
Tulcholke, B.E
Geology of Nc
CO, pp. 87–9
Pindell, J.L., 199
Caribbean evo
Mesozoic and
Mexico and
exploration. C
Palaeontologis
Research Con
251–274.
Pindell, J.L., Ba
Caribbean regi
Case, J.E. (E
North Americ
405–432.
Priem, H.N.A., E
Verdurmen, E
for episodic in
of Aruba, Net
Priem, H.N.A., E
1986. On the
batholith on A
borderland). G
Rapp, R.P., Wats
amphibolite/e
hjemites and t
Rollinson, H.R., F
the Scourian c
J. (Eds.), Evo
Grade Terrain
Royse, K.R., Kem
for the analy

Taylor, S.R., McLennan, S.M., 1985. The Continental Crust: Its Composition and Evolution. Blackwell, Oxford, 312 pp.

Tejada, M.L.G., Mahoney, J.J., Duncan, R.A., Hawkins, M.P., 1996. Age and geochemistry of basement and alkali rocks of Malaita and Santa Isabel, Solomon Islands, southern margin of Ontong Java Plateau. J. Petrol. 37, 361–394.

Thy, P., Beard, J.S., Lofgren, G.E., 1990. Experimental constraints on the origin of Icelandic rhyolites. J. Geol. 98, 417–421.

Todt, W., Cliff, R.A., Hanser, A., Hofmann, A.W., 1993. Recalibration of NBS lead standards using a $^{202}Pb+^{205}Pb$ double spike. Terra Abstracts 5, 396.

Westermann, J.H., 1932. The geology of Aruba. PhD thesis, University of Utrecht.

White, R.S., McKenzie, D.P., 1989. Magmatism at rift zones: the generation of volcanic continental margins and flood basalts. J. Geophys. Res. 94, 7685–7729.

White, R.S., Spence, G.D., Fowler, S.R., McKenzie, D.P., Westbrook, G.K., Bowen, A.N., 1987. magmatism at rifted continental margins. Nature 330, 439–444.

Winther, K.T., 1996. An experimentally based model for the origin of tonalitic and trondhjemitic melts. Chem. Geol. 127, 43–59.

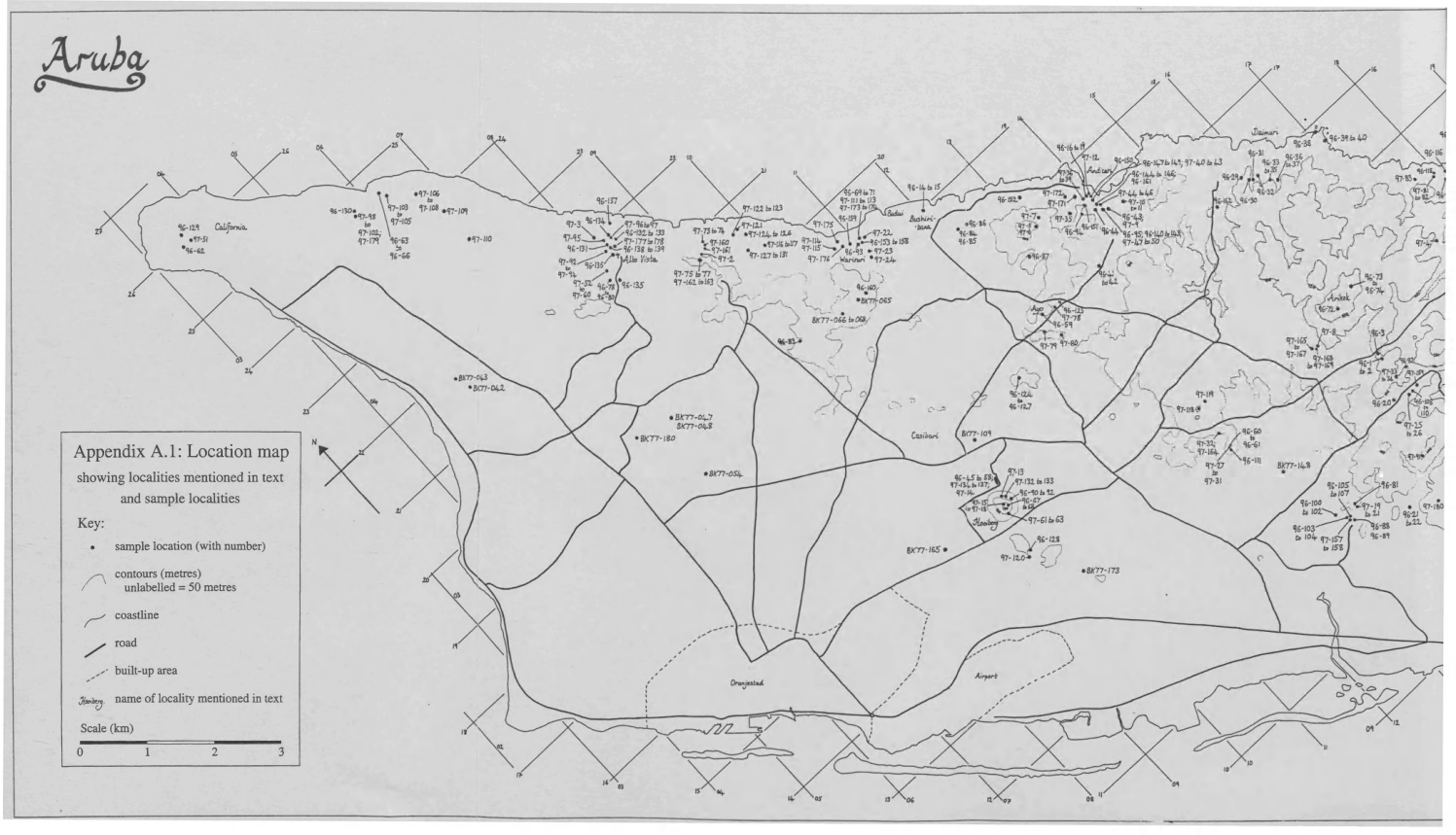
Aruba
Appendix A.1: Location map
showing localities mentioned in text and sample localities
Key:
sample location (with number)
contours (metres) unlabelled = 50 metres
coastline
road
built-up area
Hooiberg
name of locality mentioned in text
Scale (km)
0 1 2 3
N
California
Alto Vista
Savaneta
Bushiri-bana
Warawarabana
Tanki Leendert
Oranjestad
Airport
Hooiberg
Casibari
Ayo
Arikok
BK77-063
BK77-062
BK77-047
BK77-048
BK77-180
BK77-054
BK77-066 to 068
BK77-085
BK77-109
BK77-165
BK77-173
BK77-148

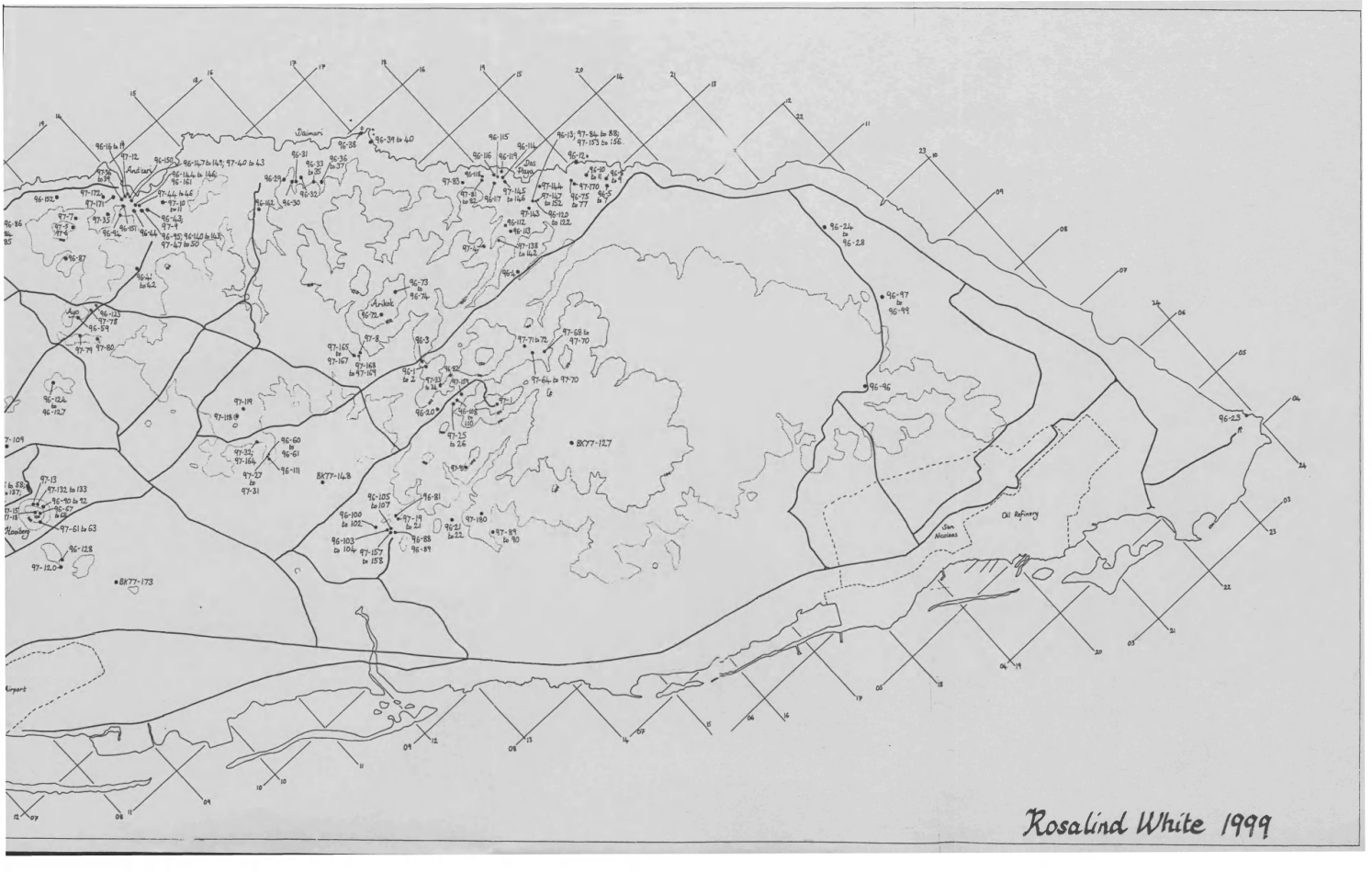
Jusari
Andoas
Arbolc
Oil Refinery
San Nicolas
BK77-12.7
BK77-14.8
BK77-173
Rosalind White 1999